

**EMEP/MSC-E Technical Report  
for Arctic Monitoring and Assessment Programme  
(AMAP)  
2002**

***Assessment of long-range transport of Hg, PCBs  
and  $\gamma$ -HCH to the Russian North***

S. Dutchak, M. Fedyunin, A. Gusev, I. Ilyin, A. Malanichev, E. Mantseva,  
Yu. Resnyansky, V. Shatalov, B. Strukov, O. Travnikov, M. Varygina,  
N. Vulykh, A. Zelenko

## SUMMARY

This report presents the results of the work fulfilled by Meteorological Synthesizing Centre East of EMEP (EMEP/MSCE-E) as a part (Activity 3) of the GEF project "Persistent Toxic Substances (PTS), Food Security and Indigenous Peoples of the Russian North". The study has been carried out under the Contract with Arctic Monitoring and Assessment Programme (AMAP) and with financial support of World Meteorological Organisation (WMO) and voluntary contribution of Co-operative Programme for Monitoring and Evaluation of the Long-Range Transmission of Air Pollutants in Europe (EMEP).

The main objective of the Activity 3 of the GEF project is to provide the assessment of long-range atmospheric transport and depositions of mercury (Hg), selected polychlorinated biphenyls (PCBs), and lindane ( $\gamma$ -HCH) to five administrative units of the Russian part of the Arctic region:

- Murmansk Oblast (Kola Peninsula)
- Nenets Autonomous Okrug (Lower part of the Pechora basin)
- Yamalo-Nenets Autonomous Okrug and Taimyr Autonomous Okrug (Taimyr Peninsula)
- Chukotka Autonomous Okrug (Chukchi Peninsula)
- Sakha Republic (Lower basin of Lena River)

According to the Contract the fulfilment of this work was divided into three stages.

***The first stage*** was aimed at the preparation of relevant meteorological information and the development and verification of atmospheric transport module for the hemispheric scale models. A special System of Diagnosis of lower Atmosphere (SDA) for generation of meteorological information for the Northern Hemisphere was elaborated. Testing the atmospheric transport module has shown that it can adequately simulate pollutant transport in the atmosphere and does not produce significant numerical errors and distortions.

***The second stage*** was devoted to the preparation of input data on emissions, geophysical data, physical-chemical properties of Hg and selected POPs and the development of hemispheric multi-compartment transport models. To provide the models with geophysical data different sources of information were considered and analyzed. These data include information on land cover, leaf area index, organic carbon content in soil, ozone, sulphur dioxide, and chemical reactant concentrations in the atmosphere.

The development of Hg and POP hemispheric models (MSCE-Hg-Hem and MSCE-POP) were carried out step by step using the modular approach. It was started with the development of atmospheric transport module common for the series of HM and POP models. Additional modules necessary for modeling mercury and selected POPs on the hemispheric scale have been also developed. The hemispheric mercury model was supplied with the module describing chemical transformations of mercury in the atmosphere. This module was elaborated using the experience of ongoing Hg model intercomparison study performed under EMEP. The hemispheric POP model was supplied with

modules describing the distribution of POPs within soil, vegetation, and seawater compartments. The model description of POP fate in the seawater compartment takes into account POP transport with sea currents, POP partitioning in seawater and the influence of ice cover dynamics in the Arctic. POP fate within soil, seawater and vegetation compartment has not been adequately explored and requires further investigations.

***The third stage*** was focused on the assessment of pollution of five selected regions of the Russian North by Hg, PCBs and  $\gamma$ -HCH from distant sources using the developed models and collected input data. This assessment includes the evaluation of concentration and deposition levels of these contaminants and contributions of main emission sources within the Russian Federation and the Northern Hemisphere to the selected areas and the Arctic as a whole. Main pathways of pollutants in question are considered.

## ***Hg***

The assessment for Hg is based on the modeling results of its long-range transport in the Northern Hemisphere. Particular attention is paid to the effect of Mercury Depletion Events (MDE) on the Arctic pollution. Satisfactory agreement of modeling results with available measurements verifies reasonable reliability of the model. Concentration levels of mercury in the ambient air and deposition fields are evaluated for all the selected regions of the Russian North. Seasonal variation of the pollution is considered. Main contributors to the contamination of the regions are determined and prevailing pathways of mercury transport are discussed.

## ***PCBs***

For the assessment of concentration and deposition levels of PCBs for the studied areas and contributions of major emission sources of the Russian Federation and other distant sources of the Northern Hemisphere several PCB congeners were selected for modeling: PCB-28, PCB-118, PCB-153, and PCB-180. These congeners make it possible to evaluate peculiarities of environmental behaviour of individual PCB congeners caused by differences in their properties between light and heavy congeners. Verification of computed concentrations and deposition fluxes against the measurements made in the Arctic and European regions is demonstrated. Detailed description of pollution levels and their seasonal variations and contributions from various emission sources to the contamination of the Russian Arctic is presented. Pathways of PCB atmospheric transport are analyzed.

## ***$\gamma$ -HCH***

Model results on levels of  $\gamma$ -HCH air concentrations in and depositions to the Russian North regions originated from emission sources of Europe and the Northern Hemisphere are presented.  $\gamma$ -HCH modeling was based on available official information and expert estimates of  $\gamma$ -HCH emissions and its usage in different regions of the Northern Hemisphere. Seasonal variations of pollution levels and contributions to depositions and air concentrations of  $\gamma$ -HCH from different source groups are estimated. Pathways of  $\gamma$ -HCH atmospheric transport are analyzed.

Detailed description of input data preparation, model development and modeling results obtained in the framework of this study are presented in this Technical Report.

## Acknowledgments

The authors deeply appreciate national experts and outer contributors who supplied the required information and data:

**Dr. Malcolm Ko** from *Atmospheric Chemistry and Dynamics Group of Atmospheric and Environmental Research (USA)* for the global data on ozone and sulfur dioxide content in the atmosphere;

**Dr. Krish Vijayaraghavan** from *Atmospheric and Environmental Research (USA)* for the global data on radical concentrations in the atmosphere;

**Prof. Ivan Holoubek** from *RECETOX – TOCOEN and Associates (Czech Republik)* for fruitful discussions, joint interpretation of observations, measurement data put at our disposal for model validation.

**Prof. Henning Rodhe** from *Department of Meteorology of Stockholm University (Sweden)* for the global data on sulfur dioxide content in the atmosphere;

**Dr. Dorota Colber** from *Institute of Marine and Coastal Sciences at Rutgers the State University of New Jersey (USA)* for the global data on the ocean primary productivity;

**Dr. Knut Breivik** from *Norwegian Institute for Air Research (Norway)* for the global data on PCB emissions;

**Prof. Kevin Jones** from *Lancaster University (UK)* for fruitful discussions and measurement data used for model validation;

**Dr. Janusz Pudykiewicz** from *Meteorological Service of Canada* for exchanging views on POP transport model development and supplied data on  $\gamma$ -HCH emissions.

**Dr. Alexey Konoplev** from *Center for Environmental Chemistry of SPA Typhoon (Russia)* for the measurement data on mercury air concentration at monitoring station Amderma;

**Dr. Franz Slemr** from *Max-Planck-Institut für Chemie (Germany)* for the measurement data on mercury concentration over the Atlantic;

We are also very much obliged to **Prof. Jozef Pacyna** from *Norwegian Institute for Air Research (Norway)* for the efficient co-operation, his reviewing and comments of the first version of the report.

Besides, the authors are very grateful to **Dr. Rulf Ebinghaus** from *Institute of Physical and Chemical Analysis of GKSS Research Center (Germany)* and **Dr. Christian Seigneur** from *Atmospheric and Environmental Research (USA)* for general informative support.

Finally, we are sincerely thankful to all **MSC-E team** and especially to **Dr. Alexey Ryaboshapko**, **Mrs. Olga Afinogenova** for the valuable remarks, **Mrs. Larissa Zayavlina** for editing the manuscript as well as to **Ms. Irina Strizhkina**, **Ms. Olga Rozovskaja** and **Mrs. Svetlana Yevdokimova** for its preparing and publishing.

## CONTENTS

<i>Introduction</i>		5
<i>Chapter 1.</i>	SELECTED REGIONS OF THE RUSSIAN ARCTIC AND FACTORS AFFECTING THEIR POLLUTION	9
1.1.	Atmospheric circulation in the Arctic region	10
1.2.	The circulation of water and sea ice in the Arctic Ocean	13
<i>Chapter 2.</i>	PHYSICAL-CHEMICAL PROPERTIES OF MERCURY AND SELECTED POPs	19
2.1.	Physical-chemical properties of mercury	19
2.2.	Physical-chemical properties of selected POPs	30
<i>Chapter 3.</i>	MODEL APPROACHES AND INPUT DATA	49
3.1.	Short review of modeling approaches used to the assessment of pollution by Hg, PCBs and HCHs on global/hemispheric scale	49
3.2.	MSCE-Hg-Hem model	52
3.3.	MSCE-POP model	64
3.4.	Meteorological data	81
3.5.	Land cover data	82
3.6.	Leaf Area Index (LAI)	83
3.7.	Chemical reactants data	83
3.8.	Data on sea currents	86
3.9.	Data on sea ice cover	89
<i>Chapter 4.</i>	EMISSION SOURCES	95
4.1.	Hg emissions	96
4.2.	PCB emissions	101
4.3.	$\gamma$ -HCH emissions	106
<i>Chapter 5.</i>	ATMOSPHERIC TRANSPORT AND DEPOSITION OF MERCURY TO THE ARCTIC REGION	113
5.1.	General description of modeling results	113
5.2.	Comparison of modeling results with measurements	117
5.3.	Arctic region	119
5.4.	Regions of the Russian North	121
5.5.	Concluding remarks	132
<i>Chapter 6.</i>	ATMOSPHERIC TRANSPORT AND DEPOSITION OF PCBs TO THE ARCTIC REGION	135
6.1.	General description of modeling results	136
6.2.	Comparison of modeling results with measurements	142
6.3.	Concentration and deposition levels in the Russian North	146
6.4.	Source-receptor relationships	150
6.5.	Congener composition analysis	157
6.6.	Evaluation of deposition of total PCB mixture to the Russian North	159
6.7.	Concluding remarks	161

<i>Chapter</i>	7.	ATMOSPHERIC TRANSPORT AND DEPOSITION OF $\gamma$ -HCH TO THE ARCTIC REGION	163
	7.1.	General description of modeling results	163
	7.2.	Comparison of modeling results with measurements	170
	7.3.	Concentration and deposition levels in regions-receptors	173
	7.4.	Source-receptor relationships	178
	7.5.	Concluding remarks	185
<i>Chapter</i>	8.	RELIABILITY OF THE ASSESSMENT RESULTS	187
	8.1.	Model verification and sensitivity analysis	187
	8.2.	Uncertainty of emission data	189
	8.3.	Modeling results vs. measurements	190
	8.4.	Concluding remarks	191
<i>Conclusions</i>			193
<i>Annex</i>	A.	MODELING RESULTS OF TRANSPORT OF PCB-28, 118 AND 180	197
<i>Annex</i>	B.	ATMOSPHERIC TRANSPORT MODULE VERIFICATION	207
<i>Annex</i>	C.	METEOROLOGICAL DATA FOR HEMISPHERIC MODELS	215
<i>Annex</i>	D.	SENSITIVITY ANALYSIS OF THE SOIL MODULE	223
<i>Annex</i>	E.	SENSITIVITY ANALYSIS OF THE OCEANIC TRANSPORT MODULE	231
<i>Annex</i>	F.	ADDITIONAL COMPUTATION EXPERIMENTS	257

## INTRODUCTION

Arctic ecosystems are very sensitive to anthropogenic impact. The contamination in the Arctic region to a considerable extent is connected with pollutants emitted from sources located far away from it. Peculiar conditions such as geographical position, low temperatures, sharply defined seasonal variations of solar radiation influence the contamination in various components of Arctic ecosystems.

According to recent investigations of the Arctic contamination the most serious impact on human health in this region inflict mercury and some POPs, in particular PCBs, dioxins and organochlorines similar to dioxins [AMAP, 2002a]. As it is reflected in a number of documents there is a public concern that indigenous population of the Arctic is among the most exposed to persistent toxic substances on the Earth [AMAP, 1998].

Persistent toxic substances are globally dispersed. Due to their physical-chemical properties they are resistant to degradation, highly volatile and capable to be accumulated in environmental compartments and in biological chains. The contamination of the Arctic region occurs through different ways. An essential role plays airborne transport of contamination from industrial regions as well as, local sources and the riverine runoff and transport by sea currents. In comparison with other natural compartments the atmosphere is one of the main pathways of contamination transport to the Arctic from remote regions of the globe.

Emission sources of the Northern Hemisphere make the most contribution to the pollution of the Arctic domain. Due to the character of atmospheric circulation in the Northern Hemisphere emission sources located in Europe and Asia play a dominating role in the contamination of the Arctic.

The main objective of this work is the assessment of the long-range atmospheric transport of Hg, selected PCBs, and  $\gamma$ -HCH to the five northern regions of the Russian Federation (administrative units): Murmansk Oblast, the Nenets Autonomous Okrug, the Yamalo-Nenets Autonomous Okrug and the Taimyr (Dolgano-Nenets) Autonomous Okrug, Sakha Republic (Yakutia), and the Chukotka Autonomous Okrug.

Physical-chemical properties of Hg and POPs and spatial distribution of emission sources require that evaluation of the long-range airborne transport to the Arctic region are made on hemispheric/global scale with the use of multi-compartment approach. To meet these requirements appropriate modeling tools should be elaborated. Modeling should provide estimates of the major pollution pathways, contamination levels in main environmental compartments and source-receptor relationships.

Extensive efforts were made for preparation of the input data for modeling. These data involved meteorological and geophysical information, physical-chemical properties of the selected substances and their emissions.

As the first step a set of meteorological information for the Northern Hemisphere was prepared. For this purpose a special System of Diagnosis of lower Atmosphere (SDA) was elaborated. The system provides meteorological information for the Northern Hemisphere on the basis of the objective analysis of meteorological fields. Using the SDA system meteorological input data for modeling were generated.

Geophysical data consist of information on land cover, leaf area index, organic carbon content in soil, ozone, sulphur dioxide, and chemical reactant concentrations in the atmosphere. These data were collected from different sources and redistributed over the model grid system.

Available emission data including both official information and expert estimates were collected and processed. Global emission inventory of Hg for 1995 [Pacyna and Pacyna, 2002] was provided by the AMAP Secretariat in the framework of this project. Estimates of Hg emissions from natural sources was performed by EMEP/MSC-E. The global emission inventory for 1930-2000 of PCB congeners was taken from [Breivik *et al.*, 2002].  $\gamma$ -HCH emission data were prepared on the basis of available official information, expert estimates and information on its use in different regions of the Northern Hemisphere.

Physical-chemical properties of Hg, selected PCBs (PCB-28, PCB-118, PCB-153, PCB-180), and  $\gamma$ -HCH were reviewed and analyzed and the model parameterization of main processes of POP behaviour in various compartments was prepared.

Model development was started from the elaboration of the atmospheric transport module for the Northern Hemisphere. This module was extensively tested and the results showed that it could adequately simulate pollutant transport in the atmosphere and did not produce significant numerical errors or distortions. For the description of peculiarities of the mentioned pollutants behaviour in different environmental compartments additional modules (for soil, seawater, vegetation) were worked out.

The hemispheric Hg model was supplied with the module describing chemical transformations of mercury in the atmosphere. This module was elaborated using the experience of ongoing Hg model intercomparison study performed under EMEP. For the hemispheric POP model additional modules describing the distribution of POPs within soil, vegetation, and seawater were elaborated. The model description of POP fate in the seawater compartment takes into account POP transport with sea currents, POP partitioning in seawater and the influence of ice cover dynamics in the Arctic. It is believed that the inclusion of these processes is of importance for proper description of POP fate on the hemispheric scale and in particularly in the Arctic region. The present level of understanding the processes taking place in soil, seawater, and vegetation compartments is insufficient and further investigations are needed.

Special attention is paid to the verification of models and their results. The analysis of sensitivity of model output to variations of different model parameters was made. The developed models participate in the model intercomparison studies, demonstrating reasonable results. Provisional modeling results of Hg and POP transport within the Northern Hemisphere and to individual regions were discussed at various workshops and conferences [Ryaboshapko *et al.*, 2002; AMAP, 2002b] and considered by the Steering Body to EMEP [EB.AIR/GE.1/2002/2].

In accordance with the objective of the project the assessment of pollution of the five selected regions of the Russian North by Hg, selected PCBs and  $\gamma$ -HCH from Russian emission sources and from sources of the whole Northern Hemisphere was made. The assessment includes the evaluation of concentration and deposition levels, their seasonal variations and source-receptor relationship for selected areas and the Arctic as a whole. Main pathways of Hg, PCBs and  $\gamma$ -HCH from remote sources to the Arctic were evaluated. Particular attention was given to the fate of these contaminants in different environmental compartments. The effect of Mercury Depletion Events (MDE) on the Arctic pollution was considered. For POPs the transport with sea currents and the effect of ice cover dynamics in the Arctic region were taken into account.

All the results, obtained in the framework of this study, including input data preparation, model development and testing, model outputs are described in this Technical Report. The report is organized in nine chapters and four annexes. Brief outline of its contents is given below.

The first chapter is devoted to a brief description of selected regions of the Russian North from the point of their view of their geographical location and climate conditions affecting the long-range transport of the pollutants under consideration. Along with the main features of air masses and seawater circulation, ice cover dynamics in the Arctic region are discussed.

The second chapter is focused on physical-chemical properties of Hg, PCBs and  $\gamma$ -HCH. Basic properties of the considered pollutants which define their behaviour in various environmental media including partitioning between the gaseous, aqueous and particle phase, removal processes and chemical degradation reactions are discussed. Besides the model description of Mercury Depletion Events (MDE) is also presented.

Chapter 3 is devoted to the model description including processes and parameterization defining the transport and behaviour of persistent toxic substances in the environment. A short review of different modeling approaches to the investigation of the global or hemispheric pollution by toxic substances is given.

Information on emissions of Hg, PCBs,  $\gamma$ -HCH used for modeling in this study and selection of main groups of sources is described in Chapter 4.

Next three Chapters (5, 6, and 7) comprise the main results of the assessment of pollution of the Russian Arctic by Hg, selected PCB congeners, and  $\gamma$ -HCH. Brief description of modeling results for the Northern Hemisphere and the Arctic region is added. General features of the Arctic pollution by these contaminants are outlined. The main attention is concentrated on the selected regions of the Russian North. Levels of concentrations in the ambient air and deposition fields along with their seasonal variations are given. Main contributors to the contamination of the regions are determined and prevailing pathways of the long-range transport are considered.

Chapter 8 is focused on model verification and uncertainties.

Main conclusions are summarized in the end of the Technical Report.

Additional information and modeling results are presented in a number of annexes. Annex A describes supplementary modeling results for PCB-28, PCB-118, and PCB-180. Annex B – atmospheric transport module, Annex C - input data for hemispheric models, Annexes D, E, F – model sensitivity analysis.

For readers convenience the basic outcome of this study is generalized in the Executive Summary issued separately.

## References

- AMAP Assessment Report [1998] Arctic Pollution Issues, Arctic Monitoring and Assessment Programme, Oslo, pp.192.
- AMAP[2002a] Arctic Pollution 2002.
- AMAP Report [2002b]:2. The Second AMAP International Symposium on Environmental Pollution of the Arctic: Extended Abstract. Rovaniemi, Finland. October 1-4, 2002.
- Breivik K., Sweetman A., Pacyna J.M., Jones K. [2002] Towards a global historical emission inventory for selected PCB congeners – a mass balance approach. 2. Emissions. *The Science of the Total Environment*, v.290, pp.199-224.
- Pacyna E.G. and J. M.Pacyna [2002] Global emission of mercury from anthropogenic sources in 1995. *WASP* 137(1), pp.149-165.
- Ryaboshapko A., R.Bullock, R.Ebinghaus, I.Ilyin, K.Lohman, J.Munthe, G.Petersen, C.Seigneur and I.Wängberg [2002] Comparison of mercury chemistry models. *Atmospheric Environment*, v.36 (24) pp.3881-3898.

## Chapter 1

## 1. SELECTED REGIONS OF THE RUSSIAN ARCTIC AND FACTORS AFFECTING THEIR POLLUTION

According to the project objectives this study is focused on the pollution evaluation of selected regions of the Russian North. This territory occupies rather large part of the Russian Federation extended as far as about 11 000 km from Norwegian border on the western edge to the Mys Dezhneva (East Cape) on the eastern one. It includes Murmansk Oblast, Nenets Autonomous Okrug, Yamalo-

Nenets and Taimyr Autonomous Okrugs, Sakha Republic (Yakutia), Chukotka Autonomous Okrug (Fig. 1.1). The model evaluation of the Russian North contamination was based on this administrative division.

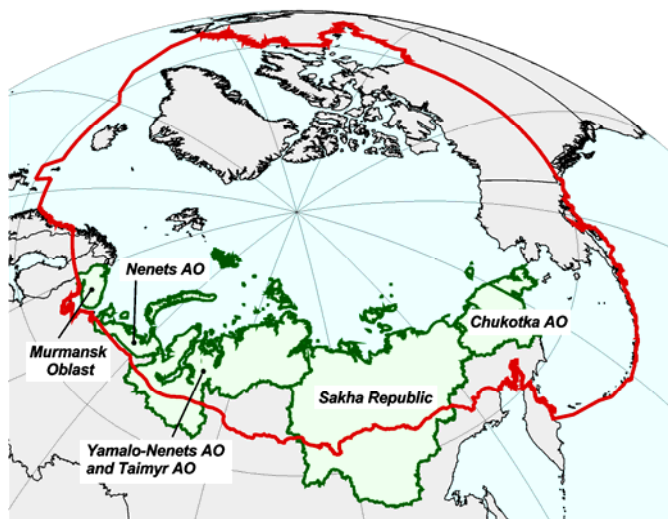


**Figure 1.1** Area of the Russian North (red line bounds the Arctic region) [AMAP, 1998]

The territory of *Murmansk Oblast* being part of the Kola Peninsula occupies about 145 thousand km<sup>2</sup>. The major part of indigenous population of Murmansk Oblast belongs to Saami group living in Lovozero and Kola districts of the eastern part of the Kola Peninsula.

*Nenets Autonomous Okrug* (Nenets AO) occupies around 177 thousand km<sup>2</sup>. It includes the lower basin of the Pechora and Indiga Rivers. The major part of its territory is tundra and forest tundra. Most of indigenous people living in this Okrug belong to Nenets.

The territory of *Yamalo-Nenets Autonomous Okrug* (Yamalo-Nenets AO) is about 750 thousand km<sup>2</sup> including the Yamal Peninsula and lower basin of the Ob River. Indigenous population of the Okrug is mostly represented by Nenets, Khanty and Yukagir. As for Nenets AO the major part of its territory is tundra and forest tundra. *Taimyr Autonomous Okrug* (Taimyr AO) territory is about 862 thousand km<sup>2</sup>. It includes the Taimyr Peninsula, lower basin of the Yenisey and Khatanga Rivers. Forests with a minor part of tundra mostly cover its area. Indigenous people living in this Okrug are Dolgan, Nenets, Nganasan, Evenk, and Enets. In computations Yamalo-Nenets AO and Taimyr AO were considered as one region.

The territory of *Sakha Republic* is about 3.1 million km<sup>2</sup>. Its Arctic area is mostly covered by tundra and forest tundra. The indigenous population of the Republic is comprised of Yakut, Even, Evenk, Yukagir, and Chukchi.

*Chukotka Autonomous Okrug* (Chukotka AO) territory is about 738 thousand km<sup>2</sup>. This Okrug is situated at the most north-eastern part of Eurasian continent. The area of this Okrug is mostly covered by tundra and forests. The indigenous population is represented by Chukchi, Eskimo (Yupik), Even, Chuvan, and Koryak.

The climate of the Russian Arctic regions is characterized by lack of solar radiation in wintertime, which leads to very low temperatures. In contrast to winter, in summer solar radiation flux is significant, but temperatures are not high because most of incoming solar energy is spent for snow or ice melting. Atmospheric circulation is characterized by cyclonic activity in all seasons, which conditions the exchange of air masses between middle and high latitudes. The western part of the Russian Arctic undergoes milder effect of the Atlantic to the highest extent in comparison with central and eastern parts because of prevailing western atmospheric flows. It is the warmest part of the Arctic and the temperature range between winter and summer is much lower than that in the eastern part of Russian North. The eastern part of the Russian North is characterized by the most severe climatic conditions.

The delivery of contaminants to the selected regions of the Russian Arctic and the Arctic as a whole depends on many factors: the atmospheric circulation, oceanic currents, ice coverage dynamic, riverine runoff to the Arctic waters, physical-geographical conditions of this region, location of emission sources, their intensity, physical-chemical properties of pollutants etc. In this section we briefly outline circulation of air masses, sea currents and ice cover dynamics in the Arctic region. More detailed analysis of processes which affect the pollution of the Arctic is given in [AMAP, 1998].

## 1.1. Atmospheric circulation in the Arctic region

The atmospheric circulation in the Arctic region is essentially different for cold and warm season. The prevailing atmospheric currents in the lower Arctic troposphere depend on the location of the following quasi-stationary baric systems in the Northern Hemisphere: Icelandic and Aleutian Low and Siberian and North American High.

In winter due to the geographical position of these systems the air parcels come to the Arctic from Europe in the northeast direction and from central Asia and Siberia (Fig. 1.2.a). The prevailing transport of air masses from the regions of North America is in the zonal direction over the North Atlantic. Thus air masses from North American continent come to the region of Scandinavia, Iceland and the Norwegian Sea and then – to the Arctic. Western regions of the Russian North (Murmansk Oblast, Nenets AO) are characterized mainly by south-western or western atmospheric flows, bringing air masses from Eastern and Central Europe as well as from central Russia. In the central regions (Yamalo-Nenets and Taimyr AO, Sakha Republic) flows with southern component prevails, thus transporting air masses from Central Russia, the Urals, South of Siberia, Central and Eastern Asia. Over easternmost region (Chukotka AO) northern flows predominate during winter.

In summer due to more uniform surface warming in comparison with the winter period the temperature gradient and consequently pressure between the pole and the equator is lower (Fig. 1.2.b). Therefore the atmospheric circulation in the Arctic is less intensive than during winter. During this period the continental high pressure systems disappear and oceanic low pressure systems weaken. Over the Arctic Ocean the high-pressure systems take place more often than in winter, defining outflow of the Arctic air in the sub-meridional direction. European region is under the impact of Azores anticyclone. Over central Eurasia and the central part of North America low-pressure systems dominate. The inflow of air masses to the Arctic mainly takes place from the Bering Sea, Aleutian Island and from the North Atlantic along the northwestern periphery of Azores anticyclone. In contrast to winter, the main peculiarity of atmospheric transport in summer over all regions of the Russian Arctic, except for Chukotka has more often the northern component. Chukotka, in its turn, is characterized by predominant transport either from the Pacific Ocean or from Eastern Asia and Russian Far East. However, the northern transport also takes place.

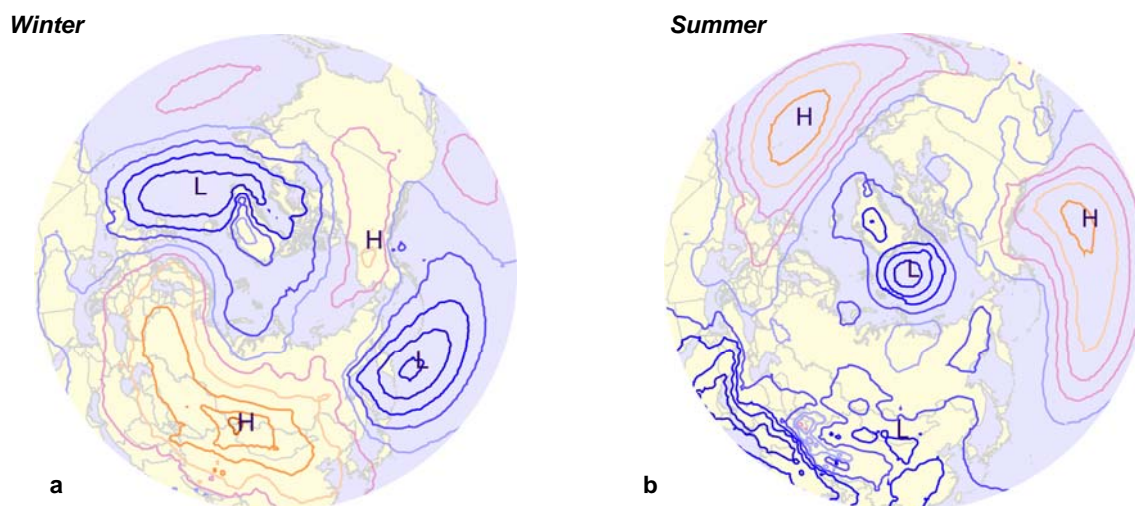


**Figure 1.2.** Location of main baric systems in the Arctic region for winter (a) and summer (b) period of 1996 based on the reanalysis data [Kalnay et al., 1996]

It is significant to note that these general features of the Arctic circulation are based on seasonal averaging. For this reason these flow directions are only most probable. Baric systems and consequently the transport direction at each specific moment can be essentially different from those estimated by averaging. It is also important to note that on the local level wind directions also can differ from prevailing directions since they can be distorted under the impact of relief, breeze circulation and other local peculiarities.

The atmospheric circulation is also responsible for precipitation pattern in the Russian Arctic. The most abundant annual precipitation take place in the western part of the Arctic and can reach 500-600 mm. From the westernmost part of the Arctic towards the east annual precipitation amount decreases. On the North of Sakha Republic precipitation are mainly within 100-150 mm. In the easternmost part of the Russian Arctic precipitation are relatively high (300 - 600 mm), which is caused by important southern transport of air masses from the Pacific Ocean, especially during summer season.

Analysis of prevailing wind directions in this or that geographical region can be made by two basic approaches – the analysis of trajectories of air particles or by typing of synoptic situations. Since in the literature comparatively little attention is given to the “climatology” of trajectories in the Russian North, the analysis of the main transport directions is based on typing of synoptic processes in the Arctic suggested by L.A. Dydina [1982].

The atmospheric circulation in the considered regions (the Kola, Yamal and Taimyr Peninsulas, Yakutia and the Chukotka Peninsula) first is characterized for the winter period and then for the summer.

In winter over the region of the Kola Peninsula cyclonic activity dominates. The prevailing direction of transport has the southern component – southwestern, southern, and southeastern. It implies that air parcels come from the northern part of Russia and from Europe. In some cases western and northwestern airflows take place, and air masses come from the Northern Atlantic and the Norwegian Sea. Under these transport patterns air masses from North America continent can reach the Kola Peninsula.

Over the Yamal Peninsula in winter cyclonic activity predominates. The prevailing transport direction has a distinct southern component. Air masses come mainly from southern and southwestern regions

of Russia and from Kazakhstan. Under certain conditions air masses reach the Yamal Peninsula from the northern part of Europe - from the Kola Peninsula, St.-Petersburg region and Scandinavia. In relatively rare cases air masses can come from the north or southeast.

Typical wintertime air mass transport to the Taimyr Peninsula occurs from the south or southwest of Russia (the southern Urals, the Caspian region, south of West-Siberian lowland) and from Kazakhstan. However, transport from the west is also possible, and some contribution of northern regions of Russia such as St.-Petersburg region and the Kola Peninsula to pollution levels over the Taimyr Peninsula is also expected.

Yakutia in winter is influenced by Siberian anticyclone. Therefore, air masses should arrive to this region mainly from the south. In some cases, and especially in the northern part of the region, the transport from the west or northwest can take place.

The Chukotka Peninsula is affected by eastern periphery of Siberian anticyclone, which conditions northern and northeastern winds for the most part of winter. Main transport directions of air masses are from Canadian Arctic Archipelago, from the Arctic Ocean and from Alaska. In some cases the northeastern fluxes arise under the impact of Canadian anticyclone. The western peripheries of cyclones over the Chukotka and Bering Seas also condition the northern and northwestern directions of winds. Penetration of cyclones from the Sea of Okhotsk to the Bering Sea can cause transport from the south, but these situations are relatively rare for wintertime.

In summer the Barents Sea and the Kola Peninsula are characterized by cyclonic activity conditioning winds in the southern and southwestern direction. Therefore the atmospheric transport from central regions of Russia as well as from Eastern Europe is expected. Another typical situation is transport of air from the northwest. In this case air masses arrive from the northern Atlantic and Scandinavia.

Atmospheric transport patterns for the Yamal Peninsula in summer time, in contrast to winter, have more probable northern direction, when air masses penetrate to the peninsula from the Arctic Ocean. However, airflows from the south, southwest and even southeast bringing air from industrial regions of Russia are also possible.

Similar to the Yamal Peninsula, typical atmospheric transport patterns to the Taimyr Peninsula in summer are characterized either by southern or by northern flows. Airflows containing the southern component can bring air masses from the Caspian region, south of West Siberia, from the southern Urals and from Kazakhstan. More probable northern currents provide inflow of air from the Arctic Ocean.

Over Yakutia in summer the transport from the north or northwest dominates. However, under certain conditions the transport of air masses from the south or southwest can take place.

Over the Chukotka Peninsula in summer time transport both from the north or northeast (the Chukotka Sea) and from the south (the Sea of Okhotsk, the Bering Sea, the Pacific Ocean) are typical. It also happens that Okhotsk cyclones are intruded to the peninsula forming southern and southwestern air fluxes. Eastern fluxes, accompanied by the outflow of moist warm air, are formed when over Siberia low pressure system is located and over the Bering, Chukotka and East Siberian Seas high pressure dominates [Zimich, 1998].

This brief analysis of atmospheric transport patterns allows us to conclude, that for the western part of the Russian Arctic the transport of air masses from southern or central parts of Russia as well as Europe is more typical. In the eastern part of the Arctic the transport from southern Russia or from the Arctic Ocean is most probable.

## 1.2. The circulation of water and sea ice in the Arctic Ocean

### Basic features of water circulation in the Arctic Ocean

The first detailed description of water circulation in the North-European basin was given in [Nansen, 1909; Helland-Hansen and Nansen, 1909]. The pattern presented by these authors has not been changed in its essential features but it was refined and complemented during the years, which followed in [Metcalf, 1960; Aagaard and Coachman, 1968; Treshnikov and Baranov, 1972; Nikiforov and Shpaikher, 1980].

According to modern conception basic elements of the horizontal circulation in the Arctic Ocean are as follows:

- Polar drift from Bering strait via the pole to the Fram strait;
- Extensive anticyclonic circulation in Amerasian Arctic sub-basin (Beaufort gyre);
- East-Greenland current; according to [Aagaard and Coachman, 1968] the overall transport of this current comprises about 30 Sv (Sverdrups, 1 Sv =  $10^6$  m<sup>3</sup>/s), i.e. approximately half the Gulfstream ;
- West-Iceland and East-Iceland currents;
- Norwegian current (it is an extension of the Atlantic warm water flow through Faeroe-Shetland strait; northwards it divides into two branches: North Cape current and Spitsbergen current.);
- North Cape current (directed eastward along the Kola Peninsula northern shore);
- Spitsbergen current (directed northward along western Spitsbergen coast);
- The system of cyclonic currents of the North-European basin (the Norwegian and Greenland Seas).

Due to sharp vertical stratification the overall motion pattern is sufficiently more complicated than the horizontal water motion outlined above. In the structure of water masses there are several layers differing in their thermohaline properties and, as a consequence, in the circulation structure. On account of limited direct measurements the three-dimensional circulation scheme can be reproduced only in a crude way. However the key features of schemes constructed by different authors have much in common. As an example Figure 1.3 demonstrates the block scheme of three-dimensional circulation in the Arctic basin after [Nikiforov et al., 1966]

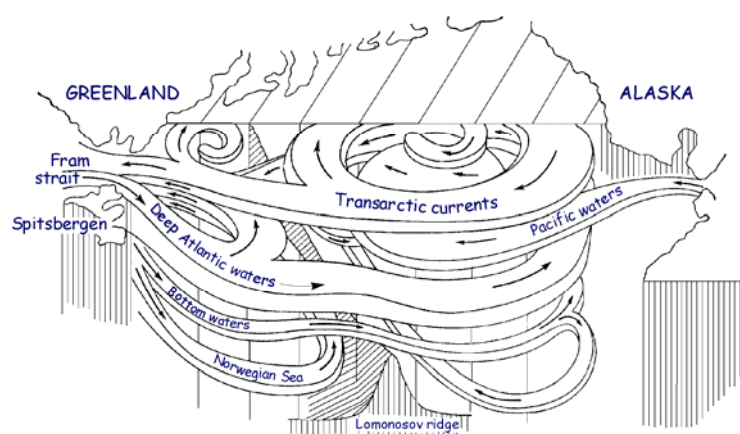


**Figure 1.3.** Block scheme of circulation in the Arctic basin after [Nikiforov et al., 1966]

Three main layers differing in water masses properties stand out in the Arctic basin along the vertical: the Arctic surface water, the Atlantic water and Deep water. The Arctic surface water includes the layer of water (30-50 m) with relatively low salinity and temperature close to freezing point as well as the underlying halocline (50-

200m). The formation of this water mass is determined by the "excess" of fresh water budget due to continental runoff. About 10% of the global runoff enters the Arctic Ocean whereas the ocean's area is only 5%, and its volume – 1.5%. The elements of the horizontal circulation listed above are referred primarily to the Arctic surface water.

Strong density stratification in the halocline prevents from the development of deep convection like that observed to the south of Greenland, which is the source of deep-water formation. Sharp stratification essentially decreases the heat exchange rate between the upper layer and the underlying layers of relatively warm Atlantic water but at the same time it restrains the vertical redistribution of contaminants coming into the surface water from the atmosphere or with runoff.

The Atlantic water mass of the Arctic basin, as it follows from the name, comes into the Arctic basin from the Atlantic Ocean initially as a surface inflow – the extension of Norwegian current, West Spitsbergen current and then submerges under the Arctic surface water. Several places where the surface flow submerges to deeper layers are known. One of them indicated on the majority of three-dimensional circulation schemes is located to the west of Spitsbergen Island.

The water exchange between the Arctic basin and the Atlantic Ocean amounts in general to the fact that Arctic cold currents carrying enormous ice masses enter the Atlantic Ocean, and from the Atlantic warm water with high salinity flows into the Arctic Ocean as submerged flow. Thus the Arctic basin is a source of water with reduced salinity relative to the North-European basin, and the Arctic Ocean as a whole – relative to the North Atlantic. It happens for two reasons – owing to permanent ice outflow to the indicated regions and due to tremendous "excess" of fresh water budget resulted from the continental runoff.

The Pacific Ocean is another source of water inflow to the Arctic Basin through the Bering Strait. The mean inflow transport is about 0.8 Sv (1 Sv =  $10^6$  m<sup>3</sup>/s.) [Coachman and Aagaard, 1988]. This average transport is superimposed by seasonal and interannual variations with amplitude of an order 1 Sv and 0.2 Sv respectively. According to [Coachman, 1993] they can reach 3 Sv to the north and 5 Sv to the south.

Evidently variations in the water transport should be directly connected with the redistribution of water contaminants.

Information about the circulation in the layer of the Atlantic waters flowing in the sub-surface layer (at depths from 200 to 900 m) is rather limited. It is deemed that the large-scale circulation is mainly counter-clockwise i.e. opposite to the general circulation of the surface water.

The Arctic deep water has two varieties: Deep water of Canadian basin and Deep water of Eurasian basin. Lomonosov ridge at depth of about 1500 m is the distinguish line between them. Water exchange with neighboring basins occurs only through the Fram strait. Its depth reaches 2600 m whereas in other places of the boundary contour (the Bering strait, straits of Canadian Archipelago, the Barents Sea) depths are essentially smaller.

In addition to the direct contaminants transport with currents there are also mechanisms of vertical mixing: turbulent mixing of convection-wind origin in the upper ocean layer, which is in action everywhere, and deep convection observed only over comparatively small regions in the Greenland, Norwegian and Labrador Seas. Deep convection is the principal source of deep water formation, which is unique for the Northern Hemisphere (in the northern latitudes of the Pacific there are no such processes). Features of the North Atlantic deep convection have been analyzed in detail by [Killworth, 1983]. An essential role in these processes belongs to the evolution of sea ice, which is considered in the next section.

## General information about sea ice

### *Geographical distribution*

Due to the climate conditions sea ice is concentrated predominantly in the polar regions of the World Ocean. Its mean annual area is nearly 26 ml.km<sup>2</sup>. Slightly less than half of it is accounted for the Northern Hemisphere. However, during a year the ice covered area varies drastically. The largest ice covered area in the Northern Hemisphere is observed in February-March, 15.4 ml.km<sup>2</sup>, the smallest area – in September, 8 ml.km<sup>2</sup> [Zakharov and Malinin, 2000].

Contrary to the Southern Hemisphere where sea ice forms a broad ring surrounding the Antarctic continent, in the Northern Hemisphere ice represents a compact massive covering the ocean area around the geographical pole. The central part of this massive is made up of so called old ice i.e. two-year and multi-year ice. Along the periphery seasonal ice is located, which completely melts in summer and reaches its maximum development in February-March.

At the boundary between the Atlantic and the Pacific there are three ice tongues stretched in the meridional direction: East-Greenland, East-Canadian and the Pacific (Fig. 1.4). Along the eastern coast of North America sea ice in winter reaches 46°N and occasionally down to 42°30'N. Along Asian continent in the Pacific Ocean ice penetrates to the south down to 43°N.

General geographical features of sea ice distribution are determined, along with seasonal cycle of incoming solar energy, by the character of circulation in polar and middle latitudes. The farthest to the south ice spreads along the eastern coast of Greenland, North America and Asia where cold sea currents flow: East Greenland, Labrador and Oya-Sio. In regions, which are under the influence of warm currents, in particular, of individual branches of North-Atlantic and Kuroshio currents the ice boundary retreats to the north. As a result there is a severe asymmetry in distribution of water temperature, salinity and sea ice between the western and eastern parts of the Atlantic and the Pacific Oceans.

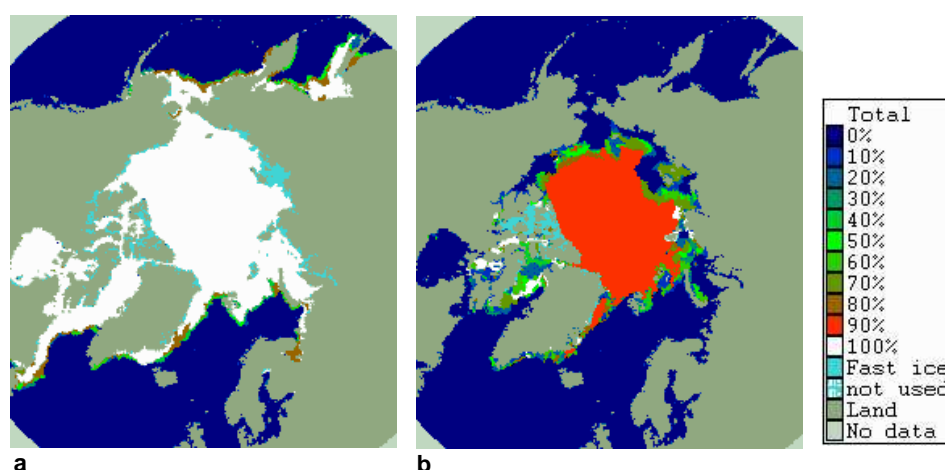


**Figure 1.4.** Sea ice compactness in the Arctic in January 1993 (a) and in August 1993 (b) from [Global Digital Sea Ice Data Bank]

Most part of ice in the Northern Hemisphere drifts under the impact of wind and sea currents. But in shallow water near coasts the ice is frequently attached to land and is motionless during long time. In March during the period of the most extensive development its area is 2 ml.km<sup>2</sup>. The fast ice is mostly developed in straits of Canadian Arctic Archipelago and in shallow water surrounding New Siberian Islands.

### ***Basic characteristics of sea ice cover***

Basic characteristics of the sea ice cover state are its compactness and thickness. Up till now information about ice thickness remained quite fragmentary due to high horizontal inhomogeneity in thickness distribution and technical difficulties in its routine observations. The modern-day pattern of ice thickness distribution in the Arctic is based primarily on data sonar measurements. The accuracy of measurements of mean ice sinking (its underwater part being 80-95% of the whole thickness) at distances of 50-100 km is 0.3-0.5 m. Generalized data on wintertime sinking of sea ice determined from measurements according to Gloersen and Campbell [Zakharov and Malinin, 2000] (an overall length of used underwater profiles is about 200 thous. km) are given in Figure 1.5.

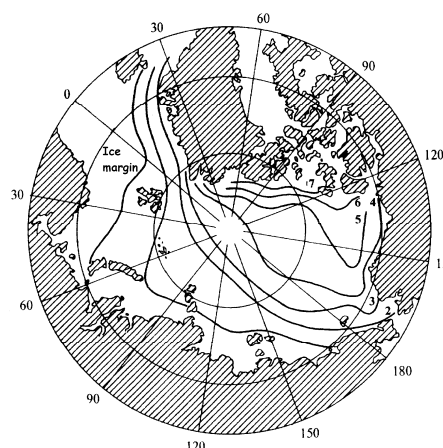


**Figure 1.5.** Mean wintertime sinking of sea ice (metres) determined from measurements according to Gloersen and Campbell [Zakharov and Malinin, 2000]

Mean annual sinking for the Arctic Ocean as a whole is 2.9 m, standard deviation 1.8 m. Mean annual sinking varies greatly depending on the region within a wide range, e.g. from 1 m in the Kara Sea and the Baffin Sea to 3.4 m in the Central Arctic and up to 4 m in the region of Canadian Arctic Archipelago. Wintertime mean values reach here 7 m. A large-scale feature of the ice thickness distribution over the Arctic Ocean is a general thickness decrease from North Greenland coast and Canadian Arctic Archipelago towards Siberian coast.

Sea ice thickness varies not only with space but over time as well e.g. seasonal variations. Every year ice melts completely over the area of about 8 ml.km<sup>2</sup>. A typical range of annual sea ice growth with subsequent melting in different regions is 0.5-2 m.

The compactness is the ratio of area covered with drifting ice to the overall area of the considered domain. It is determined by 10-ball scale according to which 0 ball means clear water and 10 balls – compact ice. The practical significance of compactness lies in the fact that it actually determines the conditions of navigation within the ice-covered areas. The scientific importance is related to the fact that it essentially governs exchange rates of substances between the atmosphere and the ocean: energy, mass and contaminants. In the Arctic basin the compactness usually rapidly increases from 1-2 balls near ice margins to 9-10 balls outside the marginal zone over the most part of the ice cover. The Arctic ice cover represents a vast area of compact ice surrounded on the outside with a narrow belt of ice with low compactness. In the Arctic Ocean seasonal compactness variations do not exceed 1.4 balls, and in the central part – 0.3 ball. Towards the margins of ice cover seasonal variations increase to 3.1 balls. This average pattern can be drastically transformed in individual years, since even in the region of the North Pole large ice-free water areas were occasionally observed.

The formation, development and decay of sea ice take place under the impact of thermodynamic (heat fluxes, phase conversions) and dynamic (ice movements under the influence of wind and sea currents) factors. This division, however, is rather conventional since, for instance, thermal state of seawater essentially depends on its dynamics. It is confirmed by the existence of vast ice-free areas in which climatic conditions are seemingly favorable for ice formation.

The analysis of present-day winter conditions in the atmosphere suggests that these conditions cannot prevent the Arctic ice cover from further expansion. Isotherm  $-2^{\circ}\text{C}$  in the atmosphere

corresponding to freezing point of seawater in some regions is as far from the ice edge as hundreds of kilometers [Zakharov and Malinin, 2000]. The climate does not prevent the sea ice cover from the development in horizontal direction. Over the entire space limited by the ice edge in the north and by air temperature isotherm  $-2^{\circ}\text{C}$  in the south. A restrictive factor in this case is the advective heat coming from the south with sea currents and compensating heat losses from the ocean surface to the atmosphere. In the central part of the Arctic basin the restrictive effect of heat advection with currents disappears since the Atlantic warm waters coming to the Arctic basin submerge under lighter freshened surface water, become overlapped by the halocline from above and sharply restrain vertical heat loss. The depth of the upper freshened layer varies from 30 to 70 m [Zakharov, 1981].

### Ice drift

Ice motion is governed by impact of wind and surface sea currents. Since the structure of surface currents, in its turn, also depends on wind impact, then large-scale features of surface water and sea ice circulation have much in common.

The first three features of large-scale water circulation listed in Section 1.1 are also distinctly expressed in the field of ice drift velocity constructed on the basis of processed data of drifting buoys (Fig. 1.6).

Ice drift velocity averaged over long time periods (about a year) can be estimated safely with the use of data on drifting stations "North Pole" (NP). The characteristic averaged velocity is 2 km/day [Zakharov, 1976], but it can reach 6.8 km/day as observed in the course of NP drift in 1937/38. This velocity may be accepted for the assessment of long-range transport of contaminants associated with the ice cover for the time intervals of about a year and more.

Another characteristic important for problems of the contaminants transport is an overall ice outflow from the Arctic basin to the North-European basin and to the Atlantic Ocean. This outflow has a pronounced seasonality with maximum in winter and minimum during summer half-year. During a year 650 thous.km<sup>2</sup> of ice come to the Greenland Sea, 420 of which fall on six winter months (November-April) and 230 – on six summer months (May-October). The mean amplitude is 530 thous.km<sup>2</sup>. The minimum ice outflow was observed in 1953/54 and comprised 390 thous.km<sup>2</sup>. The maximum outflow in 1961-62 amounted up to 920 thous.km<sup>2</sup>.

In volume units the annual ice outflow from the Arctic basin to the Atlantic and the Barents Sea through various straits is about 20000 km<sup>3</sup> [Knipovich, 1938].

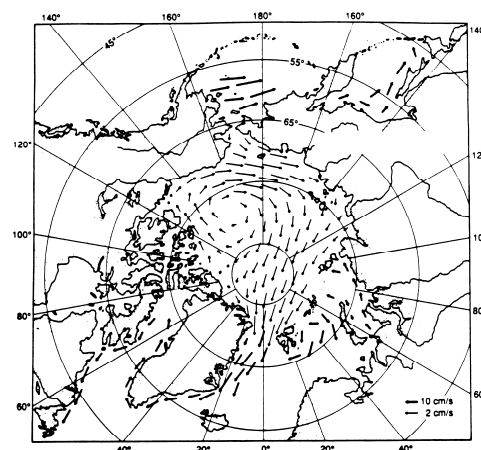


**Figure 1.6.** Mean ice drift velocity in the Arctic determined on the basis of processed data from automatic drifting buoys. The data volume is equivalent to observations of one buoy drifting during 120 years [WMO/TD-No. 127, 1987]

## References

- Aagaard K. and L.K. Coachman [1968] The East Greenland Current north of Denmark Strait. Part I. // *Arctic*, v. 21, pp. 181-200.
- Aagaard K. and L.K. Coachman [1968] The East Greenland Current north of Denmark Strait. Part II // *Arctic*, v. 21, pp. 267-290.
- AMAP Assessment Report [1998] Arctic Pollution Issues, Arctic Monitoring and Assessment Programme, Oslo.
- Calculations of three-dimensional structure of sea currents and other characteristics in the oceans of the Northern Hemisphere including the Arctic basin [2002]. Meteorological Synthesizing Centre-East. Report on scientific-research work, M, 53 p., (*in Russian*).
- Coachman L.K. [1993] On the flow field in the Chirikov Basin. *Cont. Shelf Res.*, v. 13, pp. 481-508.
- Coachman L.K. and K. Aagaard [1988] Transports through Bering Strait: Annual and inter-annual variability. *J. Geophys. Res.*, v. 93, No C12, pp. 15535-15539.
- Dydina L.A. [1982]. The peculiarities of synoptic processes development in the Arctic and their application for medium-range weather forecasts. Leningrad, Hydrometeoizdat. (*in Russian*).
- Global Digital Sea Ice Data Bank. Available at [http://www.aari.nw.ru/gdsidb/gdsidb\\_2.html](http://www.aari.nw.ru/gdsidb/gdsidb_2.html).
- Helland-Hansen B. and F. Nansen [1909] The Norwegian Sea. Rep. of Norw. Fish. Mag. Invest., v. 21, No 1, 390 p.
- Kalnay E., M.Kanamitsu, R.Kistler, W.Collins, D.Deaven, L.Gandin, M.Iredell, S.Saha, G.White, J.Woollen, Y.Zhu, Leetmaa A., Reynolds R., Chelliah M., Ebisuzaki W., Higgins W., Janowiak J., Mo K.C., Ropelewski C., Wang J., Roy Jenne, and Dennis Joseph [1996] The NCEP/NCAR 40-Year Reanalysis Project // *Bulletin of the American Meteorological Society*, 1996, vol. 77, No. 3, 437-471 p.
- Killworth P.D. [1983] Deep convection in the world ocean. *Rev. Geophys. Space Phys.*, v. 21, pp. 1-26.
- Knipovich N.M. [1938]. Hydrology of seas and brackish water (for fishing). M.-L., Pischepromizdat, 514 p. (*in Russian*).
- Metcalfe W.G. [1960] A note on water movement in the Greenland Norwegian Sea. *Deep Sea Res.*, v. 7, No 3, pp. 190-200.
- Nansen F. [1909] The oceanography of North Polar Basin. The Norw. North Polar Exped. 1893-1896 *Sci. Res.*, v. 3, No 9, 390 p.
- Nikiforov E.G. and A.O. Shpaikher [1980] Regularities of the formation of large-scale fluctuations of hydrological regime in the Arctic Ocean. L., Hydrometeoizdat, 270 p. (*in Russian*).
- Nikiforov E.G., E.B.Balyshev and N.I. Blinov [1966] On the structure of water masses in the eastern part of the Arctic basin, *Okeanologiya*, v. 6, No.1, pp.76-81, (*in Russian*).
- Scientific concept of the Arctic climate system study (ACSIS) – Report of the JSC Study Group on ACSYS [1992] WCRP-72, WMO/TD-No. v. 486, 89 p.
- Treshnikov A.F. and G.I. Baranov [1972] Circulation structure of the Arctic basin waters. L., Hydrometeoizdat, 158 p, (*in Russian*).
- WMO/TD–No.127. Report of the Second Session of the Working Group on Sea Ice and Climate (Seattle, USA, 27-31 October 1987) [1987] WMO/TD–No. 127, 97 pp.
- Zakharov V.F. [1976] Fall of temperature in the Arctic and ice cover of the Arctic seas, L., Hydrometeoizdat, 96 p. (*in Russian*).
- Zakharov V.F. [1981] Arctic ice and current natural processes, L., Hydrometeoizdat, 136 p. (*in Russian*).
- Zakharov V.F. and V.N. Malinin [2000]. Sea ice and climate. Saint-Petersburg, Hydrometeoizdat,, 92 p. (*in Russian*).
- Zimich P.I. [1998]. The atmospheric processes and the weather of the eastern Arctic. Vladivostok, Dalnauka, 256 p. (*in Russian*).

## Chapter 2

### PHYSICAL-CHEMICAL PROPERTIES OF MERCURY AND SELECTED POPs

This chapter is focused on physical-chemical properties used in the model calculations of mercury, PCB and  $\gamma$ -HCH long-range transport. The basic properties of the considered pollutants: partitioning between the gaseous, aqueous and particle phase, removal processes and chemical degradation reactions are discussed below. For all these compounds temperature dependences of some physical-chemical characteristics and degradation rate constants are given. Besides the description of Mercury Depletion Events (MDE) phenomenon is also presented.

The model parameterization for considered contaminants is based on literature data on physical-chemical properties. Some papers include the evaluation of the accuracy of physical-chemical constants. Scattering of literature values determined by experimental and computational methods can to some extent characterize uncertainty of these constants. In addition available information on standard deviations for a number of physical-chemical constants is presented in this chapter.

#### 2.1. Physical and chemical properties of mercury

Mercury undergoes numerous physical and chemical transformations in the atmosphere. Understanding and adequate reproduction of properties of mercury and its compounds is a very important condition of realistic simulation. Continuously growing knowledge of mercury behaviour in the atmosphere and modern investigations appearing in the scientific literature constrain us to revise or even substantially modify the model parameterization.

##### 2.1.1. Mercury forms in the atmosphere

Mercury appears in the atmosphere both in the elemental form and in the form of various chemical compounds. Since properties of the compounds significantly differ from each other and from elemental mercury, it is very important to define the variety of the most important mercury species transported in the atmosphere.

First and the prevailing mercury species is elemental mercury ( $Hg^0$ ). Due to its physical properties (temperature dependence of saturated vapour pressure) elemental mercury occurs in the atmosphere under the realistic conditions solely in the form of vapour. Even at the absolute temperature minimum over the Earth surface (the Antarctic, Siberia) partial pressure of mercury vapour is several times lower than the pressure of saturated vapour [Fursov, 1983; Lindqvist *et al.*, 1991].

Besides, atmospheric mercury occurs in the form of different compounds – inorganic and organic. Inorganic compounds include, first of all, mercury chloride ( $HgCl_2$ ) and mercury hydrate ( $Hg(OH)_2$ ). The composition of gaseous inorganic mercury compounds has not been adequately investigated yet [Ebinghaus *et al.*, 1999b].

Organic mercury is represented in the atmosphere mainly by compounds with one and two methyl groups. The first type of compounds include  $CH_3HgCl$ ,  $CH_3HgOH$ ,  $CH_3HgBr$  etc. and have a generalized name monomethyl mercury (MMM), the second one is  $Hg(CH_3)_2$  – dimethyl mercury (DMM).

At last, mercury in the solid phase is incorporated into the composition of aerosol particles. According to [Schroeder *et al.*, 1991], the solid phase mercury in the atmosphere can be presented by the following compounds:  $HgO$ ,  $HgS$ ,  $HgCl_2$ ,  $HgSO_4$ ,  $Hg(NO_3)_2$ .

Atmospheric transport of mercury compounds in the solid phase is mainly determined by properties of particles-carriers. One of the most important aerosol characteristics is the size distribution defining removal processes of mercury from the atmosphere. Under the conditions of continental atmosphere size distribution of particles was studied in [Milford and Davidson, 1985]. Mean aerodynamic diameter of aerosols containing mercury was found to be 0.61  $\mu m$ . G. Keeler and co-workers [Keeler *et al.*, 1995] investigated the composition and size distribution of particulate mercury in various regions of the USA. It was obtained that maximum of the distribution spectrum is shifted toward larger sizes in contaminated industrial areas, whereas it amounts to 0.68  $\mu m$  in relatively clean regions.

Another important property of particulate mercury is solubility of its compounds in cloud and precipitation water. This property is essential for mercury chemical transformations in cloud water [Ryaboshapko *et al.*, 2001]. Besides, it defines mercury availability for biota and controls thereby negative impact on the environment.

R. Ebinghaus *et al.* [1999a] assume that the insoluble part of particulate mercury in precipitation varies from 90% in contaminated regions to 10% in relatively clean ones. Another study of particulate mercury [Sakata and Marumoto, 2002] has demonstrated that only 5–50% of aerosol mercury content was leached by dilute hydrochloric acid (0.33 mol/L  $HCl$ ) in a highly contaminated urban area. Presumably, solubility of particulate mercury is even lower in neutral or sub-acid water of the cloud environment. Among mercury compounds occurring in the atmosphere bromide ( $HgBr_2$ ), iodide ( $HgI_2$ ), sulphide ( $HgS$ ) and oxide ( $HgO$ ) have the lowest solubility. According to [Brosset and Lord, 1991] 50% of mercury in rainwater is represented by insoluble compounds. This agrees with conclusions of other researchers [Fitzgerald *et al.*, 1991; Lamborg *et al.*, 1995]. Besides, C. Lamborg and co-workers point out that the portion of particulate mercury in snow is greater than in rainwater.

### 2.1.2. Physical and chemical transformations

Mercury transformations in the atmosphere include transitions between the gaseous, aqueous and solid phase, chemical reactions in the gaseous and aqueous environment. Hereafter we shall use term the “aqueous phase” for all species dissolved in cloud water and those in composition of solid particles suspended in a droplet.

#### *Inter-phase equilibrium*

All gaseous mercury compounds to this or that extent are soluble in cloud and rain droplets. Droplet sizes are small enough therefore the equilibrium between the solution and gas is established rather rapidly. As a rule, equilibrium states are described by Henry's law with allowance made for the temperature effect. The same approach can be used for the description of equilibrium between the atmospheric air and sea or lake water surface. In this section for the convenience of comparison the

water-air Henry's law constants<sup>1</sup> are given in the dimensionless form (i.e. as the ratio of concentration in the liquid to air concentration).

For the last five years no new publications have been found which could change to any extent the notion of conditions of elemental mercury equilibrium between air and water. Earlier the authors used the following temperature dependence of Henry's law constant obtained in multiple measurements of its value within the temperature range from 278K to 298K [Ryaboshapko and Korolev, 1997]:

$$H_{Hg} = 0.00984 \cdot T \exp \left[ 2800 \left( \frac{1}{T} - \frac{1}{298} \right) \right]. \quad (2.1)$$

This expression gives a value practically coinciding at 278K with that used by *W. Schroeder et al.* [1991] and by *G. Petersen et al.* [1998].

For seawater the following dependence suggested in [Wängberg et al., 1999] was used:

$$H_{Hg} = \exp(4633.3/T_w - 14.52), \quad (2.2)$$

where  $T_w$  is the seawater temperature in K.

Both expressions provide the same result at 25°C but they differ almost 2 times at 0°C. It is difficult to say whether this difference is due to the influence of seawater chemical composition.

It is assumed that the main gaseous mercury compound in the atmosphere is chloride. The most often cited values of its Henry's law constant are  $3 \cdot 10^7$  (at 298 K) and  $8.3 \cdot 10^7$  (at 283 K) [Lidqvist et al., 1984]. *J. Sommar et al.* [1999] give higher values of the constant for  $HgCl_2$  –  $4.9 \cdot 10^7$  (at 298 K) and  $3.6 \cdot 10^7$  (at 323 K). *A. Ryaboshapko et al.* [2001] roughly approximated the temperature dependence of Henry's law constant for mercury chloride in the "air-water" system by the expression:

$$H_{HgCl_2} = 1.054 \cdot 10^5 T \exp \left[ 5590 \left( \frac{1}{T} - \frac{1}{298} \right) \right]. \quad (2.3)$$

Henry's law constants of other gaseous mercury compounds and individual reactants for different values of temperature are given in Table 2.1.

As it follows from the table the major part of DMM in the "air-water" system should be in the gaseous state. The reverse relationship should be for  $CH_3HgOH$ ,  $Hg(OH)_2$  and, particularly, for  $HgO$ .

Equilibrium conditions of ozone in the "air-water" system were studied in [Sander, 1997]. In this work *R. Sander* has suggested the following expression for temperature dependence of ozone Henry's law constant:

$$H_{O_3} = 9.51 \cdot 10^{-4} T \exp \left[ 2325 \left( \frac{1}{T} - \frac{1}{298} \right) \right]. \quad (2.4)$$

Although (as it was demonstrated above) metallic mercury cannot exist in the atmosphere in the liquid or solid state its sorption by aerosol particles is possible. Quantitative characteristics of the process depend first of all on the "gas – solid matter" interface area as well as on the composition of particles.

<sup>1</sup> It should be mentioned that there are two opposite determinations of dimensional Henry's law constant in the scientific literature devoted to physical-chemical properties of mercury and POPs. Henry's law constant is traditionally expressed either as the ratio of dissolved concentration in water to gas-phase partial pressure of a chemical in the case of mercury compounds or as inverse ratio in the case of POPs. Thus for mercury we identified this value in the chapter related to physical-chemical properties as water-air Henry's law constant (H) and for POPs - as air-water Henry's law constant ( $K_H$ ).

**Table 2.1.** Henry's law constants for mercury compounds and different reactants

Compound	Henry's law constant	Temperature	Reference
$(CH_3)_2Hg$	6.7	273 K	Lindqvist and Rodhe, 1985
	3.2	298 K	
	3.2	298 K	Seigneur et al., 1994
$CH_3HgCl$	$6.25 \cdot 10^4$	288 K	Lindqvist and Rodhe, 1985
	$5.3 \cdot 10^4$	298 K	
	$5.39 \cdot 10^4$	298 K	Seigneur et al., 1994
$CH_3HgOH$	$5.9 \cdot 10^6$	288 K	Petersen, 1992
	$3.7 \cdot 10^6$	293 K	
$Hg(OH)_2$	$6.25 \cdot 10^5$	283 K	Lindqvist and Rodhe, 1985
	$3.1 \cdot 10^5$	298 K	
	$2.9 \cdot 10^5$	298 K	Seigneur et al., 1994
$HgO$	$3.2 \cdot 10^6$	?	Petersen et al., 1998
$Cl_2$	$2.7 \cdot 10^5$ *	?	Lin and Pehkonen, 1998
$\cdot OH$	600	298 K	In: [Lin and Pehkonen, 1998]
$HO_2\cdot$	$4.9 \cdot 10^4$	298 K	
$SO_2$	30	298 K	
$H_2O_2$	$1.8 \cdot 10^7$	298 K	

\* This constant was obtained on the following assumptions. Chlorine solubility in cloud drops strongly depends on pH and chloride concentration. C.-J. Lin and S. Pehkonen [1998] suggested the formula for calculations of effective Henry's law constant (mole/L/atm):

$$H_{eff} = 7.61 \cdot 10^{-2} \left( 1 + \frac{10^{-3.3}}{[Cl^-][H^+]} + \frac{10^{-10.8}}{[Cl^-][H^+]^2} \right).$$

According to data from [Baltensperger et al., 1998; Couture et al., 1998; Kimec et al., 1998; Vong et al., 1997]  $[H^+]$  and  $[Cl^-]$  concentrations in the marine atmosphere can be estimated by an order of magnitude as  $3.2 \cdot 10^{-5}$  and  $10^{-4}$  mole/L respectively. Hence it follows that effective Henry's law constant for chlorine will be equal to  $1.2 \cdot 10^4$  mole/L/atm or  $2.7 \cdot 10^5$  in the dimensionless representation.

B. Lyon et al. [1999] considered two types of particles – small (diameter 0.3  $\mu m$ ) and coarse (5.7  $\mu m$ ) and accepted that the distribution in the system is proportional to the contact surface area. The relationship of areas appeared to be equal to 93:7 respectively.

Most likely soot particles possess the highest sorption capability. C. Seigneur et al. [1998] analysed literature data published in [Krishnan et al., 1994; Livengood et al., 1995; Accurex Environmental, 1995] (cited from [Seigneur et al., 1998]) on  $Hg^0$  and  $Hg(II)$  absorption from the gaseous phase by activated charcoal and estimated redistribution coefficients  $K_{a/s}$  in the dimension "liter of air per gram of soot". The coefficient  $K_{a/s}$  was estimated to be equal to 10 L/g for  $Hg^0$  and  $3 \cdot 10^5$  L/g for  $Hg(II)$ . C. Seigneur et al. [1998] indicate that it is not clear so far whether activated charcoal and atmospheric particles have the same chemical properties. Besides the redistribution value should depend on the temperature but nothing is known about it as yet.

In the comparison of various mercury liquid-phase chemistry schemes [Ryaboshapko et al., 2001] it was demonstrated that mercury partition in the "liquid – solid matter" system considerably affects mercury accumulation in cloud and rain droplets. Above all it is defined by mercury accessibility to chemical transformations in the liquid phase and non-accessibility in the sorbed state. Soot particles contained in drops may serve as the most probable sorbent.

C. Seigneur and co-workers [Seigneur et al., 1998] also analysed data of [Thiem et al., 1976; Ma et al., 1996] (cited from [Seigneur et al., 1998]) on the absorption of  $Hg(II)$  from water by activated charcoal and estimated the redistribution coefficient  $K_{w/s}$  in the dimension "liter of water per gram of soot". For atmospheric conditions in the first approximation the coefficient is equal to 3700 L/g of  $Hg(II)$ .

Special experiments with rain water for the determination of partitioning coefficient  $K_p$  with shaking of aerosol matter in pure water and for the determination of desorption coefficient  $K_d$  showed that these coefficients are of the same order of magnitude [Seigneur *et al.*, 1998]. However,  $K_p$  varies from 100 to 600 L/g and  $K_d$  – from 200 to 1400 L/g. The experiment with adsorption of dissolved forms on sampled aerosol matter made for the determination of the adsorption coefficient  $K_a$  evidenced that  $K_a$  is lower by an order of magnitude than  $K_d$ . Most likely it is connected with the occurrence of insoluble mercury forms (oxide and sulphide) in aerosol matter. The nature of aerosol matter can drastically affect the coefficient values. Values of  $pH$  actually did not influence the investigated coefficients.

### Gas-phase reactions

In the atmosphere there is a number of chemical substances capable of oxidizing elemental mercury and its organic compounds in the gaseous phase. Photochemical processes leading to decay of molecules are also possible. The integral indicator of the significance of this or that reaction for mercury atmospheric cycle is mercury lifetime in the atmosphere relative to a given reaction. Based on this indicator it is reasonable to consider only those reactions, which make a tangible contribution to mercury atmospheric cycle. It is also important to know reaction products since their rate of scavenging from the atmosphere essentially depends on their phase state.

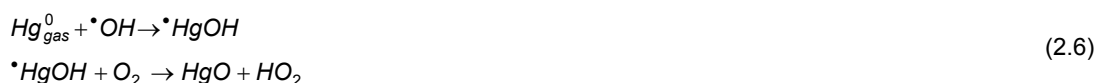
It is recognized that ozone is the most important oxidant in the gas phase. In the majority of modern models describing mercury behaviour in the atmosphere the reaction rate of oxidation by ozone suggested by *B. Hall* [1995] and equal to  $(3 \pm 2) \cdot 10^{-20}$  cm<sup>3</sup>/molec/s at 20°C is used. First of all it should be mentioned that this estimate has an essential uncertainty. *B. Hall* [1995] also investigated the temperature effect of this reaction at 22°C, 55°C and 75°C. With temperature decrease the reaction rate should decline (activation energy about 10 kJ/mole, pre-exponential multiplier  $2.1 \cdot 10^{-18}$  cm<sup>3</sup>/molec/s). With the use of these data we obtained the following temperature dependence of this reaction rate (cm<sup>3</sup>/molec/s):

$$k = 2.1 \cdot 10^{-18} \exp(-1246/T). \quad (2.5)$$

In a rough assessment mean temperature of the troposphere is 0°C, it gives the oxidation reaction rate equal to  $2.2 \cdot 10^{-20}$  cm<sup>3</sup>/molec/s. At the average concentration of ozone in the troposphere  $7.5 \cdot 10^{11}$  molec/cm<sup>3</sup> mean lifetime of elemental mercury in the troposphere relative to this reaction is about 2 years. Therefore this reaction is one of most important in the atmospheric mercury chemistry.

It is difficult to say what compound may be a product of  $Hg^0$  oxidation by ozone. Most probably the oxide is formed. *G. Petersen* and co-workers [Petersen *et al.*, 1998] consider the reaction product to be gaseous. On the contrary experts from *US EPA* [1997] suppose that actually the reaction product is immediately adsorbed by aerosol particles and then behaves itself in the atmosphere in accordance with properties of particles-carriers. We believe if mercury oxide is the product of oxidation by ozone, it cannot exist in the atmosphere as a gas due to its poor volatility [Sommar *et al.*, 2001; Schroeder and Munthe, 1998]. It should be immediately and irreversibly trapped either by particles or cloud drops.

*J. Sommar et al.* [1999; 2001] studied the reaction of elemental mercury oxidation by hydroxyl radical. The reaction can go on in two stages:



Thus, the resulting reaction can be written as follows:



with the reaction rate  $k = (8.7 \pm 2.8) \cdot 10^{-14} \text{ cm}^3/\text{molec}/\text{s}$ .

At the mean concentration of atmospheric hydroxyl  $10^6 \text{ molec}/\text{cm}^3$  the  $\text{Hg}^0$  lifetime relative to this reaction will be less than a year. Thus this reaction may be even more important than the reaction of oxidation by ozone. The high value of the  $\cdot\text{OH}$  radical oxidation rate has not been confirmed by any independent laboratory yet. Hence one should be careful operating with this high value. The temperature dependence of the reaction rate is also unknown.

The reaction of  $\text{Hg}^0$  oxidation by chlorine [Seigneur *et al.*, 1994; Tokos *et al.*, 1998] may be important for the atmosphere over the ocean:



where reaction rate  $k \leq 4 \cdot 10^{-16} \text{ cm}^3/\text{molec}/\text{s}$  at  $25^\circ\text{C}$ . B. Hall (cited from [Tokos *et al.*, 1998]) showed that the reaction rate does not depend on temperature. In the atmosphere near the oceanic water surface chlorine concentration is about  $3 \cdot 10^9 \text{ molec}/\text{cm}^3$ . Under these conditions mean lifetime of  $\text{Hg}^0$  relative to this reaction will be estimated by days. However, it should be mentioned that in the atmosphere chlorine could exist only at night, only over the ocean and only in the lowest atmospheric layer.

Gaseous hydrogen peroxide may be another oxidant of elemental mercury:



Available in the literature information about this reaction rate is contradictory. For instance, E. Constanttinou *et al.* [1995] use the rate constant up to  $4.1 \cdot 10^{-16} \text{ cm}^3/\text{molec}/\text{s}$  at  $25^\circ\text{C}$ . J.J.S. Tokos *et al.* [1998] give a considerably lower value –  $6 \cdot 10^{-19} \text{ cm}^3/\text{molec}/\text{s}$ . It is essential to note the reaction rate should strongly depend on temperature. On the base of data on activation energy (75 kJ/mole) we can suggest the following temperature dependence of the reaction rate constant ( $\text{cm}^3/\text{molec}/\text{s}$ ):

$$k = 8.4 \cdot 10^{-6} \exp(-9021/T) \quad (2.10)$$

If, as before, we take that mean temperature of the troposphere is  $0^\circ\text{C}$ , then the oxidation rate will be  $3.7 \cdot 10^{-20} \text{ cm}^3/\text{molec}/\text{s}$ . At the mean atmospheric concentration of gaseous  $\text{H}_2\text{O}_2$  equal to  $2.5 \cdot 10^{10} \text{ molec}/\text{cm}^3$  elemental mercury lifetime in the atmosphere will be about 30 years. Most likely it is the minimum value since hydrogen peroxide is a daytime oxidant [Lin and Pehkonen, 1999]. For this reason gas phase oxidation reaction of  $\text{Hg}^0$  by hydrogen peroxide can be neglected.

Mercury organic compounds, for example, DMM are sufficiently rapidly destructed in the atmosphere at the reaction with OH radical [Niki *et al.*, 1983]. The reaction product is either elemental mercury [Niki *et al.*, 1983] or MMM [Schroeder and Munthe, 1998]. The reaction rate constant is  $2 \cdot 10^{-11} \text{ cm}^3/\text{molec}/\text{s}$ . At mean radical concentration  $10^6 \text{ molec}/\text{cm}^3$  atmospheric lifetime of DMM should not exceed several hours [Lin and Pehkonen, 1999]. Besides, M. Horvat [1996] points to a possibility of photochemical destruction of DMM leading to even shorter lifetime.

Theoretically mercury reduction in the gas phase to the elemental state is not excluded. For example, photochemical destruction of molecules containing mercury can lead to the formation of  $\text{Hg}^0$  but quantitative information on such reactions is not available yet [Seigneur *et al.*, 1994].

### Aqueous-phase reactions

Schemes of aqueous-phase transformations used in modern models of mercury transport assume a simultaneous action of two mechanisms – oxidation and reduction of elemental mercury. These schemes are described in detail in the work [Ryaboshapko *et al.*, 2001]. The main oxidants may be dissolved ozone and chlorine as well as hydroxyl radical formed directly in a droplet. Sulphite complexes and hydroperoxide radical may be reducing agents. Photoreduction of some compounds is also possible. Modern ideas about aqueous-phase mercury chemistry are described in detail in the work [Lin and Pehkonen, 1999].

Many investigators studied the reaction of  $Hg^0$  oxidation by ozone in the water environment. C.-J. Lin and S. Pehkonen [1999] take the reaction rate constant equal to  $(4.7 \pm 2.2) \cdot 10^7$  (mole/L) $^{-1}$ s $^{-1}$ . In order to estimate the uncertainty of this value, Table 2.2 summarizes the rate constants used by different modellers in the chronological order. As it follows from the table the reaction rate published by J. Munthe in 1992 is used in models. The dependence of the rate on solution temperature and pH may be neglected. It may be supposed that the reaction with ozone is the basic one for elemental mercury oxidation.

**Table 2.2.** Rate constants of  $Hg^0$  oxidation by ozone in the aqueous phase

Rate constant, (mole/L) $^{-1}$ s $^{-1}$	Dependencies		Reference
	on temperature	on pH	
$(4.7 \pm 2.2) \cdot 10^7$	Independent	Independent	Munthe, 1992
$4.7 \cdot 10^7$	at 25°C	–	Seigneur <i>et al.</i> , 1994
$4.5 \cdot 10^7$	–	–	Pleijel and Munte, 1995
$4.7 \cdot 10^7$	at 25°C	–	Constantinou <i>et al.</i> , 1995
$4.5 \cdot 10^7$	–	–	Lin and Pehkonen, 1997
$4.7 \cdot 10^7$	at 5°C	–	Petersen <i>et al.</i> , 1998
$4.7 \cdot 10^7$	–	Dependent	Lin and Pehkonen, 1998
$(4.7 \pm 2.2) \cdot 10^7$	Independent * (5 - 35°C)	Independent * (5.2 - 6.2)	Lin and Pehkonen, 1999

\* Independent within the interval

$Hg^0$  oxidation by hydroxyl radical takes place only in the daytime since the radical itself is a product of photochemical reactions. C.-J. Lin and S. Pehkonen [1997] estimated that the reaction rate is equal to  $2 \cdot 10^9$  (mole/L) $^{-1}$ s $^{-1}$ . K. Gärdfeldt *et al.* [2001] suggest a very close value –  $(2.4 \pm 0.3) \cdot 10^9$  (mole/L) $^{-1}$ s $^{-1}$ .

H. Herrmann and co-workers [Herrmann *et al.*, 2000] investigated variations of hydroxyl radical concentrations in cloud water. First of all, the concentration depends on the atmosphere pollution by substances capable either to generate radicals or react with them. Besides, there is a strong dependence on a droplet size. In the daytime OH concentration variation may be roughly described by the function of square of sine.

The calculated OH concentration in water at noon is  $3.7 \cdot 10^{-15}$  mole/L. In this case the constant of pseudo-first order reaction will be  $7.4 \cdot 10^{-6}$  s $^{-1}$  [Lin and Pehkonen, 1997]. Aqueous-phase reactions of oxidation by ozone and OH radical compete: at the ozone air concentration below 4 ppb radical oxidation prevails. At concentrations more than 10 ppb the contribution of radical reaction is about 20%, and at 20 ppb – only 10%.

Under certain conditions the reaction of  $Hg^0$  oxidation by dissolved chlorine may be important. In solution chlorine may occur in two forms – hypochlorine acid (HOCl) and hypochlorite ion (OCl $^-$ ),

which relationship depends on solution  $pH$ . Oxidation by chlorine can take place mainly in the ocean atmosphere and only at night since  $Cl_2$  and  $HOCl$  are decomposed at light. Both hypochlorine acid and pyrochlorite ion can oxidize mercury [Lin and Pehkonen, 1999]:



It was considered earlier that the main agent responsible for the mercury reduction to the elemental state was sulphite ion ( $SO_3^{2-}$ ) forming unstable complexes with mercury ion [Munthe et al., 1991]. As a result of the complex decays an atom of elemental mercury comes to the aqueous phase. Photoreduction of  $Hg(OH)_2$  was indicated also as a possible reduction mechanism [Pleijel and Munthe, 1995]. During recent years radical mechanism of reduction at the reaction of mercury ion or dissolved compounds with  $HO_2$  radical was investigated [Lin and Pehkonen, 1997; 1998].

Chemistry of mercury sulphite complexes is not sufficiently studied up till now. In a general form the scheme of the sulphite mechanism at present is represented in the following way.

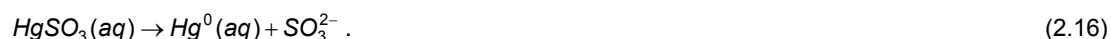
At the first step sulfur dioxide is dissolved in a water drop with the formation of three forms of 4-valent sulfur: non-dissociated  $H_2SO_3$ , bisulphite-ion ( $HSO_3^-$ ), and sulphite-ion ( $SO_3^{2-}$ ). At real  $pH$  values of cloud water within the range of 3 - 5 the bulk of  $S^{IV}$  is represented by the first two forms, although in any case concentrations of sulphite-ion trace quantities will be higher than concentrations of dissolved mercury.

Sulphite-ion can react with divalent mercury ion forming mercury sulphite. Further it combines with another sulphite-ion producing sulphite-mercury complex [Constantinou et al., 1995]:

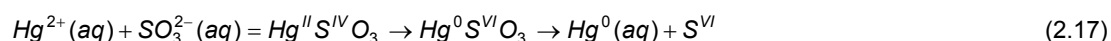


Note that G. Petersen et al. [1998] considers this pathway to be impossible on the assumption that primary the complex is formed. Then it dissociates with the formation of mercury sulphite. In any case mercury sulphite complex dominates among all other mercury compounds with four-valence sulphur [Lin and Pehkonen, 1997].

Mercury sulphite and probably sulphite-mercury complex decay and mercury is reduced to the elemental state [Constantinou et al., 1995]:



In a general form the intramolecular redox process may be represented by the following reaction chain [van Loon et al., 2000]:



Thus the availability of  $S^{IV}$  in a drop provides the action of negative feedback increasing elemental mercury concentration in a drop and preventing its additional solution from the ambient air.

G.Petersen and co-workers [Petersen et al., 1998] believe that mercury reduction process is limited by reaction of  $Hg(SO_3)_2^{2-}$  dissociation. Data on the rate of the indicated reactions are very contradictory. It is demonstrated in Table 2.3.

**Table 2.3.** Reaction rates of sulphite reduction of mercury in the aqueous phase

Reaction	Equilibrium or rate parameter	Temperature	Reference
$Hg^{2+} + SO_3^{2-} \rightarrow HgSO_3$	$5 \cdot 10^{12} M^{-1}$	25°C	Constantinou et al., 1995
$HgSO_3 + SO_3^{2-} \leftrightarrow Hg(SO_3)_2^{2-}$	$2.5 \cdot 10^{11} M^{-1}$	25°C	
$Hg(SO_3)_2^{2-} \rightarrow Hg^0$	$1 \cdot 10^{-4} s^{-1}$	25°C	
$HgSO_3 \rightarrow Hg^0 + SO_3^{2-}$	$0.6 s^{-1}$	25°C	
$Hg^{2+} + 2SO_3^{2-} \rightarrow Hg(SO_3)_2^{2-}$	$1.1 \cdot 10^{-21} ([SO_2(g)]/10^{-2pH})^2 s^{-1} *$	5°C	Petersen et al., 1998
$Hg(SO_3)_2^{2-} \rightarrow HgSO_3 + SO_3^{2-}$	$4.4 \cdot 10^{-4} s^{-1}$	5°C	
$HgSO_3 \rightarrow Hg^0$	$0.6 s^{-1}$		Munthe et al., 1991
$HgSO_3 \rightarrow Hg^0 + products$	$0.6 s^{-1}$		Lin and Pehkonen, 1999
$Hg(SO_3)_2^{2-} \rightarrow Hg^0$	0		Munthe, 1994
$Hg(HSO_3)^- \rightarrow Hg^0 + S^{VI}$	$4 \cdot 10^{-6} s^{-1}$		Munthe et al., 1991

\* Concentration of  $SO_2$  is in ppb.

While considering the importance of sulphite reduction mechanism one should take into account several things. First, if water solution has chloride, mercury ions mainly form mercury chloride [Prokofiev, 1981; Lindqvist et al., 1984; Lin and Pehkonen, 1998]. At the same time the probability of sulphite compounds formation drastically decreases. Under real atmospheric conditions the content of chloride in cloud water varies from  $2 \cdot 10^{-5}$  to  $4 \cdot 10^{-4}$  mole/L [Baltensperger et al., 1998; Couture et al., 1998; Kimec et al., 1998]. The content of chloride is particularly high in the atmosphere over the ocean – up to  $4 \cdot 10^4$  mole/L [Vong et al., 1997]. Observations in Europe under EMEP [Ilyin et al., 2001] show that chloride content in precipitation is always higher than  $2 \cdot 10^{-6}$  mole/L used in the work [Petersen et al., 1998]. The model analysis of the chemical scheme sensitivity to chloride content demonstrated that actually sulphite mechanism of reduction starts acting only when chloride concentration is lower than  $5 \cdot 10^{-6}$  mole/L [Ryaboshapko et al., 2001].

Second, sulphite in cloud water are rapidly oxidized to sulfate. According to data from [Lin and Pehkonen, 1998] in 5 hours sulphite-ion content becomes negligible and the sulphite reduction mechanism ceases to act (it is assumed that at cloud formation the bulk of sulphur dioxide is dissolved in cloud water). It is also important that at high concentrations of sulphite-ion the sufficiently stable complex  $Hg(SO_3)_2^{2-}$  (see Table 2.3) is mainly formed [Lin and Pehkonen, 1998].

Third, as it was mentioned above the probability of sulphite-ion formation is strongly dependent on solution *pH*. According to [Petersen et al., 1998] the rate of mercury-sulphite complex formation is defined by the solution acidity (see Table 2.3). Model assessments showed [Ryaboshapko et al., 2001] that sulphite reduction mechanism begins to act at *pH* more than 5.

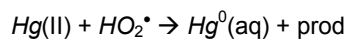
Finally, sulphite reduction rate drastically decreases with temperature decrease. According to [van Loon et al., 2000] at temperature decrease from 25°C to 0°C the rate declines more than 20 times.

C.-J. Lin and S. Pehkonen [1999] consider that in general  $SO_2$  is not important in mercury reduction since sulfur oxidation to 6-valence state goes on quickly. Ozone is the principal oxidant in the continental atmosphere both in the daytime and at night, and in the marine atmosphere – in the daytime. At night chlorine is the main oxidant in the oceanic atmosphere.

A part of oxidized mercury can be represented by hydrate. Under real conditions it can take place only at high *pH* and when chlorides are practically absent. Under the impact of solar light hydrate can

decay forming elemental mercury. Z. Xiao and co-workers [Xiao *et al.*, 1994] estimated that even at summer noon in the latitude of Stockholm this reaction is very slow ( $k = 3 \cdot 10^{-7} \text{ s}^{-1}$ ).

C.-J.Lin and S.Pehkonen [1997, 1998] found that hydroperoxide radical can be a very effective reducing agent:



According to their data the reaction rate is  $1.7 \cdot 10^4 \text{ (mole/L)}^{-1} \text{ s}^{-1}$  and typical level of  $\text{HO}_2^\bullet$  radical concentration in the liquid phase is  $1 \cdot 10^{-8} \text{ mole/L}$ . It is particularly important that this radical reacts both with free mercury ions and with molecular compounds of  $\text{HgCl}_2$  type. At the same time it is assumed that molecules of mercury compounds sorbed by particles are not accessible for this reduction mechanism. The reaction is dependent on  $\text{pH}$  but the quantitative description of this dependence is not available so far. The diurnal dynamics of the radical concentration was investigated in detail by H.Herrmann *et al.* [2000] under different external conditions. Like in the case with radical  $^\bullet\text{OH}$  in the daytime  $\text{HO}_2^\bullet$  concentration variations can be described by a function square sine. On the base of said above it seems important to include this reaction to the model calculation scheme.

It is known that the major part of cloud water does not fall out as precipitation but it is evaporated. For modeling of mercury behaviour in the atmosphere the interpretation of mercury fate after a droplet evaporation is important. The literature provides very contradictory information on this issue. Earlier it was supposed [Lindqvist *et al.*, 1991] that reactive oxidized mercury after water evaporation is reduced to the elemental form due to photo-dissociation. Only chemically persistent compounds (like  $\text{HgS}$ ) are remained in the solid state. G. Petersen *et al.* [1998] in their model assume that at drop evaporation all mercury compounds are transferred to the gaseous phase. Experts of US EPA [1997] consider that after drop evaporation an aerosol particle is formed containing in its composition all earlier dissolved and insoluble mercury compounds.

### 2.1.3. Arctic mercury depletion

Rising of mercury content in vulnerable Arctic ecosystems and increase of mercury input to human organism in the Arctic is of a particular concern [AMAP, 1998]. Only few years ago it was difficult to find any geophysical explanation of increased mercury content in the Arctic. Mercury behaviour in the atmosphere suggests that elevated  $\text{Hg}$  depositions in high latitudes are impossible. Indeed, it is commonly accepted that even if  $\text{Hg}^0$  is scavenged from the atmosphere due to dry deposition, the process can be realized only in low and middle latitudes through "soil-plant-atmosphere" interaction [US EPA, 1997].  $\text{Hg}^0$  uptake by snow cover is usually disclaimed. Oxidized gaseous and particulate  $\text{Hg}$  has restricted atmospheric lifetime, and their anthropogenic emissions in middle latitudes cannot account for noticeable contribution to total  $\text{Hg}$  deposition in the Arctic [Petersen *et al.*, 2001; Ilyin *et al.*, 2001].

However, recently discovered Mercury Depletion Events (MDE) phenomenon during springtime [Schroeder *et al.*, 1998] allows hypothesizing other ways of high  $\text{Hg}$  deposition in the Arctic (and Antarctic). The main point of the MDE consists in abrupt dropping of TGM concentration in high latitudes during springtime. The drop can be very quick (during few hours) and very deep – practically to total disappearance of elemental mercury. In a short time the TGM concentration can sharply rise to its usual values. Sometimes the period of super low  $\text{Hg}^0$  concentration can last several hours and even days [Lu *et al.*, 2001; Lindberg *et al.*, 2002; Berg *et al.*, 2001; Ebinghaus *et al.*, 2002]. Sharp droppings can repeat several times, and the total duration of the phenomenon is about 4-6 weeks.

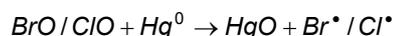
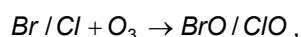
Both in the Northern and Southern Hemisphere the phenomenon can be observed only in springtime [Lu *et al.*, 2001; Ebinghaus *et al.*, 2002]. In the Northern Hemisphere it lasts from mid-March to mid-June.

Elemental mercury has relatively long atmospheric lifetime and theoretically cannot have such sharp variations [Junge, 1972]. Evidently, elemental mercury must be extremely quickly transformed into any other mercury-containing products during MDE. Most likely, they are oxidized mercury compounds presented by either gaseous oxidized forms or particulate oxidized forms. The products were experimentally determined both as reactive gaseous mercury (RGM) and  $Hg_{part}$  [Lu *et al.*, 2001; Lindberg *et al.*, 2002]. The concentration of oxidized mercury can be of the same level as usual TGM concentration (up to  $1 \text{ ng/m}^3$ ). Such concentrations are much higher than those ones, which are typically observed in the vicinity of strong anthropogenic sources.

Very probably, the phenomenon embraces only the first kilometre height of the atmospheric layer [Ebinghaus *et al.*, 2002]. This is supported by aircraft measurements of oxidation products [Schroeder *et al.*, 2001; Lindberg *et al.*, 2002]. For example, at the surface level RGM concentration was  $70 \text{ pg/m}^3$ , while at 1 km height – only  $2 \text{ pg/m}^3$  [Lindberg *et al.*, 2002]. The total gaseous mercury (TGM) concentration rises with height and achieves its ordinary values at 1 km [Schroeder *et al.*, 2001]. This height is practically coincides with the top of the boundary layer. Hence, since the oxidation process is very fast the vertical profile of oxidation products is opposite to the TGM profile.

It is commonly believed that the sunrise in the Arctic provokes quick photochemical (catalytic) oxidation of elemental mercury in reactions with Br-related radicals [Ebinghaus *et al.*, 2002]. Recently S. Lindberg *et al.* [2002] presented a possible mechanism of the Hg depletion. The mechanism suggested can be described by several consecutive:

1. Occurrence in the atmosphere sea-salt aerosol particles in the frozen form (negative air temperature is an obligatory condition)
2. Influence of UV solar radiation on concentrated on the particle surface Br/Cl compounds. The compounds can be concentrated on the surface in the process of freezing
3. Formation of halogen radicals and halogen oxide radicals as a result of autocatalytical hetherogenic reactions
4. Destruction of ozone and oxidation of elemental mercury in the following reactions:



and/or



5. Abrupt stopping step 2 when air temperature is rising above zero. Formation of a water drop instead of the frozen particle and dissolution of the salts homogeneously within the drop.

The mechanism seems to be very reasonable. However, it cannot explain an “explosion” character of the process beginning. In our opinion such a “trigger” is formation of areas of open water near seashore (or polynyas) in ice cover. In springtime ice cover becomes movable due to ice drift provoked by sea currents or wind pressure. Such alternations can be very fast – in few hours a wide area of open water can appear even at low air temperature. In this case the formation of frozen sea-salt aerosol is quite natural. S. Lindberg *et al.* [2002] showed that elevated levels of RGM accompanied very often with periods of sea-surface roughness and formation of marine aerosol.

S. Lindberg *et al.* [2002] expect that primary product of elemental mercury oxidation is RGM. Then some RGM can be converted into  $Hg_{part}$ . On the contrary, Lu *et al.* [2001] believe that RGM and  $Hg_{part}$  are formed simultaneously, and the formation of  $Hg_{part}$  is preferable. T. Berg *et al.* [2002] also observed simultaneous formation both of  $Hg_{part}$  and RGM. Lifetime of  $Hg_{part}$  and RGM even in the stable polar atmosphere is much shorter than that of  $Hg^0$ , and their deposition should lead to additional Hg pollution of the Arctic environment. Measurements of mercury concentration in snow-pack conducted in series with atmospheric observation at Barrow station (Alaska, USA) showed clearly that the depletion phenomenon is accompanied by the rise of mercury content in snow [Lindberg *et al.*, 2002]. Canadian experts provided a broad survey of mercury content in northeastern Canada and Greenland. They found that the depletion phenomenon is widespread and lead to considerable rising of mercury content in snow-pack during springtime [Lu *et al.*, 2001]. However, S.Lindberg *et al.* [2002] noted that mercury concentration in snow-pack reaches its maximum leeward from polynyas and open water areas. Besides, the concentrations drop with distance from the seashore. These facts confirm that the MDE is closely connected with seashore line.

It was noted in recent works that the depletion is connected with elevated concentrations of BrO. Satellite observations showed that both in the Arctic and the Antarctic the zones of elevated BrO concentrations have ring shape – they connected with the seashores, and they appear in spring [Steffen *et al.*, 2001; Drummond, 2001; Lu *et al.*, 2001; Ebinghaus *et al.*, 2002]. If hypothesis of BrO involvement into Hg depletion is correct, it means that not the whole Arctic is influenced by the phenomenon but only seashore zones. Most likely, that the central parts of the Arctic and Antarctic are not affected by the MDE. Nowadays it is difficult to say how far southward the phenomenon can be extended. It observed at least within the Polar Circle in the Arctic.

## 2.2. Physical-chemical properties of selected POPs

Basic differences in POP environmental behaviour result from some peculiarities of their physical-chemical properties.

The key characteristics required for modeling POP behaviour in the environment are considered below.

Saturated vapour pressure ( $p^0$ , Pa) characterizes the capability of a pure substance to be transmuted to the gaseous state (for liquid this process is called vaporization, for solid substances - sublimation). The saturated vapor pressure for subcooled liquid -  $p_L^0$  is considered in this work. The value of  $p_L^0$  depends on the air temperature and increases with increasing temperature for all considered compounds. With the help of  $p_L^0$  one can characterize the partitioning of an organic compound between its particle and gaseous phase in the atmosphere.

Partitioning of a substance between the gaseous and particle phase in the atmosphere ( $\phi$ ) is determined in accordance with the Junge-Pankow model [Junge, 1977; Pankow, 1987]. POP fraction adsorbed on particle surfaces is:

$$\phi = c\theta / (p_L^0 + c\theta), \quad (2.18)$$

where

- $c$  is the constant dependant on thermodynamic parameters of the adsorption process and on properties of aerosol particle surface ( $c = 0.17 \text{ Pa}\cdot\text{m}$  [Junge, 1977]);
- $\theta$  is the specific surface of aerosol particles,  $\text{m}^2/\text{m}^3$  ( $\theta = 1.5\cdot 10^{-4}$  for a background aerosol [Whitby, 1978]);
- $p_L^0$  is the subcooled liquid-vapour pressure, Pa.

Thus POPs with lower vapour pressure are better sorbed on atmospheric aerosol particles thereby increasing the probability of their subsequent deposition and washout with precipitation.

Air-water Henry's law constant ( $K_H$ , Pa·m<sup>3</sup>/mol) is the ratio of equilibrium partial pressure  $P_A$  of a substance in the air to its concentration in water  $C_W$  which equals the ratio of its saturated vapour pressure  $p^0$  and its solubility  $S$ , i.e. the proportion:

$$\frac{P_A}{C_W} = \frac{p^0}{S} = K_H \quad (2.19)$$

is fulfilled. Here  $K_H$  is the Henry's law constant, in this case measured in [Pa·m<sup>3</sup>/mol] on the assumption that the species concentration in water is measured in mol/m<sup>3</sup>. Expressing the saturated vapour pressure of a substance in terms of its air molar concentration using the Mendeleev-Clapeyron equation, one can represent the Henry's law constant in the dimensionless form  $K'_H$ :

$$\frac{C_A}{C_W} = K_{AW} = K'_H = \frac{K_H}{RT} \quad (2.20)$$

here  $K_{AW}$  is the dimensionless air-water partition coefficient;  
 $C_A$  is the substance concentration in air;  
 $R$  is the universal gas constant;  
 $T$  is the absolute temperature, K.

The value of the Henry's law constant is used in the description of the gaseous exchange between the atmosphere and soil, between the atmosphere and seawater, and for the determination of wet scavenging of the POP gaseous phase.

The washout ratio for the particle phase ( $W_p$ ) can be calculated by the following relationship:

$$W_p = C_p / C_{A,a} \quad (2.21)$$

where  $C_p$  is the substance concentration in precipitation in the particle phase, ng/m<sup>3</sup>;  
 $C_{A,a}$  is the substance concentration in air in the particle phase, ng/m<sup>3</sup>.

Coefficients of partitioning between different media ( $K_{OW}$ ,  $K_{OA}$  – dimensionless;  $K_{OC}$ , dm<sup>3</sup>/kg):

The octanol-water partition coefficient ( $K_{OW}$ ) is a measure of substance hydrophoby and characterizes its partitioning between water and lipid media substituted for octanol. It is determined as the ratio of equilibrium concentrations in octanol  $C_O$  (mol/l) and in water  $C_W$  (mol/l):

$$K_{OW} = C_O / C_W \quad (2.22)$$

$K_{OW}$  is used for the estimation of the partition coefficient in the organic carbon-water system ( $K_{OC}$ ), the partition coefficient in the octanol-air system ( $K_{OA}$ ), and the bioconcentration factor (BCF).

The octanol-air partition coefficient ( $K_{OA}$ ) is used for the description of a substance partitioning between air and the cuticle of plants, between the gaseous phase and the organic film of atmospheric aerosol particles, etc. In experiments this coefficient is determined by the ratio of equilibrium concentrations of a substance in octanol and air.

$$K_{OA} = C_O / C_A = K_{OW} / K_{AW} = K_{OW} \cdot RT / K_H \quad (2.23)$$

where  $C_O$  is the equilibrium concentration of a substance in octanol;  
 $C_A$  is the equilibrium concentration of a substance in air.

Additionally, this coefficient can be defined with the use of coefficients “octanol-water” and “air-water”.

The organic carbon-water partition coefficient ( $K_{OC}$ ,  $\text{dm}^3/\text{kg}$ ) is used for the description of POP sorption by soil and bottom sediments. It is determined as:

$$K_{OC} = K_P / f_{OC}, \quad (2.24)$$

where  $K_P$  is the partition coefficient equal to the ratio of POP concentration in the solid state of soil (bottom sediments) to that in the water phase;

$f_{OC}$  is the mass fraction of organic carbon in soil and bottom sediments.

Molecular diffusion coefficients ( $D_A$ ,  $D_W$ ,  $\text{cm}^2/\text{s}$ ) are used in the description of the POP air-soil exchange process. The molecular diffusion coefficient of an organic compound in air ( $D_A$ ,  $\text{cm}^2/\text{s}$ ) can be estimated by the formula [Schwarzenbach *et al.*, 1993]:

$$D_A = 10^{-3} \cdot \frac{T^{1.75} [(1/M_{air}) + (1/M)]^{1/2}}{p [\bar{V}_{air}^{1/3} + \bar{V}_m^{1/3}]^2} \quad (2.25)$$

where  $T$  is the absolute temperature, 298 K;

$M_{air}$  is the mean molecular air weight, ~29 g/mol;

$M$  is the molecular weight of an organic substance, g/mol;

$p$  is the pressure, 1 atm;

$\bar{V}_{air}$  is the mean molar gas volume in the air, ~20.1  $\text{cm}^3/\text{mol}$ ;

$\bar{V}_m$  is the molar volume of an organic substance,  $\text{cm}^3/\text{mol}$ .

For the determination of molecular diffusion coefficients for organic substances in water ( $D_W$ ,  $\text{cm}^2/\text{s}$ ), the following ratio [Schwarzenbach *et al.*, 1993] can be used:

$$D_W = \frac{13.26 \times 10^{-5}}{\mu^{1.14} \cdot (\bar{V}_m)^{0.589}} \quad (2.26)$$

where  $\mu$  is the solution viscosity in centipoise at a certain temperature, taken to be equal to water viscosity, 0.894 cps at 298K;

$\bar{V}_m$  is the mean molar volume of a substance,  $\text{cm}^3/\text{mol}$ .

For POP modeling it is necessary to know:

- temperature dependencies of physical-chemical characteristics (subcooled liquid-vapour pressure, Henry's law constant, octanol-air partition coefficient);
- data on the distribution of low volatile POPs with particle sizes in the atmosphere;
- degradation constants in environmental compartments.

The above-mentioned characteristics used for modeling PCB congeners and  $\gamma$ -HCH are described below in relevant subsections. Physical-chemical properties and the parameterizations of PCB individual congeners and  $\gamma$ -HCH used in the multi-compartment model are presented in several MSC-E reports [Pekar *et al.*, 1999, Shatalov and Malanichev, 2000, Erdman *et al.*, 2001, Shatalov *et al.*, 2001]. The analysis of physical-chemical properties of the considered POPs available in the literature as well as parameters employed by other modellers for the long-range transport evaluation allowed us to improve the model parameterization.

### 2.2.1. Polychlorinated biphenyls (PCBs)

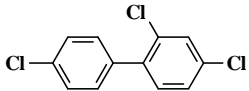
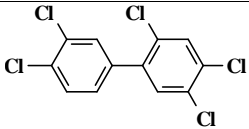
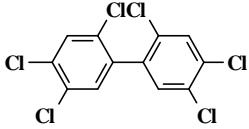
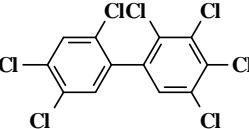
Polychlorinated biphenyls (PCBs) belong to a class of organochlorine aromatic compounds long used for industrial purposes in many countries. There are 209 PCB congeners with different physical-chemical properties and toxicity depending on the number and position of the chlorine atoms in the biphenyl molecule. According to the classification of the International Agency for Research on Cancer (IARC), PCBs belong to group 2A of probable carcinogens for man [IARC, 1987 cited from HSDB, 2002]. In addition, PCBs can affect the human reproductive system and impose toxic impacts on an embryo [Avkhimenko, 2000]. PCBs without substituents in ortho-position relative to the internuclear bond C<sub>1</sub>-C<sub>1</sub> (coplanar), as well as some PCB mono-ortho-substituted congeners, exhibit toxicity similar to that of polychlorinated dibenzo-*p*-dioxins/furans. Eleven congeners of PCBs beginning with tetra- to heptachlorinated isomers possess toxicological properties with international toxic equivalency factors from 0.00001 to 0.1 I-TEF relative to 2,3,7,8-tetrachlorodibenzo-*p*-dioxin isomer [Klyuev and Brodsky, 2000].

PCBs are typical POPs because they are persistent to external impacts. They have high thermal and photo stability and small reactive capability. Due to high lipophilicity, PCBs may be accumulated in adipose tissues of man, animals, birds and aqueous organisms. In addition, these compounds are readily sorbed on particle and soil surface. Numerous measurements demonstrate that they are omnipresent in environmental objects even in such remote regions as the Arctic [Brevik et al., 2002].

The following individual PCB congeners were selected for the evaluation of the long-range transport to the Arctic: PCB-28, 118, 153 and 180. They represent light, medium and heavy homologues of PCBs. It should be mentioned that PCB-118 possesses toxicological properties (0.0001 I-TEF). This selection was also conditioned by the fact that physical-chemical properties of these congeners are well studied and the availability of measurement data on concentrations in different natural objects allow us to verify model results.

General information on four PCB congeners is demonstrated in Table 2.4.

**Table 2.4.** Structural formulas, composition and some properties of the PCB studied

Compound	Chemical names (IUPAC)	CAS RN	Molecular formula	Molecular weight, g/mol	Structural formula
PCB-28	2,4,4'-Trichlorobiphenyl	7012-37-5	C <sub>12</sub> H <sub>7</sub> Cl <sub>3</sub>	257.5	
PCB-118	2,3',4,4',5-Pentachlorobiphenyl	31508-00-6	C <sub>12</sub> H <sub>5</sub> Cl <sub>5</sub>	326.4	
PCB-153	2,2',4,4',5,5'-Hexachlorobiphenyl	35065-27-1	C <sub>12</sub> H <sub>4</sub> Cl <sub>6</sub>	360.9	
PCB-180	2,2',3,4,4',5,5'-Heptachlorobiphenyl	035065-29-3	C <sub>12</sub> H <sub>3</sub> Cl <sub>7</sub>	395.3	

Below, physical-chemical properties of PCB congeners modeled in the AMAP project are described.

### Temperature dependence of PCB subcooled liquid-vapour pressure

The coefficients for the dependence of the subcooled liquid-vapour pressure  $p_L^0$  on the temperature in the form (2.27) for 180 PCB congeners were determined by *R.L.Falconer and T.F.Bidleman* [1994].

$$\log p_L^0 (\text{Pa}) = -A/T(K) + B. \quad (2.27)$$

These coefficients for four PCB congeners are listed in Table 2.5.

**Table 2.5.** Coefficients of the dependence of subcooled liquid-vapour pressure (Pa) on temperature for four PCB congeners [Falconer and Bidleman, 1994]

Compound	A	B
PCB-28	4075	12.20
PCB-118	4664	12.72
PCB-153	4775	12.85
PCB-180	5042	13.03

Parameters for calculating the temperature dependence of  $p_L^0$  for 32 PCB congeners were derived [Falconer and Bidleman, 1994] from previously obtained gas chromatographic data (GC). From this information the coefficients were estimated for another 148 PCBs for which vapour pressure had been reported only at a fixed temperature. According to [Falconer and Bidleman, 1994], these A values should have a similar degree of reliability as the GC results, which ranged from -16 to +18%, with a mean of +3% (percentage of literature values). The values of  $p_L^0$  (Pa) calculated by these dependences for different ambient temperatures are given in Table 2.6.

**Table 2.6.** Values of subcooled liquid-vapour pressure (Pa) at different temperatures for three PCB congeners

Compound	$P_L^0$ , Pa			
	-10°C	0°C	+10°C	+25°C
PCB-28	$5.1 \cdot 10^{-4}$	$1.9 \cdot 10^{-3}$	$6.3 \cdot 10^{-3}$	$3.4 \cdot 10^{-2}$
PCB-118	$9.7 \cdot 10^{-6}$	$4.3 \cdot 10^{-5}$	$1.7 \cdot 10^{-4}$	$1.2 \cdot 10^{-3}$
PCB-153	$4.9 \cdot 10^{-6}$	$2.3 \cdot 10^{-5}$	$9.5 \cdot 10^{-5}$	$6.7 \cdot 10^{-4}$
PCB-180	$7.2 \cdot 10^{-7}$	$3.6 \cdot 10^{-6}$	$1.6 \cdot 10^{-5}$	$1.3 \cdot 10^{-4}$

As evident from Table 2.6, for all the congeners  $p_L^0$  values increase with temperature rise, resulting in a reduction of their adsorption on particles (see Eq. (2.18)).

### Henry's law constant dependence on temperature for PCBs

The Henry's law constant is a key parameter in model calculations of the long-range transport. The temperature dependence of Henry's law constant can be expressed by Eq. (2.28):

$$\log K_H = \log K_{H298} + \frac{\Delta H_{AW}}{2.303R} \left( \frac{1}{T_0} - \frac{1}{T} \right), \quad (2.28)$$

where  $K_{H298}$  is the Henry's law constant (Pa·m<sup>3</sup>/mol) at 25°C (298K);  
 $\Delta H_{AW}$  is the enthalpy of volatilization from water, kJ/mol;  
 $R$  is the universal gas constant,  $8.314 \cdot 10^{-3}$  kJ/(mol·K);  
 $T$  is the absolute temperature, K.

Measured values of  $\Delta H_{AW}$  for relevant PCB homologous groups with from three to seven chlorine atoms are summarized in the paper [Wania, 1997] and presented in Table 2.7.

**Table 2.7.** Measured values of  $\Delta H_{AW}$  for four PCB homologous groups

Homologue groups	$\Delta H_{AW}$ , kJ/mol	Reference cited from [Wania, 1997]
Trichlorobiphenyls	61.8	<i>Burkhard et al., 1985</i>
Pentachlorobiphenyls	67.2	
Hexachlorobiphenyls	69.4	
Heptachlorobiphenyls	71.3	

From Eq. (2.28) the temperature dependence of the Henry's law constant can be expressed in the form:

$$\log K_H = -A/T(K) + B, \quad (2.29)$$

where  $A = \Delta H_{AW}/2.303R$ ;

$$B = \log K_{H298} + \Delta H_{AW}/2.303R(298).$$

Values of Henry's law constant at 25°C for four PCB congeners published in [Dunnivant et al., 1992] are given in Table 2.8. Calculation of  $K_H$  (25°C) for PCBs was performed on the basis of the Quantitative Structure-Property Relationship (QSPR) model. This model agrees well with other model predictions and is capable of accurately calculating  $K_H$  for structurally similar PCB congeners. The statistical analysis of the calculated and experimental  $\log K_H$  data showed a high regression coefficient ( $r = 0.9476$ ) and a low standard error ( $s = 0.662$  or 1.9% of the mean value), which are indicative of reasonable model predictions [Dunnivant et al., 1992].

**Table 2.8.** Values of Henry's law constant at 25°C for four PCB congeners, Pa·m<sup>3</sup>/mol

Compound	$K_{H298}$ , calculated value	Reference
PCB-28	28.58	<i>Dunnivant et al., 1992</i>
PCB-118	12.56	
PCB-153	16.48	
PCB-180	10.74	

Using  $\Delta H_{AW}$  values from Table 2.7 and Henry's law constants at 25°C from Table 2.8, the coefficients of temperature dependences of Henry's law constants (2.29) were estimated and used for modeling in this work. Table 2.9 gives selected  $A$  and  $B$  values (they are given in bold) in comparison with the temperature dependence coefficients available in the literature.

**Table 2.9.** Coefficients of the temperature dependences of Henry's law constants for four PCB congeners

Compound	A					B				
	1*	2	3	4	5	1	2	3	4	5
PCB-28	2611	<b>3227</b>	3100	1821	3418	10.22	<b>12.28</b>	11.97	7.69	12.92
PCB-118		<b>3510</b>	3535	2727	3416		<b>12.88</b>	13.44	10.71	12.70
PCB-153		<b>3625</b>	3662	3577	3413		<b>13.38</b>	14.05	13.72	12.68
PCB-180		<b>3724</b>	3910	7628	3414		<b>13.53</b>	14.71	27.16	12.49

1 – ten Hulscher et al., 1992 cited from [Pekar et al., 1999]; 2 - estimated (see text) on the basis of data from [Wania, 1997 and Dunnivant et al., 1992]; 3 – [Paasivirta et al., 1999]; 4 – [Bamford et al., 2000]; 5 – estimated on the basis of data from [Wata et al., 1995].

### Temperature dependence of the octanol-air partition coefficient for PCBs

Parameters of temperature dependences of octanol-air partition coefficients for 15 PCBs were determined by T. Harner and T.F. Bidleman [1996] for the temperature range from -10°C to + 30°C in the form:

$$\log K_{OA} = A/T(K) - B. \quad (2.30)$$

It should be mentioned that for trichlorobiphenyls the experimental dependence was estimated for PCB-29 only [Harner and Bidleman, 1996]. For this reason, coefficient  $A$  of this dependence (2.30) for PCB-28 was taken to be equal to the corresponding coefficient for PCB-29 (3792). Further, using data from Table 2.5, the subcooled liquid-vapour pressure at 20°C (293 K) was calculated. Then using the regression Eq. (2.31) derived by T.Harner and T.F.Bidleman [1996], the octanol-air partition coefficient at 20°C was estimated.

$$\log K_{OA} = (-1.268) \log p_L^0 + 6.135, \quad r^2 = 0.995 \quad (2.31)$$

Coefficient  $B$  was calculated by the formula:

$$B = A/293 - \log K_{OA}^{293}, \quad (2.32)$$

where  $K_{OA}^{293}$  is the octanol-air partition coefficient at 20°C (293K).

The dependences determined experimentally and estimated are presented in Table 2.10.

The octanol-air partition coefficients at 20°C determined on the basis of these dependences are given in Table 2.11.

**Table 2.10.** Octanol-air partition coefficient dependence on temperature for three PCB congeners

Compound	A	B	Reference
PCB-28	3792	4.63	Estimate (see text)
PCB-118	4693	5.92	Harner and Bidleman, 1996
PCB-153	4695	6.02	
PCB-180	4535	4.70	

**Table 2.11.** Octanol-air partition coefficients at 20°C for four PCBs

Compound	Chlorine atom positions	$K_{OA}$
PCB-28	2,4,4'	$2.04 \times 10^8$
PCB-118	2,3',4,4',5	$(1.21 \pm 0.10) \times 10^{10}$
PCB-153	2,2',4,4',5,5'	$(1.11 \pm 0.08) \times 10^{10}$
PCB-180	2,2',3,4,4',5,5'	$(5.64 \pm 0.71) \times 10^{10}$

### PCB molecular diffusion coefficients

The molecular diffusion coefficients of PCB-153 in air and in water were estimated by Eq. (2.25) and (2.26). Diffusion coefficients of the rest of the congeners were estimated by the following formulas:

$$\frac{D_A}{D_A^{153}} \cong \left[ \frac{M^{153}}{M} \right]^{1/2} \quad (2.33)$$

$$\frac{D_W}{D_W^{153}} \cong \left[ \frac{M^{153}}{M} \right]^{1/2}, \quad (2.34)$$

where  $D_A^{153}$  and  $D_W^{153}$  are the molecular diffusion coefficients of PCB-153 in air and in water, respectively;

$D_A$  and  $D_W$  are the molecular diffusion coefficients of a given PCB congener in air and in water, respectively;

$M^{153}$  is the molecular weight of PCB-153, g/mol (see Table 2.4);

$M$  is the molecular weight of a given PCB congener (see Table 2.4).

Table 2.12 demonstrates values of molar volumes for four PCB congeners taken from [Mackay *et al.*, 1992; Ruelle and Kesselring, 1997] and molecular diffusion coefficients for air and water calculated with the use of these values. Molecular diffusion coefficients of PCBs selected for modeling in this work were estimated on the basis of molar volume presented in [Mackay *et al.*, 1992].

**Table 2.12.** Molar volumes ( $\bar{V}$ ,  $\text{cm}^3/\text{mol}$ ) and obtained values of molecular diffusion coefficients in air and water at  $25^\circ\text{C}$  of four PCB congeners ( $D_A$ ,  $D_W$ ,  $\text{m}^2/\text{s}$ )

Compound	$\bar{V}$ , $\text{cm}^3/\text{mol}$		$D_A$ , $\text{m}^2/\text{s}$	$D_W$ , $\text{m}^2/\text{s}$
	Values	References		
PCB-28	<b>247.3</b>	Mackay <i>et al.</i> , 1992	<b><math>5.42 \cdot 10^{-6}</math></b>	<b><math>6.09 \cdot 10^{-10}</math></b>
	198.7	Ruelle and Kesselring, 1997	$5.18 \cdot 10^{-6}$	$5.87 \cdot 10^{-10}$
PCB-118	<b>289.1</b>	Mackay <i>et al.</i> , 1992	<b><math>4.82 \cdot 10^{-6}</math></b>	<b><math>5.40 \cdot 10^{-10}</math></b>
	224.5	Ruelle and Kesselring, 1997	$4.81 \cdot 10^{-6}$	$5.35 \cdot 10^{-10}$
PCB-153	<b>310</b>	Mackay <i>et al.</i> , 1992	<b><math>4.58 \cdot 10^{-6}</math></b>	<b><math>5.14 \cdot 10^{-10}</math></b>
	237.4	Ruelle and Kesselring, 1997	$4.66 \cdot 10^{-6}$	$5.14 \cdot 10^{-10}$
PCB-180	<b>330.9</b>	Mackay <i>et al.</i> , 1992	<b><math>4.38 \cdot 10^{-6}</math></b>	<b><math>4.91 \cdot 10^{-10}</math></b>
	-	Ruelle and Kesselring, 1997	-	-

Values used for modeling are given in bold.

Data of Table 2.12 show that the molecular diffusion coefficients both in air and water decrease with the increase in the degree of chlorination.

### Partitioning of PCBs between the gaseous and particle phase in the atmosphere

Fractions of PCB adsorbed on particles were calculated from Eq. (2.18) [Junge, 1977; Pankow, 1987] for the background aerosol ( $\theta = 1.5 \cdot 10^{-4} \text{ m}^2/\text{m}^3$ ) and the data of Table 2.6. Obtained values  $\phi$  for different temperatures are given in Table 2.13.

**Table 2.13.** PCB fractions adsorbed on atmospheric aerosol particles at different temperatures, %

Compound	$\phi \times 100$ , %			
	$-10^\circ\text{C}$	$0^\circ\text{C}$	$10^\circ\text{C}$	$25^\circ\text{C}$
PCB-28	5	1	0.4	0.1
PCB-118	72	37	13	2
PCB-153	84	53	21	4
PCB-180	97	88	61	16

As evident from Table 2.13, fractions of PCBs bound with particles increase with the increase of the degree of chlorination. Moreover, for all congeners the extent of adsorption increases with temperature decrease.

### PCB sorption by soil and bottom sediments

PCB sorption by soils and bottom sediments is characterized quantitatively by the organic carbon-water partition coefficient ( $K_{OC}$ ,  $\text{m}^3/\text{kg}$ ).  $K_{OC}$  for PCBs were calculated with the use of the following relation:

$$K_{OC} = 0.41 K_{OW} \text{ [Karickhoff, 1981]} \quad (2.35)$$

Table 2.14 gives partition coefficients in the "octanol-water" system selected for modeling and

partition coefficients for the “organic carbon-water” system estimated with the use of these coefficients for four PCB congeners. Besides ranges of  $\log K_{OW}$  values determined by experimental and computational methods and available in literature are presented in this table.

**Table 2.14.** Partition coefficients in the “octanol-water” and “organic carbon-water” system for four PCB congeners

Compound	Range of $\log K_{OW}^*$	Selected $\log K_{OW}$	Estimated $\log K_{OC}$ , $\text{dm}^3/\text{kg}$	$K_{OC}$ , $\text{m}^3/\text{kg}$
PCB-28	5.61-5.8	5.8 [Mackay et al., 1992]	5.41	259
PCB-118	6.39-7.12	6.74 [Hawker and Connell, 1988]	6.35	2253
PCB-153	6.72-7.75	6.9 [Mackay et al., 1992]	6.51	3257
PCB-180	6.7 - 8.27	7.36 [Hawker and Connell, 1988]	6.97	9393

\* Literature data include information from the following references: [Hawker and Connell, 1988; Mackay et al., 1992; McLachlan, 1996; Hovard and Meylan, 1997; Paasivirta et al., 1999; Sahsuvar, 1999; NIST, 2002].

As seen from Table 2.14, PCBs sorption by soils and bottom sediments increases with the number of chlorine atoms in the molecule.

### PCB wet deposition

Wet deposition is an important mechanism of PCB scavenging from the atmosphere. Total dimensionless ratio  $W_T$  for a substance washout with precipitation is determined by the Eq. (2.36):

$$W_T = W_G(1 - \phi) + W_P\phi, \quad (2.36)$$

where  $W_G$  is the washout ratio of the gas phase;  
 $W_P$  is the washout ratio of a substance associated with aerosol particles;  
 $\phi$  is the substance fraction associated with aerosol particles.

Due to sufficiently high values of Henry's law constants, the efficiency of gaseous PCB washout with precipitation is relatively low. Washout ratios  $W_G$  determined as inverse values to dimensionless Henry's law constant ( $RT/K_H$ ) at 25°C are of the order of  $10^1 - 10^2$ . Washout ratios of PCB scavenging with rain ( $W_P$ ) for particle-bound PCBs are substantially higher. [Franz and Eisenreich, 1998] summarized various published data indicating that  $W_P$  for scavenging with rain is  $10^2 - 10^6$ . For model calculations of PCB-118, PCB-153 and PCB-180, a  $W_P$  mean value equal to  $1.5 \cdot 10^5$  [Sweetman and Jones, 2000] was chosen. It should be mentioned that for gaseous and particle-bound PCB-28, the empirical washout ratio is equal to  $2.1 \cdot 10^4$  [Granier and Chevreuril, 1997]. Because the usage of theoretical ratios in preliminary calculations of this PCB leads to underestimation of scavenging with rain (this can be explained, for instance, by the occurrence of organic matter in raindrops), the above experimentally determined value of the washout ratio was used.

### PCB degradation in the environment

**The atmosphere.** Data of E.S.C.Kwok et al. [1995] show that the basic mechanism of PCB degradation in the atmosphere is reaction with hydroxyl radicals and that all other mechanisms can be neglected. The degradation process in the atmosphere is described by the following reaction:

$$\frac{dC}{dt} = -k_{air} \cdot C \cdot [OH], \quad (2.37)$$

where  $C$  is the pollutant concentration in air,  $\text{ng}/\text{m}^3$ ;  
 $[OH]$  is the air concentration of hydroxyl radical,  $\text{molec}/\text{cm}^3$ ;  
 $k_{air}$  is the degradation rate constant for air,  $\text{cm}^3/(\text{molec} \cdot \text{s})$ .

The atmospheric concentration of OH-radical shows wide seasonal and diurnal variations, as its major tropospheric source is the photochemical cleavage of ozone by sunlight [Sinkkonen and Paasivirta, 2000]. In the MSCE-POP model the variability of this factor is taken into account by the assumption that the value of the mean diurnal concentration of hydroxyl radicals depends only on the season. At a latitude of 45°N, the mean diurnal OH-radical concentration at the surface layer at a depth of 2 km is  $2 \cdot 10^6$  molec/cm<sup>3</sup> in summer,  $0.8 \cdot 10^6$  molec/cm<sup>3</sup> in spring and autumn and  $0.09 \cdot 10^6$  molec/cm<sup>3</sup> in winter at mean annual concentration  $0.8 \cdot 10^6$  molec/cm<sup>3</sup> [Yu Lu and Khall, 1991].

In modeling PCB long-range transport to the Arctic, it was reasonable to introduce the temperature dependence of rate constant of the gas-phase reaction with OH-radicals. In the work [Beyer and Matthies, 2001] this dependence is described by the Arrhenius equation:

$$k_{air} = A \cdot \exp(-E_a / RT) \quad (2.38)$$

where  $A$  is the pre-exponential multiplier value, cm<sup>3</sup>/(molec·s);

$E_a$  is the activation energy of interaction with an OH-radical in air, J/mol;

$R$  is the universal gas constant, J/(mol · K);

$T$  is the ambient temperature, K.

The same approach was applied to PCB atmospheric transport evaluation in [Sahsuvar, 1999]. Values of the pre-exponential multiplier and the activation energy for individual PCB congeners taken from [Beyer and Matthies, 2001] are displayed in Table 2.15.

**Table 2.15.** Coefficients in the equation of temperature dependence of rate constant in the reaction with OH-radical (2.38) according to [Beyer and Matthies, 2001]

Compound	$A$ , cm <sup>3</sup> /(molec·s)	$E_a$ , J/mol	Reference
PCB-28	$2.70 \cdot 10^{-10}$	13720	Anderson and Hites, 1996
PCB-118	$6.15 \cdot 10^{-11}$	12920	Degradation rate constant at 25 °C estimated with AOPWIN, version 1.90 and calculated reaction energy
PCB-153	$8.12 \cdot 10^{-11}$	15380	
PCB-180	$1.40 \cdot 10^{-10}$	17840	

The activation energy value for PCB-28 was experimentally determined and presented in [Anderson and Hites, 1996] with form  $-E_a/R$  (K) =  $1650 \pm 220$ . Uncertainty in this value is based on one standard error of the slope of the temperature dependence regression. The estimated rate constant of PCB-28 in the gas-phase reaction with OH-radical at 298 K amounts to  $1.1(0.8-1.4) \times 10^{-12}$  cm<sup>3</sup> s<sup>-1</sup> (95% confidence limits) [Anderson and Hites, 1996]. For the remaining PCBs, degradation rate constants in air at 298 K were determined using the computer program AOPWIN from molecular structure information [Beyer and Matthies, 2001]. The activation energy  $E_a$  (i.e. temperature dependence of reaction rate) of these PCBs was correlated with the degree of chlorination. Although the coefficient of determination is small ( $r^2 = 0.67$ ), the slope is significantly distinct from zero [Beyer and Matthies, 2001].

**Natural waters and soils.** PCB degradation in the aqueous and soil environment has not been thoroughly investigated. No data on temperature dependence of degradation constants in these environmental compartments have been found among relevant literature. Table 2.16 demonstrates estimates of half-lives for four PCB congeners in surface water and soils presented in [Mackay et al., 1992; Wania, 1999].

**Table 2.16.** PCB half-lives in surface water and soil according to literature data

Substance	Half-life*, h (surface water)	Half-life (soils), h	
	<i>Mackay et al.</i> , 1992; <i>Wania</i> , 1999	<i>Wania</i> , 1999	<i>Mackay et al.</i> , 1992
PCB-28	17000	10 000	55 000
PCB-118	55 000	100 000	55 000
PCB-153	55 000	550 000	55 000
PCB-180	55 000	1000 000	55 000

In recent investigations of *S.Sinkkonen and J.Paasivirta* [2000] carried out for the Baltic region, there are different estimates of four PCB half-lives, taking into account the temperature factor of surface water and soils. Table 2.17 exhibits half-lives for surface waters and soils taken from [*Sinkkonen and Paasivirta*, 2000] and the corresponding degradation constant values of the considered PCB congeners in these environmental compartments. Specifically these values were used for modeling in this work.

*Thus for modeling the hemispheric transport of the selected PCB in the Arctic region, we have used the above-discussed physical-chemical properties. The parameterization is described in section 3.3 below.*

**Table 2.17.** Degradation constants for water and soil [*Sinkkonen and Paasivirta*, 2000]

Substance	$k_d^{sea}$ , s <sup>-1</sup>	Half-life*, h. Surface water	$k_d^{soil}$ , s <sup>-1</sup>	Half-life*, h. soils
PCB-28	$1.33 \cdot 10^{-7}$	1450	$7.4 \cdot 10^{-9}$	26 000
PCB-118	$3.21 \cdot 10^{-9}$	60000	$3.21 \cdot 10^{-9}$	60000
PCB-153	$1.6 \cdot 10^{-9}$	120000	$1.17 \cdot 10^{-9}$	165 000
PCB-180	$8.02 \cdot 10^{-10}$	240000	$5.83 \cdot 10^{-10}$	330 000

\* - on the average for +7 °C

### 2.2.2. $\gamma$ -Hexachlorocyclohexane ( $\gamma$ -HCH)

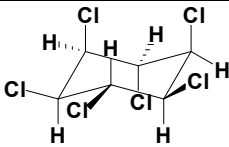
$\gamma$ -HCH is one of stereo isomers of 1,2,3,4,5,6 of hexachlorocyclohexane (HCH) referring to a group of organochlorine compounds. HCH occurs as eight stereo isomers among which  $\gamma$ -HCH possesses the highest insecticide activity.  $\gamma$ -HCH (as technical HCH or lindane) was intensively used all over the world for various purposes – for the treatment of people and animals (against ectoparasites), constructions, clothes, water (against mosquitoes), plants, forests, orchards, seeds, soil etc. [*Filov ed.*, 1990].  $\gamma$ -HCH exhibits mutagenic activity, embriotropic action and affects reproduction processes [*Izmerov ed.*, 1990]. Additionally people who have had occupational contact with this substance can develop allergies or experience other irritating effects.

$\gamma$ -HCH is one of the most volatile chemicals among organochlorine insecticides. It is poorly soluble in water but easily soluble in the majority of organic solvents. This chemical is extremely stable to temperatures up to 180°C and with acids, but in alkalis it undergoes dehydrochlorination [*HSDB*, 2002]. Once HCH isomers enter the environment, they are distributed globally and can be found in air, surface water, soil, and living organisms [*Walker et al.*, 1999]. But HCHs are much less bioaccumulative than other organochlorines because of their relatively low lipophilicity and short half-life in biota [*AMAP Assessment Report*, 1998]. HCHs are the most abundant pesticides in the Arctic

atmosphere and waters [Macdonald *et al.*, 2000]. The detectable presence of these substances in such remote regions, where lindane and technical HCH have not been used, is evidence of the long-range transport [Walker *et al.*, 1999].

Table 2.18 demonstrates general characteristics of  $\gamma$ -HCH.

**Table 2.18.**  $\gamma$ -HCH general characteristics

Compound	Chemical names (IUPAC)	CAS RN	Molecular formula	Molecular weight, g/mol	Structural formula
$\gamma$ -HCH	(1,2,4,5/3,6)-gamma stereo isomer 1,2,3,4,5,6, – hexachlorocyclohexane	58-89-9	C <sub>6</sub> H <sub>6</sub> Cl <sub>6</sub>	290.8	

$\gamma$ -HCH physical-chemical properties required for model calculations are presented below. According to predictions based on the Junge-Pankow model,  $\gamma$ -HCH was assumed to be present in the atmosphere at moderate temperatures only in the gas phase.

### Temperature dependence of $\gamma$ -HCH subcooled liquid-vapour pressure

Coefficients for the temperature dependences of  $\gamma$ -HCH subcooled liquid-vapour pressure  $p_L^0$  (2.39) available in the literature are presented in the Table 2.19.

$$\log p_L^0(\text{Pa}) = A + B/T \text{ (K)} \quad (2.39)$$

**Table 2.19.** Coefficients of  $\gamma$ -HCH subcooled liquid-vapour pressure temperature dependences

Coefficients		Notes	References
A	B		
11.15	- 3680	calculated from experimental GC data	Hinckley <i>et al.</i> , 1990
13.63	- 4416	calculated from literature data	Hinckley <i>et al.</i> , 1990
13.80	- 4330	estimated	Paasivirta <i>et al.</i> , 1999

The first temperature dependence of  $\gamma$ -HCH subcooled liquid-vapour pressure was determined by D.A.Hinckley *et al.* [1990] from experimental data using capillary gas chromatography (GC). This method provides vapour pressures within a factor of two of average literature values for nonpolar compounds. Exactly this temperature dependence was used in the MSC-E model calculations of  $\gamma$ -HCH long-range airborne transport for 1999 - 2000. Additionally it was used in [Cotham and Bidleman, 1991] for the evaluation of  $\gamma$ -HCH fluxes in the Arctic regions.

### Henry's law constant dependence on temperature for $\gamma$ -HCH

Coefficients for Henry's law constant temperature dependence for  $\gamma$ -HCH in the form (2.40) have been determined by several authors.

$$\log K_H = A + B/T \quad (2.40)$$

These coefficients are presented in Table 2.20.

**Table 2.20.** Coefficients of Henry's constant temperature dependences, Pa·m<sup>3</sup>/mol

Coefficients		Notes	References
A	B		
7.54±0.54	-2382±160	experiment, distilled water	<i>Kucklick et al.</i> , 1991
8.68±0.96	-2703±276	experiment, sea water	
11.58	-3093	estimated	<i>Paasivirta et al.</i> , 1999
9.51	-3005	experiment	<i>Jantunen and Bidleman</i> , cited from <i>Paasivirta et al.</i> , 1999
10.10	-3183	Selected for previous MSC-E modeling [ <i>Pekar et al.</i> , 1999]	<i>Jacobs and van Pul.</i> , 1996

Temperature dependence of Henry's law constant for  $\gamma$ -HCH determined experimentally by *Kucklick et al.* [1991] for distilled water and seawater was used for modeling in this work. It is necessary to mention that this temperature dependence value was also used in [*Cotham and Bidleman*, 1991] for calculating pollutant fluxes in the Arctic regions.

### $\gamma$ -HCH molecular diffusion coefficients

Molecular diffusion coefficients of  $\gamma$ -HCH were estimated from dependences (2.25) and (2.26) suggested by [*Schwarzenbach et al.*, 1993], on the basis of molar volumes taken from [*Ruelle and Kesselring*, 1997; *Mackay et al.*, 1997].  $\gamma$ -HCH molar volumes and values of molecular diffusion coefficients in air and water are given in Table 2.21.

**Table 2.21.**  $\gamma$ -HCH molar volumes and calculated molar diffusion coefficients in air and water

$V_{mol}$ , cm <sup>3</sup> /mol	Molecular diffusion coefficients, m <sup>2</sup> /s	
	Air ( $D_a$ )	Water ( $D_w$ )
179.5 [ <i>Ruelle and Kesselring</i> , 1997]	$6 \cdot 10^{-6}$	$7 \cdot 10^{-10}$
243.6 [ <i>Mackay et al.</i> , v.5, 1997]	$5 \cdot 10^{-6}$	$5.9 \cdot 10^{-10}$

Molecular diffusion coefficients of  $\gamma$ -HCH selected for modeling were estimated on the basis of molar volume presented in the work [*Ruelle and Kesselring*, 1997].

### Coefficients of partitioning $K_{OW}$ and $K_{OC}$ for $\gamma$ -HCH

Among literature at present there is a large amount of data on measured and estimated values of  $\gamma$ -HCH partitioning in the "octanol-water" and "organic carbon-water" system. According to [*Mackay et al.*, 1997], experimentally determined values of  $\log K_{OW}$  are within the range of 3.25 - 5.32 and values of  $\log K_{OC}$  – within 2.38 - 3.40. The "octanol-water" and "organic carbon-water" partition coefficients selected for modeling  $\gamma$ -HCH under this project and recommended or used by other authors are given in Table 2.22.

**Table 2.22.** Partition coefficients  $K_{OW}$  and  $K_{OC}$  for  $\gamma$ -HCH

Partition coefficient	Units	Value	Reference
$\log K_{OW}$	dimensionless	3.9	<i>Chu and Chan</i> , 2000
$\log K_{OC}$	dm <sup>3</sup> /kg	3.0	<i>Mackay et al.</i> , 1997; <i>Chu and Chan</i> , 2000

### Temperature dependence of octanol-air partition coefficient for $\gamma$ -HCH

Reasoning from the requirement of consistency in parameters  $K_{OW}$  and  $K_{OA}$ , coefficients A and B of temperature dependence for  $\gamma$ -HCH partition coefficient in an "octanol-air" system in the form of Eq. (2.30) were calculated. For this purpose, we used coefficient A of temperature dependence (2.40) of Henry's law constant for fresh water (with a reverse sign) from [Kucklick *et al.*, 1991] and reference value  $K_{OA}$  at 25°C, calculated by the formula:

$$\log K_{OA} = \log K_{OW} - \log K_H/RT \quad (2.41)$$

where  $\log K_{OW} = 3.9$  (see Table 2.22);

$\log K_H/RT$  is estimated by Eq. (2.40) taken from [Kucklick *et al.*, 1991] for 25°C.

Thus the temperature dependence of partition coefficient in the "octanol-air" system for  $\gamma$ -HCH will be of the following form:

$$\log K_{OA} = 2382/T(K) - 0.25 \quad (2.42)$$

### $\gamma$ -HCH degradation in environment

**The atmosphere.** The main process in  $\gamma$ -HCH degradation is its interaction with OH-radical. Hence, as in the case of PCBs, the degradation of this species in air will be described by second order Eq. (2.37) taking into account seasonal values of OH-radical air content at the latitude 45° N taken from [Yu Lu and Khall, 1991]. The mean seasonal [OH] concentrations used are, for winter,  $9 \cdot 10^4$  molec/cm<sup>3</sup>, for autumn and spring,  $8 \cdot 10^5$  molec/cm<sup>3</sup>, and for summer,  $2 \cdot 10^6$  molec/cm<sup>3</sup>. According to [Brubaker and Hites, 1998], the temperature dependence of rate constants of the reaction with OH-radical in air for  $\gamma$ -HCH will be of the following form:

$$k_{OH} [\text{cm}^3/(\text{molec}\cdot\text{s})] = A \exp(-Ea/RT) \quad (2.43)$$

where  $A = 6 \cdot 10^{-11} \text{ cm}^3 \text{ s}^{-1}$ ;

$Ea = 14.2 \pm 1.7 \text{ kJ/mol}$ ;

$R$  is the universal gas constant, J/(mol, K);

$T$  is the ambient temperature, K;

Thus the rate constant ( $k_{Oh}$ ) estimated [Brubaker and Hites, 1998] for 298 K ranges within  $(1.4-2.5) \times 10^{-13} \text{ cm}^3 \text{ s}^{-1}$  with a mean value equal to  $1.9 \times 10^{-13} \text{ cm}^3 \text{ s}^{-1}$ .

**Natural waters.**  $\gamma$ -HCH degrades in aqueous environments through several processes: hydrolysis, photolysis and microbial degradation. The slowest degradation takes place in ground waters; the most rapid degradation processes are biodegradation under anaerobic conditions and hydrolysis in nearly alkaline medium (pH=9) at a temperature above 20°C. In the literature there are various estimates of  $\gamma$ -HCH degradation rate constants in water for the above-mentioned processes. According to these data, half-lives of  $\gamma$ -HCH degradation in waters due to different processes vary from 3 days [Mackay *et al.*, 1997] to 1720 days [Strand and Hov, 1996].

For calculations of  $\gamma$ -HCH degradation in the aqueous environment, we selected the temperature dependence of hydrolytic decomposition of HCH isomers at different pH determined in [Ngabe *et al.*, 1993]. The rate constant for alkaline (base) hydrolysis is related to the energy of activation and absolute temperature by the Arrhenius equation:

$$\log k_b = A - E_a/(2.303RT), \quad (2.44)$$

where  $k_b$  is the second-order rate constant for the base hydrolysis of a substance in water,  $M^{-1} \cdot \text{min}^{-1}$ ;  
 $A = 15.146$  is the pre-exponential factor;  
 $E_a = 84.6 \pm 7.8$  is the energy of hydrolysis process activation, kJ/mol;  
 $R = 8.314$  is the universal gas constant, J/(mol·K);  
 $T$  is the absolute temperature, K.

According to *B.Ngabe et al.* [1993], the pseudo first-order rate constant for the hydrolysis of a substance in water depends on the activity of hydroxide ions in the solution and is connected with the second-order rate constant by the following relationship:

$$k_{DW} \cong k_b \cdot a_{OH}/60, \quad (2.45)$$

where  $k_{DW}$  is the pseudo first-order rate constant for the hydrolysis of  $\gamma$ -HCH in water,  $s^{-1}$ ;  
 $a_{OH}$  is ion activity in the solution depending on pH value and temperature.

Under conditions close to natural ones (pH=7), the half-life of  $\gamma$ -HCH in an aqueous environment due to the hydrolysis on the base of  $k_{DW}$  calculated by formulas (2.44) and (2.45) for the temperature range from 0°C to 25°C will be from 1.5 to 34 years.

**Soils.** Obviously for  $\gamma$ -HCH, as for other POPs, important factors in the soil degradation process are soil type and humus content. The current version of the MSC-E model does not operate with such details of soil-top as of yet. Therefore in this project we have selected a mean value of degradation rate constant of this substance available in the literature and used by other modellers. It is equal to  $2 \cdot 10^{-8} s^{-1}$  [*Hornsby et al.*, 1996]. The half-life of  $\gamma$ -HCH degradation in soils calculated on the basis of this rate constant amounts to 400 days. Values of  $\gamma$ -HCH half-life in soil, according to data presented in [*Mackay et al.*, 1997], vary from 3 days to 3 years.

The model parameterization is described in Section 3.3.

## References

- Accurex Environmental [1995]. Private communication to Ms. Heike Abeck, ENSR.
- AMAP Assessment Report [1998] Arctic Pollution Issues, Arctic Monitoring and Assessment Programme, Oslo, pp. 710-716.
- Anderson P.N. and R.A. Hites [1996] OH Radical Reactions: The Major Removal Pathway for Polychlorinated Biphenyls from the Atmosphere, *Environ. Sci. Technol.*, v. 30, No. 5, pp. 1756 – 1763.
- Avkhimenko M.M. [2000] Medical and ecological consequences of environmental pollution by polychlorinated biphenyls. In: Polychlorinated Biphenyls/Supertoxicants of XXI century. Information Issue No.5, Moscow, pp.14-31, (*in Russian*).
- Baltensperger U., Schwikowski M., Jost D.T., Nyeki S., Gaggeler H.W., and Poulida O., [1998]. Scavenging of atmospheric constituents in Mixed phase clouds at the high-Alpine site Jungfrauoch. Part I: Basic concept and aerosol scavenging by clouds. *Atmospheric Environment*, v.32, No. 23, pp.3975-3983.
- Bamford H.A., D.L.Poster and J.E.Baker [2000] Henry's Law Constants of Polychlorinated Biphenyl Congeners and Variation with Temperature, *Chem.Eng. Data*, v. 45, pp. 1069 – 1074.
- Berg T., Hjelbrekke A.-G., Larsen R. [2001] Heavy metals and POPs within the EMEP region 1999. EMEP/CCC –Report 9/2001.
- Berg T., Sekkesæter S., Solberg S., Steines E., Valdal A.-K., and Wibetoe G. [2002] Arctic springtime depletion of mercury in Svalbard. Book of abstracts of Symposium "EUROTRAC-2", 11-15 March 2002, Garmisch-Partenkirchen, Germany.
- Beyer A and M.Matthies [2001] Criteria for Atmospheric Long-range Transport Potential and Persistence of Pesticides and Industrial Chemicals. Umweltforschungsplan des Bundesministerium für Umwelt, Naturschutz und Reaktorsicherheit. Stoffbewertung, Gentechnik, Forderkennzeichen (UFOPLAN) 299 65 402.

- Breivik, K., Sweetman A., Pacyna, J. M. and K.C.Jones [2002] Towards a global historical emission inventory for selected PCB congeners – a mass balance approach. 1. Global production and consumption. *The Science of the Total Environment*.
- Brosset C. and Lord E. [1991] Mercury in precipitation and ambient air – a new scenario. *WASP*. v. 56, pp.493-506.
- Burkhard L.P., Armstrong D.E. and A.W. Andren [1985] Henry's Law Constants for the Polychlorinated Biphenyls. *Environ. Sci. Technol.*, v.19, pp.590-596.
- Chu W. and Chan K.-H. [2000] The prediction of partitioning coefficients for chemicals causing environmental concern, *The Science of the Total Environment*, v. 248, pp. 1-10.
- Constantinou E., Wu X.A. and Seigneur C. [1995] Development and application of a reactive plume model for mercury emissions. *Water, Air and Soil Pollution*, 80, 1-4, 325-335.
- Cotham W.E. and T.F. Bidleman [1991] Estimating the atmospheric deposition of organochlorine contaminants to the Arctic. *Chemosphere*, v. 22, pp.165-188.
- Couture M.D., Banic C.M., Schemenauer R.S., Leitch W.R., and Wiebe H.A., [1998]. Comparison of the chemistry of fog water from mountain sites and cloud water from airborne platforms. In: "Proceedings of the First International Conference on Fog and Fog Collection", Eds. R.S.Schemenauer and H.Bridgman. International Development Research Center, Ottawa, Canada, pp. 109-112.
- Drummond J.R. [2001] The view from above: Passive sounding of the troposphere from space. IGAC Newsletter, No 25, December 2001, pp.2-6.
- Dunnivant F.M., Elzerman A.W., Jurs P.C., Hasan M.N., [1992], Quantitative Structure-Property Relationships for Aqueous Solubilities and Henry's Law Constants of Polychlorinated Biphenyls, *Environ. Sci. Technol.*, v. 23, No. 10, pp. 1250 – 1253.
- Ebinghaus R., H.H. Kock, C. Temme, J.W.Einax, A.G.Löwe, A.Richter, J.P.Birrows and W.H.Schroeder [2002] Antarctic Springtime Depletion of Atmospheric Mercury. *Environ. Sci. Technol.*, v.36, pp.1238-1244.
- Ebinghaus R., R.M.Tripathi, D.Walischlager and S.E.Lindberg [1999a] Natural and anthropogenic mercury sources and their impact on the air-surface exchange of mercury on regional and global scales. In: Ebinghaus R., Turner R. R., Lacerda de L. D., Vasiliev O., and Salomons W. (Eds.) Mercury contaminated sites. Springer, Berlin, pp.3-50.
- Ebinghaus R., R.R.Turner, L.D. de Lacerda, O. Vasiliev and W. Salomons (Eds.) [1999b] *Mercury contaminated sites*. Springer, Berlin. 538 p.
- Erdman L., A.Gusev and N.Pavlova [2001] Atmospheric Input of Persistent Organic Pollutants to the Mediterranean Sea. WMO, Map Technical Reports Series No.130
- Falconer R.L. and T.F. Bidleman [1994] Vapor pressures and predicted particle/gas distributions of polychlorinated biphenyl congeners as functions of temperature and ortho-chlorine substitution. *Atmos. Environ.*, v.28, pp.547-554
- Filov V.A. ed. [1990] Harmful chemicals, Hydrocarbons. Halogen derivatives of hydrocarbons. Handbook, L.: Chemistry, 732 p. (in Russian).
- Fitzgerald W. F., R.P.Mason and G.M.Vandal [1991] Atmospheric cycling and air-water exchange of mercury over mid-continental lacustrine regions. *WASP*. v. 56, pp. 745-767.
- Franz T.P. and S.J. Eisenreich [1998] Snow scavenging of polychlorinated biphenyls and polycyclic aromatic hydrocarbons in Minnesota. *Environ. Sci Technol.*, v.32, pp.1771-1778.
- Fursov V. Z. [1983]. Gaseous mercury method of mineral deposits exploration activities. Moscow, Nauka, 203 p. (in Russian).
- Gårdfeldt K., X. Feng, J. Sommar and O. Lindqvist [2001]. Total gaseous mercury exchange between air and water at river and sea surfaces in Swedish coastal regions. *Atmospheric Environment*, 35, 3027-3038.
- Granier L.K. and Chevreuil M. [1997] Behaviour and spatial and temporal variations of polychlorinated biphenyls and lindane in the urban atmosphere of the Paris area, France. *Atmospheric Environment*, v.31, No.22, pp.3787-3802.
- Hall B. [1995]. The gas phase oxidation of mercury by ozone. *Water, Air and Soil Pollution*, v.80, No. 1-4, 301-315.
- Harner T. and T.F. Bidleman [1996] Measurements of octanol-air partition coefficients for polychlorinated biphenyls. *Chem. Eng. Data*, v.41, pp.895-899.
- Hawker D.W. and D.W.Connell [1988] Octanol-water partition coefficients of polychlorinated biphenyl congeners. *Environ. Sci. Technol.*, v.22, pp.382-387.
- Hazardous Substances Databank (HSDB) [2002]: <http://toxnet.nlm.nih.gov>.
- Herrmann H., B.Ervens, H.-W.Jacobi, R.Wolke, P.Nowacki and R.Zellner [2000]. CAPRAM2.3: A chemical aqueous phase radical mechanism for tropospheric chemistry. *Journal of Atmospheric Chemistry*, v.36, pp.231-284.
- Hincley D.A., T.F.Bidleman and W.T. Foreman [1990] Determination of vapor pressures for non-polar and semi-polar organic compounds from gas chromatographic retention data. *Chem. Eng. Data*, v.35, No 3, pp.232-237.
- Hornsby A.G., Wauchope R.D., Herner A.E. [1996] Pesticide Properties in the Environment, Springer-Verlag, New York, Inc,
- Horvat M. [1996]. Mercury analysis and specification in environmental samples. In: Global and Regional Mercury Cycles: Sources, Fluxes and Mass Balances. Ed. By W.Baeyens, R.Ebinghaus and O.Vasiliev. NATO ASI Series, 2. Environment v. 21. Kluwer Academic Publ., Dordrecht, pp. 1-31.
- Howard P. H. and W.M. Meylan Eds. [1997] Handbook of physical properties of organic chemicals, CRC Lewis Publishers, Boca Raton, New York, London, Tokyo.
- IARC Monographs on the Evaluation of the Carcinogenic Risk of Chemicals to Man. [1987] Geneva: World Health Organization, International Agency for Research on Cancer, 1972-Present. (Multivolume work), p. S7 71.
- Ilyin I., A. Ryaboshapko, O.Travnikov, T.Berg and A.G.Hjellbrekke [2001]. Evaluation of transboundary transport of heavy metals in 1999. Trend Analysis. EMEP Report, June 3/2001. MSC-E, Moscow, 2001.
- Iwata H., S.Tanabe, K.Uedo and R. Tatsukawa [1995], Persistent Organochlorine Residues in Air, Water, Sediments, and Soils from the Lake Baikal Region, Russia, *Environ. Sci. Technol.*, v. 29, No. 3, pp. 792-801.

- Izmerov N.F. ed. [1990]. Lindane. In series "Scientific reviews of the Soviet literature related to toxicity and hazard of chemicals". The Centre of international projects of the State Committee on Science and Technology, 40, pp.9-10, (in Russian).
- Jacobs C.M.J. and W.A.J. van Pul [1996] Long-range atmospheric transport of persistent organic pollutants. 1: Description of surface –Atmosphere exchange modules and implementation in EUROS. National Institute of Public Health and the Environment, Bilthoven, The Netherlands. Report No. 722401013.
- Junge C. [1972] The cycle of atmospheric gases – natural and man made. Quarterly Journal of the Royal Meteorological society, v.98, No 418, pp.711-729.
- Junge C.E. [1977] Basic considerations about trace constituent in the atmosphere is related to the fate of global pollutant. In: Fate of pollutants in the air and water environment. Part I, I.H. Suffet (ed.) (Advanced in *Environ. Sci. Technol.*, v.8), Wiley-Interscience, New York.
- Karickhoff S. W. [1981] Semiempirical estimation of sorption of hydrophobic pollutants on natural sediments and soil, *Chemosphere*, v.10, pp.833-846.
- Keeler G., Glinsorn G., and Pirrone N. [1995]. Particulate mercury in the atmosphere: its significance, transport, transformation and sources. *Water, Air and Soil Pollution*, v.80, pp.159-168.
- Kimec G., Zwodziak A., K. Acker and W.Wieprecht [1998]. Cloud/fog water chemistry at high elevation in the Sudeten mountains, south-western Poland. Proceedings of the First International Conference on Fog and Fog Collection. Vancouver, Canada, July 19-24, pp. 69-72.
- Klyuev N.A. and E.S. Brodsky [2000] Determination of polychlorinated biphenyls in the environment and biota. In Poychlorinated Biphenyls/Supertoxicants of XXI century. Information Issue No.5, Moscow, pp. 31-63 (in Russian).
- Krishnan S.V, B.K. Gullet and W.Jozewicz [1994] Sorption of elemental mercury by activated carbons. *Environmental Science and Technology*, v.28, pp.1506 – 1512.
- Kucklick J.R., D.A.Hinckley and T.F.Bidleman [1991] Determination of Henry's law constants for hexachlorocyclohexanes in distilled water and artificial seawater as a function of temperature. *Marine chemistry*, v.34, pp.197-209.
- Kwok E.S.C., Atkinson R. and J.Arey [1995] Rate constants for the gas-phase reactions of the OH radical with dichlorobiphenyls, 1-chlorodibenzo-p-dioxin, 1,2-dimethoxybenzene, and diphenyl ether: estimation of OH radical reaction rate constants for PCBs, PCDDs, and PCDFs. *Environ. Sci. Technol.*, v.29, No.6, pp.1591-1598.
- Lamborg C.H., W.F.Fitzgerald, G.M.Vandal and K.P.Rolfhus [1995]. Atmospheric mercury in northern Wisconsin: sources and species. *Water, Air and Soil Pollution*, v.80, pp.189-198.
- Lin C. -J. and S.O.Pehkonen [1999] The chemistry of atmospheric mercury: a review. *Atmospheric Environment*, v.33, pp. 2067–2079.
- Lin C.-J. and S.O.Pehkonen [1998]. Two-phase model of mercury chemistry in the atmosphere. *Atmospheric Environment*, v.32, No 14/15, pp. 2543-2558.
- Lin C.-J. and S.O. Pehkonen [1997] Aqueous free radical chemistry of mercury in the presence of iron oxides and ambient aerosol. *Atmospheric Environment*, v.31, pp.4125-4137.
- Lindberg S.E., S.Brooks, C.-J. Lin, K.J. Scott, M.S. Landis, R.R. Stevens, M. Goodsite and A.Richter [2002] Dynamic oxidation of gaseous mercury in the Arctic troposphere at polar sunrise. *Environmental Science and Technology*, v.36, 1245-1256.
- Lindqvist O. and H.Rodhe [1985]. Atmospheric mercury - a review. *Tellus*, v.37B, pp.136-157.
- Lindqvist O., A.Jernelöv, K.Johansson and H.Rodhe [1984]. Mercury in the Swedish environment: Global and local sources. National Swedish Environment Protection Board, Report PM 1816, 91 p.
- Lindqvist O., K.Johanson, M.Aastrup, A.Anderson, L.Bringmark, G.Hovsenius, L.Hakanson, A.Iverfeld, M.Meili and B. Timm [1991]. Mercury in the Swedish environment - recent research on causes, consequences and corrective methods. *Water, Air and Soil Pollution*, v.55, pp.1-261.
- Livengood D., H.S. Huang, M.H. Mendelsohn and J.M. Wu [1995] Development of mercury control enchantments for flue-gas cleanup system. EPRI/DOE *International Conference on Managing Hazardous and Particulate Air Pollutants*.
- Lu J. Y., Schroeder W. H., Barrie L. A., Steffen A., Welch H. E., Martin K., Lockhart W. L., Hunt R. V., Boila G., Richter A. [2001] Magnification of atmospheric mercury deposition to polar regions in springtime: the link to tropospheric ozone depletion chemistry. *Geophys. Res. Letters*. v.28. No.17, pp.3219-3222.
- Lyon B., G.Rice, O.R.Bullock and P.Selby [1999] Modelling the local scale atmospheric fate of anthropogenic mercury emissions. In: *Mercury as a Global Pollutant. 5th International Conference*, Rio de Janeiro, May 23-28. Book of abstracts, p. 110.
- Macdonald R.W., Barrie L.A., Bidleman T.F., Diamond M.L., Gregor D.J., Semkin R.G., Strachan W.M., Li Y.F., Wania F., Alaee M., Alexeeva L.V., Backus S.M., Bailey R., Bewers J.M., Gobel C., Halsall C.J., Harner T., Hoff J.T., Jantunen L.M.M., Lockhart W.L., Mackay D., Muir D.C.G., Pudykiewicz J., Reimer K.J., Smith J.N., Stern G.A., Schroeder W.H., Wagemann R., Yunker M.B. [2000] Contaminants in the Canadian Arctic: 5 years of progress in understanding sources, occurrence and pathways. *The Science of the Total Environment*, v. 254, pp. 93-234.
- Mackay D., Wan Ying Shiu, Kuo Ching Ma. [1992] Illustrated handbook of physical-chemical properties and environmental fate for organic chemicals, v. II, Lewis Publishers, p. 209-216.
- Mackay D., Wan Ying Shiu, Kuo Ching Ma. [1997] Illustrated Handbook of Physical-Chemical Properties and Environmental Fate for Organic Chemicals, v.5, pp. 479 – 489, 567 – 571.
- McLachlan M.S. [1996] Bioaccumulation of Hydrophobic Chemicals in Agricultural Food Chains, *Environ. Sci. Technol.*, v. 30., No. 1, pp. 252 – 259.
- Milford J.B. and C.I.Davidson [1985] The Sizes of Particulate Trace Elements in the Atmosphere - A Review. *JAPCA*, v. 35, No. 12, pp. 1249-1260.
- Munthe J. [1992] The aqueous oxidation of elemental mercury by ozone. *Atmospheric Environment*, 26A, 8, 1461-1468.

- Munthe J. [1994] The atmospheric chemistry of mercury: kinetic studies of redox reactions. In C.J.Watras and J.W.Huckabee (eds.), Mercury Pollution: Integration and Synthesis, Lewis Publishers, Ann Arbor, Michigan, pp.273-279.
- Munthe J., Z.F. Xiao and O. Lindqvist [1991] The aqueous reduction of divalent mercury by sulfite. *Water, Air and Soil Pollution*, v.56, pp.621-630.
- Ngabe B., T.F.Bidleman and R.L.Falconer [1993] Base Hydrolysis of  $\alpha$  - and  $\gamma$  - Hexachlorocyclohexane, *Environ. Sci. Technol.*, v. 27, No. 9, pp. 1930-1933.
- Niki H., P.D.Maker, C.M.Savage and L.P.Breitenbach [1983] A long-path Fourier transform study at the kinetics and mechanism for the HO-radical initiated oxidation of dimethyl mercury. *J.Phys.Chem.*, v.87, pp.4978-4981.
- NIST[2002]  
<http://chem.sis.nlm.nih.gov/chemidplus/cmplxqry.html>
- Paasivirta J., S. Sinkkonen, P.Mikelson, T.Rantio and F. Wania [1999] Estimation of vapor pressures, solubilities and Henry's law constants of selected persistent organic pollutants as functions of temperature, *Chemosphere*, v. 39, No. 5, pp. 811-832.
- Pankow J.F. [1987] Review and comparative analysis of the theories on partitioning between the gas and aerosol particulate phases in the atmosphere. *Atmos. Environ.*, v.21, pp.2275-2283.
- Pekar M., N. Pavlova, A. Gusev, V. Shatalov, N. Vulikh, D. Ioannisian, S. Dutchak, T. Berg and A.-G. Hjelbrekke [1999] Long-Range transport of selected persistent organic pollutants. EMEP Report 4/99.
- Petersen G. [1992]. Belastung von Nord- und Ostsee durch ökologisch gefährliche Stoffe am Beispiel atmosphärischer Quecksilberverbindungen. GKSS-Forschungszentrum Geesthacht, Forschungsvorhaben 104 02 726, 53 p.
- Petersen G., J.Munthe, K. Pleijel, R. Bloxam and A.V.Kumar [1998] A comprehensive Eulerian modelling framework for airborne mercury species: Development and testing of the tropospheric chemistry module (TCM). *Atmospheric Environment*, v. 32, No. 5, pp. 829-843.
- Petersen G., R. Bloxam, S. Wong, J. Munthe, O. Krüger, S. Schmolke, and A.V. Kumar [2001] A comprehensive Eulerian modelling framework for airborne mercury species: model development and applications in Europe. *Atmospheric Environment*, v.35, pp.3063-3074.
- Pleijel K. and J. Munte [1995]. Modelling the atmospheric mercury cycle - chemistry in fog droplets. *Atmospheric Environment*, v.29, No.12, pp.1441-1457.
- Prokofiev A.K. [1981]. Chemical forms of mercury, cadmium and zinc in fresh water systems. *Advances in Chemistry*, v. 50, No 1, pp. 54-84 (in Russian).
- Ruelle P. and U.W. Kesselring [1997] Aqueous solubility prediction of environmentally important chemicals from the mobile order thermodynamics. *Chemosphere*, v. 34, No. 2, pp. 275-298.
- Ryaboshapko A. and V. Korolev [1997] Mercury in the atmosphere: estimates of model parameters. Meteorological Synthesizing Centre - East, EMEP/MSC-E Report 7/97, August 1997, Moscow, 60 p.
- Ryaboshapko A., I. Ilyin, R. Bullock, R.Ebinghaus, K. Lohman, J.Munthe, G.Petersen, C.Seigneur and I.Wangberg [2001]. Intercomparison study of numerical models for long-range atmospheric transport of mercury. Stage I. Comparison of chemical modules for mercury transformations in a cloud/for environment. Moscow, MSC-East, EMEP Technical Report 2/2001.
- Sahsuvar L. [1999], Modelling Physical Chemical Properties and Pathways of Polychlorinated Biphenyls in the Atmosphere, Centre for Atmospheric Chemistry, York University, Toronto, Ontario, pp. 141 and Appendixs.
- Sakata M. and K. Marumoto [2002] Formation of atmospheric particulate mercury in the Tokyo metropolitan area. To be published in *Atmospheric Environment*.
- Sander R. [1997] Henry's law constants available on the Web. EUROTRAC Newsletter, No.18, pp.24-25, <http://www.science.yorku.ca/cac/people/sander/res/henry.html>
- Schroeder W.H. and J. Munthe [1998] Atmospheric mercury - an overview. *Atm. Environ.*, v.32, No 5, pp. 809-822.
- Schroeder W.H., G. Yarwood and H. Niki [1991] Transformation processes involving mercury species in the atmosphere. *Water Air Soil Pollut.*, v.56, pp.653-666.
- Schroeder W.H., G.C. Edwards, P.E. Rasmussen, R.J. Kemp, G. Dias, D. Wallace, A. Steffen and J.Y. Lu [2001] Mercury: Rising? Or falling? Book of Abstracts, *6th International Conference on Mercury as a Global Pollutant* (October 15-19, 2001, Minamata, Japan), p. 42.
- Schroeder W.H., K.G. Anlauf, L.A. Barrie, J.Y. Lu, A. Steffen, D.R. Schneeberger and T.Berg [1998] Arctic springtime depletion of mercury. *Nature*, v.391, pp.331-332.
- Schwarzenbach R.P., P.M.Gschwend and D.M.Imboden [1993] Environmental organic chemistry. John Wiley&Sons Inc., New York.
- Seigneur C., H.Abeck, G.Chia, M.Reinhard, N.S.Bloom, E.Prestbo and P.Saxena [1998] Mercury adsorption to elemental carbon (soot) particles and atmospheric particulate matter. *Atmospheric Environment*, v.32, No 14/15, pp. 2649-2657.
- Seigneur C., J. Wrobel and E.Constantinou [1994] A chemical kinetic mechanism for atmospheric inorganic mercury. *Environmental Science and Technology*, v.28, No. 9, pp.1589-1597.
- Shatalov V. and Malanichev A., [2000], Investigation and assessment of POP transboundary transport and accumulation in different media, Part II, EMEP Report 4/2000, pp. 79
- Shatalov V., A.Malanichev, N.Vulykh, T.Berg and S.Manø [2001] Assessment of POP transport and accumulation in the environment. EMEP Report 4/2001, Moscow.
- Sinkkonen S. and J.Paasivirta [2000] Degradation half-life times of PCDDs, PCDFs and PCBs for environmental fate modelling. *Chemosphere*, v.40, pp.943-949.
- Sommar J., D.Strömberg and O.Lindqvist [1999] Distribution equilibrium of mercury (II) chloride between water and air applied to flue gas scrubbing. In: *Mercury as a Global Pollutant. 5th International Conference*, Rio de Janeiro, May 23-28, Book of abstracts, p. 129.

- Sommar J., K.Gärdfeldt, D.Strömberg and X. Feng [2001] A kinetic study of the gas-phase reaction between the hydroxyl radical and atomic mercury. *Atmospheric Environment*, v.35, pp.3049-3054.
- Steffen A., W.H. Schroeder, G. Hoenniger, U. Platt, J. Fuentes, W. Lawson, W. Strachan [2001] Springtime experiments during Canadian high Arctic atmospheric mercury depletion events. Book of Abstracts, *6th International Conference on Mercury as a Global Pollutant* (October 15-19, 2001, Minamata, Japan), p. 30.
- Strand A. and Ø. Hov [1996] A model strategy for the simulation of chlorinated hydrocarbon distributions in the global environment. *Water, Air and Soil Pollution*, v.86, pp.283-316.
- Sweetman A.J. and Jones K.C. [2000] Declining PCB concentrations in the U.K. atmosphere: evidence and possible causes. *Environmental Science and Technology*, v.34, No. 5, pp.863-869.
- Thiem L., D.Badorek and J.T.O'Connor [1976] Removal of mercury from drinking water using activated carbon. American Water Works Association. v.68, pp.447 – 451.
- Tokos J.J.S., B.Hall, J.A.Calhoun and E.M.Prestbo [1998] Homogeneous gas-phase reaction of Hg<sup>0</sup> with H<sub>2</sub>O<sub>2</sub>, O<sub>3</sub>, CH<sub>3</sub>I, and (CH<sub>3</sub>)<sub>2</sub>S: implications for atmospheric Hg cycling. *Atmospheric Environment*, v.32, No 5, pp.823-827.
- US-EPA [1997] Mercury Study Report to Congress. Vol. III, Fate and Transport of Mercury in the Environment. US-EPA-452/R-97003.
- Van Loon L., E.Mader and S.L.Scott [2000] Reduction of the aqueous mercuric ion by sulfite: UV spectrum of HgSO<sub>3</sub> and its intermolecular redox reaction. *J. Phys. Chem. A.*, v.104, pp.1621-1626.
- Vong R.J., B.M.Baker, F.J.Brechtel, R.T.Collier, J.M.Harris, A.S. Kowalski, N.C. McDonald and L.M. McInnes [1997] Ionic and trace element composition of cloud water collected on the Olympic peninsula of Washington State. *Atmospheric Environment*, v.31, pp.1991-2001.
- Walker K., Vallero D.A., Lewis R.G. [1999] Factors influencing the distribution of lindane and other hexachlorocyclohexanes in the environment. *Environmental Science and Technology*, v. 33, No. 24, pp.4373-4378.
- Wängberg I., S.R. Shcmolke, R. Ebinghaus, J. Munthe, P. Schager and A.Iverfeldt [1999]. Estimates of the air-sea exchange of gaseous mercury in the southern Baltic Sea, summer and winter 1997-1998. In: *Mercury as a Global Pollutant. 5th International Conference, Rio de Janeiro, May 23-28. Book of abstracts*, p. 133.
- Wania F. [1997] Modelling Sea-Air Exchange of Persistent Organic Pollutants: Focus on Temperature and Other Seasonal Parameters. In: *Sea-Air Exchange: Processes and Modelling*. Ed. by J.M.Pacyna, D.Broman and E.Lipiatou 1998, pp.161-190.
- Wania F. [1999] Global Modeling of Polychlorinated Biphenyls, WECC (Wania Environmental Chemists Corp.) Report 1/99, p.22.
- Whitby K.T. [1978] The Physical Characteristics of Sulphur Aerosols. *Atmospheric Environment*, v.12, pp.135 – 159.
- Xiao Z.F., J. Munthe, D. Strömberg and O.Lindqvist [1994] Photochemical Behavior of Inorganic Mercury Compounds in Aqueous Solution. In: *Mercury Pollution: Integration and Synthesis*, ed. by C.J.Watras and J.W.Huckabee, Lewis Publishers, Boca Raton, pp. 581-592.
- Yu Lu and M.A.K. Khall [1991] Tropospheric OH: model calculation of spacial, temporal and secular variations. *Chemosphere*, v. 23, pp.397-444.

# Chapter 3

## MODEL APPROACHES AND INPUT DATA

This chapter is devoted to the description of modeling approaches to the assessment of long-range transport and contamination of the regions of the Russian North by Hg, PCBs and  $\gamma$ -HCH. The global character of these pollutants requires appropriate approaches to the assessment of their dispersion in the atmosphere. There are at least several reasons for the hemispheric or global consideration of the atmospheric pollutant dispersion. Firstly, volatile contaminants such as mercury and some POPs emitted to the atmosphere have essentially global atmospheric residence time estimated as long as months or even years and can be airborne transported practically over the whole globe [Ebinghaus *et al.*, 1999; Vulykh and Putilina, 2000]. Moreover, after being deposited to the Earth's surface these pollutants can be re-emitted to the atmosphere from areas situated far from traditionally considered industrial regions. Besides, the consideration of contamination of such remote regions as the Arctic at the hemispheric or global level seems to be reasonable.

Modeling approaches used in a number of studies of environment pollution by Hg, PCBs, and  $\gamma$ -HCH on the global or hemispheric scale are briefly outlined in Section 3.1. Following sections contain the description of the models developed at MSC-E. These models are based on the same atmospheric transport scheme. They are referred to three-dimensional Eulerian models. Therefore it is rather appropriate to talk about series of models describing transport of certain pollutants than about separate models. Nevertheless, the models contain peculiarities describing the behaviour of the mentioned pollutants in the compartments. Thus, mercury model more concentrated on complicated chemical transformations of mercury in the atmosphere, whereas POP model includes a developed description of persistent organic pollutants in the environmental compartments. The hemispheric model of mercury long-range transport (**MSCE-Hg-Hem**) is described in Section 3.2. The appropriate model for evaluation of hemispheric pollution by POPs (**MSCE-POP**) is presented in Section 3.3. To avoid duplication of description of common components the atmospheric transport scheme is described in detail only in for MSCE-Hg-Hem (Section 3.2) and just mentioned for MSCE-POP (Section 3.3). Instead, peculiarities of pollutant transformations and behaviour in the media are highlighted for both models.

The chapter also contains the description of input data required for the models. Meteorological data are described in Section 3.4. Information on land cover and leaf area index is presented in Sections 3.5 and 3.6 respectively. Section 3.7 contains a short description of data on air concentrations of chemical reactants. Data on ocean currents and sea ice are characterized in Sections 3.8 and 3.9.

### 3.1. Short review of modeling approaches used to the assessment of pollution by Hg, PCBs and HCHs on global/hemispheric scale

A great number of different studies of the Arctic pollution have been performed recently [AMAP, 1998]. Most of them were carried out using various measurement campaigns aiming at the investigation of contamination of the environment within this region. Only a few of them included the application of mathematical models. The application of modeling to the assessment of the environmental contamination recently takes on great significance. In spite of uncertainties in models and in the input information, model approaches are improved and become a useful tool for the investigation of dispersion and behaviour of contaminants in the environment. Modeling can complement the information on HM and POP content in different Arctic environmental compartments

obtained using measurement campaigns. In particular it can provide data on concentrations in air and other media with a certain spatial and temporal resolution. Modeling results can be used for the analysis of contamination pathways to the Arctic and for investigations of source-receptor relationship. Besides models can be used for the projection of contamination levels employing various emission scenarios. Here we would like to describe briefly some of them related to such chemicals as Hg, PCBs, and HCHs, which are of concern in this study.

## Hg

The Danish Hemispheric Eulerian Model system (DEHM) was developed and recently applied to estimate the transport of mercury to the Arctic. The earlier version of the model was used in AMAP phase I [AMAP, 1998], and the model has been described in several papers (e.g. *Christensen* [1997, 1999]; *Barrie et al.* [2001]). The modeling system includes a meteorological model based on the PSU/NCAR Mesoscale Model version 5 (MM5) [Grell et al., 1995] and a 3-dimensional air pollution model DEHM. The description of chemical transformations of mercury is based on the scheme from the GKSS model [Petersen et al., 1998]. In the present version there are 13 mercury species in the gaseous, aqueous and particulate phase. The model includes the parameterization of springtime mercury depletion events in the Arctic atmosphere. It is assumed that during the Arctic polar sunrise the oxidation rate affecting the transformation of  $\text{Hg}^0$  to  $\text{HgO}$  increases by 25% in the boundary layer over sea ice under sunny conditions. Dry deposition velocities of the reactive gaseous mercury species are determined on the basis of the resistance method. For wet deposition of reactive and particulate mercury simple scavenging coefficient different for in-cloud and sub-cloud scavenging is applied [Christensen, 1997]. The model was used for the simulation of mercury long-range transport and deposition for the period from October 1998 to December 2000 on the basis of the new global inventory of mercury emissions for 1995 on a  $1^\circ \times 1^\circ$  grid [Pacyna and Pacyna, 2002], which includes mercury speciation. No re-emission from land and oceans is considered in the model. As the initial concentration and boundary conditions the concentration of  $1.5 \text{ ng/m}^3$  of  $\text{Hg}^0$  is used. The model results suggest that mercury depletion events in the Arctic atmosphere are of an essential importance. The total deposition of mercury in the area north to the Polar Circle is increased from 78 to 181 tonnes per year in model runs without and with depletion parameterization.

Another model used for the simulation of mercury species in the gaseous and aqueous phase is a Eulerian Multiscale Global/Regional Atmospheric Heavy Metals Model (GRAHM) developed at Canadian Meteorological Centre (CMC). The development of this model was started from an operational weather forecasting model Global Environmental Model (GEM) [WMO, 2000]. The model is based on solving a set of dynamic equations for all meteorological processes and includes a description of mercury species chemical transformations in the atmosphere. The mercury chemical scheme is adapted from G.Petersen et al. [1998]. For the description of contamination mass conserving 3-D quasi-monotonic semi-Lagrangian mass conserving scheme is employed. The discretization in time is based on the two-time-level semi-Lagrangian scheme. The model is capable to use variable resolution in vertical as well as in horizontal direction. Therefore it can operate with different scales and can produce both global distribution of mercury concentrations in the atmosphere and high-resolution regional concentration fields. The model was applied to simulation of global mercury distribution using emission inventory of anthropogenic mercury sources for 1990 of GEIA [Pacyna et al., 1996]. However, this inventory does not contain information on mercury speciation, vertical distribution of emissions and point sources.

Another approach to the identification of sources of Canadian High Arctic pollution by total gaseous mercury (TGM) is based on the 10-day back trajectory cluster analysis and the potential source contribution function (PSCF) model [Lin et al., 2001]. To investigate the long-range transport and source-receptor relationship of atmospheric pollutants a receptor model called PSCF has been developed. Using the combination of chemical measurements and computed backward trajectories of

air parcels to the points of observations (receptor sites), the PSCF model is capable to identify potential sources and pathways of a pollutant. Along with this model the cluster analysis of backward trajectories was applied to analyze the regional transport patterns and to project possible sources of pollutants. On the base of these techniques the study of potential sources and dominant pathways of Canadian High Arctic pollution by mercury was performed using the 1995 TGM concentrations measured at Alert site. The 10-day backward trajectories were computed by the trajectory model HYSPLIT4. According to the results of the study the long-range transport events occur only in the cold seasons. The potential source regions are located in Eurasia, Northern America and Europe. During the Arctic summer elevated TGM concentrations can be caused by the exchange of volatile mercury between the air and the underlying surface.

### ***PCBs and HCHs***

A simple global two-dimensional model for studying the fate of organochlorines in the environment is presented in [Strand and Hov, 1996]. This paper describes the application of the developed model to the simulation of  $\alpha$  and  $\gamma$ -HCH distribution in three environmental compartments: atmosphere, soil and seawater. Only the most important processes are included into this multicompartment model. These are the transport within the atmosphere, wet deposition with precipitation, exchange with sea and soil compartments, sedimentation and degradation. The model was used to study the distribution of  $\alpha$ - and  $\gamma$ -HCH with the use of data for the period 1960-1989. The results show that in spite of the coarse resolution and a certain level of simplification the model is able to reproduce reasonably well the observed atmospheric and oceanic levels of HCHs. It was shown that the major part of emitted HCH (92%) was partitioned to the ocean compartment due to its very significant capacity. From this amount 21% was contained in the surface waters and 71% - in deep waters.

The application of a global-scale multicompartment transport model to the evaluation of environmental fate of pesticides (hexachlorocyclohexanes) is presented in [Koziol and Pudykiewicz, 2001]. The model developed permits to give a realistic representation of interaction between such environmental compartments as the atmosphere, hydrosphere, cryosphere, and soil system. Along with the atmospheric part it includes the simulation of exchange between the air and the underlying surface (water, soil, snow, and ice). The atmospheric transport is described on the basis of equations in a general contra variant form. The terrain following spherical coordinate system is chosen with horizontal resolution  $2^\circ \times 2^\circ$ . The model includes the soil module for simulation of diffusion and convection of a pollutant within the soil. The computations were based on two-year meteorological data of Global Reanalysis data set for 1993-1994, climatological data, and estimations of HCHs' application during the simulated period. The computed concentrations were compared with observations made in the high Arctic at sites Alert, Ny-Alesund, Dunai, and Tagish. The comparison indicates that the results of the model are in a good agreement with measured air concentrations and their trends. According to the modeling results India seems to be the most significant source of pollution by HCHs. Other potential sources of HCHs can be located in Central Europe, the Ukraine, North Africa, and Mexico.

The fugacity-based mass balance model was developed to determine the global distribution of selected persistent organic pollutants [Wania and Mackay, 1999]. The global environment is represented in the model as the 10 latitudinal bands or climatic zones each of which is divided into a set of well-mixed compartments, namely, the atmosphere, land, freshwater and seawater. It includes transport and exchange processes between these compartments, degradation, partitioning of chemicals between the gaseous and particulate phase in air, as well as between the dissolved phase and suspended matter in water. This version of the model has no vertical division of the atmospheric compartments and processes of advection and diffusion. Air temperatures and exchange rates between atmospheric compartments are defined as seasonally varying parameters. The model

developed was applied to simulation of  $\alpha$ -HCH global distribution [Wania *et al.*, 1999]. Based on this simulation seasonal variations and long-term trends of  $\alpha$ -HCH concentrations in the atmosphere and ocean water were assessed. The model reproduced the latitudinal dependence of measured  $\alpha$ -HCH concentrations in air and reversible air-sea exchange for the period 1960-1996. Differential persistence of chemicals in different climate zones and temperature-controlled partitioning between the atmosphere and the underlying surface were indicated as the most significant factors for the global distribution of HCHs. The model results suggest that the most part of applied  $\alpha$ -HCH was degraded within the soil compartment where it was used and a small fraction was transferred to the terrestrial and marine environment of the Arctic region via the atmosphere and rivers. However even this small amount can result in elevated levels of HCH concentrations in this area. The most important sources of the Arctic pollution by this chemical were temperate and boreal climatic zones. The Arctic Ocean can be the final sink for the  $\alpha$ -HCH where it is accumulated and degraded with the half-life of about ten years.

The updated version of the model was also used in the study of the global historical fate of PCBs [Wania, 1999]. The modifications include vertically layered representation of the atmosphere, a forest canopy compartment, and some other improvements of parameterization of the processes. The simulation was based on the estimates of emission of seven PCB isomers into the global environment from 1930 to 2000. It was assumed that the chemical composition of these emissions was constant throughout the considered period and all the release of PCBs occurred to the atmosphere. The results are of a preliminary character they are deviating within an order of magnitude in comparison with measurements. Based on the model results it was obtained that the total amount of seven PCBs released during the period of 1930-2000 was distributed within the environment in the following way: 64% was degraded, 18% was transported to the deep sea and 1% was buried in fresh water sediments, and 17% was dispersed within various environmental compartments. The analysis of congeneric composition of PCBs in different media suggests that the polar atmosphere is represented by lighter congeners and their amount there tends to increase with time. It was concluded that there is a need to perform computations for individual PCB chemicals rather than for the chemical mixture with average properties since the simulated fate of various congeners is different to a significant extent. It was indicated that even relatively minor fractions of the global PCB emissions being transported northward result in elevated levels of the PCB concentrations in the polar region.

The approaches used in these studies and their results were carefully studied prior to set up investigations in the framework of this project. To achieve the goals of the present study the dynamic Eulerian hemispheric models were considered to be suitable for the evaluation of pathways and spatial distribution of contamination in different environmental compartments and to provide estimates of source-receptor relationships. The description of models developed for this study is presented below in this chapter.

### 3.2. MSCE-Hg-Hem model

The scheme of model treatment of main mercury processes in the atmosphere is presented in Figure 3.1. Mercury enters the atmosphere from anthropogenic and natural sources. They include point (coal-fired power plants, waste incinerators, volcanoes etc.) and diffuse area sources (mill tailings, municipal wastes, geologically enriched soils) [Jackson, 1997; Gustin *et al.*, 1999]. Whereas anthropogenic emissions contain a number of mercury species (elemental mercury vapour, oxidized gaseous and particulate mercury), natural emissions mostly consist of elemental vapour. Moreover, mercury vapour is emitted to the atmosphere from the sea surface due to marine biota activity [Kim and Fitzgerald, 1986]. Detailed description of mercury emission sources is presented in Chapter 4.

Once emitted to the atmosphere mercury is transported through it with the air masses (advective transport) and dispersed by eddy diffusion. During the pathway in the atmosphere mercury species undergo physical and chemical transformations resulting in their mutual redistribution. Thus, elemental mercury is oxidized by such oxidants as ozone and OH radical. Besides, it is dissolved in cloud water and takes part in aqueous-phase oxidation and reduction reactions, formation of sulphite and chloride complexes, which are in turn adsorbed by soot particles. The model chemical scheme is described in detail in Section 3.2.2. Mercury species are removed from the atmosphere by means of surface uptake and precipitation scavenging. The model parameterization of dry and wet deposition processes is considered in Section 3.2.3.

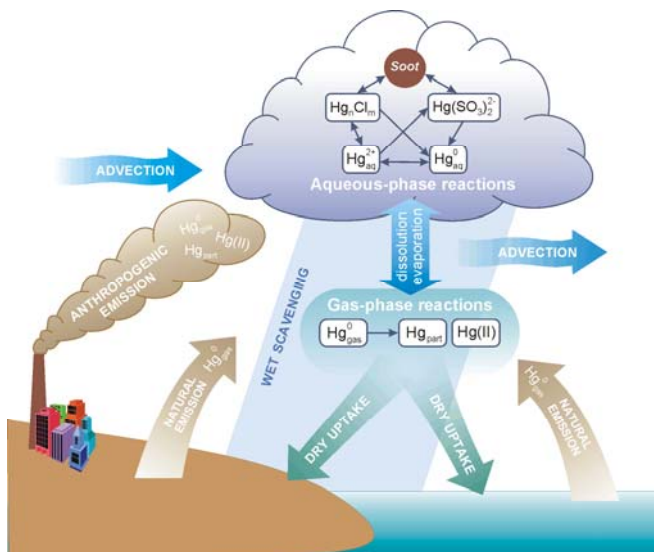


**Figure 3.1.** The model scheme of mercury behaviour in the atmosphere

The model computation domain covers the whole Northern Hemisphere with spatial resolution 2.5° both in zonal and meridional directions. The surface grid structure of the model domain is shown in Figure 3.2. To avoid a singularity at the pole point, peculiar to the spherical coordinates, the grid has a special circular mesh of radius 1.25° including the North Pole. In the vertical direction the model domain consists of eight irregular levels of terrain-following sigma-pressure ( $\sigma$ -p) coordinate defined as a ratio of local atmospheric pressure to the ground surface pressure [Jacobson, 1999]. The vertical grid structure of the model is presented in Figure 3.3.

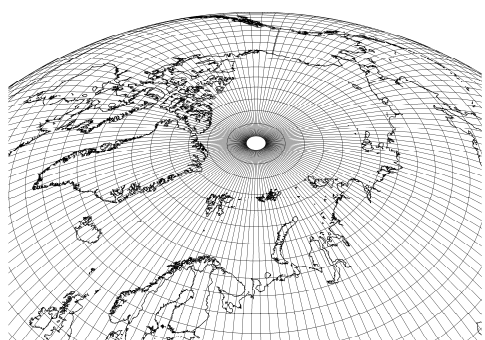


**Figure 3.2.** Horizontal grid structure of the model domain. Geographical coordinates with 2.5° × 2.5° resolution and the pole grid cell

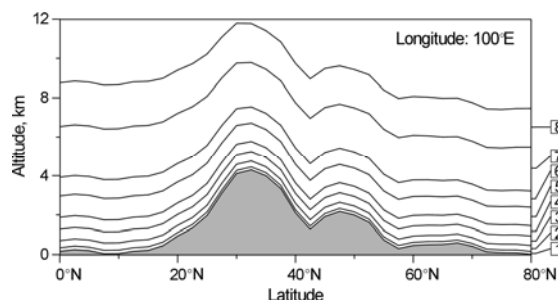


**Figure 3.3.** Vertical grid structure of the model domain. Eight terrain-following  $\sigma$ -levels: 1 –  $\sigma = 0.99$ ; 2 – 0.96; 3 – 0.91; 4 – 0.85; 5 – 0.77; 6 – 0.68; 7 – 0.55; 8 – 0.4

### 3.2.1. Atmospheric transport

The model description of mercury atmospheric transport is based on the three-dimensional advection-diffusion equation adapted to the ( $\sigma$ - $p$ ) coordinate [see e.g. *Jacobson, 1999*]:

$$\frac{\dot{\Gamma}\mathcal{D}}{\dot{\Gamma}\mathcal{D}}(q_i p_s) = -\nabla_H \cdot (q_i p_s \mathbf{V}_H) - \frac{\dot{\Gamma}\mathcal{D}}{\dot{\Gamma}\mathcal{D}}(q_i p_s \sigma) + \frac{\dot{\Gamma}\mathcal{D}}{\dot{\Gamma}\mathcal{D}} \left[ K_z \frac{g^2 \rho^2}{\rho_s^2} \frac{\dot{\Gamma}\mathcal{D}}{\dot{\Gamma}\mathcal{D}}(q_i p_s) \right] + C_i + S_i - R_i \quad (3.1)$$

Here  $q_i = c_i/\rho$  is mixing ratio of  $i^{\text{th}}$  mercury species;

$c_i$  and  $\rho$  are the mercury species volume concentration and the local air density;

$\sigma = d\sigma/dt$  is the vertical scalar velocity in the  $\sigma$ - $p$  coordinate;

$\nabla_H$  and  $\mathbf{V}_H$  denote vectors of horizontal divergence operator and horizontal wind velocity respectively;

$K_z$  is the vertical eddy diffusion coefficient; and  $g$  is the gravitational acceleration.

In Eq. (3.1) we omitted horizontal components of eddy diffusion because of the coarse horizontal grid resolution. The local air density  $\rho$  is coupled with air temperature  $T_a$  and surface pressure  $p_s$  through the equation of state:

$$\rho = \frac{\sigma p_s}{R_a T_a}, \quad (3.2)$$

where  $R_a$  is the humid air gas constant.

The first two terms on the right hand side of Eq. (3.1) describe horizontal and vertical advection of a pollutant in the atmosphere. The third term represents vertical eddy diffusion, the fourth considers species mutual chemical transformations ( $C_i$ ), and the last two terms describe bulk pollutant sources ( $S_i$ ) and removal processes ( $R_i$ ). Eq. (3.1) is solved by means of the time-splitting technique [*Yanenko, 1971; Marchuk, 1975; McRae et al., 1982*]. Following this method, Eq. (3.1) is decomposed into several separate sub-equations describing different physical and chemical processes, which are solved successively during each time step.

#### *Advection*

In spherical coordinates the sub-equation of Eq. (3.1) describing horizontal advection has the following form:

$$\frac{\partial}{\partial t}(q_i p_s) = -\frac{1}{R_E \cos \varphi} \left[ \frac{\partial}{\partial \lambda}(q_i p_s V_\lambda) + \frac{\partial}{\partial \varphi}(q_i p_s V_\varphi \cos \varphi) \right] \quad (3.3)$$

where  $\lambda$  and  $\varphi$  are the geographical longitude and latitude;

$R_E$  is the Earth radius;

$V_\lambda$  and  $V_\varphi$  are zonal and meridional components of the wind velocity respectively.

Moreover, the former term in the square brackets describes the zonal advective transport, while the latter term represents the meridional one.

Eq. (3.3) is numerically solved using Bott flux-form advection scheme [*Bott, 1989a; 1989b*]. This scheme is mass conservative, positive-definite, monotone, and is characterized by comparatively low artificial diffusion [see e.g. *Dabdub and Seinfeld, 1994*]. In order to reduce the time-splitting error in strong deformational flows the scheme has been modified according to [*Easter, 1993*]. The original

Bott scheme has been derived in the Cartesian coordinates. To apply the scheme to the transport in spherical coordinates it has been modified taking into account peculiarities of the spherical geometry. Detailed description of the Bott advection scheme in the spherical coordinates is presented in [Travnikov, 2001].

The vertical advection part of Eq. (3.1) is written as follows:

$$\frac{\partial}{\partial t}(q_i p_s) = -\frac{\partial}{\partial \sigma}(q_i p_s \sigma). \quad (3.4)$$

This one-dimensional advection equation is solved using the original Bott scheme generalized for a grid with variable step  $\Delta\sigma$ .

### **Vertical velocity**

The very important issue for any air quality model is the mass consistency. It means that supplied wind and air density fields (surface pressure  $p_s$  is a full analog of air density in  $\sigma$ - $p$  coordinate system) should satisfy the continuity Eq. (3.5):

$$\frac{\partial p_s}{\partial t} + \nabla_H \cdot (p_s \mathbf{V}_H) + \frac{\partial}{\partial \sigma}(p_s \sigma) = 0. \quad (3.5)$$

In the terms of an air quality model it implies that the model maintain a uniform mass mixing ratio field of an inert tracer [Odman and Russel, 2000]. It is exactly realized only if the air quality model and a meteorological model supplying input data have the same *discretization*, i.e. grid structure, time step, and finite-difference formulation. However, many transport models (including considered one) have discretization different from that used in the data supplying meteorological model. Besides, time resolution of the meteorological data (6 hours for the model involved) is often considerably lower than the model time resolution defined by the stability condition (15-45 minutes). It requires temporal interpolation of the meteorological data. All mentioned above can lead to a considerable mass inconsistency and the uniform tracer field cannot be maintained. To adjust input meteorological fields to the model discretization vertical wind velocity  $\sigma$  is calculated from the continuity Eq. (3.5) at each step using the procedure similar to that suggested in [Odman and Russel, 2000].

Since the non-linear advection scheme is used for vertical advection, it is difficult to derive the vertical velocity directly from Eq. (3.5). Instead one can solve Eq. (3.5) using exactly the same procedure as for Eq. (3.3) and (3.4) for one time step and equate the obtained value of surface pressure to that interpolated from the input data. As a result for each vertical column of the computation domain we obtain system of non-linear equations:

$$p_s = F_k(\boldsymbol{\sigma}) \quad k = 1, \dots, N. \quad (3.6)$$

Here  $\boldsymbol{\sigma} = (\sigma_1, \dots, \sigma_N)$  is the vector of vertical wind velocities at the upper boundaries of  $\sigma$ -layers;

$N$  is the number of the layers.

Solving the Equations system (3.6) for  $\boldsymbol{\sigma}$  at each vertical column and taking into account boundary condition at the surface  $\sigma_0 = 0$  we obtain field of vertical wind velocities. We apply standard FORTRAN library MINPACK (<http://www.netlib.org/minpack/>) for the solution of the non-linear Equations system (3.6).

### ***Eddy diffusion***

Vertical eddy diffusion is described by the following equation:

$$\frac{\partial}{\partial t}(q_i p_s) = \frac{\dot{\Gamma} \partial}{\dot{\Gamma} \partial} \left[ K_z \frac{g^2 \rho^2}{p_s^2} \frac{\dot{\Gamma} \partial}{\dot{\Gamma} \partial} (q_i p_s) \right]. \quad (3.7)$$

Vertical eddy diffusion coefficient  $K_z = K_z(\lambda, \varphi, \sigma)$  is supplied by the atmospheric boundary layer module of the meteorological data preparation system (see Annex C). Non-linear diffusion Eq. (3.7) has been approximated by the second-order implicit numerical scheme in order to avoid restrictions of the time step caused by possible sharp gradients of species mixing ratio  $q_i(\sigma)$ . The obtained finite-difference equation is solved by means of the sweep method.

### ***Initial and boundary conditions***

The model computation domain has two boundaries: upper and equatorial. Long residence time of mercury in the atmosphere requires setting appropriate initial and boundary conditions to take into account mercury contained in the computation domain before the computations and the input fluxes of mercury through the boundaries.

According to the numerous measurements carried out for last decades [e.g. see *R.Ebinghaus et al.*, 1999] elemental mercury  $Hg^0$  is more or less uniformly distributed over the Northern Hemisphere (background concentrations are around 1.7 ng/m<sup>3</sup>). Vertical distribution of  $Hg^0$  is also rather uniform [*Banic et al.*, 1999]. Therefore we prescribed uniform distribution of elemental mercury concentration at the upper boundary – 0.185 pptv (corresponding to about 1.5 ng/m<sup>3</sup> at 1 atm and 20°C). On the other hand, some gradient of total gaseous mercury (TGM) was observed over the ocean between the Northern and Southern Hemispheres [e.g. see *Banic et al.*, 1999]. According to *R.Ebinghaus et al.* [2001] mean concentrations of TGM over the Northern and Southern Hemispheres are 1.7 and 1.3 ng/m<sup>3</sup> respectively. Elemental mercury makes up the main part of TGM. Summarizing the measurement data from [*Slemr*, 1996] we set the gradient of  $Hg^0$  to 0.05 ng/m<sup>3</sup>/degree at the equatorial boundary. Since the residence time of other mercury species in the atmosphere is considerably shorter we neglected their input through the boundaries. Currently, only atmospheric module is adequately developed for the mercury transport description. Therefore, the lower boundary at the Earth surface is closed. The mercury fluxes through the lower boundary are indirectly considered by deposition and “natural emission and re-emission” processes.

To fill up the model domain with mercury from anthropogenic sources of different regions and continents (it is necessary for the inter-continental transport assessment) we performed a computation run for the period of one year without any boundary and initial conditions. Then we used the obtained concentrations of mercury species as initial conditions for the regular computation run. Besides, the contribution of different sources to mercury incoming through the upper boundary is assumed to be the same as at the highest atmospheric layer.

### **3.2.2. Atmospheric chemistry**

The overview of main physical and chemical processes of mercury transformation in the atmosphere is given in Section 2.1. The current model parameterization is mostly based on the chemical scheme developed by *G.Petersen et al.* [1998]. In order to adjust the original scheme for global long-term calculations it was simplified taking into account only the most important reactions [*Ryaboshapko et al.*, 1999]. Fast irreversible reactions were assumed to be instantaneous, while reversible ones were

replaced by appropriate equilibrium conditions. Besides, up-to-date ideas of mercury atmospheric chemistry were also represented.

Mercury occurs in the atmosphere in various forms in gaseous, aqueous, and solid phase, which are undergo numerous physical and chemical transformations. The model considers the following mercury forms: gaseous elemental  $Hg_{gas}^0$ , gaseous oxidized  $Hg(II)$  (mostly  $HgCl_2$ ); particulate oxidized  $Hg_{part}$ ; and four liquid phase forms - elemental dissolved  $Hg_{aq}^0$ , mercury ion  $Hg_{aq}^{2+}$ , sulphite complex  $Hg(SO_3)_2^{2-}$ , and aggregate of chloride complexes  $Hg_nCl_m$ . The main mercury transformations in the atmosphere are schematically described in the Figure 3.4

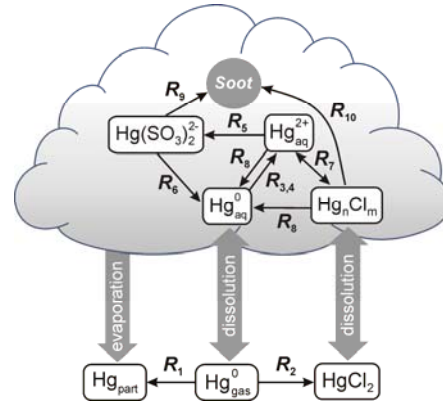


Figure 3.4. Scheme of physical and chemical transformations of mercury in the atmosphere

### Gaseous phase

One of the most important gas phase reactions is oxidation of elemental mercury by ozone ( $R_1$ ):



Since, ozone is always in plenty under ordinary atmospheric conditions this second-order reaction is described by a first-order rate expression with the reaction rate constant depending on the reactant concentration:

$$R_1 = -\frac{d[Hg_{gas}^0]}{dt} = k'_1[Hg_{gas}^0], \quad (3.9)$$

$$k'_1 = k_1[O_3]_{gas}, \quad k_1 = A \exp(-E_a / (R_{univ}T))$$

where  $A = 2.1 \cdot 10^{-18} \text{ cm}^3/(\text{molec}\cdot\text{s})$ ;  $E_a = 10.36 \text{ kJ/mole}$ ;  $R_{univ} = 8.31 \text{ J}/(\text{mole}\cdot\text{K})$ ; and ozone concentration  $[O_3]_{gas}$  is in  $\text{molec}/\text{cm}^3$  [Hall, 1995].

It is believed that the product of the reaction is particulate mercury (see Section 2.1.2). Monthly mean fields of ozone concentration over the whole Northern Hemisphere were taken from [Wang et al., 1998] and then adapted to the model grid (see Section 3.7).

Gas phase oxidation of elemental mercury by chlorine can be noticeable in the ocean boundary layer during night time ( $R_2$ ):



with the reaction rate expression:

$$R_2 = -\frac{d[Hg_{gas}^0]}{dt} = k'_2[Hg_{gas}^0] \quad (3.11)$$

$$k'_2 = k_2[Cl_2]_{gas},$$

where  $k_2 = 3.7 \cdot 10^{-18} \text{ cm}^3/(\text{molec}\cdot\text{s})$  and chlorine concentration  $[Cl_2]_{gas}$  is in  $\text{molec}/\text{cm}^3$ .

We adopted air concentrations of chlorine in the atmosphere suggested by *C.Seigneur et al.* [2001] described in Section 3.7. Although chlorine concentrations are low (about 100 ppt) in comparison with those of ozone, it could make up considerable contribution to oxidation of elemental mercury due to high reaction rate constant (Eq. 3.11).

Another possible significant oxidant is hydroxyl radical. Its influence on mercury oxidation could be comparable with that of ozone. However, because of absence of reliable data on the reaction rate constant (see Section 2.1.2) we did not include it into the scheme.

### ***Aqueous phase***

In the cloud environment elemental gaseous mercury  $Hg_{gas}^0$  is dissolved in cloud water (see Fig. 3.4). This process is described by equilibrium conditions with Henry's law constant (non-dimensional) depending on the air temperature (Eq. 2.1).

Dissolved elemental mercury  $Hg_{aq}^0$  is oxidized by ozone producing mercury oxide  $HgO$ , which is very short-lived in the liquid phase and is rapidly transformed to the mercury ion  $Hg_{aq}^{2+}$  ( $R_3$ ). Thus, the resulting reaction can be written as follows:



with the reaction rate expression:

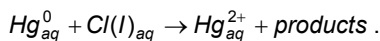
$$R_3 = -\frac{d[Hg_{aq}^0]}{dt} = k'_3[Hg_{aq}^0]; \quad (3.13)$$

$$k'_3 = k_3 H_{O_3} [O_3]_{gas},$$

where  $k_3 = 7.8 \cdot 10^{-14}$  (molec/cm<sup>3</sup>)<sup>-1</sup>s<sup>-1</sup>, ozone concentration  $[O_3]_{gas}$  is in molec/cm<sup>3</sup>.

This reaction rate constant is derived from values presented in Table 2.2 taking into account equilibrium conditions of ozone dissolution in cloud water. Temperature dependence of non-dimensional Henry's law constant  $H_{O_3}$  for ozone is described by Eq. 2.4.

Elemental mercury in aqueous phase is also oxidized by dissolved chlorine  $Cl(I)_{aq}$  with formation of mercury ion  $Hg_{aq}^{2+}$  ( $R_4$ ):



Reaction rate expression for this reaction has the following form:

$$R_4 = -\frac{d[Hg_{aq}^0]}{dt} = k'_4[Hg_{aq}^0]; \quad (3.14)$$

$$k'_4 = k_4 H_{Cl_2} [Cl_2]_{gas},$$

where  $k_4 = 3.3 \cdot 10^{-15}$  (molec/cm<sup>3</sup>)<sup>-1</sup>s<sup>-1</sup>, chlorine concentration  $[Cl_2]_{gas}$  is in molec/cm<sup>3</sup>, non-dimensional Henry's law constant  $H_{Cl_2}$  is presented in Table 2.1.

Mercury ion  $Hg_{aq}^{2+}$  reacts in the solution with sulphite ions  $SO_3^{2-}$  resulting in the formation of mercury sulphite complex  $Hg(SO_3)_2^{2-}$  ( $R_5$ ) [Petersen *et al.*, 1998]:



The reaction rate is determined by the air concentration of  $SO_2$  and the cloud water  $pH$  (see Table 2.3):

$$R_5 = -\frac{d[Hg_{aq}^{2+}]}{dt} = k'_5[Hg_{aq}^{2+}] ; \quad (3.16)$$

$$k'_5 = k_5[SO_2]_{gas}^2 \cdot 10^{4pH} ,$$

where  $k_5 = 1.8 \cdot 10^{-42}$  (molec/cm<sup>3</sup>)<sup>2</sup>s<sup>-1</sup>, and  $[SO_2]_{gas}$  is in molec/cm<sup>3</sup>.

The sulphite complex  $Hg(SO_3)_2^{2-}$  is dissociated to mercury sulphite  $HgSO_3$ , which is unstable, and is readily reduced to  $Hg_{aq}^0$ . Thus, the reduction process ( $R_6$ ) can be described as:



with the reaction rate expression:

$$R_6 = -\frac{d[Hg(SO_3)_2^{2-}]}{dt} = k_6[Hg(SO_3)_2^{2-}] , \quad (3.18)$$

where  $k_6 = 4.4 \cdot 10^{-4}$  s<sup>-1</sup>.

This process increases the amount of dissolved elemental mercury in a droplet hampering further dissolution of gaseous mercury. Hence, the scheme implies negative feedback controlling elemental mercury uptake from the air.

Mercury ion  $Hg_{aq}^{2+}$  also takes part in a number of reactions leading to the formation of various chloride complexes  $Hg_nCl_m$  ( $R_7$ ). These reversible reactions in the first approximation can be replaced by equilibrium concentrations of free mercury ions and mercury in the aggregate of chloride complexes ( $[HgCl^+]$ ,  $[HgCl_2]$ ,  $[HgCl_3]$ ,  $[HgCl_4^{2-}]$ ). The equilibrium ratio of the appropriate mercury concentrations depends upon water content of chloride ion  $[Cl^-]$  and is defined as follows [Lurie, 1971]:

$$r_1 = \frac{[Hg_nCl_m]_{aq}}{[Hg_{aq}^{2+}]} = \frac{[Cl^-]_{aq}}{1.82 \cdot 10^{-7}} + \frac{[Cl^-]_{aq}^2}{6.03 \cdot 10^{-14}} + \frac{[Cl^-]_{aq}^3}{8.51 \cdot 10^{-15}} + \frac{[Cl^-]_{aq}^4}{8.51 \cdot 10^{-16}} . \quad (3.19)$$

Besides, aqueous chemistry includes reduction of divalent mercury  $Hg(II)_{aq}$  (both mercury ion  $Hg_{aq}^{2+}$  and chloride complexes  $Hg_nCl_m$ ) in reaction with hydroperoxy radical  $HO_2^{\bullet}$  ( $R_8$ ):



The appropriate reaction rate has the following expression:

$$R_8 = -\frac{d[Hg(II)_{aq}]}{dt} = k'_8[Hg(II)_{aq}]; \quad (3.21)$$

$$k'_8 = k_8 H_{HO_2} [HO_2^*]_{gas},$$

where  $k_8 = 2.8 \cdot 10^{-17} (\text{molec/cm}^3)^{-1} \text{s}^{-1}$ , hydroperoxy radical concentration  $[HO_2^*]_{gas}$  is in  $\text{molec/cm}^3$ .

Monthly mean fields of concentration of hydroperoxy radical over the whole Northern Hemisphere were taken from [Spivakovsky *et al.*, 2000] and then adapted to the model grid (see Section 3.7). Temperature dependence of non-dimensional Henry's law constant  $H_{HO_2}$  for hydroperoxy radical is taken from [Jacobson, 1999]:

$$H_{HO_2} = 4.89 \cdot 10^4 \exp \left[ 6639.4 \left( \frac{1}{T} - \frac{1}{298} \right) \right]. \quad (3.22)$$

Sulphite and chloride complexes can be adsorbed and desorbed by soot particles in the aqueous phase ( $R_9, R_{10}$ ). Comparatively fast equilibrium of these two reverse processes can also be described by means of "dissolved-to-adsorbed ratio". Based on the appropriate reaction rates it could be taken equal to 0.2 in both cases [Petersen *et al.*, 1998]:

$$r_2 = \frac{[Hg(SO_3)_2^{2-}]_{aq}}{[Hg(SO_3)_2^{2-}]_{soot}} = \frac{[Hg_n Cl_m]_{aq}}{[Hg_n Cl_m]_{soot}} = 0.2. \quad (3.23)$$

As it was mentioned above one can distinguish three groups of mercury compounds being in equilibrium. The first group (A) contains elemental mercury in the gaseous and dissolved phase; the second one (B) consists of the mercury sulphite complex both dissolved and on soot particles; and the third group (C) includes free mercury ions, dissolved mercury chloride complexes and those on soot particles and gaseous mercury chloride:

$$\begin{aligned} A &= Hg_{gas}^0 + Hg_{aq}^0; \\ B &= \left\{ Hg(SO_3)_2^{2-} \right\}_{dis} + \left\{ Hg(SO_3)_2^{2-} \right\}_{soot}; \\ C &= Hg_{aq}^{2+} + \left\{ Hg_n Cl_m \right\}_{dis} + \left\{ Hg_n Cl_m \right\}_{soot} + \left\{ HgCl_2 \right\}_{gas}. \end{aligned} \quad (3.24)$$

According to this simplified scheme and introduced notations mercury transformations in the liquid phase are described by the following system of the first-order differential equations:

$$\begin{cases} \frac{d[A]}{dt} = -\alpha k'_2[A] + \beta k_4[B] + k'_5 \delta [C], \\ \frac{d[B]}{dt} = -\beta k_4[B] + \gamma k'_3[C], \\ \frac{d[C]}{dt} = -\gamma k'_3[C] + \alpha k'_2[A] - k'_5 \delta [C]. \end{cases} \quad (3.25)$$

Here  $\alpha = H_{Hg} L_w / (1 + H_{Hg} L_w)$  is the fraction of mercury in the A group corresponding to the dissolved form, and  $L_w$  is the non-dimensional liquid water content defined as volume of cloud water per unit volume. Parameter  $\beta = r_2 / (1 + r_2)$  denotes mercury fraction of the B group in the dissolved phase.

Value  $\gamma = r_2 r_3 / (r_2 r_3 + r_1 r_3 + r_1 r_2)$  is the fraction of mercury in the C group corresponding to the mercury ion  $Hg_{aq}^{2+}$ , whereas  $\delta = \gamma(1+r_1)$  is fraction of divalent mercury  $Hg(II)_{aq}$  in C group. Parameter  $r_3 = H_{HgCl_2} L_w / (1 + H_{HgCl_2} L_w)$  is the fraction of mercury chloride  $HgCl_2$  in cloud water. The analytical solution of the equations system with appropriate initial conditions defines mercury evolution in the aqueous phase during one time step.

The non-dimensional liquid water content  $L_w$  is evaluated according to parameterization suggested in [Hongisto, 1998]. It is equal to  $10^{-7}$  for clouds without precipitation;  $3 \cdot 10^{-7}$  for the large-scale cloudiness with precipitation; and  $10^{-6}$  for the convective cloudiness with precipitation. Cloud cover data for the two types of cloudiness (large-scale and convective) is provided by the meteorological data preparation system (Annex C).

### Mercury Depletion Events

Taking into account general ideas and review of the literature (see Section 2.1.3) on Mercury Depletion Events phenomenon (MDE) we adopt the following assumptions for the model parameterization.

1. We assume that MDE can occur only over open seawater areas, which were previously covered with ice during winter period. We exclude a possibility of penetration of  $BrO$  precursors through ice cover. Hence, we think that MDE can take place over coastal zones of the Arctic Ocean. Only those grid cells are taken into account, which cover both land and sea.
2. We suppose that the water surface was previously covered with ice if air temperature in a given point was permanently lower than  $-3^\circ C$  during wintertime (assumed seawater freezing point). Then in springtime the temperature became higher than  $0^\circ C$ , and ice melting started. Besides, during springtime ice-drift becomes more intensive and areas of open water appear. Conditionally we “switch on” the MDE module if air temperature during previous 24 hours was higher than  $0^\circ C$ . We understand the conventional character of such a “trigger” because open water can appear at low negative temperatures.
3. We assume that total duration of MDE during springtime in any point does not exceed 4 weeks and MDE takes place every day (instantly at noon) during this period. The MDE module can be “switched on” only within the period from April to June.
4. We believe that during the MDE concentration of elemental mercury near the surface layer drops down from its usual level to  $0.1 \text{ ng/m}^3$ . Oxidation of  $Hg^0$  leads to the formation of RGM (50%) and  $Hg_{part}$  (50%). The oxidized products are partly scavenged from the atmosphere within a given modeling grid cell, partly transported outside it and scavenged later.
5. We accept that the MDE covers the lowest 1 kilometre height layer of the atmosphere. Within this layer the intensity of the phenomenon linearly decreases with height to zero at the top of the layer. Hence, during the MDE elemental mercury has rising profile from  $0.1 \text{ ng/m}^3$  at the surface to its usual values at 1 km height. Contrary, oxidized forms have dropping profile from their maximum at the surface to their usual values at 1 km height.

We took the Arctic definition accepted within the AMAP programme (Fig. 3.5). It covers the terrestrial and marine areas north of the Arctic Circle, north of  $62^\circ N$  in Asia and  $60^\circ N$  in North America, modified to include the marine areas north of the Aleutian chain, Hudson Bay, and parts of the North Atlantic Ocean including the Labrador Sea.



Figure 3.5. AMAP Arctic area [AMAP, 1998]

### 3.2.3. Removal processes

Mercury is removed from the atmosphere due to dry uptake of particulate and gaseous species by the underlying surface and through the scavenging of both the gas-phase and aqueous forms with precipitation. Appropriate sub-equation of Eq. (3.1) describing removal processes of  $i^{\text{th}}$  species is as follows:

$$\frac{\partial q_i}{\partial t} = -(\Lambda_i^d + \Lambda_i^w + \Lambda_i^{aq})q_i \quad (3.26)$$

where  $\Lambda_i^d$ ,  $\Lambda_i^w$ , and  $\Lambda_i^{aq}$  are the rates of dry, wet deposition and removal of the aqueous phase respectively.

Since surface pressure is not changed in this processes, we have divided both parts of the original equation by  $p_s$ . All the removal processes are considered in the model successively.

#### *Dry deposition*

Particular mercury as well as some gaseous species is removed from the atmosphere through the contact with the underlying surface. They approach the ground surface (soil, rocks, vegetation, water etc.) due to advection, diffusion or sedimentation processes and stick to or react with it. This process is described by a part of Eq. (3.26) referred to the surface level:

$$\left. \frac{\partial q_i}{\partial t} \right|_{surf} = -\Lambda_i^d q_i \Big|_{surf} \quad (3.27)$$

where the rate of dry deposition (uptake)  $\Lambda_i^d$  is proportional to dry deposition velocity  $V_d^i$ :

$$\Lambda_i^d = V_d^i \left( \frac{g\sigma}{R_a T_a} \right)_{surf} \quad (3.28)$$

Here subscript *surf* denotes values related to the ground surface. It should be noted that the expression in the parenthesis characterizes transformation from Cartesian to ( $\sigma$ - $p$ ) coordinate system and equals to inverse absolute value of the Jacobian ( $J = -R_a T_a / g\sigma$ ).

In the current version of the model we apply a simplified parameterization of the dry deposition velocity for aerosol particles developed in [Pekar, 1996]. This approach is based on measured deposition velocities [Sehmel, 1980] as functions of aerosol size ( $d$ ), roughness of the underlying

surface ( $z_0$ ) and friction velocity parameter ( $u_*$ ). Reasoning from the analysis of scientific literature (see Section 2.1) it is adopted that mercury particle-carriers have characteristic mass median diameter  $d = 0.7 \mu\text{m}$  and dry deposition velocities of particulate mercury are described by the following formulas:

$$V_d^{part} = \begin{cases} (0.02u_*^2 + 0.01)(z_0 10^3)^{0.33}, & \text{land} \\ 0.15u_*^2 + 0.013, & \text{sea} \end{cases}$$

here  $V_d^{part}$  is in cm/s,  $z_0$  in m, and  $u_*$  in m/s.

Currently, only two types of underlying surface are distinguished in the parameterization of dry deposition of particulate mercury (land and seawater surface). It is proposed to introduce specification of dry deposition on different types of land cover (forests, grassland, deserts etc.)

Dry deposition velocity of gaseous oxidized mercury  $Hg(\text{II})$  is taken the same as for nitric acid  $V_d^{oxid} = 0.5 \text{ cm/s}$  due to similarity of their properties [Petersen et al., 1995]. This parameter does not vary seasonally and with different type of the underlying surface.

Dry uptake of elemental gaseous mercury  $Hg_{gas}^0$  by various types of underlying surface is not adequately defined yet. Some experts [US EPA, 1997] suppose that this type of mercury removal is not an essential sink on a regional and global scale. It is assumed that absorption of  $Hg_{gas}^0$  by vegetation takes place only if its concentration exceeds so-called "compensation point" (about  $20 \text{ ng/m}^3$ ). It implies that the absorption is realized only in the immediate vicinity of emission sources [Lyon et al., 1999]. According to another viewpoint [Lin and Pehkonen, 1999] dry uptake of elemental mercury is considered to be the dominating mechanism of mercury removal from the atmosphere. T.Bergan and H. Rodhe [2001] also note that elemental mercury uptake is an important mechanism of the global mercury cycle, but it is poorly considered in the literature.

Summarizing available literature data [Travnikov and Ryaboshapko, 2002] we adopt the following parameterization of the process. There is no dry uptake of elemental gaseous mercury by water surface and land surface not covered by vegetation. It is also absent during nighttime. Over the vegetated surface during daytime dry uptake velocity has the following form:

$$V_d^{gas} = \begin{cases} 0, & T_s \leq T_0 \\ A_d \frac{T_s - T_0}{T_1 - T_0} \cos \theta_s, & T_0 < T_s \leq T_1 \\ A_d \cos \theta_s, & T_s > T_1 \end{cases}$$

here  $T_s$  is the surface temperature,  $T_0 = 273 \text{ K}$  and  $T_1 = 293 \text{ K}$ ;

$A_d$  is equal to  $0.03 \text{ cm/s}$  for forests and  $0.01 \text{ cm/s}$  for other vegetation types;

$\theta_s$  is the solar zenith angle calculated according to [Jacobson, 1999].

### Wet scavenging

Scavenging of aerosol particles and soluble gases by precipitation is one of the most effective mechanisms of mercury removal from the atmosphere. First of all it concerns particulate  $Hg_{part}$  and gaseous oxidized  $Hg(\text{II})$  mercury forms. Wet scavenging rate  $\Lambda_i^w$  in Eq. (3.26) is proportional to precipitation intensity  $I_p(\sigma)$  and can be roughly approximated by the following expression:

$$\Lambda_i^w = W_i I_p(\sigma) \left( \frac{g\sigma}{R_a T_a} \right)_{surf} \frac{(q_i I_p)_{surf}}{\int q_i I_p(\sigma) d\sigma} \quad (3.29)$$

where  $W_i$  is the washout ratio of the  $i^{\text{th}}$  species defined as a ratio of the species concentration in precipitation to the concentration in the surface air.

The last ratio in (3.29) takes into account variation of precipitation intensity with altitude. This approach is aimed at fitting simulated concentration in precipitation of scavenged species to measured ones using empirical values of the washout ratios  $W_i$ .

It is assumed that presence of  $Hg$  does not affect properties of a particle with respect to wet scavenging (it make up only a minor part of the particle mass). Instead, wet scavenging of particles mainly depends on their size distribution spectrum. Both  $Hg_{part}$  [Milford and Davidson, 1985] and  $SO_4^-$  [Whitby, 1978; Schryer, 1982; Kiehl and Briegleb, 1993; Weiss et al., 1977] are accumulated in sub-micron size mode (0.1 – 1  $\mu\text{m}$ ). Allen et al. [2001] also demonstrated that more than 50% of  $Hg_{part}$  mass is settled on particles with diameter below 1  $\mu\text{m}$ . Therefore, the value of washout ratio peculiar to sulphate particles  $W_{part} = 5 \cdot 10^5$  [Iversen et al., 1989] was adopted for the parameterization of  $Hg_{part}$  wet removal. Washout ratio of gaseous oxidized mercury is taken to be equal to that of nitric acid  $W_{oxid} = 1.4 \cdot 10^6$  [Petersen et al., 1995; Jonsen and Berge, 1995].

### Aqueous phase removal

All aqueous-phase mercury species are scavenged from the atmosphere by precipitation with the removal rate:

$$\Lambda_i^{aq} = \frac{g\sigma}{R_a T_a} \frac{\Delta I_p}{L_w \Delta \sigma} \quad (3.30)$$

where  $\Delta I_p$  is the increment of precipitation within a grid cell. It is taken to be zero for negative values.

All aqueous-phase species scavenged by precipitation during its falling down return back to the atmosphere in the particulate form if precipitation is entirely evaporated before the ground.

### 3.3. MSCE-POP model

This chapter contains a description of the current version of the MSCE-POP model, which was employed for calculations of PCB and  $\gamma$ -HCH transport over the Northern Hemisphere. This model is multicompartment 3-dimensional, and includes descriptions of POP behaviour in different environmental media (atmosphere, soil, seawater, vegetation, sea ice and snow), incorporated as different program modules. Spatial resolution of the model is  $2.5 \times 2.5^\circ$  except for the seawater and ice/snow modules, which operate with resolution  $1.25 \times 1.25^\circ$ . The following sections give a detailed description of these modules as well as a general structure of the model.

### 3.3.1. General structure

Modeling of POP transport requires the physical-chemical properties of considered POPs, their emissions and also meteorological and geophysical data (Fig 3.6).

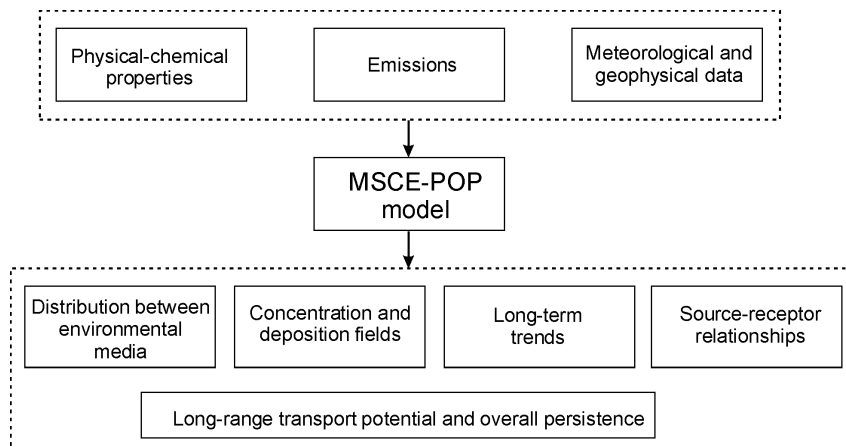


**Figure 3.6.** *Input and output data of the MSCE-POP multicompartment model*

Output model information includes:

- fields of deposition and concentration in environmental media and long-term trends of contamination in them;
- distribution of a pollutant between environmental media;
- source-receptor relationships;
- long-range transport potential and overall persistence.

The main environmental compartments included in the model are (Fig. 3.7):

- atmosphere;
- soil;
- seawater;
- vegetation;
- sea ice and snow.

It is assumed that POPs are emitted to the atmosphere from which they may be uptaken by the underlying surface (soil, seawater, sea ice/snow, vegetation) or leave the calculation domain as a result of transport. The following processes affecting the long-range transport of POP are included in the model:

#### ***The atmosphere:***

- transport with advection and diffusion;
- partitioning of a pollutant between the gaseous and particulate phase;
- wet and dry deposition of the particulate and gaseous phase to the underlying surface;
- degradation.

**Vegetation:**

- gaseous exchange with the atmosphere;
- defoliation.

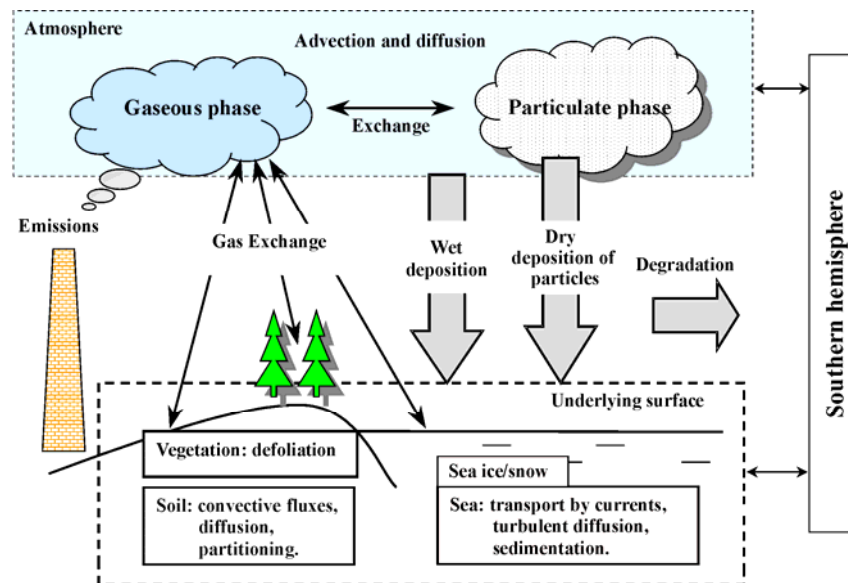


**Figure 3.7.** The scheme of processes included into the MSCE-POP hemispheric model

**Soil:**

- gaseous exchange with the atmosphere;
- partitioning between the gaseous, solid and liquid phase;
- vertical transport of a pollutant by convective water fluxes and diffusion;
- degradation.

**Seawater:**

- gaseous exchange with the atmosphere;
- transport of a pollutant by sea currents and turbulent diffusion;
- redistribution between the dissolved and particulate phase;
- sedimentation;
- degradation.

**Sea ice/snow:**

- accumulation of POPs in the snow and ice medium,
- gas phase exchange between the snow and the atmosphere,
- fluxes into the seawater as a result of snow and ice melting,
- fluxes from the seawater to the ice cover during ice bottom/lateral accretion,
- horizontal transport with drifting ice,
- degradation in the snow pack and ice.

We believe that these processes, included in the current version of the MSCE-POP hemispheric model, are vital for the description of POP transport in the environment. This statement is substantiated by a review of literature and a model sensitivity study. The latter is exemplified in Annexes D, E.

The following sections present the description of individual modules of the MSCE-POP model.

### 3.3.2. The atmosphere

This section describes processes included in the atmospheric module of the MSCE-POP hemispheric model. These processes are: partitioning of a pollutant between the gaseous and particulate phase; wet and dry deposition of both phase to the underlying surface; and degradation. Advection and diffusion schemes of the model are the same as in the MSCE-Hg-Hem model, which is described in Section 3.2.

#### *Gas/particle partitioning*

Characterization of POP partitioning between the gas and particulate phase of a pollutant is performed using subcooled liquid vapour pressure  $p_{OL}$  (Pa). According to the Junge-Pankow model [Junge, 1977; Pankow, 1987] the POP fraction  $\varphi$  adsorbed on atmospheric aerosol particles equals to:

$$\varphi = \frac{c \cdot \theta}{p_{OL} + c \cdot \theta}, \quad (3.31)$$

where  $c$  is the constant dependant on the thermodynamic parameters of the adsorption process and on the properties of aerosol particle surface. It is assumed  $c = 0.17 \text{ Pa}\cdot\text{m}$  [Junge, 1977] for background aerosol;

$\theta$  is the specific surface of aerosol particles,  $\text{m}^2/\text{m}^3$  ( $\theta = 1.5 \cdot 10^{-4} \text{ m}^2/\text{m}^3$  for background aerosol [Whitby, 1978]); to assess the influence of this assumption rough experimental calculations are made (see Annex F).

Parameter  $p_{OL}$  is pollutant-dependent and depends greatly on temperature. This dependence essentially affects the long-range transport of a pollutant and is included in the model in the form:

$$p_{OL} = p_{OL}^0 \exp \left[ -a_P \left( \frac{1}{T} - \frac{1}{T_0} \right) \right], \quad (3.32)$$

where  $T$  is the ambient temperature, K;

$T_0$  is the reference temperature, K;

$p_{OL}^0$  is the value of  $p_{OL}$  at the reference temperature  $T_0$ ;

$a_P$  is the coefficient of the vapour pressure temperature dependence, K.

#### *Dry deposition of the particulate phase*

Dry deposition flux of the particulate phase  $F_{dry}^P$  ( $\text{ng}/\text{m}^2/\text{s}$ ) is a product of dry deposition velocity  $V_d$  (m/s) and particle air concentration  $C_P$  ( $\text{ng}/\text{m}^3$ ) taken at an air reference level coinciding with the middle of the lowest atmospheric layer:

$$F_{dry}^P = V_d C_P, \quad (3.33)$$

where the dry deposition velocity from the reference level  $z_a$  is calculated according to the resistance analogy using the equation:

$$V_d = \left( r_a + 1/V_d^{surf} \right)^{-1}. \quad (3.34)$$

Here  $r_a$  is the aerodynamic resistance for turbulent transport of a pollutant from  $z_a$  to  $z_b$ , s/m;  
 $z_b$  is the height of the surface layer, m;  
 $V_d^{surf}$  is the surface dry deposition velocity from the surface layer height  $z_b$ , which is estimated by special models for different landcover.

Aerodynamic resistance  $r_a$  is calculated using the following equation [Tsyro and Erdman, 2000]:

$$r_a = \frac{0.74}{\kappa u_*} \left[ \ln \left( \frac{z_a}{z_b} \right) - \psi_h \left( \frac{z_a}{L} \right) + \psi_h \left( \frac{z_b}{L} \right) \right], \quad (3.35)$$

where  $\kappa = 0.4$  is the van Karman constant;  
 $u_*$  is the friction velocity, m/s;  
 $\psi_h$  is the similarity function for heat.

The values of deposition velocity to the underlying surface  $V_d^{surf}$  are calculated for sea, soil and forest separately.

Sea. Velocity of dry deposition over sea ( $V_d^{sea}$ ,  $z_b = 10$  m), cm/s is calculated by the equation:

$$V_d^{sea} = A_{sea} u_*^2 + B_{sea}, \quad (3.36)$$

where  $u_*$  is the friction velocity, m/s;  
 $A_{sea}$  and  $B_{sea}$  are the constants dependant on the effective diameter of particle-carriers of a considered pollutant.

(regression equation obtained by *M.Pekar* [1996] from [*Lindfors et al.*, 1991] data).

Soil. Velocity of dry deposition over soil ( $V_d^{soil}$ ,  $z_b = 1$  m), cm/s is given as follows:

$$V_d^{soil} = (A_{soil} u_*^2 + B_{soil}) z_0^{C_{soil}}, \quad (3.37)$$

where as above  $u_*$  is the friction velocity;  
 $z_0$  is the surface roughness, mm  
 $A_{soil}$ ,  $B_{soil}$ ,  $C_{soil}$  are the constants dependant on effective diameters of particle-carriers of considered POP;

(regression equation obtained by *M.Pekar* [1996] from [*Sehmel*, 1980] data).

Forest. Velocity of dry deposition to a forest ( $V_d^{forest}$ ,  $z_b = 20$  m), (adapted by *L.Erdman* [Tsyro and Erdman, 2000] from [*Ruijgrok et al.*, 1997]), m/s:

$$V_d^{forest} = E \frac{u_*^2}{u_h}, \quad (3.38)$$

where  $u_h$  is the wind speed at forest height  $h = z_b$ ;

$$E = \alpha u_*^\beta \left( 1 + \gamma \exp \left( \frac{RH - 80}{20} \right) \right) \quad (3.39)$$

is the total collection efficiency for particles within the forest canopy and  $\alpha$ ,  $\beta$  and  $\gamma$  are the experimental coefficients, depending on effective diameters of particles-carriers.

In the current model version it is assumed that the relative humidity of air is 80% of the average. Wind speed at forest height  $u_h$  (m/s) is calculated using the following equation:

$$u_h = \frac{u_*}{\kappa} \left[ \ln \left( \frac{z_b - d_0}{z_0} \right) - \psi_m \left( \frac{z_b - d_0}{L} \right) + \psi_m \left( \frac{z_0}{L} \right) \right], \quad (3.40)$$

where  $\kappa = 0.4$  is the van Karman constant;  
 $d_0 = 15$  m is zero-plane displacement;  
 $z_0 = 2$  m is the roughness length;  
 $L$  is the Monin-Obukhov parameter;  
 $\psi_m$  is the universal correction function for the atmospheric stability for momentum.

Two types of forest are distinguished in the model: deciduous forest and coniferous forest. It is assumed that dry deposition velocities to forest are calculated by Eq. (3.38) for deciduous forests during the vegetative period (only from May to September). For the remaining time, dry deposition velocities for areas covered by deciduous forests are calculated as for soil Eq. (3.37). For areas covered by coniferous forests dry deposition velocities are calculated by Eq. (3.38) throughout the year.

The amount of pollutant deposited to forest is distributed between soil and leaves/needles in accordance with the distribution coefficient  $K_{vs}$ , which is pollutant-dependent.

The coefficients  $A_{sea}$ ,  $B_{sea}$ ,  $A_{soil}$ ,  $B_{soil}$ ,  $C_{soil}$ ,  $\alpha$ ,  $\beta$  and  $\gamma$ , as well as the distribution coefficient  $K_{vs}$  between soil and leaves/needles for forests, are a part of model parameterization for a particular chemical.

### **Wet deposition**

Wet depositions of the gaseous and particulate phase are distinguished in the model. For the description of gaseous phase scavenging with precipitation, the instantaneous equilibrium between the gaseous phase in the air and the dissolved phase in precipitation is assumed:

$$C_w^d = W_g C_a^g, \quad (3.41)$$

where  $C_w^d$  is the dissolved phase concentration in precipitation water, ng/m<sup>3</sup>;  
 $C_a^g$  is the gaseous phase concentration in air, ng/m<sup>3</sup>;  
 $W_g = 1/K_H$  is the dimensionless washout ratio for the gaseous phase;  
 $K'_H$  is the dimensionless Henry's law constant.

The latter is temperature-dependent and is given by the equation:

$$K'_H = \frac{H_0}{RT} \exp \left[ -a_H \left( \frac{1}{T} - \frac{1}{T_0} \right) \right], \quad (3.42)$$

where  $T$  is the ambient air temperature, K;  
 $T_0$  is the reference temperature;  
 $R$  is the universal gas constant, J/(mol·K),  
 $a_H$  is the coefficient of Henry's law constant temperature dependence, K;  
 $H_0$  is the value of Henry's law constant at reference temperature, Pa·m<sup>3</sup>/mol.

For the description of particle bound phase scavenging with precipitation, the washout ratio determined experimentally is used:

$$C_w^s = W_p C_a^p, \quad (3.43)$$

where  $C_a^p$  is the particle bound phase concentration in the air surface layer,  $\text{ng}/\text{m}^3$ ;  
 $C_w^s$  is the suspended phase concentration in precipitation water,  $\text{ng}/\text{m}^3$ ;  
 $W_p$  is the dimensionless washout ratio for the particulate phase.

Since the meteorological data used in the model provide information for precipitation intensity in all vertical layers, wet deposition is calculated in each layer both for the gaseous and particulate phase of the pollutant.

The constants  $H_0$ ,  $a_H$ , and  $W_g$  are parameters unique to each POP.

### **Degradation**

The degradation process in the atmosphere is described by the reaction of a pollutant with OH radicals:

$$\frac{dC}{dt} = -k_{air} \cdot C \cdot [\text{OH}], \quad (3.44)$$

where  $C$  is the pollutant concentration in air (gaseous phase),  $\text{ng}/\text{m}^3$ ;  
 $[\text{OH}]$  is the concentration of OH radical,  $\text{molecules}/\text{cm}^3$ ;  
 $k_{air}$  is the degradation rate constant for air,  $\text{cm}^3/\text{s}/\text{molecules}$ ,

whose temperature dependence is provided by the equation:

$$k_{air} = A \cdot \exp(-E_a / RT), \quad (3.45)$$

where  $A$  is the exponential multiplier;  
 $E_a$  is the activation energy;  
 $R$  is the universal gas constant;  
 $T$  is the ambient temperature.

Parameters  $A$  and  $E_a$  depend on pollutant properties.

This equation is applied for the gaseous phase of a pollutant. Currently the process of degradation of a pollutant associated with particles is not included in the model due to lack of information on this topic. It should be mentioned that degradation under Arctic conditions (low temperatures, short daylight) is insignificant in comparison with that in the middle latitudes.

OH radical concentrations in the atmosphere vary substantially depending on many factors (latitude, cloudiness, day time, season, some atmospheric properties, etc.). At present, in the model as a first approximation, OH radical concentrations have no diurnal variations and depend only on the season. According to [Yu Lu and Khall, 1991] the following values were accepted:

Winter  $[\text{OH}] = 9 \cdot 10^4$ , fall, spring  $[\text{OH}] = 8 \cdot 10^5$ , summer  $[\text{OH}] = 2 \cdot 10^6$ .

To assess the influence of this assumption rough experimental calculations are made (see Annex F). Temporal and spatial variations of this parameter will be taken into account in the model in the near future.

### ***Gaseous exchange with underlying surface***

Gaseous exchange between the atmosphere and underlying surface is based on the resistance analogy. Gaseous exchange takes place with soil, vegetation, seawater and sea ice (snow). Its description is given in corresponding sections devoted to the mentioned media (types of underlying surface).

#### **3.3.3. Soil**

The soil module is based on the model developed by of *C.M.J. Jacobs and W.A.J. van Pul* [1996].

In the model, soil is separated into five horizontal layers of different thicknesses. The thicknesses of the layers are chosen individually for each pollutant considered, namely, for PCBs these are  $\Delta z_i = 0.01, 0.05, 0.2, 0.8$  and 3 cm from above, and for  $\gamma$ -HCH –  $\Delta z_i = 0.5, 0.5, 1, 2$  and 11 cm [*Shatalov et al.*, 2001]. In the current version of the model the following processes are included: partitioning of the pollutant between various phases in soil; vertical diffusion and advection with water flux; gaseous exchange with the atmosphere; and the degradation of the pollutant.

#### ***Partitioning in soil***

The total volume concentration in soil  $C$  is expressed via the mass concentration  $C^s$  of a pollutant sorbed by the soil matter, the volume concentration  $C^d$  of a pollutant dissolved in the soil water, and the gas-phase volume concentration  $C^g$  of a pollutant in the soil air,  $\text{ng/m}^3$ :

$$C = \rho_s C^s + \theta C^d + a C^g \quad (3.46)$$

where  $\rho_s = 1350$  is the bulk soil density,  $\text{kg/m}^3$ ;  
 $\theta = 0.3$  is the volumetric water content in soil;  
 $a = 0.2$  is the volumetric air content in soil.

The concentration in each phase may be represented by  $C$  using the soil partitioning coefficients  $R_s$ ,  $R_d$  and  $R_g$ :

$$C = R_s C^s = R_d C^d + R_g C^g, \quad (3.47)$$

where  $R_d = \rho_s K_d + \theta + a K_H$ ;  $R_s = R_d / K_d$ ;  $R_g = R_d / K'_H$ ;  
 $K_d = f_{OC} K_{OC}$  is the slope of the adsorption isotherm;  
 $f_{OC}$  is the fraction of organic carbon in soil;  
 $K_{OC}$  is the organic carbon distribution coefficient;  
 $K'_H$  is the dimensionless Henry's law constant (see above).

#### ***Vertical transport***

The migration of a pollutant over the vertical profile in soil is assumed to be due to diffusion and transport with the convective water flux  $J_w$  (equal to mean annual precipitation intensity  $h_p$ ,  $\text{m/c}$ ). The corresponding equation is:

$$\frac{\partial C}{\partial t} + \frac{J_w}{R_d} \frac{\partial C}{\partial z} = D_E \frac{\partial^2 C}{\partial z^2}, \quad (3.48)$$

where  $D_E$  is the effective gas-liquid diffusion coefficient,  $m^2/s$ .

The coefficient  $D_E$  is determined by:

$$D_E = \frac{\xi_g D_g}{R_g} + \frac{\xi_l D_l}{R_d}, \quad (3.49)$$

where  $D_g, D_l$  are the molecular diffusion coefficients for gas and liquid;  
 $\xi_g = a^{10/3} / \phi^2, \xi_l = \theta^{10/3} / \phi^2$  are gas and liquid tortuosity factors;  
 $\phi$  is the porosity of soil (assumed  $\phi = 0.5$ ).

### Gaseous exchange with the atmosphere

Gaseous exchange between soil and the atmosphere is parameterized using the resistance analogy.

The gaseous flux of POP from the atmosphere into the soil is driven by the difference between atmospheric gas concentration  $C_a^g$  at the air reference level  $z_a$  (equal to half the height of the lower atmospheric layer) and the soil gas-phase concentration  $C_s^g$  at the soil reference level at depth  $z_s = \Delta z_1 / 2$  ( $\Delta z_1$  – is the upper soil layer thickness). In the course of pollutant transport from the air reference level to the soil reference level it overcomes three resistances (see Fig. 3.8).

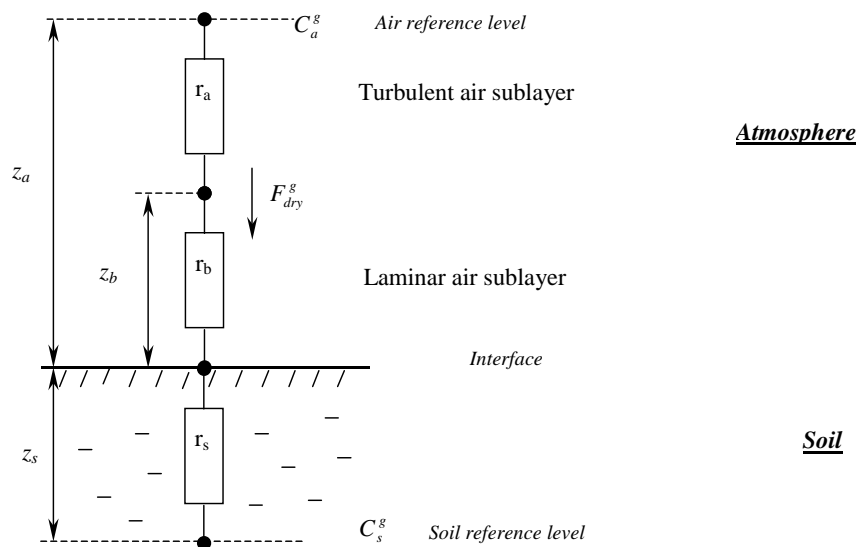


**Figure 3.8.** Resistance scheme used for the description of gaseous exchange between atmosphere and the soil

- Turbulent air sublayer resistance  $r_a$ , s/m that is, the resistance to transport through the turbulent air sublayer (from  $z_a$  to  $z_b$ . The latter is laminar sublayer height);
- Laminar surface air sublayer resistance  $r_b$ , s/m that is, the resistance to transport through the laminar surface air sublayer ( $z_b$ ) to the interface;

- Surface soil resistance  $r_s$ , s/m that is, the resistance to transport from the surface soil interface to the soil reference level ( $z_s$ ).

Hence, the formula for atmosphere/soil flux is:

$$F_{dry}^g = \frac{C_a^g - C_s^g}{r_a + r_b + r_s}, \quad (3.50)$$

where  $r_a$  is given by formula (3.35), and:

$$C_s^g = \frac{C(z_1)}{R_g} \frac{2D_E / \Delta z_1}{(2D_E / \Delta z_1 + J_w / R_d)}, \quad (3.51)$$

$$r_s = \frac{1}{R_g (2D_E / \Delta z_1 + J_w / R_d)}, \quad (3.52)$$

$$r_b = \frac{2}{\kappa u_*} \left( \frac{Sc}{Pr} \right)^{2/3}, \quad (3.53)$$

where  $Pr = 0.71$  is the Prandtl number;

$Sc = n/D_a$  is the Schmidt number;

$n = 1.5 \cdot 10^{-5}$  is the kinematic viscosity of air,  $m^2/s$ ;

$D_a$  is the molecular diffusion coefficient of a pollutant in air,  $m^2/s$ ;

$D_E$  is the effective molecular gas-liquid diffusion coefficient,  $m^2/s$ ;

$J_w$  is the convective water flux equal to mean annual precipitation intensity, m/c;

$R_d, R_g$  are the soil partitioning coefficients, dimensionless;

$u_*$  is the friction velocity, m/s.

## Degradation

The degradation process in soil is described as a first-order process by the equation:

$$\frac{dC}{dt} = -k_{soil} C, \quad (3.54)$$

where  $C$  is the pollutant concentration in soil,  $ng/m^3$ ;

$k_{soil}$  is the degradation rate constant for soil,  $s^{-1}$ .

The degradation rate constant  $k_{soil}$  is a part of model parameterization for a given pollutant. It is assumed, as a first approximation, that doubling of the degradation rate constant occurs with each 10K temperature increase. This temperature dependence was adapted from [Lammel *et al.*, 2001].

### 3.3.4. Vegetation

Three types of vegetation are distinguished in the model: coniferous forest, deciduous forest, and grass. Coefficients governing exchange processes between the atmosphere and vegetation are determined separately for each of the above vegetation types. Furthermore, we consider forest litter as an intermediate medium between vegetation and soil. In essence this medium can be viewed as an upper soil layer. The description of these media is placed in this section.

### *Gaseous exchange with the atmosphere*

The equation describing atmosphere/vegetation exchange has the following form:

$$\frac{dC_V}{dt} = \frac{1}{R_{tot}} (C_a^g - C_V / K_{Va}), \quad (3.55)$$

where  $C_a^g$  is the air concentration of a pollutant;  
 $C_V$  is the concentration in vegetation of a given type;  
 $K_{Va}$  is the bioconcentration factor (BCF);  
 $R_{tot}$  is the total resistance to the gaseous exchange given by the formula:

$$R_{tot} = R_a + a_V / k, \quad (3.56)$$

where  $R_a$  is the aerodynamic resistance of the turbulent atmospheric layer (see formula 3.27 above);  
 $k$  is the mass transfer coefficient, m/s;  
 $a_V$  is the specific surface area of vegetation,  $m^2/m^3$  (assumed value is 8000, see [Duyzer and van Oss, 1997]).

The total amount of pollutant in vegetation of a given type in a certain grid cell is then expressed by the equation:

$$Q = C_V \frac{S \cdot LAI}{a_V}, \quad (3.57)$$

where  $S$  is the area covered by vegetation of a given type within a grid cell;  
 $LAI$  is the particular leaf area index for the considered type of vegetation.

*Parameterization of BCF.* The bioconcentration factor is determined by the following equation [McLachlan and Horstmann, 1998]:

$$K_{Va} = mK_{OA}^n, \quad (3.58)$$

where  $K_{OA}$  is the partitioning coefficient between octanol and air;  
 $m, n$  are the regression coefficients presented in Table 3.1.

**Table 3.1.** Regression parameters for Equation (3.58)

	Grass [Thomas et al., 1998]	Forest, [McLachlan and Horstmann, 1998],	
		Coniferous	Deciduous
m	22.91	38	14
n	0.445	0.69	0.76

While calculating BCF using Eq. (3.58) the temperature dependence of  $K_{OA}$  should be taken into account. In the model it is assumed that:

$$K_{OA} = K_{OA}^0 \exp \left[ a_K \left( \frac{1}{T} - \frac{1}{T_0} \right) \right], \quad (3.59)$$

where as earlier  $T_0 = 283.15$  K is the reference temperature;  
 $K_{OA}^0$  is the  $K_{OA}$  value at the reference temperature;  
 $a_K$  is the coefficient of  $K_{OA}$  temperature dependence, K.

*Parameterization of the mass transfer coefficient k.* According to [Pekar et al., 1999], the mass transfer coefficient is directly proportional to the value of  $K_{OA}$ . Hence, for the evaluation of the temperature dependence of  $k$  the following formula can be used:

$$k = k_0 \exp \left[ a_K \left( \frac{1}{T} - \frac{1}{T_0} \right) \right], \quad (3.60)$$

where  $k_0$  is the  $k$  value at the reference temperature, based on the data given in [McLachlan and Horstmann, 1998] for forests and in [Pekar et al., 1999] for grass.

The values of  $K_{OA}^0$  and  $a_K$  are pollutant-dependent and their values are given in Chapter 2.

### ***Defoliation and transport to soil from forest litter***

A description of the defoliation process is also included in the model. It is assumed that part of the pollutant transported from vegetation to the forest litter is proportional to the decrease of leaf area index. For coniferous trees defoliation was described as a first-order process with a life-time  $T_{1/2} = 2$  years. In view of the permanent character of seasonal LAI variation in the tropical zone, for all types of vegetation in that zone defoliation was described as a first-order process with a life-time  $T_{1/2} = 0.5$  years. Mentioned life-times are preliminary and may be refined in the future.

The transmission of a pollutant from fallen leaves to the underlying soil was described as a first order process with the life-time depending on the latitude. On the base of the Technical Note 1/2002 [Vassilyeva and Shatalov, 2002], the life-time for the polar calculation cells was selected as  $T_{1/2} = 20$  years, for the equatorial the life-time was assumed as  $T_{1/2} = 0.1$  year. Between polar and equatorial zones, life-time is calculated using linear dependence in logarithmic scale. We admit that this is rather crude spatial parameterization, which may be improved in the future.

### ***Degradation***

There is very little data on degradation rates of considered chemicals in vegetation. For this reason, the degradation process in vegetation is not considered at present. A more detailed discussion of this question with rough estimation of degradation rates in vegetation for some POPs can be found in [Pekar et al., 1999]. On the basis of preliminary investigations, the degradation process in forest litter was introduced to the model as a first-order process with a degradation constant rate two times higher than of that in soil.

### **3.3.5. Seawater**

This section contains a general description of the processes included in the seawater module of the current version of the hemispheric MSCE-POP model.

The calculation domain is divided into 15 vertical layers with depths of 12.5, 37.5, 65, 105, 165, 250, 375, 550, 775, 1050, 1400, 1900, 2600, 3500, 4600 metres. Horizontal resolution is  $1.25^\circ \times 1.25^\circ$ , that is, two times less than the atmospheric one. More detailed spatial resolution for the ocean module allows for consideration of dynamical processes in the ocean on appreciably smaller scales than in the atmosphere. For example, this spatial resolution produces a reasonable description of sea currents nearby the coastal line.

### Basic equation

The equation for the dynamics of total concentration, including a description of advection, turbulent diffusion, degradation and sedimentation can be written as follows:

$$\frac{Dc}{Dt} = K_H \Delta_H c + \frac{\partial}{\partial z} (K_V \frac{\partial c}{\partial z}) - v_{sed} \frac{\partial c_p}{\partial z} - k_d c, \quad (3.61)$$

where  $c, c_p$  are POP total and particulate phase concentrations;

$\frac{D}{Dt}$  is the total derivative in time;

$\Delta_H$  is the Laplace operator in horizontal variables;

$K_V(z)$  and  $K_H$  are the coefficients of vertical and horizontal diffusion;

$v_{sed}$  is the sedimentation rate constant, which is estimated by the Stokes formula:

$$v_{sed} = \frac{g(\rho_p - \rho_w)d_p^2}{12\mu} \quad (3.62)$$

where  $g$  is gravitational acceleration,  $m/s^2$ ;

$\rho_p$  is mean density of particles,  $kg/m^3$ ;

$\rho_w$  is water density,  $kg/m^3$ ;

$d_p$  is the diameter of seawater particles,  $m$ ;

$\mu$  is dynamic viscosity of seawater,  $kg/m/s$ .

Fields of sea current velocities, and the depth of the upper mixed layer, used to calculate vertical turbulent diffusion, are taken from the ocean dynamic model.

### POP partitioning between different phases

POP redistribution between the dissolved phase, and the phase associated with particles, essentially affects the dynamics of POP concentration fields in the marine environment. Under the condition of instantaneous phase equilibrium establishment it is possible to consider that the relationship is always fulfilled:

$$c^p = k^p c^d \quad (3.63)$$

where  $c^p$  is the concentration of POP sorbed on particles;

$c^d$  is the concentration of POP dissolved in water;

$k^p$  is the partition coefficient between the particle and dissolved phase.

In its turn  $k^p$  may be estimated by the expression:

$$k^p = k_p^o K_p c_{prt} \quad (3.64)$$

where  $k_p^o$  is the fraction of organic matter in a particle;

$K_p$  is the equilibrium constant for sorption/desorption processes (proportional to the octanol-water coefficient  $K_{OW}$ );

$c_{prt}$  is particle concentration.

### ***Air/seawater mass exchange***

For POP flux through the sea surface the following expression is used

$$F_z|_{z=0} = \alpha_1(c_a^g / K'_H(T) - c^d)((1 - \alpha_2)D_w / \delta + \alpha_2 K_{HR} h_f) + F_{gw} + F_{pd} + F_{pw}, \quad (3.65)$$

where:

$$\delta = \delta_0 \exp(-0.15 \cdot U_a),$$

$$\alpha_1 = 1.75 - 0.75 \exp(-0.18 \cdot U_a),$$

$$\alpha_2 = 1 - \exp(-0.01 \cdot U_a).$$

- $c_a^g$  is the POP gas-phase concentration in the lower layer of the atmosphere;
- $c^d$  is the dissolved POP concentration in upper layer of the sea;
- $K'_H(T)$  is the dimensionless Henry's law constant depending on temperature;
- $D_w$  is the molecular diffusion coefficient in water;
- $\delta_0$  is the surface molecular layer depth at zero wind speed;
- $U_a$  is the wind speed absolute value near the surface;
- $h_f$  is the foam settling rate at the sea surface;
- $F_{gw}$  is the POP gas-phase flux with precipitation;
- $F_{pd}$  is the flux of POP associated with particles in the atmosphere as a result of particle dry deposition;
- $F_{pw}$  is the flux of POP associated with particles in the atmosphere as a result of particle washout with precipitation;
- $\alpha_1$  is the coefficient introduced for the description of surface sea area increase due to wave disturbance;
- $\alpha_2$  describes the relative sea surface area covered with foam at strong wind.

A more detailed description of these processes is given in [Strukov *et al.*, 2000].

Further development of the hemispheric model is associated with the refinement of the partitioning of a pollutant between the dissolved and particle phase, as well as sedimentation process. These processes strongly influence the fate of pollutants in the marine environment, and affect air concentrations over sea through gaseous exchange fluxes.

### ***POP transport with ice cover***

While POP transport modeling takes place within the scale of the globe it is necessary to consider the effect of ice coverage over the vast areas of the polar region. Sea ice plays the role of a screen between the seawater and the atmosphere. At the same time POP may be accumulated in ice itself and in the snow on it. The process of POP exchange with the atmosphere takes place on the upper snow-ice surface. When snow and ice are melting on the upper surface, or ice is melting on the lower or lateral surfaces, POP passes to the water environment. In the case of ice accretion on the lower or lateral ice surfaces, POP can penetrate into the ice medium. Furthermore, POP trapped by the sea ice and snow may be transported with ice drift. The scheme of basic processes in the atmosphere/snow/ice/seawater system is presented in Figure 3.9.

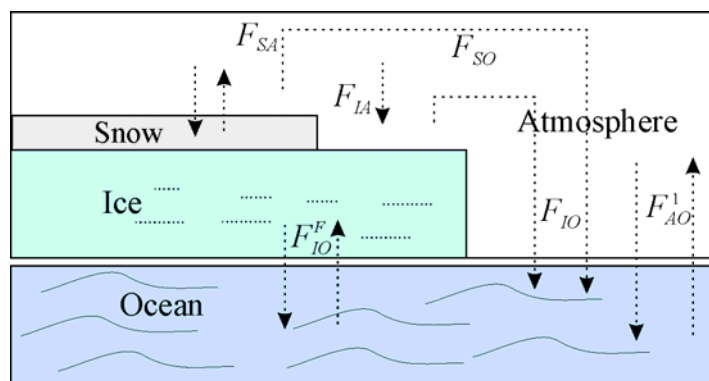


**Figure 3.9** The scheme of POP fluxes in the system atmosphere-snow/ice-seawater

$F_{SA}$  – flux between the atmosphere and the snow pack (snow on the ice surface),  $F_{SO}$  – flux from the upper surface of the snow pack into seawater (snow on the ice surface),  $F_{IA}$  – flux from the atmosphere onto the upper ice surface (no snow),  $F_{IO}$  – flux into the seawater from the upper ice surface (no snow),  $F_{IO}^p$  – flux between the seawater and the ice medium (particle phase only). Fluxes downward are considered to be positive.

POP flux between the atmosphere and seawater without sea ice may be represented as:

$$F_{AO}^0 = F_z|_{z=0} = F_d^g + F_w^g + F_d^p + F_w^p, \quad (3.66)$$

where  $F_d^g$  is POP gas phase flux between the seawater and the atmosphere;

$F_w^g$  is the gas phase flux from the atmosphere to the seawater with precipitation;

$F_d^p$  is the atmospheric dry deposition flux of POP with particles to the seawater;

$F_w^p$  is the flux of POP with particles depositing with precipitation.

To take into account the screening effect of sea ice,  $F_{AO}^0$  should be substituted for the expression:

$$F_{AO}^1 = F_{AO}^0(1 - A), \quad (3.67)$$

where  $A$  is ice compactness in dimensionless units ( $A = S_i / S$ ,  $S_i$  – ice square on sea square  $S$ ).

POP molecules in the snow-ice environment may be found in different physical states: in the gaseous phase, in snow-ice pores, sorbed on surface ice crystals (the surface phase), incorporated into organic particles contained in the snow-ice medium (the particle phase), dissolved in water, if any, in the snow or ice medium. As a first approximation the following simplifications are made:

- equilibrium between POP different phases is instantly established;
- snow and ice are not saturated by water, i.e. the POP aqueous phase is absent in the ice coverage;
- POP entering the ice surfaces with the help of active vertical mixing mechanisms (hummocking and others) are distributed in the ice medium.

In accordance with these assumptions the total concentration of the gaseous and surface phase ( $\text{kg}/\text{m}^3$ ) in snow pack is denoted as  $c_{sn}$ ; the total concentration of the gaseous and surface phase in the ice medium ( $\text{kg}/\text{m}^3$ ) – as  $c_{ic}$ ; concentration of the particle phase in the snow ( $\text{kg}/\text{m}^3$ ) – as  $c_{sc}^p$ ; and the concentration of the particle phase in the ice thickness ( $\text{kg}/\text{m}^3$ ) – as  $c_{ic}^p$ . The thickness of the snow cover on the ice and the ice thickness are denoted by  $h_{sn}$  and  $h_{ic}$ , respectively. The values of  $h_{sn}$ ,  $h_{ic}$ ,

may depend on the horizontal co-ordinates  $\lambda$ ,  $\varphi$  and time  $t$  concentration. Values  $c_{sn}$ ,  $c_{in}$ ,  $c_{sn}^p$ ,  $c_{ic}^p$  may also depend on the vertical co-ordinate  $z$ . In view of the essentially smaller vertical scale, in comparison with the horizontal, vertically averaged values of concentrations  $c_{sn}$ ,  $c_{in}$ ,  $c_{sn}^p$ ,  $c_{ic}^p$  will be considered. The area specific mass of different POP phases for the snow and ice, in accordance with ice compactness, may be represented by the expression:

$$m_{sn} = Ac_{sn}h_{sn}, \quad m_{sn}^p = Ac_{sn}^p h_{sn}, \quad m_{ic}^p = Ac_{ic}^p h_{ic}, \quad m_{is} = Ac_{is}h_{ic} \quad (3.68)$$

The balance equation of the considered POP fluxes for snow and ice medium and for the ice surface may be written as:

- for the sum of gaseous and surface phases of the snow pack:

$$\frac{dm_{sn}^g}{dt} = (F_d^g + F_w^g + F_{SO}^g)A - F_{Sd}^g, \quad (3.69)$$

- where  $F_d^g$  is the atmospheric dry deposition flux of gaseous POP between the atmosphere and snow;  
 $F_w^g$  is the atmospheric wet deposition flux of gaseous POP from the atmosphere (previously defined);  
 $F_{SO}^g$  is the flux of the gaseous and surface phases of POP from the upper snow surface into seawater;  
 $F_{Sd}^g$  is the degradation rate of gaseous and surface phases in snow.

- for the particle phase in the snow pack:

$$\frac{dm_{sn}^p}{dt} = (F_d^p + F_w^p + F_{SO}^p)A - F_{Sd}^p, \quad (3.70)$$

- where  $F_d^p, F_w^p$  are the atmospheric dry and wet deposition fluxes of POP with particles (previously defined);  
 $F_{SO}^p$  is the flux of the particle phase of POP from the upper snow surface into seawater;  
 $F_{Sd}^p$  is the degradation rate of the particle phase in snow.

- for the sum of the gaseous and surface phase in the ice:

$$\frac{dm_{is}^g}{dt} = (F_w^g + F_{IO}^g)A - F_{Id}^g, \quad (3.71)$$

- where  $F_{IO}^g$  is the flux of the surface phase of POP from the upper ice surface into seawater;  
 $F_{Id}^g$  is the degradation rate of the surface phase in ice.

The gaseous phase in the ice medium is neglected due to the small volume of the pores in the ice.

- for the particle phase in the ice medium:

$$\frac{dm_{ic}^p}{dt} = (F_d^p + F_w^p + F_{IO}^p)A - F_{Id}^p. \quad (3.72)$$

- where  $F_{IO}^p$  is the flux of the particle phase of POP between bottom and lateral ice surfaces and seawater;  
 $F_{Id}^p$  is the degradation rate of the particle phase in ice.

In these balance equations the total derivative for the two-dimensional problem is taken into consideration. Horizontal POP mass transport is realized with the ice drift along velocity fields ( $u_{ic}$ ,  $v_{ic}$ ), where  $u_{ic}$  – meridian,  $v_{ic}$  – zonal components of ice velocities.

The undefined mass fluxes in the right sides of Eq. (3.69) – (3.72) are represented by the following relationships.

The flux of the gaseous phase between the atmospheric and snow pack.

$$F_d^g = \frac{(c_a^g - c_{surf})}{r + r_{surf}}. \quad (3.73)$$

Here  $c_a^g$  is the gas phase concentration in the atmosphere;

$r$  is resistance to the atmospheric flux;

$$r_{surf} = \frac{h_{sn}}{2\phi_{sn}^{4/3} D_g}; \quad c_{surf} = c_{gsn} = c_{sn} / R_{sn}^g;$$

$D_g$  is the POP molecular diffusion coefficient in gas;

$$\phi = \frac{\rho_w - \rho_{sn}}{\rho_w} \quad \text{is snow porosity;}$$

$\rho_w, \rho_{sn}$  are water and snow density respectively,

The expression for  $F_d^g$  may be derived from the model of POP exchange between soil and the atmosphere [Pekar et al., 1998] under the condition that the water phase is absent. The coefficient  $R_{sn}^g$  in the relationship for  $c_{surf}$  is expressed through snow porosity, snow density, specific surface area of crystals  $s_{sn}$  and the coefficient of equilibrium between the gas and surface phase  $K_{ia}$  [Koziol and Pudykiewicz, 2001].

$$R_{sn}^g = \phi + \rho_{sn} s_{sn} K_{ia} \quad (3.74)$$

The values  $K_{ia}$  are connected with the POP solubility  $C_w$  and Henry's law constant:

$$\log(K_{ia}) = 0.769 \cdot \log(C_w) - 5.966 - \log(K'_H(T_{sn})), \quad (3.75)$$

where  $T_{sn}$  is snow temperature.

- For the sum of gaseous and surface phase fluxes from snow surface into the seawater (snow on the ice surface), presuming that in the majority of cases melting water leaks into the seawater through cracks and ice-holes on the ice cover (because of ice compactness  $A$  almost everywhere is less than 1):

$$F_{SO} = -dh_{sn} c_{sn} \quad \text{at} \quad h_{sn} > 0, \quad (3.76)$$

where  $dh_{sn}$  is snow cover melting rate.

- For the particle phase flux between the seawater and snow with the same assumptions

$$F_{SO}^p = -dh_{sn} c_{sn}^p \quad \text{at} \quad h_{sn} > 0 \quad (3.77)$$

- For the surface phase flux into seawater from the upper ice surface.

$$F_{IO} = -dh_{is}c_{ic} \quad \text{at } h_{is} > 0, \quad (3.78)$$

where  $dh_{is}$  is the ice melting rate on the upper ice surface.

- For the particle flux into seawater from the upper ice surface.

$$F_{IO}^p = -dh_{is}c_{ic}^p \quad \text{at } h_{is} > 0, \quad (3.79)$$

For the particle phase between the ice medium and seawater on the bottom / lateral surfaces of ice:

$$F_{IO}^p = -dh_{ib}c_{ic}^p \quad \text{at } dh_{ib} > 0 \quad (\text{melting}) \quad (3.80)$$

$$F_{IO}^p = -dh_{ib}c_w^p \quad \text{at } dh_{ib} \leq 0, \quad (\text{accretion})$$

where  $dh_{ib}$  is the ice melting rate on the lower ice surface;

$c_w^p$  is concentration of the particle phase in the water surface layer.

It is considered that at ice bottom/lateral surfaces accretion POP gas and surface phase do not enter the new ice ("freezing" effect). POPs on particles in water enter the forming ice with the particles. The availability of organic particles trapped by sea ice with POP adsorbed molecules is confirmed by numerous observations [Pfirman *et al.*, 1995].

POP degradation rates are represented by appropriate linear dependence on POP concentration:

$$F_{sd} = k_{snd}m_{sn}, \quad F_{sd}^p = k_{snd}^p m_{sn}^p, \quad F_{id} = k_{icd}m_{ic}, \quad F_{id}^p = k_{icd}^p m_{ic}^p, \quad (3.81)$$

where  $k_{snd}$ ,  $k_{snd}^p$ ,  $k_{icd}$ ,  $k_{icd}^p$  are the degradation rate constants of a substance.

Initial data for modeling, namely, fields of ice compactness, the snow cover and ice thicknesses, their melting rates, and surface temperatures are described in Section 3.9. They are calculated on the basis of the ice dynamic model, which is described in Annex E.

### 3.4. Meteorological data

The System of Diagnosis of the Lower Atmosphere (SDA) developed by Hydrometeorological Centre of Russia [Frolov *et al.*, 1994; Rubinstein *et al.*, 1997,1998; Frolov *et al.*, 1997 a,b,c] provides a set of meteorological data for the hemispheric multi-compartment models. The list of these parameters is presented in Table 3.2. The horizontal resolution of information produced by SDA system is  $2.5^\circ \times 2.5^\circ$ . Along the vertical  $\sigma$ -coordinates are used with 9 layers up to the level of 0.26 hPa.

The SDA system consists of the following main units:

- unit of initial data including the control and correction of errors,
- unit of boundary conditions,
- hydrodynamic prognostic model,
- post-processing unit.

**Table 3.2.** Meteorological parameters supplied by the SDA system for the Northern Hemisphere with resolution of 2.5°x2.5°

Parameter	Notation	Type
Wind velocity	$V_A, V_\phi$	bulk
Air temperature	$T_a$	bulk
Surface pressure	$p_s$	surface
Precipitation rate	$l_p$	bulk
Water vapour mixing ratio	$q_w$	bulk
Large-scale cloudiness	$C_L$	bulk
Convective cloudiness	$C_C$	bulk
Surface temperature	$T_s$	surface
Vertical eddy diffusion coefficient	$K_z$	bulk
Roughness of the underlying surface	$z_0$	surface
Friction velocity	$u^*$	surface
Monin-Obukhov length	$L_{MO}$	surface
Soil humidity	$M_s$	surface
Snow cover height	$h_s$	surface

### 3.5. Land cover data

Land cover information is used for correct description of deposition and exchange processes between atmosphere and different types of underlying surface. For this purpose we use 24-category USGS Land Use/Land Cover dataset obtained from NCAR Mesoscale Modeling System (MM5) [Guo and Chen, 1994]. This selection is conditioned by the availability of more detailed information on underlying surface types with high spatial resolution (10'x10'). Each grid cell is characterized by several types of surface proportional their area. Table 3.3 contains the description of USGS Land Use/Land Cover System Legend.

Since the formulation of the models described in this report does not require detailed specification of data on the underlying surface, the original 24-categories of land cover were reduced to six general categories (deciduous forests, coniferous forests, grassland, urban and built-up land, bare land and glaciers, water bodies) and redistributed over the model grid.

As an example we present here the spatial distribution of two land cover categories from reduced set: deciduous forests and grassland within the Northern Hemisphere (Fig. 3.10).

**Table 3.3.** USGS Land Use/Land Cover System Legend

No	Description
1	Urban and Built-Up Land
2	Dryland Cropland and Pasture
3	Irrigated Cropland and Pasture
4	Mixed Dryland/Irrigated Cropland and Pasture
5	Cropland/Grassland Mosaic
6	Cropland/Woodland Mosaic
7	Grassland
8	Shrubland
9	Mixed Shrubland/Grassland
10	Savanna
11	Deciduous Broadleaf Forest
12	Deciduous Needleleaf Forest
13	Evergreen Broadleaf Forest
14	Evergreen Needleleaf Forest
15	Mixed Forest
16	Water Bodies
17	Herbaceous Wetland
18	Wooded Wetland
19	Barren or Sparsely Vegetated
20	Herbaceous Tundra
21	Wooded Tundra
22	Mixed Tundra
23	Bare Ground Tundra
24	Snow or Ice

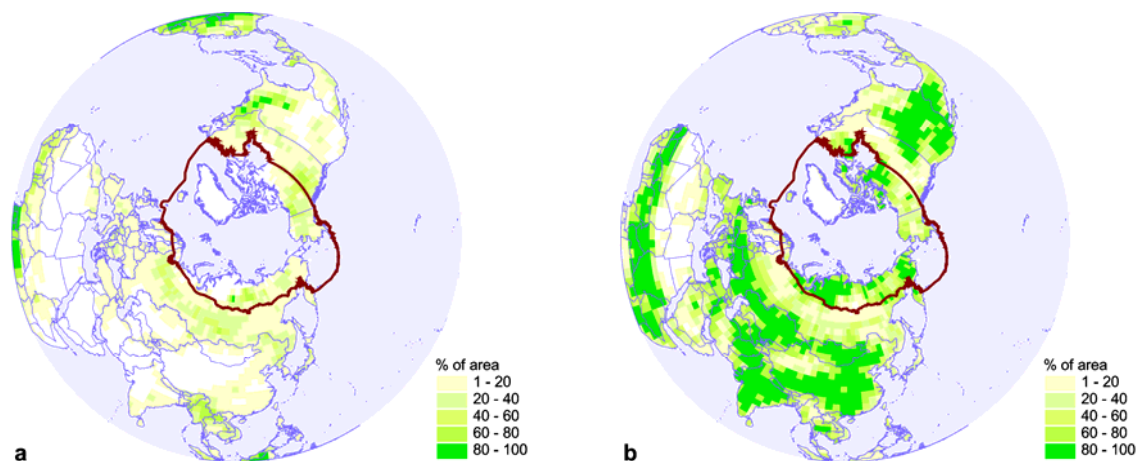


**Figure 3.10.** Fraction of the area covered by deciduous forests (a) and grassland (b) in the Northern Hemisphere

### 3.6. Leaf Area Index (LAI)

Leaf Area Index (LAI) data set is used for the description of POP gaseous exchange between the atmosphere and vegetation. The Leaf Area Index for a given grid cell implies the ratio between the area of leaves in this cell to its total area ( $\text{m}^2/\text{m}^2$ ). The geographically resolved leaf area index data with monthly resolution was adopted from CD-ROM of NASA Goddard Space Flight Center [Sellers *et al.*, 1994, 1995] and translated from  $1^\circ \times 1^\circ$  to  $2.5^\circ \times 2.5^\circ$  model grid. Consistency of these data in relation to the land cover information was investigated by correlation analysis.

### 3.7. Chemical reactants data

As it was mentioned in Section 3.2 mercury species take part in chemical reactions of oxidation and reduction both in the gaseous and aqueous phase. To describe chemical transformations one should know spatial and temporal distribution of the reactant concentrations (such as ozone, sulfur dioxide and hydroperoxy radical) in the atmosphere.

Global monthly mean data on ozone,  $\text{SO}_2$  concentration in the atmosphere were kindly provided by Dr. Malcolm Ko [Wang *et al.*, 1998; Chin M. *et al.*, 1996]. For hydroperoxy radical ( $\text{HO}_2$ ) we used monthly mean data from Dr. Clarissa Spivakovsky [Spivakovsky *et al.*, 2000]. The original data were interpolated to the model grid for the Northern Hemisphere. Air concentrations of  $\text{HO}_2$  were decreased by a factor of 10 in the cloud environment to account for its reduced photochemical activity and heterogeneous chemistry within clouds [Seigneur *et al.*, 2001]. Besides,  $\text{HO}_2$  concentrations were assumed to be zero at night. The resulted data are briefly described below.

Spatial distribution of ozone concentration in the lowest model layer is demonstrated in Figure 3.11. As seen from the figure elevated values of ozone concentration occur in the middle latitudes around the Northern Hemisphere. The highest ozone concentrations correspond to elevated regions of the Earth surface (within the model grid resolution): the Himalayas, the Rocky Mountains, and Greenland etc. Figure 3.12 shows vertical profiles of ozone concentration in the atmosphere. Each line of the plot demonstrates mean annual ozone concentration averaged along a latitude as a function of altitude

above the sea level. Blue, green, and red lines correspond to the North Pole, 45 °N, and the Equator respectively. According to the figure, ozone concentration increases with altitude in all cases. Besides, the increment is greater for high latitudes than for low ones. Thus, one can expect more intensive mercury oxidation by ozone at the upper troposphere.

Figure 3.13 shows spatial distribution of sulfur dioxide concentration in the surface air of the Northern Hemisphere. The highest concentrations of  $\text{SO}_2$  correspond to the most industrially loaded regions such as Europe, the eastern part of North America, Far East and etc. As it is shown in Figure 3.14  $\text{SO}_2$  concentration decreases with altitude practically at all latitudes (except slight growth at high altitudes over the equator). The elevated value of  $\text{SO}_2$  concentration in the ground air of the middle latitudes (green line) reflects location of main sulfur sources.

Spatial distribution of hydroperoxy radical  $\text{HO}_2$  in the surface air of the Northern Hemisphere is shown in Figure 3.15. As seen from the figure there is well pronounced gradient of  $\text{HO}_2$  concentrations from high latitudes to low ones. Besides, concentrations are more significant over land than over the ocean. Vertical distribution of  $\text{HO}_2$  concentration (Fig. 3.16) has maximum at approximately 4-5 km altitude for all latitudes. Since dissolved in cloud water  $\text{HO}_2$  takes part in aqueous-phase reactions of mercury reduction, one can expect more intensive reduction processes in low latitudes over land.

The model chemistry considers both gaseous- and aqueous-phase oxidation of elemental mercury by chlorine ( $\text{Cl}_2$ ). Currently, the direct production of  $\text{Cl}_2$  is very poorly characterized. As it is mentioned in [Keen *et al.*, 1999] sea-salt aerosol is the major source of reactive  $\text{Cl}$  gases (particularly  $\text{Cl}_2$ ) in the global troposphere. Average  $\text{Cl}$  content as sea-salt near the sea surface is estimated to be in the range 50-250 nmol  $\text{Cl}$   $\text{m}^{-3}$ . Besides, according to the results of general circulation modeling [Erickson *et al.*, 1999] average annual sea-salt  $\text{Cl}$  concentration varies in the Northern Hemisphere from about 150 nmol  $\text{Cl}$   $\text{m}^{-3}$  near the equator up to 500 nmol  $\text{Cl}$   $\text{m}^{-3}$  in the Northern Atlantic. Following C. Seigneur *et al.* [2001] we adopt air concentration of molecular chlorine in the lowest model layer over the ocean to be 100 ppt at nighttime and 10 ppt during the day and zero concentration over land. Besides, for the aqueous-phase chemistry cloud water was characterized by  $\text{pH}$  equal to 3.5 and water content of chloride ion [ $\text{Cl}^-$ ] as much as  $7 \cdot 10^{-5}$  mole/L [Acker *et al.*, 1998].

To estimate the sensitivity of modeling results to chlorine concentration two additional model runs were performed with  $\text{Cl}_2$  concentration value an order of magnitude lower (10 pptv) and higher (1 ppbv). The results show that, though, 10 times decrease of the  $\text{Cl}_2$  concentration leads up to 80% decrease of oxidized gaseous mercury  $\text{Hg}^{2+}$  over the oceans, changes of total gaseous mercury (TGM) do not exceed 5% and the decrease of annual mercury deposition flux achieves the value of 25% only in the northern parts of the Atlantic and the Pacific. As to the regions of concern, changes of mean annual TGM and deposition flux are considerably lower in this area. Increase of  $\text{Cl}_2$  concentration by an order of magnitude result in more significant changes: oxidized gaseous mercury  $\text{Hg}^{2+}$  increases several times in some marine regions, whereas mean annual TGM decreases by about 20% (mostly in the North Atlantic and the Pacific again). Annual deposition flux increases up to twice in these regions. However, changes of both mean annual TGM and deposition flux in the High Arctic and regions of the Russian North do not exceed 10%.

The model chemical scheme sensitivity to the value of chloride ion content in cloud water was investigated in [Ryaboshapko *et al.*, 2001]. It was shown that the chemical scheme is sensitive only to very low values of chloride ion content (about  $1 \cdot 10^{-6}$  mole/L). Additional calculation run with the chloride ion content  $1 \cdot 10^{-6}$  mole/L showed that maximum changes of TGM concentration of about 5% are over industrial regions. Appropriate changes of total annual  $\text{Hg}$  deposition reaches 40% in those regions but do not exceed 15% in the Arctic.

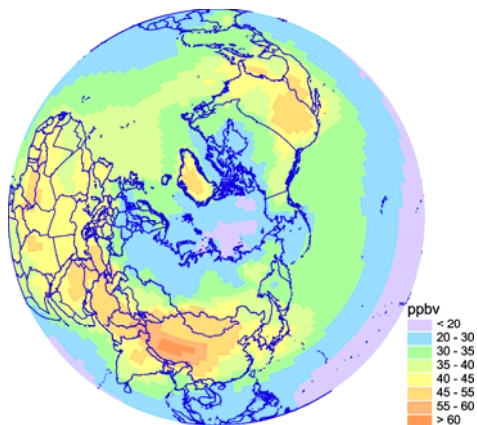


**Figure 3.11.** Spatial distribution of ozone concentration in the ground air of the Northern Hemisphere

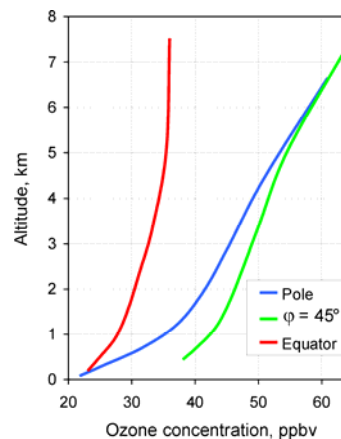


**Figure 3.12.** Vertical profiles of ozone concentration averaged along different latitudes of the Northern Hemisphere

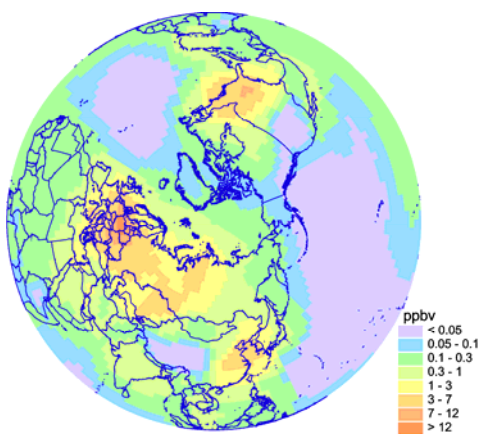


**Figure 3.13.** Spatial distribution of SO<sub>2</sub> concentration in the ground air of the Northern Hemisphere

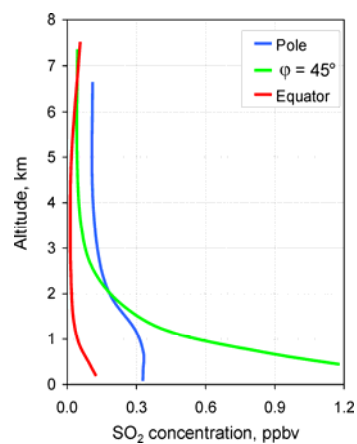


**Figure 3.14.** Vertical profiles of SO<sub>2</sub> concentration averaged along different latitudes of the Northern Hemisphere

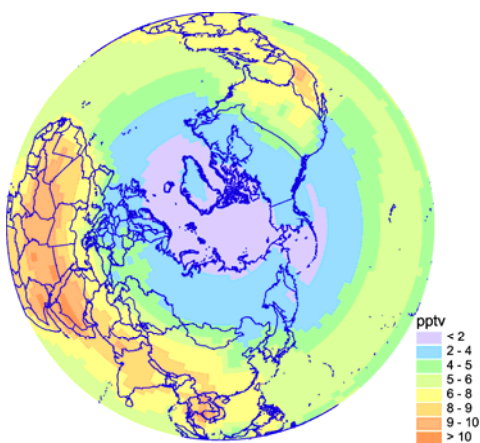


**Figure 3.15.** Spatial distribution of HO<sub>2</sub> radical concentration in the ground air of the Northern Hemisphere

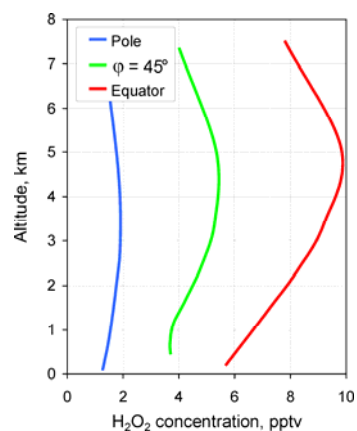


**Figure 3.16.** Vertical profiles of HO<sub>2</sub> radical concentration averaged along different latitudes of the Northern Hemisphere

### 3.8. Data on sea currents

The combined hemispheric model of the pollutants transport and diffusion, being developed under this project, consist of two main parts: atmospheric and oceanic. To determine the oceanic fields necessary for the transport-diffusion calculation (ocean currents, sea water properties), an ocean general circulation model (OGCM) is being used. The OGCM, which has been developing since early 90s, is based on primitive equations written in spherical coordinates [Resnyansky and Zelenko, 1991; 1992; 1999]. The following text will be put to the report instead of the above phrase: The former OGCM version had the limitation - the artificial zonal wall at 80N was placed, so that a near-pole area was excluded from the computational domain. During the second stage of the project implementation the model computational code was generalized in a special way to enable the inclusion of a near pole region into the model domain. The generalization involved the special finite differencing for the near-pole grid points taking into account the singularity of the latitude-longitude coordinate system. The model grid and bathymetry was constructed basing on data from the electronic version WOA98 oceanographic atlas [NOAA Atlas, 1998] (Fig. 3.17).

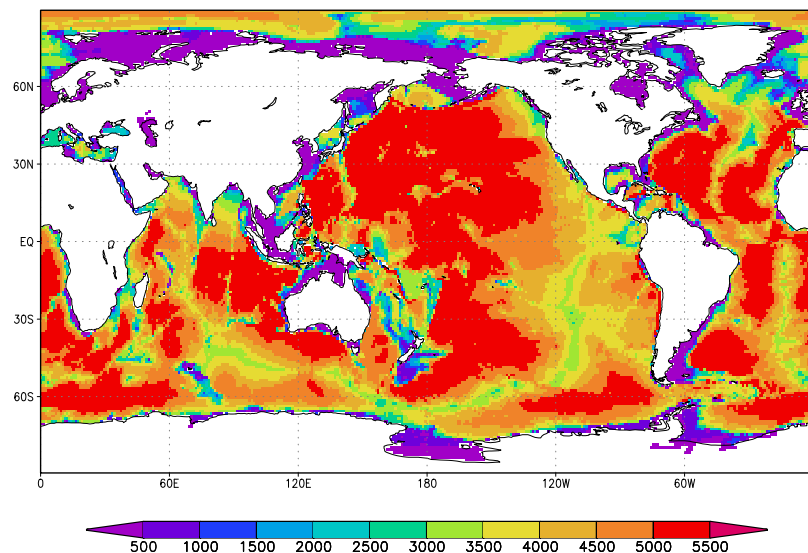


**Figure 3.17.** The  $1^\circ \times 1^\circ$  bathymetry (in meters) of the World Ocean used as input for the construction of OGCM computational domain

The surface boundary conditions necessary to compute the evolution of oceanographic fields in OGCM are expressed in terms of atmospheric forcing: wind stress, heat and fresh water fluxes. This forcing, varying with time and horizontal space, has been determined from the NCAR/NCEP re-analysis data [Kalnay *et al.*, 1996].

One more modification of the OGCM involves the incorporation of observed data on sea surface temperature and ice cover distribution, which permits to improve the quality of the derived ocean characteristics.

A number of relatively short numerical experiments have been performed in order to tune the OGCM parameters. Figure 3.18 shows the integral transport stream function obtained after a two-month model integration in the global domain including the Arctic basin. As it is seen, the modified OGCM

version quite successfully simulates basic circulation elements of the Arctic basin [Holland *et al.*, 1996; Zhang *et al.*, 1998] – the transpolar water movement from the Chukot Peninsula to the Fram Strait, the cyclonic gyre northward of Severnaya Zemlya, the anticyclonic circulation in the Bofourt Sea.

The final configuration of the OGCM has been formed for a global domain with a horizontal resolution  $1.25^\circ \times 1.25^\circ$  and with 15 levels in the vertical direction. Mean daily three-dimensional fields of ocean currents velocity and two-dimensional fields of the mixed layer depth were calculated for the further usage in hemispheric MSCE-POP transport model.

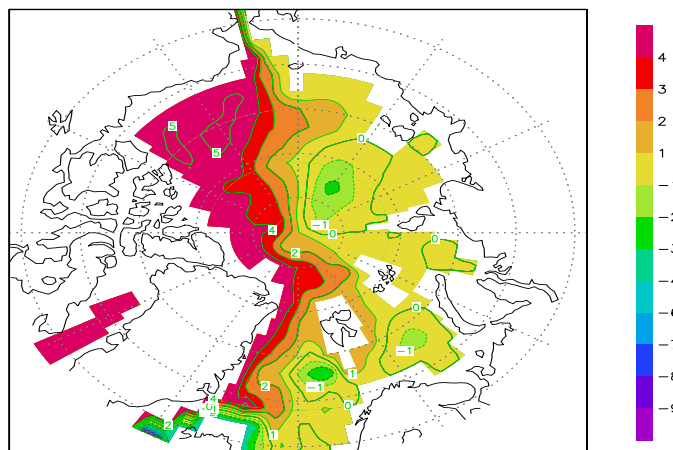


**Figure 3.18.** Transport stream function in the Arctic basin. The water moves in such a way that higher function values are at right hand side of the observer moving with water. Values are in Sverdrups ( $1 \text{ Sv} = 10^6 \text{ m}^3/\text{s}$ )

To illustrate obtained results several examples of obtained data on sea currents are given below. The Atlantic water mass of the Arctic basin, as it follows from the name, comes into the Arctic basin from the Atlantic Ocean initially as a surface inflow – the extension of Norwegian current, West Spitsbergen current and then submerges under the Arctic surface water. Several places where the surface flow submerges to deeper layers are known. One of them indicated on the majority of three-dimensional circulation schemes is located to the west of Spitsbergen Island. This submerging is reproduced in the ocean general circulation model used for the contaminants transport simulations. Figure 3.19 presents the distributions of the meridional current velocity component within two zonal sections across the Fram strait. It is clearly seen that the northward current detected in the latitude  $76.25^\circ\text{N}$  in the surface layer off the western coast of Spitsbergen Island is transformed into the flow submerging within the layer from 500 to 2500 m in the latitude  $80^\circ\text{N}$ . This pattern of abrupt submerging is typical of other places of inflow of the Atlantic water under the Arctic surface water.

The Pacific Ocean is another source of water inflow to the Arctic Basin through the Bering Strait. The mean inflow transport is about 0.8 Sv ( $1 \text{ Sv} = 10^6 \text{ m}^3/\text{s}$ ) [Coachman and Aagaard, 1988]. This average transport is superimposed by seasonal and interannual variations with amplitude of an order 1 Sv and 0.2 Sv respectively. According to [Coachman, 1993] they can reach 3 Sv to the north and 5 Sv to the south.

These features of temporal variability of the water exchange through Bering Strait are fairly well reproduced (Fig.3.20.a) by the ocean general circulation model. Similar variability occurs in other passages, through which the Arctic Ocean communicates with neighboring basins, for instance in Fram strait (Fig.3.20.b).

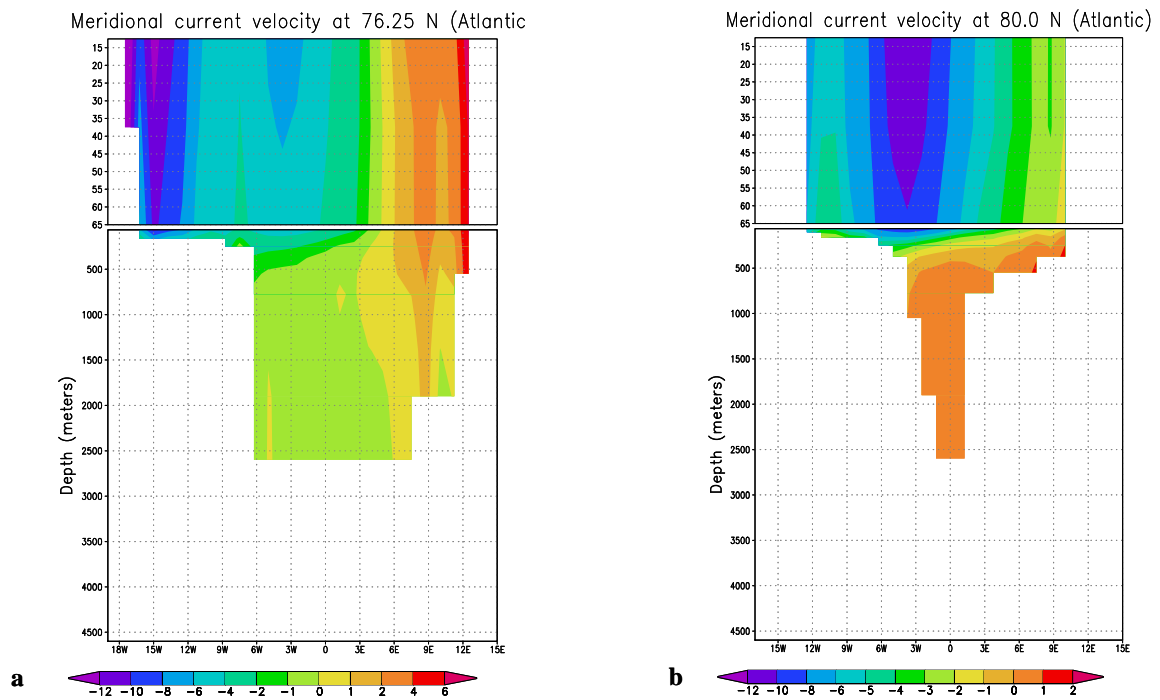


**Figure 3.19** The distribution of the meridional current velocity component (cm/s) within two zonal cross-sections through Fram strait along the latitudes 76.25° N (a) and 80°N (b). The velocity is averaged over the last (1997) year of the tree year ocean general circulation model integration on the 1.25°x1.25° grid within the computation domain involving the North Pole. Note: The velocity color scale is non-uniform: contour interval is 1 cm/s for velocities up to ±2 cm/s and 2 cm/s for velocities modules over 2 cm/s

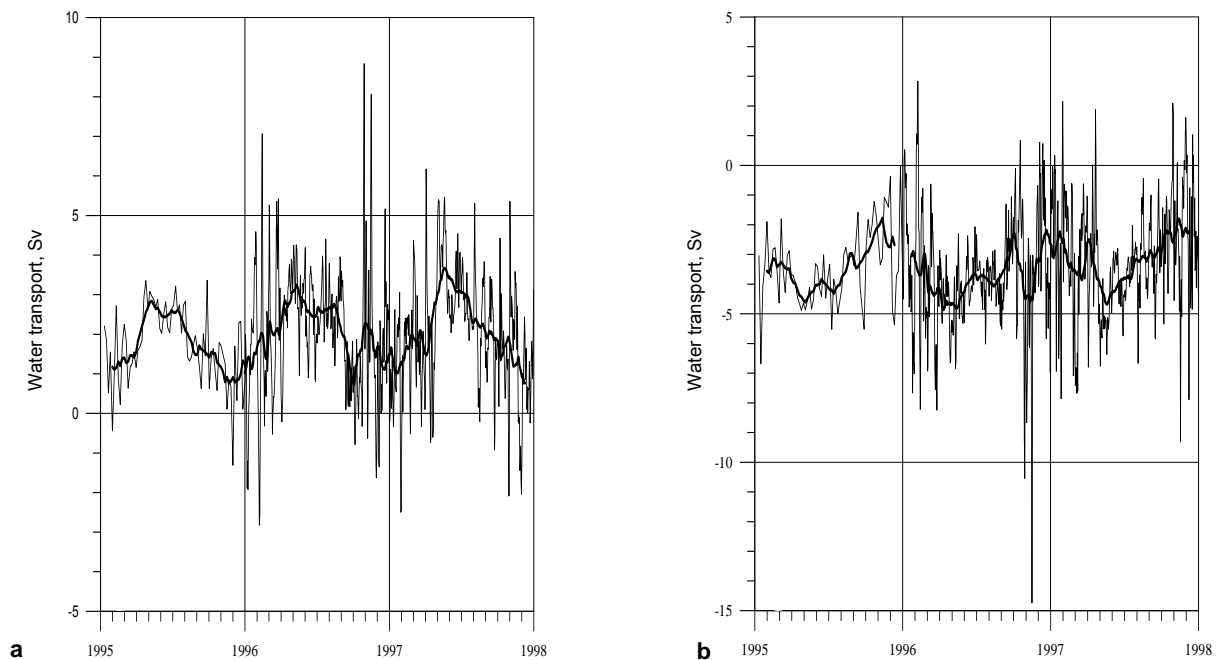


**Figure 3.20** Temporal variations of the overall transports through Bering strait (a) and Fram strait (b) over three years of 1.25°x1.25° grid model integration with daily atmospheric forcing derived from the NCEP/NCAR reanalysis. The flow transport is measured in Sverdrups (Sv, 1 Sv = 10<sup>6</sup> m<sup>3</sup>/s). Positive values correspond to the northward water transport (from the Pacific to the Arctic Ocean In the Bering Strait and from the Atlantic to the Arctic Ocean in the Fram Strait). During 1995 the flow transport values are derived in each 5 days, during 1996-97- in a day. The bold line shows 45 days running mean

### 3.9. Data on sea ice cover

The sea ice in polar regions is a mixture of open water, thin first-year ice, thicker multiyear ice, ice hummocks, snow at the top surface of ice, etc., i.e. presents non-uniform, non-isotropic medium. In this version of a simple model the sea ice is represented by three media: uniform ice, snow pack on the top of ice and open water. The evolution of the sea ice cover is governed by dynamic and thermodynamic processes. Current sea ice model includes the following processes:

- vertical heat fluxes between snow / ice and the atmosphere,
- vertical heat fluxes between ice and ocean,
- thermodynamic processes in polynyas,
- evolution of snow cover on the top of sea ice,
- ice cover dynamics in cavitation approximation,
- horizontal advection.

The heat balance equation at the upper ice surface (or snow if any) depends on heat flux due to evaporation from the surface (latent heat flux), sensible heat flux, downward long-wave radiation flux, downward short-wave (direct and scattered) solar radiation, surface albedo, and surface temperature.

The formation of new ice at the water surface in polynyas and marginal regions is determined by the net heat flux directed from the ocean to the atmosphere.

The snow pack dynamics involves precipitation, evaporation, melting and conversion of snow into ice.

The cavitation approximation in dynamics implies the resistance to compression (convergence), but absence of shear stress and resistance to divergence. In the dynamics equations there are terms of Coriolis forces, the stress induced by wind and sea currents, gravity forces arising due to sloping sea surface, and stress gradient due to ice compression.

The advection transport in the model affects all mass and thermodynamic parameters connected with sea ice.

Mean monthly output fields of the sea ice dynamics model, prepared as input data for sea ice POP transport model are

- ice thickness,
- ice compactness,
- ice / snow surface temperature,
- snow thickness on the top of ice,
- snow melting rate,
- ice melting rate at the upper boundary,
- ice melting rates at the lower and lateral boundaries.

Figure 3.21 demonstrates the simulated distribution of sea ice thickness and compactness for December and August. A large-scale structure of simulated fields is mainly consistent with distributions obtained from observations. The basic large-scale structure is well enough reproduced in

fields of ice thickness in winter and summer – the region of the most powerful perennial ice (Fig. 3.21 c,d).

Considering the obtained results as a whole it should be mentioned that model calculations make it possible to estimate characteristics of sea ice representing basic large-scale features of its evolution. In particular these data are applicable to the evaluation of impact on contaminants dispersion of such processes as ice screening impeding the exchange between the ocean and the atmosphere and comparatively long accumulation of contaminants in ice and their “rapid” discharge to the ocean during melting. To obtain more detailed and accurate data on ice cover evolution more comprehensive approach should be applied.

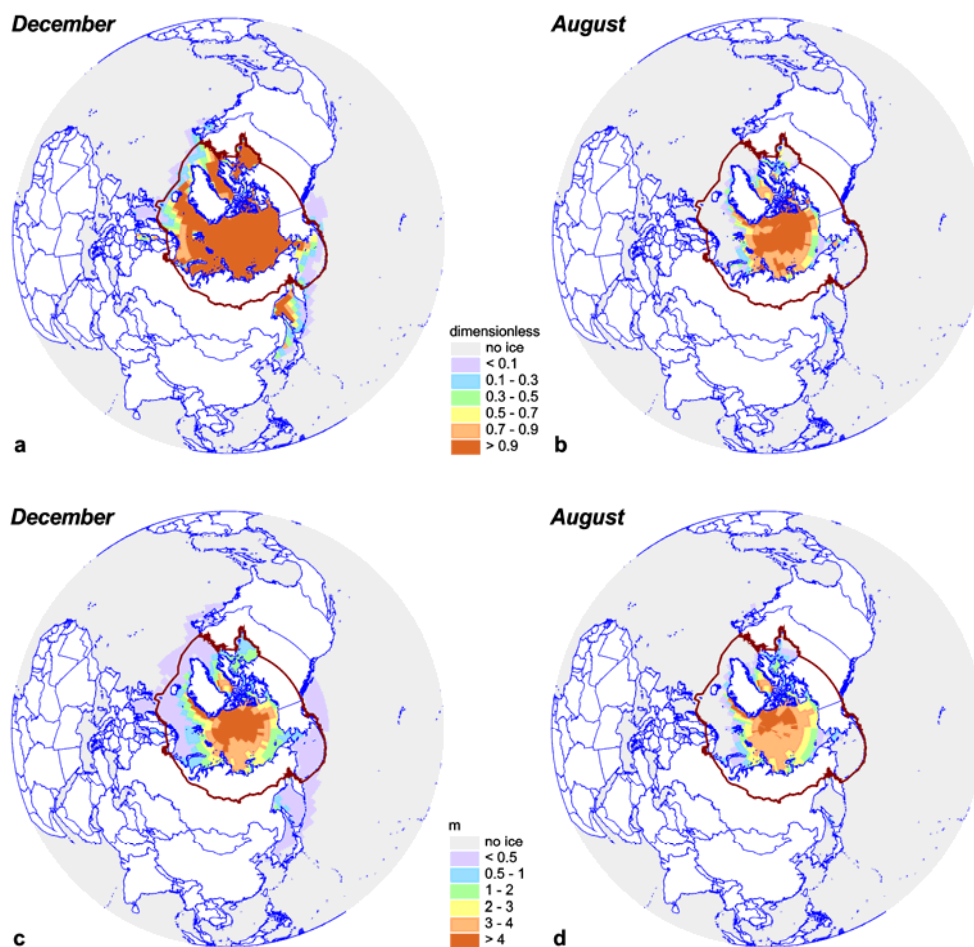


**Figure 3.21.** Simulated distribution of ice compactness (a,b) and thickness (c, d) in December and August

## References

- Acker K., D.Moller, W.Wieprecht, D.Kalass and R.Auel [1998] Investigations of ground-based clouds at the Mt. Brocken. *Fresenius. Anal. Chem.* v.361, pp.59-64.
- Allen A.G., Nemitz E., Shi J.P., Harison R.M and Greenwood J.C. [2001]. Size distribution of trace metals in atmospheric aerosols in the United Kingdom. *Atmos. Environ.*, v.32, pp.4581 – 4591.
- AMAP Assessment Report [1998] Arctic Pollution Issues, Arctic Monitoring and Assessment Programme, Oslo.
- Banic C. M., W. H. Schroeder and A. Steffen [1999] Vertical distribution of total gaseous mercury in Canada. Book of abstracts, 5<sup>th</sup> International Conference on Mercury as a Global Pollutant, 23-28 May 1999, Rio de Janeiro.
- Barrie L. A., Y. Yi, U. Lohmann, W.R.Leaith, P. Kasibhatla, G.-J. Roelofs, J. Wilson, F. McGovern, C. Benkovitz, M.A. Meliere, K. Law, J. Prospero, M. Krutz, D.Bergmann, C. Bridgeman, M. Chin, J. Christensen, R. Easter, J. Feichter, A. Jeuken, E. Kjellstrom, D. Koch, C. Land and P. Rasch [2001]. A comparison of large scale atmospheric sulphate aerosol models (cosam): overview and highlights. *Tellus* v. 53, No.B, pp. 615-645.
- Bergan T. and H. Rodhe [2001] Oxidation of elemental mercury in the atmosphere; constraints imposed by global scale modelling. *J. Atm. Chem.* v. 40, pp.191-212.
- Bott A. [1989a] A positive definite advection scheme obtained by nonlinear renormalization of the advective fluxes. *Monthly Weather Review*, v.117, pp. 1006-1015.
- Bott A. [1989b] Reply to comment on "A positive definite advection scheme obtained by nonlinear renormalization of the advective fluxes." *Monthly Weather Review*, v. 117, pp.2633-2636.
- Chin M. et al. [1996] A global three-dimensional model of tropospheric sulfate, *J. Geophys. Res.* v.101, pp.18667-18690.
- Christensen J. H. [1999]. An overview of Modelling the Arctic mass budget of metals and sulphur: Emphasis on source apportionment of atmospheric burden and deposition. Modelling and sources: A workshop on Techniques and associated uncertainties in quantifying the origin and long-range transport of contaminants to the Arctic. Report and extended abstracts of the workshop. AMAP report 99:4.
- Christensen J.H. [1997] The Danish Eulerian Hemispheric Model - a three-dimensional air pollution model used for the Arctic. *Atmospheric environment*, v.31, No.24, pp.4169 – 4191.
- Coachman L.K. [1993] On the flow field in the Chirikov Basin. *Cont. Shelf Res.*, v. 13, pp. 481-508.
- Coachman L.K. and K. Aagaard [1988] Transports through Bering Strait: Annual and inter-annual variability. *J. Geophys. Res.*, v. 93, No C12, pp. 15535-15539.
- Dabdub D. and J.H. Seinfeld [1994] Numerical advective schemes used in air quality models – sequential and parallel implementation. *Atmos. Environ.* v.28, pp.3369-3385.
- Duyzer J.H., van Oss R.F., Verhagen H.L.M., Vervaart M. and B.Boeke [1997] Determination of deposition parameters of a number of persistence organic pollutants by laboratory experiments. TNO-report TNO-MEP-R97/150.
- Easter R. C. [1993] Two modified versions of Bott's positive-definite numerical advection scheme. *Monthly Weather Review*, v.121, pp.297-304.
- Ebinghaus R., C. Temme, H.H.Kock, A. Löwe and W.H.Schroeder [2001] Depletion of atmospheric mercury concentrations in the Antarctic. Book of Abstracts, 6<sup>th</sup> International Conference on Mercury as a Global Pollutant, 15-19 October 2001, Minamata, Japan.
- Ebinghaus R., R.M. Tripathi, D.Walischlager and S.E.Lindberg [1999] Natural and anthropogenic mercury sources and their impact on the air-surface exchange of mercury on regional and global scales. In: Ebinghaus R., Turner R. R., Lacerda de L. D., Vasiliev O., and Salomons W. (Eds.) Mercury contaminated sites. Springer, Berlin, 3-50.
- Erickson D.J., III, C. Seuzaret, W.C. Keene, and S.L. Gong [1999] A general circulation model based calculation of HCl and ClNO<sub>2</sub> production from sea salt dechlorination: Reactive Chlorine Emissions Inventory. *J. Geophys. Res.*, v. 104, No.D7, pp.8347-8372
- Frolov A., A.Vaznik, E.Astahova, J.Alferov, D.Kiktev, I.Rosinkina and K.Rubinstein [1997a] A System of diagnosis of lower atmosphere for monitoring transboundary pollutant transport. *Meteorology and Hydrology*, No 4, pp.5-15.
- Frolov A., A.Vaznik, E.Astahova, J.Alferov, D.Kiktev, I.Rosinkina and K.Rubinstein [1997b] A System of diagnosis of lower atmosphere for monitoring transboundary pollutant transport. The main algorithms. *Meteorology and Hydrology*, No 5, pp.5-13.
- Frolov A., A.Vaznik, E.Astahova, J.Alferov, D.Kiktev, I.Rosinkina and K.Rubinstein [1997c] A System of diagnosis of lower atmosphere for monitoring transboundary pollutant transport: Precipitation and clouds. *Meteorology and Hydrology*, No.6, pp.5-15.
- Frolov A., K.Rubinstein, I.Rosinkina, A.Vajnik, D.Kiktev, E.Astachova and J.Alferov [1994] A System of diagnosis of lower atmosphere for of transboundary air pollutant transport. EMEP/MSC-E and RHMC report 1/94.
- Grell G.A., J Dudhia and D.R.Stauffer, [1995] A Description of the Fifth-Generation Penn State/NCAR Mesoscale Model (MM5). NCAR/TN-398+STR. NCAR Technical Note. June 1995. Mesoscale and Microscale Meteorology Division. National Center for Atmospheric Research, Boulder, Colorado, pp.122.
- Guo, Y.-R., and S. Chen [1994] Terrain and land use for the fifth-generation Penn State/NCAR mesoscale modelling system (MM5): Program TERRAIN. NCAR Tech. Note, NCAR/TN-397+IA, 119 pp. [Available from the National Center for Atmospheric Research, P. O. Box 3000, Boulder, CO 80307.]
- Gustin M. S., S.Lindberg, F.Marsik, A.Casimir, R.Ebinghaus, G.Edwards, C.Hubble-Fitzgerald, R.Kemp, H.Kock, T.Leonard, J.London, M.Majewski, C.Montecinos, J.Owens, M.Pilote, L.Poissant, P.Rasmussen, F.Schaedlich, D.Schneeberger, W.Schroeder, J.Sommar, R.Turner, A.Vette, D.Wallschlaeger, Z.Xiao and H. Zhang H. [1999] Nevada STORMS project: Measurement of mercury emissions from naturally enriched surfaces. *J. Geophys. Res.* v.104, No D17, pp. 21831-21844.

- Hall B. [1995] The gas phase oxidation of mercury by ozone. *WASP* 80, pp.301-315.
- Holland D.M., L.A.Mysak, J.M.Oberhuber [1996] Simulation of the mixed-layer circulation in the Arctic Ocean. – *J. Geophys. Res.*, 101, №C1, p.1111-1128.
- Hongisto M. [1998] HILATAR, a regional scale grid model for the transport of sulphur and nitrogen compounds. FMI Contributions No. 21, Finnish Meteorological Institute, Helsinki, Finland.
- Iversen T., J.Saltbones, H.Sandnes, A.Eliassen and O.Hov [1989] Airborne transboundary transport of sulphur and nitrogen over Europe - model descriptions and calculations. EMEP/MSC-W Report 2/89, Meteorological Synthesizing Centre - West, Oslo, Norway.
- Jackson T. A. [1997] Long-range atmospheric transport of mercury to ecosystems, and the importance of anthropogenic emissions - a critical review and evaluation of the published evidence. *Environ. Rev.* v.5, pp. 99-120.
- Jacobs C.M.J. and W.A.J. van Pul [1996] Long-range atmospheric transport of persistent organic pollutants, I: Description of surface - atmosphere exchange modules and Implementation in EUROS. National institute of public health and the environment, Bilthoven, the Netherlands. Report No722401013.
- Jacobson M. Z. [1999] *Fundamentals of atmospheric modeling*. Cambridge University Press. 656 p.
- Jonsen J.E. and E. Berge [1995] Some preliminary results on transport and deposition of nitrogen components by use of Multilayer Eulerian Model. EMEP/MSC-W Report 4/95, Meteorological Synthesizing Centre – West, Oslo, Norway.
- Junge C.E. [1977] Basic considerations about trace constituent in the atmosphere is related to the fate of global pollutant. In: Fate of pollutants in the air and water environment. Part I, I.H. Suffet (ed.) (Advanced in *Environ. Sci. Technol.*, v.8), Wiley-Interscience, New York.
- Kalnay E., M. Kanamitsu, R. Kistler, W. Collins, D. Deaven, L. Gandin, M. Iredell, S. Saha, G. White, J. Woollen, Y. Zhu, A. Leetmaa, R. Reynolds, M. Chelliah, W. Ebisuzaki, W.Higgins, J. Janowiak, K. C. Mo, C. Ropelewski, J. Wang, Roy Jenne, Dennis Joseph [1996] The NCEP/NCAR 40-Year Reanalysis Project. - Bulletin of the American Meteorological Society, v. 77, No 3, p.437-471.
- Keene W.C., M. Aslam, K. Khalil, D.J. Erickson, III, A. McCulloch, T.E. Graedel, J.M. Lobert, M.L. Aucott, S.L. Gong, D.B. Harper, G. Kleiman, P. Midgley, R.M. Moore, C. Seuzaret, W.T. Sturges, C.M. Benkovitz, V. Koropalov, L.A. Barrie, and Y.F. Li [1999] Composite global emissions of reactive chlorine from anthropogenic and natural sources: Reactive Chlorine Emissions Inventory. *J. Geophys. Res.* v.104, No.D7, pp.8429-8440.
- Kiehl J.T. and B.P. Briegleb [1993] The relative roles of sulfate aerosols and greenhouse gases in climate forcing. *Science*, v. 260, pp.311 – 314.
- Kim J. P. and W.F.Fitzgerald [1986] Sea-air partitioning of mercury in the Equatorial Pacific Ocean. *Science*, v.231, pp.1131-1133.
- Kozioł A.S. and J.A. Pudykiewicz [2001] Global-scale environmental transport of persistent organic pollutant. *Chemosphere*, v.45, pp.1181-1200.
- Lammel G., J.Feichter and A.Leip [2001] Long-range transport and multimedia partitioning of semivolatile organic compounds: a case study on two modern agrochemicals. Report No.324.
- Lin C.-J. and S.O.Pehkonen [1999] The chemistry of atmospheric mercury: a review. *Atmos. Environ.* v.33, pp.2067-2079.
- Lin C.-J., M.-D. Cheng and W. Schroeder [2001] Transport patterns and potential sources of total gaseous mercury measured in Canadian high Arctic in 1995. *Atmospheric Environment.*, v.35, pp.1141-1154.
- Lindfors V., S.M.Joffe and J.Damski [1991] Determination of the wet and dry deposition of sulphur and nitrogen compounds over the Baltic sea using actual meteorological data. Finnish Meteorological Institute Contributions N 4, Helsinki.
- Lurie Yu. Yu. [1971] *Handbook for Analytical Chemistry*. Khimiya, Moscow, 454 p.
- Lyon B., G. Rice, O.R.Bullock and P.Selby [1999] Modelling the local scale atmospheric fate of anthropogenic mercury emissions. In: Mercury as a Global Pollutant. 5<sup>th</sup> International Conference, Rio de Janeiro, May 23-28, 1999. Book of abstracts, p. 110.
- Marchuk G. I. [1975] *Methods of numerical mathematics*. Springer-Verlag, New York. 316 p.
- Milford J.B. and Davidson C.I. [1985] The sizes of particulate trace elements in the atmosphere - A review. *JAPCA*, v. 35, No.12, pp.1249-1260
- Mclachlan M. and M.Horstmann [1998] Forests as filters of airborne organic pollutants: a model. *Environ. Sci. Technol.*, v.32, pp. 413-420.
- McRae G.J., W.R. Goodin and J.H. Seinfeld [1982] Numerical solution of the atmospheric diffusion equation for chemically reacting flows. *Journal of Computational Physics*, v.45, pp.1-42.
- NOAA Atlas [1998] NOAA Atlas NESDIS No. 27-32. U.S. Gov. Printing Office, Wash., D.C.
- Odman M. T. and A.G. Russell [2000] Mass conservative coupling of non-hydrostatic meteorological models with air quality models. In: Gryning S.-E. and Batchvarova E. (Eds.) Air pollution modelling and its application XIII. Kluwer Academic/Plenum Publishers, New York, pp. 651-660.
- Pacyna J.M. [1996] Emission inventories of atmospheric mercury from anthropogenic sources. In: Global and Regional Mercury Cycles: Sources, Fluxes and Mass Balances. Ed. By W.Baeyens, R.Ebinghaus and O.Vasiliev. NATO ASI Series, 2. Environment, v. 21. Kluwer Academic Publ., Dordrecht, pp. 161-177.
- Pacyna, E. G. and Pacyna J. M. [2002] Global emission of mercury from anthropogenic sources in 1995. *WASP*. v.137, No. 1, pp.149-165.
- Pankow J.F. [1987] Review and comparative analysis of the theories on partitioning between the gas and aerosol particulate phases in the atmosphere. *Atmos. Environ.*, v.21, pp.2275-2283.
- Pekar M. [1996] Regional models LPMOD and ASIMD. Algorithms, parametrization and results of application to Pb and Cd in Europe scale for 1990 MSC-E Report 9/96, September.
- Pekar M., A.Gusev, N.Pavlova, B.Strukov, L.Erdman, I.Ilyin and S.Dutchak [1998] Long-range transport of selected POPs. Development of transport models for lindane, polychlorinated biphenyls, benzo[a]pyrene. EMEP/MSC-E Report 2/98, Parts I.

- Pekar M., N.Pavlova, A.Gusev, V.Shatalov, N.Vulikh, D.Ioannisian, S.Dutchak, T.Berg and A.-G. Hjelbrekke [1999] Long-range transport of selected persistent organic pollutants. Development of transport models for polychlorinated biphenyls, benzo[a]pyrene, dioxins/furans and lindane Joint report of EMEP Centres: MSC-E and CCC, EMEP Report 4/99.
- Petersen G., A.Iverfeldt and J. Munthe [1995] Atmospheric mercury species over central and northern Europe. Model calculations and comparison with observations from the nordic air and precipitation network for 1987 and 1988. *Atmos. Environ.* v.29, pp.47-67.
- Petersen G., J.Munthe, K. Pleijel, R. Bloxam and A.V.Kumar [1998] A comprehensive Eulerian modelling framework for airborne mercury species: Development and testing of the tropospheric chemistry module (TCM). *Atmospheric Environment*, v. 32, No. 5, pp. 829-843.
- Pfirman S.L., H.Eicken, D.Bauch and W.F. Weeks [1995] The potential transport of pollutants by Arctic sea ice. *Science of the Total Environment* (NLD), v.159, pp.129-146.
- Resnyansky Yu.D. and A.A.Zelenko [1991] Parametrization of the upper mixed layer in an ocean general circulation model. - *Izvestiya of the USSR Academy of Sciences. Atmosphere and Ocean Physics*, v.27, No 10, pp.1080-1088.
- Resnyansky Yu.D. and A.A.Zelenko [1992] Numerical realization of the ocean general circulation with parametrization of the upper mixed layer. *Proceedings of the USSR Hydrometcentre*, v.323, pp.3-31.
- Resnyansky Yu.D. and A.A.Zelenko [1999] Effects of synoptic variations of atmospheric forcing in an ocean general circulation model: direct and indirect manifestation. *Meteorology and Hydrology*, No.9 pp.66-77.
- Rubinstein K. and D.Kiktev [1998] Comparison System of the Atmospheric Lower-Layer Diagnostic System(SDA) for Pollution Transfer Modeling of MSC - East(Moscow) and MSC - West(Oslo). *Proceeding of International Conference of Air Pollution Modeling and Simulation*. Paris, 26-29 October 1998.
- Rubinstein K., Frolov A., Vaznik A., Astachova E., Rosinkina I., Kiktev D. and J.Alferov [1997] Diagnostic System of Atmosphere Lower-Layer for Pollution Transfer Modelling. *Revista. International de Contaminational. Ambienal*, v.13, No.1, pp.23-34.
- Ruijgrok, W. Tieben H. and P.Eisinga [1997] The dry deposition of particles to a forest canopy: a comparison of model and experimental results. *Atmospheric Environment*, v.31, pp. 399-415.
- Ryaboshapko A., I.Ilyin, A.Gusev, O.Afinogenova, T.Berg and A.-G. Hjelbrekke [1999] Monitoring and modelling of lead, cadmium and mercury transboundary transport in the atmosphere of Europe. Joint report of EMEP centres: MSC-E and CCC, EMEP Report 3/99, Meteorological Synthesizing Centre – East, Moscow, Russia.
- Ryaboshapko A., Ilyin I., Bullock R., Ebinghaus R., Lohman K., Munthe J., Petersen G., Segneur C., Wangberg I. [2001] Intercomparison study of numerical models for long-range atmospheric transport of mercury. Stage I: Comparison of chemical modules for mercury transformations in a cloud/fog environment. EMEP/MSC-E Technical report 2/2001, Meteorological Synthesizing Centre – East, Moscow, Russia
- Schryer D.R. (editor) [1982] Heterogeneous atmospheric chemistry. American Geophysical Union, Washington.
- Sehmel G. A. [1980] Particle and gas dry deposition: a review. *Atmos. Environ.* v.14, pp. 983-1011.
- Seigneur C., Karamchandani P., Lohman K., Vijayaraghavan K., and Shia R.-L. [2001] Multiscale modeling of the atmospheric fate and transport of mercury. *J. Geophys. Res.* v.106, No.D21, pp.27795-27809.
- Sellers P.J., S.O. Los, C.J. Tucker, C.O. Justice, D.A. Dazlich, G.J. Collatz, and D.A. Randall [1994] A global 1 by 1 degree NDVI data set for climate studies. Part 2: The generation of global fields of terrestrial biophysical parameters from the NDVI. *International Journal of Remote Sensing*, v.15, No.17, pp.3519-3545.
- Sellers P.J., S.O. Los, C.J. Tucker, C.O. Justice, D.A. Dazlich, G.J. Collatz, and D.A. Randall [1995]. A revised land surface parameterization (SiB2) for atmospheric GCMs. Part 2: The generation of global fields of terrestrial biophysical parameters from satellite data. Submitted to *Journal of Climate*.
- Shatalov V., A.Malanichev, N.Vulykh, T.Berg and S.Manø [2001] Assessment of POP transport and accumulation in the environment. EMEP Report 4/2001, Moscow.
- Slemr F. [1996] trends in atmospheric mercury concentrations over the Atlantic ocean and the Wank Summit, and the resulting concentrations on the budget of atmospheric mercury. In: Baeyens W., Ebinghaus R. Vasiliev O. (Eds.), *Global and Regional Mercury Cycles: Sources, Fluxes and Mass Balances*. NATO-ASI-Series, Kluwer Academic Publishers, Dordrecht, The Netherlands, pp. 33-84.
- Spivakovsky C.M., J.A.Logan, S.A.Montzka, Y.J.Balkanski, M.Foreman-Fowler, D.B.A.Jones, L.W.Horowitz, A.C.Fusco, C.A.M.Brenninkmeijer, M.J.Prather, S.C.Wofsy, M.B.McElroy [2000] Three-dimensional climatological distribution of tropospheric OH: Update and evaluation, *J.Geophys.Res.*, v.105, pp.8931-8980.
- Strand A. and Ø.Hov [1996] A model strategy for the simulation of chlorinated hydrocarbon distributions in the global environment. *Water, Air and Soil Pollution*, v.86, pp.283-316.
- Strukov B., Resnyansky Yu., Zelenko A., Gusev A. and V.Shatalov [2000] Modelling long-range transport and deposition of POPs in the European region with emphasis to sea currents. EMEP/MSC-E Report 5/2000.
- Thomas G., Smith K.E.C., Sweetman A.J. and K.C.Jones [1998] Further studies on air-pasture transfer of polychlorinated biphenyls. *Environmental Pollution*, v.102, pp.119 - 128.
- Travnikov O. [2001] Hemispheric model of airborne pollutant transport. EMEP/MSC-E Technical Note 8/2001, Meteorological Synthesizing Centre - East, Moscow, Russia.
- Travnikov O. and Ryaboshapko A. [2002] Modelling of mercury hemispheric transport and depositions. EMEP/MSC-E Technical Report 6/2002, Meteorological Synthesizing Centre - East, Moscow, Russia.
- Tsyro S. and L.Erdman [2000] Parametrization of aerosol deposition processes in EMEP MSC-E and MSC-W transport models. EMEP/MSC-W Technical Note.

- US EPA [1997] Mercury Study Report to Congress. Vol. III, Fate and Transport of Mercury in the Environment. US-EPA-452/R-97003.
- Vassilyeva G. and V. Shatalov [2002] Behaviour of persistent organic pollutants in soil. MSC-E Technical Note 1/2002.
- Vulykh N. and Putilina V. [2000] Hexachlorobenzene: Properties, emissions and content in the environment. *EMEP/MS-CHE Technical note 6/2000*, Meteorological Synthesizing Centre – East, Moscow, Russia.
- Wang Y. J. et al. [1998] Global simulation of tropospheric O<sub>3</sub>-NO<sub>x</sub>-hydrocarbon chemistry 2: Model evaluation and global ozone budget. *J. Geophys. Res.* v.103, pp. 10727-10755.
- Wania F. [1999] Global Modelling of Polychlorinated Biphenyls. June 1999.
- Wania F. and D.Mackay [1999] Global Chemical Fate of  $\alpha$ -Hexachlorocyclohexane. 2. Use of a Global Distribution Model for Mass Balancing, Source Apportionment, and Trend Prediction. *Environmental Toxicology and Chemistry*, v.18, No.7, pp.1400-1407.
- Wania F., D.Mackay, M.McLachlan, A.Sweetman and K.Jones [1999] Global Modelling of Polychlorinated Biphenyls. Synopsis of Research Conducted under the 1998/99 Northern Contaminants Program. Indian and Northern Affairs, Canada, pp.61-70.
- Weiss R.E., Waggoner A.P., Charlson R.J., and Ahlquist N.C. [1977] Sulfate aerosol: its geographical extent in the mid-western and southern United States. *Science* v.195, pp.979 – 981.
- Whitby K.T. [1978] The Physical Characteristics of Sulphur Aerosols. *Atmos. Environ.*, v.12, pp.135 – 159.
- WMO [2000] Report and proceedings of the WMO/EMEP/UNEP workshop on modelling of atmospheric transport and deposition of persistent organic pollutants and heavy metals (Geneva, Switzerland, 16-19 November 1999).
- Yanenko N. N. [1971] *The method of fractional steps. The solution of problems of mathematical physics in several variables*. Springer-Verlag, New York. 160 p.
- Yu Lu and M.A.K. Khalil [1991] Tropospheric OH: model calculation of spatial, temporal and secular variations. *Chemosphere*, v. 23, pp.397-444.
- Zhang J., W.D.Hibler III, M.Steele and D.A.Rothrock [1998] Arctic ice-ocean modeling with and without climate restoring. *J. Phys. Oceanogr.*, v.28, No 2, pp.191-217.

## Chapter 4

## EMISSION SOURCES

Available emission data of Hg, PCBs and  $\gamma$ -HCH for the Northern Hemisphere were collected. Emission sources were divided into several groups according to their geographical location. The key criterion for the selection of this or that region as an aggregate of emission sources is the possible influence of emissions from this region on the Russian North. The number of the selected regions is different for different pollutants. The general division of the Northern Hemisphere into aggregate regions of emission sources is presented in Figure 4.1. For brevity sake we introduce generalized names for some regions, e.g. so-called "Central Asia" actually includes Central, Western, and Southern Asia. Here one should note that composition of some regions varies from pollutant to pollutant. Selected regions of emission sources for all considered pollutants are presented in Table 4.1.



**Figure 4.1.** *Regions of the Northern Hemisphere considered in the source-receptor analysis*

**Table 4.1.** *Selected regions of the Northern Hemisphere*

Hg	PCBs	$\gamma$ -HCH
1. Russia	1. Russia	1. Russia
2. Northern Europe	2. North-western Europe	2. Western Europe
3. Western Europe	3. South-eastern Europe	3. Eastern Europe
4. Eastern Europe	4. Americas	4. Southern Europe
5. Southern Europe	5. South-eastern Asia (including China and Japan)	5. Americas
6. Americas	6. Central Asia (including India) and Africa	6. China
7. Central Asia (including India)		7. India
8. China		8. Asia (Central and South-eastern Asia)
9. Japan		9. Africa
10. South-eastern Asia		
11. Africa		

As one can see from the table among mercury sources China and Japan were isolated as individual emitters. For  $\gamma$ -HCH it seemed important to consider emissions of China and India separately, whereas Northern Europe is not included since  $\gamma$ -HCH emissions in this region are absent in 1996. The Americas (North and South) were considered as one source due to long distances from the Russian North.

Due to close location and significant influence of some regions of the Russian Federation on the Russian North pollution we subdivided the territory of Russia into twelve regions according to the current administrative division and their potential impact on the Arctic ecosystems.

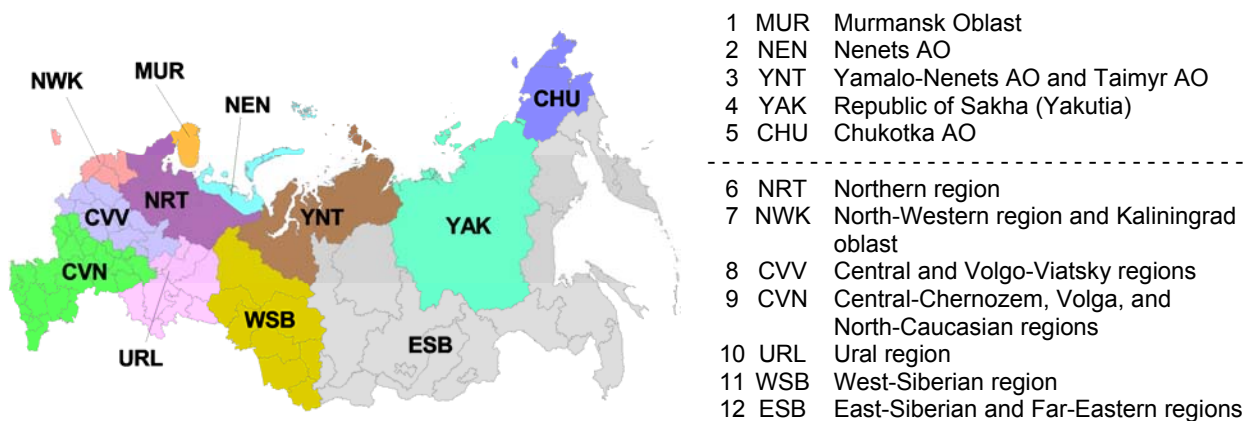


Figure 4.2. Location of twelve aggregated regions of Russian Federation chosen for the source-receptor analysis

Location of chosen regions of the Russian Federation is presented in Figure 4.2. The figure contains specification of the regions along with their codes. The first five regions are also considered as receptors. Below the description of emission data for each pollutant of concern, namely, Hg, PCBs, and  $\gamma$ -HCH, is given.

## 4.1. Hg emissions

### *Anthropogenic sources*

Anthropogenic constituent of mercury emission to the atmosphere dominates over industrial and urbanized regions of the world. To evaluate the anthropogenic input of mercury in the Northern Hemisphere we utilize the latest available global emission inventory for 1995 [Pacyna and Pacyna, 2002]. The digital emission data were provided in the framework of the current project by secretariat of AMAP. The original dataset has global coverage with resolution  $1^\circ \times 1^\circ$  and mercury chemical speciation into three forms: elemental  $Hg^0$ , gaseous oxidized  $Hg^{2+}$ , and particulate  $Hg_{part}$ . Besides it distinguishes area and point sources, the latter ones are divided into three categories according to their height (below 50 m, 50-150 m, higher 150 m). To adapt the emission of each species to the model input it has been redistributed to the model grid ( $2.5^\circ \times 2.5^\circ$ ) assuming uniform distribution over a grid cell. It is assumed that sources of the first two height categories emit to the lowest model layer, whereas those of the third one emit to the second layer.

Spatial distribution of anthropogenic mercury emission density in the Northern Hemisphere is presented in Figure 4.3 (for each species individually). As seen from the figures the most significant emission sources are in Eastern Asia, Europe and the Eastern part of North America. Some emissions are also in Hindustan and Arabian Peninsula. The total anthropogenic mercury emission from the Northern Hemisphere is estimated as 1887 tonnes per year.

In order to assess mercury transport to the Russian North the whole hemispheric emission field was divided into several continents and regions (see Table 4.1): Russia, Northern Europe, Western Europe, Eastern Europe, Southern Europe, Africa, Central Asia (including India), South-Eastern Asia (excluding China and Japan), China, Japan, and the Americas.

Relative contributions of each continent or region to the total mercury emission in the Northern Hemisphere are presented in Figure 4.4. According to the diagram more than one third (34%) of the

total mercury is emitted from China. Considerable emissions are also in Central Asia (14%), the Americas (11%), Japan (9%), and Russia (8%). The contributions of other regions do not exceed 7%.

Figure 4.5 shows contributions of different regions of Russian Federation to its total emission. Central-Chernozem, Volga, and North-Caucasian regions (CVN, 22%), Ural region (URL, 22%), and Central and Volgo-Viatsky regions (CVV, 20%) are the sources, which make the main contribution to the total anthropogenic emission of mercury in Russian Federation.

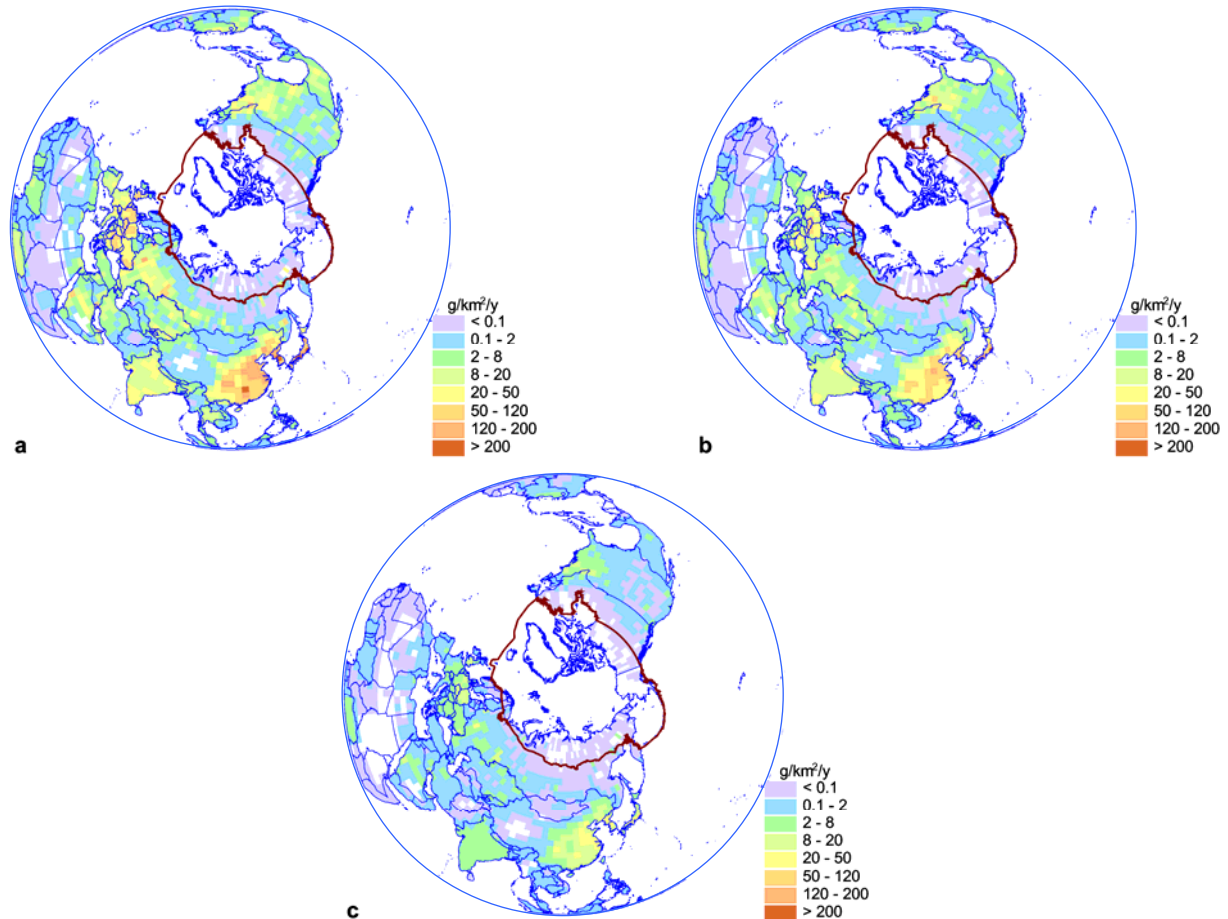


**Figure 4.3.** Spatial distribution of mercury anthropogenic emissions density in the Northern Hemisphere in 1995: (a) –  $Hg^0$ ; (b) –  $Hg^{2+}$ ; (c) –  $Hg_{part}$ ,  $g/km^2/y$

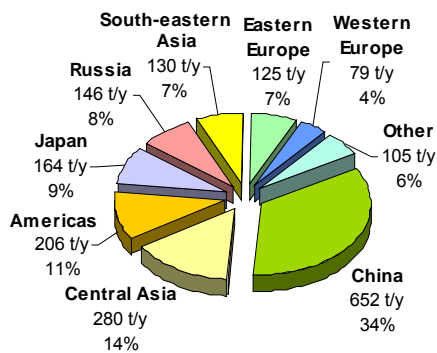


**Figure 4.4.** Relative contribution of different continents and regions to the total anthropogenic emission of mercury in the Northern Hemisphere

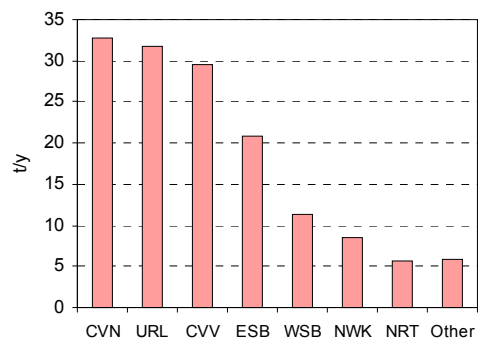


**Figure 4.5.** Contribution of different regions to the total anthropogenic emission of mercury in Russian Federation

Annual emissions of each mercury species from different regions in the Northern Hemisphere are summarized in Table 4.2. It should be noted that average speciation (over continents of the Northern Hemisphere) is approximately 58% of  $Hg^0$ , 33% of  $Hg^{2+}$ , and 9% of  $Hg_{part}$ .

**Table 4.2.** Annual anthropogenic emission of mercury species in the Northern Hemisphere, t/y

Region	$Hg^0$	$Hg^{2+}$	$Hg_{part}$
China	372	223	57
Central Asia	151	103	26
Americas	113	72	20
Japan	97	53	15
Russia	94	41	11
South-eastern Asia	80	39	10
Eastern Europe	72	42	11
Western Europe	53	21	6
Africa	33	21	5
Southern Europe	27	10	3
Northern Europe	3	2	1

### Natural sources and re-emission

Estimates of the global natural emission and re-emission of mercury available in the literature are very uncertain (see Table 4.3). The most reasonable of them vary from 700 to 3200 t/y for the continents and from 600 to 2900 t/y for the World Ocean (here we do not consider evidently overestimated values more than  $1 \cdot 10^4$  t/y). Detailed survey of natural emission fluxes was made by the authors in [Travnikov and Ryaboshapko, 2002]. In the current assessment we decided to consider two emission scenarios to evaluate possible uncertainty of natural emission and re-emission. The first one is based on highest emission estimate [Seigneur et al., 2001] – 2000 t/y from land and 2000 t/y from the ocean (Scenario I). The second scenario utilizes the lowest estimate from [Lamborg et al., 2002] - 1460 t/y from land and 800 t/y from the ocean (Scenario II). Here we do not distinguish natural emission and re-emission of mercury.

**Table 4.3.** Natural mercury emissions and reemission to the atmosphere

Emission value, t/y			Reference	Note
Land	Ocean	Total		
		$1.9 \cdot 10^5$	Jaworowski et al., 1981 (quoted in Geological Survey of Canada, 1995)	
	2900		Kim and Fitzgerald, 1986	$\pm 1800$ t/y
730	1770	2500	Nriagu, 1989	
		3000	Lindqvist et al., 1991	From 2000 to 9000 t/y
		$2.9 \cdot 10^4$	Geological Survey of Canada, 1995	3500 t/y for Canada only
1000	2000	3000	Fitzgerald and Mason, 1996	1400 t/y of re-emission from the ocean
1400-3200			Lindberg et al., 1998	
1000			Carpi and Lindberg, 1998	
700			Ebinghaus et al., 1999	500 t/y in mercury belts
2000	2000	4000	Seigneur et al., 2001	1500 t/y of re-emission from land
1320	1100	2420	Bergan and Rodhe, 2001	Without re-emission
1460	800	2260	Lamborg et al., 2002	400 t/y of re-emission from the ocean and 460 t/y from land

We distinguish five types of the Earth surface: (1) glaciers, (2) seawater, (3) background soils, (4) soil of the geochemical mercury belts, and (5) soil of mercury deposit areas. Mercury emission fluxes differ for different surface types. Glaciers of the Northern Hemisphere include Greenland, permanent ice of the Arctic and high-mountain glaciers. It is presumed that there is no mercury emission from this type of the surface.

To distribute mercury emission over the ocean we accept the idea suggested by *J.Kim and W.Fitzgerald* [1986] that mercury emission intensity is proportional to biological productivity in seawater. For this purpose we utilize monthly mean data on the ocean primary production of carbon (see Fig. 4.6) described in [*Behrenfeld and Falkowski, 1997*] and available through the Internet (<http://marine.rutgers.edu/opp/>). According to the data global primary productivity is equal to  $4.6 \cdot 10^{13}$  kg C/y. Since about 60% of the global ocean primary production falls on the Northern Hemisphere we assess the total ocean mercury emission in the Northern Hemisphere as 1200 t/y for Scenario I and 500 for Scenario II.

The entire continental area in the Northern Hemisphere constitutes approximately 75% of the global land area (excluding Greenland and the Antarctic). Thus, the total natural emission of mercury from land in the Northern Hemisphere can be roughly assessed as 1500 t/y for Scenario I and 1100 for Scenario II. Mercury flux from the land significantly depends on soil mercury content. From this point of view we divide land surface into three categories according to the adopted soil classification: background soils, soils of mercury belts, and soils of mercury deposits. Location of geochemical mercuriferous belts and productive mercury deposits areas are schematically shown in Figure 4.7. These data were generalized from [*Jonasson and Boyle, 1971; Gustin et al., 1999*] and adapted to the model grid. In the current assessment we do not take into account any influence of vegetation on the emission process.

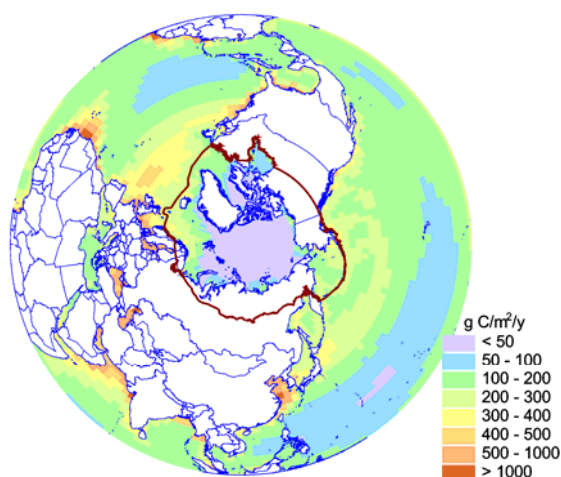


**Figure 4.6.** Spatial distribution of annual primary production of carbon in the ocean of the Northern Hemisphere [*Behrenfeld and Falkowski, 1997*], g C/m<sup>2</sup>/y

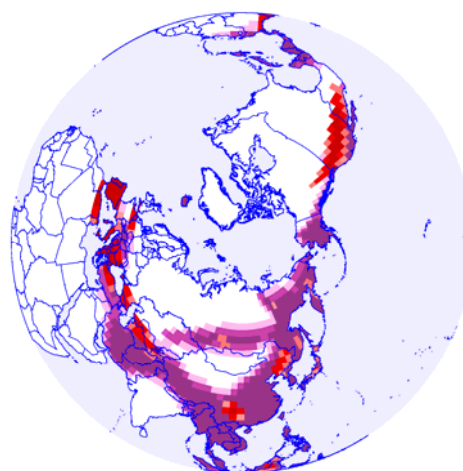


**Figure 4.7.** Generalized map of geochemical mercuriferous belts (magenta color) and productive deposit areas (red color) in the Northern Hemisphere [*Jonasson and Boyle, 1971; Gustin et al., 1999*]

As it was mentioned in Section 2.1 temperature dependence on mercury emission flux can be described by an Arrhenius type equation. Besides, empirically derived activation energies of the process have close values both for background (17.3 - 29.4 kcal/mole) and for enriched soils (25.2 kcal/mole). To parameterize the temperature dependence we choose value 20 kcal/mole for all soil

types. On the contrary, we consider pre-exponential factor depending on the soil type: the factor for background soil is five times lower than for soils of the mercury belts, and ten times lower than for the deposits areas. Besides, the emission flux is assumed to be zero for negative values of the soil temperature in the centigrade scale. Fitting total land emission in the Northern Hemisphere to the adopted value we obtain the following temperature dependence of the mercury flux from soil:

$$F_{Hg} = \begin{cases} A_s \exp(-10^4 / T_s), & T_s > T_0 \\ 0, & T_s \leq T_0 \end{cases}$$

Here mercury flux  $F_{Hg}$  is in  $\text{ng/m}^2/\text{h}$ ;  $A_s$  is equal to  $6.4 \cdot 10^{14}$  for background soils,  $3.2 \cdot 10^{15}$  for the mercury belts, and  $6.4 \cdot 10^{15}$  for deposit areas; surface temperature  $T_s$  is in K and  $T_0 = 273$  K. Currently we do not consider dependence of the mercury emission flux on insolation. It is assumed that mercury is emitted to the atmosphere in the elemental form both from land and from the ocean.

Resulting spatial distribution of mean annual mercury emission from natural sources is shown in Figure 4.8 for both scenarios. As one can see from the figure the highest mercury emissions from land correspond to mercuriferous belts and deposit areas (compare with Fig. 4.7). Mercury fluxes at the high latitudes are considerably lower even for the mercury belts due to low soil temperature. Emission flux from seawater is lowest in the Middle Pacific and the highest in internal seas and coastal waters at low latitudes. There is no mercury emission from Greenland and from seawater near the pole because of permanent glaciers.

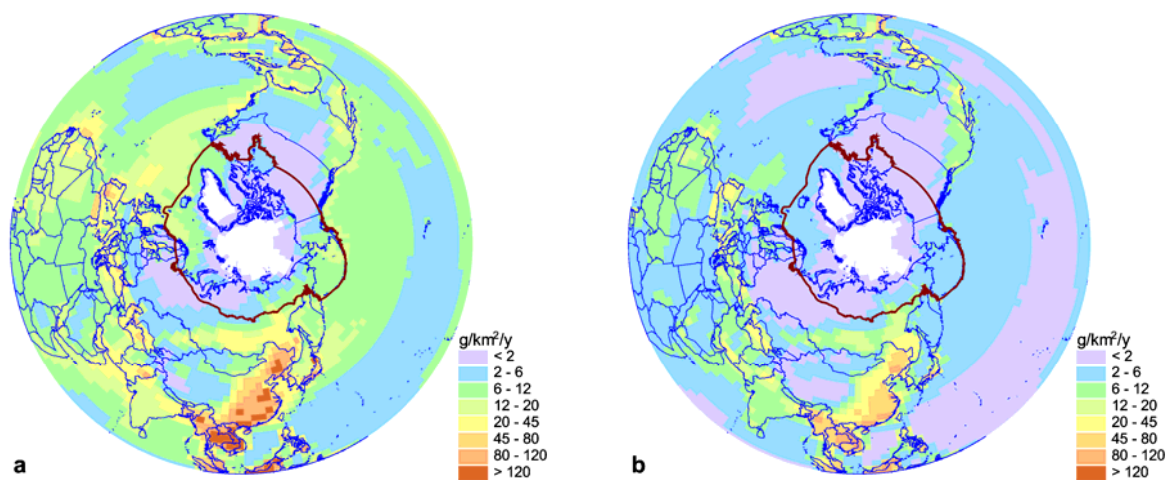


**Figure 4.8.** Spatial distribution of mean annual natural emission density of mercury in the Northern Hemisphere: (a) – Scenario I, (b) – Scenario II

Figures 4.9.a and 4.9.b illustrate seasonal variation of natural mercury emission basing on Scenario I. As one can see variation of land emission flux is considerably higher (up to an order of magnitude) than that of seawater due to greater amplitude of land surface temperature alteration. Moreover, a significant part of the surface has no mercury emission in wintertime due to negative surface temperatures.

To assess influence of natural sources from different parts of the Northern Hemisphere the emission field was divided into 8 general parts: Europe, Asia, the Americas, Africa, the Atlantic Ocean, the Pacific Ocean, the Indian Ocean, and the Arctic Ocean.

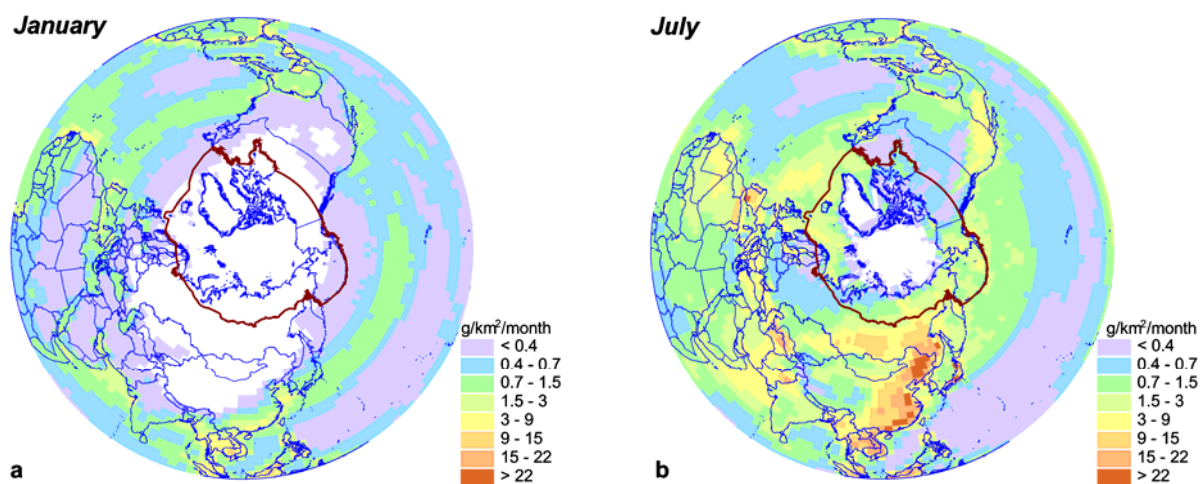


**Figure 4.9.** Spatial distribution of monthly mean natural emission density of mercury in the Northern Hemisphere (Scenario I), g/km<sup>2</sup>/month

## 4.2. PCB emissions

This section outlines the data on PCB emissions which were used in the AMAP project for the assessment of the impact of the different regions of the Northern Hemisphere on the contamination of the Russian North. The global emission inventory of 22 PCB congeners for 1930-2000 was prepared by *K. Breivik et al.* [2002b]. The inventory was based on historical data on global production and consumption of these PCBs [Breivik et al., 2002a]. A concise review of the data presented in papers [Breivik et al., 2002a,b] and of the Northern Hemisphere PCB emission sources selected for modeling purposes is given below.

### 4.2.1. PCB emission estimates according to [Breivik et al., 2002a,b]

Mixtures of chlorinated biphenyls with varying numbers of chlorine atoms and with different sets of individual homologues and congeners have been produced in many countries under various trade names: Aroclor (USA), Clophen (West Germany), Kanechlor (Japan), Delor (Czechoslovakia), Pyroclor (United Kingdom), Sovol, Sovtol (Russia) and others. The total global production of PCBs from 1930 to 1993 amounted to approximately 1.3 million t. More than 70% was accounted for by tri-, tetra and penta-chlorinated biphenyls. To quantify the production of the 22 selected congeners for the period under consideration, data on the production and chemical composition of the individual technical mixtures (for example, Aroclor 1242) were used. In the absence of required data from some producers, the annual production of individual congeners and homologues were estimated by a set of annual production-weighted default compositions.

The authors assessed the global consumption pattern by compiling information on import, export and national consumption of PCBs by country and year, including restrictions on PCB imports in various countries and regions. The inventory of PCB global consumption involves estimates for 114 countries. The results suggest that almost 97% of the intentionally produced PCBs have been used in the Northern Hemisphere.

To go from data on the prolonged historical production of PCBs to calculations of historical global emissions (from 1930 to 2000), a dynamic mass balance model was developed, parameterized and

applied. With the use of a 1-year time step, four usage sub-categories (open usage, small capacitor usage, nominally closed usage and closed usage), four disposal source categories (landfills, open burning, waste incineration and destruction) and two accidental release pathways (spillage to soil and fires) were considered. The contribution of an individual congener to the total emission for a specific year and country was determined from information on annual national consumption and by means of a number of model parameters: usage factors, product lifetimes, disposal factors, accidental release factors, degradation factors and emission factors.

Taking into account the uncertainties of model parameters in the default emission estimate (i.e. Mid estimate) two additional scenarios were considered – High and Low emissions. Some of the most relevant model parameters were adjusted within reported or anticipated ranges. The emissions of 22 individual PCB congeners were evaluated for 114 countries for the period of 1930 to 2000, with allowance made for High, Middle and Low emission scenarios. The total historical global emissions of the 22 PCB congeners for the Low and High scenarios were 440 and 91722 t. The default (Mid) emission value was estimated at 7709 t. The relative importance of historical emissions from three major source categories (usage, waste disposal and accidental release) and total historical emissions by congener were estimated in this paper for the three emission scenarios. Table 4.4 shows some estimates obtained with the use of the High emission scenario for four selected PCB congeners.

**Table 4.4.** *Total historical emissions (t) and relative importance of historical emissions from the major source categories (%) for four individual congeners (High scenario)*

Emission, t	PCB-28	PCB-118	PCB-153	PCB-180
	11658	3047	2596	1037
Contributions:				
Use, %	83	13	16	5
Waste disposal, %	6	54	49	58
Accidental release, %	11	33	35	37

According to the data presented, usage is the predominant emission pathway for less chlorinated PCB congeners; for more chlorinated PCBs it is waste disposal (especially open burning). One of the most substantial results of this work is the assessment of the temperature impact on both the absolute value of PCB emissions as well as on the PCB emission patterns.

Thus in the work [Breivik *et al.*, 2002b] temporal and spatial distribution of the global emissions of individual PCB congeners, which is a reflection of the global consumption pattern, were determined for the first time. The diversity of historical usage, waste disposal and accidental release pathways made the problem of filling the gaps between the consumption and emissions difficult and led to an equally complex and diverse true emission pattern. Due to the tremendous uncertainties at the temporal and spatial scales involved in this emission inventory, the actual emission values should be considered as order-of-magnitude estimates.

#### **4.2.2. PCB emission sources in the Northern Hemisphere**

Spatial distribution of PCB emissions in the Northern Hemisphere obtained on the basis of the High emission scenario available in [Breivik *et al.*, 2002b] and used for modeling within the framework of this project is shown in Figure 4.10 with the example from 1996. The total emissions of 22 PCB congeners from the Northern Hemisphere in 1996 are equal to 662 t. The four considered congeners made a combined contribution of about 20% to this value. At the same time, total emissions of PCB-28 from the Northern Hemisphere in 1996 was about 80 t, that of PCB-118 – about 23 t, that of PCB-153 – about 16 t and that of PCB-180 – about 4.5 t. For emission distribution over the grid with spatial

resolution  $2.5^{\circ} \times 2.5^{\circ}$ , a 1990 population distribution data set available from the CGEIC website (<http://www.ortech.ca/cgeic>) was used. Population density is considered a suitable surrogate parameter, as the PCB consumption is generally linked to the use of electrical equipment [Breivik *et al.*, 2002a].

To investigate the impact of different PCB sources on the contamination of the considered regions-receptors within the Russian North six main groups were set apart:

1. Americas
2. North-western Europe
3. South-Eastern Europe
4. Central Asia and Africa
5. South-eastern Asia
6. Russia.

According to *K.Breivik et al.* [2001b] contributions of these groups to PCB total emissions during the period from 1930 to 2000 are presented in Figure 4.11. The chief contribution of Americas to PCB emissions in the Northern Hemisphere is accounted for by the USA. From the perspective of total production, the USA produced PCBs from 1930 to 1977 amounting to about 642 kt making up more than half of the historically produced PCBs. At the same time, the USA was responsible for as much as 46% of the total historical global PCB consumption. A sizable contribution of North-western Europe (15%) to historical total emissions in the Northern Hemisphere was made mostly by inputs from West Germany (total production approximately 159 kt), France (total production approximately 135 kt) and the United Kingdom (total production approximately 67 kt), the region being at the same time a major consumer of PCBs (7.1%, 4.1% and 2% of total historical global consumption, respectively). During the considered period Russia was responsible for 7% of the total emission within the Northern Hemisphere. Russian production of PCBs amounted to 173.8 kt, 60% of which utilized in the national consumption, which was 7.9% of total global consumption. Southern and Eastern Europe contributions to historical total emissions in the Northern Hemisphere total 11%. Czechoslovakia, Spain and Italy produced PCBs in substantial quantities in this region. The contribution of South-eastern Asia to historical emissions of the Northern Hemisphere was 7%. In this region, Japan played a dominant role (total production approximately 59 kt; contribution to global consumption - about 4%).

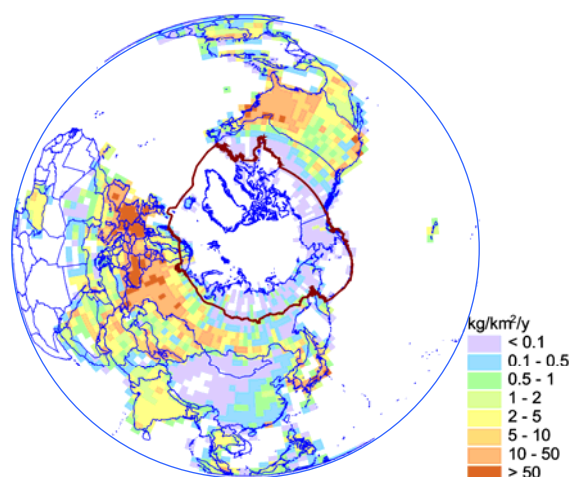


**Figure 4.10.** Spatial distribution of the total emissions of 22 PCB congeners in the Northern Hemisphere in 1996,  $\text{kg}/\text{km}^2/\text{y}$

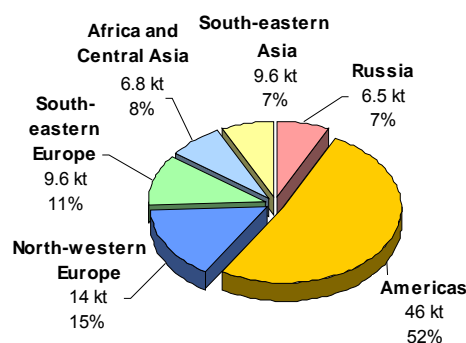


**Figure 4.11.** Distribution of PCB historical emissions in the Northern Hemisphere (1930-2000)

PCB emission dynamics in the major source groups of the Northern Hemisphere in 1930-2000 estimated on the basis of data available in [Breivik et al., 2002a] is plotted in Figure 4.12. In the majority of countries, PCB emissions have reached their maximum by the 70s, i.e. during a period of widespread intensive consumption of products containing these chemicals. PCB peak production in 1970 amounted to 75.5 kt. At that time, the USA made the largest contribution to emissions. Western Europe (namely West Germany) and Japan also contributed significantly. In these countries and in a number of others, PCB emissions had drastically decreased by the 1980s due to limitation or complete prohibition of use of these species. In Russia emissions were at a maximum in the 1990s. The temporal variation in emissions in Russia shown in Figure 4.12 reflects the prolonged period of PCB production and consumption there. In fact PCB production ceased in Russia only in 1993 and the consumption of PCB-containing products still persists [AMAP, 2000].

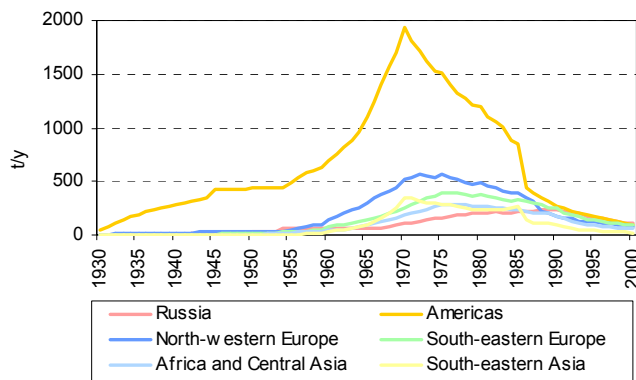


Figure 4.12. PCB emission dynamics in countries and regions in 1930-2000, t/y

In comparison with the distribution of contributions of the major source groups to the total historical emissions in the Northern Hemisphere (Fig. 4.11), a similar distribution for 1996 (selected for model computations) differs appreciably. Figure 4.13 demonstrates the relative contribution of the major source groups to the total PCB emissions of the Northern Hemisphere in 1996, estimated on the basis of data from [Breivik et al., 2002a]. Thus the USA's contribution to emissions within the Northern Hemisphere had decreased almost in half by 1996. In contrast, the combined contribution of East and South Europe reached 19% and the contribution of Russia increased up to 23% and actually became equal to that of the USA. A detailed division of Russian sources into 12 groups was made in accordance with the following criteria - location (in the Arctic zone or nearby), PCB quantities in functioning equipment, in wastes and the amounts of PCBs released into the environment. According to the inventory of PCBs in the Russian Federation [AMAP, 2000], the highest amount of PCBs in PCB-containing equipment was detected in the Central-Chernozem, Volga and North Caucasus regions (34% in whole). The highest PCB amount in wastes was detected in the Urals region (46%) [AMAP, 2000]. These regions are also distinguished by the maximum total amount of PCBs released from functioning and phased out equipment [AMAP, 2000].

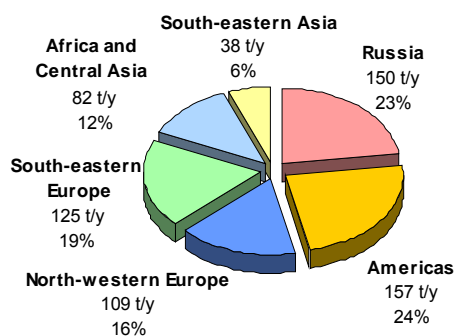


Figure 4.13. Contribution of the major source groups of the Northern Hemisphere to the total PCB emissions in 1996

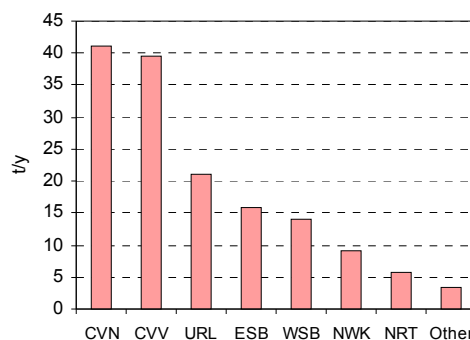


Figure 4.14. Contributions of different Russian regions to PCB emissions in 1996

Contributions to PCB emissions of region-sources within the Russian Federation (Fig.4.2) [Breivik *et al.*, 2002b] are illustrated in Figure 4.14. The diagram demonstrates that the main contribution to PCB total emissions in the Russian Federation originate in the central and southern regions of the European part of Russia. This is in agreement with the estimates presented in the *AMAP Report* [2000].

### 4.2.3. Seasonal variations of PCB emissions

Model calculations of individual PCB congeners were carried out on the basis of the global emission inventory of PCBs given in the work [Breivik *et al.*, 2002b]. This expert estimate does not include an evaluation of the seasonal variation of PCB emissions. The climatic (temperature) dependence of emissions was determined only for such source categories as soils and landfills. The emission factors (for temperatures of 5, 10 and 20°C) developed for these sources were allocated to the considered countries, based on global temperature maps. However, according to [Breivik *et al.*, 2002b] these source categories presumably contribute less to the total emissions. Nevertheless K.Breivik *et al.* [2002b] mentioned that temperature is expected to affect the emission pattern of PCBs that are capable of volatilization at ambient temperatures (the continuous sources).

It can be supposed that in actuality PCB emissions vary seasonally having higher values in summer (warmer months) due to more active volatilization in accordance with individual PCB congener volatility. At present, however, quantifying seasonal variations is difficult because of uncertainties in emission factors, the absence of necessary data and peculiarities of contributions made by various source categories to PCB emissions in specific countries. Furthermore, in a number of other expert estimates of PCB emissions, for instance, for the European region [Baart *et al.*, 1995] the characteristics of total emission variability over the year are also not available. Therefore in model calculations seasonal variations of PCB emissions were not taken into account.

### 4.2.4. Uncertainties of PCB emission estimates

Basic uncertainties involved in estimates of the global consumption and emissions of PCB individual congeners according to K. Breivik *et al.* [2002 a,b] are:

#### *Uncertainties in estimates of global production and consumption*

1. Due to deficient information, the inventory of PCB global production did not include the amount of these substances produced in factories of Poland, East Germany and Austria.
2. Data on production reported for a period in excess of one year (e.g. a 5-year period) were uniformly distributed over the indicated period.
3. The highest uncertainty in the global production estimate lies in default homologue and congener composition (e.g. for France, Spain and Italy) and variability between characteristic technical mixture compositions.
4. For individual congeners the uncertainty in the global production estimate increased for the period after the 70s due to the increased number of PCB producers. Nevertheless, recent data are more accurate than the data from the past.
5. In realization of the method of global consumption estimation, a number of assumptions were made. Reliable information was available only for countries with traditionally high consumption of PCBs. For other countries, assumptions based on trade between different countries and regions were made using Gross Domestic Product as a surrogate parameter.

6. Approximately 70 non-OECD countries are not involved in the estimate; otherwise, the probable consumption in them would be about 6% of the total export in countries of this category. It is presumed that it introduced minor uncertainties into the general inventory.

### ***Uncertainty in the emission estimate***

1. The representativeness and accuracy of emission factors are the major source of uncertainties in a given estimate of emissions.
2. The global movement of PCB-containing products and wastes between countries was not considered in detail.
3. In view of the deficiency of reasonable estimates of the detailed spatial patterns, potential "point sources" of PCB atmospheric emissions were not considered separately. For the same reason incidental or unwanted formation of PCBs and emissions from the combustion process (de novo synthesis) were also not considered.

Uncertainties of estimates in global consumption and emissions will grow with the increase of the specification level (e.g. more detailed usage and waste disposal categories). Clearly the supposed uncertainties in emission estimates appear higher than the uncertainty in production estimates.

## **4.3. $\gamma$ -HCH emissions**

This section discusses data on emissions of  $\gamma$ -HCH, an isomer of hexachlorocyclohexane (HCH), used in modeling in the AMAP project. HCH is an organochlorine insecticide of a complex action widely used all over the world since the 1940s [Li *et al.*, 1996]. This insecticide has two main compositions - technical HCH (with a range of  $\gamma$ -HCH content from 8 to 15%) and lindane (containing not less than 99% of  $\gamma$ -isomer). By the end of the 1970s the application of technical HCH was the basic source of  $\gamma$ -HCH. Its maximum usage in 1981 was approximately 334 kt [Li *et al.*, 1998]. The majority of the developed countries prohibited the application of HCH in the 1970s. At that time the usage of technical HCH in North America was prohibited in Canada and the USA, but it was still used in Mexico until 1983 [Walker *et al.*, 1999]. At a later time lindane becomes the basic source of  $\gamma$ -HCH. For instance, in China the production and application of technical HCH was prohibited in 1983 and in 1991 lindane was coming into use [Li *et al.*, 1998, Macdonald *et al.*, 2000]. In Europe 81 kt of lindane [Breivik *et al.*, 1999] was applied from 1970 to 1996. Due to the prohibition of lindane in a number of countries, according to [Breivik *et al.*, 1999]  $\gamma$ -HCH use in Europe in 1996 was about one third of its level observed in the 1970s. Nevertheless in some countries of the Northern Hemisphere it was still in use until the late 1990s [AMAP, 1998; Walker *et al.*, 1999].

### **4.3.1. *Data on $\gamma$ -HCH use and emissions in the Northern Hemisphere***

The official data on  $\gamma$ -HCH emissions submitted by countries to the UN ECE Secretariat are used for the assessment of gridded emissions in the Northern Hemisphere. Only 13 countries have submitted their totals for at least one year for the period of 1990-2000 [Vestreng and Klein, 2002]. In the 1990s a number of expert estimates of  $\gamma$ -HCH application and emissions both on the regional and global scale

were made. In particular *Y.-F. Li et al.* [1996] have collected data on global use of technical HCH and  $\gamma$ -HCH for 1980 and 1990 and distributed over the grid with spatial resolution  $1^\circ \times 1^\circ$  in accordance with the distribution of cultivated land areas. In further works [*Li et al.*, 1998; *Li*, 1999a,b] the global inventory of HCH use and its spatial distribution have been refined. Within the framework of the POPCYCLING-Baltic project an inventory of  $\gamma$ -HCH use and emissions and their spatial distribution in Europe from 1970 to 1996 was made [*Breivik et al.*, 1999; *Pacyna et al.*, 1999]. As there is no integral pattern of  $\gamma$ -HCH emissions in the Northern Hemisphere at the moment, some emission scenarios based on official and expert estimates had to be worked out. A brief description of  $\gamma$ -HCH emission data for 1990-96 used in modeling is given below.

### 4.3.2. Official data on HCH use and emissions

Table 4.5 demonstrates the official data for Europe and the USA used in modeling [*Vestreng and Klein*, 2002].

It should be mentioned that application of these data to model calculations was complicated by the absence of comments on HCH isomer composition. For this reason, it was accepted that the available data refer to  $\gamma$ -HCH emissions.

**Table 4.5.** Official HCH emission data used in modeling, t/y

Country	Official emission data						
	1990	1991	1992	1993	1994	1995	1996
Austria					12.000	8.056	8.640
Croatia	9.400						12.800
Denmark					0.061		
Germany					15.000		
Hungary	9.281	0.060	0.012	0.462	0.798	1.650	2.400
Netherlands	0		0		0	0	0
Norway			0	0	0	0	0
Spain	9.204	9.204	6.705	5.917	10.650	9.598	9.730
United Kingdom	100.013	86.189	74.756	65.250	57.301	50.616	44.963
USA							0.235

In the former USSR  $\gamma$ -HCH was used extensively as a pesticide during the years 1987-91. In spite of its prohibition in 1990, the use of remaining quantities in agriculture, forest and municipal economy continued until 1996 [*Fedorov and Yablokov*, 1999, *List of chemical and biological ...*, 1994]. Thus  $\gamma$ -HCH use in Russia in 1997 was assumed to be zero. The use of  $\gamma$ -HCH in the European part of Russia in 1990, equal to 923 tonnes was estimated on the basis of the data on pesticide application in this region [*Revich et al.*, 1999]. To get from  $\gamma$ -HCH use to its emissions, an emission factor for lindane agricultural use equal to 0.5 was employed [*Atmospheric Emission Inventory Guidebook*, 1999]. For the Asian part of the Russian Federation,  $\gamma$ -HCH emissions in 1990-96 were evaluated on the basis of information about the application of this insecticide in agriculture in different regions of the Russian Federation available in reports by Roshydromet [*Year-books*, 1992, 1993, 1999]. Aside from that, the amount of  $\gamma$ -HCH used in the Irkutsk region were estimated on the basis of data from *L.P. Ignatieva and M.F. Savchenko* [1994]. According to the obtained data,  $\gamma$ -HCH application tended to decrease from 1987 to 1997. Table 4.6 shows the dynamics of  $\gamma$ -HCH emissions over European and Asian Russia estimated by interpolation of published national data on the use of this pesticide.

Information about lindane use in Uzbekistan was found in [*Ananieva et al.*, 1990].

**Table 4.6.** Dynamics of  $\gamma$ -HCH emissions over European and Asian Russia, t/y

Russia	1990	1991	1992	1993	1994	1995	1996
European part	461.5	395.6	329.6	263.7	197.8	131.9	65.9
Asian part	47.8	29.0	12.3	5.1	2.3	1.1	0.5

### 4.3.3. Expert estimates of $\gamma$ -HCH use and emissions in a number of countries and regions in the Northern Hemisphere

Because official data are inadequate for the compilation of  $\gamma$ -HCH emission scenario for the Northern Hemisphere, they were complemented by expert estimates. In particular data on  $\gamma$ -HCH emissions in Europe from 1970 to 1996 [Pacyna *et al.*, 1999] was used, determined under the POPCYCLING-Baltic project from the inventory of the application of this insecticide in European countries [Breivik *et al.*, 1999]. In this expert estimate, the spatial distribution of  $\gamma$ -HCH emissions and use in Europe were determined on the basis of crop area as a surrogate parameter.

**Table 4.7.**  $\gamma$ -HCH application in a number of countries of the Northern Hemisphere in 1990, t/y

Country	Use in 1990
Algeria	14
Canada	284
China	100
Honduras	137
India	7650
Mexico	261
Niger	397
Pakistan	3
USA	114
Total	8960

To assess emission totals, in some countries within the Northern Hemisphere we employed expert estimates of  $\gamma$ -HCH application on the global scale from [Li *et al.*, 1996; Li *et al.*, 1998 and Li *et al.*, 1999a]. Table 4.7 presents data on the use of this insecticide in 1990 [Li *et al.*, 1996 and Macdonald *et al.*, 2000].

According to [Macdonald *et al.*, 2000], since 1995 usage of  $\gamma$ -HCH in China has been approximately 500 t/y and since 1991  $\gamma$ -HCH use in India has remained at approximately 3600 t/y.

### 4.3.4. $\gamma$ -HCH emission sources in the Northern Hemisphere

The scenario of  $\gamma$ -HCH emissions in the Northern Hemisphere for 1990-96 based on official data and expert estimates is shown in Table 4.8. According to these data the total  $\gamma$ -HCH emissions from the Northern Hemisphere in 1996 amounted to 3445 t.

**Table 4.8.**  $\gamma$ -HCH emissions in the Northern Hemisphere based on official data and expert estimates, t/y

Sources	1990	1991	1992	1993	1994	1995	1996
Americas	398	389	379	370	360	351	341
Asia	84	84	83	83	83	83	83
Eastern Europe	37	22	17	19	18	20	20
Western Europe	419	362	642	643	658	633	632
Southern Europe	337	295	277	21	25	33	47
Northern Europe	3	5	4	3	0	0	0
Africa	206	206	206	206	206	206	206
Russia	509	425	342	269	200	133	66
China	50	50	50	50	50	250	250
India	3825	1800	1800	1800	1800	1800	1800

The approach of *J.Pacyna et al.* [1999b] was used to obtain  $\gamma$ -HCH emission distribution. We used crop area distribution for the evaluation of emission distribution in the Northern Hemisphere over the grid with spatial resolution  $2.5^\circ \times 2.5^\circ$ .  $\gamma$ -HCH emission distribution for 1996 selected for calculations is demonstrated in Figure 4.15.

For the model calculations, nine groups of sources in the Northern Hemisphere were formed:

1. Americas
2. Eastern Europe
3. Western Europe
4. Southern Europe
5. Russia
6. Asia
7. Africa
8. China
9. India

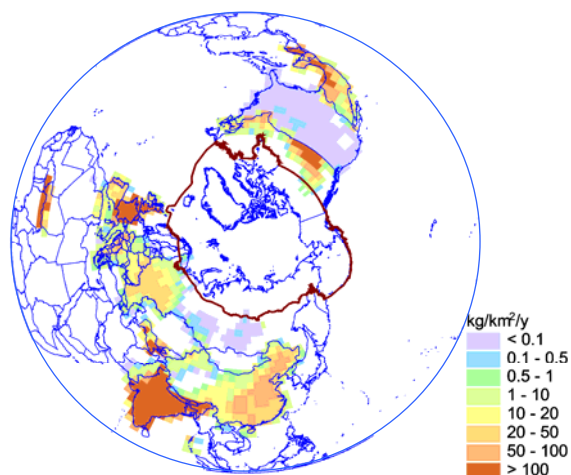
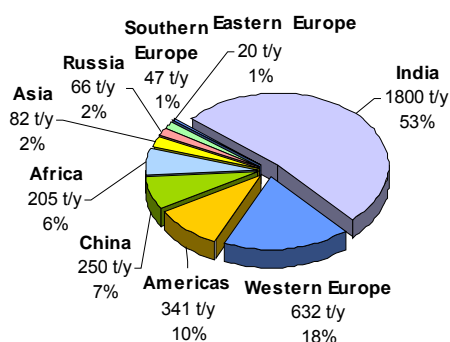


**Figure 4.15.**  $\gamma$ -HCH emission spatial distribution in the Northern Hemisphere in 1996, kg/km<sup>2</sup>/y

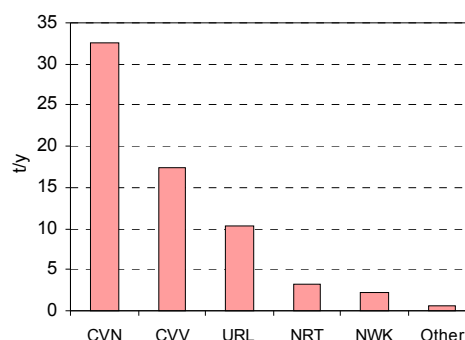
China and India were isolated as separate sources as historically they were significant producers and consumers of this insecticide over a long period of time. For instance, in connection with extensive application of technical HCH in the 60s and 70s China's consumption of  $\gamma$ -HCH was highest in the world [Macdonald et al., 2000]. Beginning from 1994 Northern European emissions are assumed to be zero and for this reason this region was not included as a group of sources in model calculations for 1996. Russian sources are presented in Figure 4.2.

Figure 4.16 demonstrates contributions of source groups identified in our scenario to  $\gamma$ -HCH overall emissions within the Northern Hemisphere in 1996.

As seen from the diagram the highest contribution made the following sources – India, since it was the most significant consumer of this insecticide in agriculture in this time period and Western Europe. Russia's contribution in the indicated year totalled 2%.



**Figure 4.16.** Contribution of different sources to  $\gamma$ -HCH emission in the Northern Hemisphere for 1996



**Figure 4.17.** Contributions of different regions of the Russian Federation to  $\gamma$ -HCH emissions for 1996

As mentioned above, the territorial proximity of a number of regions of the Russian Federation to the Arctic set the stage for finer specification of Russian  $\gamma$ -HCH sources. Figure 4.17 illustrates contributions of Russian region-sources to  $\gamma$ -HCH total emission as it follows from the scenario used.

Figure 4.17 shows that the largest emission value (33 t) from Russia was released from sources located in Central-Chernozem, Volga and North-Caucasus regions.

### 4.3.5. Seasonal variations of $\gamma$ -HCH emissions

According to [Strand and Hov, 1996] the use of pesticides varies over the year and is concentrated in the growing season. The seasonal trend is most characteristic in mid-latitudes where the growing season is short. In connection to this, the application in the 30°N - 60°N latitude zone is therefore assumed to follow the function:

$$2F_{appl} = \frac{F_{totallp}}{365} \left[ \sin \left( 2\pi \frac{\text{day}}{365} - \frac{\pi}{2} \right) + 1 \right] \quad (4.1)$$

where  $F_{appl}$  is the daily emission to the atmosphere and soil;  
 $F_{totappl}$  is the annual emission;  
 day is the Julian day.

In the tropics the application of pesticides is assumed to be constant over the year [Strand and Hov, 1996].

### *Uncertainties in $\gamma$ -HCH emission estimates*

The main uncertainty is connected with the country-based usage of  $\gamma$ -HCH which may be uncertain in itself. K.Brevik et al. [2001] believe that uncertainties of  $\gamma$ -HCH consumption in Europe [Brevik et al., 1999] are the consequences of the following peculiarities of the original data:

- Uncertainties regarding whether usage in a given region reported for active ingredient or plus diluting agents;
- The distinction between technical HCH and lindane usage when no information on the subject is given;
- The use of ratios describing HCH to total insecticide usage in estimating HCH consumption (in countries where only information on insecticide usage was available).

As it was mentioned in [Pacyna et al., 1999], the accuracy of data increases from the 1970s to the 1990s reflecting the availability of more reliable information. According to [Li, 1999b] in some regions of the Northern Hemisphere data on the consumption of this insecticide were not kept while in other regions this information was confidential.

Another source of uncertainties arises from distribution of estimated emission over cropland areas as HCH consumption for other purposes unconnected with agriculture was not considered. On the other hand the distribution of emissions over cropland areas results in the appearance of an artificial value of  $\gamma$ -HCH emissions even in the Murmansk Oblast where some agricultural land is available. In the assessment of emissions on the basis of consumption values we used averaged emission factor for lindane applied in agriculture thereby introducing an additional uncertainty. This approach does not

take into account that the share of  $\gamma$ -HCH emitting directly to the air to a great extent depends on the method of the pesticide application.

Substantial source of uncertainties in this emission scenario originates from the rather rough description of seasonal variations of  $\gamma$ -HCH emissions used in the model.

## References

- AMAP Assessment Report [1998] Arctic Pollution Issues, Arctic Monitoring and Assessment Programme, Oslo, pp. 192.
- AMAP Report 2000: 3. PCB in the Russian Federation: Inventory and proposals for priority remedial actions. Arctic Monitoring and Assessment Programme (AMAP), Oslo, 2000, published by: Centre For International Project (CIP), Moscow, 2000.
- Ananieva K.B., Vishnevskaya O.V., Dudchenko V.A. [1990]. Contamination of soils and surface water by chlororganic pesticides in Uzbekistan. In "Investigation of the environmental pollution of Central Asia region. Methods of prediction and the assessment of impact. Proceedings of the Central Asian Regional Scientific-Research Hydrometeorological Institute named after V.A. Bugaev. Issue 138, No. 219, pp. 103-109, (*in Russian*).
- Atmospheric Emission Inventory Guidebook [1999] Use of Pesticides and Limestone. UNECE/EMEP Task Force on Emission Inventories. Technical report No 30, Second Edition, A joint EMEP/CORINAIR Production, Edited by Stephen Richardson, B1060-2.
- Baart A., Berdowski J., van Jaarsveld J. and K.Wulffraat [1995] Calculation of atmospheric deposition of contaminants on the North Sea. TNO-MEP-R 95/138, Delft, The Netherlands.
- Behrenfeld M.J. and P.G.Falkowski [1997] Photosynthetic derived from satellite-based chlorophyll concentration. *Limnol. Oceanogr.*, v.42, No.1, pp.1-20.
- Bergan T. and H.Rodhe [2001] Oxidation of elemental mercury in the atmosphere; constraints imposed by global scale modelling. *J. Atm. Chem.* v.40, pp.191-212.
- Breivik K., Pacyna J., Munch J. [1999] Use of  $\alpha$ -,  $\beta$ - and  $\gamma$ -hexachlorocyclohexane in Europe, 1970-1996. *The Science of the Total Environment*, v. 239, pp. 151-163.
- Breivik K., Sweetman A., Pacyna J.M., Jones K. [2002a] Towards a global historical emission inventory for selected PCB congeners – a mass balance approach. 1. Global production and consumption. *The Science of the Total Environment*, v. 290, pp. 181-198.
- Breivik K., Sweetman A., Pacyna J.M., Jones K. [2002b] Towards a global historical emission inventory for selected PCB congeners – a mass balance approach. 2. Emissions. *The Science of the Total Environment*, v. 290, pp. 199-224.
- Breivik K., Wania F., Pacyna J. [2001] Sources and Environmental Cycling of POPs in the Baltic Sea region: Case studies for  $\alpha$ -HCH and  $\gamma$ -HCH using the POPCYCLING-Baltic model. EMEP/CCC-Report 4/2001.
- Carpi A. and Lindberg S. E. [1998] Application of a teflon<sup>TM</sup> dynamic flux chamber for quantifying soil mercury flux: tests and results over background soil. *Atmos. Environ.* v.32, No.5, pp.873-882.
- CGEIC website: Canadian Global Emissions Interpretation Centre, <http://www.ortech.ca/cgeic>.
- Ebinghaus R., Tripathi R. M., Walischlager D., and Lindberg S. E. [1999] Natural and anthropogenic mercury sources and their impact on the air-surface exchange of mercury on regional and global scales. In: Ebinghaus R., Turner R. R., Lacerda de L. D., Vasiliev O., and Salomons W. (Eds.) Mercury contaminated sites. Springer, Berlin, pp.3-50.
- Fedorov L.A. and A.B. Yablokov [1999] Pesticides – toxic stress for biosphere and man, Moscow, Nauka, pp.22-29, (*in Russian*).
- Fitzgerald W. F. and Mason R. P. [1996] The global mercury cycle: oceanic and anthropogenic aspects. In: Baeyens W., Ebinghaus R. Vasiliev O. (Eds.), Global and Regional Mercury Cycles: Sources, Fluxes and Mass Balances. NATO-ASI-Series, Kluwer Academic Publishers, Dordrecht, The Netherlands, pp. 85-108.
- Geological Survey of Canada [1995] The significance of natural sources of metals in the environment. Report prepared for the UN-ECE LRTAP (HM) Convention, 28 May 1995.
- Gustin M. S., Lindberg S., Marsik F., Casimir A., Ebinghaus R., Edwards G., Hubble-Fitzgerald C., Kemp R., Kock H., Leonard T., London J., Majewski M., Montecinos C., Owens J., Pilote M., Poissant L., Rasmussen P., Schaedlich F., Schneeberger D., Schroeder W., Sommar J., Turner R., Vette A., Wallschlaeger D., Xiao Z., and Zhang H. [1999] Nevada STORMS project: Measurement of mercury emissions from naturally enriched surfaces. *J. Geophys. Res.* 104, No.D17, pp.21831-21844.
- Ignatieva L.P. and M.F. Savchenko [1994]. Hygiene of pesticide application in Siberia, Publication of the Irkutsk State University, p.16, (*in Russian*).
- Jaworowski et al., 1981 (quoted in *Geological Survey of Canada*, 1995.)
- Jonasson I. R. and Boyle R. W. [1971] Geochemistry of mercury. Spatial Symposium on Mercury in Man's Environment, Environment Canada, 15-16 February 1971, Ottawa, Canada pp. 5-21.
- Kim J. P. and Fitzgerald W. F. [1986] Sea-air partitioning of mercury in the Equatorial Pacific Ocean. *Science* 231, 1131-1133, Behrenfeld and Falkowski, 1997.
- Lamborg C. H., Fitzgerald W. F., O'Donnell J., and Torgersen T. [2002] A non-steady-state compartmental model of global-scale mercury biogeochemistry with interhemispheric atmospheric gradients. *Geochimica et Cosmochimica Acta* v.66, No.7, pp.1105-1118.
- Li Y.F. [1999a] Global technical hexachlorocyclohexane usage and its contamination consequences in environment: from 1948 to 1997. *The Science of the Total Environment*, v. 232, pp. 123-160.
- Li Y.F. [1999b] Global gridded technical hexachlorocyclohexane usage inventories using a

- global cropland as a surrogate. *J. Geophys. Research*, V. 104, No. D19, pp. 23,785-23,797.
- Li Y.F., Bidleman T.F., Barrie L.A., McConnell L.L.. [1998] Global hexachlorocyclohexane use trends and their impact on the Arctic atmospheric environment. *J. Geophys. Research*, v. 25, No. 1, pp. 39-41.
- Li, Y. F., A. McMillan and T. Scholtz [1996] Global HCH usage with 1x1 longitude/latitude resolution, *Env. Sci. and Technol.*, v.30, pp.3525-3533.
- Lindberg S.E., P.J.Hanson, T.P.Meyers, and K.-H.Kim [1998] Air/surface exchange of mercury vapor over forests – the need for a reassessment of continental biogenic emissions. *Atmos. Environ.* v.32, pp.895-908.
- Lindqvist O., Johanson K., Aastrup M., Anderson A., Bringmark L., Hovsenius G., Hakanson L., Iverfeld A., Meili M., and Timm B. [1991] Mercury in the Swedish environment – recent research on causes, consequences and corrective methods. *WASP* v.55, pp.1-261.
- List of chemical and biological means against pests, diseases of plants and against weed, growth regulators of plants and pheromones permitted for use in agriculture including farm and municipal economy for 1992-96. [1994], Moscow, Kolos, pp. 297-299, (*in Russian*).
- Macdonald R.W., Barrie L.A., Bidleman T.F., Diamond M.L., Gregor D.J., Semkin R.G., Strachan W.M., Li Y.F., Wania F., Alaei M., Alexeeva L.V., Backus S.M., Bailey R., Bewers J.M., Gobel C., Halsall C.J., Harner T., Hoff J.T., Jantunen L.M.M., Lockhart W.L., Mackay D., Muir D.C.G., Pudykiewicz J., Reimer K.J., Smith J.N., Stern G.A., Schroeder W.H., Wagemann R., Yunker M.B. [2000] Contaminants in the Canadian Arctic: 5 years of progress in understanding sources, occurrence and pathways. *The Science of the Total Environment*, v. 254, pp. 93-234.
- Nriagu J. O. [1989] A global assessment of natural sources of atmospheric trace metals. *Nature* v.338, pp.47-49.
- Pacyna J.M. et al. [1999] Final report for Project POPCYCLING-Baltic. EU DGXII, Environment and Climate Program ENV4-CT96-0214. Available on CD-rom including technical report, the emission and environmental databases as well as the POPCYCLING-Baltic model. NILU, P.O. Box 100, N-2027 Kjeller, Norway.
- Pacyna, E. G. and Pacyna J. M. [2002] Global emission of mercury from anthropogenic sources in 1995. *WASP* 137, No.1, pp.149-165C.
- Revich B.A., Radilov A.S., Triger YU.A., Danilina A.E. [1999] The model of national strategy and plan of actions for abatement and elimination of POP emissions, Edited by B.A. Kurlyandsky. National strategy and plan of actions for abatement and elimination of persistent organic pollutants (POPs). Subregional meeting, Moscow. Centre of International Projects, (*in Russian*).
- Seigneur C., Karamchandani P., Lohman K., Vijayaraghavan K., and Shia R.-L. [2001] Multiscale modeling of the atmospheric fate and transport of mercury. *J. Geophys. Res.* v.106, No.D21, pp.27795-27809.
- Strand A. and Hov Ø., [1996] A model strategy for the simulation of chlorinated hydrocarbon distributions in the global environment. *Water, Air and Soil Pollution* 86, 283-316.
- Vestreng V., Klein H. [2002] Emission data reported to UNECE/EMEP: Quality assurance and trend analysis & Presentation of WebPab. MSC-W Status Report 2002. EMEP/MSW-W Note 1/2002. July 2002.
- Walker K., Vallero D.A., Levis R. G. [1999] Factors influencing the distribution of lindane and other hexachlorocyclohexanes in the environment. *Env. Sci. and Technol.*, v.33, No. 24, pp.4373-4378.
- Year-book. Monitoring of pesticides in natural objects of the Russian Federation. [1992] Book 1, Part 1, p.244, (*in Russian*).
- Year-book. Monitoring of pesticides in natural objects of the Russian Federation. [1993] Book 1, Obninsk, p.115, (*in Russian*).
- Year-book. Monitoring of pesticides in natural objects of the Russian Federation in 1997. [1999], Saint-Petersburg, Hydrometeoizdat, p. 71, (*in Russian*).

## Chapter 5

**ATMOSPHERIC TRANSPORT AND DEPOSITION OF MERCURY  
TO THE ARCTIC REGION**

Mercury airborne contamination of the Arctic as a whole and regions of the Russian North are described in this chapter. The assessment is based on the modeling results of mercury long-range transport in the Northern Hemisphere. Since the Arctic is exposed to the adverse impact of distant polluted regions (especially, in the case of such global pollutant as mercury), peculiarities of mercury transport in the Northern Hemisphere are briefly described in the beginning. Particular attention is paid to the effect of Mercury Depletion Events (MDE) on the Arctic pollution based on the accepted parameterization. The consistency of the modeling results is verified by the comparison with available measurements. Further, general features of the Arctic region pollution by mercury are outlined. Finally, detailed description of the Russian North regions pollution by mercury is presented. Concentration levels of mercury in the ambient air and deposition fields are evaluated for all the selected regions. Seasonal variation of the pollution is considered. Main contributors to the contamination of the regions are determined and prevailing pathways of mercury transport are discussed.

**5.1. General description of modeling results**

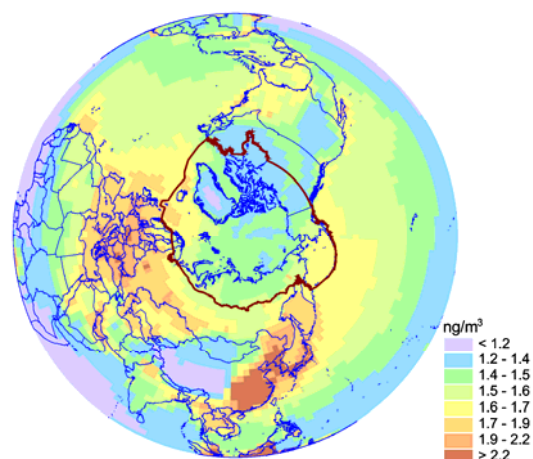
Computations of the atmospheric mercury transport and deposition in the Northern Hemisphere have been performed for 1996 by means of the developed model (Chapter 3). The calculation run for the period of one year have been carried out using emission data described in Section 4.1 and the appropriate initial and boundary conditions (Section 3.2). To take into account the long atmospheric residence time of mercury we performed two-year spin-up of the model using the same meteorological data. Results of mercury transport modeling in the Northern Hemisphere are described below.

***Concentration levels and deposition fields***

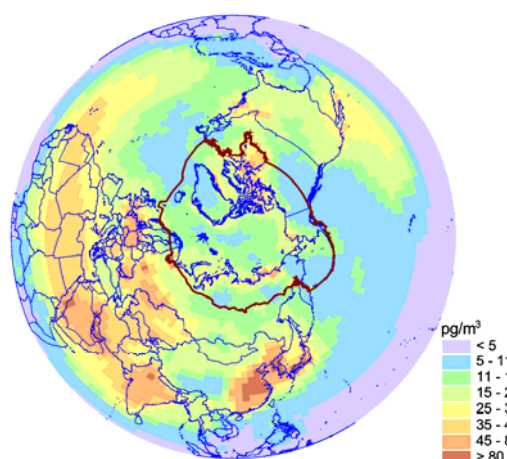
Mercury concentration in the ambient air and deposition fluxes to the ground is the primary information characterizing a negative impact of the pollutant on the human health and the environment. Figure 5.1 shows calculated spatial distribution of mean annual concentration of total gaseous mercury (TGM) in the surface air of the Northern Hemisphere. The modelling results presented below are arithmetical means of the calculations obtained using two natural emission and re-emission scenarios (see Section 4.1). Analysis of the difference between two emission scenarios is presented at the end of the section. According to the modeling results TGM is more or less uniformly distributed over the Northern Hemisphere. This fact agrees with numerous measurements carried out for last several decades [e.g. see *Ebinghaus et al.*, 1999]. As seen in the figure TGM concentration in the Northern Hemisphere varies from about 1 ng/m<sup>3</sup> (under local conditions) in elevated remote regions (Greenland, the Himalayas) to some ng/m<sup>3</sup> in industrialized areas. One can clearly distinguish two the most contaminated regions: Eastern Asia with concentrations up to 5 ng/m<sup>3</sup> and Europe (more than 2 ng/m<sup>3</sup>). High values of gaseous mercury concentration in these regions can be explained by significant both anthropogenic and natural mercury emissions (see Figs. 5.2 and 5.9). There are pronounced gradients of TGM concentration over the Atlantic and Pacific Oceans. In both cases, concentration decreases from middle latitudes to the equator. It agrees with gradients of TGM measured over the oceans [*Slemr*, 1996; *Lamborg et al.*, 2002].

Figure 5.2 demonstrates spatial distribution of particulate mercury ( $Hg_{part}$ ) in the ambient air. Besides in Southeast Asia and Europe, comparatively high concentrations of particulate mercury occur in Hindustan and the Arabian Peninsula being consistent with the emission data (Fig. 5.2). Due to low amount of precipitation over Africa  $Hg_{part}$  flows across this continent and reaches the Atlantic.

Spatial distribution of reactive gaseous mercury (RGM) concentration is shown in Figure 5.3. The residence time of this mercury form in the atmosphere is short due to high solubility and deposition rate. Therefore concentration of gaseous oxidized mercury quickly decreases from regions with major emission sources to remote ones.



**Figure 5.1.** Spatial distribution of mean annual air concentration of total gaseous mercury (TGM) in the surface air of the Northern Hemisphere



**Figure 5.2.** Spatial distribution of mean annual air concentration of particulate mercury ( $Hg_{part}$ ) in the surface air of the Northern Hemisphere

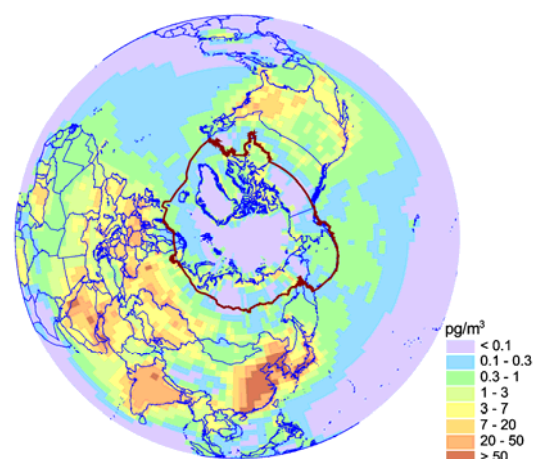


**Figure 5.3.** Spatial distribution of mean annual air concentration of reactive gaseous mercury (RGM) in the surface air of the Northern Hemisphere

Common feature of  $Hg_{part}$  and RGM concentration patterns is elevated mercury content in the coastal areas of the Arctic Ocean. This is a direct consequence of the mercury depletion events (MDE). According to the model parameterization of MDE (Section 3.2) during springtime elemental mercury in the lower troposphere is partially transformed to particulate and RGM forms in the vicinity of the Arctic coast. Long-term effect of the phenomenon will be discussed below.

Figure 5.4 presents distribution field of total annual deposition flux of mercury in the Northern Hemisphere. As seen from the figure the most considerable fluxes take place in the middle latitudes. The highest depositions are in the main emission regions: Southeast Asia, Europe, and the eastern part of North America. As for the rest, the deposition pattern, to some extent, corresponds to the annual precipitation amount field, since wet deposition plays a dominating role in the mercury removal process. Influence of MDE on the deposition fluxes within the Arctic region is illustrated in the enlarged fragment. More detailed consideration of the MDE effect is presented in the next subsection.

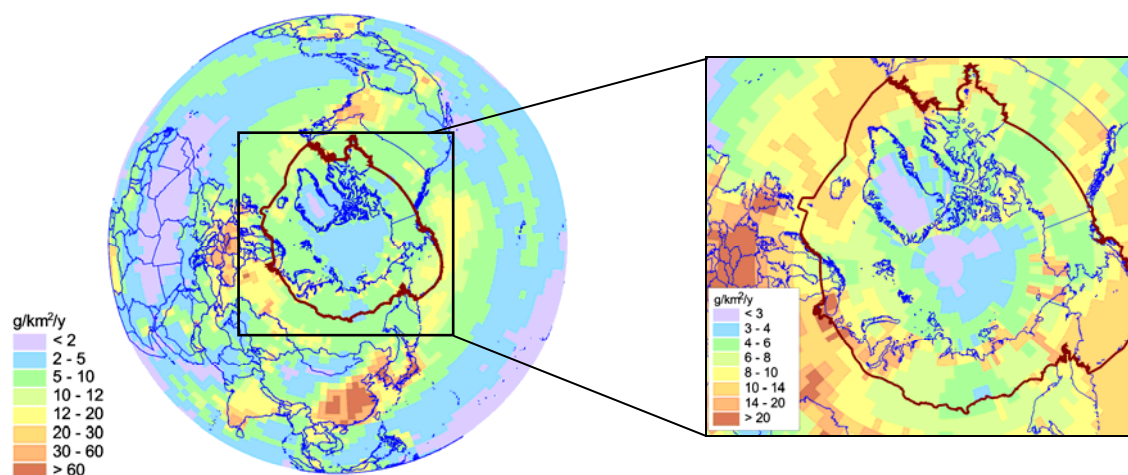


**Figure 5.4.** Annual deposition density of total mercury in the Northern Hemisphere. The enlarged fragment shows elevated mercury deposition over the Arctic coast due to MDE

As it was mentioned in Section 4.1 we performed calculation using two natural emission and re-emission scenarios: Scenario I is the upper limit of the emission estimates; Scenario II is the lower one. It was obtained that differences of mean annual TGM concentration obtained using both scenarios are more noticeable over the ocean because difference between two scenarios of emission from the ocean is more significant (1200 t/y and 500t/y) than that from land (1500t/y and 1100 t/y). Differences of the total deposition flux are insignificant over industrial regions because of considerable contribution of anthropogenically emitted short-lived mercury forms to deposition in these regions. One should note that uncertainty of both TGM concentration and total deposition flux due to uncertainty natural emission and re-emission does not exceed 20% in middle and high latitudes.

### *Mercury Depletion Events (MDE)*

Nature of mercury depletion events taking place during the Arctic sunrise is still unclear to some extent. Proposed hypothesis of the MDE mechanism [Lindberg *et al.*, 2002] includes complicated chemistry involving formation of halogen related radicals. Development of detailed model scheme of MDE phenomenon is the subject of a separate study. In the current research we attempt to estimate roughly long-term effect of MDE on the Arctic pollution using a simplified parameterization (see Section 3.2).

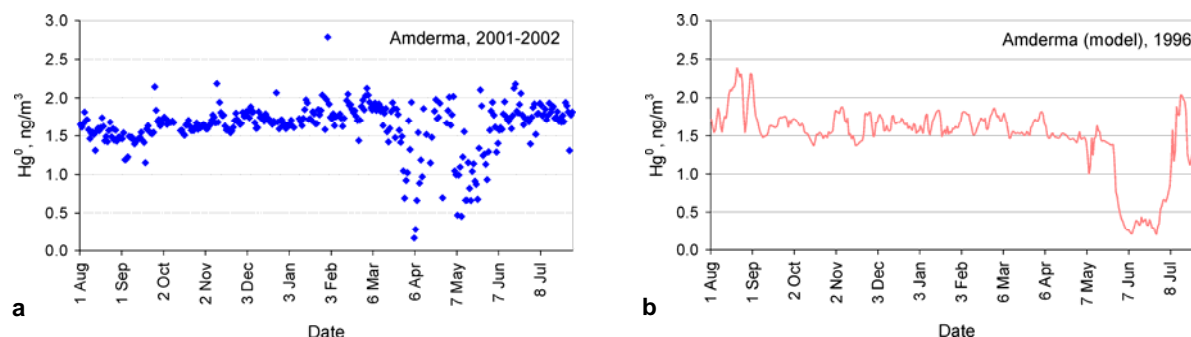


**Figure 5.5.** Daily mean air concentrations of elemental mercury at monitoring station Amderma (Russia): (a) – measured in 2001-2002; (b) – modeled on the base of 1996

The model ability to simulate MDE is illustrated in Figure 5.5. Daily mean concentrations of elemental mercury in air measured in 2001-2002 at monitoring station Amderma (Nenets AO; 69°43'N, 61°37'E)

are presented in Figure 5.5. The measurements were performed within the Joint Canada/Russia project on installation and operation of air monitoring station at Amderma in frame of AMAP (AMAP, Environment of Canada, Air Zone Inc.), and the data was kindly provided by Dr. Konoplev from Center for Environmental Chemistry of SPA "Typhoon" (Russia). As seen from the figure significant drops in elemental mercury concentration takes place at this location in the period from end of March till middle of June. Figure 5.5(b) shows modeled air concentrations of  $Hg^0$  at the same location. Since model calculations were performed for 1996, only qualitative comparison is possible. As one can see from the figure the model reproduces in general the depth of  $Hg^0$  concentration decrease and the duration of the phenomenon. However, simulated MDE phenomenon is shifted in time to summer months due to conditional parameterization of MDE triggering mechanism in the model based on air temperature (Section 3.2). Besides, due to coarse spatial resolution of the model grid it is not able to simulate high variability of  $Hg^0$  concentration during MDE. Nevertheless, the applied approach allows estimating qualitatively long-term effect of MDE on the Arctic pollution taking into account the temporal shift mentioned above.

As it is shown in the enlarged fragment of Figure 5.4 such a short-term phenomenon as MDE, lasting for several weeks per year, can considerably increase annual deposition of mercury in some regions of the Arctic. First of all it relates to marine and terrain areas adjacent to the Arctic coast. To examine the effect of MDE on the Arctic contamination, two computation runs have been conducted. In the first case MDE phenomenon was included into the model, in the second one it was not. The net Influence of MDE on total annual mercury deposition is illustrated in Figure 5.6. The figure shows the difference between deposition fluxes obtained in two computation runs – with and without MDE. As seen MDE can contribute more than 50% to annual deposition to areas adjacent to the Arctic coast (about 300 km northward and southward the coast): the Queen Elizabeth Islands, Hudson Bay, the White Sea, Gulf of the Ob River, the Laptev Sea coast etc. Low negative values show that increased deposition fluxes due to MDE in some regions lead to decreased fluxes in other ones. Thus, a considerable amount of mercury does not reach the pole during springtime being scavenged due to MDE over the coastal and contiguous regions.

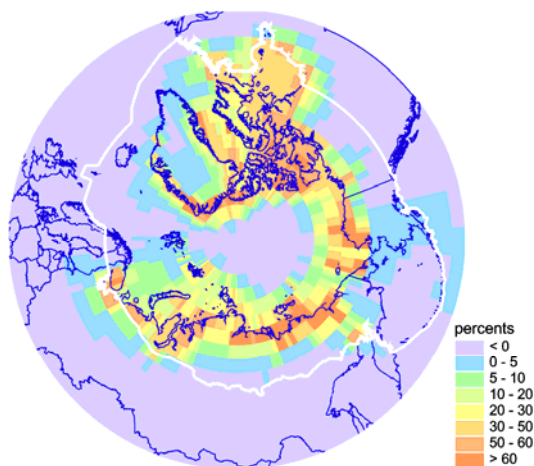


**Figure 5.6.** Net Influence of MDE on the total annual mercury deposition. The field presents the difference between two computation runs – with and without MDE. White curve shows limits of the AMAP domain

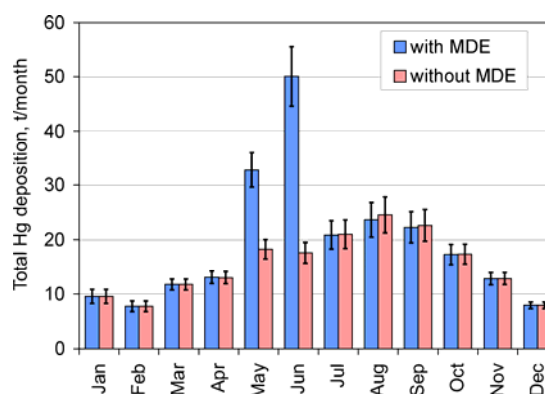


**Figure 5.7.** Seasonal variation of total annual mercury deposition to the Arctic with and without MDE. Intervals show difference between two emission scenarios

Figure 5.7 shows seasonal variation of total annual mercury deposition to the Arctic in both cases. As one can see from the figure, the model predicts the most pronounced effect of MDE in May and June (taking into account the temporal shift mentioned above), when monthly depositions to the Arctic

increased twice or even more. The performed calculations predict that deposition of mercury to the Arctic due to MDE can amount to about 50 t/y (~20% of total annual deposition). It is somewhat lower recent estimates (about 100 t/y) obtained by other authors [Chistensen, 2001].

## 5.2. Comparison of modeling results with measurements

To verify the modeling results the calculated mercury concentrations in the air and deposition fluxes were compared with available monitoring data. Currently, only limited number of measurement data on the annual basis is available for 1996 from the AMAP programme [Berg and Hjellbrekke, 1999], the EMEP monitoring network [Berg and Hjellbrekke, 1998] and North American NADP/MDN network [NADP/MDN, 2002]. The monitoring stations performed regular measurements of mercury in 1996 are listed in Table 5.1. Besides, taking into account restricted number of annual air concentration measurements we included episodic observations and measurements for other years available from the literature. Description of this data is presented in Table 5.2. All sites involved the comparison shown in Figure 5.8.

**Table 5.1.** Monitoring stations involved in the model verification

Station	Code	Latitude	Longitude
<i>AMAP</i>			
Alert	CA420	82°28'N	62°30'E
<i>EMEP network</i>			
Westerland	DE1	54°55'N	8°18'E
Zingst	DE9	54°26'N	12°44'E
Pallas	FI96	67°58'N	24°7'E
Mace Head	IE31	53°19'N	9°54'W
Spitsbergen	NO42	78°54'N	11°53'E
Lista	NO99	58°06'N	6°34'E
Rörvik	SE2	57°25'N	11°56'E
Bredkälen	SE5	63°51'N	15°20'E
Vavihill	SE11	56°01'N	13°09'E
Aspvreten	SE12	58°48'N	17°23'E
<i>NADP/MDN network</i>			
Everglades National Park	FL11	25°23'N	80°41'W
Marcell Experimental Forest	MN16	47°32'N	93°28'W
Waccamaw State Park	NC08	34°10'N	78°25'W
Pettigrew State Park	NC42	35°45'N	76°22'W
Longview	TX21	32°23'N	94°43'W
Brule River	WI08	46°45'N	91°30'W
Popple River	WI09	45°48'N	88°24'W
Trout Lake	WI36	46°03'N	89°39'W

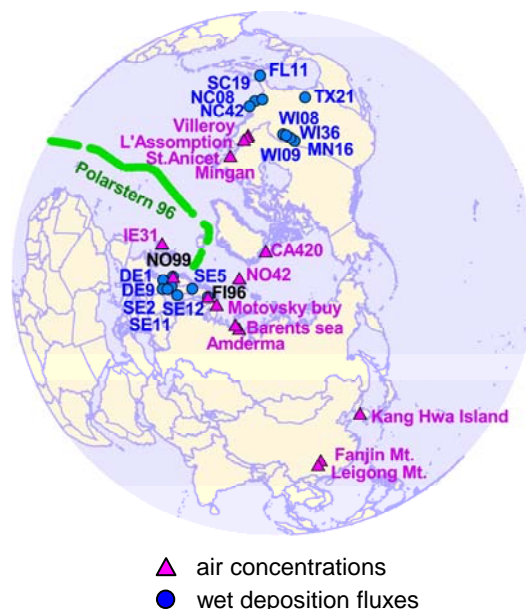


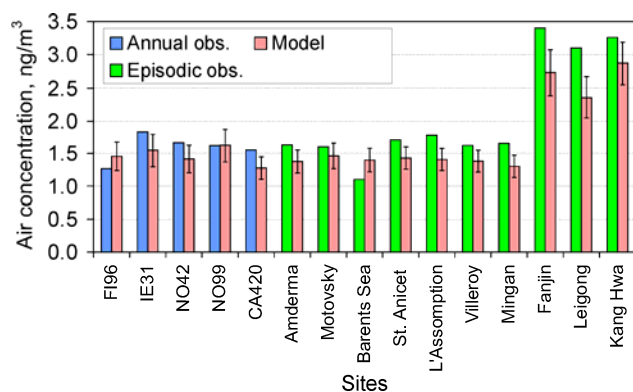
**Figure 5.8.** Location of the monitoring sites

**Table 5.2** Episodic measurement campaigns involved in the model verification

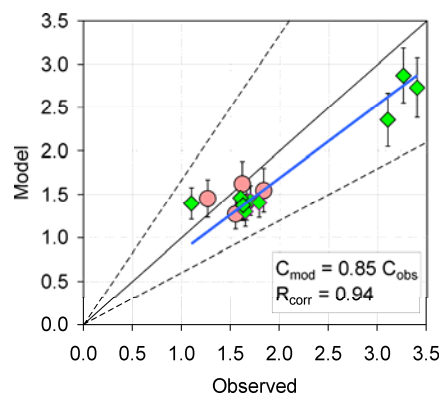
Location	Year	Observ	Model	Reference
Middle Atlantic (Polarstern '96)	1996	1.33-2.12	1.06-1.67	Temme et al., 2003
Motovsky and Kola Bays,	1996	1.6	1.46	Golubeva et al., 2003
Northern Sea Rout	1997	1.1	1.4	
Amderma	2001-2002	1.63	1.37	Konoplev, 2003
Quebec (Canada)	1998			Poisant, 2000
St. Anicet		1.7	1.43	
L'Assomption		1.79	1.4	
Villeroy		1.62	1.38	
Mingan		1.65	1.3	
Guizhou (China)	Multi-year			Tan et al., 2000
Fanjin Mt.		3.4	2.73	
Leigong Mt.		3.1	2.36	
Kang Hwa Island (Korea)	2001	3.26	2.87	Kim et al., 2002

Figure 5.9 shows observed and modeled mean annual mercury concentrations in the ambient air. Only five annual measurements are available for 1996 (blue bars). Other measurements (green bars) were obtained in short term episodic campaigns (e.g. in Motovsky Bay, Barents Sea, Kang Hwa Island) or relate to other years and, therefore, are less reliable in the comparison. Intervals show uncertainty due to natural emission and re-emission (based on two emission scenarios). As one can see the model adequately reproduces annual air concentrations, however, some underestimation is registered at most of episodic sites. As seen from Figure 5.10 the discrepancy observed and modeled values does not exceed 40% with high correlation coefficient (0.94).

The comparison of the observed and modeled annual wet deposition fluxes is presented in Figure 5.11. As seen from the figure the modelled values satisfactorily conform to the measured ones both for European and for North American stations. Variations due to uncertainty of natural emission are even smaller compared to the air concentrations, because most of the stations are located in industrial regions. Regression analysis of wet deposition fluxes is shown in Figure 5.12. As seen the slope of the regression line is close to unity and the discrepancy for all the stations does not exceed a factor of two (dashed lines). The correlation coefficient amounts to 0.54.



**Figure 5.9.** Observed and modeled mean annual TGM concentrations in the ambient air in 1996. Intervals show difference between two emission scenarios



**Figure 5.10.** Observed versus modeled mean annual mercury concentrations. Red circles show annual measurements in 1996, green diamonds – episodic campaigns. Dashed lines show discrepancy interval of 40%

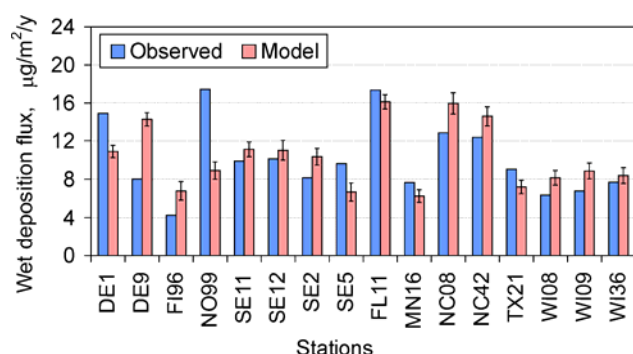


**Figure 5.11.** Observed and modeled annual wet deposition fluxes of mercury. Intervals show difference between two emission scenarios

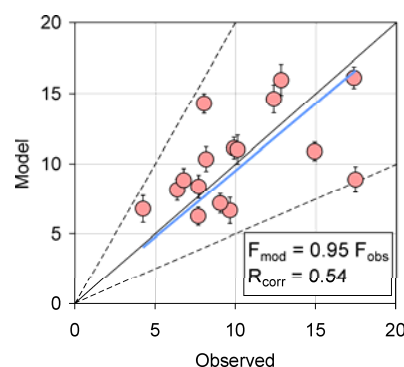


**Figure 5.12.** Observed versus modeled annual wet deposition fluxes of mercury. Intervals show difference between two emission scenarios. Dashed lines show discrepancy interval of a factor of two

To verify the model ability to simulate background mercury concentrations in the ambient air measurement data obtained during the Atlantic cruise on the research ship *Polarstern* in October-November 1996 [Temme *et al.*, 2003]. The data was kindly provided by Dr. Franz Slemr from Max-Planck-Institut für Chemie (Germany). The measurements TGM in the surface air were performed during the ship itinerary through the Northern and Middle Atlantic in the Northern Hemisphere (see Fig. 5.8) and further in the Southern Hemisphere. The original half-an-hour-accumulated data was averaged to obtain daily means. Figure 5.13 shows measured and modeled TGM concentrations over the Atlantic Ocean as a function of geographical latitude. As seen from the figure the model reproduces mercury concentrations close to the observed ones in the Middle Atlantic. More significant discrepancy is in the Northern Atlantic where influence of episodic transport of mercury from anthropogenic sources is possible.

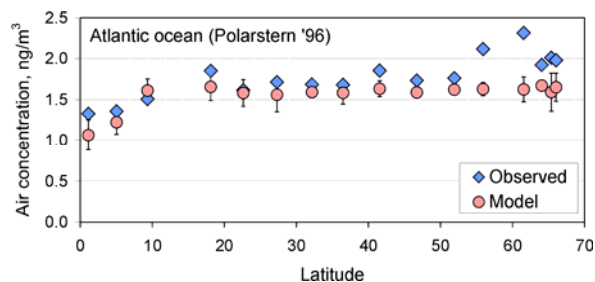


**Figure 5.13.** Daily mean concentrations of TGM in the surface layer measured during *Polarstern* '96 cruise in the Atlantic and modeled for the same locations

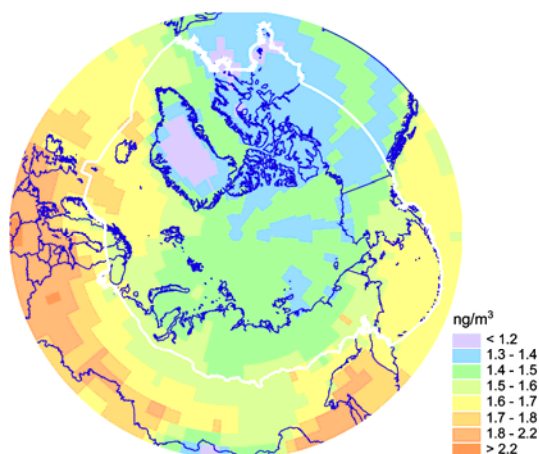
### 5.3. Arctic region

Mercury contamination of the Arctic has a number of characteristic features peculiar to the region as a whole. In this section we consider general modeled results of the Arctic contamination by mercury.

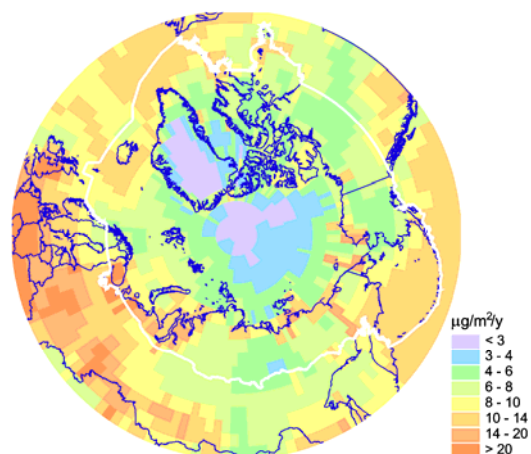
#### *Levels of concentration and depositions*

Figure 5.14 shows levels of mercury concentration in the ambient air of the Arctic region. Here and further we use the AMAP domain limits [AMAP, 1998] as a definition of the Arctic region. As seen from the figure air concentration of mercury in the Arctic varies from 1.2 ng/m<sup>3</sup> over Greenland to 2 ng/m<sup>3</sup> in the North Atlantic. Besides, elevated values of concentration occur in the Bering Sea. In the first case this is result of the long-range transport from European sources, in the second one – mainly the influence of mercury sources from Southeast Asia. Mean annual concentrations of mercury over the Arctic Ocean and Asian part of Russia are around 1.5 ng/m<sup>3</sup>.

Spatial distribution of annual mercury deposition to the Arctic is presented in Figure 5.15. As one can see, the deposition field varies more significantly – from less than 3 g/km<sup>2</sup> per year in Greenland and near the pole to more than 20 g/km<sup>2</sup> per year over areas adjacent to the Arctic coast. The reasons for that variability are annual precipitation pattern (defining wet depositions) and mercury depletion events. Considerable depositions are also in the North Atlantic and the Bering Sea.



**Figure 5.14.** Spatial distribution of mean annual air concentration of total gaseous mercury (TGM) in the Arctic region. White curve shows limits of the AMAP domain



**Figure 5.15.** Spatial distribution of total annual deposition of mercury in the Arctic region. White curve shows limits of the AMAP domain

### Main contributors to the Arctic pollution

Due to the high transport potential of mercury in the atmosphere many anthropogenic and natural sources from different regions of the Northern Hemisphere contribute to the Arctic pollution. Figure 5.16 demonstrates relative contributions of anthropogenic and natural sources to the annual mercury deposition to the Arctic. Unidentified sources describe mercury coming through the equator. Here we do not distinguish primary emission sources and re-emission of mercury previously deposited to the ground. As it is seen contribution of anthropogenic sources varies from 40% to 49%, whereas natural sources contributes from 44% to 54%.

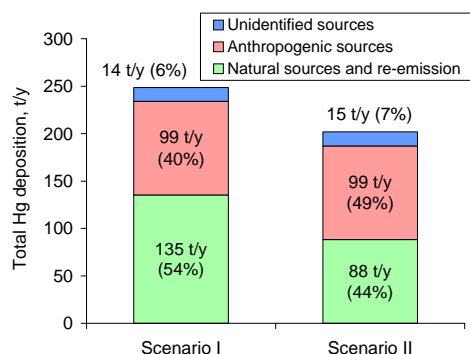


**Figure 5.16.** Contribution of different types of sources of the Northern Hemisphere to the annual deposition of mercury to the Arctic. Unidentified sources describe mercury coming through the equator

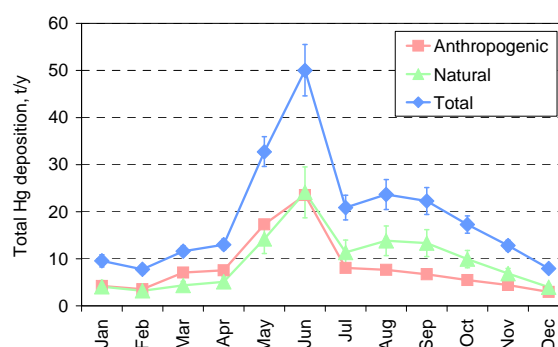


**Figure 5.17.** Seasonal variation of total mercury deposition of to the Arctic. Intervals show difference between two emission scenarios

Seasonal variation of total mercury deposition of to the Arctic is illustrated in Figure 5.17. A significant influence of MDE on the Arctic deposition is predicted in the end of spring and beginning of summer (here one should take account of the temporal shift mentioned in Section 5.1), when total deposition amounts to 50 tonnes per month. Deposition of anthropogenic mercury is defined mostly by variation of precipitation, whereas deposition from natural sources and re-emission is considerably influenced by the temperature dependence of the emission process, it leads to the increase of natural emissions in the late summer.

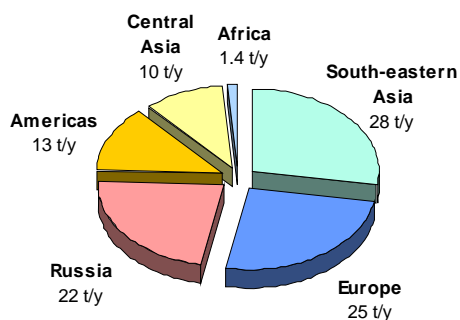


**Figure 5.18.** Contribution of different regions to the annual deposition of mercury to the Arctic from **anthropogenic** sources

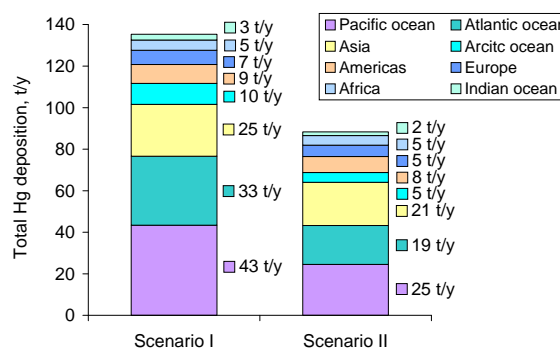


**Figure 5.19.** Contribution of different regions to the annual deposition of mercury to the Arctic from **natural** sources and **re-emission**

The contribution of different regions of the Northern Hemisphere to the total annual deposition to the Arctic from anthropogenic and natural sources are shown in Figures 5.18 and 5.19 respectively. As one can see the most significant contributors to anthropogenic mercury deposition are sources located in South-east Asia, Europe and Russia. The most significant contributions to the natural component of annual deposition to the Arctic are from the Pacific and Atlantic oceans, and from Asia. Keeping in mind that the parameterization of natural emission and re-emission processes contain considerable uncertainty and, on the other hand, natural emission cannot be controlled by any political decisions we shall pay more attention to deposition from anthropogenic sources.

## 5.4. Regions of the Russian North

Mercury contamination of the Russian North contains both common features peculiar to the Arctic region and some distinctions determined by local conditions. This section contains a detailed consideration of contamination of the Russian North regions by mercury. We shall consider five selected regions: Murmansk Oblast (MUR), Nenets AO (NEN), Yamalo-Nenets AO and Taimyr AO (YNT), Sakha Republic (Yakutia) (YAK), and Chukotka AO (CHU).

### Levels of concentration and depositions

Figure 5.20 shows spatial distribution of mean annual concentration of TGM in the ambient air of regions of the Russian North. It is seen that mean annual concentration varies slightly over this territory (from 1.4 to 1.8 ng/m<sup>3</sup>). There are elevated concentration levels in Murmansk Oblast and in central Sakha Republic related mostly to local emission sources. Besides, there is some gradient of mercury concentration southward in such regions as Yamalo-Nenets AO, Sakha Republic and Chukotka AO. Possible reason is a considerable decrease of elemental mercury concentration over the Arctic coast during springtime caused by mercury depletion events.

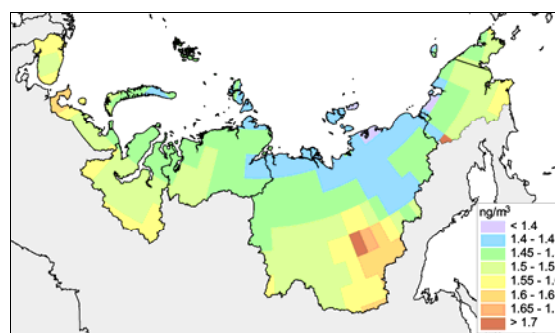


**Figure 5.20.** Spatial distribution of mean annual air concentration of TGM in the Russian North

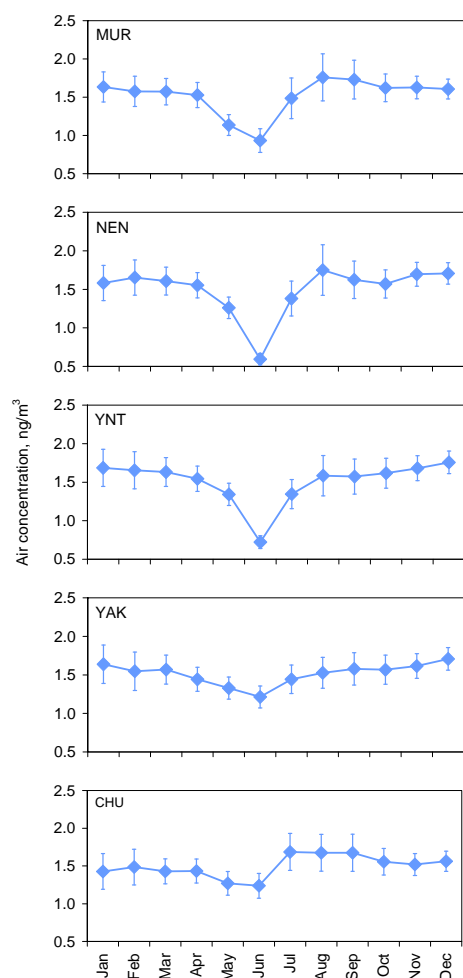


**Figure 5.21.** Seasonal variation of average concentration of TGM in the regions of Russian North. Intervals show difference between two emission scenarios

The effect of MDE on seasonal variation of mercury concentration in the ambient air is illustrated in Figure 5.21. As seen from the figure the lowest concentrations in all the regions are observed in June. The strongest decrease occurs in Nenets AO (down to 0.7 ng/m<sup>3</sup>), whereas in Sakha Republic and Chukotka AO it is not so significant (concentration is about 1.4 ng/m<sup>3</sup>). This can be explained by large interior territory for the former and significant influence of transport from Asian sources for the latter. Slightly elevated concentrations in last months of summer can be explained by increased natural emission (and re-emission) of mercury in the late summer due to higher surface temperature during this season.

Spatial distribution of mercury air concentration in two different months (June and December) is illustrated in Figures 5.22 and 5.23. In June (Fig. 5.22) low concentrations (lower than 0.6 ng/m<sup>3</sup>) are clearly seen over the Arctic coast due to MDE. The most significant decrease is over Gulf of the Ob River, the Laptev Sea and the East Siberian Sea coasts. High concentration values in the southern part of Sakha Republic and the Pacific coast of Chukotka AO are caused by long-range transport from South-eastern Asia (mostly from China). Concentration levels of mercury in December (Fig. 5.23) are comparatively higher for two reasons: coastal zones are not exposed to MDE phenomenon any more, and lower air temperature leads to higher air density and in turn volume concentrations. Besides, some of the regions (Nenets AO, Yamalo-Nenets AO and Taimyr AO and Sakha Republic) are subjected to a significant influence of Russian and other European sources.

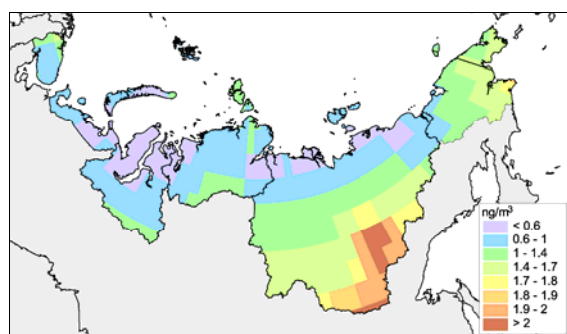


**Figure 5.22.** Spatial distribution of monthly mean concentration of TGM in the Russian North in June

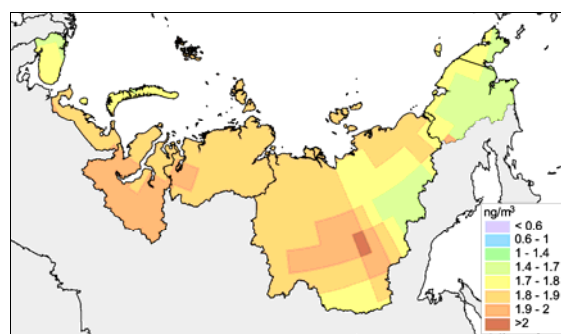


**Figure 5.23.** Spatial distribution of monthly mean concentration of TGM in the Russian North in December

Spatial distribution of total annual deposition flux of mercury is shown in Figure 5.24. The highest depositions are to the coast of the Arctic Ocean due to MDE, where annual deposition flux can exceed  $20 \text{ g/km}^2$ . The lowest depositions (less than  $5 \text{ g/km}^2/\text{y}$ ) are in central Sakha Republic because of a small amount of annual precipitation in this region. Total annual deposition of mercury to Murmansk Oblast is  $3 \text{ t/y}$ , to Nenets AO -  $3.7 \text{ t/y}$ , to Yamalo-Nenets AO and Taimyr AO -  $14.5 \text{ t/y}$ , to Sakha Republic -  $20.7 \text{ t/y}$ , and to Chukotka AO -  $7 \text{ t/y}$ .

Seasonal variation of total mercury deposition flux averaged over the regions is illustrated in Figure 5.25. For comparison variation of precipitation amount is also presented. As seen from the figure seasonal variation of deposition in general well correspond to that of precipitation, because wet deposition with precipitation is the dominating mechanism of mercury scavenging from the atmosphere. The exception is high depositions to all regions during May and June when mercury depletion events (MDE) take place. Deposition fluxes in these months can several times exceed those during the rest of the year. The highest exceeding is in Murmansk Oblast, because according to the model parameterization almost all its territory is exposed to MDE (see Fig. 5.6).

Variation of spatial distribution of mercury deposition fluxes during a year is shown in Figures 5.26 and 5.27. As it is expected the most intensive depositions in June (Fig. 5.26) are over areas of the Arctic coast where MDE takes place. In December (Fig. 5.27) depositions are considerably lower in all the regions and especially in Sakha Republic due to low precipitation amount.

Characteristic values of mean annual air concentrations and total annual deposition flux for each region are summarized in Table 5.3.

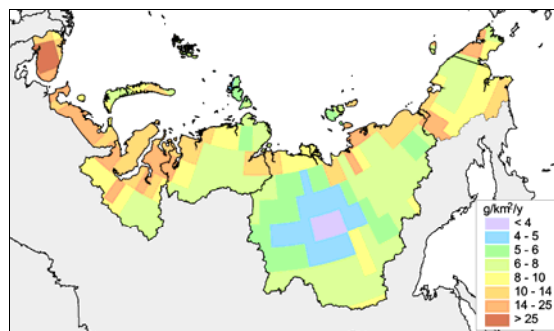


**Figure 5.24.** Spatial distribution of annual deposition flux of total mercury to the Russian North

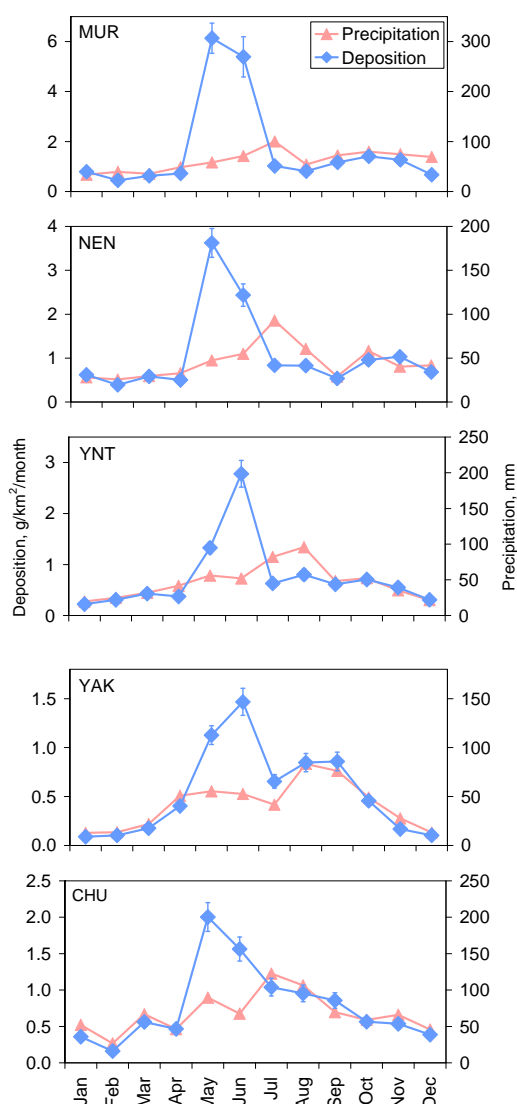


**Figure 5.25.** Seasonal variation of average deposition flux of total mercury in the regions of the Russian North. Intervals show difference between two emission scenarios

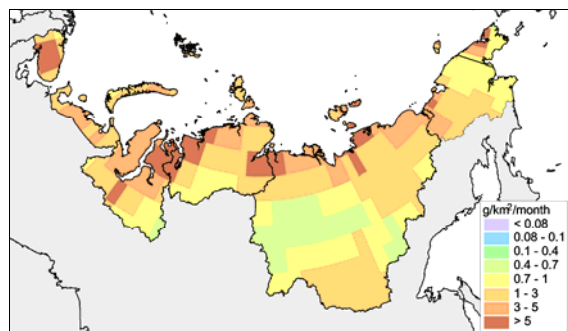


**Figure 5.26.** Spatial distribution of monthly deposition flux of total mercury in the Russian North in June

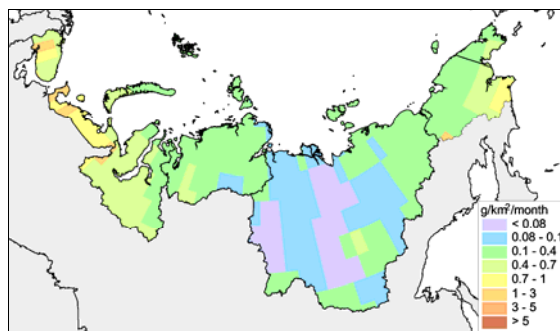


**Figure 5.27.** Spatial distribution of monthly deposition flux of total mercury in the Russian North in December

**Table 5.3.** Characteristic values of air concentrations and total annual deposition flux in five selected regions of the Russian North

Region	Air concentrations, ng/m <sup>3</sup>			Total annual deposition flux, g/km <sup>2</sup> /y		
	min	max	average	min	max	average
Murmansk Oblast	1.52	1.62	1.56	8	30	21
Nenets AO	1.44	1.66	1.52	6	26	14
Yamalo-Nenets AO and Taimyr AO	1.43	1.58	1.5	5	15	10
Sakha Republic	1.38	1.75	1.5	3	17	7
Chukotka AO	1.38	1.71	1.5	6	18	10

Relative contribution of different regions to the pollution of the Russian North is analyzed in the next subsection. Since methylmercury naturally formed from inorganic mercury by biological activity in aquatic compartments, makes the most significant adverse impact of mercury on the human health and the environment, we shall pay further more attention to deposition of airborne mercury to the surface.

### *Contribution of different regions to the pollution of the Russian North*

Dispersion of mercury in the global atmosphere and, in particular, source-receptor relationships have some peculiarities. Due to long residence time of mercury in the atmosphere (about 1 year) it is able to flow with air mass around the globe (one or more times) until it is deposited to the ground. Therefore pollution of remote regions by mercury, in contrast to short-lived pollutants (e.g. lead), looks not as direct transport from source region to a receptor region but rather as the contribution of locally emitted mercury to the global mercury pool in the atmosphere (so-called 'global background'), mixing, and further deposition to the surface. However, in some cases episodic or seasonal influence of large regional sources on pollution of a certain region can even dominate over the global background.

To determine contributors to the pollution of a certain region of the Russian North we distinguish emission sources located in different regions of the Northern Hemisphere as it was described in Chapter 4. We differentiate sources from Russia, Eastern, Western, Northern and Southern Europe, Central Asia, China, Japan, South-east Asia (without China and Japan), both Americas, and Africa. Besides, Russian sources are subdivided into several regions listed in Table 5.3 along with their codes used in the text. The location of the regions is shown in Figure 5.28.

**Table 5.4.** Regions of Russia considered in the source-receptor analysis

Region	Code
Murmansk Oblast	MUR
Nenets AO	NEN
Yamalo-Nenets AO and Taimyr AO	YNT
Sakha Republic (Yakutia)	YAK
Chukotka AO	CHU
Northern Region	NRT
North-Western region and Kaliningrad Oblast	NWK
Central and Volga-Viatsky regions	CVV
Central-Chernozem, Volga, and North-Caucasian regions	CVN
Ural region	URL
West-Siberian region	WSB
East-Siberian and Far-Eastern regions	ESB

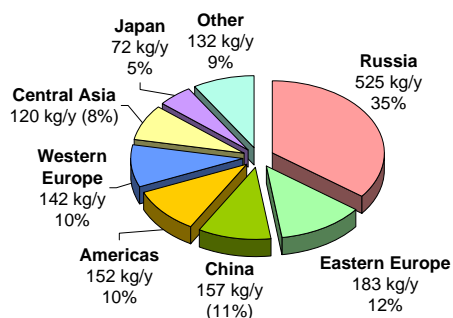
**Figure 5.28.** Location of Russian regions

For the evaluation of source-receptor relationships mercury emitted from each source region is considered separately. However, due to significant number of the source regions (30 including natural sources) calculations for all regions are performed simultaneously. To avoid uncertainties connected with the model non-linearity all the processes (advection, diffusion, chemistry, deposition etc.) are computed for total pollutant mass re-calculating contribution of each source region after each process. Thus, if at some time step contribution of  $i^{\text{th}}$  source to mercury mass  $m$  in a gridcell is  $\alpha_i$  and due to some process the mass  $m$  is increased by value  $\delta m$  with fraction of  $i^{\text{th}}$  source  $\beta_i$ , then contribution of  $i^{\text{th}}$  source to mercury mass in the gridcell at the next time step will be  $\alpha'_i = (\alpha_i m + \beta_i \delta m) / (m + \delta m)$ . This procedure is performed for each mercury species separately.

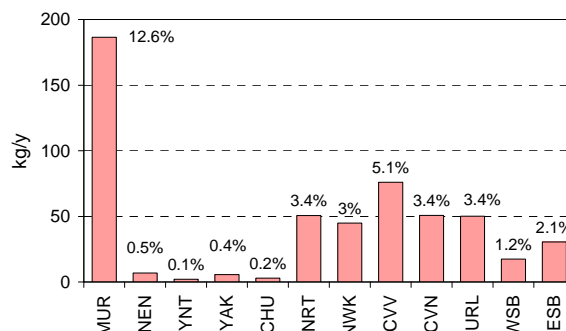
**Murmansk Oblast (MUR).** Murmansk Oblast is one of northwestern regions of Russia located on the Kola Peninsula. That is why influence of European sources (both Russian and external) is most important for this region. Figures 5.29 and 5.30 illustrate contributions of major external and Russian sources to annual mercury deposition to Murmansk Oblast from anthropogenic sources. As seen the largest contribution is made by Russian internal sources (35%). Among them about 13% is from its own sources (MUR) and 18% from other Russian European regions (NRT, NWK, CVV, CVN and URL). The most important external sources are Eastern Europe (12%), China (11%), Americas (10%), and Western Europe (10%). The category “Others” here and for other receptor-regions contains Northern and Southern Europe, South-east Asia (excluding China and Japan), and Africa due to their insignificant contributions.

Figure 5.31 shows seasonal variation of relative contributions of different regions to mercury deposition to Murmansk Oblast. As one can see from the diagram relative contribution of Russian sources is the most variable: It alters from about 50% in February to about 25% in June. This alteration is mainly determined by variation of relative contribution of own sources of Murmansk Oblast (white line). This fact can be explained by the consideration of absolute deposition values (see Fig. 5.32). The absolute value of total deposition from Murmansk Oblast sources varies slightly during the year. Instead, deposition from other Russian regions changes considerably (the same is for external regions).

The reason for increasing contribution of remote sources in May and June is MDE. Indeed, products of MDE (gaseous oxidized and particulate mercury) are the most effectively scavenged from the atmosphere in comparison with other mercury forms.



**Figure 5.29.** Relative contributions of regions of the Northern Hemisphere to annual mercury deposition to Murmansk Oblast from anthropogenic sources



**Figure 5.30.** Contribution of Russian regions to annual mercury deposition to Murmansk Oblast from anthropogenic sources

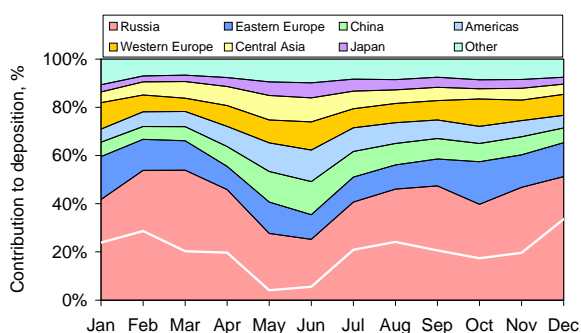


**Figure 5.31.** Seasonal variation of relative contributions of different regions to mercury deposition to Murmansk Oblast. White line shows contribution of own sources of Murmansk Oblast

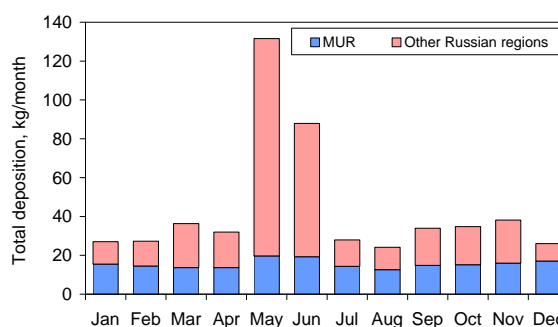


**Figure 5.32.** Seasonal variation of total mercury deposition to Murmansk Oblast from anthropogenic sources of Russian regions

Besides, these forms are also primarily emitted to the atmosphere from anthropogenic sources. Due to a short residence time in the atmosphere gaseous oxidized and particulate mercury are mostly deposited in the vicinity of emission sources. That is why the contribution of MDE to deposition of these forms from local sources is insignificant. On the contrary, mercury from remote sources reaches the region mostly in form of elemental vapour and is not deposited effectively. While during MDE elemental mercury is transformed into short-lived forms and its deposition increases.

In January and October more intensive transport of mercury from European sources takes place (see Fig. 5.31). This transport is illustrated in Figure 5.33 for January.

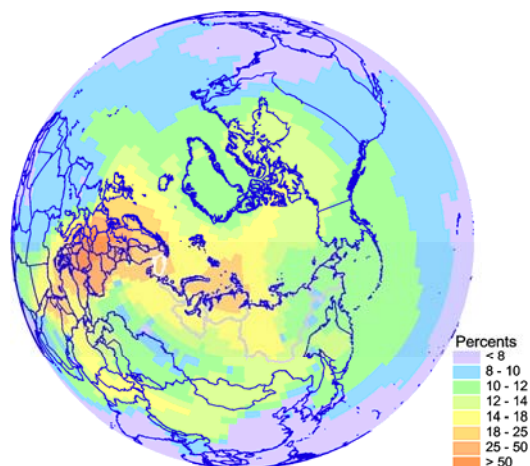


**Figure 5.33.** Spatial distribution of relative contribution of East European sources to concentration of anthropogenic mercury in the ambient air in January. White curve shows Murmansk Oblast

**Nenets AO (NEN).** Nenets AO is located in the northern part of European Russia. Therefore main features of its long-range pollution are similar to those of Murmansk Oblast. The distinction is more significant influence of Russian regions. Figures 5.34 and 5.35 show the relative contribution of different regions to total annual deposition of mercury to Nenets AO from anthropogenic sources. The largest contribution is made by Russian sources again (35%). However, in comparison to Murmansk Oblast, own sources of Nenets AO contribute only 7% from the total deposition, whereas combined contribution of other Russian European regions (NRT, NWK, CVV, CVN and URL) is more significant (24%). The most important of them are Northern region (NRT), Central and Volga-Viatsky regions (CVV). The most significant external contributors are Eastern Europe (13%), China (11%), Americas (10%), Western Europe (9%), and Central Asia (9%).

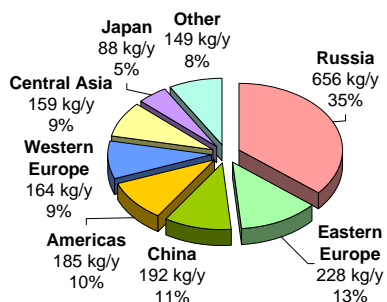


**Figure 5.34.** Relative contributions of regions of the Northern Hemisphere to annual mercury deposition to Nenets AO from anthropogenic sources

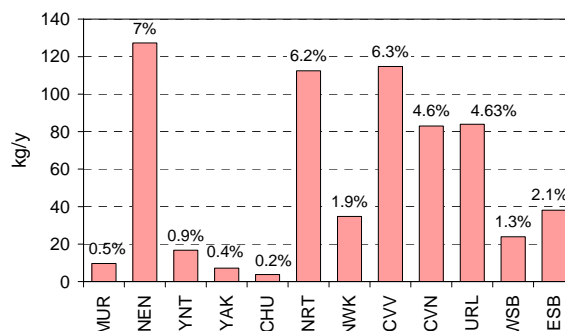


**Figure 5.35.** Contribution of Russian regions to annual mercury deposition to Nenets AO from anthropogenic sources

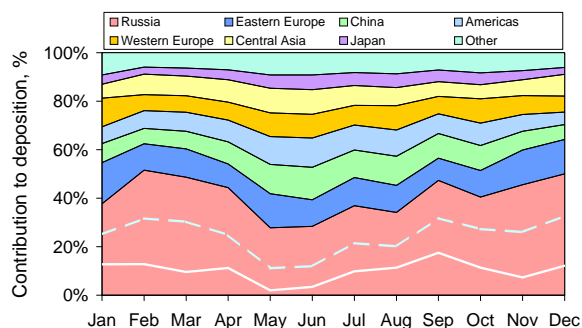


**Figure 5.36.** Seasonal variation of relative contributions of different regions to mercury deposition to Nenets AO. White solid line shows the contribution of own Nenets sources, dashed line – combined contribution of three the most important regions (NEN, NRT and CVV)

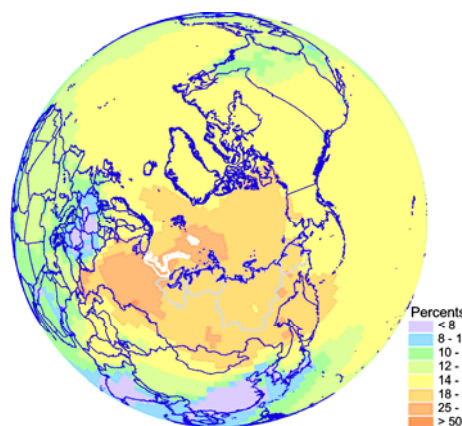


**Figure 5.37.** Spatial distribution of relative contribution of Russian European sources (NRT, NWK, CVV, CVN, and URL) concentration of anthropogenic mercury in the ambient air in November. White curve shows Nenets AO

Seasonal variation of relative contributions from different sources is presented in Figure 5.36. As in the case of Murmansk Oblast the contribution of Russian sources is the most variable. However, in this case the variation is determined not only by own Nenets sources but also by sources from Northern, Central and Volga-Viatsky regions (see dashed line in Fig. 5.36). Beside MDE months (May and June) depositions from these sources are significant in March and November. The transport of mercury from Russian European regions sources (NRT, NWK, CVV, CVN, and URL) in November is illustrated in Figure 5.37. The contribution of all external sources increases during MDE in May and June. Moreover, the transport from Eastern and Western European sources make up some essential contribution in January.

**Yamalo-Nenets AO and Taimyr AO.** Location of Yamalo-Nenets AO and Taimyr AO in northern part of western Siberia accounts for the fact that Asian sources become play a noticeable role in their pollution, however, European ones still continue to exert a considerable effect. As seen from Figure 5.38 up to 30% of mercury annually deposited to these regions is from Russian sources. One should note that the contribution of own sources of Yamalo-Nenets AO and Taimyr AO is comparatively low (about 3%), whereas three major Russian contributors (CVV, CVN, and URL) make up 16% of total deposition (see Fig. 3.39). Two major external contributors are China (12%) and Eastern Europe (12%). A considerable impact is also from Americas (11%), Central Asia (11%) and Western Europe (9%).

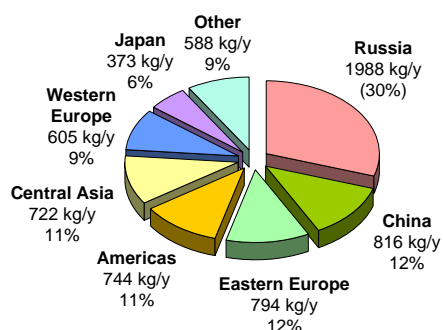


**Figure 5.38.** Relative contributions of regions of the Northern Hemisphere to annual mercury deposition to Yamalo-Nenets AO and Taimyr AO from anthropogenic sources

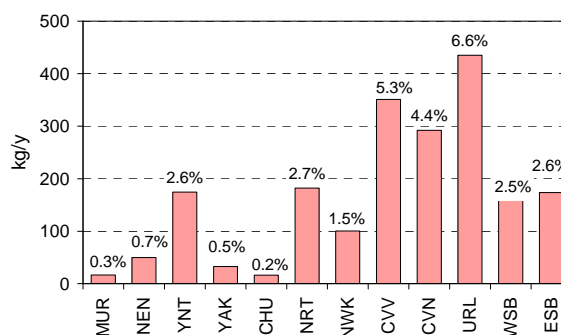


**Figure 5.39.** Contribution of Russian regions to annual mercury deposition to Yamalo-Nenets AO and Taimyr AO from anthropogenic sources

Seasonal variations of relative contributions are shown in Figure 5.40. As seen variation of Russian sources has in general the same shape as those of Murmansk Oblast and Nenets AO (with maximum in February and minima May and June) but with lower amplitude. It could be explained by insufficient influence of own sources (white solid line). On the other hand, the seasonal variation is substantially defined by the impact of one of the main internal contributors – Ural region (dashed line). As usual, contribution of external regions increases during MDE in June. Besides, transport from China affects more significantly in September, Eastern and Western Europe contribute more essentially in January, whereas contribution of Central Asia increases in February and December. Mercury transport from Central Asian sources northward in December is shown in Figure 5.41.

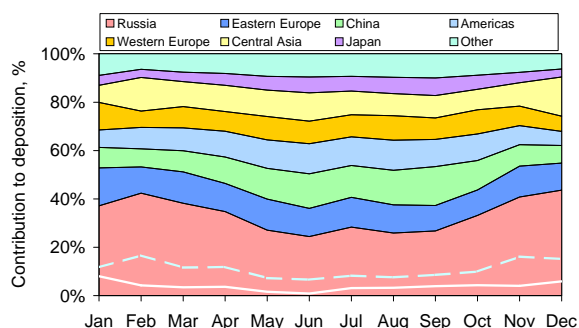


**Figure 5.40.** Seasonal variation of relative contributions of different regions to mercury deposition to YNT. White solid line shows the contribution of own sources, dashed line – combined contribution of own and Ural region sources

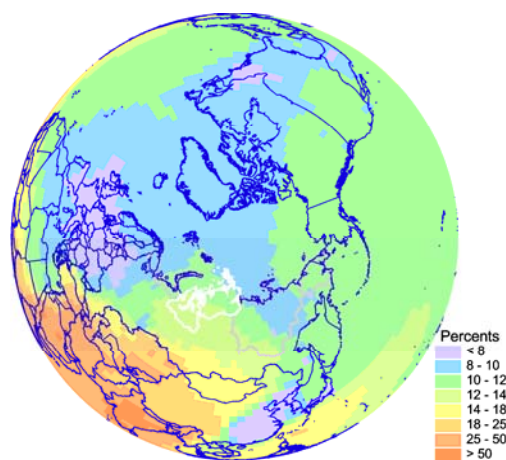


**Figure 5.41.** Spatial distribution of relative contribution of Central Asian sources to concentration of anthropogenic mercury in the ambient air in December. White curve shows Yamalo-Nenets AO and Taimyr AO

**Sakha Republic (Yakutia)** Sakha Republic is a large region covering the northern and central parts of Eastern Siberia. In spite of insignificant total emission, influence of its own sources is substantial due to a large territory and peculiarities of atmospheric circulation in central Siberia. Besides, Asian sources become dominating in this region. As seen from Figure 5.42 Russian regions contribute about 30% of total annual mercury deposition to Sakha Republic. Among them the most significant contribution is made by own sources of this region (see Fig. 5.43). Major external contributors are China (15%), Americas (11%), Eastern Europe (11%), and Central Asia (10%).

As one can see from Figure 5.44 seasonal variation of the relative contributions are mostly defined by own sources of the region. Their contribution (white solid line) varies from several percent in the beginning of summer up to 20-30% in winter months. Substantial contribution of regional sources in wintertime can be explained by reduced airborne transport to the region due to Siberian Anticyclone traditionally prevailing over winter months. As to external sources, impact of China reaches its maximum in September (up to 20%). Airborne transport of mercury from Chinese sources in September is illustrated in Figure 5.45. It flows northeast from China and reaches Sakha Republic through the Sea of Okhotsk. The contribution of other regions slightly differs from month to month.

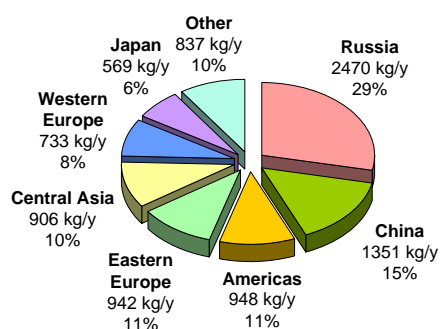


**Figure 5.42.** Relative contributions of regions of the Northern Hemisphere to annual mercury deposition to Sakha Republic from anthropogenic sources

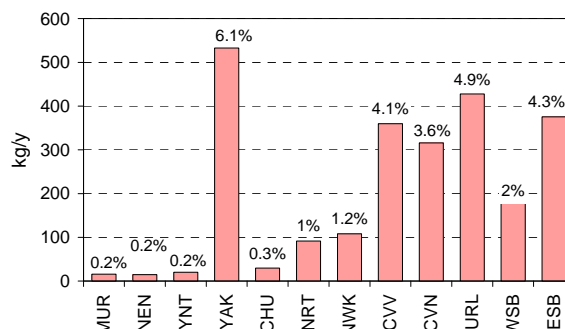


**Figure 5.43.** Contribution of Russian regions to annual mercury deposition to Sakha Republic from anthropogenic sources

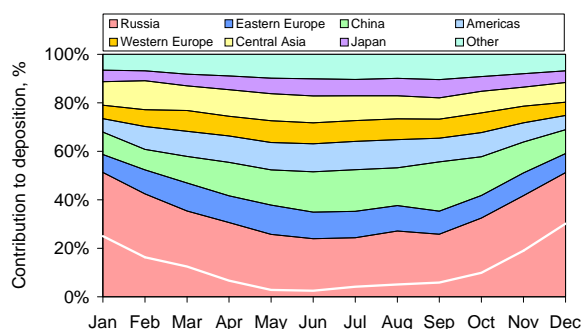


**Figure 5.44.** Seasonal variation of relative contributions of different regions to mercury deposition to Sakha Republic. White solid line shows contribution of own sources

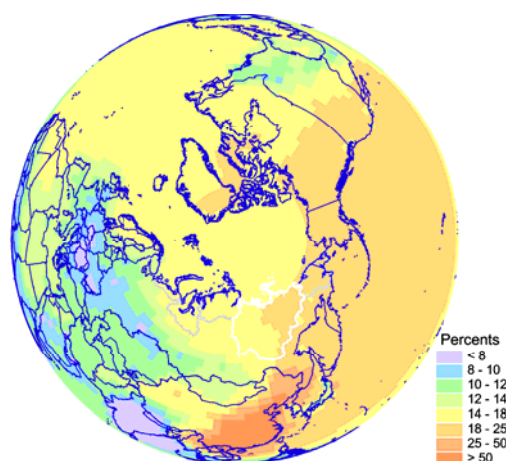


**Figure 5.45.** Spatial distribution of relative contribution of Chinese sources to concentration of anthropogenic mercury in the ambient air in September. White curve shows Sakha Republic

**Chukotka AO.** Chukotka AO is the most eastward remote region of Russia. Its location far away from major industrial regions accounts for the fact that global background of mercury has a substantial effect on the region pollution. Figure 5.46 demonstrates relative contributions of different regions to annual mercury deposition to Chukotka AO. As seen the main contributor is still Russia (26%), however, contribution of China is also considerable (17%). Among others one can distinguish Americas (11%), Central Asia (10%), and Eastern Europe (10%). The contribution of own sources of Chukotka AO is insignificant comparing with emission sources located in Eastern Siberia and Far East (Fig. 5.47). However, influence of major emission regions from European Russia (CVV, CVN, URL) is also noticeable.

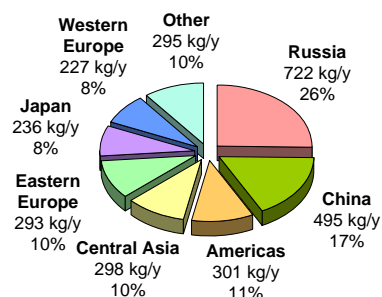


**Figure 5.46.** Relative contributions of regions of the Northern Hemisphere to annual mercury deposition to Chukotka AO from anthropogenic sources

As it is shown from Figure 5.48 relative contributions of regions to mercury deposition to Chukotka AO vary slightly during a year. It could be explained by predominance of the global background over episodic transport from neighboring regions. Own sources of Chukotka AO only slightly affect deposition to the region. Russian internal sources permanently make up a substantial contribution (about 20%) with some increase in February due to intensive zonal transport across the entire territory of Russia. Significant mercury depositions to Chukotka AO during of the year are also from Chinese sources.

Because of prevailing airflow transport from South-east Asia eastward and north-eastward, Chukotka AO is almost permanently exposed to mercury from Chinese and other Asian sources.

China is one of major emitters of mercury to the atmosphere. Its contribution to the total mercury emission in the Northern Hemisphere makes up to 35% (see Section 4.1). Therefore, influence of Chinese emission sources could be noticeable even for pollution of such remote regions as the Arctic. Figure 5.49 illustrate seasonal patterns of mercury airborne transport to regions of the Russian North from anthropogenic emission sources located in China. As one can see from the figure the dominating direction of the transport from China is eastward to the Pacific. In late winter and spring months its influence is mostly confined by the Pacific Ocean. However, starting from middle of summer mercury from Chinese sources penetrates the Arctic through the Bering Sea and Alaska. In autumn it is transported through the Sea of Okhotsk and attains to eastern regions of the Russian North. In this period contribution of such distinct source region as China to mercury concentration in air of Chukotka AO and Sakha Republic can reach 20%.

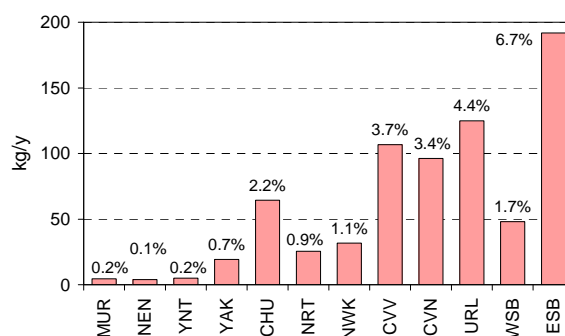


**Figure 5.47.** Contribution of Russian regions to annual mercury deposition to Chukotka AO from anthropogenic sources

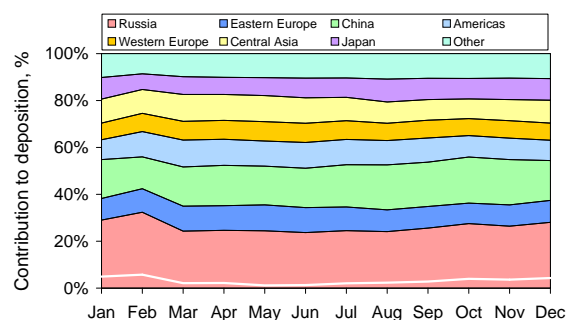


**Figure 5.48.** Seasonal variation of relative contributions of different regions to mercury deposition to Chukotka AO. White solid line shows contribution of own sources

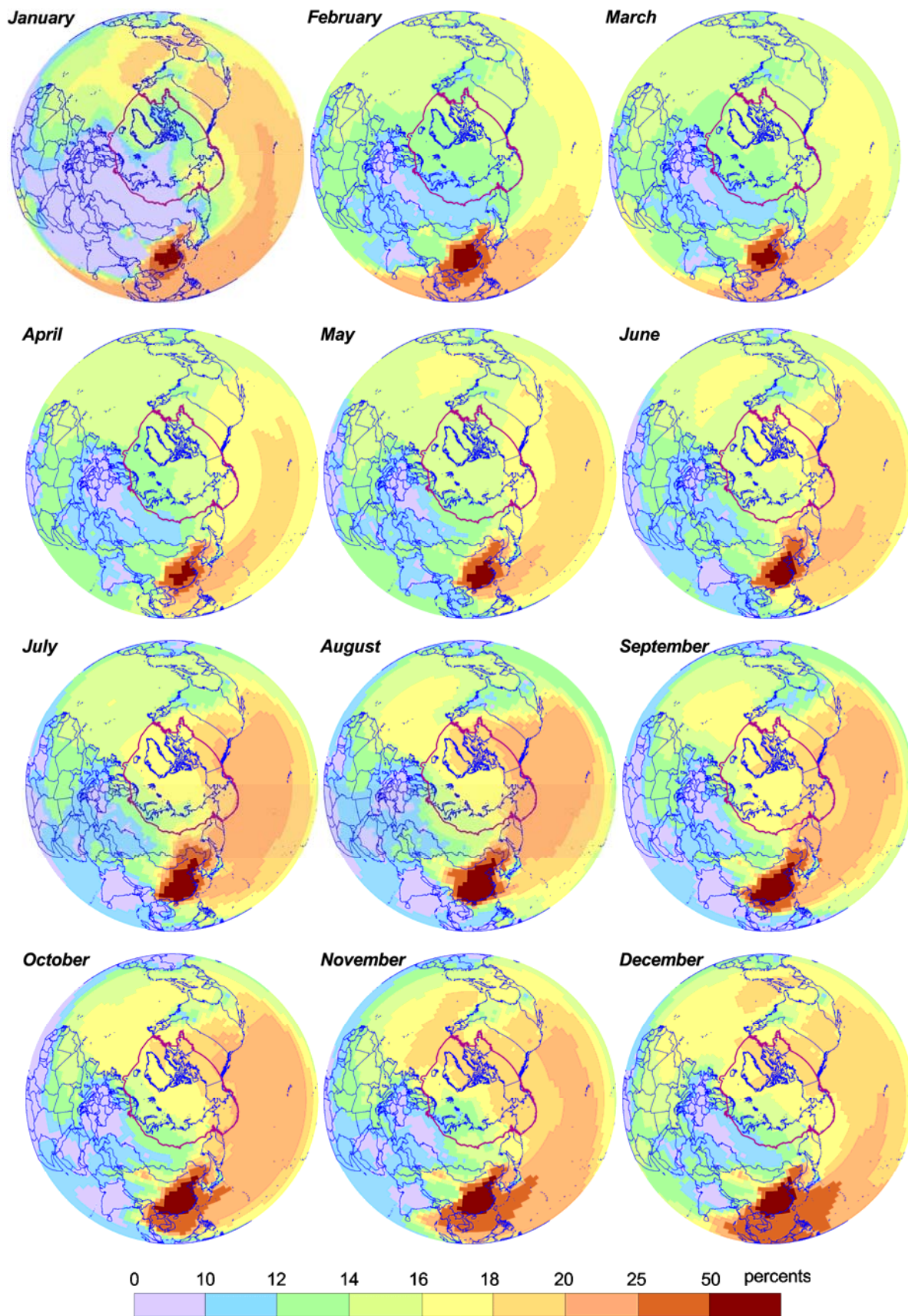


Figure 5.49. Contribution of Chinese sources to concentration of anthropogenic mercury in the ambient air of the Northern Hemisphere

## 5.5. Concluding remarks

Summarizing investigation results presented above one can conclude the following:

- The developed model of mercury long-range airborne transport and depositions on the hemispheric scale can be successively applied to the assessment of mercury concentration levels in the ambient air and deposition fluxes to the surface in the Northern Hemisphere and some particular regions as the Arctic. Satisfactory agreement of modeling results with available measurements verifies reasonable reliability of the model.
- Airborne transport of mercury from remote industrial regions noticeably contributes (up to 40%) to the pollution of the Arctic as a whole and regions of the Russian North, in particular.
- Such short-term phenomenon as mercury depletion events occurring in the Arctic during springtime sunrise does substantially affect the pollution load of this region by mercury considerably increasing (up to 60%) annual mercury depositions in areas adjacent to the Arctic coast (200-300 kilometers northward and southward the coast).
- Natural mercury sources and re-emission of previously deposited mercury are able to contribute considerably to mercury contamination of the Arctic regions. However, the uncertainty of their contributions is still significant.
- Mercury concentration levels in the ambient air slightly vary over all regions of the Russian North (mean annual values 1.4-1.8 ng/m<sup>3</sup>). Deposition fluxes vary more significantly (from 4 to 25 g/km<sup>2</sup>/y) depending on precipitation amount. The highest depositions are over areas adjacent to the Arctic coast due to mercury depletion events.
- For all regions of the Russian North influence of Russian emission sources dominates over that of external regions. The main external contributors of the Russian North pollution are Eastern and Western Europe, China, Americas, and Central Asia. Relative importance of these contributors varies for different regions of the Russian North. Mercury depletion events phenomenon results in increased role of external sources in the regions pollution.
- Contribution of own regional sources is the most important for **Murmansk Oblast**, but episodic transport of mercury from Eastern and Western European sources can also significantly influence the region pollution.
- Along with own sources of **Nenets AO** emissions from regions of European part of Russia considerably contribute to pollution of this region. Besides, airborne transport from Eastern and Western European sources is also noticeable.
- Ural region and two central regions of European Russia (CVV and CVN) make up the main contribution to the pollution of **Yamalo-Nenets AO and Taimyr AO** from Russian sources, whereas own regional sources do not play a significant role. Main external contributors are China, Eastern Europe, Americas and Central Asia.
- Own regional sources make substantial contribution to pollution of **Sakha Republic**, especially, in wintertime when transport from external sources is reduced. In other seasons episodic transport of mercury from China considerably affect the region pollution.
- Emission sources from Eastern Siberia and Far East are dominating over other Russian regions in regard to mercury contamination of **Chukotka AO**. The main external contributor to the region pollution is China, which contribution is comparable with that of Russian sources and slightly varies during the year.

## References

- AMAP [1998] *AMAP Assessment report: Arctic pollution issues*. Arctic Monitoring and Assessment Programme (AMAP), Oslo, Norway. 859 p.
- Berg T. and Hjelmbrekke A.-G. [1998] Heavy metals and POPs within the ECE region. EMEP/CCC Report 7/98, Norwegian Institute for Air Research, Kjeller, Norway
- Berg T. and Hjelmbrekke A.-G. [1999] AMAP Datareport: Atmospheric subprogramme. NILU OR 16/99, Norwegian Institute for Air Research, Kjeller, Norway
- Christensen J. [2001] Modeling of mercury with the Danish Eulerian hemispheric model. International Workshop on Trends and Effects of Heavy Metals in the Arctic. McLean, Virginia, 18-22 June 2001.
- Ebinghaus R., Turner R. R., Lacerda de L. D., Vasiliev O., and Salomons W. (Eds.) [1999] *Mercury contaminated sites*. Springer, Berlin. 538 p.
- Golubeva N., Burtseva L., Matishov G. [2003] Measurements of mercury in the near-surface layer of the atmosphere of the Russian Arctic. *Sci. Tot. Envir.*, in press
- Kim K.-H., Kim M.-Y., Kim J., Lee G. [2002] The concentrations and fluxes of total gaseous mercury in a western coastal area of Korea during late March 2001. *Atmos. Environ.* v.36, 3413-3427
- Konoplev A. [2003] Private communication.
- Lamborg C. H., Fitzgerald W. F., O'Donnell J., and Torgersen T. [2002] A non-steady-state compartmental model of global-scale mercury biogeochemistry with interhemispheric atmospheric gradients. *Geochimica et Cosmochimica Acta.* v.66, No.7, pp.1105-1118.
- Lindberg S. E., Brooks S., Lin C.-J., Scott K. J., Landis M. S., Stevens R. R., Goodsite M., and Richter A. [2002] Dynamic oxidation of gaseous mercury in the Arctic troposphere at polar sunrise. *Environ. Sci. Technol.* v.36, pp.1245-1256
- NADP/MDN [2002] *National Atmospheric Deposition Program (NRSP-3)/Mercury Deposition Network*. (<http://nadp.sws.uiuc.edu/mdn/>)
- Poisant L. [2000] Total gaseous mercury in Quebec (Canada) in 1998. *Sci. Tot. Envir.*, v. 259, pp.191-201
- Slemr F. [1996] Trends in atmospheric mercury concentrations over the Atlantic ocean and the Wank Summit, and the resulting concentrations on the budget of atmospheric mercury. In: Baeyens W., Ebinghaus R. Vasiliev O. (Eds.), *Global and Regional Mercury Cycles: Sources, Fluxes and Mass Balances*. NATO-ASI-Series, Kluwer Academic Publishers, Dordrecht, The Netherlands, pp.33-84
- Tan H., He J.L., Liang L., Lazoff S., Sommer J., Xiao Z.F., and Lindqvist O. [2000] Atmospheric mercury deposition in Guizhou, China. *Sci. Tot. Envir.*, v. 259, 223-230
- Temme C., Slemr F., Ebinghaus R., Einax J.W. [2003] Distribution of mercury over the Atlantic Ocean in 1996 and 1999 - 2001, *Atmos. Environ.*, in press



## Chapter 6

**ATMOSPHERIC TRANSPORT AND DEPOSITION OF PCBs  
TO THE ARCTIC REGION**

This section contains the results of the assessment of environmental pollution by polychlorinated biphenyls (PCBs) in selected regions of the Russian North for 1996. Levels of concentrations and depositions of PCBs, and contributions to the contamination in these areas made by major emission sources of the Russian Federation and other distant sources within the Northern Hemisphere are estimated. This assessment is carried out on the basis of simulations using the MSCE-POP hemispheric multicompartiment model.

Modeling PCB redistribution over the environment is complicated due to of a large number of individual PCB congeners (more than 200), whose fates in the environment differ considerably. This results from the variety of these congeners' physical-chemical properties as well as from the variety of congener compositions of PCB mixtures used in different countries of the Northern Hemisphere. The information needed for model evaluation of transport and environmental accumulation of individual PCB congeners is rather limited. The most thoroughly investigated are the following of 7 PCB congeners: PCB-28, 52, 101, 118, 138, 153 and 180. For these congeners sufficient information on physical-chemical properties and measurement data is available. The information on emissions is at present available for 22 PCB congeners [Breivik *et al.*, 2002] including the above mentioned group of 7 congeners. On the other hand, the main interest in PCB assessment is focused on toxic PCB congeners. International toxic equivalency factors are assigned to 12 PCB congeners: PCB-77, 81, 105, 114, 118, 123, 126, 156, 157, 167, 169 and 189. For the toxic congeners, data on emissions are available for only three (PCB-105, 118 and 123). In order to cover a wide spectrum of PCB congeners' behaviour in the environment we have selected PCB-28, 118, 153 and 180 in view of the availability of emission and measurement data. These congeners have different physical-chemical properties and represent light (PCB-28), heavy (PCB-180) and toxic (PCB-118) congeners. A detailed description is given of the main processes of PCB behaviour in the environment using as an example PCB-153. Peculiarities in the behaviour of congeners are exemplified by PCB-28, 118 and 180 (see Annex A).

PCBs continue to be detected in the environment far from areas where they were originally used and despite efforts to restrict their emissions. It is believed that the major reasons for this are their ability to be transported long-range and their high persistence in the environment. Apart from atmospheric and seawater transport these pollutants can undergo a number of deposition/re-emission (multi-hop) cycles, the so-called "grasshopper effect". For proper model description of the re-emission process, long-term accumulations in environmental media should be assessed. On the basis of numerical experiments [Shatalov *et al.*, 2000, 2001] it was obtained that a preliminary calculation covering a 25-year period (model spin-up) is sufficient for medium saturation. Thus, for the pollution assessment of the Russian North in 1996 model preliminary calculations were carried out for the period of 1970 to 1995 for each congener considered. The initial conditions for calculations for 1996 were taken from the model spin-up.

Hemispheric annual emission data for the calculation from 1970 to 1996 were adapted from [Breivik *et al.*, 2002] (details in Section 4.2). The emission data is very uncertain, therefore three emission scenarios (Low, Mid and High) are presented in this work. Pilot calculations made by the MSCE-POP model indicated that the results obtained by using the High emission scenario give more reasonable

agreement with observed pollution levels. This suggests that in spite of prohibition on the PCB production, significant emissions could still continue.

The original emission data is given as total values for individual countries. Spatial distribution was made on the basis of population density distribution. Since there is no information about seasonal variations, PCB emissions were uniformly distributed over the year. It seems that the consideration of seasonal emission variations can significantly improve model results.

Apart from pollution level assessment, an analysis of the contributions of major sources to the contamination of the Russian North in 1996 was made. To this end PCB emission sources of the Northern Hemisphere were divided into 17 source groups (Section 4.2). Separate model runs were carried out for the assessment of pollution transport from each source group with the assumption of zero emissions from other sources and with zero initial conditions. These calculations allow us to evaluate the contributions of each emission source to depositions to and concentrations in the Russian North. A special run, with zero emissions and initial conditions obtained during the model spin-up, was performed to evaluate the influence of historical emissions on the contamination of the Russian North in 1996. The difference between pollution levels estimated by calculation on the basis of total emissions and sum of calculation results obtained from separate model runs does not exceed 3% for the considered areas of the Russian North.

The following section contains a general description of modeling results of four selected PCB congeners for the Northern Hemisphere. The verification of computed PCB concentrations in air and precipitation and deposition fluxes is presented in Section 6.2. A detailed description of PCB-153 pollution levels in the Russian North is given in Section 6.3. Similar results for other modeled congeners can be found in Annex A. Section 6.4 is devoted to the analysis of contributions from various emission sources to the contamination of the selected region. Section 6.5 contains information on PCB congener composition in regions of the Russian North.

## 6.1. General description of modeling results

This section gives calculation results of four model runs for PCB-153, 28, 118 and 180. Long-term trends in accumulation (during model spin-up 1970-95) and distribution between media (atmosphere, soil, seawater and vegetation) on the hemispheric scale for 1996 are described. Special attention is focused on the Arctic.

### *Redistribution between environmental media*

The accumulation process in the environmental media of the whole hemisphere during model spin-up is analysed. The dynamics of the accumulation process for PCB-153 in media along with the emission trend are presented in Figure 6.1. The emissions increase up to 1985 after which time they begin to decrease (Fig. 6.1.a). This leads to an immediate decrease of the content in the atmosphere and vegetation. After 1986, PCB-153 contents in all environmental compartments decrease (Fig. 6.1.b-e). The maximum of soil and seawater concentrations in 1986 testifies to the fact that the processes of degradation in and re-volatilization from these media are comparable with those of depositions and gaseous exchange, that is, that saturation is attained.

However, the rate of content reduction in the media is different. The lowest reduction rate is determined for soil, followed by sea, air and vegetation. Due to large accumulation capacities, low mass exchange rates and the high persistence of PCB-153 in soil and seawater, the rate of decrease

in content in these media is much slower than for emissions. The content decrease in the remaining media lags behind the emission reduction as well. For example, the delay of concentration decrease in air (Fig. 6.1.b) can be explained by re-emission flux from soil, keeping air pollution content. Changes in vegetation content (Fig. 6.1.c) are similar to the atmospheric ones due to high rate of mass exchange flux between these media.

Dynamics of total content and emissions during 1970-96 are given in Figure 6.1.f.

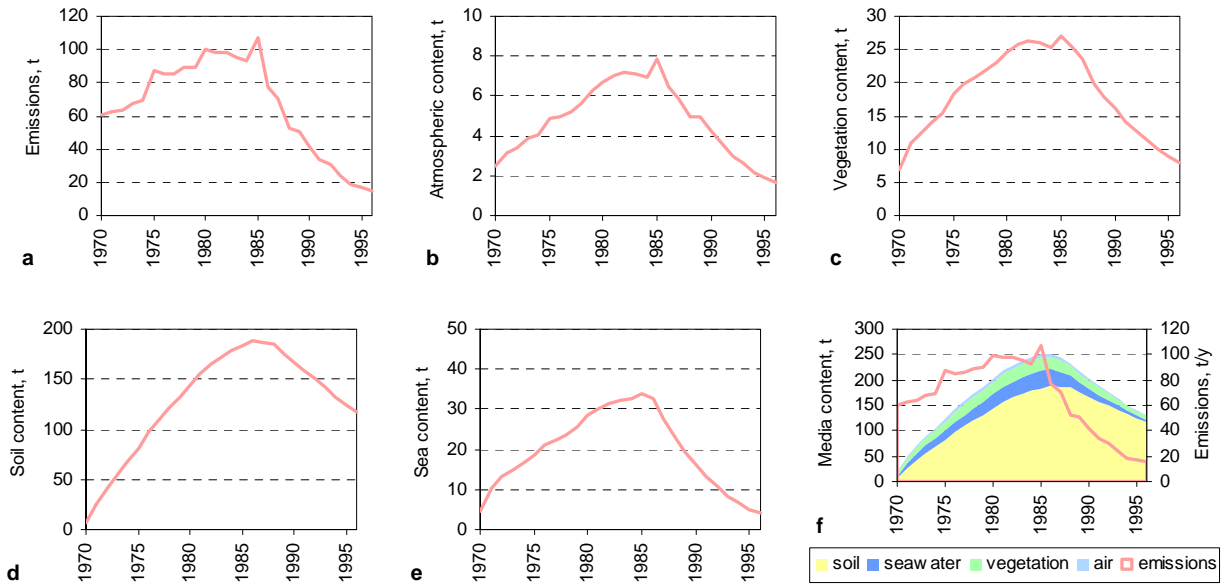


**Figure 6.1.** Trends of PCB-153 emissions and content in the Northern Hemisphere during model spin-up

Trends of medium contents and emissions of PCB-28, 118 and 180 are given in Figure 6.2. These diagrams indicate that medium saturation is also attained for these pollutants. The peculiarity of PCB-28 is that emissions decrease right from 1970 (Fig. 6.2.a). Medium saturation is attained in 1976, followed by a decrease in content. PCB-118 and 180 accumulation (Fig. 6.2.b and Fig. 6.2.c) is similar to that of PCB-153 (Fig. 6.1.f). It should be noted that in comparison with other congeners, PCB-180 soil content decrease after emission reduction is the slowest

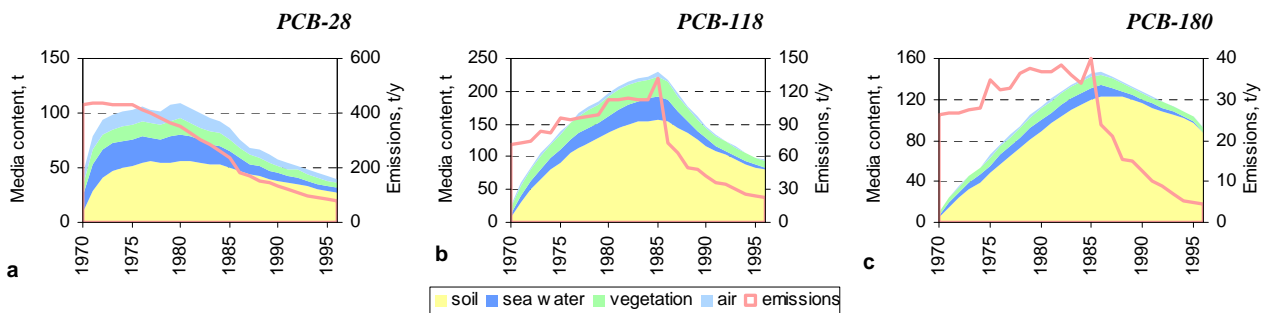


**Figure 6.2.** Trends in emissions and accumulation of PCB-28 (a), PCB-118 (b) and PCB-180 (c) in the Northern Hemisphere during model spin-up

The distribution of considered congeners between environmental compartments in late 1996 due to long-term accumulation is presented in Figure 6.3. As seen from the diagrams, the bulk of PCBs tend to be accumulated in the soil environment. PCB-180 is accumulated in soil to a greater extent than PCB-153, PCB-118, PCB-28. A tangible part of PCB-28 is contained in vegetation, sea and air.

Thus, we can conclude, that for all considered congeners medium saturation is attained. This testifies to the fact that the calculation period is long enough to reasonably describe contamination levels in all environmental compartments. The second conclusion is that soil is the main reservoir for PCBs. According to model assessment, substantial soil content can inflict a noticeable impact on the contamination of the atmosphere and other media against the background of emission reduction due to the re-emission process.

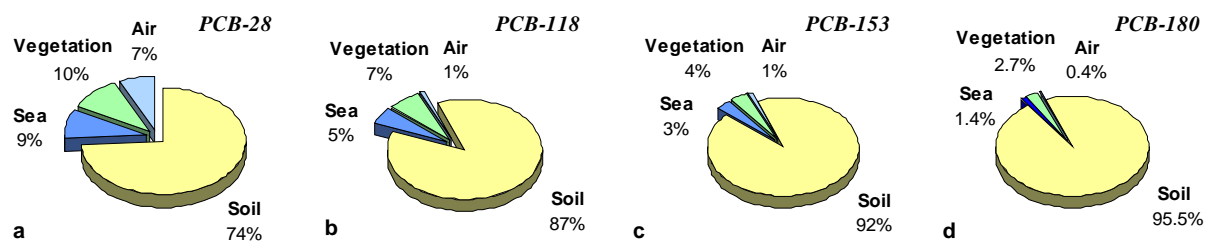


**Figure 6.3.** Distribution of PCB congeners between environmental media of the Northern Hemisphere by the end of 1996

### *Spatial distribution of contamination*

This section is aimed just at a brief description of spatial distribution of PCB contamination over the Northern Hemisphere. We would like to make a note of the contamination levels characteristic of some regions and to describe some peculiarities of PCB spatial distribution. A more detailed description of the contamination in the Arctic and especially in the five selected regions of the Russian North are presented below.

Spatial distribution of PCB-153 depositions and concentrations in environmental media for the whole Northern Hemisphere in 1996 was evaluated. Figure 6.4 displays maps of emissions, concentrations in air, soil, vegetation and seawater, and depositions. As to depositions we consider wet and dry depositions for the particulate phase plus wet deposition of the gaseous phase (so-called “direct” depositions). The importance of this value is connected with the possibility of its comparison with observed data. The gaseous exchange flux between the atmosphere and the underlying surface is evaluated separately due to the importance of the re-emission process. These processes are analysed in Section 6.3.

The most significant emission sources of PCBs are located in the European and North American regions (Fig. 6.4.a). The areas of highest atmospheric pollution are situated in the same regions (Fig. 6.4.b). Air concentrations in contaminated regions range from 5 to 20  $\text{pg}/\text{m}^3$  in America, and reach more than 20  $\text{pg}/\text{m}^3$  in Europe. Atmospheric transport from remote sources leads to a relatively large contribution to air contamination levels in the Russian North (1-3  $\text{pg}/\text{m}^3$ ).

The deposition map is presented in Figure 6.4.c. High deposition fluxes – more than 0.5  $\text{g}/\text{km}^2/\text{y}$  occur in Central Europe. Considerable fluxes 0.2-0.5  $\text{g}/\text{km}^2/\text{y}$  occur over most of Europe and the East part of Northern America. The deposition fluxes for the Russian North are in the range of 0.05-0.2  $\text{g}/\text{km}^2/\text{y}$ . There is a clear gradient of deposition reduction from the western to the eastern part of the Russian North. For the Arctic region the typical deposition level is 0.01-0.05  $\text{g}/\text{km}^2/\text{y}$ . A considerable part of the PCBs deposited over the Arctic Ocean are accumulated in the sea ice. The pollutant accumulated in sea ice can be transported with ice over a long distance with a subsequent discharge to the Ocean caused by the melting of ice. Description of the role of sea ice in POP transport is given in Annex E.

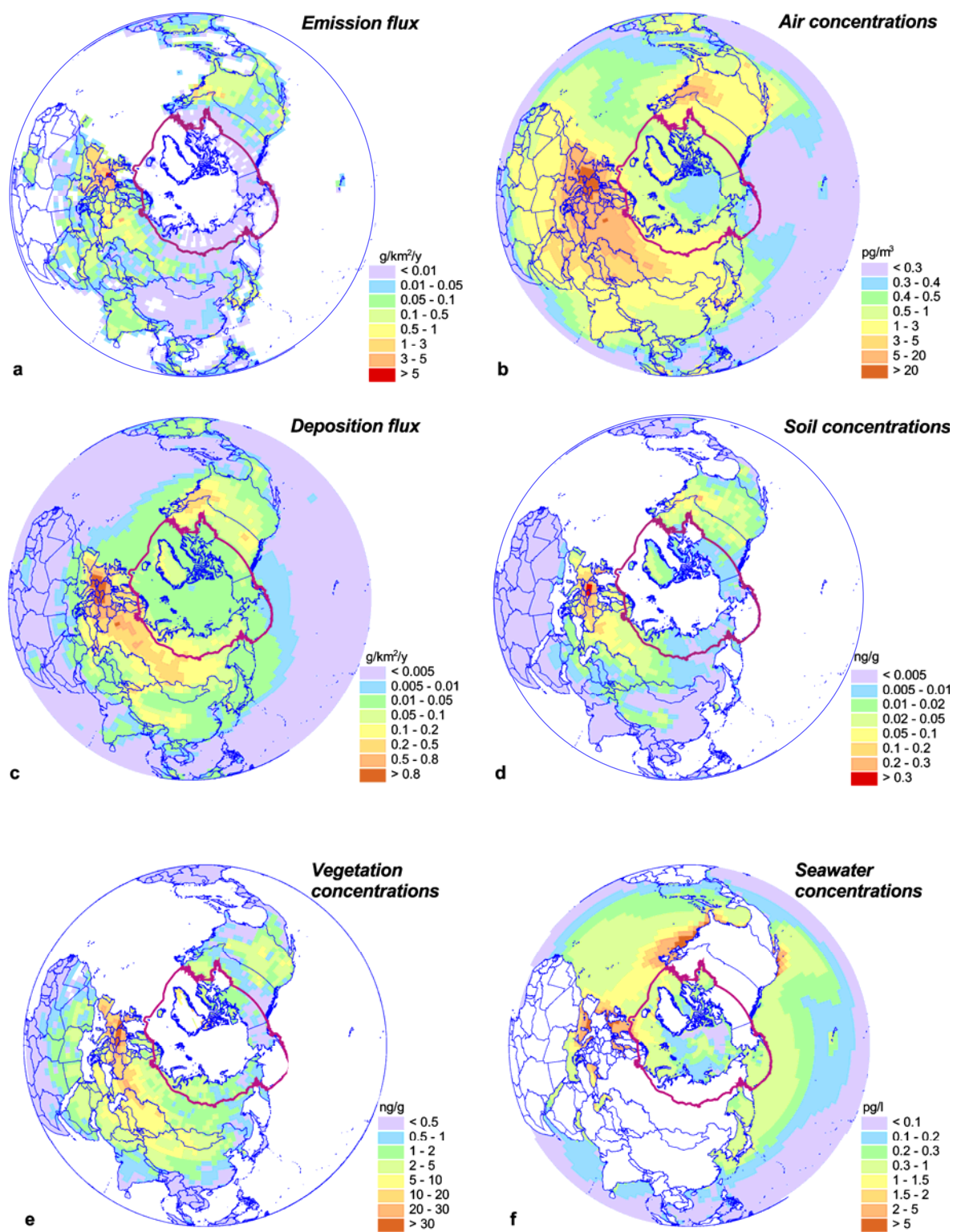


**Figure 6.4.** PCB-153 annual emissions, depositions and concentrations in media in the Northern Hemisphere in 1996

Depositions over land lead to PCB accumulations in soil. Figure 6.4.d presents spatial distribution of averaged concentrations in soil. Averaging is made over the whole depth of the soil calculation domain. Pollutant accumulation in soil is determined by a long-term deposition process. For example, concentrations 0.1-2 ng/g are observed both in regions with high deposition fluxes over Central Europe and in regions with low deposition, in particular, in the UK. This phenomenon is explained by the fact that in the 1970-s the UK PCB emission sources were rather significant, after which their intensity decreased.

The next terrestrial medium is vegetation. Calculated spatial distribution of concentrations in vegetation is presented by Figure 6.4.e. PCBs penetrate to vegetation mainly by the means of gaseous exchange with the atmosphere and dry deposition of the particulate phase. The typical range of concentrations near the main emission sources in the European region is 10-30 ng/g. Throughout most of Asia concentrations in vegetation range from 0.5 to 10 ng/g. The same level is characteristic of Northern America.

Another important medium is seawater. Figure 6.4.f presents the concentration field in this medium. High concentration levels are obtained in the coastal waters not far from main emission sources. For example, the typical range of seawater concentrations in the Mediterranean and Northern seas is 1.2-4 pg/l. In some regions these concentrations can reach 4 pg/l and more.

In the marine environment, pollutant can be transported from one region to another by sea currents. For example, the exchange of water masses between the Atlantic Ocean and the Arctic Ocean occurs in two directions (see Chapter 1). The inflow to the Arctic Ocean takes place along Norwegian and Russian coast, the outflow - along the coast of Greenland. These pathways of pollution transport with seawater are evident in the considered map. Seawater with PCB concentrations of 0.4-1.2 pg/l flow into the Arctic region along the Norwegian and Russian coast and the water masses with concentrations in the range of 0.1-0.4 pg/l flow from the Arctic Ocean to the Northern Atlantic along the coast of Greenland. Seawater pollution in the Arctic Ocean is noticeably affected by sea ice cover, which accumulates and transports a pollutant and hampers the gas exchange between the atmosphere and seawater. A detailed description of the influence of sea currents and ice cover on seawater contamination is given in Annex E.

Similar maps with the spatial distribution of calculated concentrations and depositions for PCB-28, 118 and 180 are given in Annex A.

### ***Contamination of the Arctic region***

In this chapter we would like to focus on the contamination of the Arctic region by PCB-153 in 1996. Figure 6.5 shows that relatively high deposition levels (0.1-0.5 g/km<sup>2</sup>/y) take place in the west part of the Russian North. Lower levels (0.05-0.1 g/km<sup>2</sup>/y) are characteristic of its east part. The deposition range of 0.01-0.1 g/km<sup>2</sup>/y is typical for the American North. Depositions over the Arctic Ocean are less than 0.05 g/km<sup>2</sup>/y.

The contributions of different regions to PCB-153 depositions to the Arctic are subject to seasonal variations. Below we examine some characteristic features of seasonal variations of contributions made by emission sources in the Americas and North-Western Europe. Figure 6.6 shows seasonal variations of relative contributions of different regions to PCB-153 deposition to the Arctic. As one can see from the diagram the relative contribution of sources from North-Western Europe is the most variable: it changes from about 70% in January to about 25% in May. On the other hand the influence of the Americas is only 5% in January but in May it amounts to 26%, being comparable with the contribution of North-Western Europe.

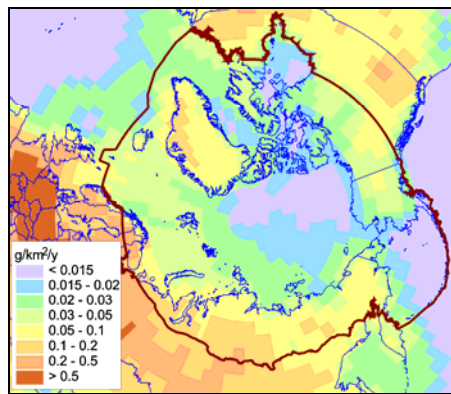


**Figure 6.5.** Annual depositions of PCB-153 in the Arctic region

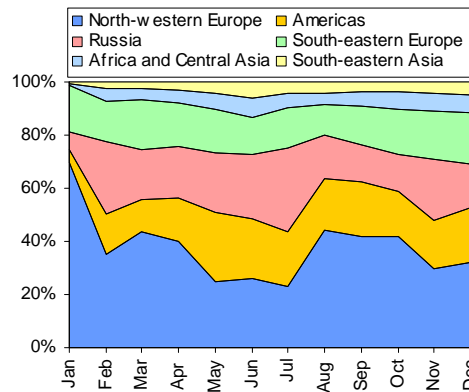


**Figure 6.6.** Seasonal variation of relative contributions of different regions to PCB-153 deposition to the Arctic

These noticeable variations are explained by peculiarities of atmospheric circulation in the Arctic in various seasons and seasonal variations of temperature, precipitation and degradation rates. Seasonal variations of emissions are not considered. To illustrate pathways of atmospheric transport, simulation results of PCB-153 transport from two groups of sources (the Americas and North-Western Europe) for 1996 were examined. In Figure 6.7 (a,b) air concentrations of PCB-153 emitted in the Americas and North-Western Europe in January are shown. The fields of air concentrations originating from the same sources in May are given in Figure 6.7 (c,d).

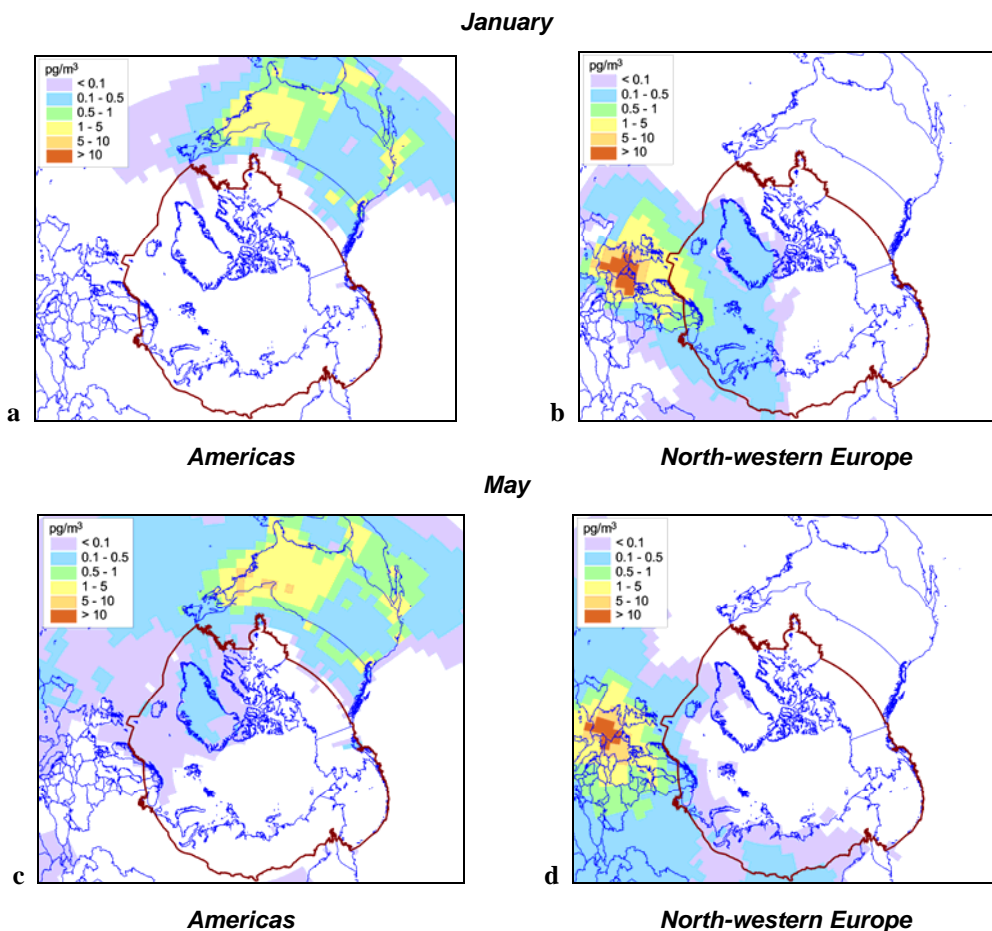


**Figure 6.7.** Air concentrations of PCB-153 emitted in Americas and North-western Europe for January and May

As seen from the maps, PCB-153 from American sources mainly penetrates into the Arctic in May, whereas from European ones - in January. On the whole, the basic contribution to Arctic pollution is made by European emission sources in the cold season. This is in line with the annual pattern of atmospheric circulation in the Arctic region. According to it the mean flow in winter is from Eurasia into the Arctic, and from the Arctic into North America.

Annual contributions of different emission sources to depositions to the Arctic region in 1996 are shown in Figure 6.8. The main group of sources contributing to this region is North-Western Europe (about 40%), which is then followed by Russia (19%), the Americas (17%), South-Eastern Europe (16%). The share of all other sources amounts to 8%.

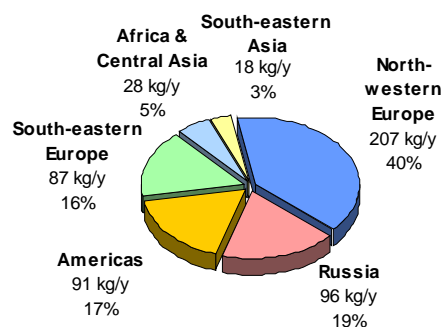


Figure 6.8. Contributions of different emission sources to PCB-153 deposition to the Arctic region in 1996

## 6.2. Comparison of modeling results with measurements

In this section the computed PCB concentrations in air and precipitation and deposition fluxes are verified using the available measurement data. Data for the comparison were taken from several sources including measurements at sites within the AMAP region [Berg and Hjellbrekke, 1999], observations of the EMEP monitoring network [Berg et al., 1996, 1997; Berg and Hjellbrekke, 1998; Brorström-Lundén et al., 2000], and literature data for 1989-96. This information is primarily concerned with PCB air concentrations. Less data are available on concentrations in precipitation and on deposition fluxes. The verification of model results is made by the comparison of mean annual concentration values. For this purpose, available observations were analysed. A number of studies of PCB concentrations obtained for relatively short periods of duration or otherwise episodic measurement campaigns were not taken into account.

Table 6.1. Monitoring sites selected for the comparison with model results for PCBs

Station	Code	Latitude	Longitude
Stórhöfði	IS91	63° 24'N	20° 17'W
Rörvik	SE2	57° 25'N	11° 56'E
Pallas	FI96	67° 58'N	24° 07'E
Ny Ålesund	NO42	78° 54'N	11° 53'E
Kosetice	CZ3	49° 35'N	15° 05'E
Alert	CA420	82° 28'N	62° 30'W
Tagish	CA1	60° 18'N	134° 16'W
Dunai	RU17	73° 59'N	124° 30'E
Kårvatn	NO39	62° 47'N	8° 53'E
Svanvik	NO47	69° 27'N	30° 02'E
Hazelrigg		54° 3'N	2° 50'W



Figure 6.9. Location of monitoring sites selected for the comparison with model results for PCBs

The locations of the sites are depicted in Figure 6.9. Table 6.1 contains coordinates of these stations. Data on PCB concentrations measured at the EMEP network were available from the following sites: Storhöfði (IS91), Rörvik (SE2), Pallas (FI96), Ny Ålesund (NO42), and Košetice (CZ3). Measurements of PCB concentrations within the Arctic region were available from Tagish, Dunai, and Alert sites. In addition, data from two Norwegian sites, Karvatn and Svanvik, were used [Oehme *et al.*, 1995]. Observations of PCB concentrations at the semi-rural site Hazelrigg [Coleman *et al.*, 1998] were also used in the comparison. The comparison of mean annual air concentrations of four PCB congeners (PCB 28, 118, 153, and 180) for the period of 1989-96 is presented in Figure 6.10. Most of the computed values of air concentrations (95%) are within a factor of 4 with respect to observed levels. As it can be seen from the figure and Table 6.2, in general the model overestimates atmospheric concentrations of the heavier congeners 180 and 153. For PCB-118 computed concentrations are rather close to measured ones. Computed mean annual air concentrations of PCB-28 are somewhat lower than observed ones. Although the number of sites for the analysis is relatively small, a correlation between observed and computed concentrations can be found. This testifies to the fact that the model reasonably represents spatial distribution of selected PCB congeners in air.

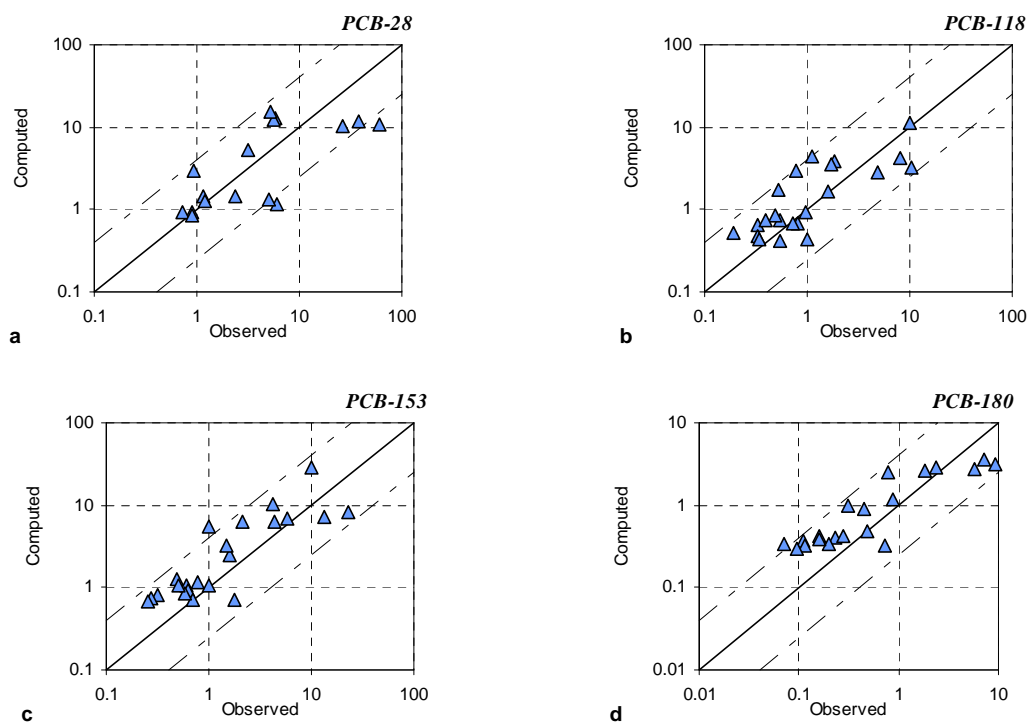


**Figure 6.10.** Scatter plots of mean annual concentrations of four PCB congeners in the surface air,  $\text{pg}/\text{m}^3$ . Measured and computed PCB air concentrations are shown using the logarithmic scale. Dashed lines on the diagrams limit the area with agreement between the measured and computed values within a factor of 4

**Table 6.2.** Comparison of measured and computed mean annual air concentrations of four PCB congeners and correlation between measured and computed values

	Mean observed, $\text{pg}/\text{m}^3$	Mean computed, $\text{pg}/\text{m}^3$	Mean ratio, Obs/Mod	Correlation
PCB-28	10.27	5.76	1.74	0.5
PCB-118	2.14	2.13	0.98	0.7
PCB-153	3.39	4.34	0.80	0.5
PCB-180	1.58	1.24	0.87	0.8

Next eight figures (Fig. 11.a-h) present more detailed comparison for individual years and sites grouped by two relatively large areas - European and Arctic region.

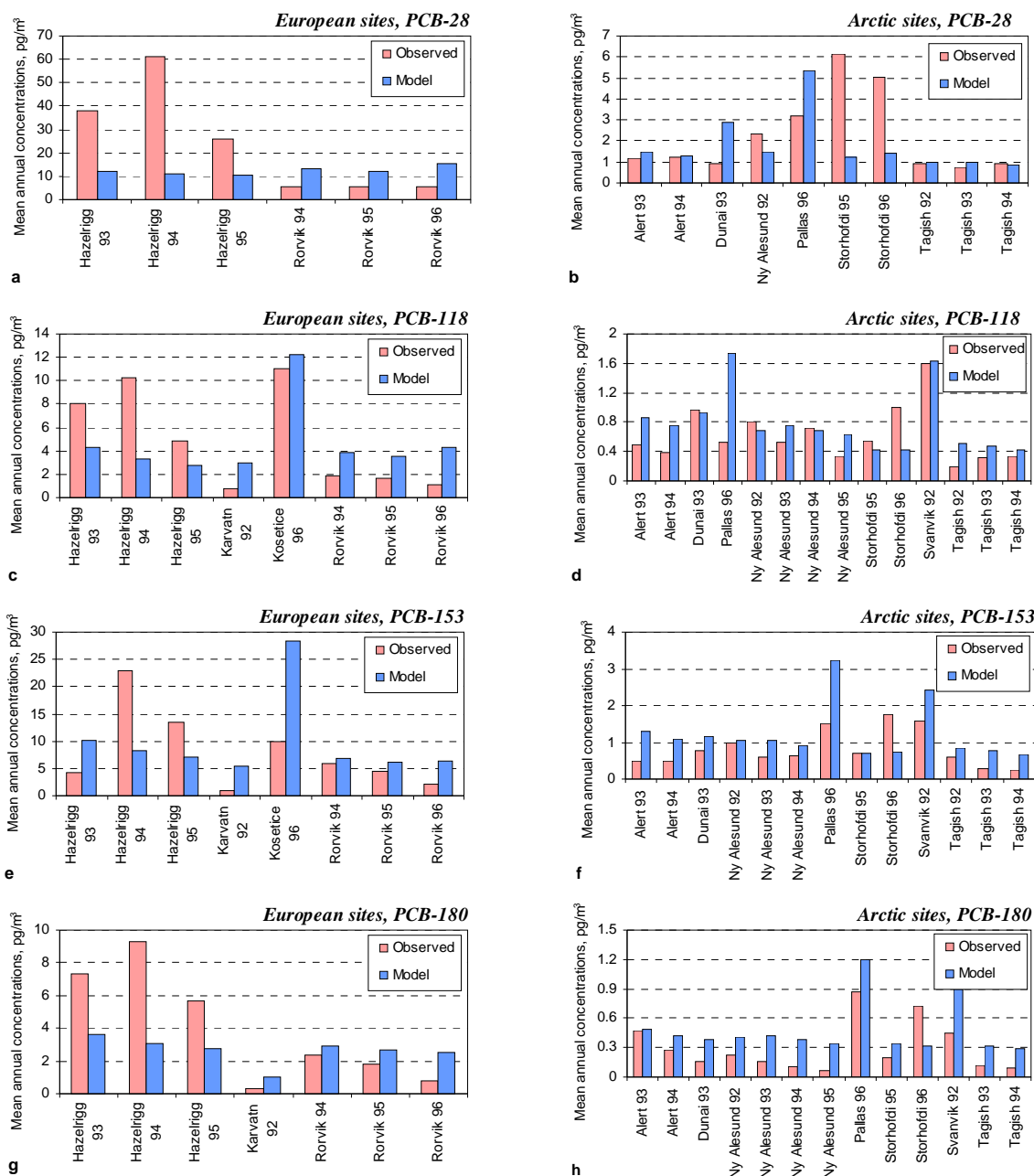


**Figure 6.11.** Comparison of mean annual concentrations of four PCB congeners in the surface air of European and the Arctic regions for the period 1989-96,  $\text{pg}/\text{m}^3$

The comparison of measured and computed concentration in precipitation of four PCB congeners for site Stórhöfði in 1995 and 1996 is given in Table 6.3.

The most significant discrepancies were found for Hazelrigg site. This site is located in semi-rural area of the United Kingdom. It is a single semi-rural station for this region (others are urban), therefore it is included into the comparison. Significantly higher levels of measured PCB concentrations at this site in comparison with the computed ones are most likely connected with the proximity of local emission sources.

**Table 6.3.** Comparison of computed mean annual PCB concentrations in precipitation for 1995 and 1996 with measurements made at Stórhöfði (IS91), ng/l

	Mean observed, 1995	Mean observed, 1996	Mean computed, 1996
PCB-28	0.243	0.160	0.028
PCB-118	0.042	0.037	0.019
PCB-153	0.037	0.070	0.031
PCB-180	0.067	0.041	0.032

Since the values of concentration in precipitation and of deposition flux strongly depend on precipitation amount the comparison of measured and computed values for these parameters should be carried out only for 1996 (meteorology of this year was used in calculation). However, such comparison is complicated by the deficiency of available measurement data for 1996. Therefore, additional measurements for 1995 were used in the comparison. Deposition fluxes include dry and wet particle depositions and wet gas deposition. Data on concentrations in precipitation for 1995-96 were found for Icelandic site Stórhöfði (IS91) and on deposition fluxes - for Pallas (FI96) and Rorvik (SE2).

The comparison of PCB concentrations in precipitation for this site shows that the computed values of three congeners (118, 153, 180) are quite close to the observed values. The comparison with measurement results of 1996 is better than with that of 1995 because in calculations meteorological parameters of 1996 were used. More significant disagreement is found for PCB-28. The computed value for this congener is significantly lower than measured one. It might be connected with uncertainties in emission data. It may be confirmed by the fact that the computed air concentration for this site is underestimated too (Figure 6.11.b). The second reason for the discrepancy may be the uncertainty connected with parameterization of washout process for this congener. To improve the parameterization of this process more information about simultaneously measured concentrations in air and precipitation are needed.

The comparison of computed and observed PCB deposition fluxes were made for two sites, Rörvik (SE2) and Pallas (FI96), for 1995 and 1996 (Figure 6.12).

Results of the comparison show that the computed deposition fluxes for these two sites are 3-5 times higher than measured ones for PCB-118, PCB-153, and PCB-180. The same can be noted for the computed air concentrations, which are 2-3 times higher than measured values. For PCB-28 the computed deposition fluxes were in a satisfactory agreement with observed values.

In conclusion it can be noted that the computed concentrations are close to measured PCB concentration levels at several sites located in the Arctic and European regions. Most of computed air concentration values are within a factor of 4 in comparison with measurements. Model air concentrations of four PCB congeners correlate rather well with observed ones.

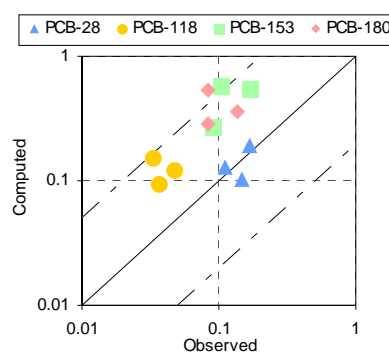


**Figure 6.12.** Scatter plot of calculated annual deposition fluxes of four PCB congeners in comparison with measured ones at Rörvik (1995, 1996) and Pallas (1996), g/km<sup>2</sup>/y. Observed and computed deposition fluxes are shown using logarithmic scale. Dashed lines limit the area of agreement within a factor of 5 between measured and computed values

The comparison of concentrations in precipitation and deposition fluxes was limited by the deficiency of available measurements for 1996. Computed concentrations of PCB-118, 153, 180 in precipitation for Stórhöfði (IS91) are in a good agreement with measured ones. However, the model underestimated observed concentration levels of PCB-28 at this site within a factor of four. Computed deposition fluxes compared to observed ones at Pallas and Rörvik are 3-5 times higher. At the same time model estimates of PCB-28 deposition fluxes agreed rather well with measurements made at these sites.

It should be mentioned that the measurement database for this comparison is rather limited. Therefore for more thorough verification of model results it is necessary to have more measurements in other regions of the Northern Hemisphere.

### 6.3. Concentration and deposition levels in the Russian North

This section contains information on pollution levels of PCB-153 in the Russian North. Spatial distribution of annual means as well as seasonal variation of contamination is examined for each considered region (Murmansk Oblast, Nenets AO, Yamalo-Nenets AO and Taimyr AO, Sakha Republic and Chukotka AO). Similar information on other congeners (PCB-28, PCB-118, PCB-180) can be found in Annex A.

Deposition fluxes include wet scavenging of the gaseous and particulate phase plus dry depositions of PCB associated with particles. Net gaseous exchange flux between the atmosphere and the underlying surface is considered separately due to the importance of re-emission process for PCBs. Due to a reversible character of gaseous exchange the flux can be directed to the underlying surface (positive value) as well as to the atmosphere (negative value, re-emission).

#### 6.3.1. Spatial distribution

Figures 6.13 and 6.14 display spatial distributions of mean annual air concentrations and annual deposition fluxes of PCB-153 over the selected regions of the Russian North for 1996. There is a clear latitudinal gradient of air concentrations from the western to eastern parts of the Russian North. Relatively high air concentrations ( $2-4 \text{ pg/m}^3$ ) take place in Murmansk Oblast, Nenets AO and in the southern part of Yamalo-Nenets and Taimyr AO. Moderate values ( $1-2 \text{ pg/m}^3$ ) are characteristic of the northern part of Yamalo-Nenets and Taimyr AO and Sakha Republic. Chukotka AO is characterized by low values ( $<1 \text{ pg/m}^3$ ).

Spatial pattern of deposition fluxes is of similar character. Rather high values ( $> 150 \text{ mg/km}^2/\text{y}$ ) are determined for Murmansk Oblast, Nenets AO and the southern part of Yamalo-Nenets and Taimyr AO as well as for the western part of Sakha Republic. Moderate values ( $70 - 150 \text{ mg/km}^2/\text{y}$ ) are determined for the northern part of Yamalo-Nenets and Taimyr AO, Sakha Republic and the western part of Chukotka AO. The northern part of the Russian North is characterized by lower values of deposition fluxes ( $<70 \text{ mg/km}^2/\text{y}$ ).

In addition to the fields of air concentrations and annual deposition fluxes spatial distribution of PCB-153 concentration in seawater within the Arctic region is presented (Fig. 6.15). The highest concentrations in seawater are obtained for coastal waters of Murmansk Oblast ( $>1.2 \text{ pg/l}$ ). Moving to the east, seawater concentrations go down, reaching values of  $0.2-0.4 \text{ pg/l}$ . In some regions of Yamalo-Nenets AO and Taimyr AO, Yakutia and Chukotka AO water concentrations are less than  $0.2 \text{ pg/l}$ .

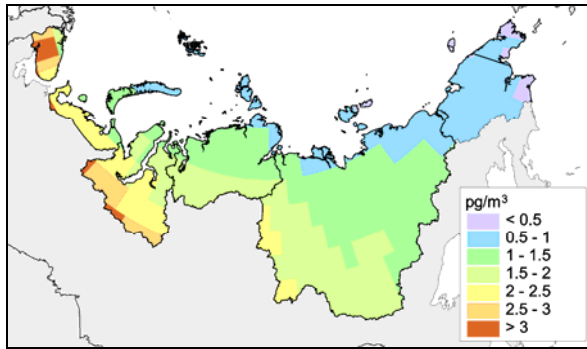


**Figure 6.13.** Mean annual air concentrations of PCB-153 in the Russian North,  $\text{pg}/\text{m}^3$

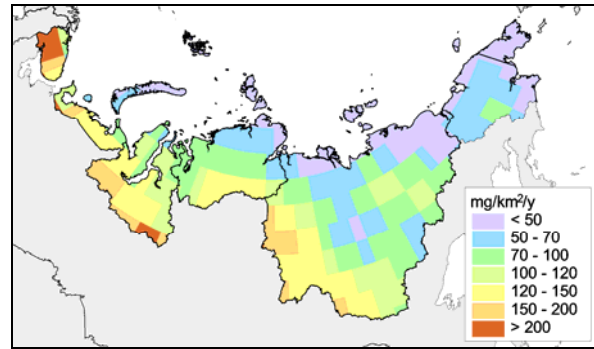


**Figure 6.14.** Deposition of PCB-153 in the Russian North calculated for 1996,  $\text{mg}/\text{km}^2/\text{y}$

Seawater concentration pattern illustrates the inflow of PCB-153 from the North Atlantic with sea currents. It should be mentioned that the results obtained for the marine environment are rather preliminary. At present stage of model development we do not consider the contamination transport by rivers, therefore there is a certain underestimation of PCB concentrations in coastal seawater. In further investigations of the Arctic contamination, the effect of pollutant transported by rivers should be taken into account.

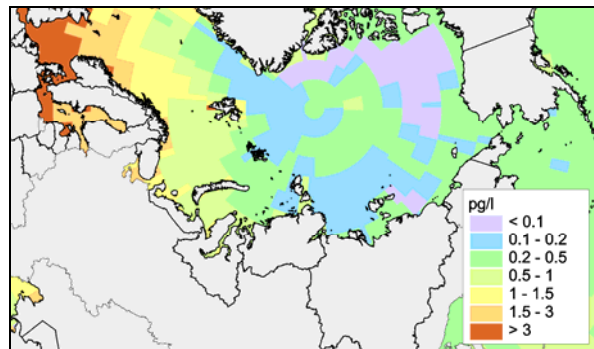


**Figure 6.15.** Mean annual PCB-153 seawater concentrations near the Russian North,  $\text{pg}/\text{l}$

### 6.3.2. Annual averages

Mean annual air concentrations, annual deposition and net gaseous exchange fluxes along with their spatial variations for each region are summarized in Table 6.4. It can be seen that air concentrations (sum of gas and particle phases) varies from 0.4 to 4.1  $\text{pg}/\text{m}^3$  over the Russian North. Averaged net gaseous flux over the most part of the territory is negative (except for Nenets AO). It means that in these regions the evaporation process prevails over dry gaseous deposition. This is conditioned by large amount of PCBs accumulated in environmental media (mainly in soil) during the period from 1970 to 1995 and essential reduction of air concentrations caused by emission reduction. Annual deposition fluxes vary along the territory of the Russian North more than within an order of magnitude (16 – 373  $\text{mg}/\text{km}^2/\text{y}$ ).

**Table 6.4.** Annual contamination levels and their spatial variation of the Russian North regions by PCB-153 in 1996

Region	Air concentration, $\text{pg}/\text{m}^3$			Depositions*, $\text{mg}/\text{km}^2/\text{y}$			Gas exchange, $\text{mg}/\text{km}^2/\text{y}$		
	Mean	Min	Max	Mean	Min	Max	Mean	Min	Max
Murmansk Oblast	2.6	1.3	4.1	208	70	333	-71	-248	139
Nenets AO	1.7	0.5	3.8	97	27	373	15	-302	100
Yamalo-Nenets AO and Taimyr AO	1.8	0.5	3.3	106	27	216	-44	-167	58
Sakha Republic	1.4	0.4	2.3	89	16	224	-77	-208	14
Chukotka AO	0.7	0.4	1	51	16	74	-34	-64	18

\* depositions include wet and dry particle deposition and wet gaseous deposition

## Seasonal variations

In this subsection we discuss main tendencies of contamination level variability defined by meteorological parameters (winds, temperature and precipitation). Since emissions are considered to be uniform throughout the year (discussion on this topic is in chapter 4.2.3) the obtained seasonal variations are caused by meteorological and geophysical conditions only (wind speed and direction, temperature, leaf area index, etc.). The main dependencies of seasonal variations of monthly averaged contamination levels are described in detail on the example of Murmansk Oblast. Variations of air concentrations, deposition flux, and net gaseous flux for Murmansk Oblast are presented in Figure 6.16. Variations of temperature and precipitation are also presented for the sake of explanation of characteristic behaviour of contaminant over 1996.

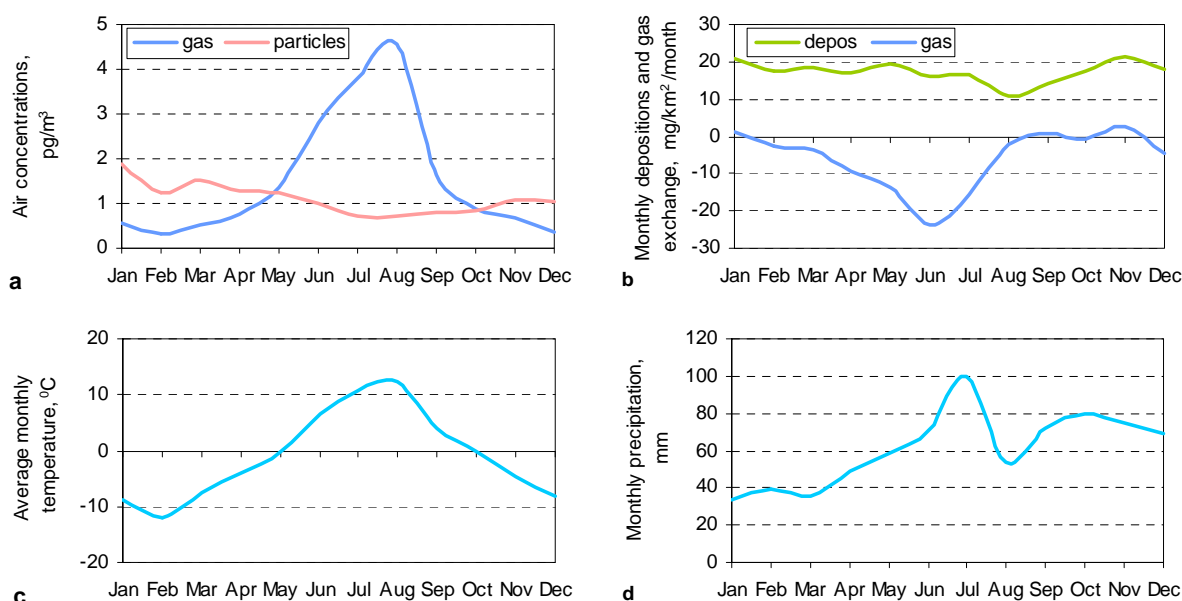


**Figure 6.16.** Seasonal variations of PCB-153 contamination levels in Murmansk Oblast for 1996

Monthly mean air concentrations of the gaseous phase vary within an order of magnitude over the year, reaching the maximum value in August (about  $5 \text{ pg/m}^3$ ). This maximum coincides with the peak temperature. The particulate phase concentrations do not change so drastically and reach their maximum in winter (about  $2 \text{ pg/m}^3$ ). They dominate over the gaseous phase within the cold season. This tendency is explained by the dependence of partitioning between phases on temperature and by the fact that gaseous PCBs are removed more efficiently at low temperatures.

As it was mentioned above, annual depositions include wet gas and particle depositions plus dry particle deposition. The deposition flux ranges from 10 to  $22 \text{ mg/km}^2/\text{month}$  (Fig. 6.16.b). On the whole depositions follow the tendency of the particulate phase concentration within the year. The decrease of deposition flux in August coincides with maximum value of temperature and is explained by temperature dependence of gas/rainwater partitioning coefficient and by lower precipitation amount (Fig. 6.16.d).

The behaviour of net gaseous flux is somewhat more complicated (Fig. 6.16.b). Its value varies from 3 to  $-24 \text{ mg/km}^2/\text{month}$  over the year. In the cold period gaseous phase concentrations of the underlying surface are rather low therefore the flux is positive. This means that PCBs mainly deposit to the underlying surface from the atmosphere. During warm season re-emission process takes place.

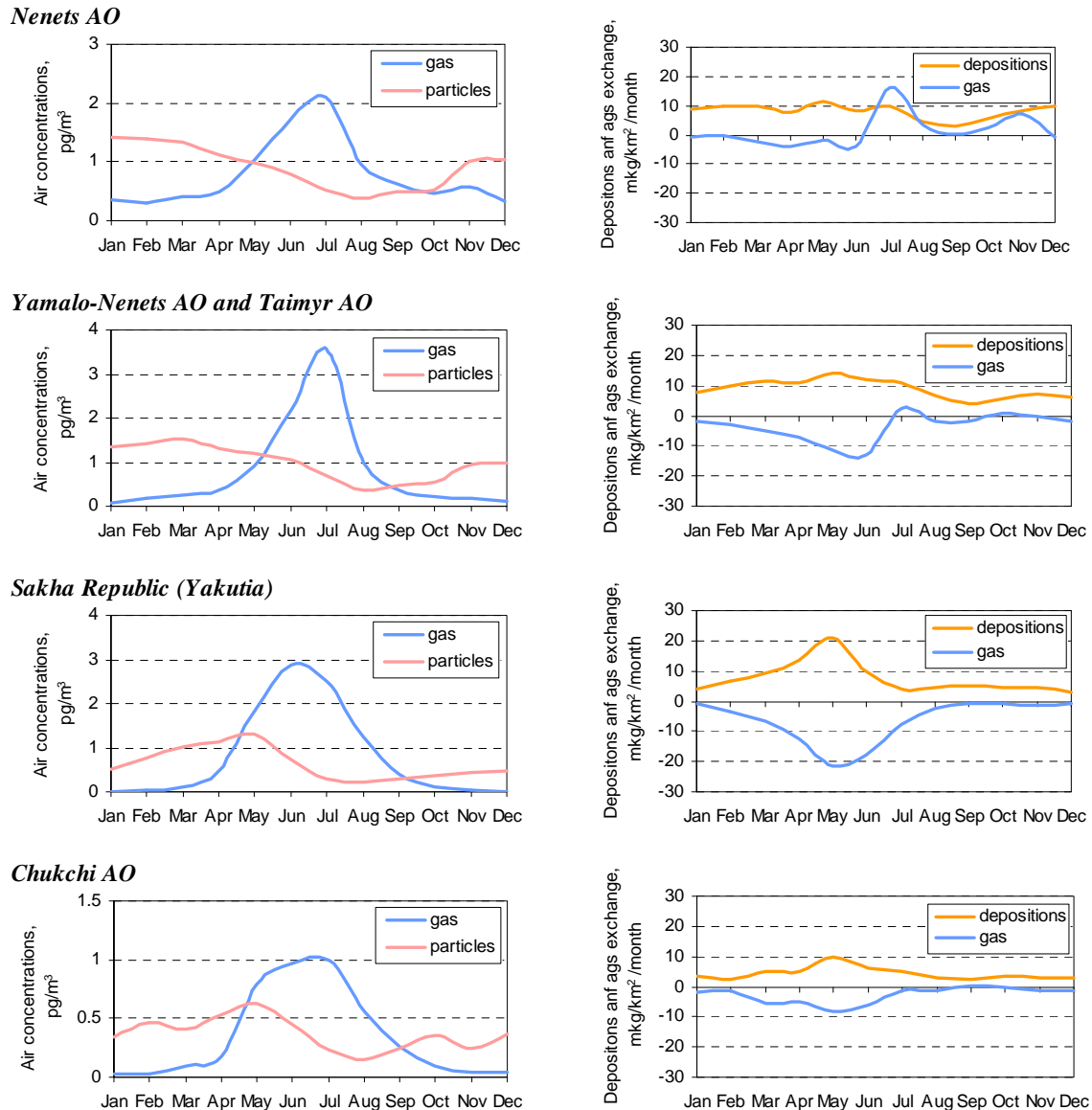


Figure 6.17. Seasonal variations of PCB-153 contamination levels in regions of the Russian North for 1996

Calculated seasonal variations of PCB-153 pollution levels in other regions of the Russian North are demonstrated by plots in Figure 6.17 along with variations of temperature and precipitation (Fig. 6.18). General tendencies can be explained in the same way as in the case of Murmansk Oblast. As a special feature we can indicate positive values of the gaseous flux in summer time in Nenets AO, Yamalo-Nenets AO, and Taimyr AO.

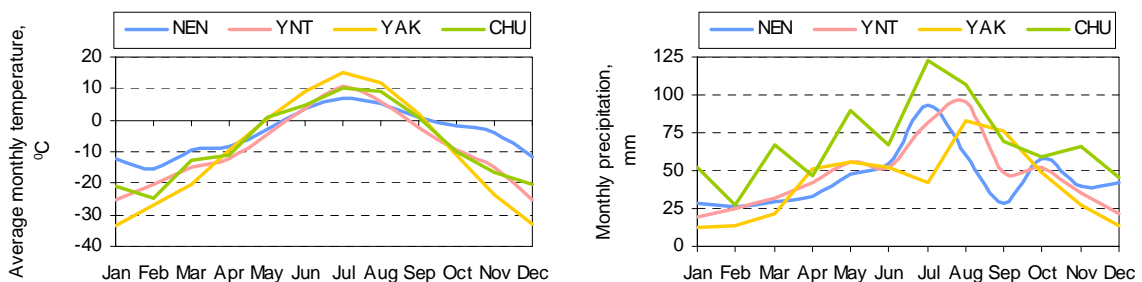


Figure 6.18. Seasonal variations of temperature and precipitation in regions of the Russian North for 1996

The above described pollution levels are caused by both emissions of the considered year and re-emission from environmental media (soil mainly). The influence of this last process amounts to 30-80% depending on the congener and region. Taking into account that re-emissions cannot be controlled by any political decisions we focus on the influence of emissions of 1996.

## 6.4. Source-receptor relationships

This section contains information on contributions from different emission sources of the Northern Hemisphere to PCB contamination of the Russian North (selected 5 region-receptors) in 1996. Contamination in regions-receptors is formed both by emissions of the considered year (1996) and by amount of pollutant accumulated in the environment during the period preceding the reference year (1990 – 1995). Calculations show that large fraction of concentrations in soil and seawater over regions of the Russian North are formed by PCBs earlier accumulated in environmental media. Keeping in mind that the historical emission cannot be controlled by any political decisions we shall pay the main attention to deposition from anthropogenic sources.

The Northern Hemisphere is divided into 6 large source-regions – Russia, the Americas, North-western Europe, South-eastern Europe, South-eastern Asia, Africa and Central Asia (Fig.6.19.a, see also Section 4.2). For more detailed examination of influence of Russian sources on the contamination of the Russian North, Russia is subdivided into 12 individual source regions, 5 of them are located in the Russian North and are at the same time considered as the regions-receptors (Fig. 6.19.b, Table 6.5).

Figure 6.20.a displays contributions of different source groups to the overall Northern Hemisphere emissions. Figure 6.20.b presents values of emissions from different regions of Russia. As above, we consider an example of PCB-153. Information on other congeners is collected in Annex A. The most significant emission sources in the Northern Hemisphere are located in North-western Europe (about 4.4 t/y, 30%), then come South-eastern Europe, America, Africa and Central Asia (Fig.6.20.a). Russian emissions take the fifth place. Due to proximity to regions under investigation, it is important to consider Russian emissions in detail (Fig.6.20.b). It should be noted, that total own emissions of 5 regions-receptors of the Russian North (MUR, NEN, YNT, YAK, CHU) are rather low. Therefore PCB contamination of Russian North is mainly formed due to the long-range transport from other regions with substantial emission levels.

**Table 6.5.** Russian emission sources and their codes. The first 5 sources are also receptors in the Russian North

		Code	Russian sources
Sources	Receptors	MUR	Murmansk Oblast
		NEN	Nenets AO
		YNT	Yamalo-Nenets AO and Taimyr AO
		YAK	Sakha Republic (Yakutia)
		CHU	Chukotka AO
		NRT	Northern region
		NWK	North-western region and Kaliningrad Oblast
		CVV	Central and Volga-Viatsky regions
		CVN	Central-Chernozem, Volga, and North-Caucasian regions
		URL	Ural region
		WSB	West-Siberian region
		ESB	East-Siberian and Far-Eastern regions

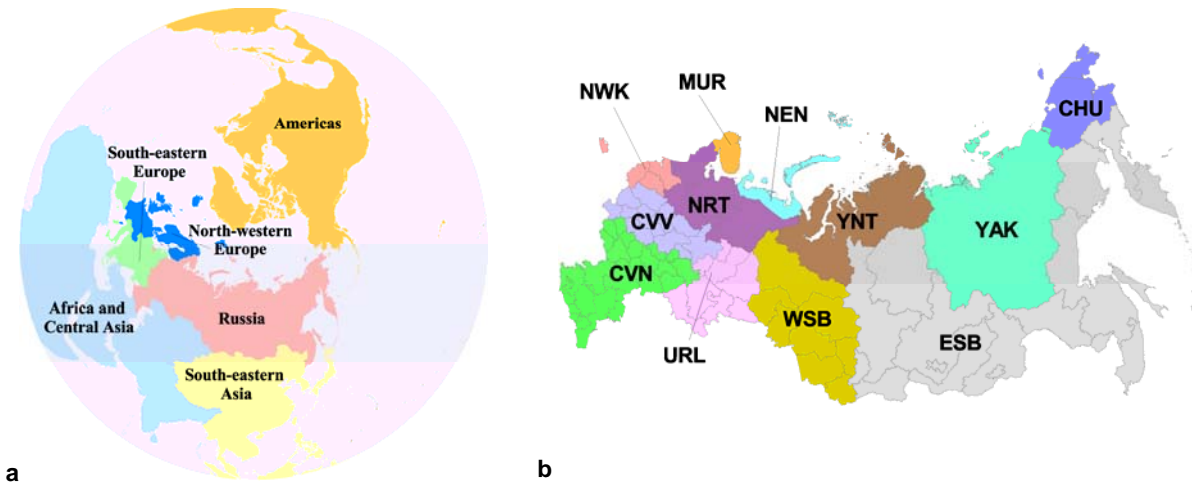


Figure 6.19. Splitting emission sources into groups, (a) – rough scheme, (b) – specification of Russian sources

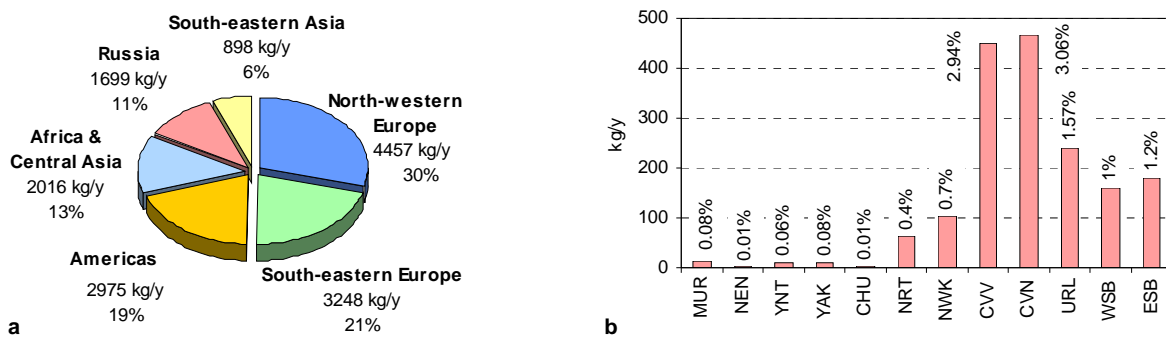


Figure 6.20. Contributions of different emission source groups of PCB-153 to the hemispheric emissions in 1996: source-regions in the Northern Hemisphere (a), detailed splitting of Russian sources (b)

**Murmansk Oblast.** Here we consider the contributions of various emission sources to depositions and concentrations in Murmansk Oblast in 1996. Contributions of emission sources of the Northern Hemisphere and Russia to depositions to Murmansk Oblast are illustrated by Figure 6.21 a – b. As seen the largest contribution is made by Russian sources (44%), although their emission fraction is only 11% (Fig.6.21.a). Then come more significant, but remote emission sources, namely North-western Europe (35%) and South-eastern Europe (14%). The minor influence of sources located in the Americas, Africa and Central Asia and South-eastern Asia (in sum 7%) can be explained by their significant remoteness from Murmansk Oblast.

Russian contribution to depositions to Murmansk Oblast is formed mainly by own Murmansk sources (about 22%) in spite of a small fraction of Murmansk Oblast in total Russian emissions (Fig.6.21.b).

Contributions of different emission sources to air and soil concentrations are given in Figures 6.21.c and 6.21.d. As seen from the figures, these contributions are almost the same as for depositions. For example, Russian contributions to depositions and concentrations in air and soil are from 44% to 47%, respectively. Similar situation is observed also for other regions.

Inputs of different emission sources to deposition are subject to seasonal variations determined by meteorological conditions (wind speed and direction, precipitation amount and temperature). Figure 6.22 displays seasonal variations of contributions of main source groups to deposition to this region in absolute (a) and relative (b) values for 1996.

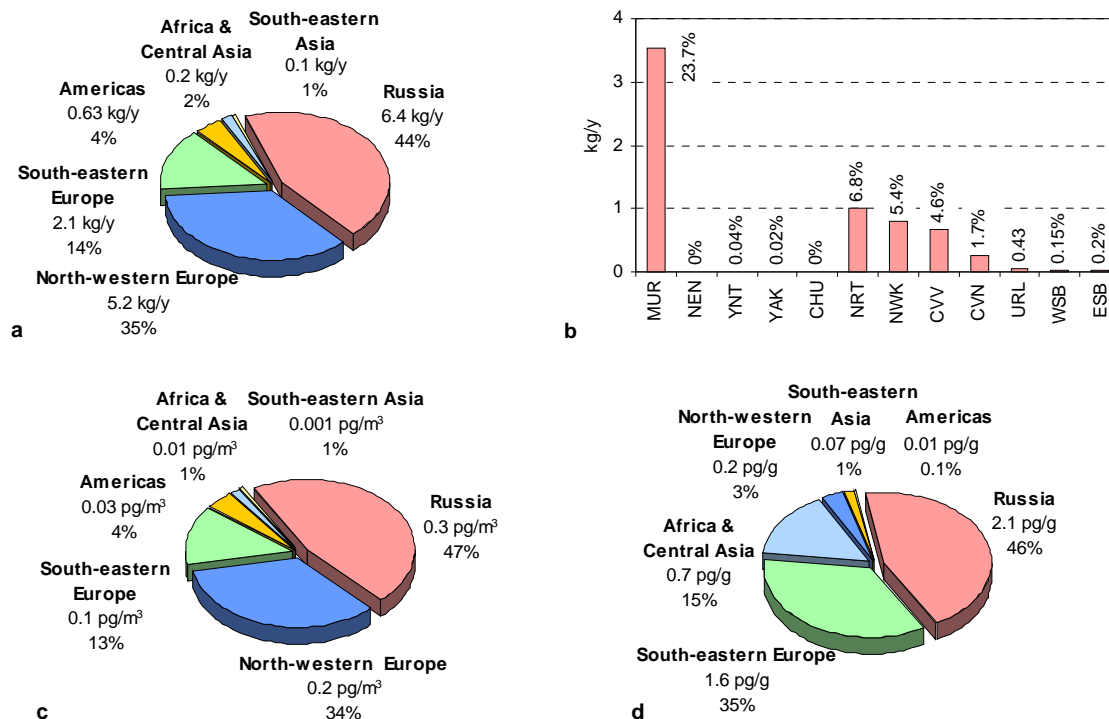


**Figure 6.21.** Contributions of different emission sources to PCB-153 depositions (a - source-regions in the Northern Hemisphere, b - detailed splitting of Russian sources), and concentrations in air (c) and in soil (d) of Murmansk Oblast in 1996

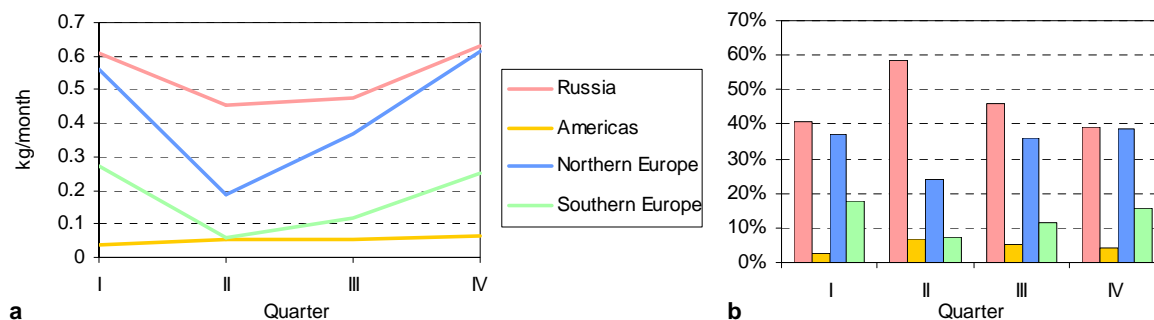


**Figure 6.22.** Seasonal variations of contributions of different emission sources to PCB-153 depositions to Murmansk Oblast (I-IV quarters of 1996)

As it was shown above, the main contributions to depositions are made by Russia and North-western Europe (Fig.6.22). The depositions are higher in the cold season, than in the warm one (Fig.6.22.a). This can be explained by the fact that at high temperature the particulate fraction of PCB decreases, leading to the decrease of depositions (the second quarter). Rates of decrease for various sources are different. For example in the second quarter the decrease of depositions from North-western Europe sources is stronger than that from Russian sources. This leads to the decrease of the fraction of North-western Europe sources in the second quarter among others (Fig.6.22.b). It happens because north-west winds are rare in this period and because of a large transport distance from North-western Europe to Murmansk Oblast. In the third quarter total depositions increase. Due to prevailing north-west winds in the cold period, the contribution to depositions from sources of North-western Europe increase and its fraction becomes equal to that of Russian sources.

**Nenets Autonomous Okrug.** The contributions of different source groups to the pollution of Nenets AO are similar to that of Murmansk Oblast. Contributions of Russia and North-western Europe are slightly lower (41 and 31%), but contributions of South-eastern Europe and America are slightly higher (18% and 6%) in comparison with Murmansk Oblast (Fig.6.23.a). The structure of Russian contribution to depositions to this region is principally different from that for Murmansk Oblast. The main contributions (15%) are made by Central and Volga-Viatsky regions and (10%) by the Northern region (Fig.6.23.b). The contribution of local sources for this region is negligible. Therefore, the long-range transport plays a leading role in the contamination of Nenets AO since basic contributions to pollution of this region is made by remote sources.

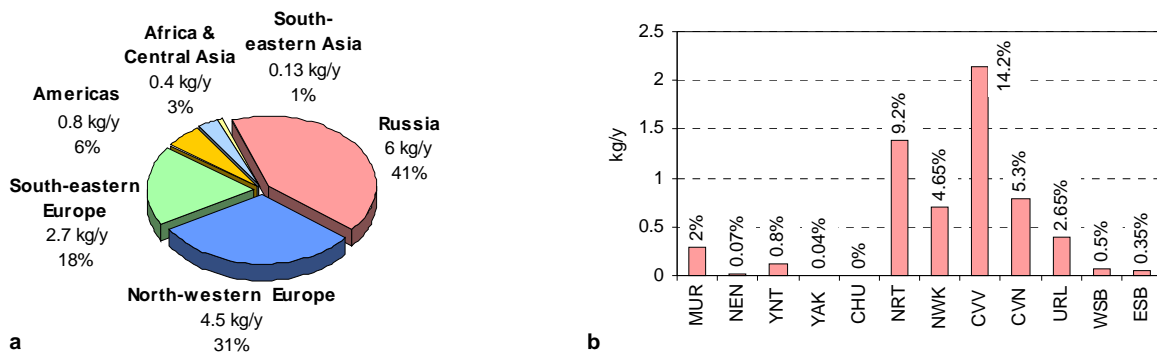


**Figure 6.23.** Contributions of different emission sources to PCB-153 depositions to Nenets AO in 1996. (a) – from source-regions in the Northern Hemisphere, (b) - detailed splitting of Russian contribution

Seasonal variations of contributions of main source groups to deposition to Nenets AO in absolute (a) and relative (b) values in 1996 are displayed in Figure 6.24.

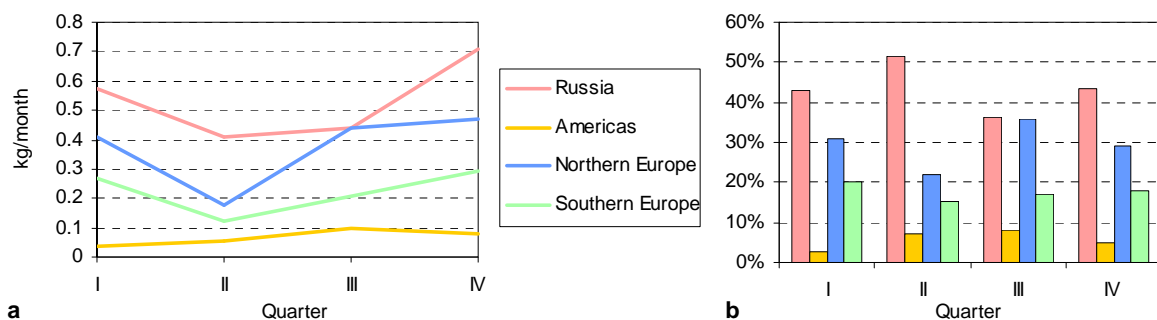


**Figure 6.24.** Seasonal variations of contributions of different emission sources to PCB-153 depositions to Nenets AO (I-IV quarters of 1996)

The main contributions to depositions to the region are made by North-western Europe, South-eastern Europe and Russia. The situation is quite similar to that of Murmansk Oblast - the depositions decrease in the warm period (the second quarter) and increase in the cold period (Fig. 6.24.a). The rates of decrease for various sources are different. For example in the second quarter the decrease of depositions from North-western Europe source is stronger than that of Russian sources. This leads to the decrease of the fraction of North-western European sources in the second quarter in comparison with others (Fig. 6.24.b). The reason for that is just the same as for Murmansk Oblast.

**Yamalo-Nenets and Taimyr Autonomous Okrugs.** For this region substantial contribution to the depositions is made by Russian (47%), North-western (26%) and South-eastern (16%) European emission sources (Fig. 6.25.a). The largest contribution of Russian sources is obtained from Central and Volga-Viatsky regions (12%). Then come the contribution of internal emission sources of the considered region (9%).

Seasonal variations of contributions of main source groups to deposition to Yamalo-Nenets AO and Taimyr AO in absolute (a) and relative (b) values for 1996 are shown in Figure 6.26.

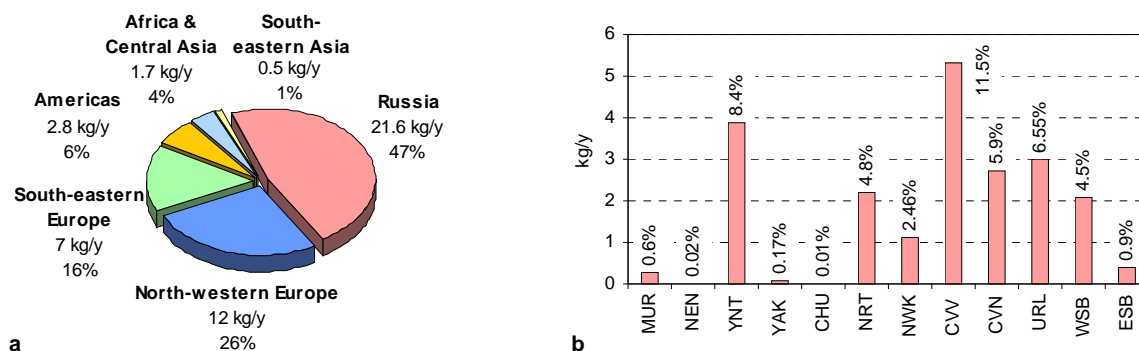


**Figure 6.25.** Contributions of different emission sources to PCB-153 depositions to Yamalo-Nenets and Taimyr AO in 1996. (a) – from source-regions in the Northern Hemisphere, (b) - detailed splitting of Russian contribution

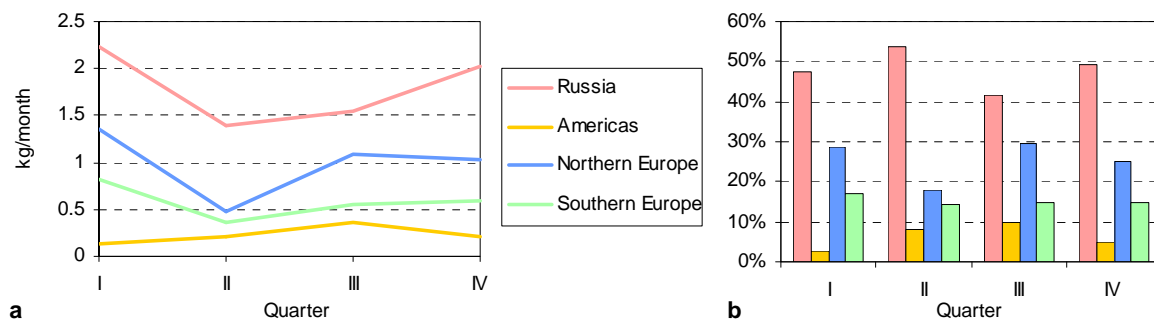


**Figure 6.26.** Seasonal variations of contributions of different emission sources to PCB-153 depositions to Yamalo-Nenets AO and Taimyr AO (I-IV quarters of 1996)

Seasonal variations of contributions of different emission sources to PCB-153 depositions are the same as in Nenets AO. Depositions decrease from the first to the second quarter and then go up. The rate of increase of depositions from North-western Europe sources is higher in comparison with those of Russian ones. There is a difference for the fourth quarter, when depositions from North-western Europe remain less than depositions from Russia. This can be explained by the fact that the considered region is located to the east from Nenets AO. Therefore southern and south-western winds transport of the pollutant from Russian sources in considerable amounts.

**Sakha Republic (Yakutia).** Contributions to depositions to Sakha Republic from sources of the Northern Hemisphere are presented in Figure 6.27.a. As for other regions the major contribution to depositions is made by Russia (38%). Then come North-western Europe (23%) and South-eastern Europe (16%). Contributions from American sources to the pollution of this region become tangible (contrary to the above considered regions) and comparable with that of local sources – about 11%.

As to Russian emission sources (Fig. 6.27.b), the main contribution is made by own sources of Yakutia (11%). Then come CVV, CVN, URL, WSB, ESB with contributions from 4% to 6%.

Seasonal variations of contributions of main source groups to deposition to Sakha Republic in absolute (a) and relative (b) values in 1996 are displayed in Figure 6.28.

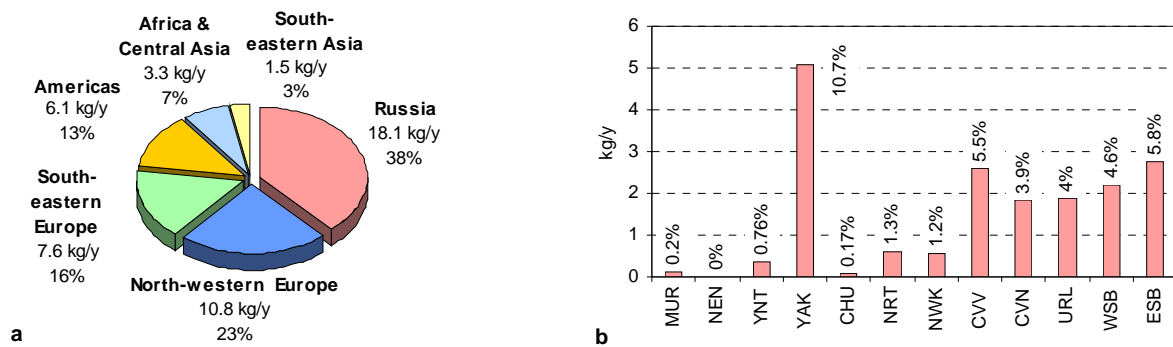


**Figure 6.27.** Contributions of different emission sources to PCB-153 depositions to Sakha Republic (Yakutia) in 1996. (a) – from source-regions in the Northern Hemisphere, (b) - detailed splitting of Russian contribution

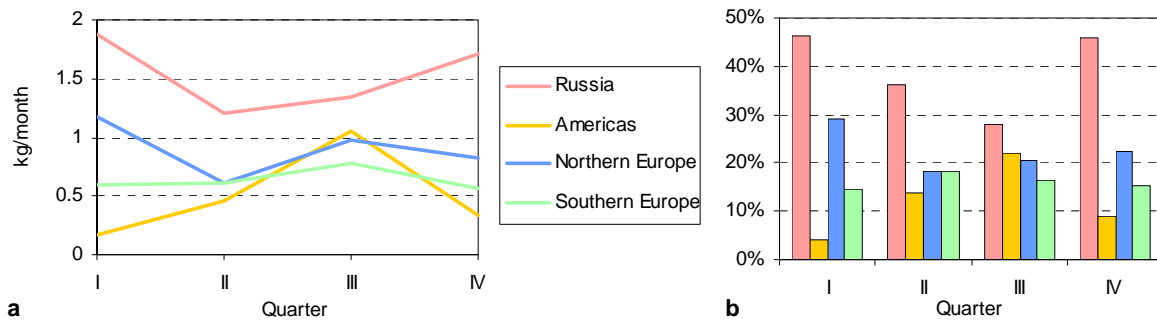


**Figure 6.28.** Seasonal variations of contributions of different emission sources to PCB-153 depositions to Sakha Republic (I-IV quarters of 1996)

The main difference of seasonal variations in this region in comparison with previous ones is that contributions from American sources in this region became more significant. Due to meteorological conditions contributions of these sources are growing from the first to the third quarters and drop down in the fourth quarter. Fast increase of contributions from American sources leads to the increase of their relative input and at the same time to the decrease of relative input from North-western European and Russian sources in this region in the second and the third quarters.

**Chukotka Autonomous Okrug.** For this region considerable contributions to depositions are made by Russian (25%), North-western (22%) and South-eastern (19%) European emission sources (Fig. 6.29.a). In comparison with Yakutia, the contribution from the Americas increased up to 17%, that is explained by specific geographical location and meteorological features of this region.

Contributions to depositions from Russian sources are presented in Figure 6.29.b. The main contribution is made by emissions of Chukotka AO itself (8%), then come East-Siberian and Far-Eastern regions (5%).

Seasonal variations of contributions of main source groups to deposition to Chukotka AO in absolute (a) and relative (b) values in 1996 are displayed in Figure 6.30.

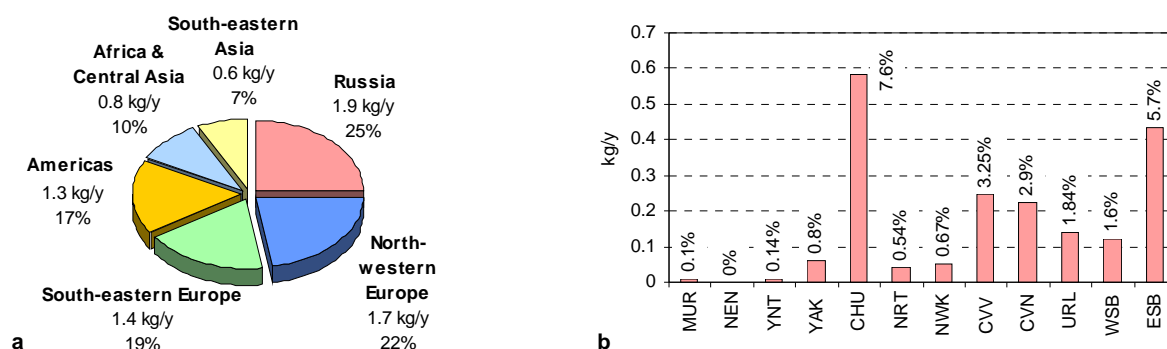


**Figure 6.29.** Contributions of different emission sources to PCB-153 depositions to Chukotka AO in 1996. (a) – from source-regions in the Northern Hemisphere, (b) - detailed splitting of Russian contribution

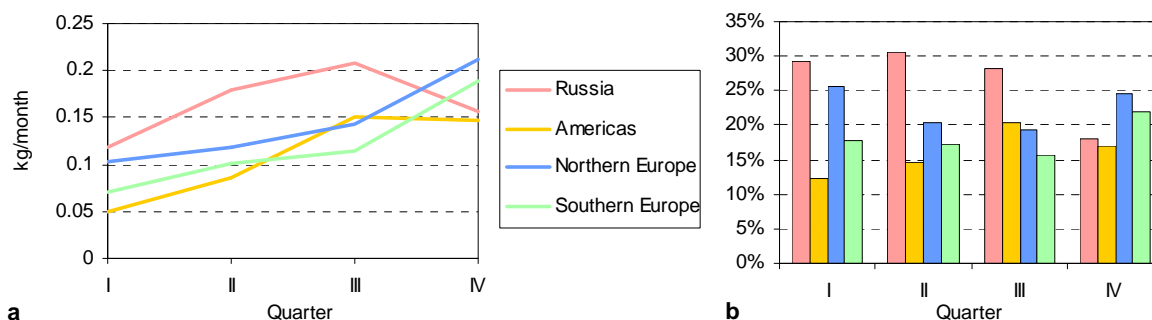


**Figure 6.30.** Seasonal variations of contributions of different emission sources to PCB-153 depositions to Chukotka AO (I-IV quarters of 1996)

Increase of depositions from the considered emission sources takes place for the period from the first to the fourth quarters (Fig. 6.29.a). There is an exception for Russian sources, which decrease beginning from the third quarter. Further increase of contributions from American sources with respect to those of North-western and South-eastern Europe determine the character of seasonal variations of relative inputs of different source groups in the region. These inputs from Russian sources are greater in the second and the third quarters. On the contrary relative inputs North-western and South-eastern Europe sources are maximum in the first and the fourth quarters.

Thus, from the analysis of contributions of different emission sources to PCB contamination of the selected regions of the Russian North the following results were obtained:

- contributions of different emission sources to the formation of air and soil concentrations are similar to their contributions to deposition formation.
- major contribution to PCB-153 pollution of the Russian North is made by Russian emission sources, then come North-western and South-eastern Europe, and the Americas.
- among Russian sources the strongest influence on the pollution of the considered regions is made by its own emissions. This is true for Murmansk Oblast, Sakha Republic and Chukotka AO. Nenets AO and Yamalo-Nenets AO and Taimyr AO are influenced mainly by Central and Volga-Viatsky regions.

### 6.5. Congener composition analysis

Simulations of long-range transport and accumulation of four PCB congeners (PCB-28, PCB-118, PCB-153 and PCB-180) make it possible to compare the peculiarities of environmental behaviour of different PCB congeners during their long-range transport. In particular, changing of PCB congener composition in air during their transport is of particular interest. Clearly, this analysis is of preliminary character and the results may be changed in the course of further refinement of PCB physical-chemical properties and emission data.

The diagrams of Figure 6.31 present PCB congener composition (in this section we consider congener composition of the mixture of 4 selected PCB congeners) in air of different regions-receptors of the Russian North in comparison with that of emissions. Figure 6.31.a displays the congener composition formed by all emission sources of the Northern Hemisphere during the period from 1970 to 1996.

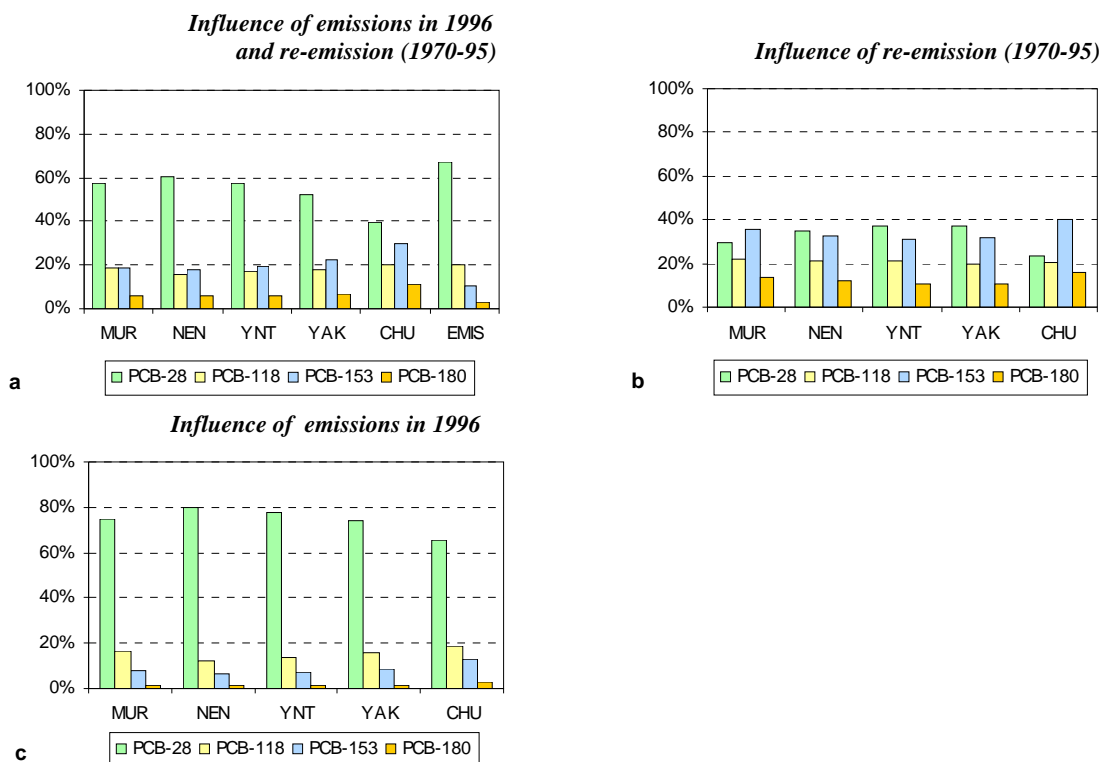
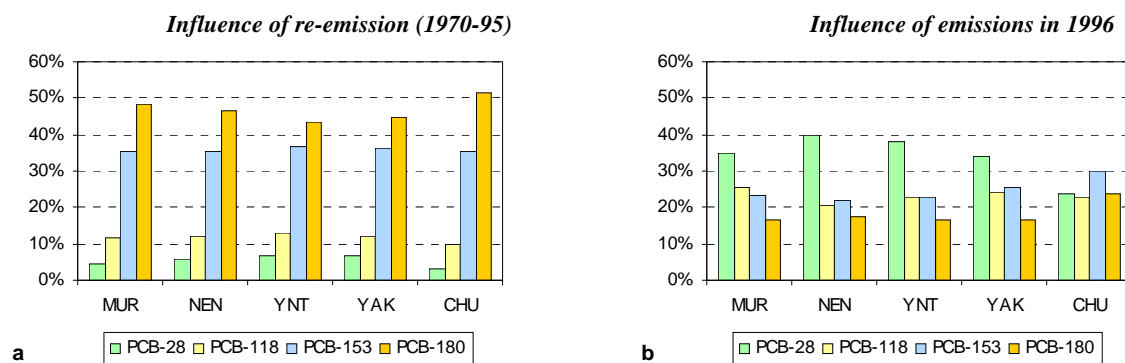


Figure 6.31. PCB congener composition in air of different regions-receptors of the Russian North in 1996

For all regions-receptors, the fraction of PCB-28 is highest and PCB-180 is lowest, in compliance with their fraction in emissions (last column in Fig. 6.31.a). The other congeners are in the intermediate position. It should be noted that the congener composition of four selected PCB congeners vary from region to region. This congener composition for 1996 may be split into two parts: formed by re-emission process caused by PCB accumulations in media during the period from 1970-95 (Fig. 6.31.b) and formed by emission in 1996 (Fig. 6.31.c). In the first case we consider results of the model run for 1996 with zero emission and initial concentrations obtained from model spin-up (1970-95). In the second case the results of the model run with zero initial concentrations in all the media and emission of 1996 are considered.

The most contribution to the congener composition due to re-emission is made by PCB-28 and PCB-153 (Fig. 6.31.b). Considering the congener composition caused only by emissions of 1996 (Fig. 6.31.c), it should be noted that PCB composition in air in general follows that of emissions, being different for individual regions.

Thus, one of the most important factors, influencing PCB congener composition in air, is congener composition of emissions. To demonstrate the role of physical-chemical properties and atmospheric transport in the formation of PCB congener composition, it is interesting to exclude the emission factor from the consideration. To this end we normalized air congener compositions to their emissions and show results in Figure 6.32. By this normalization we have obtained PCB congener composition in air under the assumption that emissions of all four congeners equal one another. The congener composition caused by re-emission processes (Fig. 6.32.a) is normalized by total emissions from 1970-95, and the congener composition caused by emissions of 1996 (Fig. 6.32.b) is normalized by emissions of this year.



**Figure 6.32.** PCB congener composition in air of different regions-receptors in 1996 (equal emission totals)

From Figure 6.32.a it is clearly seen, that the heavier congener is the greater re-emission influences on air pollution. This may be explained by higher degradation half-life in soil for heavy congeners and higher soil capacity for them. As to emissions of 1996, Figure 6.32.b demonstrates that fraction of PCB-28 is higher than fractions of other congeners for all regions-receptors excluding Chukotka AO.

Simple normalization to emissions keeps the uncertainty of different congener composition of emission sources located in different countries. To get over this uncertainty it is interesting to consider the congener composition of air concentrations transported from a single emission source with equal fractions of each congener. More reliable estimates may be obtained if we consider one region-source and regions-receptors located in increasing distance. This experiment is shown in Figure 6.33, where normalized emissions only from Murmansk Oblast are considered. As seen from the diagram, there are certain variations in congener composition of PCB mixture transported from Murmansk Oblast to

five regions-receptors. However, these differences are less significant than those caused by different congener composition of different emission sources.

Thus, in the atmosphere of the Russian North PCB-28 dominates, then come PCB-118, 153 and PCB-180. For different regions-receptors, the composition of PCB mixture is different. The main factor affecting the air congener composition is emissions.

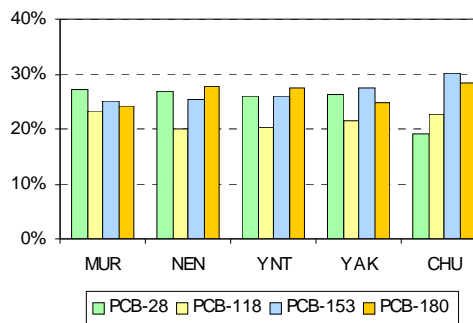


**Figure 6.33.** PCB congener composition in air of different regions-receptors in 1996 caused by Murmansk emission sources (equal emission totals)

## 6.6. Evaluation of deposition of total PCB mixture to the Russian North

The aim of this section is to give a rough estimate of total deposition of the whole PCB mixture to five regions-receptors of the Russian North and to the Arctic as a whole. To do that the fractions of four selected congeners (PCB-28, 118, 153 and 180) in total 1996 emissions of 22 congeners included in the emission inventory by [Breivik et al., 2002] from different source groups were calculated in accordance with the cited work (Table 6.6).

**Table 6.6.** Relative contributions (%) of selected four congeners to total emission of 22 PCB congeners for different source groups (according to [Breivik et al., 2002])

Source group	PCB-28	PCB-118	PCB-153	PCB-180
Russia	13.8	4.5	1.1	0.2
America	11.2	2.9	2.1	0.8
North-Western Europe	11.0	2.9	4.1	1.2
South-Eastern Europe	12.6	3.4	2.6	0.7
Africa and Central Asia	12.3	3.4	2.6	0.7
South-Eastern Asia	10.5	3.9	2.6	0.7

Using these data four estimates of total deposition of the mixture of 22 PCB congeners to regions-receptors and to the Arctic were performed under the assumption that all PCB emissions consists totally of one of the four considered congeners (PCB-28, PCB-118, PCB-153 or PCB-180). The results of evaluation are summarized in Table 6.7.

**Table 6.7.** Annual deposition of the mixture of 22 PCB congeners to five regions-receptors and to the Arctic estimated on the basis of physical-chemical properties of four selected congeners

Regions-receptors	Deposition of mixture of 22 PCB congeners (tonnes) evaluated via properties of				Range (%)
	PCB-28	PCB-118	PCB-153	PCB-180	
Murmansk Oblast	0.78	0.84	0.82	0.84	7
Nenets AO	0.90	0.82	0.80	0.66	38
Yamalo-Nenets AO and Taimyr AO	2.3	2.4	2.6	2.6	14
Republic of Sakha	1.8	2.2	2.6	2.6	46
Chukotka AO	0.19	0.30	0.38	0.39	109
Arctic region	19.7	19.1	23.0	22.2	20

Clearly, such estimates disregard differences of physical-chemical properties of different PCB congeners assigning properties of one of the congeners to the whole mixture. This leads to essential differences in obtained estimates, which can reach factor 2 in some regions of the Russian North (Chukotka AO). For the Arctic as a whole the range of the obtained estimates is about 20%.

Relatively small difference between estimates obtained by properties of different congeners can be explained by the fact that at high content of light congeners in the Arctic air, their deposition velocities are essentially lower than for heavy congeners. The combined effect of these two opposite-directed factors leads to close values of depositions evaluated on the basis of properties of different congeners. These considerations show that averages of deposition values calculated with the help of properties of four selected congeners can serve as an estimate of depositions of the mixture of 22 PCB congeners to different regions-receptors within a factor of two.

The evaluation of total depositions of 22 PCB congeners to regions-receptors can be done in different ways. First, one can assume that all emissions of 22 PCB congeners are distributed between four considered congeners in equal fractions (25% scenario). Then the estimate of total deposition will be arithmetical mean of estimates obtained by properties of each four congeners. Further, one can assume that all emissions of 22 PCBs are distributed between four congeners according to their fractions in total emissions (4 congener scenario). Finally, all emissions of 22 PCB congeners can be divided into four groups (di+trichlorinated PCBs, tetra+pentachlorinated PCBs, hexachlorinated PCBs and hepta+octachlorinated PCBs). It is supposed that these groups are transported with properties of PCB-28, 118, 153 and 180, respectively (4 group scenario). The results of all three estimates are presented in Table 6.8.

**Table 6.8.** *Estimated annual deposition of the mixture of 22 PCB congeners to five regions-receptors and to the Arctic, tonnes*

Regions-receptors	25% scenario	4 congener scenario	4 group scenario
Murmansk Oblast	0.82	0.79	0.80
Nenets AO	0.80	0.87	0.87
Yamalo-Nenets AO and Taimyr AO	2.5	2.36	2.37
Republic of Sakha	2.3	2.01	1.99
Chukotka AO	0.31	0.24	0.23
Arctic region	21.0	20.1	20.0

All these estimates are close enough to one another.

Further, according to estimates of the work [Breivik *et al.*, 2002], the share of considered there 22 PCB congeners *in the production of total PCB mixture* amounts is about 43%. If we assume (clearly, this assumption is a very rough one) that the share of these 22 congeners *in PCB emissions* is also close to 50%, we can evaluate annual deposition of total PCB mixture to five regions-receptors and to the Arctic (Table 6.9). These values are obtained using 4 group scenario from Table 6.8. The obtained estimate of total PCB deposition to the Arctic (40 tonnes) agrees well with the estimate by R.W. Macdonald with co-authors [Macdonald *et al.*, 1999] (45 tonnes).

**Table 6.9.** *Estimated depositions of total PCB mixture to selected regions, tonnes*

	Murmansk Oblast	Nenets AO	Yamalo-Nenets AO and Taimyr AO	Republic of Sakha	Chukotka AO	Arctic region
Annual deposition of PCB mixture	1.6	1.7	4.8	4.0	0.46	40

## 6.7. Concluding remarks

As a result of the model assessment of PCB pollution levels and contributions of main emission sources, the following conclusions were made:

1. Model evaluation gives spatial distribution of depositions and concentrations in air, soil, seawater and vegetation for PCB-28, 118, 153, and 180 for 1996. For model verification, air concentrations were compared with measurements. The comparison demonstrated that for all considered congeners about 95% of results are within a factor of 4.
2. Air concentrations of PCB-153 in the Russian North in 1996 vary from 0.7 to 2.6  $\text{pg}/\text{m}^3$ , the depositions - from 0.05 to 0.21  $\text{g}/\text{km}^2/\text{y}$ . The pollution level decreases, concurrent with the distance from main emission sources from Murmansk Oblast to Chukotka AO. The pattern for the other congeners is similar.
3. As to emissions of 1996, source-receptor analysis shows that the highest contributions to pollution of the Russian Arctic are made by Russian and North-western and South-eastern Europe emission sources. Among Russian sources for the regions of Murmansk Oblast, Yakutia and Chukotka AO, the highest contributions are made by their own local sources. For Nenets AO, and Yamalo-Nenets AO and Taimyr AO, a considerable contribution is made by the Central and Volga-Viatsky regions.
4. Seasonal variations of air contamination of the Russian North are substantial and different for each region-receptor. The influence of region-sources on receptors depends on the season and may be explained by the character of atmospheric transport.
5. Investigation of congener composition in the air of the Russian North reveals that PCB-28 dominates, followed by PCB-118, 153 and 180. For different region-receptors, the composition of the PCB mixture is slightly different. The main factor affecting the air congener composition is emissions.
6. Rough estimation of the contamination of the Russian North by the total PCB mixture has been done on the basis of four congener transport simulations taking into account the fractions of these congeners in the entire PCB mixture.

## References

- Baart A., J.Berdowski, J.van Jaarsveld and K.Wulffraat [1995] Calculation of atmospheric deposition of contaminants on the North Sea. TNO-MEP-R 95/138, Delft, The Netherlands.
- Berg T., and Hjellbrekke A.-G. [1998]. Heavy metals and POPs within the ECE region. Supplementary data for 1989-1996. EMEP/CCC-Report 7/98, 103 p.
- Berg T., and Hjellbrekke A.-G. [1999]. AMAP Datareport: Atmospheric Subprogramme. NILU, OR-16-99, 100 p.
- Berg T., Hjellbrekke A.-G. and N. Ritter [1997]. Heavy metals and POPs within the ECE region. Additional data. EMEP/CCC-Report 9/97, 79 p.
- Berg T., Hjellbrekke A.-G., and Skjelmoen J.E. [1996]. Heavy metals and POPs within the ECE region. EMEP/CCC-Report 8/96, 187 p.
- Brevik K., A. Sweetman, J. Pacyna and K. Jones. [2002] Towards a global historical emission inventory for selected PCB congeners – a mass balance approach 2. Emissions. *The Science of the Total Environment*. In press.
- Coleman P. J., Donovan B.J., Campbell G.W., Watterson J.D., Jones K.C., Lee R.G.M., Peters A.J. [1998] Results from the Toxic Organic Micropollutants (TOMPS) network: 1991 to 1997. AEAT-2167, Issue 2.
- Brorström-Lundén E., E.Junedal, H.Wingfors and S.Juntto [2000] Measurements of the Atmospheric Concentrations and the Deposition Fluxes of Persistent Organic pollutants (POPs) at the Swedish West Coast and in the northern Fennoscandia.

- Macdonald R.W., T.F., Bidleman, D.C.G., Muir, L.M. Jantunen and T. Harner [1999] Arctic Mass Budgets - a look at HCH, toxaphene and PCBs, Annex 14., In Modelling and Sources: A Workshop on Techniques and Associated Uncertainties in Quantifying the Origin and Long-Range Transport of Contaminants to the Arctic. AMAP Report 99:4.
- Oehme M., J.Haugen and M.Schlabach [1995] Ambient air levels of persistent organochlorines in spring 1992 at Spitsbergen and the Norwegian mainland: comparison with 1984 result and quality control measures. *The Science of Total Environment*, v.160/161, pp.139-152.
- Shatalov V. and A.Malanichev, [2000], Investigation and assessment of POP transboundary transport and accumulation in different media, Part I and II, EMEP Report 4/2000.
- Shatalov V., A.Malanichev, N.Vulykh, T.Berg and S.Manø [2001] Assessment of POP transport and accumulation in the environment. EMEP Report 4/2001, Moscow.

## Chapter 7

**ATMOSPHERIC TRANSPORT AND DEPOSITION OF  $\gamma$ -HCH TO THE ARCTIC REGION**

This section contains a model evaluation of  $\gamma$ -HCH air concentrations, depositions and pathways of long-range transport to the Russian North in 1996 with the use of a source-receptor scheme. The realization of the source-receptor scheme used in this chapter is quite the same as for PCBs (see Chapter 6).  $\gamma$ -HCH emission sources were split into groups as described earlier in Chapter 4 (see also Fig. 7.19.a and b below).

$\gamma$ -HCH transport was simulated for the period from 1990 to 1996 to evaluate accumulation in main environmental media (soil, seawater, vegetation).

The calculations are made by using the hemispheric version of the MSCE-POP model (see Section 3.3 above) and cover the territory of the whole Northern Hemisphere. Such spatial coverage is reasonable for the assessment of  $\gamma$ -HCH contamination of the Russian North from remote regions such as North America and Asia.

**7.1. General description of modeling results*****Redistribution between environmental media***

In the course of the model run for the period from 1990 to 1996, detailed spatial distributions of contamination in main environmental media (atmosphere, soil, seawater and vegetation) as well as deposition fluxes over the Northern Hemisphere with resolution  $2.5^{\circ} \times 2.5^{\circ}$  were obtained under the assumption that initial media content in the beginning of 1990 is zero. These results were used to assess the contents of main media over the whole hemisphere (that is, the total amount of the pollutant accumulated in such media as atmosphere, soil, seawater and vegetation) in 1996 and to examine the dynamics of the accumulation process. Figure 7.1 displays trends of  $\gamma$ -HCH accumulations during the simulated period (1990–96) in these media. For the sake of comparison, the dynamics of  $\gamma$ -HCH emissions used in modeling is also presented.

According to the emission data used, total emissions in the Northern Hemisphere decreases from 1990 to 1991, and then remains at an approximately constant level (Fig. 7.1.a). It can be observed that the process of accumulation takes place differently in each environmental compartment. Namely, the dynamics of  $\gamma$ -HCH content in the atmosphere and vegetation follows the emission dynamics (Figs. 7.1.b and c). Contents in soil and seawater (Figs. 7.1.d and e) grow quickly during the first three years of the simulation period and beginning in 1993 become more or less stable.

Since a stabilization of content in all the environmental media has been reached to some extent by the end of 1996, redistribution of  $\gamma$ -HCH in the end of the simulation period allows one to select media with the highest accumulation of the pollutant. The redistribution of  $\gamma$ -HCH between environmental compartments over the whole Northern Hemisphere by the end of the simulation period is shown in Figure 7.2.

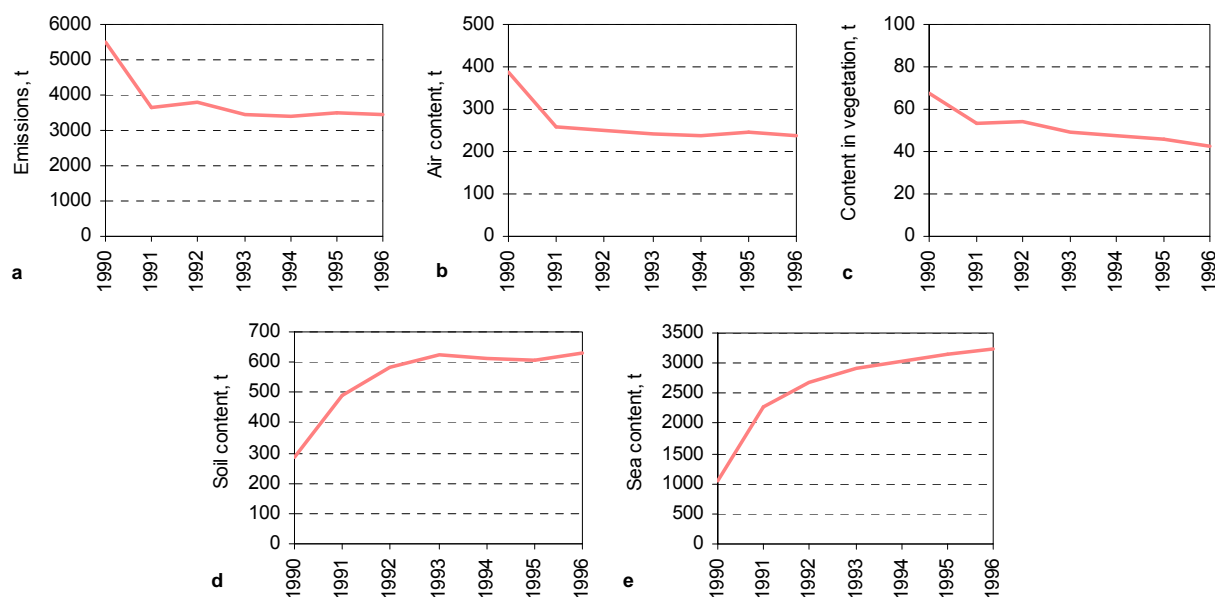


**Figure 7.1.** Trends of  $\gamma$ -HCH emissions and accumulation in main environmental media and in the whole environment during 1990 – 1996 (calculations with initial media content equal to zero)

According to this distribution seawater is the main media accumulating  $\gamma$ -HCH (it contains about 80% of the whole environmental content). This conclusion coincides with that made in [Strand and Hov, 1996]. Thus, atmosphere/gas exchange, transport by sea currents and the influence of sea ice (see Annex E) seem to be essential in the description of the fate  $\gamma$ -HCH in the environment. Soil accumulated a somewhat less, though still considerable fraction of  $\gamma$ -HCH.

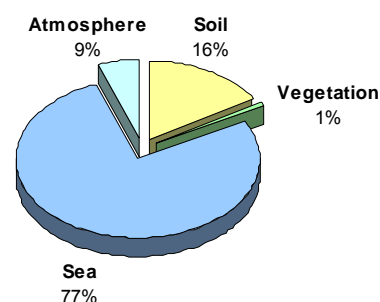


**Figure 7.2.** Calculated redistribution of  $\gamma$ -HCH between environmental compartments by the end of 1996

### ***Spatial distribution of contamination***

Further, calculation results allow one to perform more detailed analysis of the contamination of environmental media, that is, to evaluate spatial distribution of  $\gamma$ -HCH contamination by the end of the simulation period (1996). Figure 7.3 shows spatial distributions of average annual  $\gamma$ -HCH depositions and concentrations in the lower atmospheric layer and upper seawater layer in comparison with that of emissions.

Maps of concentrations and depositions indicate that high levels of concentrations and depositions are mainly characteristic of regions with high emissions. However, the transport of  $\gamma$ -HCH from emission sources to remote regions both in the atmosphere and sea is also noticeable (e.g. atmospheric transport from European and Indian sources towards the North-East). This will be demonstrated below in more detail

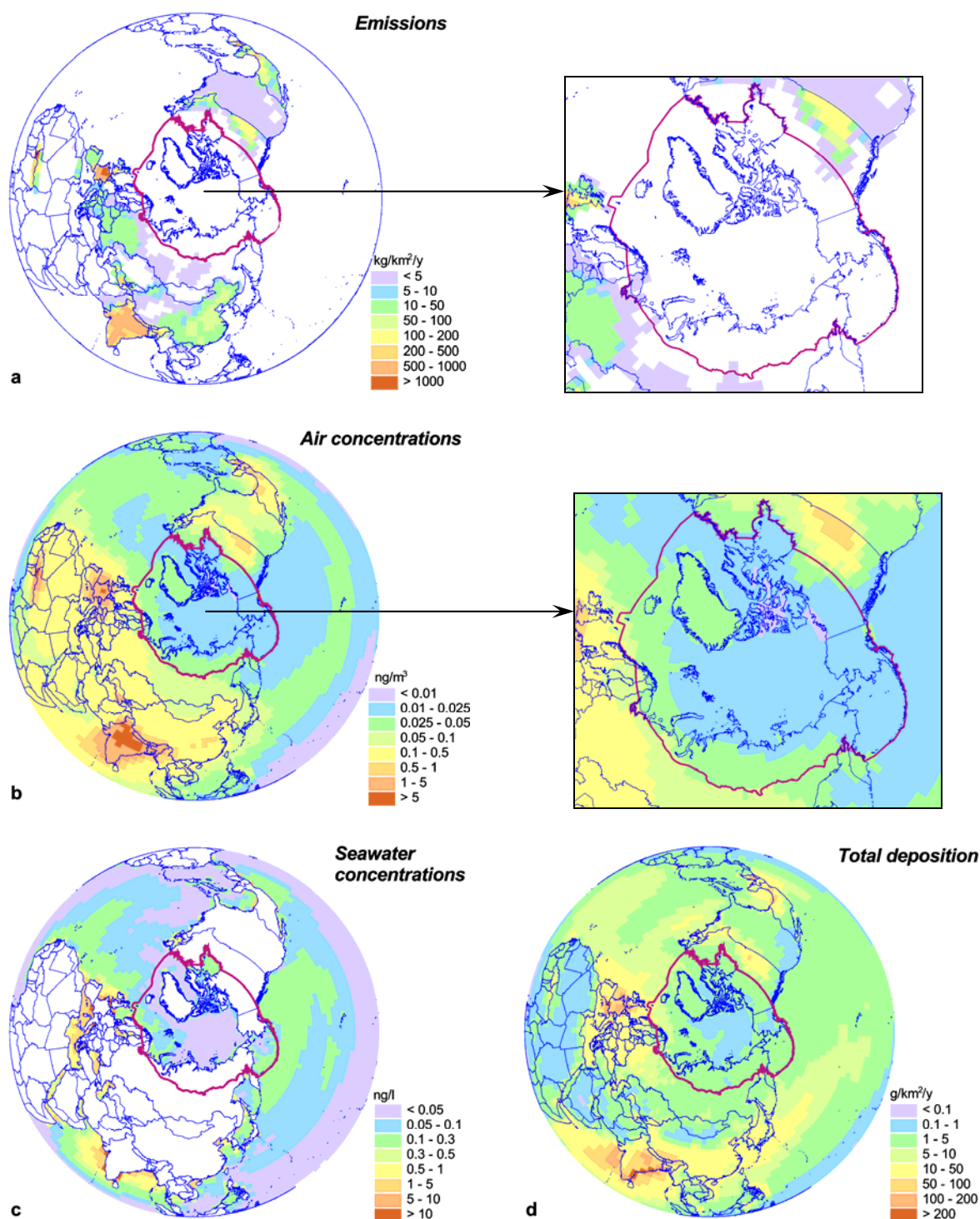


**Figure 7.3.** Calculated spatial distribution of average annual  $\gamma$ -HCH deposition and concentrations in atmosphere and seawater in comparison with emissions for 1996

### Contamination of the Arctic region

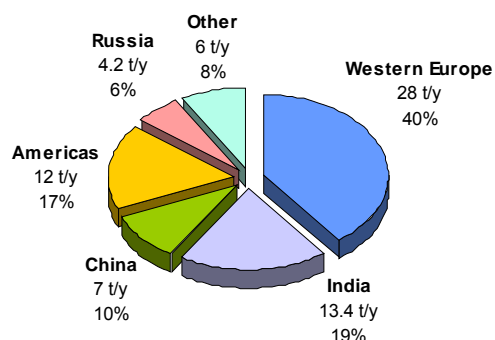
Calculated spatial distributions of air concentrations and depositions allow us to evaluate pollution levels in the Arctic (AMAP region, see Fig. 7.3). Table 7.1 contains the annual averages of air concentrations and depositions over the Arctic calculated for 1996.

**Table 7.1.** Annual averages of air concentrations and deposition flux in the Arctic region in 1996

	Min	Max	Aver
Air concentrations, ng/m <sup>3</sup>	0.0086	0.11	0.023
Deposition flux, g/km <sup>2</sup> /y	0.22	17	2.4

The calculated total amount of  $\gamma$ -HCH deposited to the Arctic region in 1996 equals 78 tonnes. Due to the high deposition velocity over sea (according to the model assumption it is twice higher on the average than that over land) and taking into account that an essential part of the area is covered by ocean (about 60% according to [AMAP, 1998]) the total amount of  $\gamma$ -HCH deposited to sea area in 1996 is estimated at 58 tonnes. Due to the high persistence of the pollutant in a sea environment, depositions of  $\gamma$ -HCH to seawater for the period from 1990 to 1996 form sufficiently high seawater concentrations in the region (up to 1 ng/l and more). It must be taken into account that at present the model underestimates seawater concentrations since some pathways of the pollutant to the region are not taken into account (e.g., inflow with rivers).

Modeling results allow one also to evaluate the contributions of different emission sources to the contamination of the Arctic region (Fig. 7.4). The main group of sources contributing this region is Western Europe (about 40%), followed by India (19%), America (17%), China (10%) and Russia (6%). The share of all other sources amounts to 8%.

**Figure 7.4.** Contributions of different emission sources to the deposition to the Arctic region in 1996

In spite of the fact that anthropogenic emissions in the Arctic region are practically nonexistent (Fig. 7.3.a) contamination in this region is noticeable. Here air concentration levels can reach up to 0.11 ng/m<sup>3</sup> and deposition flux can reach 17 g/km<sup>2</sup>/y. Seawater concentrations near the regions of the Russian North are in the range 0.1 – 2 ng/l. These concentrations (as well as concentrations in soil) are the result of long-term accumulation process (see above) and the so-called cold condensation effect. To demonstrate this effect latitudinal distributions of contamination in main media in the polar region (60° and higher) were calculated (since there is no soil at latitudes higher than 80°, the plot for soil concentrations is presented for latitudes from 60° to 80° only).

Calculations show that though main emission sources are located in the middle latitudes (not higher than 70 degrees North), concentration levels in all main environmental compartments show a very slow decrease in the polar zone concurrent with latitude (or no decrease at all, see Figs. 7.5.a–c). This effect can be explained by more effective accumulation of  $\gamma$ -HCH at low temperatures and indicates that this pollutant tends to accumulate in regions with a cold climate.

One more proof of **cold condensation** is demonstrated by the comparison of the latitudinal distribution of soil concentrations with that of emissions (Fig. 7.6).

From the plot it is seen that maxima in latitudinal distribution of soil concentrations shift to the north with respect to maxima of emission distribution and the maximum of soil concentrations located at higher latitudes is much more pronounced.

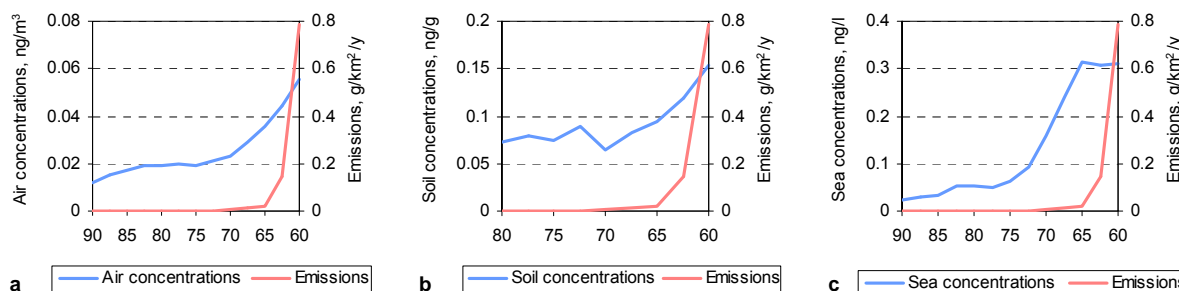


**Figure 7.5.** Calculated latitudinal distribution of  $\gamma$ -HCH concentrations in the atmosphere (a), soil (b) and seawater (c) in the polar zone

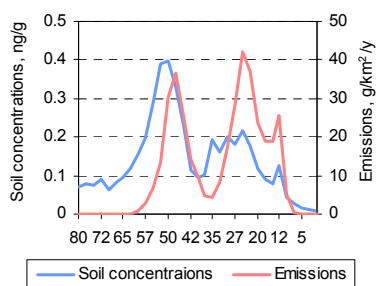


**Figure 7.6.** Calculated latitudinal distribution of  $\gamma$ -HCH concentrations in soil over the whole hemisphere

### Pathways of atmospheric $\gamma$ -HCH transport to the Arctic

Spatial distributions of contamination calculated over the entire Northern Hemisphere allow one also to evaluate pathways of  $\gamma$ -HCH transport from different groups of sources to the Arctic in various media.

Here we present the analysis of  $\gamma$ -HCH transport from the two largest groups of sources: India and West Europe. The process of atmospheric transport of  $\gamma$ -HCH from Indian sources in 1996 under the assumption of initial concentrations of zero in all environmental compartments is displayed month by month in Figure 7.7.

One can see that in the beginning of the year (January – March)  $\gamma$ -HCH transport takes place mainly in an eastward direction. From April to August  $\gamma$ -HCH is transported in a northward direction to the Russian North and the Arctic region due to the cyclonic character of wind patterns in the region. Then the character of wind patterns change and from September the process of atmospheric outflow from the Arctic and transport in an eastward direction takes place. In accordance with model estimates,  $\gamma$ -HCH from Indian sources can be transported to the Russian North and the Arctic region passing around Tibet from its southern-eastern side.

The transport from West-European sources is shown in Figure 7.8.

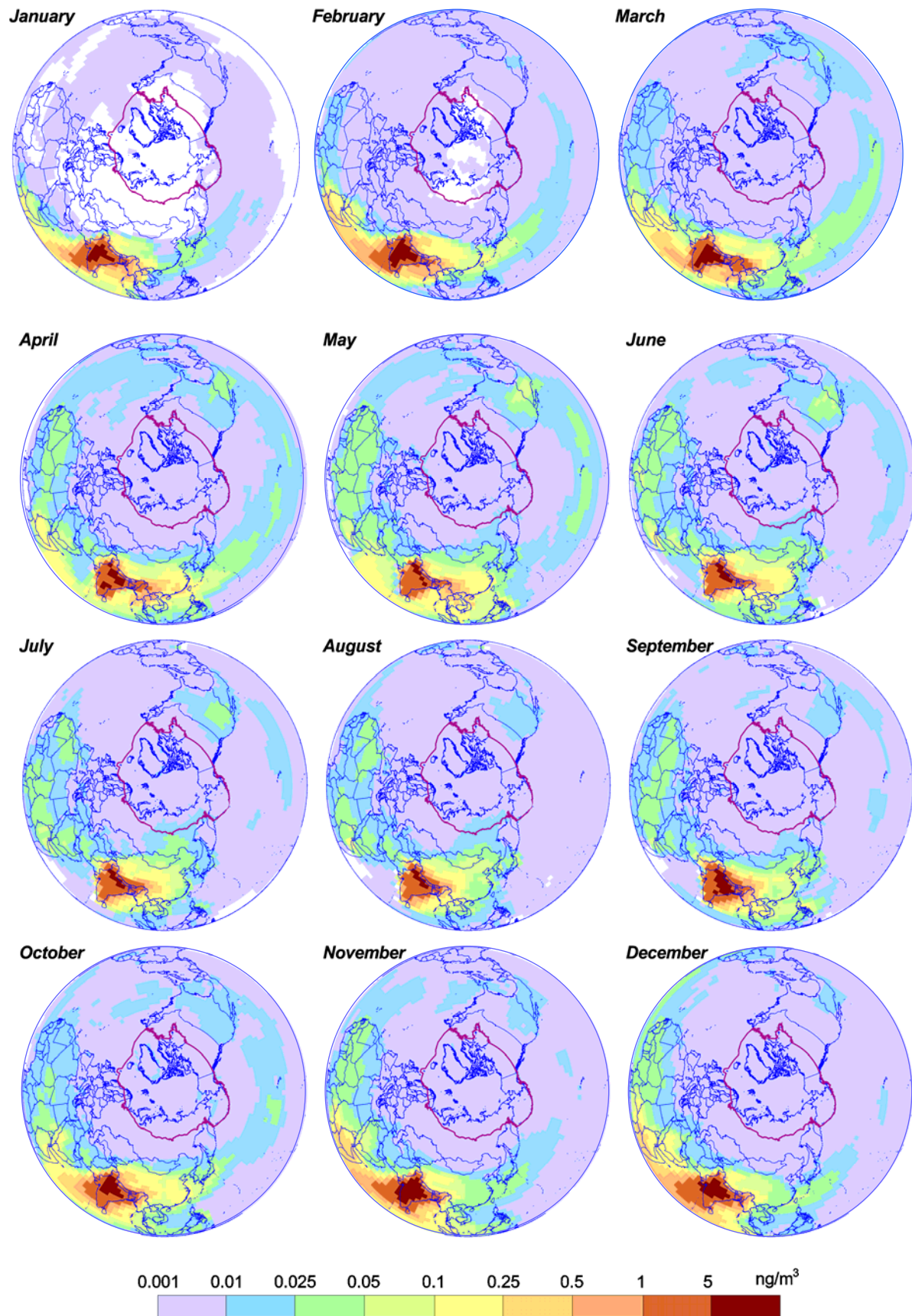


Figure 7.7. Monthly dynamics of  $\gamma$ -HCH transport from Indian sources for 1996 (air concentrations)

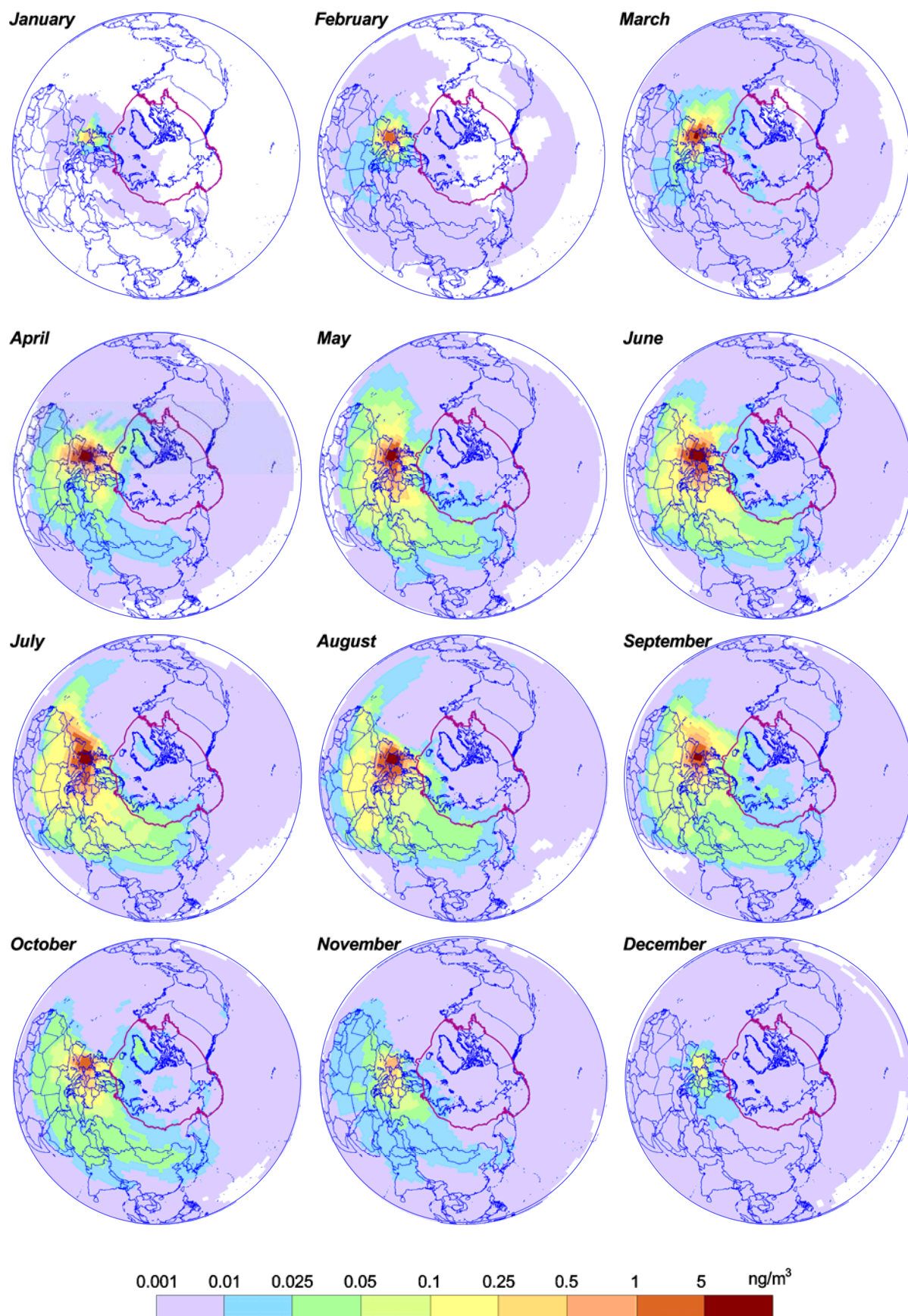


Figure 7.8. Monthly dynamics of  $\gamma$ -HCH transport from West-European sources for 1996 (air concentrations)

Maps of monthly averaged air concentrations show that the transport of  $\gamma$ -HCH from West-European sources to the Arctic as a whole and to the Russian North in particular takes place from January to September in eastward and north-eastward directions. The decrease of air concentrations in the period from October to December is explained by an emission decrease due to seasonal variations assumed in the model for this group of sources (see Section 4.3).

This analysis can be extended to the analysis of source-receptor relationships for selected regions of the Russian North. This will be done below (see Section 7.4).

Calculated spatial distributions of  $\gamma$ -HCH contamination in the Northern Hemisphere also make it possible to calculate average contamination levels in region-receptors. However, prior to that we wish to present a description of comparison between measurements and calculations to elucidate the reliability of calculated estimates.

## 7.2. Comparison of modeling results with measurements

The aim of this section is to compare calculated values of air concentrations and depositions with available measurement data. For the comparison we used annual averages of measured  $\gamma$ -HCH concentrations in the ambient air and precipitation for the period from 1990 to 1996, available in the EMEP database (Chemical Coordinating Centre of EMEP) [Löfblad *et al.*, 1995, Berg *et al.*, 1996, Berg *et al.*, 1997, Berg and Hjellbrekke, 1998, Berg and Hjellbrekke, 1999]. Part of the air concentration values calculated for the Arctic region were compared with measurement data available in [AMAP, 1999]. In addition, results of national measurement campaigns [Brorström-Lundén *et al.*, 2000; *Reviews of the environmental background ...*, 1994 – 1996, Hoff *et al.*, 1996, IADN Results to 1996] and some literature data [Halsall *et al.*, 1998; Harner *et al.*, 1999] were included in the comparison study carried out for air concentrations of different regions of the Northern Hemisphere. However, taking into account that computation period begins from 1990, sufficient accumulation levels in media are achieved only by 1993 and we carry out the comparison for the period from 1993 to 1996.

Figure 7.9 presents a map of the geographical locations of measurements used for the comparison. The map indicates that measurement data are available for different regions: North-west Europe, the Arctic zone, the Great Lakes region, and the Baikal region. It is readily seen that the monitoring data on  $\gamma$ -HCH concentrations in air, in contrast to those in precipitation, were available for a number of measurement sites situated in the Arctic region specifically (Pallas, Ny Ålesund, Tagish, Dunai, Alert, etc.). As evident from the map, spatial coverage of air concentration measurements is much larger than that of precipitation. The majority of sites monitoring  $\gamma$ -HCH concentration in precipitation are located in Europe. Certainly, for better validation of calculation results more measurements both in air and in precipitation are needed.



▲ air concentrations ● concentration in precipitation

**Figure 7.9.** Location of measurement sites used for the comparison. Circles: measurements of air concentrations, triangles: measurements of concentrations in precipitation

In the comparison, annual means of  $\gamma$ -HCH measurements in air and precipitation were used. Namely, mean annual air concentrations are mean arithmetic values of presented data. Mean concentration in precipitation is precipitation weighted arithmetic average. All the measured values were statistically processed. Additionally, all data have been checked for outliers. For example, very high values in the EMEP database, which are beyond the scope of four-fold mean root square deviation in the log-normal distribution have not been taken into account. It might well be pointed out that available observed data, as a rule, cover prolonged time periods thereby providing the possibility to compare the dynamics of air and precipitation contamination by  $\gamma$ -HCH for a given monitoring station.

### 7.2.1. Air concentrations

Table 7.2 contains the comparison results of measured and calculated concentrations in the surface air layer of the European and Arctic regions for the period from 1993 to 1996.

**Table 7.2.** Comparison of measured and calculated values of concentrations in the surface air layer,  $\text{pg}/\text{m}^3$  and calculation to measurement ratio for Europe and the Arctic

Site	Location		Year	Measured			Calculated	Calc/meas ratio
	Long	Lat		Min	Max	Aver		
SE2 <sup>1)</sup>	11.93	57.42	1994	11	199	51.2	195.00	3.81
			1995	6	78	25	176.00	7.04
			1996	6	50	26	167.00	6.42
SE12 <sup>5)</sup>			1996			83.43	74.6	0.89
NO99 <sup>2)</sup>	6.56	58.1	1993	12.1	282.7	53.52	178.00	3.33
			1994	1.99	1000.3	122.89	160.00	1.30
			1995	7.4	593.5	64.98	149.00	2.29
			1996	15.8	132.6	60.72	154.00	2.54
NO42 <sup>3)</sup>	11.88	78.9	1993	3.3	38.3	14.4	25.00	1.74
			1994	5.31	62.1	16.1	24.00	1.49
			1995	5.98	41.1	13.13	23.20	1.77
			1996	4.87	39.1	12.85	20.00	1.56
FI96 <sup>1)</sup>	24.12	67.97	1996	4.2	24	11	54.2	4.93
IS91 <sup>4)</sup>	-20.25	63.45	1995	0	50	14.19	36.8	2.59
			1996	3.6	32.3	9.64	33.6	3.49
Tagish <sup>5)</sup>	-134.27	60.3	1993	3.33	25.1	10.95	15.9	1.45
			1994	4.36	138	14.21	15.8	1.11
Alert <sup>5)</sup>	-62.5	82.45	1993	1.92	410	18.53	15	0.81
			1994	0.15	57.85	10.7	14.6	1.36
Barguzin BR <sup>6)</sup>	109.5	54.2	1993	2.0	204	15	104	6.93
			1994	2.0	366	38	92.8	2.44
			1995	3.0	860	154	87.1	0.57
Dunai <sup>7)</sup>	124.5	74.99	1993	3.68	22.7	9.83	27.4	2.79
Barents Sea <sup>8)</sup>	43.7	76.4	1996	13.3	67.8	36.2	16.7	0.46
North East Arctic <sup>8)</sup>	-85.2	83.7	1996	5.3	35.6	14.9	20.5	1.38
North Pole <sup>8)</sup>	-166.1	88.3	1996	12.2	18.8	15	14.9	0.99
Average								2.5
Correlation between measured and calculated values								0.5

<sup>1)</sup> Brorström-Lundén et al., 2000

<sup>5)</sup> AMAP, 1999

<sup>2)</sup> Berg et al., 1996; Berg and Hjellbrekke, 1998

<sup>6)</sup> Reviews of the environmental background .... 1994 – 1996

<sup>3)</sup> Berg et al., 1996; AMAP, 1999

<sup>7)</sup> Halsall et al., 1998

<sup>4)</sup> Berg et al., 1996; Berg et al., 1997

<sup>8)</sup> Harner et al., 1999

The ratios of calculated to measured values (see last column of Table 7.2) show that **the model on average overestimates air concentrations 2.5 times and the correlation between calculated and measured values is 0.5**. A good agreement is obtained at the Canadian sites Alert and Tagish (located inside the Arctic region); measurement data were taken from [AMAP, 1999]. Large discrepancies are obtained at Swedish site SE2 (Rörvik) [Brorström-Lundén et al., 2000]. However, at Swedish site SE12 (Aspvreten), calculations and measurements [AMAP, 1999] agree well enough. Most likely reason for these discrepancies is connected with uncertainties in spatial distribution of emissions.

Large discrepancies between measurement and modeling results occur at the Great Lakes sites [Hoff et al., 1996, IADN Results to 1996]. However, because spatial distribution of emissions from Canada is of a conventional character (it is based on crop area distribution and as a result a large amount of emissions in Canada is assumed to be located near the Great Lakes region) these measurements were not included into the comparison. Refinement of spatial distribution of emissions in this region should improve agreement between calculated and measured concentrations in this region.

The results of the comparison are presented in the form of a scatter plot. The scatter plot in the Figure 7.10 illustrates differences between calculated and measured annual air concentrations. Most of computed concentrations are within a factor of five with respect to measured values. The zone of “factor of five” is shown in the diagram by the dashed lines. When the station is located within this zone, annual average computed value for this station is no more than five times higher or no less than five times lower than the measured value. A logarithmic scale is applied for better display of the entire range of measured and computed values. The measurements at the Great Lakes are depicted by blue triangles. Over 75% of comparisons are within a factor of four.

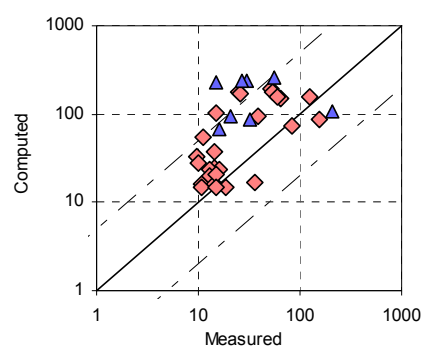


**Figure 7.10.** Computed versus measured annual average  $\gamma$ -HCH concentrations in air in 1996,  $\text{ng}/\text{m}^3$

From the plot it is seen that only three values are outside factor five (except for measurements near the Great Lakes).

### 7.2.2. Concentrations in precipitation

Table 7.3 presents the comparison between calculated and measured mean annual concentrations in precipitation. Available measurement data on  $\gamma$ -HCH content in precipitation were obtained at the EMEP monitoring stations. As it was mentioned above, these data cover only the European region, in particular its northern part.

For the concentration in precipitation, all computed values are within a factor of three with respect to measurements, with an average measurement to calculation ratio of 1.15. The correlation between measured and computed values is 0.82. It should be mentioned that a satisfactory correlation of  $\gamma$ -HCH concentrations in air and precipitation is due to more reliable emission distribution in the European region taken from [Pacyna et al., 1999] and used in our model calculations.

**Table 7.3.** Comparison of measured and calculated values of concentrations in precipitation, ng/l and calculation to measurement ratio

Site	Location		Year	Measured			Calculated	Calc/meas ratio
	Long	Lat		Min	Max	Aver		
DE1 <sup>1)</sup>	8.3	54.9	1993	3.2	80.5	9.28	7.60	0.82
			1995	0.13	20.0	6.32	7.02	1.11
			1996	1.8	180	10.38	7.09	0.68
DE9 <sup>2)</sup>	12.7	54.4	1995	0.13	20.0	6.52	5.57	0.85
IE2 <sup>2)</sup>	6.4	53	1994	0.05	5.2	1.43	2.65	1.85
			1995	0.5	7.5	2.15	2.63	1.22
			1996	0.5	8	2.04	2.74	1.34
IS91 <sup>3)</sup>	20.3	63.6	1995	0	6.83	0.44	0.89	2.02
			1996	0.07	2.6	0.27	0.76	2.81
NO99 <sup>2)</sup>	6.5	58.1	1993	0.83	74.36	8.45	4.34	0.51
			1994	0.61	70.6	9.98	4.06	0.41
			1995	0.66	60.46	5.54	3.88	0.70
			1996	2.06	24.6	8.01	4.47	0.56
Average								1.15
Correlation								0.82

<sup>1)</sup> Lövblad et al., 1995<sup>2)</sup> Berg et al., 1996<sup>3)</sup> Berg and Hjellbrekke, 1999

The scatter plot in Figure 7.11 illustrates differences between calculated and measured annual concentrations in precipitation. The 'factor of two' agreement between computed and measured annual concentrations lies between the dashed lines. As in the case of air concentrations, logarithmic scale is applied.

It is seen that **about 80% of all computed concentrations are within a factor of two with respect to measured values.**

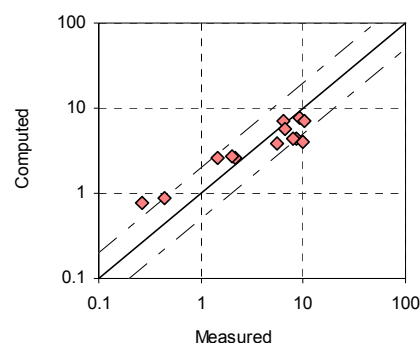


**Figure 7.11.** Computed versus measured annual average  $\gamma$ -HCH concentrations in precipitations in 1996, ng/l

### 7.3. Concentration and deposition levels in regions-receptors

This section is devoted to evaluation of concentration levels and their seasonal variations in five regions-receptors:

- Murmansk Oblast (MUR),
- Nenets Autonomous Okrug (NEN),
- Yamalo-Nenets Autonomous Okrug and Taimyr Autonomous Okrug (YNT),
- Sakha Republic (Yakutia, YAK),
- Chukotka Autonomous Okrug (CHU).

### Spatial distributions

Figures 7.12–7.14 illustrate levels of air concentrations and depositions in five regions-receptors in the Russian North obtained by the end of calculation period (1996). Because of importance of marine environment for  $\gamma$ -HCH we present also the map of seawater concentrations.

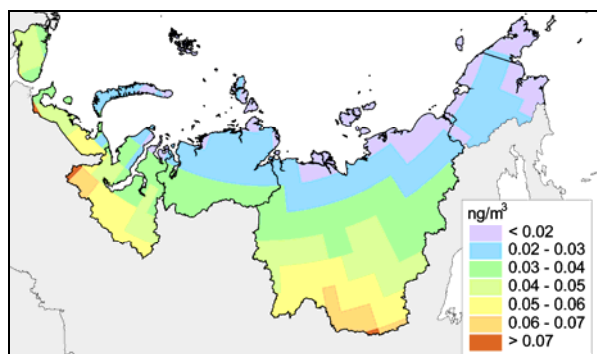


**Figure 7.12.** Air concentrations in the Russian North calculated for 1996

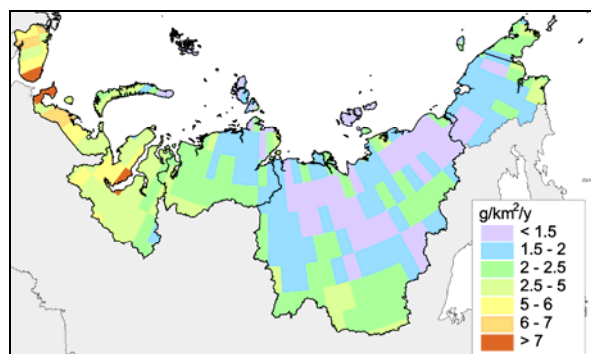


**Figure 7.13.** Deposition in the Russian North calculated for 1996

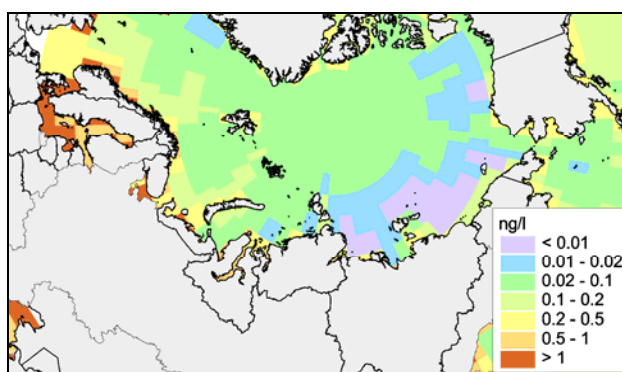


**Figure 7.14.** Seawater concentrations near the Russian North calculated for 1996

Higher air concentration levels (from 0.02 to 0.07  $\text{ng}/\text{m}^3$ ) are characteristic of Murmansk Oblast, Nenets AO and of the south of Yamalo-Nenets AO and Sakha Republic. Lower levels (from 0.01 to 0.3  $\text{ng}/\text{m}^3$ ) are characteristic of Taimyr AO, Chukotka AO and of the north of Sakha Republic. Similarly, deposition fluxes are larger for Murmansk Oblast, Nenets AO and Yamalo-Nenets AO (from 2 to 7  $\text{g}/\text{km}^2/\text{y}$  and more) and lower in Taimyr AO, Sakha Republic and Chukotka AO (0.1 – 3  $\text{g}/\text{km}^2/\text{y}$ ).

Calculated marine concentrations near borders of the Russian North regions are from 0.01 to 1  $\text{ng}/\text{l}$ . The map of marine concentrations illustrate also that the inflow of  $\gamma$ -HCH from European sources with sea currents take place mainly from the North Atlantic: higher concentrations are calculated near the Northern part of the Scandinavian Peninsula and Spitsbergen. This fact agrees with evaluation of marine inflow of  $\gamma$ -HCH to the Arctic made in [AMAP, 1998]. We note, however, that at present the model underestimates concentrations in seawater. At present development of model descriptions of seawater and soil environments is in progress (see Annexes D, E).

### Annual averages and their spatial variations

On the basis on the above spatial distributions (Figs. 7.12–7.14) average levels of deposition and air concentration levels in regions-receptors and their spatial variations were evaluated. The results are shown in Figure 7.15 (bars mean spatial variations of annual means inside each region). The corresponding numerical values are presented in Table 7.4.

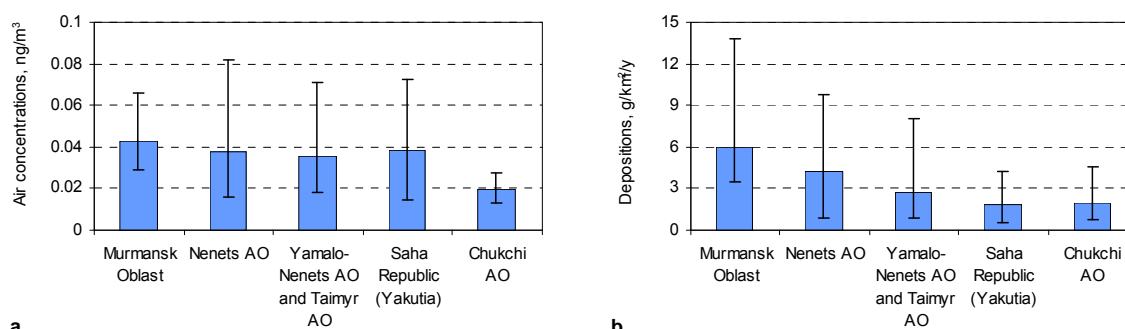


**Figure 7.15.** Contamination levels in the regions of the Russian North calculated for 1996: annual averages and their spatial variations: air concentrations (a), depositions (b)

**Table 7.4.** Deposition and air concentration levels in regions-receptors

Region	Air concentrations, ng/m <sup>3</sup>			Deposition flux, g/km <sup>2</sup> /y		
	Min	Max	Aver	Min	Max	Aver
Murmansk Oblast	0.029	0.066	0.043	3.5	13.8	6.0
Nenets AO	0.016	0.082	0.038	0.9	9.7	4.3
Yamalo-Nenets AO and Taimyr AO	0.018	0.071	0.036	0.8	8.0	2.7
Sakha Republic	0.014	0.072	0.038	0.5	4.3	1.8
Chukotka AO	0.013	0.027	0.020	0.75	4.6	1.9

The calculated air concentration levels in the first four regions (Murmansk Oblast, Nenets AO, Yamalo-Nenets AO and Taimyr AO, and Sakha Republic) are similar. Average concentrations in Chukotka AO are two times lower. This is explained by the geographical location of the latter region. Annual averages of deposition flux values change more essentially from region to region. This is mainly caused by different values of precipitation flux in these regions (see below the analysis of seasonal variations).

Up to the moment we have considered annual averages of concentrations and depositions. However, seasonal variations of air concentrations and depositions are high in the northern regions due to high temperature changes and play an important role for the Arctic region. Below we consider seasonal variations of air concentrations and depositions for all five regions-receptors.

### Seasonal variations

Monthly averages of air concentrations and depositions for Murmansk Oblast are presented in Figure 7.16 together with variations of temperature and precipitation amount.

Monthly averages of atmospheric concentrations in Murmansk Oblast vary from 0.02 to 0.07 ng/m<sup>3</sup>. It is seen that maximum concentrations are reached in August and September. This is due to high

enough temperatures (5 – 10° C) and by seasonal variations of emissions. Dry deposition flux (flux of gaseous exchange) is determined by atmospheric concentrations and temperature. The dependence of this flux on temperature is inverse. Namely, the more temperature is, the less are atmosphere/soil and atmosphere/sea exchange fluxes. For instance, moderate values of air concentrations and high enough temperature in June (10° C) lead to the decrease of dry deposition flux compared with values in neighbouring months. In addition wet depositions are affected by precipitation amount. In particular, this is the reason for higher value of wet deposition flux in July in comparison with that in June and August.

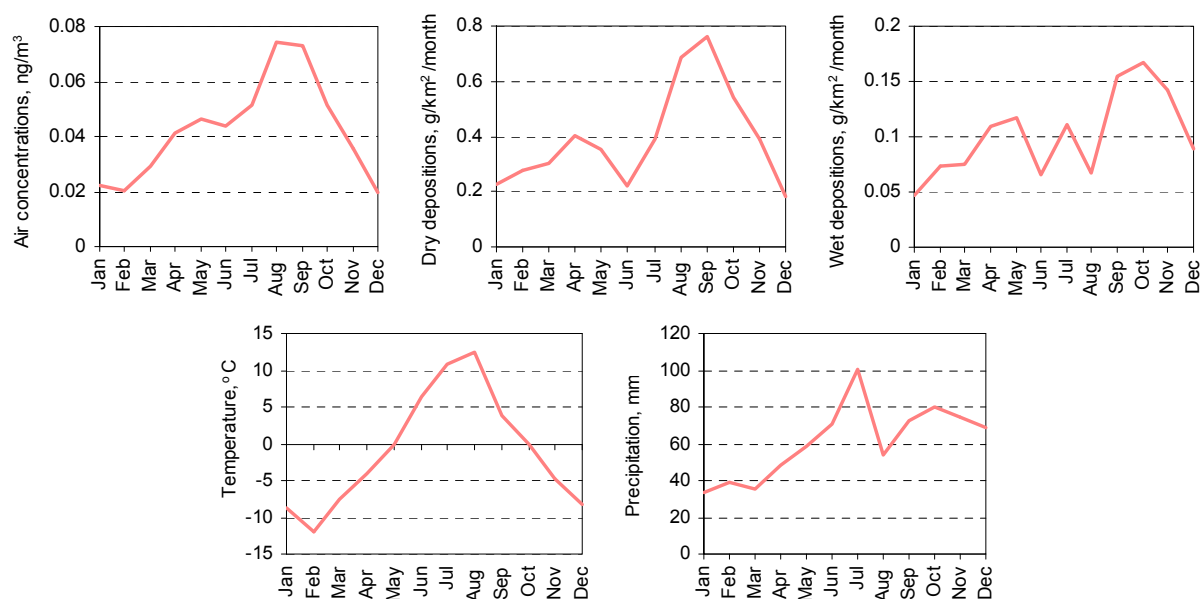
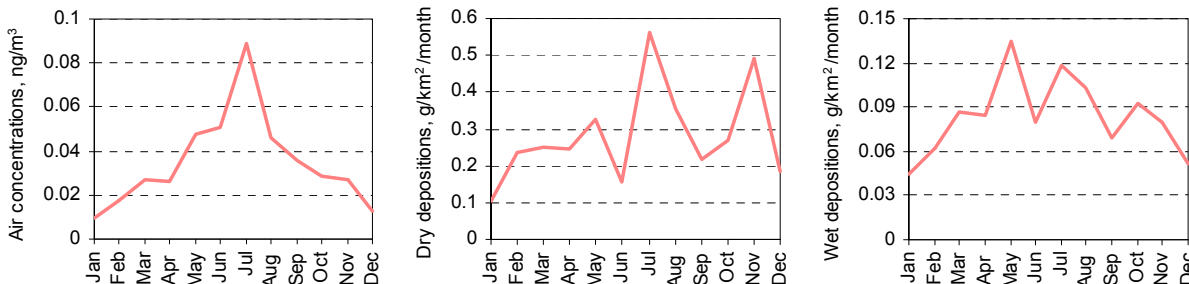


**Figure 7.16.** Seasonal variations of air concentrations and depositions (in comparison with temperature and precipitation amount) in Murmansk Oblast

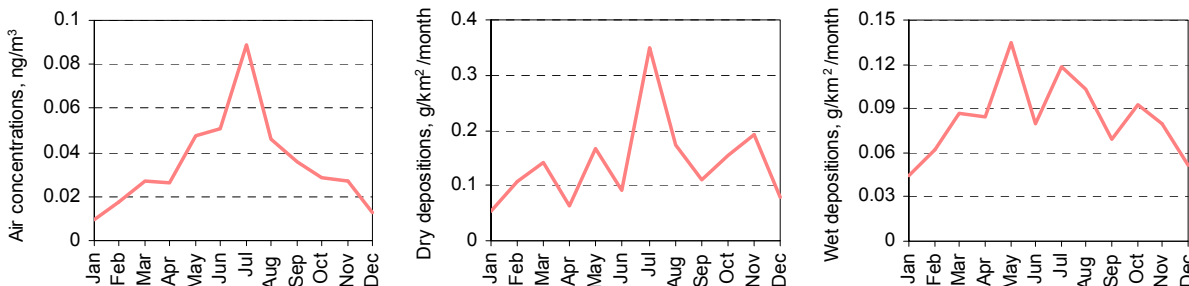
Plots of seasonal variations for the rest four regions of the Russian North are presented in Figure 7.17. For comparison Figure 7.18 displays plots of monthly averages of temperature and precipitation in these four regions.

The processes determining concentrations and depositions in these regions are of the same character as above. Less concentration levels in Chukotka AO are explained by their larger distance from main emission sources. Comparatively high values of wet deposition flux in this region with lower air concentrations are explained by high values of precipitation amount which are about 1.5 times higher than in Nenets AO, Yamalo-Nenets AO and Taimyr AO, and Sakha Republic. It is seen that minimum values of wet deposition flux correspond in general to minima of precipitation amount for each region. Close to constant values of dry deposition flux from January to April in Sakha Republic and Chukotka AO is explained by relatively low rate of increase of atmospheric concentrations together with high temperature gradients which are characteristic of these regions.

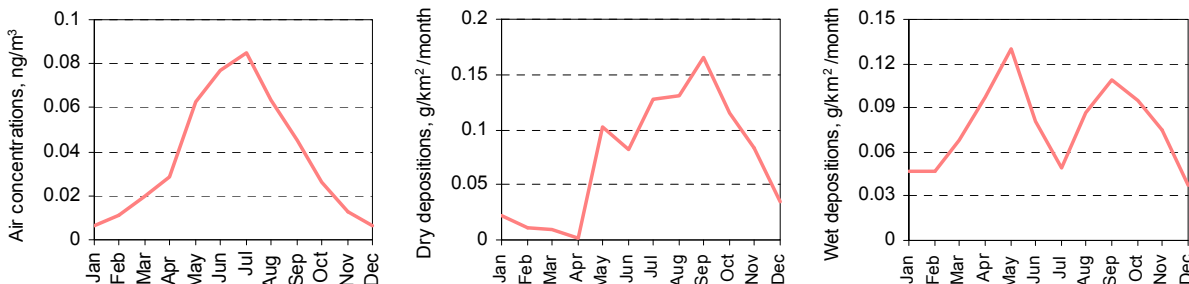
**Nenets Autonomous Okrug**



**Yamalo-Nenets Autonomous Okrug and Taimyr Autonomous Okrug**



**Sakha Republic**



**Chukotka Autonomous Okrug**

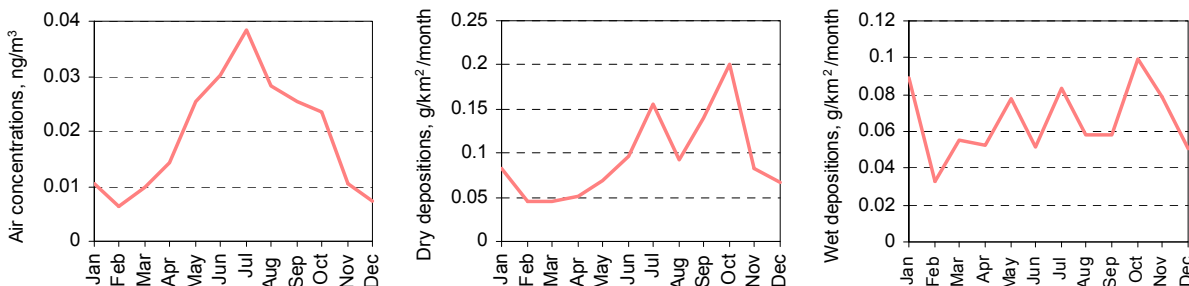


Figure 7.17. Seasonal variations of air concentrations and depositions in four regions of the Russian North

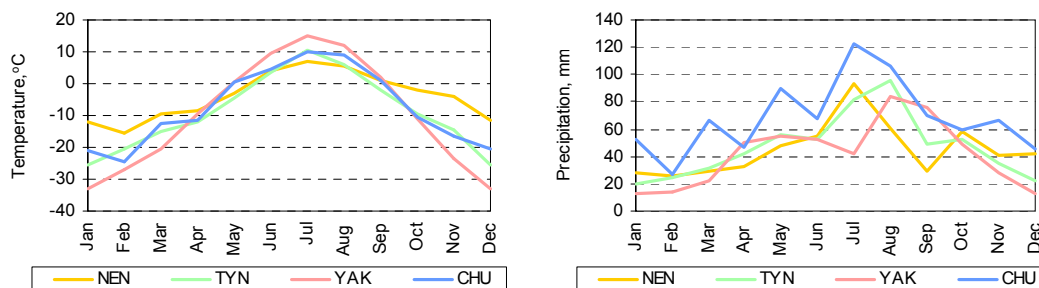


Figure 7.18. Seasonal variations of temperature and precipitation amount in four regions of the Russian North

## 7.4. Source-receptor relationships

Contamination in regions-receptors is formed both by emissions of the considered year (1996) and by amount of pollutant accumulated in the environment during the period preceding the reference year (1990 – 1995). Calculations show that about 40% of concentrations in soil and seawater over regions of the Russian North are formed by  $\gamma$ -HCH earlier accumulated in environmental media.

Similar to the case of PCBs keeping in mind that the historical emission cannot be controlled by any political decisions we shall pay the main attention to deposition from anthropogenic sources. Namely, the influence of different groups of sources on the contamination of regions-receptors is evaluated. The analysis of contributions from different sources is performed into two steps. First we use rough splitting of sources within the Northern Hemisphere. Namely, we combine all Russian sources in one group (Fig. 7.19.a). Then we use more detailed splitting of Russian sources (Fig. 7.19.b).

Names of Russian source groups influencing the contamination of the Russian North together with their abbreviations are presented in Table 7.5.

The contributions of different groups of sources to the total hemispheric emissions are shown in Figure 7.20.

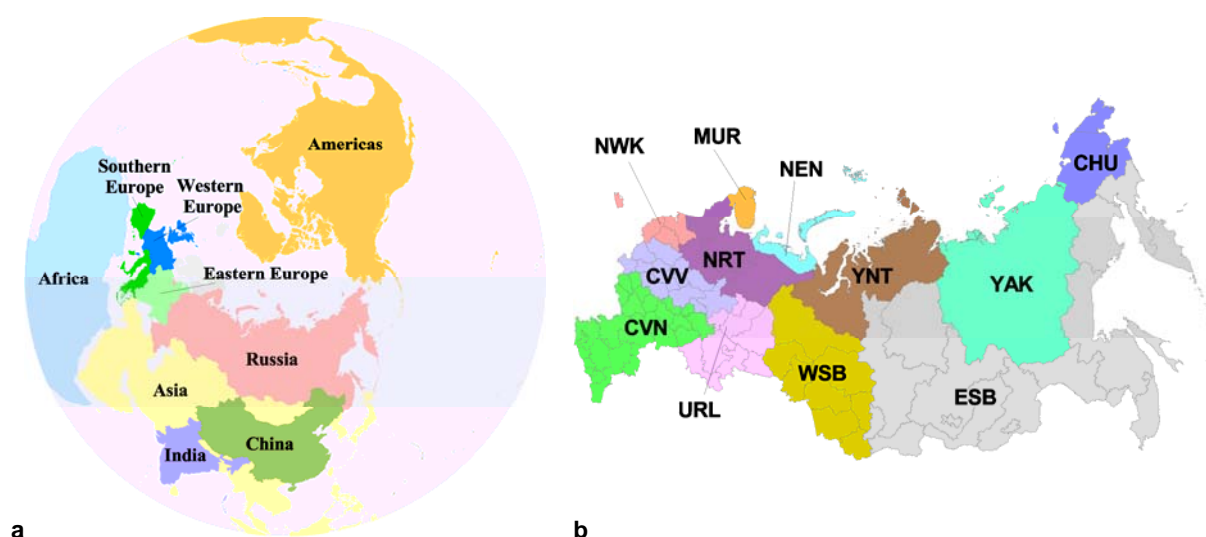


**Figure 7.19.** Splitting emission sources into groups, (a) – rough scheme, (b) – specification of Russian sources

**Table 7.5.**  $\gamma$ -HCH source groups in the Russian Federation

Name	Abbreviation	Name	Abbreviation
Murmansk Oblast *	MUR	North-Western region and Kaliningrad Oblast	NWK
Nenets AO	NEN	Central and Volga-Viatsky regions	CVV
Yamalo-Nenets AO and Taimyr AO	YNT	Central-Chernozem, Volga, and North-Caucasian regions	CVN
Sakha Republic (Yakutiya)	YAK	Ural region	URL
Chukotka AO	CHU	West-Siberian region	WSB
Northern region	NRT	East-Siberian and Far-Eastern regions	ESB

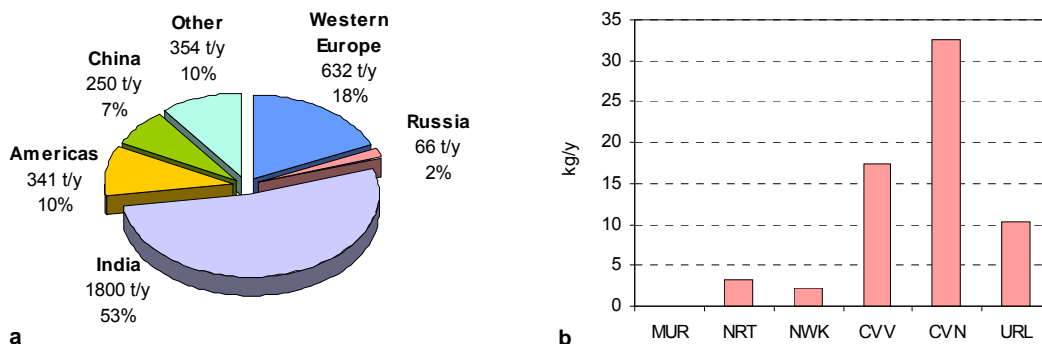


Figure 7.20. Contributions of different emission source groups to the hemispheric emissions in 1996: rough scheme (a), detailed splitting of Russian sources (b)

Due to local peculiarities and peculiarities of the wind pattern the contributions of these groups to the contamination of regions-receptors can be different from that shown in Figure 7.20 for emissions.

**Murmansk Oblast.** We begin with the consideration of contributions of these source groups to depositions and concentrations in main environmental media (atmosphere, soil, seawater) first with rough splitting scheme where all Russian sources are considered as one group.

Sources of West-Europe make the largest contribution to deposition to Murmansk Oblast (more than 50%). Russia is responsible for 17%. Then come India (9%), North America (7%) and China (4%). Contributions of all other sources account for 9% (Fig. 7.21).

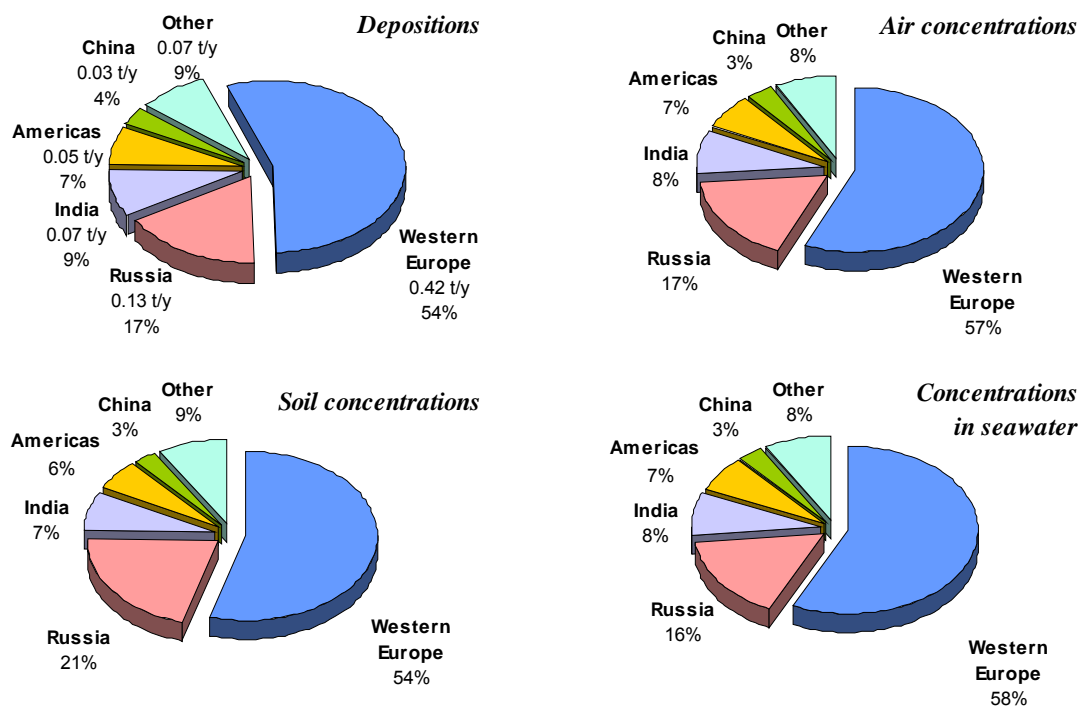


Figure 7.21. Contributions of different emission source groups (rough scheme) to annual mean air concentrations and depositions for Murmansk Oblast in 1996

It is seen that contributions of different source groups to all media are almost the same as for depositions. Similar situation is observed also for other regions-receptors. Below we shall present pie charts for depositions only.

The detailed analysis of Russian contribution to Murmansk Oblast is presented in Figure 7.22.

Russian contribution to depositions to Murmansk Oblast is mostly made by Central and Volga-Viatsky regions (40 kg or 5.1%) and Central-Chernozem, Volga, and North-Caucasian regions (34 kg or 4.3%). Then comes the contribution from the Northern region (23 kg or 2.9%) and from Murmansk Oblast itself (19 kg or 2.4%). The inputs from the north-western region and Kaliningrad Oblast and Ural region are comparatively small.

The inputs of different emission sources to deposition to the considered region are subject to seasonal variations determined both by seasonal variations of emissions and by differences in meteorological conditions. Figure 7.23 displays seasonal variations of contributions of main source groups to deposition to this region in absolute (a) and relative (b) values in 1996.

As it was shown above, main contributions to depositions to the region are made by Western Europe and Russia. Due to seasonal variations of emissions from both source groups their contributions to deposition to the region enlarge from the first to second quarter. However, due to wind pattern (on the average winds of western direction are prevailing in the region) the contributions from Western Europe are growing faster than that from Russian sources. This leads to a slight growth of contribution to depositions from Western Europe sources and diminishing of contribution of Russian sources. This process is even more pronounced from second to third quarters since in this period northern and western wind directions are prevailing in the region. In the fourth quarter due to emission reduction the contribution from Russian sources drops and it becomes comparable with contributions from American, Chinese and Indian sources. This leads to further decrease of relative contributions from Russian sources to overall deposition to the considered region.

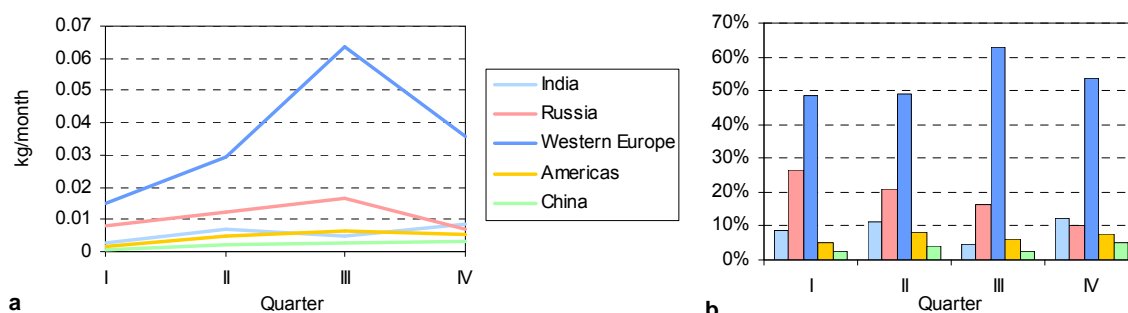


**Figure 7.23.** Seasonal variations of contributions of different groups of emission sources to depositions to Murmansk Oblast in 1996

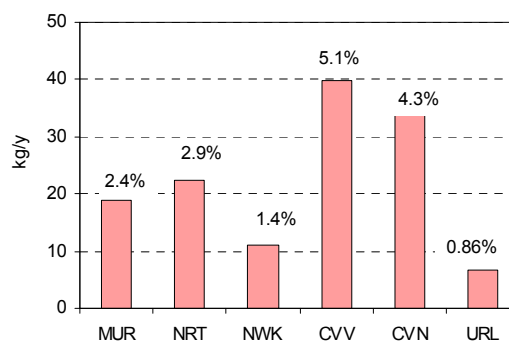


**Figure 7.22.** Relative inputs of different groups of Russian emission sources to the overall Russian contributions to depositions to Murmansk Oblast

**Nenets Autonomous Okrug.** For this region the order of main contributors to depositions is the same as for Murmansk Oblast. However, the contribution of West Europe is decreased and of Russia is increased. This is evidently caused by geographical location of source groups with respect to receptors. The structure of Russian contribution to depositions to this region is similar to that for Murmansk Oblast though the influence of Ural region increases. The main exception is that the contribution of sources of Murmansk Oblast to depositions is negligible for this region.

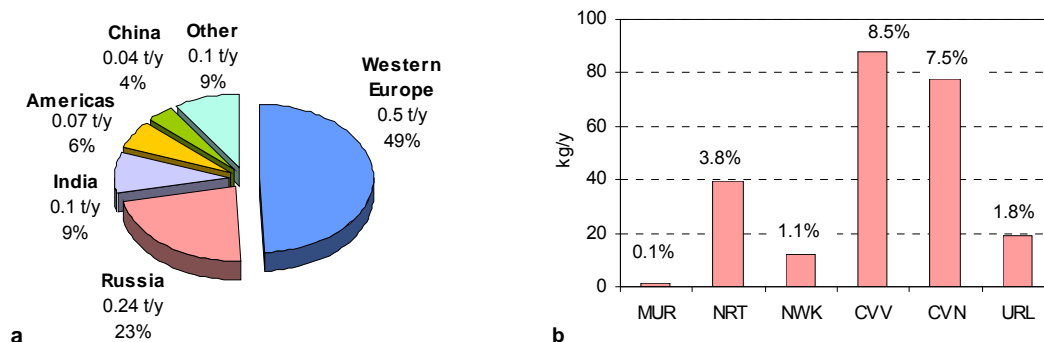


**Figure 7.24.** Contributions of different emission source groups to annual depositions for Nenets AO in 1996; rough scheme (a), detailed analysis of Russian contribution (b)

Seasonal variations of contributions of main source groups to deposition to Nenets AO in absolute (a) and relative (b) values in 1996 are displayed in Figure 7.25.

Again, main contributions to depositions to the region are made by Western Europe and Russia. Here the situation is quite similar to that in Murmansk Oblast though the influence of winds of the Northern direction in the third quarter is much higher (in spite of high emission values we obtain decrease of contribution from Russian sources to depositions to Nenets AO). Further, the contributions from Russian sources to this region are twice larger than for Murmansk Oblast. As a result, relative influence of American, Chinese and Indian sources is less and we obtain slight increase of relative input of Russian sources to depositions in the fourth quarter.

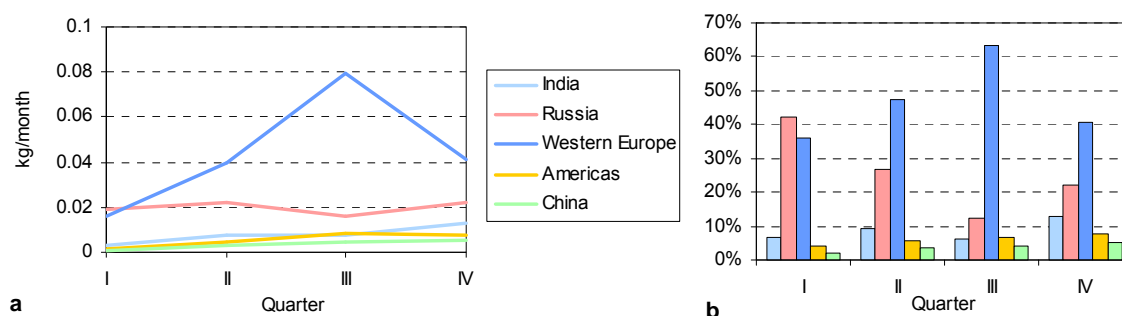


**Figure 7.25.** Seasonal variations of contributions of different groups of emission sources to depositions to Nenets AO in 1996

**Yamalo-Nenets Autonomous Okrug and Taimyr Autonomous Okrug.** For this region main contributors to depositions are similar to that for Nenets AO. The structure of Russian contribution to depositions here are also similar to that for Nenets AO, the influence of Ural region being further increased. The relative input from sources of Central-Chernozem, Volga, and North-Caucasian regions became even slightly larger than that from Central and Volga-Viatsky regions.

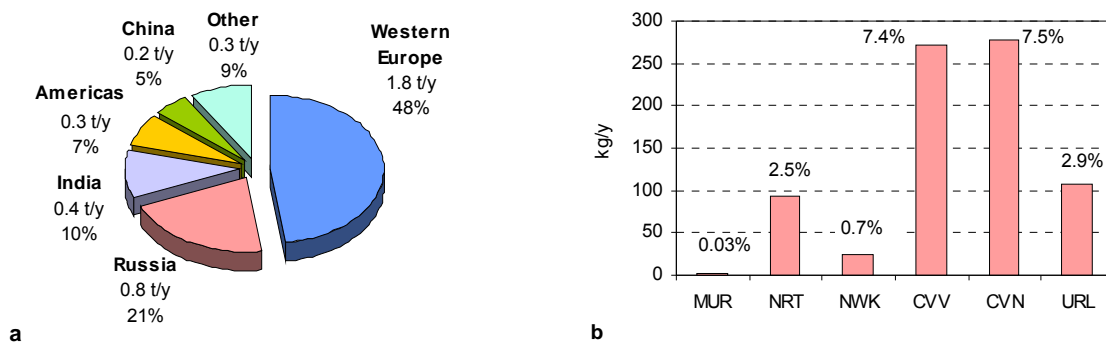


**Figure 7.26.** Contributions of different emission source groups to annual depositions to Yamalo-Nenets AO and Taimyr AO in 1996; rough scheme (a), detailed analysis of Russian contribution (b)

Seasonal variations of contributions of main source groups to deposition to Yamalo-Nenets AO and Taimyr AO in absolute (a) and relative (b) values in 1996 are shown in Figure 7.27.

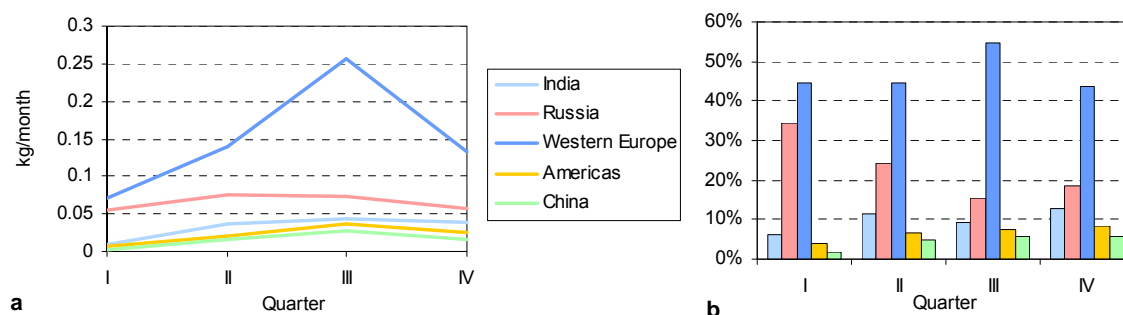


**Figure 7.27.** Seasonal variations of contributions of different groups of emission sources to depositions to Yamalo-Nenets AO and Taimyr AO in 1996

Here the situation is just the same as in Nenets AO except for the fact that the contributions from Western Europe sources are essentially decreased (up to three times) and contributions from Russian sources are increased more than twice. This leads to total increase of fraction of Russian sources in deposition to the region though temporal pattern of seasonal variation is the same as for Nenets AO.

**Sakha Republic (Yakutia).** Here the influence of West Europe remains to be essential with respect to depositions (36%). However, the contribution of India becomes essential (about 19%). Contributions of China, America and Russia are about the same (approximately 10%). Among Russian source groups the influence of Ural region (2%) and Central-Chernozem, Volga, and North-Caucasian regions (4.5%) increases on the account of decreasing contributions from Northern region and Central and Volga-Viatsky regions (0.8 and 3.4%, respectively).

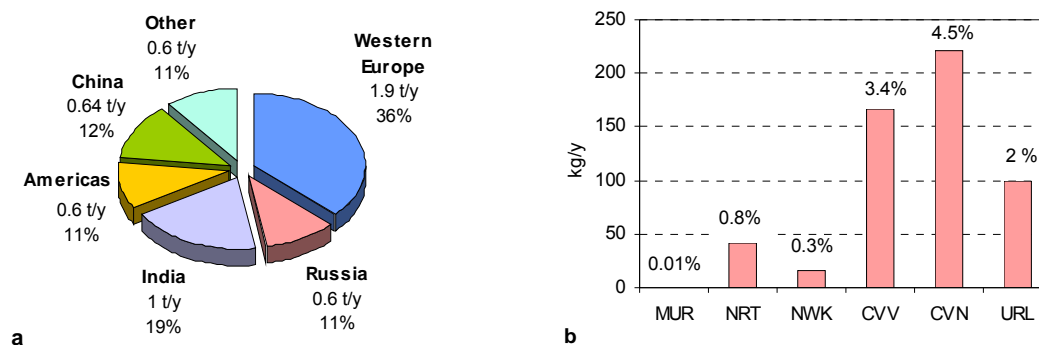


**Figure 7.28.** Contributions of different emission source groups to annual depositions for Sakha Republic in 1996; rough scheme (a), detailed analysis of Russian contribution (b)

Seasonal variations of contributions of main source groups to deposition to Sakha Republic in absolute (a) and relative (b) values in 1996 are displayed in Figure 7.29.

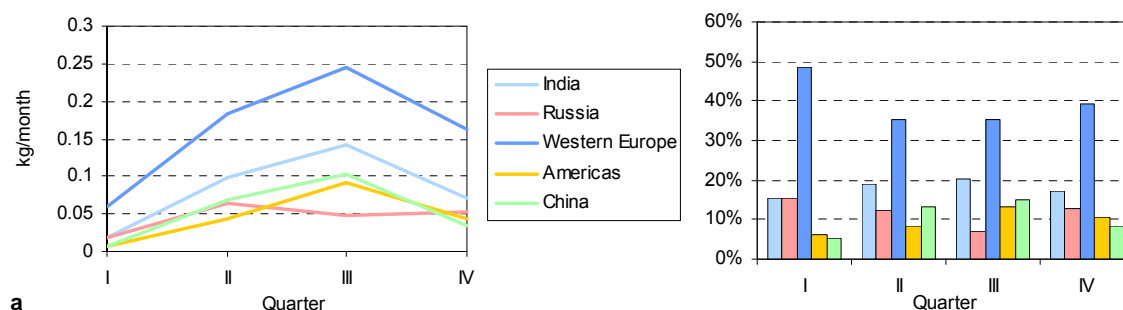


**Figure 7.29.** Seasonal variations of contributions of different groups of emission sources to depositions to Sakha Republic in 1996

The main difference of seasonal variations in this region is that contributions from American, Chinese and Indian sources in this region became more valuable than from Russian sources in second and third quarters. Due to meteorological conditions contributions of these sources are growing from first to third quarters and drop down in the fourth quarter. We recall that for Indian and Chinese sources no seasonal variations are supposed so that the mentioned seasonal variations of these sources are completely due to meteorology (the analysis of  $\gamma$ -HCH pathways from Indian and West-European sources is given in Section 7.1 above). Fast increase of contributions from American, Chinese and Indian sources leads to the increase of their relative input and at the same time to decrease of relative input of the contributions from West-European and Russian sources in this region in second and third quarters.

**Chukotka Autonomous Okrug.** For this region India becomes the main contributor to depositions together with West Europe (about 27% each). Then comes China (19%), America (11%) and Russia (5%). Contributions of all the rest sources is about 10% (Fig. 7.30).

The input of Ural region to contributions from Russian sources remains at the same level as for Sakha Republic and the inputs from Central-Chernozem, Volga, and North-Caucasian regions increased up to 2.3%.

Relative inputs from each source group to each region-receptor are explained by their geographical locations and directions of  $\gamma$ -HCH transport pathways over the Northern Hemisphere.

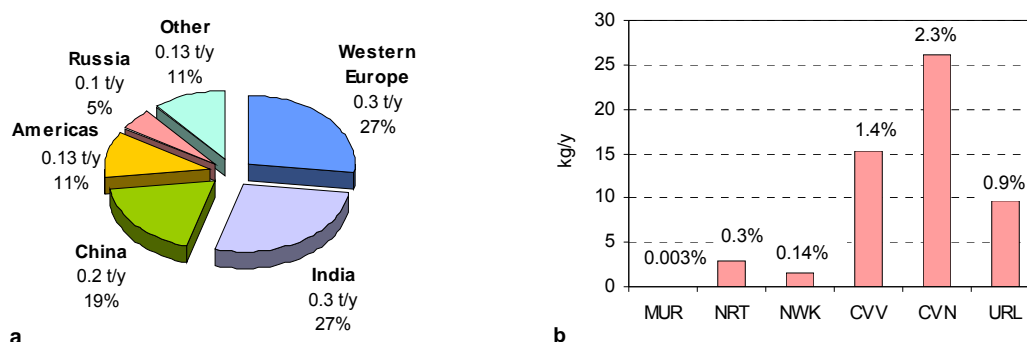


**Figure 7.30.** Contributions of different emission source groups to annual depositions for Chukotka AO in 1996; rough scheme (a), detailed analysis of Russian contribution (b)

Seasonal variations of contributions of main source groups to deposition to Chukotka AO in absolute (a) and relative (b) values in 1996 are displayed in Figure 7.31.

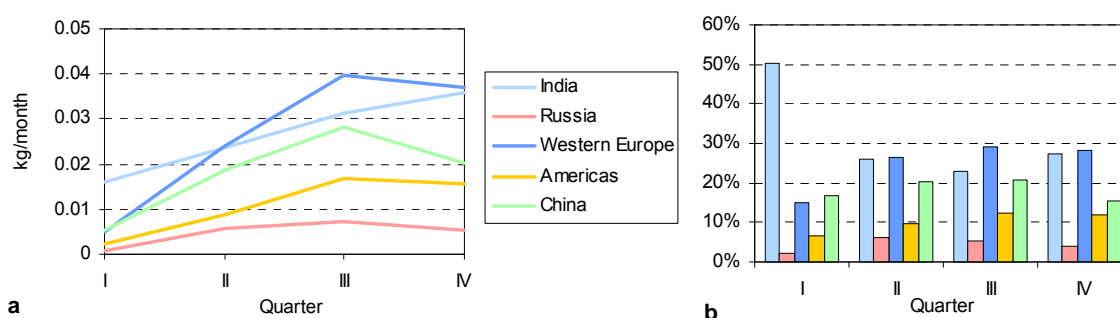


**Figure 7.31.** Seasonal variations of contributions of different groups of emission sources to depositions to Chukotka AO in 1996

Further increase of contributions from American, Chinese and Indian sources together with strong decrease of contributions from West-European and Russian sources determine the character of seasonal variations of relative inputs of different source groups in the region. These inputs from Indian sources are greater in first and fourth quarters. Inversely, for all other source groups (Russia, America, China and Western Europe) relative inputs are maximum in second and third quarters.

## 7.5. Concluding remarks

$\gamma$ -HCH contamination levels in the Russian North, source allocation budget and pathways of  $\gamma$ -HCH transport were evaluated with the use of the hemispheric POP multicompartment transport model. As a result:

1. Air concentration levels in the region-receptors are within a range 0.01 – 0.09 ng/m<sup>3</sup>, and deposition flux is from 1 to 14 g/km<sup>2</sup>/y. Calculated air concentration levels in four regions (Murmansk Oblast, Nenets AO, Yamalo-Nenets AO and Taimyr AO, and the Sakha Republic) are close to one another. Average concentrations in Chukotka AO are two times lower. Annual averages of deposition flux values change more significantly from region to region. They decrease in the east direction. The main direction of  $\gamma$ -HCH marine transport is from the North-Atlantic region.
2. The main medium accumulating  $\gamma$ -HCH is seawater. About 80% of all  $\gamma$ -HCH content in the environment over the Northern Hemisphere is contained in this medium. The total calculated amount of  $\gamma$ -HCH deposited in the Arctic region in 1996 is equal to 78 tonnes including 58 tonnes deposited into the Arctic Ocean.
3. Contamination levels in region-receptors undergo substantial seasonal variations. These variations are due to atmospheric circulation, temperature and precipitation regime and variations in emissions.
4. The main emission sources influencing the contamination of the Russian North are West Europe, Russia, India, America and China. For the three west region-receptors (Murmansk Oblast, Nenets AO, and Yamalo-Nenets AO and Taimyr AO), the relative contributions of West-European and Russian sources are the most significant (about 50% and 20%, respectively). For eastern region-receptors (Sakha Republic and Chukotka AO), the influence of West-European sources is about 30 – 35%. Here, the relative contributions of Indian and Chinese sources are more significant (20 – 25% and 15 – 20%, respectively), influence of Russian sources becomes smaller (5 – 10%) however the influence of North American sources becomes more substantial (about 11%).
5. Contributions of different groups of Russian sources to depositions on region-receptors were evaluated. The sources from the northern region (NRT) significantly contribute to the Murmansk Oblast and Nenets AO (3%). The contribution of these sources is somewhat less to Yamalo-Nenets AO and Taimyr AO (2.5%) and relatively small to the Sakha Republic and Chukotka AO (0.8 and 0.3%, respectively). The influence of the north-western region and Kaliningrad Oblast (NWK) is relatively small on all region-receptors (from 0.1 to 1.4%). Sources from the Central and Volga-Viatsky regions affect significantly (and almost equally) all region-receptors (1.4 – 8.5%). The same is observed for sources from Central-Chernozem, Volga, and North-Caucasus regions (CVN). The contributions of Ural sources are smaller to the Murmansk Oblast (0.8%) and higher to the Sakha Republic (2%).
6. Pathways of  $\gamma$ -HCH transport from main source groups to region-receptors were examined. It was found that the marine pathway is significant for sea concentrations near the Russian North borders.
7. Calculations overestimate air concentrations. On the average they agree with available measurements within a factor of 2.5, with correlation 0.5. Over 50% of comparisons are within a factor of 3 and only three of them are outside of factor 5. Concentrations in precipitation agree with measurements within a factor of 1.15 on the average, with correlation 0.82. For further refinement of these estimates, refinement in emission data is needed.

## References

- AMAP [1998] *AMAP Assessment report: Arctic pollution issues*. Arctic Monitoring and Assessment Programme (AMAP), Oslo, Norway.
- AMAP [1999], *AMAP Datareport: Atmospheric Subprogramme*, Berg T. and Hjellbrekke, NILU: OR-16-99, Norwegian Institute for Air Research, p.100.
- Berg T. and A.-G.Hjellbrekke [1999] Heavy metals and POPs within the ECE region, 1997, EMEP/CCC-Report 7/99, p.98.
- Berg T., A.-G.Hjellbrekke and J.E.Skjelmoen [1996] Heavy metals and POPs within the ECE region. EMEP/CCC-Report 8/96, p.187.
- Berg T., A.-G.Hjellbrekke and N.Ritter [1997]. Heavy metals and POPs within the ECE region. Additional data. EMEP/CCC-Report 9/97, 79 p.
- Berg T., and A.-G.Hjellbrekke [1998]. Heavy metals and POPs within the ECE region. Supplementary data for 1989-1996. EMEP/CCC-Report 7/98, p.105.
- Brorström-Lundén E., E.Junedal, H.Wingfors and S.Juntto [2000] Measurements of the Atmospheric Concentrations and the Deposition Fluxes of Persistent Organic pollutants (POPs) at the Swedish West Coast and in the northern Fennoscandia, p.65.
- Hallsall C.J., R.Bailey, Stern G.A., Barrie L.A., Fellin P., Muir D.C.G., Rosenberg B., Rovinsky F.Ya., Kononov E.Ya., Pastukhov B., 1998, Multi-year observations of organohalogen pesticides in the Arctic atmosphere, *Environmental Pollution*, v. 102, pp. 51-62.
- Harner T., Kylin H., Bidleman T.F., Strachan W.M.J. [1999] Removal of  $\alpha$  - and  $\gamma$  - Hexachlorocyclohexane and Enantiomers of  $\alpha$  - Hexachlorocyclohexane in the Eastern Arctic Ocean, *Environ. Sci. Technol.*, v. 33, No. 8, pp.1157 – 1164.
- Hoff R.M., W.M.J.Strachan, Sweet C.W., Chan C.H., Shackleton M., Bidleman T.F., Brice K.A., Butniston D.A., Cussion S., Gatz D.F., Harlin K., Schroeder W.H. [1996] Atmospheric deposition of toxic chemicals to the Great Lakes: a review of data through 1994. *Atmos. Environ.*, v. 30, No.20, pp.3505-3527.
- IADN Results to 1996, Atmospheric Deposition of Toxic Substances to the Great Lakes: IADN Results to 1996, published by Environment Canada and the United States Environmental Protection Agency, 2000, p.121.
- Lövblad G., A.-G.Hjellbrekke, K.Sjoberg, J.E.Skjelmoen, J.Schaug [1995] Data Report 1993. EMEP/CCC-Report 8/95.
- Pacyna J.M. et al. [1999] Final report for Project POPCYCLING-Baltic. EU DGXII, Environment and Climate Program ENV4-CT96-0214. Available on CD-rom including technical report, the emission and environmental databases as well as the POPCYCLING-Baltic model. NILU, P.O. Box 100, N-2027 Kjeller, Norway.
- Review of the environmental background state over Russia in 1993. [1994] Moscow, Hydrometeoizdat, (in Russian).
- Review of the environmental background state over Russia in 1994. [1995] Moscow, Hydrometeoizdat, (in Russian).
- Review of the environmental background state over Russia in 1994. [1996] Moscow, Hydrometeoizdat, (in Russian).
- Strand A. and Ø.Hov [1996] A model strategy for the simulation of chlorinated hydrocarbon distributions in the global environment. *Water, Air and Soil Pollution* v.86, pp.283-316.

## Chapter 8

## RELIABILITY OF THE ASSESSMENT RESULTS

In this chapter we summarize main results of the activity devoted to the model testing, verification of modeling results and evaluation of their uncertainty.

### 8.1. Model verification and sensitivity analysis

#### *Advection scheme*

Advection scheme used in the atmospheric module is based on widely applied and extensively tested Bott scheme adapted to the spherical co-ordinates (Section 3.2). To verify the scheme operation consistency in particular conditions of the spherical co-ordinates (especially in the vicinity of the pole) standard advection tests have been performed. Detailed description of the tests is presented in Annex B. The main conclusions of the tests are the advection scheme does not produce considerable distortions of transported substances (dispersion error) and has comparatively low artificial diffusion. Besides, the scheme is stable in strong deformational flows and does not produce observable time-splitting error.

#### *Atmospheric transport*

Simulation of a tracer airborne transport in real atmospheric conditions has been tested on the base of lead. It is commonly assumed that lead occurs in the atmosphere solely in solid phase as a part of aerosol particles. In the frame of the study, modeling results obtained by the hemispheric model were compared with available measurements and results of regional model of heavy metal atmospheric transport (MSCE-HM). The MSCE-HM model has been verified in a number of intercomparison campaigns with other regional models [Sofiev *et al.*, 1996; Gusev *et al.*, 2000; Ryaboshapko *et al.*, 2001] and has been qualified by means of sensitivity and uncertainty studies [Travnikov, 2000]. Thus, its results can be considered as quite reliable within European region. The verification procedure is described in detail in Annex B.

It was concluded that results of a tracer airborne transport modeling are in satisfactory agreement both with available measurements and with results of regional MSCE-HM model, and discrepancy does not exceed a factor of two in both cases. Thus, the developed atmospheric module can satisfactorily simulate airborne transport of an inert tracer in the atmosphere.

#### *Atmospheric chemistry*

Chemical scheme of mercury transformation in the atmosphere was verified in comparison with other mercury transport models and with measurements during the models intercomparison study [Ryaboshapko *et al.*, 2002; Ryaboshapko *et al.*, in press]. The comparison has shown that all the models involved apply similar physical and chemical principles of mercury transformations and their

results are in reasonable agreement. Besides, newest findings of the most advanced scientific models were included to the model chemical scheme.

Sensitivity of the model chemical scheme to atmospheric parameters (air temperature, pH, liquid water content) and concentration of main chemical reactants (such as ozone, sulfur dioxide, etc.) was studied in [Ryaboshapko *et al.*, 2001]. The most important parameters for certain atmospheric conditions were determined and their description in the model scheme was refined.

### ***Gas/particle partitioning***

The application of the constant value of the specific aerosol surface to the calculation of gas/particle partitioning can lead to uncertainties of depositions and mean annual air concentrations ranging within about 20-30% for the Russian North. For other regions of the Northern Hemisphere the uncertainty can be higher. In further model development the spatial distribution of the specific aerosol surface should be taken into account (Annex F).

### ***Degradation***

Atmospheric degradation can be significant sink of low chlorinated PCBs, which present in the atmosphere mainly in gaseous phase. One of the most important processes of PCB destruction in the atmosphere is reaction with OH radical. The atmospheric concentrations of OH radical depend on a lot of factors (latitude, cloudiness, day time, season, etc.). At present in the model as a first approximation OH radical concentrations have no diurnal variations and depend only on a season. To assess the influence of this assumption rough calculation experiments are made (Annex F).

### ***Oceanic transport and ice cover***

Oceanic transport module describing behaviour of POPs in the marine environment was verified in comparison with available measurements of PCB in seawater [Strukov *et al.*, 2000]. Measurements from different depths of the Northern Atlantic were involved in the comparison. The results showed reasonable agreement between modeled and observed values.

An extensive analysis of the oceanic transport module sensitivity to some processes affecting POP transport and accumulation in the environment is presented in Annex E. In particular, influence of the partitioning between dissolved and adsorbed forms as well as ice cover effect on POP transport is considered. The most substantial details of the processes are outlined and appropriate parameterization is selected.

### ***Soil accumulation***

Sensitivity of the soil module, describing POP transformation and accumulation in the soil environment to such processes as transport with dissolved organic carbon and distribution between dissolved and adsorbed forms, is studied in Annex D. In particular, it is demonstrated that proper description of this processes can considerably improve the modeling of POP accumulation in soil and soil/atmosphere exchange processes.

## 8.2. Uncertainty of emission data

Emission data are among the most important input information drastically influencing the modeling results [Travnikov, 2000]. Therefore, assessment of emission uncertainty requires separate consideration.

### *Mercury*

Uncertainty analysis of anthropogenic mercury emission estimates appropriate to the utilized emission data was published in [Pacyna and Pacyna, 2001]. As it was mentioned in this work uncertainty of the emission estimates can be evaluated per source categories as follows:

- Stationary fossil fuel combustion:  $\pm 25\%$
- Non-ferrous metal production:  $\pm 30\%$
- Iron and steel production:  $\pm 30\%$
- Cement production:  $\pm 30\%$
- Waste disposal: up to a factor of 5

Taking into account different contribution of the source categories to mercury emission from different continents the emission uncertainty can vary from 25% to more than 100% from continent to continent.

Estimates of natural mercury emission and re-emission contain higher uncertainty. As it follows from Table 5.2 the global estimates available from the literature (disregarding evidently overestimated values) varies almost twice. Besides, conventional character of the spatial distribution of emission fluxes contributes additional uncertainty. Thus, uncertainty of natural emission and re-emission of mercury potentially reaches a factor of two.

### *PCBs*

Analysis of emission estimates uncertainties for PCB is presented in Section 4.2 of the report. The main sources of the uncertainty are identified as follows:

- The representativeness and accuracy of emission factors are the major source of uncertainties.
- The global movement of PCB-containing products and wastes between countries was not considered in detail.
- Potential “point sources” of PCB atmospheric emissions, incidental formation, and emissions of PCB from the combustion process (*de novo* synthesis) were not considered separately.

Besides, uncertainties of estimates in global consumption and emissions will grow with the increase of the specification level (e.g. more detailed usage and waste disposal categories).

## *$\gamma$ -HCH*

Uncertainties of  $\gamma$ -HCH emission estimates are analyzed in Section 4.3. It is concluded that:

- The main uncertainty is connected with the country-based usage of  $\gamma$ -HCH that may be uncertain themselves.
- Another source of uncertainties arises from distribution of estimated emission over cropland areas since HCH consumption for other purposes unconnected with agriculture was not considered.
- Substantial source of uncertainties originates from the rather rough description of seasonal variations of  $\gamma$ -HCH emissions used in the model

### **8.3. Modeling results vs. measurements**

The most important analysis of modeling results accuracy is comparison of calculated values with measured ones. However, one should note that measuring data with appropriate spatial and temporal representativeness are often unavailable for statistically correct analysis.

#### *Mercury*

Comparison of mercury modeling results with available measurements is presented in Section 5.2. Nineteen monitoring station from Europe and North America are involved in the comparison. It is demonstrated that the model quite well reproduces annual air concentrations at these stations and the discrepancy does not exceed 40%. Modeled deposition fluxes satisfactorily conform to the measured ones. The discrepancy for all the stations does not exceed a **factor of two** with the correlation coefficient 0.54.

#### *PCBs*

Model results on PCB transport was verified by comparison computed concentrations in air and precipitation and deposition fluxes with available measurement data (Section 6.3). Measured data on PCB-28, 118, 153 and 180 from eleven sites for the period from 1989-96 were used in comparison. The comparison showed that most of computed air concentration values were within a **factor of four** with regard to measurements. Modeled concentrations of all considered PCB congeners correlate rather well with observed air concentrations. Computed concentrations of some congeners in precipitation also agreed quite well with measured ones, but for others distinction is significant.

#### *$\gamma$ -HCH*

Comparison of calculated and observed  $\gamma$ -HCH concentrations in the ambient air and precipitation is based on monitoring and literature data (Section 7.2). Available measurements on  $\gamma$ -HCH air concentrations cover the Arctic, European and Baikal regions, whereas the data on concentrations in precipitation are mostly from the European region. The comparison showed that the model overestimates  $\gamma$ -HCH air concentrations on average 2.5 times with correlation between measured and calculated values about 0.5. Besides, more than 75% of compared values are within a **factor of four**. Reasonable agreement was obtained for measured and modeled concentrations of  $\gamma$ -HCH in precipitation: on average calculated concentrations 1.2 times overestimate measured ones with correlation coefficient 0.8.

## 8.4. Concluding remarks

Summarizing mentioned above we can conclude that models involved in the assessment are extensively tested and can be considered as sufficiently reliable within the confidence limits. Uncertainties of modeled air concentrations and deposition fluxes could be roughly estimated by a factor of two for mercury results and by a factor of four for PCB and  $\gamma$ -HCH. Uncertainties of the relative contributions of different sources to the total deposition to some region (source-receptor relationships) are assumed to be lower. More precise quantitative estimates of the model uncertainties require comprehensive sensitivity and uncertainty analysis of the models with respect to all the processes and input parameters.

## References

- Gusev A., Ilyin I., Petersen G., van Pul A., Syrakov D., and Pekar M. [2000] Long-range transport model intercomparison studies. EMEP/MSC-E Technical note 2/2000, Meteorological Synthesizing Centre – East, Moscow, Russia
- Pacyna, J. M. and Pacyna E. G. [2001] An assessment of global and regional emissions of trace metals to the atmosphere from anthropogenic sources worldwide. *The Canadian Journal of Environmental Reviews*, v.9, pp.1-30
- Ryaboshapko A., Ilyin I., Bullock R., Ebinghaus R., Lohman K., Munthe J., Petersen G., Segneur C., Wangberg I. [2001] Intercomparison study of numerical models for long-range atmospheric transport of mercury. Stage I: Comparison of chemical modules for mercury transformations in a cloud/fog environment. EMEP/MSC-E Technical report 2/2001, Meteorological Synthesizing Centre – East, Moscow, Russia
- Ryaboshapko A., Bullock R., Ebinghaus R., Ilyin I., Lohman K., Munthe J., Petersen G., Segneur C., Wangberg I. [2002] Comparison of mercury models. *Atmos. Environ*, v.36, pp.3881-3898
- Ryaboshapko A., Ilyin I., Artz R., Bullock R., Christensen J., Cohen M., Dastur A., Davignon D., Draxler R., Munthe J., Petersen G., Syrakov D. [in press] Intercomparison Study of Numerical Models for Long-Range Atmospheric Transport of Mercury Stage II. Comparison of modelling results with observations obtained during short-term measuring campaigns. EMEP/MSC-E Technical report.
- Sofiev M., Maslyayev A., and Gusev A. [1996] Heavy metal model intercomparison. Methodology and results for Pb in 1990. *EMEP/MSC-E Report 2/96*, Meteorological Synthesizing Centre – East, Moscow, Russia
- Strukov, B.S., Resnyansky Yu.D., Zelenko A.A., Gusev A.V., and Shatalov V.E. [2000] Modelling long-range transport and deposition of POPs in the European region with emphasis to sea currents. EMEP/MSC-E Technical report 5/2000, Meteorological Synthesizing Centre – East, Moscow, Russia
- Travnikov O. [2000] Uncertainty analysis of heavy metals long-range transport modelling. *EMEP/MSC-E Technical note 9/2000*, Meteorological Synthesizing Centre – East, Moscow, Russia



## CONCLUSIONS

*The assessment of the long-range atmospheric transport and depositions of mercury (Hg), selected polychlorinated biphenyls (PCBs), and lindane ( $\gamma$ -HCH) to the selected five administrative units of the Russian part of the Arctic region has been carried out on the simulation results of 1996.*

*This assessment involves:*

- *Development of the System of Diagnosis of lower Atmosphere (SDA) for generation of meteorological data for hemispheric modeling.*
- *Adaptation of geophysical data, information on land cover, leaf area index, organic carbon content in soil, and chemical reactant concentrations in the atmosphere for the hemispheric scale.*
- *Survey of physical-chemical properties of Hg and selected POPs and their model parameterization.*
- *Collection and processing of official emission data and expert estimates within the hemispheric scale.*
- *Elaboration and testing of atmospheric transport module common for Hg and POPs transport models.*
- *Development of hemispheric Eulerian model oriented on peculiarities of mercury behaviour in the Arctic region, in particular mercury depletion events.*
- *Development of hemispheric multicompartiment model for the evaluation of POP concentrations in various environmental compartments (air, soil, vegetation, seawater, ice cover) with special emphases on POP transport by sea currents and on ice cover dynamics in the Arctic.*
- *Evaluation of transport pathways and the contamination load of the considered pollutants to the Russian North and to the Arctic as a whole from Russian sources and sources located within the Northern Hemisphere.*

### Basic outcome

#### *Mercury (Hg)*

The assessment of pollution by Hg using the developed hemispheric MSCE-Hem-Hg model is based on the global inventory of mercury emissions. Major conclusions drawn from modeling results obtained for 1996 are presented below.

- Atmospheric long-range transport of mercury from industrial regions of the Northern Hemisphere markedly contributes to the pollution of the Arctic as a whole, and regions of the Russian North in particular. Natural sources as well as the re-emission of previously deposited mercury can make a considerable contribution to Arctic contamination.

- Mercury concentration levels in the ambient air slightly vary over all regions of the Russian North (mean annual values 1.4-1.8 ng/m<sup>3</sup>). Deposition fluxes vary more significantly (from 4 to 25 g/km<sup>2</sup>/y) depending on the precipitation amount. The highest depositions are over areas adjacent to the Arctic coast due to mercury depletion events.
- For all the regions of the Russian North the influence of Russian emission sources dominates over those of external regions. The main external contributors to the pollution of the Russian North are Eastern and Western Europe, China, the Americas, and Central Asia. The relative importance of these contributors varies in different regions of the Russian North. Mercury depletion events phenomenon results in an increased role being played by external sources in the pollution of the region.
- The largest contribution to mercury deposition in **Murmansk Oblast** is made by Russian sources (35%) from which 13% belongs to the sources of this region. The most important external sources are Eastern Europe (12%), China (11%), the Americas (10%), and Western Europe (10%).
- Similar contributions to the pollution of Murmansk AO are obtained for **Nenets AO**. The most important contribution is made by Russian mercury emission sources (35%). Along with local sources from **Nenets AO** (7%) emissions from the regions of the European part of Russia considerably contribute to the pollution of this region (24%). The most important external contributors are Eastern Europe (13%), China (11%), and the Americas (10%).
- The Ural region and two central regions of European Russia (CVV and CVN) make up the main contribution (16%) to the pollution of **Yamalo-Nenets AO and Taimyr AO** from Russian sources (30%), whereas regional sources do not play a substantial role. The main external contributors are China (12%), Eastern Europe (12%), the Americas (11%) and Central Asia (11%).
- Russian regions contribute about 30% of the total annual mercury deposition to **Sakha Republic**. Among them the most significant contribution is made by regional sources (6%). Major external contributors are China (15%), the Americas (11%), Eastern Europe (11%), and Central Asia (10%).
- Similar to other regions of the Russian North the main contribution to the pollution of **Chukotka AO** is made by Russian sources (26%). Emission sources from Eastern Siberia and the Far East dominate over other Russian regions in the mercury contamination of **Chukotka AO**. The main external contributor to the pollution of the region is China (17%), whose contribution is comparable with that of Russian sources and slightly varies during the year. Among others, the Americas contribute 11% and Central Asia 10%.

### ***Polychlorinated biphenyls (PCBs)***

The assessment of pollution by PCBs is based on the modeling results of the long-range transport of four selected PCB congeners (PCB-28, PCB-118, PCB-153, PCB-180) within the Northern Hemisphere for 1996. These results were obtained using the developed hemispheric multicompartiment MSCE-POP model and the global historical inventory of PCB emissions. The main conclusions are presented below.

- Model evaluation of pollution by PCBs has provided concentrations of selected congeners in the main environmental compartments (atmosphere, soil, seawater and vegetation) and their depositions for 1996. Verification of modeling results showed a reasonable agreement between computed values and available measurements of PCB concentrations in air and in precipitation. The application of the constant value of the specific aerosol surface to the calculation of gas/particle partitioning leads to uncertainties in depositions and mean annual air concentrations

ranging within about 20-30% for the Russian North. For other regions of the Northern Hemisphere the uncertainties are higher. In further model development the spatial distribution of the specific aerosol surface should be taken into account.

- PCB-153 concentrations gradually decrease from 2.6 pg/m<sup>3</sup> in Murmansk Oblast to 0.7 pg/m<sup>3</sup> in Chukotka AO. The decrease in deposition flux ranges from 200 mg/km<sup>2</sup>/y to 50 mg/km<sup>2</sup>/y. A similar pattern of concentration and deposition variations is observed for other congeners.
- PCBs accumulated mostly in soil. Heavy PCB congeners make the highest contribution to long-term accumulation. According to preliminary estimates, the fraction of air concentrations caused by the re-emission process from soil amounts to 30-80%, depending on the congener and region.
- The largest contribution to the depositions in **Murmansk Oblast** is made by Russian sources (44%). Among other emission sources significant contributions are made by North-Western Europe (35%) and South-Eastern Europe (14%). **Murmansk Oblast** depositions are formed mostly by local sources (about 22%).
- The contributions of different source groups to the pollution of **Nenets AO** are similar to those of Murmansk Oblast. Contributions of Russia and North-Western Europe are slightly lower (41% and 31%), but contributions of South-Eastern Europe and the Americas are slightly higher (18% and 6%) in comparison with Murmansk Oblast. The main contribution from sources in the Russian Federation is made by the Central and Volgo-Viatsky regions (15%) and by the Northern region (10%). The contribution of local sources to **Nenets AO** is negligible.
- Major contributions to the depositions to **Yamalo-Nenets and Taimyr AO** are made by Russia (47%), North-Western Europe (26%) and South-Eastern Europe (16%). Among the Russian sources the largest contribution to depositions is made by the Central and Volgo-Viatsky regions (12%).
- Russia (38%), North-Western Europe (23%) and South-Eastern Europe (16%) are major contributors to depositions in **Sakha Republic**. Among the Russian sources of PCB emissions, the main contribution is made by regional sources (13%).
- The most essential contributors to depositions in **Chukotka AO** are the following: Russia (25%), North-Western Europe (22%) and South-Eastern Europe (19%). A comparable contribution is also made by American sources (17%). The main contribution from Russian sources is made by emissions from **Chukotka AO** itself (8%).
- These estimates of contributions to the selected regions are based on PCB-153 data. The contributions of other congeners are given in Annex A.

### *γ-Hexachlorocyclohexane (γ-HCH)*

A Model evaluation of pollution by  $\gamma$ -HCH was made with the use of the hemispheric multicompartiment MSCE-POP model and available emission data. The collected emission dataset is not consistent and does not include all sources of the Northern Hemisphere. Pathways of  $\gamma$ -HCH transport from main source groups to regions-receptors were examined.

- Air concentration levels in regions-receptors are within the range 0.05 – 0.5 ng/m<sup>3</sup>, and deposition flux is from 1 to 10 g/km<sup>2</sup>/y. Air concentration levels in four regions (Murmansk Oblast, Nenets AO, Yamalo-Nenets AO and Taimyr AO, and Sakha Republic) are similar to one another. Average concentrations in Chukotka AO are two times lower. Annual deposition flux values decrease more substantially from region to region, in an eastward direction.

- $\gamma$ -HCH accumulates mainly in seawater. About 80% of all  $\gamma$ -HCH content in the environment is contained in this medium. An essential part of  $\gamma$ -HCH is transported to the Arctic by sea currents from the Atlantic Ocean. It was found that the marine pathway is significant for marine concentrations near the borders of the Russian North.
- The main contribution to  $\gamma$ -HCH depositions in **Murmansk Oblast** is made by sources in Western Europe (54%), followed by Russia - 17%, and India - 9%. The Russian contribution to depositions is mostly made by sources from the Central and Volgo-Viatsky regions (5%) and Central-Chernozem, Volga, and North-Caucasian regions (4%).
- Similar to Murmansk Oblast, major contributions to the pollution of **Nenets AO** are made by emission sources from Western Europe (49%), Russia (23%), and India (9%). The main sources in the Russian Federation are the Central and Volgo-Viatsky regions (8%) and Central-Chernozem, Volga, and North-Caucasian regions (8%).
- For **Yamalo-Nenets and Taimyr AO** the major contributors are Western Europe (48%), Russia (21%), and India (10%). The main sources in the Russian Federation are the Central and Volgo-Viatsky regions (7%) and Central-Chernozem, Volga, and North-Caucasian regions (8%).
- The major contributors to the pollution of the **Sakha Republic** are the following: Western Europe (36%), India (19%), and Russia (11%). The main sources in the Russian Federation are the Central and Volgo-Viatsky regions (3%) and Central-Chernozem, Volga, and North-Caucasian regions (4%).
- For **Chukotka AO** main contributions to contamination are made by India (27%), Western Europe (27%), China (19%), and the Americas (11%). The contribution of Russian sources accounts for 5%.
- Contamination levels in regions-receptors undergo substantial seasonal variations due to changes in meteorological conditions and variations in emissions.

Some general conclusions could be made on the ground of the performed investigations:

- Europe, North America, and South-eastern Asia are the most sizeable emission sources of mercury, PCBs and  $\gamma$ -HCH. The bulk of Russian emissions are located in the European part of the Russian Federation. Due to geographical location and meteorological conditions, European sources make the basic contribution to the contamination of western regions of the Russian North. Asian and North American sources play more significant roles in the pollution of the eastern territories of the Russian Arctic, though the contribution of European sources is still considerable.
- The obtained results make it possible to predict contamination levels in the Russian Arctic for the near future. The analysis of the emission data shows that mercury emissions decrease in Europe and North America, whereas they grow in South-eastern Asia. The influence of Asian sources may become prevailing, thus contamination levels of this pollutant in some regions of the Russian North may increase in the future. As to  $\gamma$ -HCH, its usage is prohibited in most countries, although it is still utilized in Asia. Thus the relative influence of Asian countries on pollution of the Russian Arctic by  $\gamma$ -HCH is likely to increase. At the same time PCB contamination levels are expected to decrease with emission reduction, though contamination due to accumulation in environmental media remains significant.

## Annex A

## MODELING RESULTS ON TRANSPORT OF PCB-28, 118 AND 180

This annex contains the calculated data on contamination levels of PCB-28, 118 and 180 in 1996. At first the contamination of the whole hemisphere is considered, then pollution levels of the Russian North are presented. The last section is devoted to source-receptor relationships for the selected regions of the Russian North.

## PCB-28

*Contamination of the North Hemisphere*

This section presents the model results on contamination levels of PCB-28 in the Northern Hemisphere in 1996. The spatial distributions of annual emission and deposition fluxes as well as mean annual concentrations in the air surface layer and soil concentrations averaged over the whole depth of soil calculation domain are given in Figure A.1. Depositions mean the sum of wet and dry particle deposition and wet gas depositions.

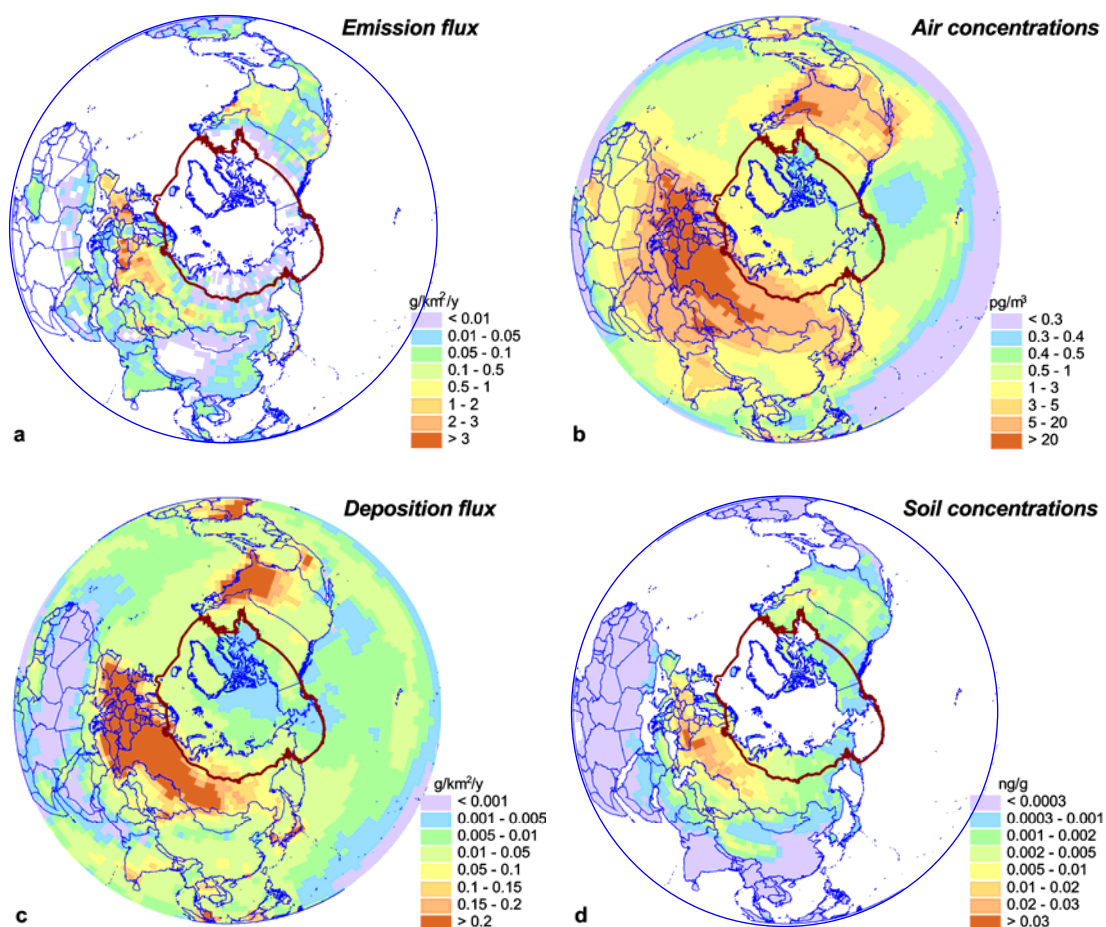
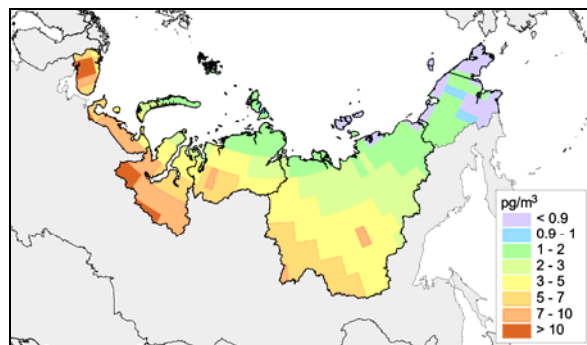


Figure A.1. PCB-28 emissions and contamination levels in 1996

## Concentrations and depositions in the Russian North

In this section, spatial distributions of annual mean air concentrations and annual depositions of PCB-28 in the Russian North in 1996 are presented (Figs. A.2, A.3). Table A.1 contains the information on annual contamination levels in the regions of the Russian North and their spatial variations.



**Figure A.2.** Mean annual air concentrations of PCB-28 in the Russian North,  $\text{pg}/\text{m}^3$

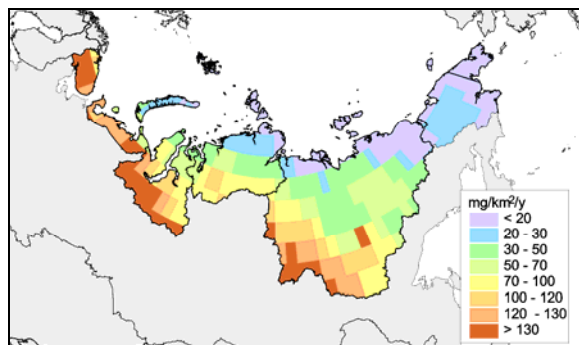


**Figure A.3.** Deposition of PCB-28 in the Russian North calculated for 1996,  $\text{mg}/\text{km}^2/\text{y}$

**Table A.1.** Annual contamination levels of the Russian North regions by PCB-28 in 1996 and their spatial variations

Region	Air concentration, $\text{pg}/\text{m}^3$			Depositions, $\text{mg}/\text{km}^2/\text{y}$			Gas exchange, $\text{mg}/\text{km}^2/\text{y}$		
	Min	Max	Mean	Min	Max	Mean	Min	Max	Mean
Murmansk Oblast	3.4	18.6	8.2	61	320.1	164.7	113	1496.8	528.1
Nenets AO	1.2	15.2	5.7	11.7	284.4	86.1	9.2	1021.9	395.5
Yamalo-Nenets AO and Taimyr AO	1	13.1	5.2	8.6	220.8	82.1	-38.8	787.9	119.2
Sakha Republic	0.7	7.2	3.4	6	157.3	66.4	-77.3	125	-11.5
Chukotka AO	0.5	1.3	0.9	5.3	27.6	18.4	-21.1	90.8	13.1

## Contributions of different emission sources to the pollution of the Russian Arctic

In this section contributions of different emission sources to the PCB-28 emissions in the Northern Hemisphere and Russia in 1996 are presented in Figure A.4. Figure A.5 depicts contributions of these sources to depositions to the regions of the Russian North and to the Arctic region as a whole.

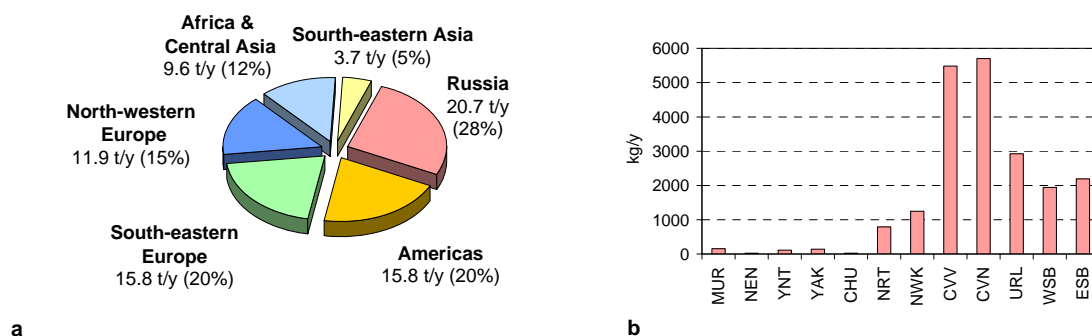
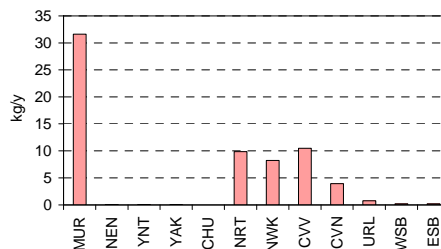
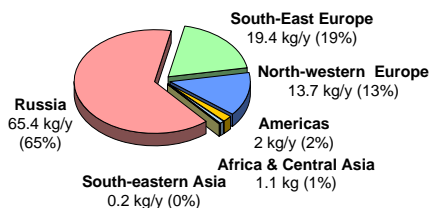


**Figure A.4.** Contributions of different emission source groups of PCB-28 to the hemispheric emissions in 1996: source regions in the Northern Hemisphere (a), detailed splitting of Russian sources (b)

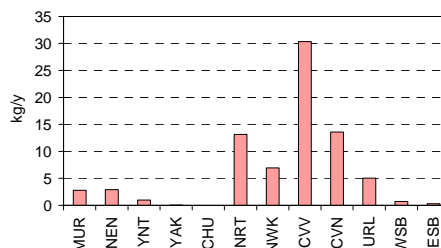
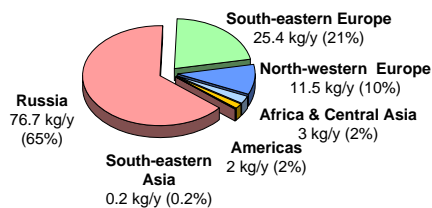
**Contributions of the Northern Hemisphere sources to depositions**

**Contributions of Russian sources to depositions**

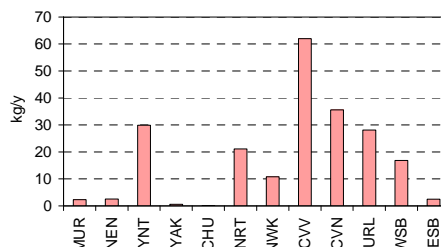
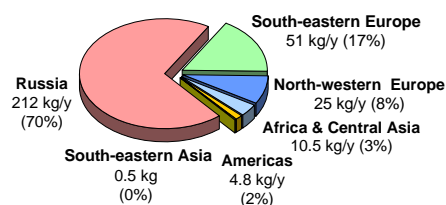
**Murmansk Oblast**



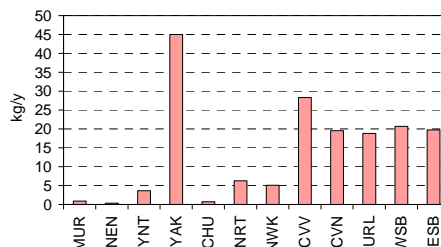
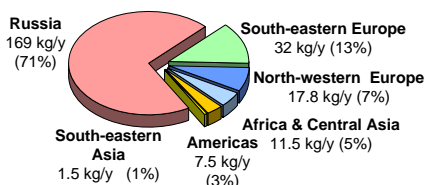
**Nenets AO**



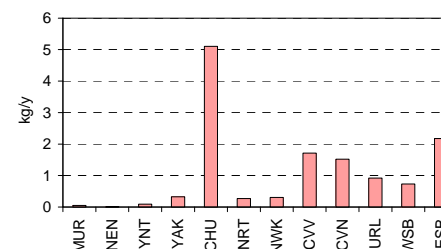
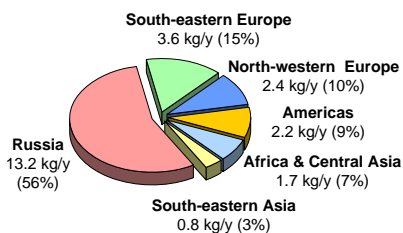
**Yamalo-Nenets AO and Taimyr AO**



**Sakha Republic (Yakutia)**



**Chukotka AO**



**the Arctic**

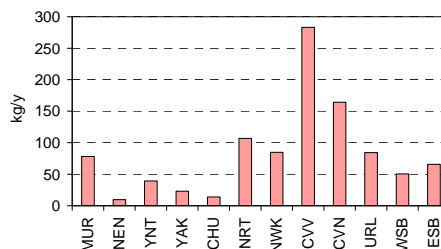
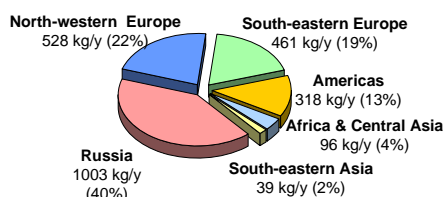


**Figure A.5.** Contributions of different emission sources to PCB-28 depositions to regions of Russian North and to the Arctic as a whole in 1996

## PCB-118

### *Contamination of the North Hemisphere*

This section presents the model results on contamination levels of PCB-118 in the Northern Hemisphere in 1996. The spatial distributions of annual emission and deposition fluxes as well as mean annual concentrations in the air surface layer and soil concentrations averaged over the whole depth of soil calculation domain are given in Figure A.6. Depositions mean the sum of wet and dry particle deposition and wet gas depositions.

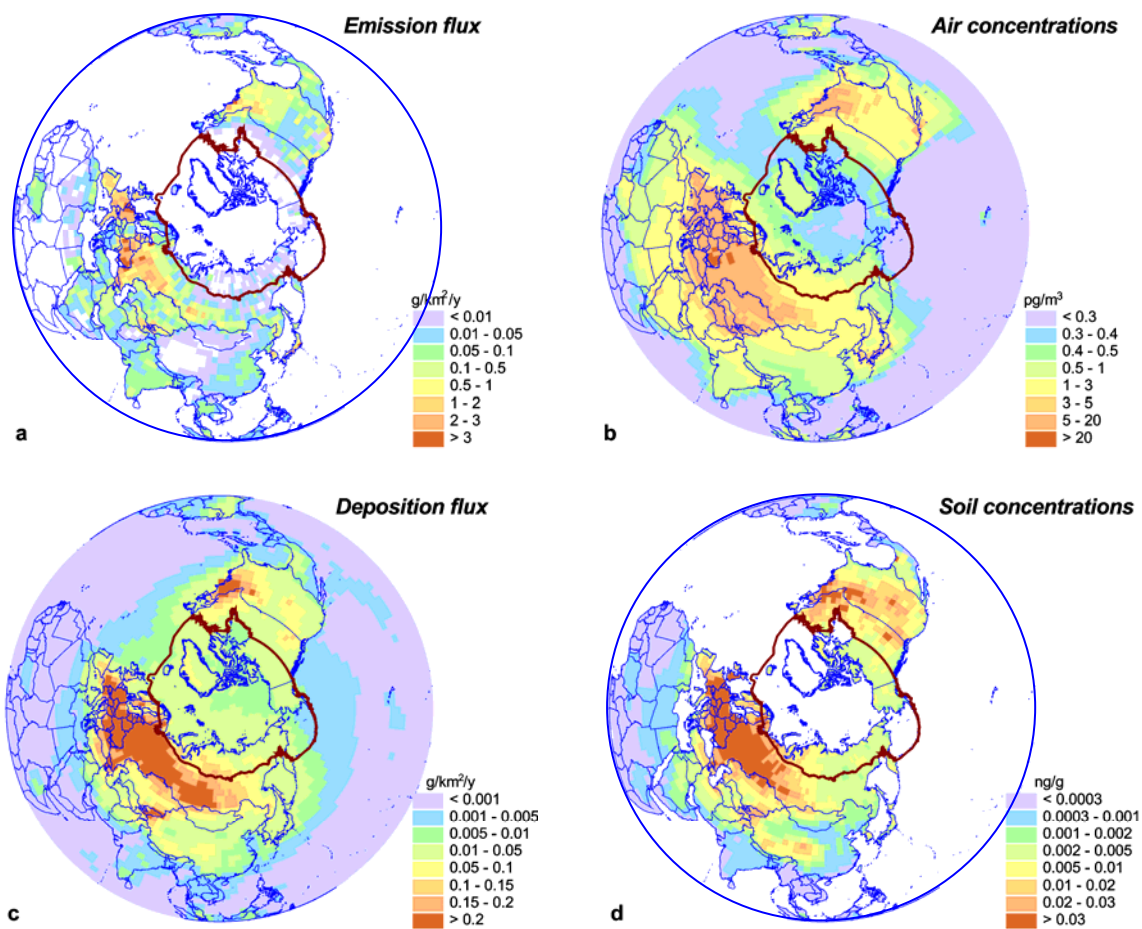


**Figure A.6.** PCB-118 emissions and contamination levels in 1996

### *Concentrations and depositions in the Russian North*

In this section, spatial distributions of annual mean air concentrations and annual depositions of PCB-118 in the Russian North in 1996 are presented (Figs. A.7, A.8). Table A.2 contains the information on annual contamination levels in the regions of the Russian North and their spatial variations.

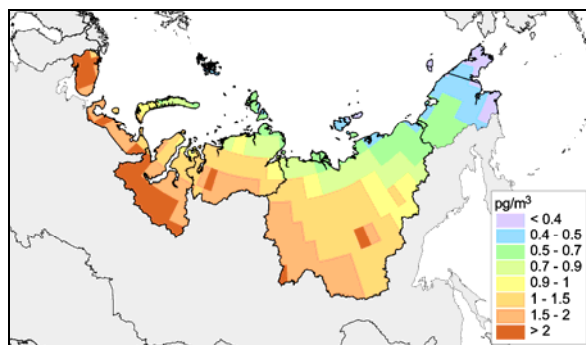


**Figure A.7.** Mean annual air concentrations of PCB-118 in the Russian North in 1996,  $pg/m^3$

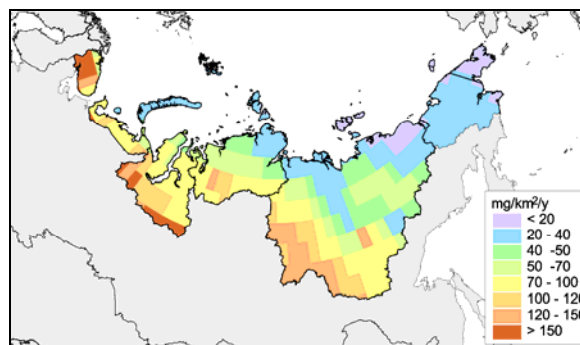


**Figure A.8.** Deposition of PCB-118 in the Russian North in 1996,  $mg/km^2/y$

**Table A.2.** Annual contamination of the Russian North regions by PCB-118 in 1996 and their spatial variations

Region	Air concentration, $pg/m^3$			Depositions, $mg/km^2/y$			Gas exchange, $mg/km^2/y$		
	Min	Max	Mean	Min	Max	Mean	Min	Max	Mean
Murmansk Oblast	1.1	5.7	2.6	48.2	376.6	169.2	-59.4	274.8	67.4
Nenets AO	0.4	4	1.5	19.6	335.4	72.2	-113	244.4	100.3
Yamalo-Nenets AO and Taimyr AO	0.4	3.5	1.6	19.1	189.1	81.8	-85	152.9	10.2
Sakha Republic	0.3	2.5	1.2	11.8	176.9	66.7	-136.9	17.9	-36.1
Chukotka AO	0.3	0.6	0.5	9	39.5	28.3	-23	24	-8.3

### Contributions of different emission sources to the pollution of the Russian Arctic

In this section, contributions of different emission sources to the PCB-118 emissions in the North Hemisphere in 1996 is presented in Figure A.4. Figure A.5 depicts contributions of these emission sources to depositions to the regions of the Russian North and to the Arctic as a whole.

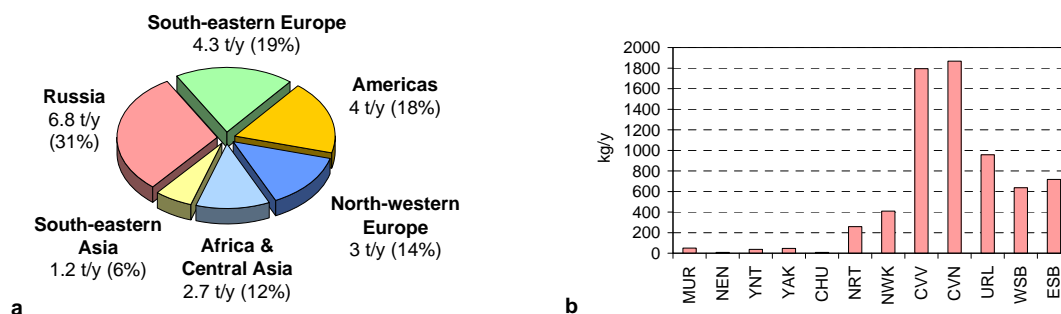


**Figure A.9.** Contributions of different emission source groups of PCB-118 to the hemispheric emissions in 1996: source-regions in the Northern Hemisphere (a), detailed splitting of Russian sources (b)

**Contributions of the Northern Hemisphere sources to depositions**

**Contributions of Russian sources to depositions**

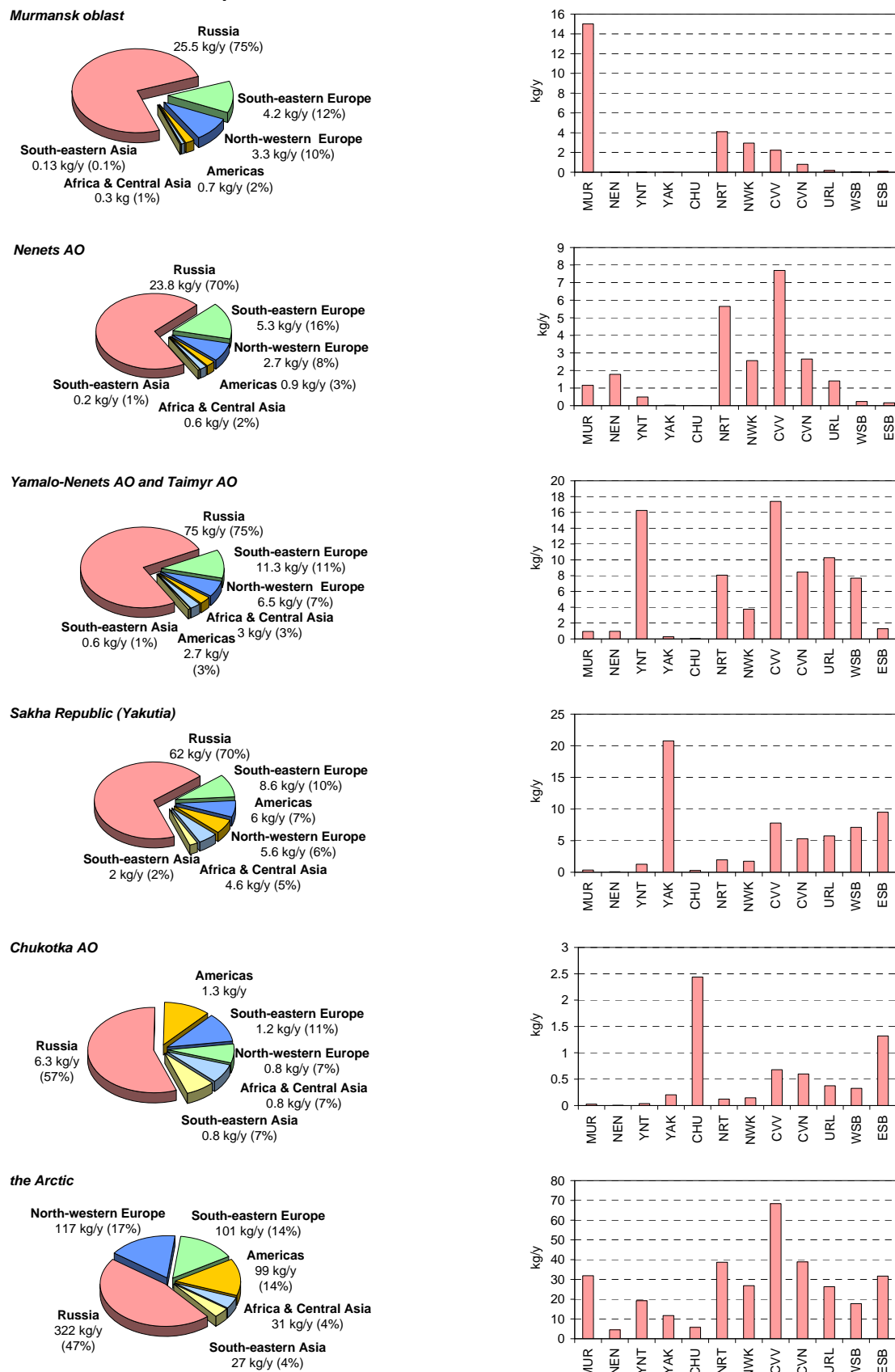


**Figure A.10.** Contributions of different emission sources to PCB-118 depositions to regions of Russian North and to the Arctic as a whole in 1996

## PCB-180

### *Contamination of the North Hemisphere*

This section presents the model results on contamination levels of PCB-180 in the Northern Hemisphere in 1996. The spatial distributions of annual emission and deposition fluxes as well as mean annual concentrations in the air surface layer and soil concentrations averaged over the whole depth of soil calculation domain are given in Figure A.11. Depositions mean the sum of wet and dry particle deposition and wet gas depositions.

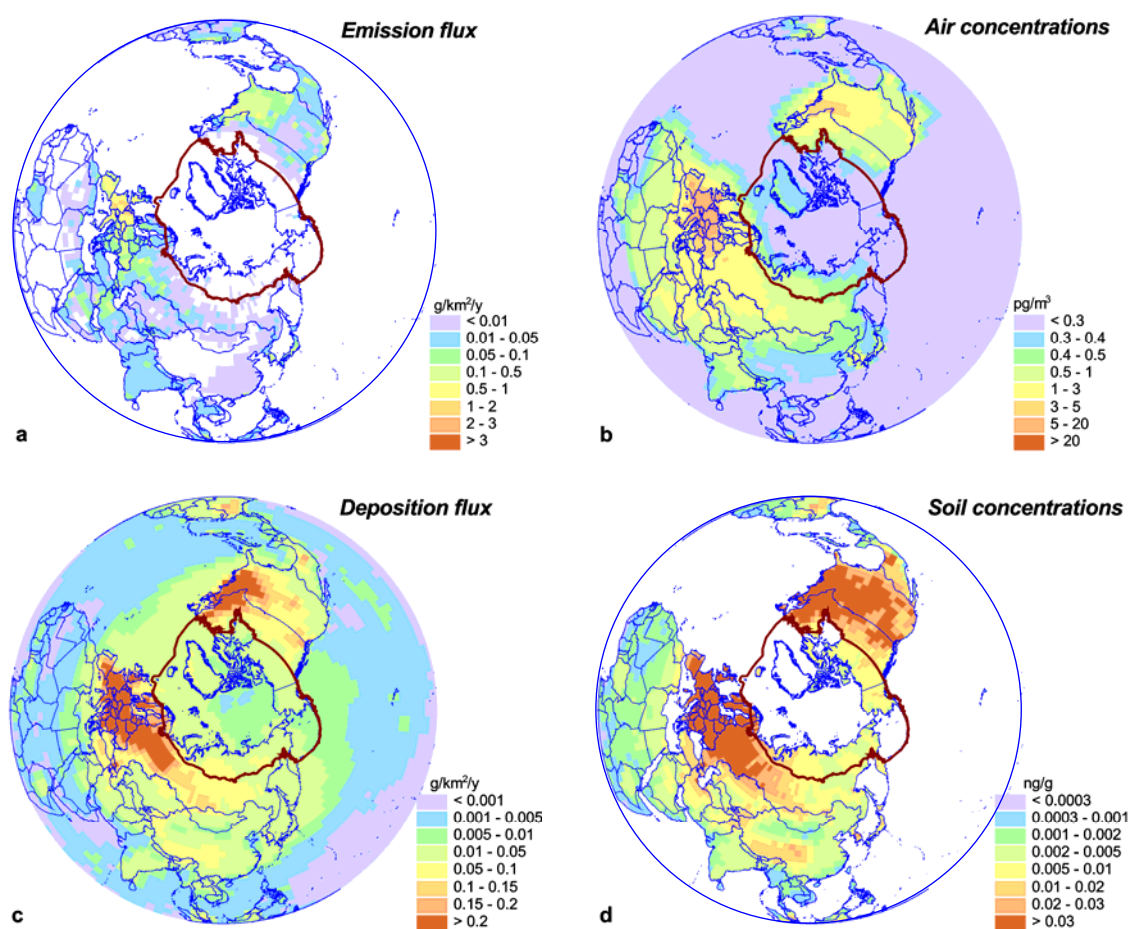
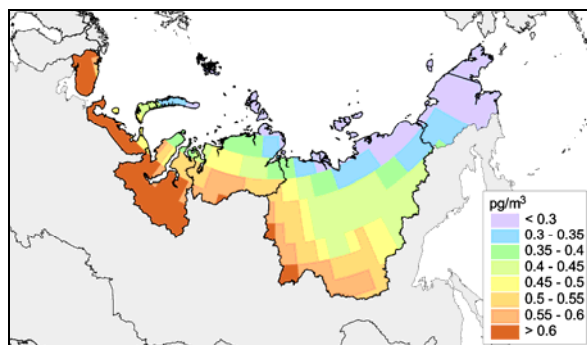


Figure A.11. PCB-180 emissions and contamination levels in 1996

### *Concentrations and depositions in the Russian North*

In this section, spatial distributions of annual mean air concentrations and annual depositions of PCB-180 in the Russian North in 1996 are presented (Figs A.12, A.13). Table A.3 contains the information on annual contamination levels in the regions of the Russian North and their spatial variations.



**Figure A.12.** Mean annual air concentrations of PCB-180 in the Russian North in 1996,  $\text{pg/m}^3$

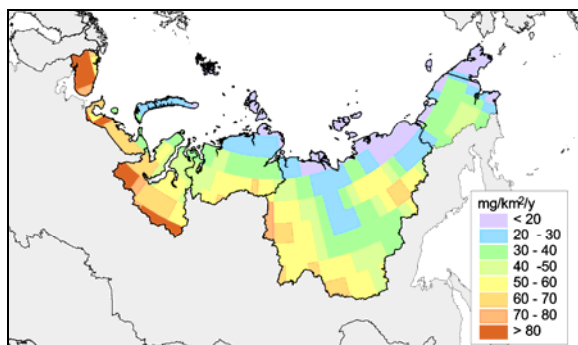


**Figure A.13.** Deposition of PCB-180 in the Russian North in 1996,  $\text{mg/km}^2/\text{y}$

**Table A.3.** Annual contamination of the Russian North regions by PCB-180 in 1996 and their spatial variations

Region	Air concentration, $\text{pg/m}^3$			Depositions, $\text{mg/km}^2/\text{y}$			Gas exchange, $\text{mg/km}^2/\text{y}$		
	Min	Max	Mean	Min	Max	Mean	Min	Max	Mean
Murmansk oblast	0.5	1.2	0.9	47	188	123	-160	9.4	-70
Nenets AO	0.2	1.1	0.6	12	204	53	-168	8	-20
Yamalo-Nenets AO and Taimyr AO	0.2	0.9	0.6	12	114	52	-90	0.8	-29
Sakha Republic	0.1	0.7	0.5	6.9	96	43	-92	1.2	-38
Chukotka AO	0.1	0.4	0.3	9	48	32	-40	2.6	-23

### Contributions of different emission sources to the pollution of the Russian Arctic

In this section, contributions of different emission sources to the PCB-180 emissions in the North Hemisphere in 1996 is presented in Figure A.14. Figure A.15 depicts contributions of these emission sources to depositions to the regions of the Russian North and to the Arctic as a whole.

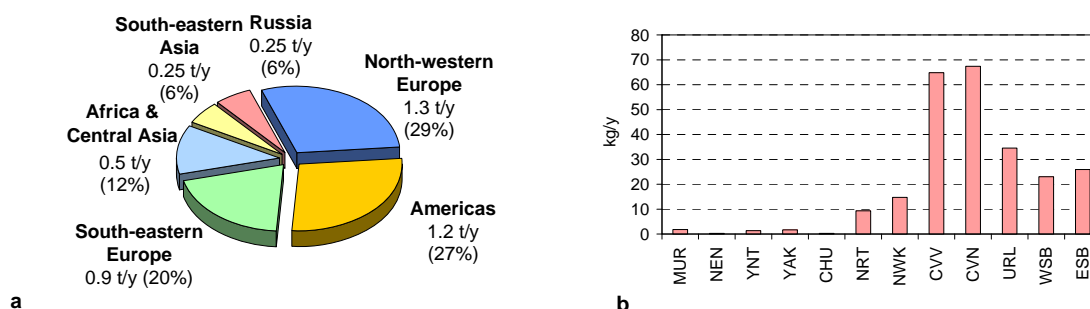
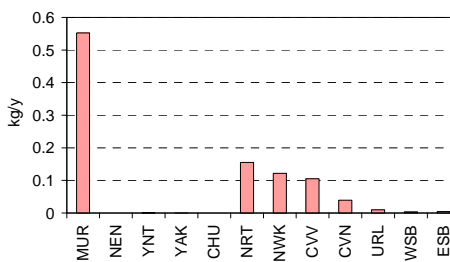
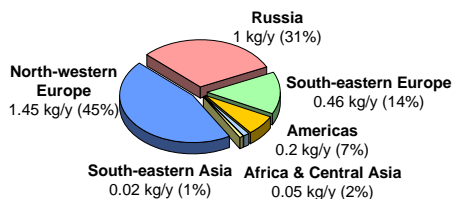


**Figure A.14.** Contributions of different emission source groups of PCB-180 to the hemispheric emissions in 1996: source-regions in the Northern Hemisphere (a), detailed splitting of Russian sources (b)

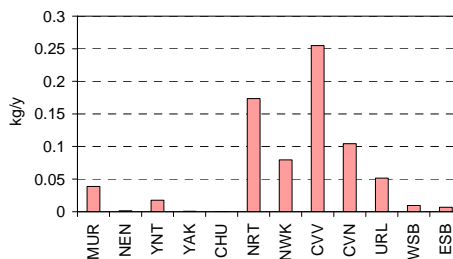
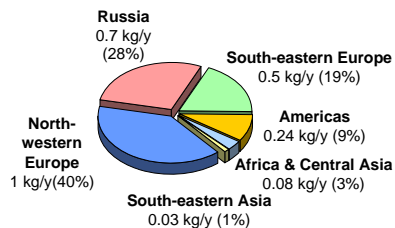
**Contributions of the Northern Hemisphere sources to depositions**

**Contributions of Russian sources to depositions**

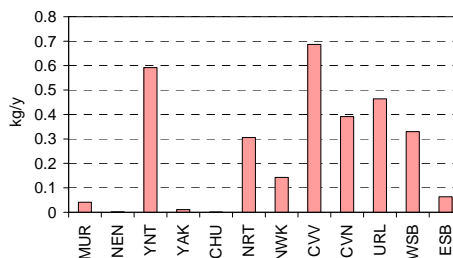
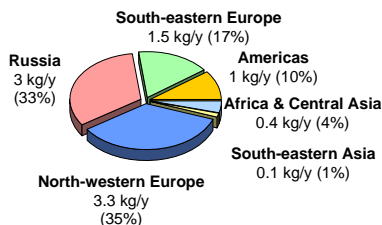
**Murmansk oblast**



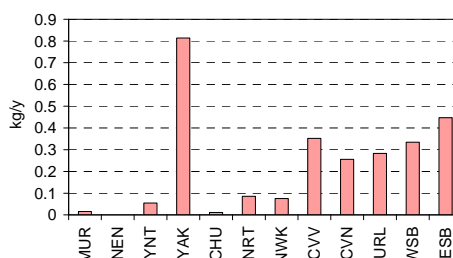
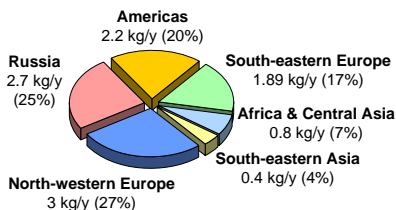
**Nenets AO**



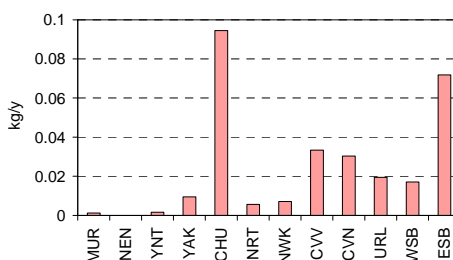
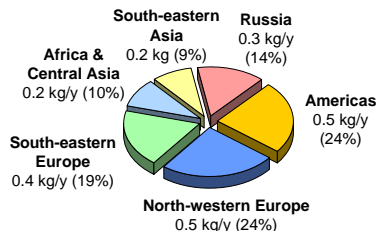
**Yamalo-Nenets AO and Taimyr AO**



**Republic of Sakha (Yakutia)**



**Chukotka AO**



**the Arctic**

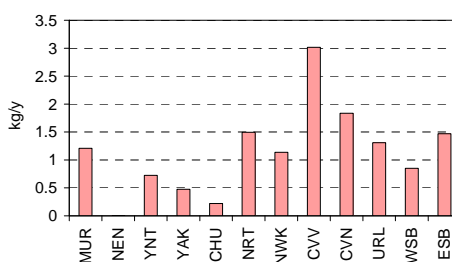
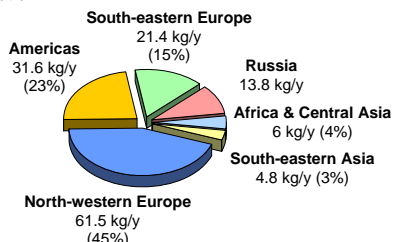


**Figure A.15.** Contributions of different emission sources to PCB-180 depositions to regions of Russian North and to the Arctic as a whole in 1996



## Annex B

## ATMOSPHERIC TRANSPORT MODULE VERIFICATION

The atmospheric transport scheme of the models developed is described in Chapter 4. This annex contains description of some numerical experiments verifying the transport module consistency.

## B.1 Testing of the advection scheme

*Horizontal advection*

To examine the consistency of the constructed advection scheme the classical Smolarkiewicz numerical experiments [Smolarkiewicz, 1982] have been performed. In the first experiment initial distribution of  $\psi$  is transported in the uniform rotational flow. In the second one transformation of the initial distribution in the strong deformational flow is considered. In both numerical experiments cone-shaped initial distribution has been determined with  $\psi=110$  at the top and  $\psi=10$  at the bottom of the cone (arbitrary units).

The objective of the rotational flow experiment is to examine the model ability to simulate a pollutant horizontal advective transport and to evaluate artificial diffusion of the numerical scheme. The wind field of the rotational flow is shown in Figure B.1 as well as the initial cone shaped distribution. The axis of the rotational flow is sloped down from the Earth axis with the angle  $30^\circ$  and the center of the initial distribution is located at the latitude  $20^\circ\text{N}$ . Since the flow is non-divergent the uniform distribution should remain uniform, while the cone-shaped one theoretically should be transported as a solid body. However, in reality the cone is smoothed down due to the artificial diffusion.

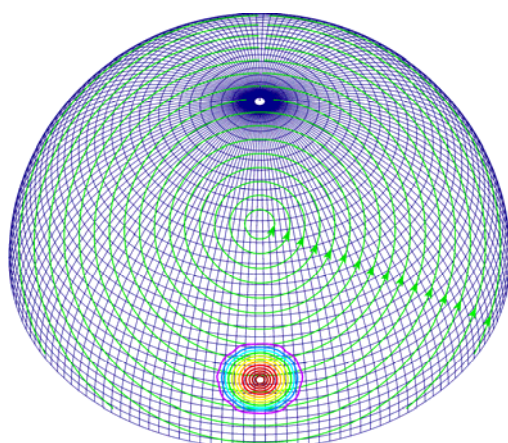


**Figure B.1.** Conditions of the rotational flow numerical experiment: Wind streamlines and the initial cone-shaped distribution. Concentric circles denote isolines of  $\psi$  value with step  $\Delta\psi = 8$  (arbitrary units)

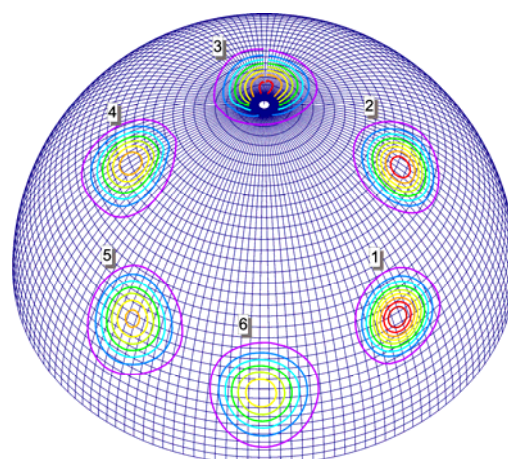


**Figure B.2.** Results of the rotational flow numerical experiment. Concentric circles denote isolines of  $\psi$  value with step  $\Delta\psi = 8$  (arbitrary units): 1 – after 1/6 of the full revolution; 2 – 1/3; 3 – 1/2; 4 – 2/3; 5 – 5/6; 6 – after the full revolution

Results of the test are presented in Figure B.2. The numbered sets of concentric circles show the cone location and shape at different moments of the revolution with time step  $\Delta t=1/6$  of the whole revolution period. As seen from the figure the cone only slightly changes its shape due to numerical dispersion and artificial diffusion after the whole revolution. It has become lower (about 60% of the original height) and its circular shape has been somewhat disturbed. Thus, the advection scheme does not produce considerable distortions and has comparatively low artificial diffusion.

The objective of the deformational flow experiment is to examine the model stability in strong deformational flows and evaluate possible time-splitting error [Bott, 1993; Easter, 1993; Clappier, 1998]. The velocity field and the initial cone-shaped distribution for the deformational flow experiment are presented in Figure B.3 in spherical coordinates. Zonal and meridional components of the wind are determined by the following formulas:

$$V_{\lambda} = 4 \sin(4\lambda) \sin(4\varphi - \pi/2),$$

$$V_{\varphi} \cos \varphi = 4 \cos(4\lambda) \cos(4\varphi - \pi/2).$$

As it is seen from the figure the wind field is built up from sets of symmetrical vortices. Since the flow is non-divergent again a uniform distribution should remain uniform except zones where mass from the initial cone incoming. But anyway values of  $\psi$  should remain limited at any point of the domain.

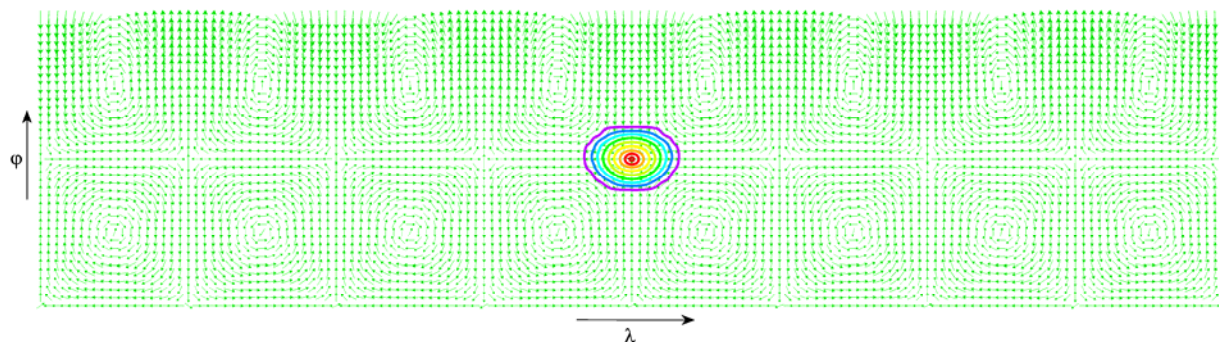


**Figure B.3.** Conditions of the deformational flow numerical experiment: Wind velocity vectors and the initial cone-shaped distribution. Concentric circles denote isolines of  $\psi$  value with step  $\Delta\psi = 10$  (arbitrary units)

Results of the experiment are presented in Figure B.4. Figure B.4.a shows the initial cone-shaped distribution in the spherical coordinates. Figures B.4.b–e illustrate transformation of the distribution in the deformation flow and correspond to different time moments (or different numbers of iterations). As one can see the mass is coming along the boundaries of the vortices and is penetrating to the neighboring ones. The main difference from the original deformational flow experiment [Smolarkiewicz, 1982] is sharing of the mass between the remote vortices through the pole (see Fig.B.4.d). This is peculiar feature of the spherical geometry. The maximum value of  $\psi$  distribution decreases in time, that is the model is stable to the deformational flow. Besides, there is no observable time-splitting error.

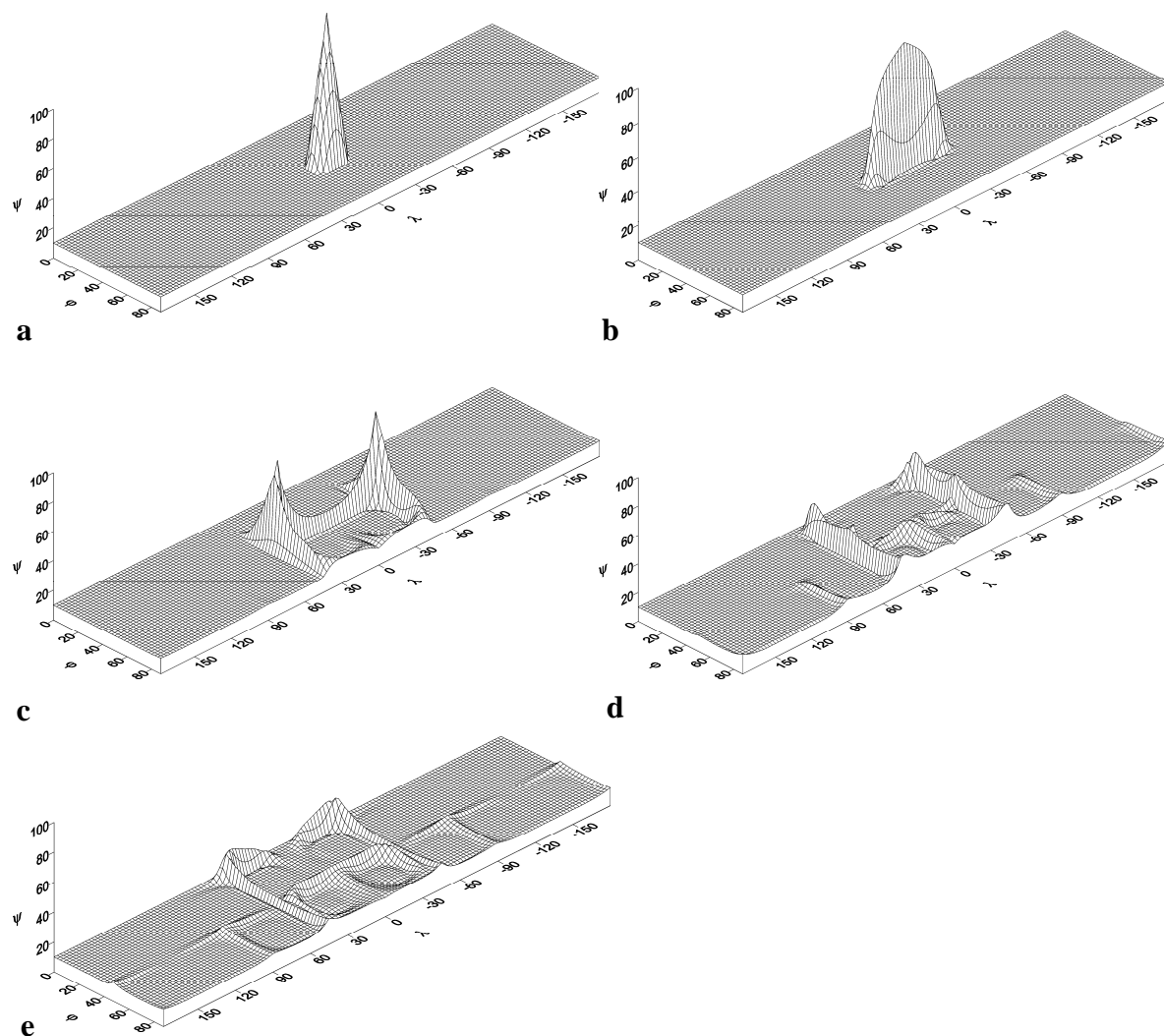


**Figure B.4.** Results of the deformational flow numerical experiment  $\psi$  distribution: (a) – initial; (b) – after 130 iterations; (c) – 390 iterations; (d) – 650 iterations; (e) – 810 iterations

### Vertical advection

To examine the vertical advective transport in combination with the horizontal one a number of numerical experiments have been performed. One of them is presented below. Two-dimensional advective transport is considered. Conditions and results of the experiment are shown in Figure B.5. The real orography corresponding to 100°E longitude is utilized as a underlying surface. To simulate straight-line transport of the initial distribution in the terrain-following coordinates the uniform wind field has been determined along the horizon (see Fig.B.5.a). For this purpose we had to apply

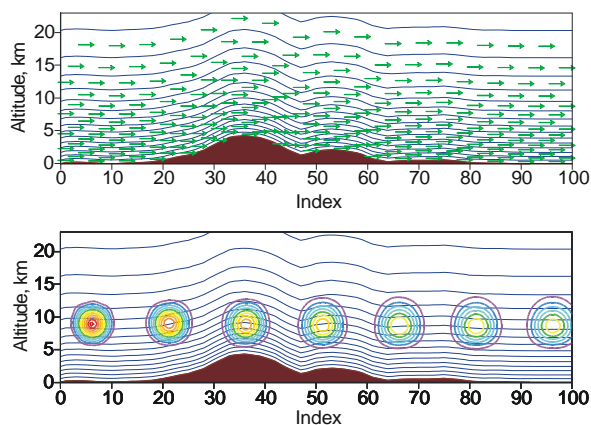


**Figure B.5.** Wind field (a) and results (b) of the numerical experiment for the vertical advection

unrealistic “transparent” boundary conditions at the surface: The wind can freely flow in and out through the surface. The main objective of the experiment is to examine the model ability to adequately simulate the advective transport in the atmosphere without influence of the curvilinear sigma coordinate. The cone-shaped initial distribution is determined in the left side of the domain (see Fig.B.5.b) and moves to the right. As one can see from the figure the cone is transported along straight line, and somewhat smoothing of the initial shape is observed due to the artificial diffusion. The originally circular shape is slightly disturbed because of the non-uniform grid.

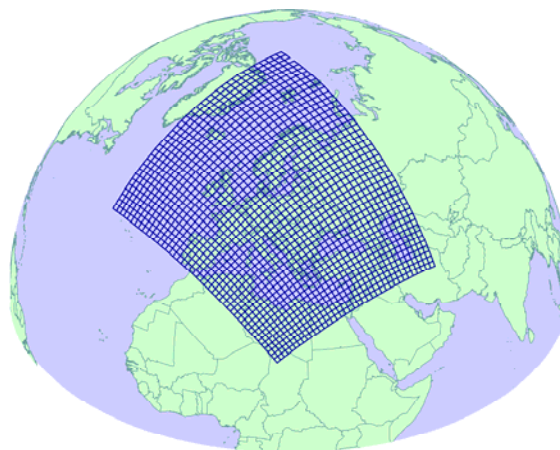
## B.2 Verification of the atmospheric transport module

The atmospheric module requires to be verified against some reliable results of other models or measurements. First of all we compared modeling results obtained by the hemispheric model with those by regional MSCE-HM model of heavy metal atmospheric transport. The MSCE-HM model has been developed and employed in operational regime for the last several years. It has been verified in a number of intercomparison campaigns with other regional models [Sofiev *et al.*, 1996; Gusev *et al.*, 2000; Ryaboshapko *et al.*, 2001] and has been qualified by means of sensitivity and uncertainty studies [Travnikov, 2000]. Thus its results can be considered as quite reliable within European region. In the other verification procedure the hemispheric model results were compared with measurement data available within the EMEP monitoring network. In both cases lead airborne transport was considered.

### *Comparison with regional MSCE-HM model*

The regional MSCE-HM model is a three-dimensional Eulerian-type model operating within the EMEP domain (see Fig.B.6). The model grid covers whole Europe, the Mediterranean Sea, and part of the Atlantic Ocean with spatial resolution  $50 \text{ km} \times 50 \text{ km}$ . In the vertical it consists of 5 atmospheric layers up to approximately 4 km. Detailed description of the model can be found in [Ryaboshapko *et al.*, 1999].

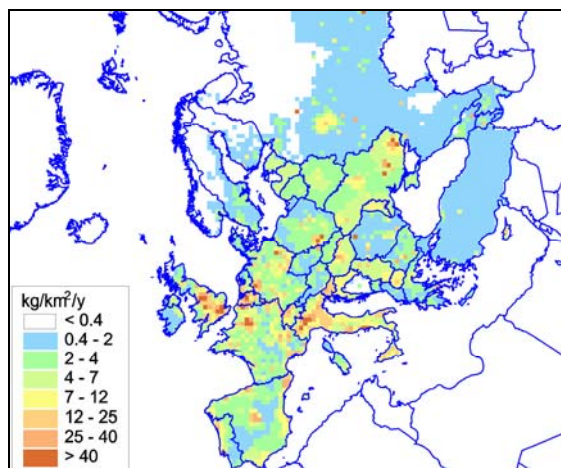
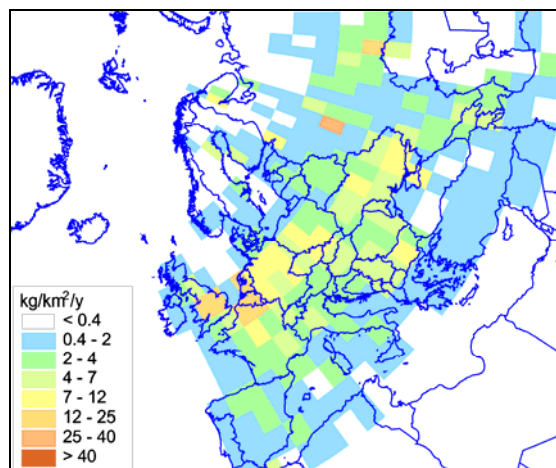
Conditions of the comparison are summarized in Table B.1. Both models were employed to calculate the long-range transport and deposition of antropogenic lead in 1990. Each model used its own computation domain and spatial resolution. In both cases we used meteorological data for 1990. The MSCE-HM model utilized official anthropogenic emission data from the EMEP inventory while the hemispheric model operated with the GEIA Global Lead Emission Inventory for 1989 [Pacyna *et al.*, 1995]. Only European emission sources were considered from the whole hemispheric field. Since the official EMEP data considerably differ from the GEIA inventory, we had to reduce the latter by multiplying the emission field by a correction factor ( $\sim 0.6$ ) to equalize the total emissions from Europe in both cases. The spatial fields of lead antropogenic emission density for regional MSCE-HM and hemispheric models are presented in Figures B.7 and B.8 respectively.



**Figure B.6.** *Computation domain of the regional MSCE-HM model (EMEP domain)*

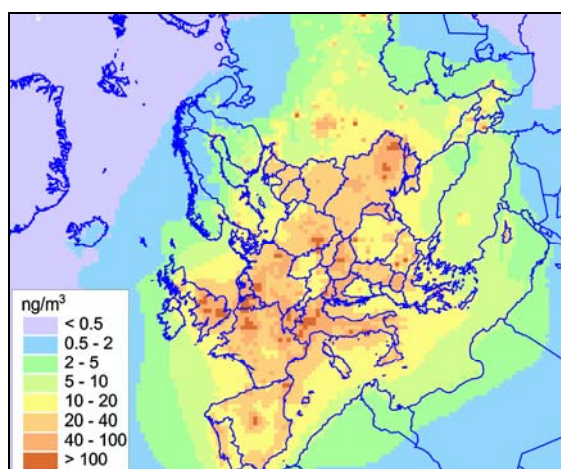
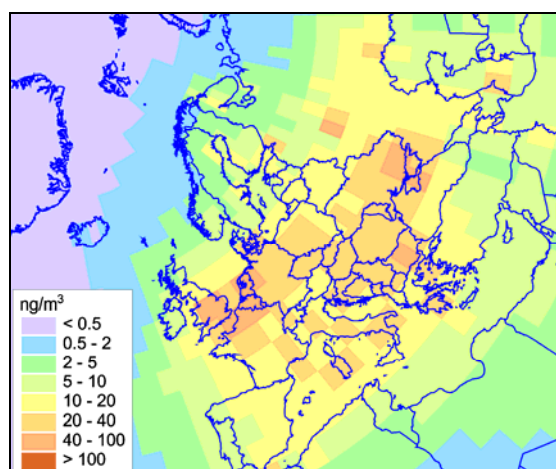
**Table B.1.** Conditions of the hemispheric and regional MSCE-HM models comparison study

Characteristics	Hemispheric model	MSCE-HM model
Objective	Lead long-range transport and deposition in 1990	
Computation domain	Northern Hemisphere	EMEP domain
Spatial resolution	2.5° × 2.5°	50 km × 50 km
Meteorological data	for 1990	for 1990
Emission data	Reduced GEIA inventory for 1989	Official data from the EMEP inventory for 1990

**Figure B.7.** Lead anthropogenic emission density in 1990 (official data from the EMEP inventory)**Figure B.8.** Lead anthropogenic emission density in 1989 (reduced GEIA Inventory)

As seen from the figures, considerably lower resolution of the hemispheric model leads to rougher distribution of the anthropogenic emissions smoothing all emission peaks (Fig. B.8). Besides, the emission fields have some spatial distinctions. First of all one has to mention significantly higher emission levels for the regional model (Fig. B.7) in Northern Italy and in Spain.

Results of the model comparison are presented in Figures B.9–B.14. Figures B.9 and B.10 show spatial distributions of mean annual lead concentration in surface air obtained by the MSCE-HM and hemispheric models respectively.

**Figure B.9.** Spatial distribution of mean annual lead concentration in the surface air obtained by the *regional MSCE-HM model***Figure B.10.** Spatial distribution of mean annual lead concentration in the surface air obtained by the *hemispheric model*

Here one should take into account that the models have quite different advection schemes, spatial resolutions, and utilize different emission data. Nevertheless, the spatial distribution fields in both cases look quite similar. The regions with the highest lead concentrations coincide as a whole, except several regions (e.g. Northern Italy, Spain etc.), where the hemispheric model produce considerably lower values. The reason for the distinction is different emission fields for the regional and hemispheric models as it was mentioned above (compare Fig. B.6 and B.7). The models produce very close background lead concentrations in air far from industrial regions (e.g. the Atlantic Ocean and the Arctic) characterizing long-range lead transport. It is natural that the concentration field of the hemispheric model is smoother (without significant peaks) than that of the regional one due to lower spatial resolution. Besides, the hemispheric model predicts more considerable lead transport outside the domain eastward and south-eastward. A similar situation is for the spatial distributions of total annual lead deposition (compare Fig. B.11 and B.12).

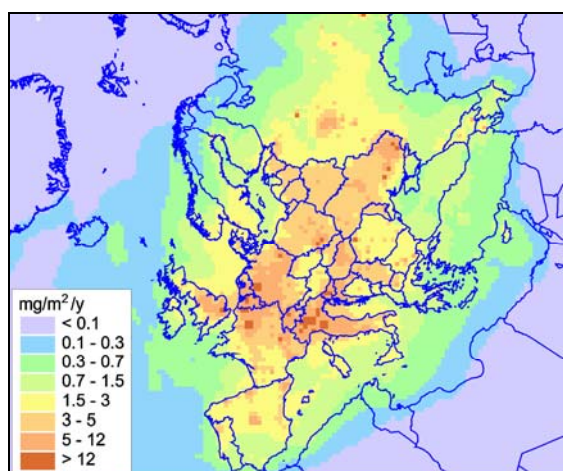


**Figure B.11.** Spatial distribution of total annual lead deposition obtained by the **regional MSCE-HM model**

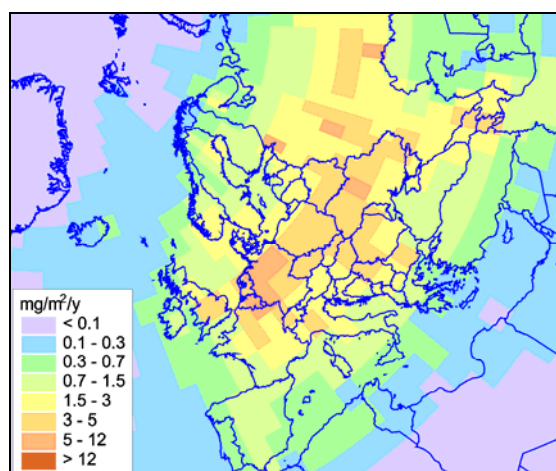


**Figure B.12.** Spatial distribution of total annual lead deposition obtained by the **hemispheric model**

Quantitative comparison of the concentration and deposition fields obtained by the regional and hemispheric models has been performed by means of regression analysis and is presented in Figures B.13 and B.14. We compared values of mean annual lead concentration in air (Fig. B.13) and total annual lead deposition (Fig. B.14) obtained by both models at grid points of the EMEP domain. To avoid excessive overloading of the figures we present only one sixth of all the grid cells uniformly distributed over the domain. As seen from the figures the slopes of the regression line are quite close to unity (solid blue line) and correlation coefficients (R) are higher than 0.7 in both cases. The significant overshoots of the regional model results can be explained by considerably higher resolution and correspond to points with the highest emission. As a whole the most points are within a “factor of two” limits (dashed blue lines).

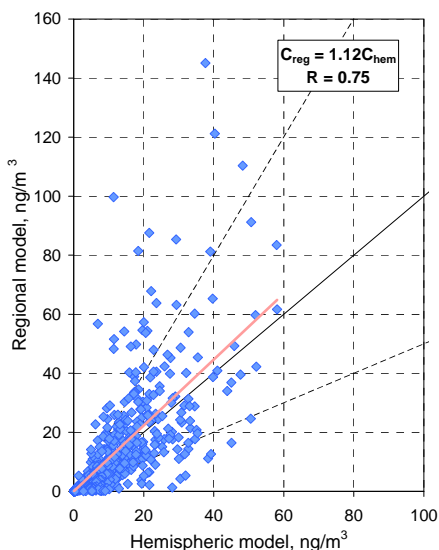


**Figure B.13.** Comparison of the mean annual lead concentration fields obtained by the regional MSCE-HM and hemispheric models. Equation  $C_{reg} = AC_{hem}$  describes the regression line with the slope  $A$ ;  $R$  is the correlation coefficient

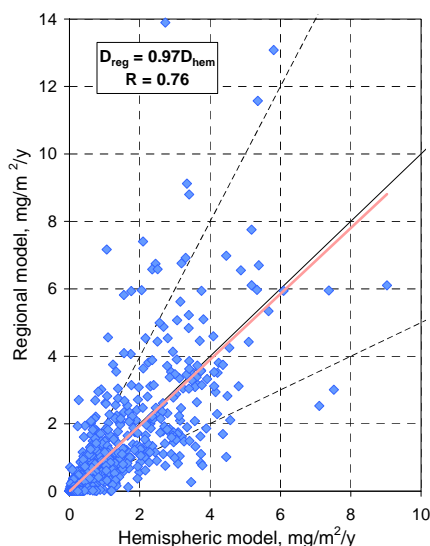


**Figure B.14.** Comparison of the annual total lead deposition fields obtained by the regional MSCE-HM and hemispheric models. Equation  $D_{reg} = AD_{hem}$  describes the regression line with the slope  $A$ ;  $R$  is the correlation coefficient

### Comparison with measurements

In order to verify the hemispheric model consistency we also compared the modeling results with the available measurements. The original (not reduced) emission data for lead in 1989 from the GEIA Inventory [Pacyna *et al.*, 1995] were used for the modeling. The measurement data for lead in 1989 were taken from the EMEP monitoring network [Berg *et al.*, 1996]. The comparison of the observed and modeled mean annual lead concentrations in the surface air and annual wet deposition fluxes are presented in Figures B.15 and B.16 respectively. As seen from the figures the modeling results are in a satisfactory agreement with observations in both cases. The model overestimates the observed air concentrations at the most monitoring stations (see Fig. B.15). As one can see from the regression analysis (Figs. B.15.b and B.16.b) the discrepancy of the modeling results and measurements mostly does not exceed a factor of two.

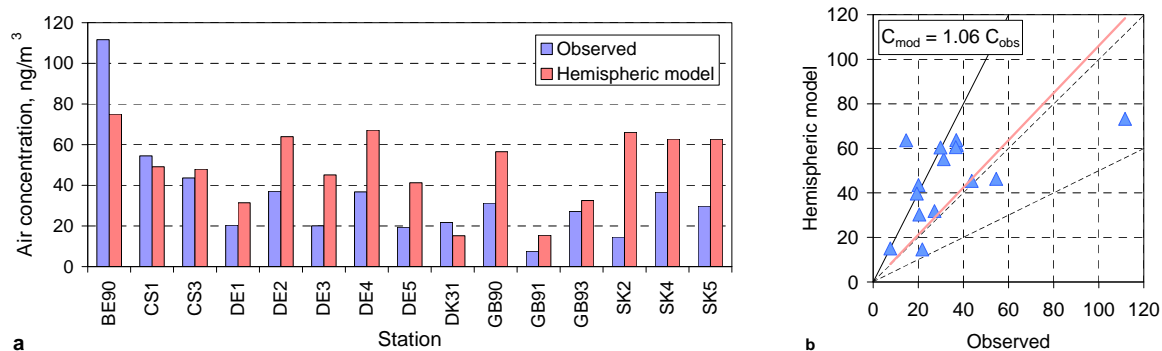


**Figure B.15.** Observed and modeled mean annual lead concentrations in the surface air,  $ng/m^3$

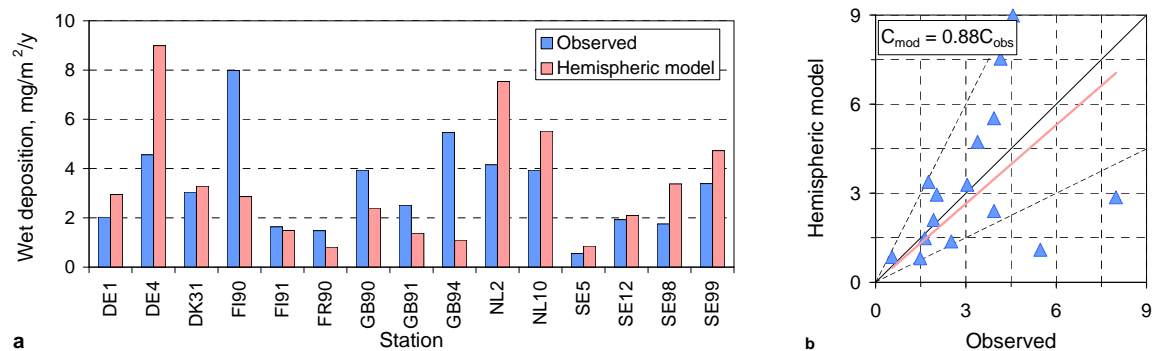


**Figure B.16.** Observed and modeled annual wet deposition fluxes, mg/m<sup>2</sup>/y

## References

- Berg T., A.-G. Hjellbrekke and J.E. Skjelmoen [1996]: Heavy metals and POPs within the ECE region. EMEP/CCC-Report 8/96. Norwegian Institute for Air Research.
- Bott A. [1993] The monotone area-preserving flux-form advection algorithm: Reducing the time-splitting error in two-dimensional flow fields. *Monthly Weather Review*, v.121, pp.2637-2641.
- Clappier A. [1998] A correction method for use in multidimensional time-splitting advection algorithms: Application to two- and three-dimensional transport. *Monthly Weather Review*, v.126, pp. 232–242.
- Easter R. C. [1993] Two modified versions of Bott's positive-definite numerical advection scheme. *Monthly Weather Review*, v.121, pp.297-304.
- Gusev A., Ilyin I., Petersen G., van Pul A., Syrakov D., and Pekar M. [2000] Long-range transport model intercomparison studies. EMEP/MSC-E Technical note 2/2000, Meteorological Synthesizing Centre – East, Moscow, Russia.
- Pacyna J. M., Scholtz M. T., and Li Y.-F. [1995] Global Budgets of Trace Metal Sources, *Environmental Reviews*, v.3, pp.145-159.
- Ryaboshapko A., Ilyin I., Gusev A., Afinogenova O., Berg T. and Hjellbrekke A.-G. [1999] Monitoring and modelling of lead, cadmium and mercury transboundary transport in the atmosphere of Europe. Joint report of EMEP centres: MSC-E and CCC, EMEP Report 3/99, Meteorological Synthesizing Centre – East, Moscow, Russia
- Ryaboshapko A., Ilyin I., Bullock R., Ebinghaus R., Lohman K., Munthe J., Petersen G., Segneur C., Wangberg I. [2001] Intercomparison study of numerical models for long-range atmospheric transport of mercury. Stage I: Comparison of chemical modules for mercury transformations in a cloud/fog environment. EMEP/MSC-E Technical report 2/2001, Meteorological Synthesizing Centre – East, Moscow, Russia
- Smolarkiewicz P. K. [1982] The three-dimensional Crowley advection scheme. *Monthly Weather Review*, v.110, pp.1968-1983.
- Sofiev M., Maslyayev A., and Gusev A. [1996] Heavy metal model intercomparison. Methodology and results for Pb in 1990. EMEP/MSC-E Report 2/96, Meteorological Synthesizing Centre – East, Moscow, Russia.
- Travnikov O. [2000] Uncertainty analysis of heavy metals long-range transport modelling. EMEP/MSC-E Technical note 9/2000, July, 2000.

## Annex C

## METEOROLOGICAL DATA FOR HEMISPHERIC MODELS

This annex to the report provides a brief description of the preparation of meteorological data for modeling.

Meteorological information for the pollution long-range transport modeling is prepared by a special system developed at Hydrometeorological Centre of Russia. This System of Diagnosis of the lower Atmosphere (SDA) is based on the experience gained in the development and maintaining of the system of meteorological information supply for regional HM and POP transport models of EMEP/MSC-E [Frolov *et al.*, 1994; Rubinstein *et al.*, 1997,1998; Frolov *et al.*, 1997a,b,c]. Below we will briefly describe main features of SDA and its main units.

### *Description of SDA basic principles*

SDA provides meteorological information for the Northern Hemisphere on the basis of the objective analysis of meteorological fields and data on the oceanic surface temperature fields. The horizontal resolution of SDA system is  $2.5^{\circ} \times 2.5^{\circ}$ . The vertical structure of SDA output information is presented by 9 layers in  $\sigma$ -coordinates (Table C.2). The list of meteorological parameters produced by SDA is presented in Table C.1.

**Table C.1.** List of meteorological parameters on longitude-latitude grid for the Northern Hemisphere with resolution of  $2.5^{\circ} \times 2.5^{\circ}$

Element	Type	Levels	Purpose
1. Wind velocity (zonal component)	Instantaneous	9 levels	atmospheric transport
2. Wind velocity (meridional component)	Instantaneous	9 levels	atmospheric transport
3. Analogue of vertical velocity in sigma-coordinate system (at the upper boundary of the layer)	Instantaneous	9 levels (at layer boundaries)	atmospheric transport
4. Temperature	Instantaneous	9 levels	reaction rates
5. Water vapour mixing ratio	Instantaneous	9 levels	volumes of gridcells, conversion of mixing ratios to volume concentrations
6. Large-scale cloudiness	Mean 6 hours	9 levels	wet scavenging
7. Convective cloudiness	Mean 6 hours	9 levels	wet scavenging
8. Precipitation	Accumulated during 6 hours	9 levels	wet scavenging
9. Coefficient of vertical turbulence	Instantaneous	4 lower levels (at layer boundaries)	mixing along the vertical
10. Monin-Obukhov length	Instantaneous	Surface	dry deposition
11. Friction velocity	Instantaneous	Surface	dry deposition
12. Surface pressure	Instantaneous	Surface	transport along the vertical, volumes of gridcells
13. Surface temperature	Instantaneous	Surface	natural emissions, soil-atmosphere exchange
14. Roughness length	Instantaneous	Surface	dry deposition
15. Soil moisture of surface	Instantaneous	Surface	POP transport in soil, atmosphere-soil exchange processes
16. Snow cover height	Instantaneous	Surface	natural emissions

**Table C.2.** Level numbers and  $\sigma$  values in the middle of the layers used in the SDA

<i>N</i>	1	2	3	4	5	6	7	8	9
$\sigma$	0.99	0.96	0.91	0.85	0.775	0.68	0.56	0.39	0.19

### ***SDA technological scheme***

In the developed system the preparation of data is made according to the following steps:

- The preparation of an annual set of initial information. Gridded data obtained by objective analysis made by Hydrometeorological Centre of Russia are used as initial information. These data include horizontal wind components, temperature, and humidity on the standard isobaric surfaces with 12-hour interval. Initial data can have some gaps and errors. The data of NCAR/NCEP reanalysis are used as additional input. For this case a special procedure is developed for the control and correction of possible errors in initial data.
- As the next step the hydrodynamic prognostic model of Hydrometeorological Centre of Russia (version T40L15) is run for 36-hour period with the initial data based on the previous step results and data of weekly analysis of the sea surface temperature and sea ice distribution. Modeling results are recorded for each 6-hour interval.
- To obtain the initial data for the next model run the prognostic fields produced by the model are mixed with results of the objective analysis. Weighted multipliers for each type of the field are specially selected by a number of numerical experiments.
- Computed meteorological parameters are interpolated to the required spatial structure (horizontal and vertical).
- In the new spatial structure diagnostic calculations of the analogue of vertical velocity and of all the parameters of the boundary layer are performed.
- The data are aggregated according to periods (4 periods round the clock) with possible subsequent compression.
- At the final step the analysis and control of the output meteorological information is performed.

The main units of SDA technological system are the following:

- unit of initial data preparation including the control and correction of errors,
- unit of preparation of boundary conditions,
- computational unit with the use of the hydrodynamic prognostic model,
- post-processing unit including the computations of the boundary layer parameters.

### ***Brief description of SDA units***

#### ***Hydrodynamic prognostic model***

There are two main aims of the use of the prognostic model in SDA. First of all, every 6 hours model fields of meteorological parameters are mixed up with diagnostic fields thus forming the initial data for the subsequent 6-hour model run. In addition to this, the major part of the parameters in Table C.1 are not measurable and hence are not included in the results of the objective analysis. Therefore, these parameters are computed by the model.

This model described in work [Kurbatkin et al., 1994] is based on numerical integration of a set of hydrodynamic equations for baroclinic atmosphere in hydrostatic approximation. Along the vertical  $\sigma$  coordinate is used, where  $\sigma = P/P_S$ ,  $P$  is atmospheric pressure and  $P_S$  is surface pressure. The set of equations is as follows:

$$\frac{\partial \bar{v}}{\partial t} + \bar{v} \cdot \nabla \bar{v} \sigma \frac{\partial \bar{v}}{\partial \sigma} + f \cdot \bar{k} \times \bar{v} + \nabla \Phi + RT_v \nabla \ln p = \bar{P}_H \quad (\text{C.1})$$

$$\frac{\partial \Phi}{\partial \sigma} = -\frac{RT_v}{\sigma} \quad (\text{C.2})$$

$$\frac{\partial T'}{\partial t} \left( \frac{\partial p}{\partial \sigma} \right) + \nabla \cdot (\bar{v} \frac{\partial p}{\partial \sigma}) + \frac{\partial}{\partial \sigma} \left( \sigma \frac{\partial p}{\partial \sigma} \right) = 0 \quad (\text{C.3})$$

$$\frac{\partial T'}{\partial t} + \nabla \cdot (\bar{v} T') - (\nabla \cdot \bar{v}) T' + \sigma \frac{\partial T_v}{\partial \sigma} - \frac{\chi \omega}{p} T_v = P_T \quad (\text{C.4})$$

$$\frac{\partial q}{\partial t} + \nabla \cdot (\bar{v} q) - (\nabla \cdot \bar{v}) q + \sigma \frac{\partial q}{\partial \sigma} = P_q \quad , \quad (\text{C.5})$$

where  $\bar{v}$  is wind velocity vector;  $p$  is pressure;  $\bar{k}$  is unit vector;  $\Phi$  is geopotential;  $R$  is gas constant for dry air;  $q$  is water vapour mixing ratio.  $T_v$  is virtual temperature,  $T'$  is deviation of temperature from standard profile  $T_0(\sigma)$ . Terms  $P_H$ ,  $P_T$  and  $P_q$ , stand for non-adiabatic or subgrid processes. These terms are derived by means of parameterizations. Term  $\sigma$  means analogue of velocity in vertical direction.

The equation set is solved by the spectral method with triangle truncation on the hemispheric scale in the atmospheric layer between the Earth surface ( $\sigma = 1$ ) and the upper level ( $\sigma = 0$ ).

The computations are carried out by T40 version of the model corresponding to the spatial resolution 2.5 degree on Gaussian (non-uniform along latitude) grid. Along the vertical the atmosphere is divided into 15 layers. Basic prognostic and diagnostic variables of the model are calculated for the middle of each layer. Values of vertical velocity analogues and radiation fluxes are calculated at the layer boundaries. Specific  $\sigma$  values at the basic model levels are presented in Table C.3. As the scheme of integration over time, the semi-implicit scheme of Nemchinov-Sadokov-Rober is used. This model considers basic physical processes within the atmosphere and at the underlying land surface important for large-scale numerical weather forecast and atmospheric circulation modeling. Below a brief description of these processes will be given.

**Table C.3.** Level numbers and  $\sigma$  values in the middle of the layers used in the hydrodynamic prognostic model

N	15	14	13	12	11	10	9	8
$\sigma$	0.99	0.96	0.91	0.85	0.77	0.68	0.59	0.5
N	7	6	5	4	3	2	1	
$\sigma$	0.45	0.34	0.26	0.19	0.15	0.07	0.05	

Horizontal macroturbulence. For the parameterization of horizontal turbulence processes a linear scheme of a fourth order is used. In this model version it is assumed that the horizontal diffusion coefficient has the following value:  $K_H = 8 \times 10^{14} \text{ m}^2/\text{s}$ .

Vertical diffusion transport. In the free atmosphere fluxes of the impulse, enthalpy and moisture are calculated on the basis of  $K$ -theory. The coefficient of vertical turbulence is determined by the

hypothesis on mixing length. It is supposed that this coefficient depends on the wind shear and static stability. The parameterisation for the surface layer is based on Monin-Obukhov similarity theory.

Large-scale condensation. The parameterization is based on the fact that precipitation takes place when the humidity exceeds critical values which for “warm” clouds (with the temperature at the upper boundary higher than  $-12^{\circ}\text{C}$ ) is 2 g/kg. In subcooled clouds all the condensed moisture precipitates. Besides the effect of rain drops evaporation is taken into account and corrections for negative humidity values resulted from approximation errors are made.

Convective processes. In the parameterization of wet convective processes the scheme of Kuo penetrating convection is used. Vertical and horizontal convective turbulent fluxes of the momentum, enthalpy and moisture are not considered in this version of the model, since it is supposed that their impact on the atmospheric circulation is negligible.

Solar radiation. The parameterization scheme for radiation processes considers main effects of solar radiation on the atmosphere and ground surface. The effect of cloudiness and aerosol are considered in detail. The lower troposphere is the field of main interest in view of supplying the models with the data for computation of pollutant transport. For the lower troposphere the diurnal variation plays an essential role in the reproduction of circulation. It inflicts a considerable impact on near surface processes and therefore it is introduced in diurnal and annual variations of short-wave length radiation.

Calculations of land surface temperature. Temperature of the land surface is a prognostic variable. It is assumed that land is represented by a thin layer (0.42 m) of soil where the local exchange of moisture and heat with the atmosphere takes place. Temperature is calculated on the basis of heat balance conditions, including long-wave and short-wave radiation fluxes, latent and sensible heat turbulent fluxes and heat flux to the surface. Energy transfers because of water freezing or snow melting are considered as well.

Parameterisation of land hydrology. It is assumed that soil is divided into two layers. While calculating moisture variations in the upper soil layer, snow melting, moisture input due to precipitation and its diminishing due to evaporation as well as diffusive exchange with the lower layer are taken into account. The horizontal transport of moisture in soil is absent.

## ***Boundary conditions***

At the upper and lower boundaries kinematic conditions are prescribed:

$$\sigma = 0 \text{ at } \sigma = 0 \text{ and } \sigma = 1$$

and at  $\sigma = 0$  the condition of absence of heat, moisture and impulse fluxes is also used.

As lower boundary conditions we use fields of the surface temperature (recalculated in the computation process), ocean surface temperature (prescribed), *sea ice distribution (prescribed)*, temperature at the depth of  $D = 0.42$  m ( $T_D$ ) (prescribed), soil moisture content (recalculated in the computation process), snow cover height (prescribed). In addition, fields of the roughness height and surface albedo (corrected for ice and snow in the course of computations) are used. Fields of sea ice distribution and ocean surface temperature were provided by National Centre of Environmental Predictions (the USA NCEP/NOAA).

### Computation of boundary layer parameters

The main task of computation of boundary layer parameters is the definition of vertical structure of meteorological variables inside the atmospheric boundary layer (ABL), up to the height about 1500 m and computation of vertical turbulent diffusion coefficients on four lower levels, friction velocity, and Monin-Obukhov length scale.

The problem is to determine the vertical structure of ABL on the basis of meteorological variables (horizontal wind speed components  $(u, v)$ , air temperature  $T$  and its specific humidity  $q$ ) at the prescribed boundaries:

ABL upper boundary:

$$z = h \sim 1500 \text{ m } (\sim 850 \text{ hPa}): \quad u = u_h, \quad v = v_h, \quad T = T_h, \quad q = q_h \quad (\text{C.6})$$

underlying surface,

$$z = 0 \text{ (or } z = z_0 \text{ - roughness level)} \quad u = 0, \quad v = 0, \quad T = T_0, \quad q = q_0 \quad (\text{C.7})$$

It is assumed that fields of wind speed, temperature and air humidity are statistically stationary and statistically uniform along the horizontal. It is also assumed that within ABL it is possible to neglect vertical variations of radiation heat flux. On these assumptions all point statistical characteristic of meteorological fields (mean values of  $u$ ,  $v$ ,  $T$ ,  $q$  and characteristic of turbulence) should be directly dependent only on the height above the underlying surface. Functional expressions for these dependencies are determined from equations for momentum, heat and moisture transport. Hence the formulated model can be interpreted as a hydrodynamic interpolator of meteorological variables within ABL [Zilitinkevich et al., 1978]:

$$f(v - v_g) + \frac{1}{\rho} \frac{\partial \tau_x}{\partial z} = 0, \quad (\text{C.8})$$

$$-f(u - u_g) + \frac{1}{\rho} \frac{\partial \tau_y}{\partial z} = 0, \quad (\text{C.9})$$

$$\frac{\partial F_T}{\partial z} = 0, \quad (\text{C.10})$$

$$\frac{\partial F_q}{\partial z} = 0. \quad (\text{C.11})$$

where  $\tau_x = -\rho \overline{u'w'}$  and  $\tau_y = -\rho \overline{v'w'}$  are the components of vertical momentum flux;

$F_T = \rho c_p \overline{T'w'}$  and  $F_q = \rho \overline{q'w'}$  are vertical turbulent fluxes of heat and moisture, respectively;

$u$ ,  $v$ , and  $w$  are wind velocity components;

$T$  is air temperature;

$q$  is specific humidity;

$\rho$  is air density;

$c_p$  is air specific heat capacity at constant pressure;

$u_g$  and  $v_g$  are geostrophic wind components;

$f$  is Coriolis parameter;

$P$  is atmospheric pressure. The prime sign indicates turbulent fluctuations and the bar above means statistical averaging.

In order to close the equation set (C.8 – C.11) first order closure scheme is used. First order closure schemes determine the link between vertical gradients of substances and their vertical fluxes:

$$\left. \begin{aligned} \tau_x / \rho &= -\overline{u'w'} = k_m \partial u / \partial z \\ \tau_y / \rho &= -\overline{v'w'} = k_m \partial v / \partial z \end{aligned} \right\}, \quad (C.11)$$

$$F_T / (\rho c_p) = \overline{T'w'} = -k_T (\partial T / \partial z + g / c_p), \quad (C.13)$$

$$F_q / \rho = \overline{q'w'} = -k_q \partial q / \partial z. \quad (C.14)$$

where  $g/c_p$  is adiabatic lapse rate;  
 $g = 9.8 \text{ m/sec}^2$  is gravity acceleration;  
 $c_p = 1 \cdot 10^{-3}$  is specific air heat capacity at constant pressure, J/(kg·K);  
 $k_m$ ,  $k_T$  and  $k_q$  are turbulent mixing coefficients for momentum, heat and moisture, respectively.

Following commonly accepted practice, it is assumed that turbulent mixing coefficients for heat and moisture are equal:

$$k_T = k_q \equiv k_H, \quad (C.15)$$

Formulas used for calculation of the coefficients in Ekman layer are as follows [Smith, 1993]:

$$k_m = l_m^2 f_m(Ri) \left| \frac{\partial \mathbf{u}}{\partial z} \right|, \quad (C.16)$$

$$k_H = l_H l_H f_H(Ri) \left| \frac{\partial \mathbf{u}}{\partial z} \right|, \quad (C.17)$$

where  $Ri$  is the local Richardson number,

$$Ri = \frac{\partial B / \partial z}{|\partial \mathbf{u} / \partial z|^2} = \frac{g[(1/T)(\partial T / \partial z + g / c_p) + 0.61 \partial q / \partial z]}{|\partial \mathbf{u} / \partial z|^2}, \quad (C.18)$$

Stability functions  $f_m$  and  $f_H$  are computed according to the formulas:

$$f_m = f_H = 1 / (1 + c_1 Ri) \quad \text{at } Ri \geq 0, \quad (C.19)$$

$$\left. \begin{aligned} f_m &= 1 - c_1 Ri / [1 + (c_1 / c_2)(l_m / l_H)(-Ri)^{1/2}] \\ f_H &= 1 - c_1 Ri / [1 + (c_1 / c_3)(l_m / l_H)(-Ri)^{1/2}] \end{aligned} \right\} \quad \text{at } Ri < 0. \quad (C.20)$$

Here  $l_m$  and  $l_H$  are mixing lengths at neutral stratification, derived from the work [Blackadar, 1962]:

$$l_m(z) = \kappa z / (1 + \kappa z / \lambda_m), \quad (C.21)$$

$$l_H(z) = \kappa z / (1 + \kappa z / \lambda_H), \quad (C.22)$$

where  $c_1 = 10$ ,  $c_2 = 4$ ,  $c_3 = 25$  are empirical coefficients;  
 $\kappa = 0.4$  is von Karman constant;  
and  $\lambda_m$  and  $\lambda_H$  are the asymptotic values of mixing length, proportional to the boundary layer depth.  
In this work it is assumed that  $\lambda_m = \lambda_H = 0.2 \cdot h = 0.2 \times 1500 \text{ m} = 300 \text{ m}$ .

The surface layer is described on the basis of Monin-Obukhov similarity theory. According to the theory vertical gradients of wind velocity  $\partial \mathbf{u} / \partial z$ , of potential temperature  $\partial \theta / \partial z$  and specific humidity  $\partial q / \partial z$  are described by dimensionless functions of dimensionless height  $\zeta = z/L$ :

$$\frac{\partial \mathbf{u}}{\partial z} = \frac{\mathbf{u}_*}{\kappa z} \varphi_m(\zeta), \quad (4.1)$$

$$\frac{\partial \theta}{\partial z} = \frac{\partial T}{\partial z} + \frac{g}{c_p} = \frac{T_*}{\kappa z} \varphi_T(\zeta), \quad (C.23)$$

$$\frac{\partial q}{\partial z} = \frac{q_*}{\kappa z} \varphi_q(\zeta), \quad (C.24)$$

where  $\mathbf{u}_*$ ,  $T_*$  are  $q_*$  are the scaling parameters for velocity (friction velocity), temperature and air moisture.

Traditionally equations for ABL refer to z-coordinate system where vertical distances are determined in geometrical units. At the same time the system supplying pollution transport models with meteorological information uses  $\sigma$ -levels. In this connection ABL equations are rewritten in the  $\sigma$ -system. The problem is solved by the iteration method with subsequent determination of coefficients dependent on the solution of the system. The iteration process is continued until the difference between solutions on the two subsequent iterations is less than a small threshold level.

### ***Correction of precipitation fields***

Precipitation amounts in SDA are computed by the hydrodynamical model. At the same time there is a network of more than 4000 synoptic stations measuring precipitation amounts. Special procedure was developed in order to use these station data for correction of modeled precipitation amounts. The procedure includes the following stages:

- Control of station data and distribution of them within equal temporal intervals
- Objective analysis of atmospheric precipitation
- Correction of vertical distribution of precipitation amounts.

Objective analysis is based on approach of optimal interpolation. The details of the correction procedure one can find in work [Rubinstein et al., 2002].

## References

- Blackadar A.K. [1962] The vertical distribution of wind and turbulent exchange in a neutral atmosphere. *J. Geophys. Res.*, v.67, No. 8, pp. 3095-3102.
- Frolov A., A.Vaznik, E.Astahova, J.Alferov, D.Kiktev, I.Rosinkina and K.Rubinstein [1997a] A System of diagnosis of lower atmosphere for monitoring transboundary pollutant transport. *Meteorology and Hydrology*, No 4, pp.5-15.
- Frolov A., A.Vaznik, E.Astahova, J.Alferov, D.Kiktev, I.Rosinkina and K.Rubinstein [1997b] A System of diagnosis of lower atmosphere for monitoring transboundary pollutant transport. The main algorithms. *Meteorology and Hydrology*, No. 5, pp.5-13.
- Frolov A., A.Vaznik, E.Astahova, J.Alferov, D.Kiktev, I.Rosinkina and K.Rubinstein [1997c] A System of diagnosis of lower atmosphere for monitoring transboundary pollutant transport: Precipitation and clouds. *Meteorology and Hydrology*, N.6, pp.5-15.
- Frolov A., K.Rubinstein, I.Rosinkina, A.Vajnik, D.Kiktev, E.Astachova and J.Alferov [1994] A System of diagnosis of lower atmosphere for of transboundary air pollutant transport. EMEP/MSC-E and RHMC report 1/94.
- Kurbatkin G.P., Degtarev A.I. and A.V.Frolov [1994] Spectral model of the atmosphere, initialization and database for numeric weather forecasts. – Sn.-P., Hydrometeoizdat, p.184.
- Rubinshtein K. G., Tsyrlunikov M. D., Bagrov A. N and Alferov Yu. V. [2002]. Correction of precipitation fields from observational data for preparing information for pollution transport models. *Meteorology and Hydrology*, 10, pp.34 - 50 (in Russian).
- Rubinstein K. and D.Kiktev [1998] Comparison System of the Atmospheric Lower-Layer Diagnostic System(SDA) for Pollution Transfer Modeling of MSC - East(Moscow) and MSC - West(Oslo). Proceeding of International Conference of Air Pollution Modeling and Simulation. Paris, 26-29 October 1998.
- Rubinstein K., Frolov A., Vaznik A., Astachova E., Rosinkina I., Kiktev D. and J.Alferov [1997] Diagnostic System of Atmosphere Lower-Layer for Pollution Transfer Modelling. *Revista. International de Contaminational. Ambienal.* v.13, No. 1, pp.23-34.
- Smith R.H.B. [1993] Subsurface, surface and boundary layer processes. Unified Model Documentation Paper No. 24, Climate Research, Meteorological Office, Bracknell, UK, 54 pp.
- Zilitinkevich S.S., A.S. Monin and D.V. Chalikov [1978] Interactions of the atmosphere and the ocean. In: *Physics of the Ocean.* v. 1 Ocean Geophysics. Moscow, Nauka, pp. 208 - 339, (in Russian).

## Annex D

### SENSITIVITY ANALYSIS OF THE SOIL MODULE

The behaviour of persistent organic pollutants in such environmental compartments as soil, vegetation and seawater strongly influence on their long-range transport. However, POP behaviour in these media is determined by a number of processes of different importance. For the development of POP transport multicompartment models the investigation of the influence of processes affecting POP behaviour in environmental compartments (that is, ***sensitivity study with respect to processes***) is of major importance. In this Annex we perform sensitivity study with respect to some processes governing POP behaviour in soil. The behaviour of POPs in seawater compartment will be considered in the Annex E.

The processes of accumulation in and volatilization from soil are of importance for some POPs such as PCBs, PCDD/Fs and others. In particular, according to model calculations [Shatalov *et al.*, 2001], re-emission PCB flux from soil in Europe in the late 1990s is comparable with anthropogenic emissions and became in some countries a main source of air contamination together with transboundary transport.

The description of behaviour of POPs in soil and of atmosphere/soil exchange process used in MSCE-POP model is rather simplified and does not take into account some processes having considerable influence on POP fate in soil (transport with the dissolved organic carbon, dynamic redistribution between different soil phases, convection fluxes along macropores, leaching to rivers, bioturbation and others). At present the work aimed at refinement of model description of some processes governing the behaviour of POPs in soils is ongoing (see [Vassilyeva and Shatalov, 2002]). Here we consider the results of numerical experiments evaluating possible influence of vertical transport with dissolved organic carbon and dynamic redistribution of POPs between different phases in soil. More detailed analysis of these processes and choice of parameters used for such evaluation are considered in the above cited report.

***Transport with dissolved organic carbon.*** Dissolved organic carbon (DOC) is a component of soil solute for almost all soil types. The most interesting fraction of DOC is mobile dissolved organic carbon, which can be readily transported along soil micro- and macropores. DOC concentration in soil solute depends on soil type and, in particular, on fraction of organic content in soil of given type. As a first approximation the quantity of mobile organic carbon is about 1% of total organic carbon content in soil.

***Redistribution between different soil phases.*** In the context of high storage capacity of the soil solid phase for some POPs, the processes of their sorption and desorption to soil solution are of a particular importance. At present in the model a concept of instantaneous equilibrium between dissolved POP fraction and that sorbed on solid soil organics is used. However, recently more and more evidences appear that real sorption-desorption exchange between POPs and soil differ drastically from equilibrium ones. It is connected with soil organics heterogeneity and low availability of POPs located in micropores. Due to a high volume of POP molecule and its continuous interaction with the hydrophobic surface while moving inside the soil organics micropores, the establishment of thermodynamic equilibrium between the dissolved and sorbed phase requires considerable time (usually from one to six months). POP desorption in the inverse direction is also non-uniform and delayed.

## D.1. Model assumptions

To evaluate the influence of the above processes on soil concentrations of POPs (and, as a consequence, on the process of atmosphere/soil gaseous exchange) numerical experiments simulating processes of POP accumulation in soil and their re-volatilization from soil were performed. Calculations were carried out for the simplified environmental configuration consisting of one atmospheric layer (representing surface atmospheric layer in the real environment) and five soil layers of different thickness (Figure D.1).

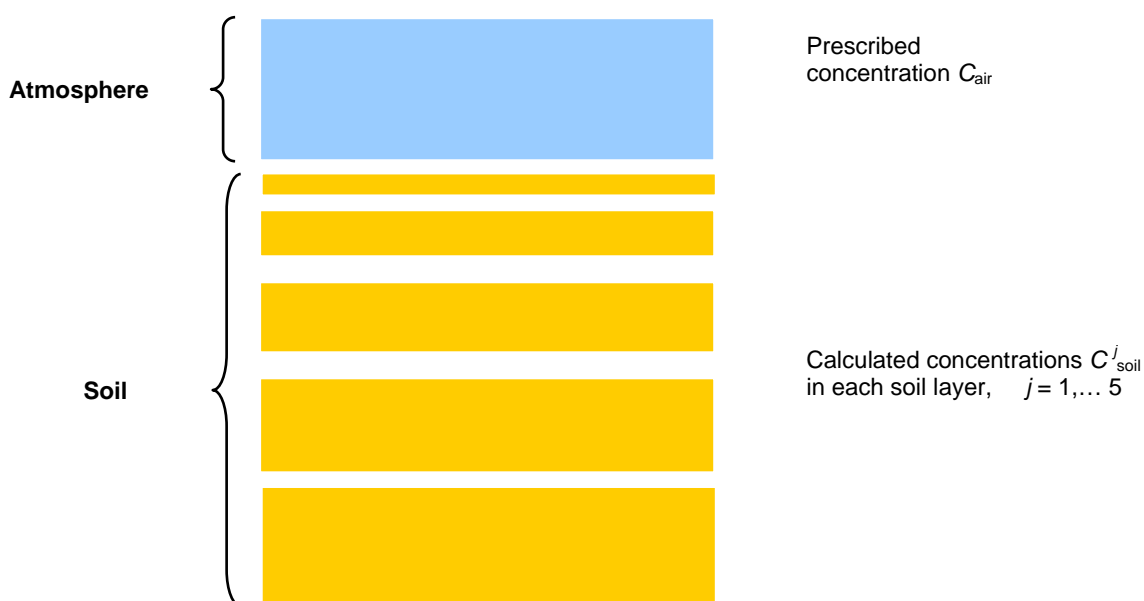


**Figure D.1.** Simplified model of the environment used in sensitivity study of selected soil processes

In simulations concentration ( $C_{air}$ ) in the atmosphere was prescribed at some conventional level and then soil concentrations in all five soil layers ( $C_{soil}^j$ ) were computed (more detailed description of numerical experiments is given below).

Modeling was carried out with the use of the soil module of the MSCE-POP model (the description can be found on <http://www.msceast.org/pops/media.html>). Initially it was taken from [Jacobs and van Pul, 1996] and based on the theory of [Jury et al., 1983].

According to this scheme, a pollutant entering soil from the atmosphere is distributed between the gaseous ( $f_{air}$ ), liquid ( $f_{liquid}$ ) and solid ( $f_{solid}$ ) soil phases in accordance with equilibrium coefficients  $K_{AW}$  and  $f_{OC}K_{OC}$ , hereby the equilibrium is set up immediately. At present the scheme is complemented with the fraction of dissolved organic matter ( $f_{DOC}$ ) and with the fraction of the chemical non-equilibrium sorbed by solid phase ( $f_{non-equil}$ ) or low available with individual degradation rate (Fig. D.5).

The share of a substance sorbed by DOC is calculated by the partition coefficient of equilibrium partitioning between DOC and the dissolved phase  $f_{DOC}K_{DOC}$ . In this context it is assumed that the DOC fraction is 1% of total organic matter in soil  $f_{DOC} = 0.01f_{SOM}$ .  $K_{DOC}$  is assessed through the linear correlation between logarithmic  $K_{DOC}$  and  $K_{OW}$  has been determined for the majority of POPs. These dependences obtained by J. Poershman and F.D. Kopinke [2001] for PAHs and PCBs are respectively:

$$\log K_{DOC} = 0.98 \log K_{OW} - 0.39$$

$$\log K_{DOC} = 0.93 \log K_{OW} - 0.54.$$

Note that the pollutant associated with DOC is transported with the soil solution.

According to model assumptions the solid non-equilibrium sorbed fraction is sorbed by 70% of soil organic matter. The rest organic chemical is equilibrium sorbed by the remaining 30% of soil organic matter. The exchange between these phases takes place according to the first order kinetic equation with characteristic time  $T_{non-equil,50} = 1$  year. It is also assumed that the non-equilibrium sorbed fraction degrades “slowly”. Its degradation is practically coincides with the degradation rate of humus itself with half-life 25 years. A pollutant equilibrium sorbed by SOM is “rapidly” degraded with the rate constant depending on an individual pollutant.

The scheme of a pollutant distribution between different soil components is shown in Figure D.2.

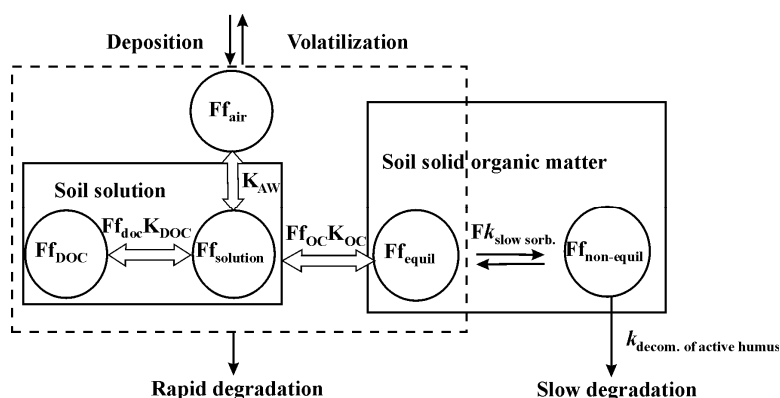


**Figure D.2.** Model realization of POP partitioning between soil components and its degradation

Following the scheme used, the pollutant migration over the soil horizon is conditioned by diffusion processes in the liquid and gaseous phase and by the transport of the real dissolved and sorbed to DOC fractions of a pollutant together with the liquid flow  $J_w$ . The vertical soil profile is represented by 5 calculation layers with boundary on (from top to bottom) 1) - 0.01, 2) - 0.05, 3) - 0.2, 4) - 0.8 and 5) - 3 cm.

The general formulation of the numerical problem was as follows. PCB-153 was selected as a characteristic POP, which physical-chemical properties were used in the experiment. This is due to the fact that the properties of this indicator congener are often used for calculations of the long-range transport of PCB mixture [Pekar *et al.*, 1998].

Besides it was demonstrated [Shatalov *et al.*, 2001] that soil is the most important accumulating compartment in calculations of PCB transport. Physical-chemical properties of PCB-153 at temperature 25°C can be found in [Shatalov *et al.*, 2001]. Modeling was performed at soil organic carbon content  $f_{OC} = 5\%$  typical of usual chernozem. The wet precipitation flux was assumed equal to  $J_w = 10$  cm/year.

In calculations two periods were considered – the accumulation time (5 years), during which PCB atmospheric concentration was 1 ng/m<sup>3</sup> and the clearance interval with air concentration assumed equal to zero. It was considered that pollutant input to soil takes place only due to gas exchange with the atmosphere. The calculations resulted in the profile of pollutant vertical distribution. This profile allows drawing conclusions about the penetration depth variation and about the dependence on the involvement to the model of the considered processes.

## D.2. Evaluation of the effect of POP fraction sorbed by dissolved organic matter

To assess the DOC effect on POP transport, the calculation results with and without consideration of DOC sorbed fraction are considered below (Fig. D.3).

The comparison of the curves depicted in Figure D.3 indicates that the consideration of DOC phase increases the pollutant concentration in soil as much as 1.75 times during the accumulation period (5 years). It is explained by more intensive transport of a pollutant sorbed on DOC together with the water flow.

This process also significantly affects pollutant distribution down to soil profile. As evident from Figures D.4.a and b, the consideration of DOC phase slightly increases the depth of POP penetration. For example, by the end of 5<sup>th</sup> year the concentration in the third layer (Fig. D.4.a) is 5 times higher than that obtained without DOC phase (Fig. D.4.b).

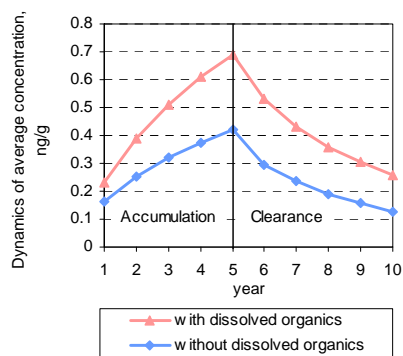


**Figure D.3.** The comparison of calculation results of POP accumulation in soil and soil clearance with and without DOC consideration

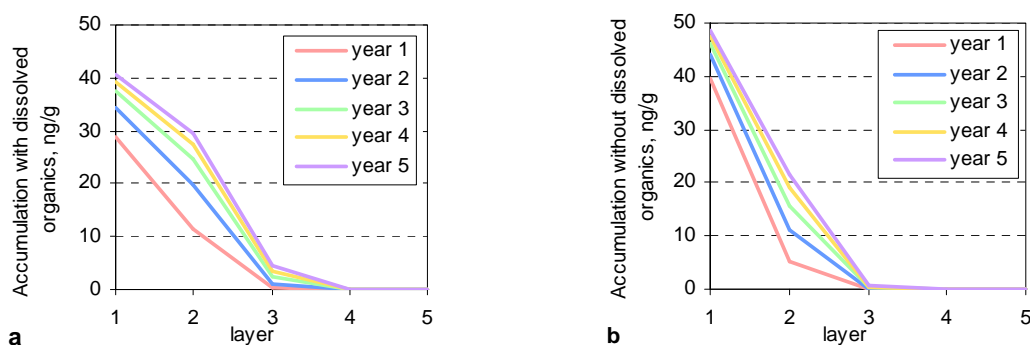


**Figure D.4.** POP concentrations in the soil layers (1-5) during the accumulation period (5 years). Calculations with (a) and without (b) DOC consideration

The dynamics of vertical profile within the clearance period is demonstrated by Figure D.5. Calculations show that at the stage of clearance the concentration of DOC phase considerably slows down soil clearance (Fig. D.5.a and b). With the consideration of DOC phase (Fig. D.5.a) as before the concentration in the 3<sup>rd</sup> layer is 5 times higher than that obtained without DOC consideration (Fig. D.5.b).

Thus the numerical experiment demonstrated that the consideration of POP sorption by dissolved organics enhances POP migration down to soil profile and influences their accumulation in soil.

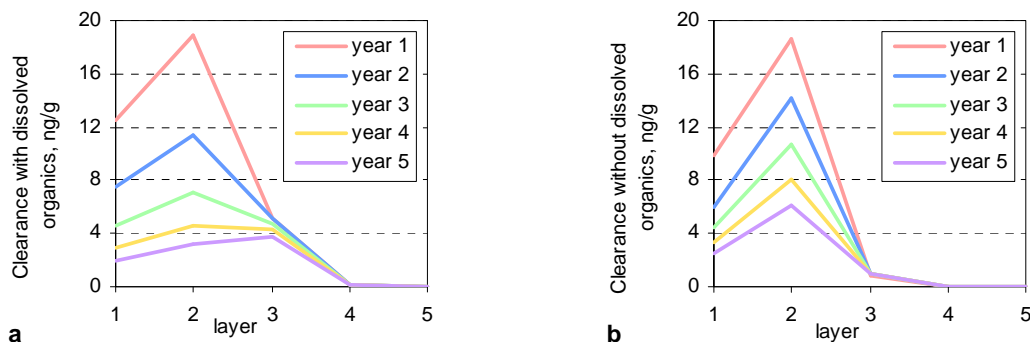


**Figure D.5.** Pollutant concentrations in soil layers (1-5) during clearance period (5 years). Calculations performed with (a) and without (b) DOC consideration

### D.3. Evaluation of the effect of non-equilibrium sorbed POP fraction

To evaluate the influence of non-equilibrium sorbed POP fraction the description of a kinetic process of redistribution between equilibrium and non-equilibrium soil fractions was added to the model. Calculation results with and without consideration of this fraction are presented by plots in Figure D.6. During 5-year accumulation period with the consideration of this fraction at first the process proceeds slower but by the end of the period it is slightly more rapid than without the consideration of this fraction.

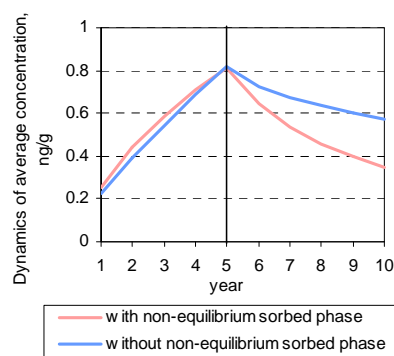


**Figure D.6.** The comparison of calculation results with and without consideration of non-equilibrium sorbed POP fraction

An additional calculation run of PCB accumulation during 20-year's period shows that the consideration of the low available fraction leads to a tangible increase of soil capacity resulted from the low intensity of degradation processes in this phase. As to the clearance period the consideration of the non-equilibrium sorption leads to slower decline of the pollutant concentration. In particular, by the end of the period the difference reaches 1.7 times.

The consideration of this fraction also influences the pollutant vertical distribution in soil (Fig. D.7). As follows from Figures D.7.a and b the consideration of the non-equilibrium fraction slightly increases the penetration depth of the pollutant. For instance, by the end of accumulation period (5<sup>th</sup> year), the POP concentration in the 3<sup>rd</sup> layer with the consideration of the non-equilibrium sorbed fraction (Fig. D.7.a) is somewhat higher than those obtained without its consideration (Fig. D.7.b). As to the 1<sup>st</sup> layer the pattern is reverse.

The dynamics of vertical profile of soil contamination during the clearance period is presented by plots in Figure D.8. The comparison of these plots indicated that the consideration of the discussed phase substantially decelerates soil self-clearance. It can be mentioned that with the consideration of this fraction the concentration in the 1<sup>st</sup> layer calculated with allowance of non-equilibrium sorption (Fig. D.8.a) is 5 times higher than without the fraction consideration (Fig. D.8.b).

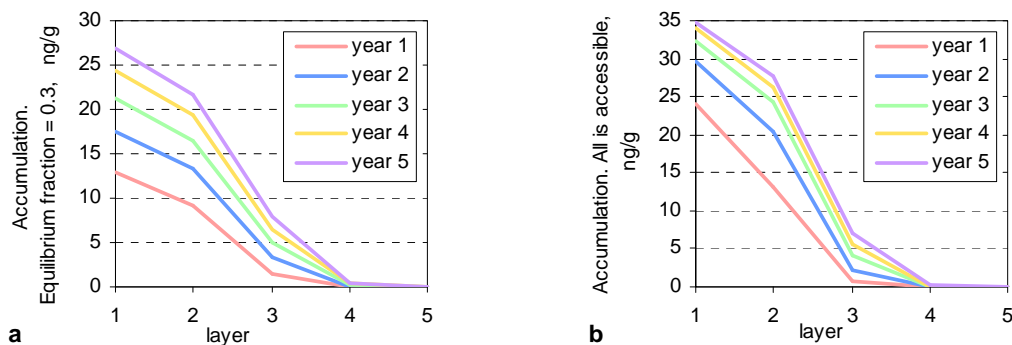


**Figure D.7.** POP concentration in the soil layers (1-5) during the accumulation period (5 years). Calculations with (a) and without (b) consideration of the non-equilibrium sorbed POP fraction

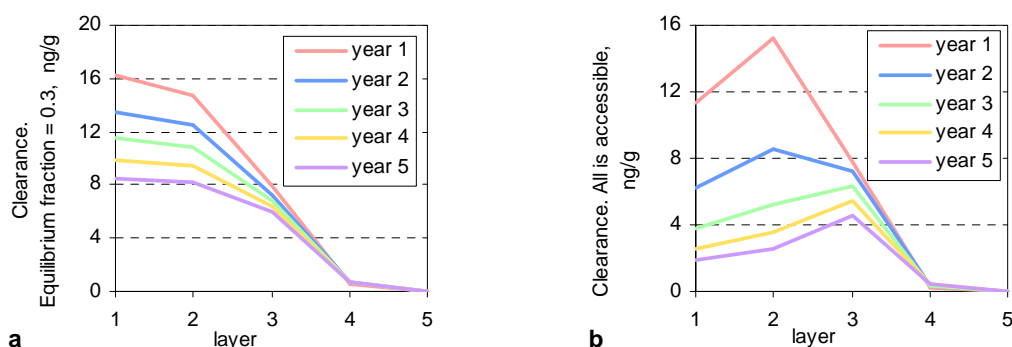


**Figure D.8.** POP concentrations in the soil layers (1-5) at the stage of clearance (5 years). Calculations with (a) and without (b) consideration of the low available fraction

These results are in agreement with the literature data concerning the delayed self-purification of soil contaminated with POPs and with long preservation of the aged POP residues [Alexander, 1994], as well as with the results of durated revolatilization of POPs from soil [Duyzer, van Oss, 1997].

Thus the consideration of kinetics of POP sorption by particulate soil organic matter appreciably changes the pollutant vertical distribution, particularly during the clearance period, what increases this period substantially.

#### D.4. Model refinement

On the basis of the above described investigations a scheme describing POP redistribution between different phases in soil and vertical transport with dissolved organics was included into MSCE-POP model description. This scheme includes the following POP phases in soil:

- gaseous (POP in the intercellular air);
- dissolved;
- sorbed on dissolved organic carbon;
- sorbed on readily accessible soil organics fraction;
- sorbed on potentially accessible soil organics fraction.

The model assumes the concept of instantaneous equilibrium between all phases but the last. The exchange between two last phases is described by a kinetic equation of first order.

## References

- Alexander M. [1994] Biodegradation and bioremediation. Academic press, San Diego and others. p.302.
- Duyzer J.H., van Oss R.F., Verhagen H.L.M., Vervaart M. and B.Boekee [1997] Determination of deposition parameters of a number of persistence organic pollutants by laboratory experiments. TNO-report TNO-MEP-R97/150.
- Jacobs C.M.J. and W.A.J. van Pul [1996] Long-range atmospheric transport of persistent organic pollutants, I: Description of surface - atmosphere exchange modules and Implementation in EUROS. National institute of public health and the environment, Bilthoven, the Netherlands. Report No722401013.
- Jury W.A., W.F.Spencer and W.J.Farmer [1983] Behaviour assessment model for trace organics in the soil. *Environ. Qual.* v.12, pp.558-564.
- Poerschmann J. and F.-D. Kopinke [2001] Sorption of very hydrophobic Organic Compounds (VHOCs) on dissolved humic organic matter (DOM). 2. Measurement of sorption and application of Flory-Huggins concept to interpret the data. *Environ. Sci. Technol.*, v.35, pp. 1142-1148.
- Shatalov V., A.Malanichev, N.Vulykh, T.Berg and S.Manø [2001] Assessment of POP transport and accumulation in the environment. EMEP Report 4/2001, Moscow.
- Vassilyeva G. and V. Shatalov [2002] Behaviour of persistent organic pollutants in soil. MSC-E Technical Note 1/2002.



## Annex E

## SENSITIVITY ANALYSIS OF THE OCEANIC TRANSPORT MODULE

In this Annex we present sensitivity studies with respect to some processes governing POP behaviour in soil and seawater environmental compartments.

The World Ocean is one of the most capacious medium for some persistent organic pollutants. POPs enter the seawater mainly from the atmosphere by depositions and gaseous exchange as well as with river run-offs. Concentration field variations in the World Ocean take place due to seawater horizontal and vertical currents, POP partitioning between the dissolved phase and phases sorbed of different suspended particles and dissolved organic compounds, deposition of sorbed phases together with sedimentating particles, resuspension processes in the near bottom layers, degradation and a number of other processes. With the availability of ice coverage on the sea surface, POPs from the atmosphere are accumulated on the ice surface and drift with ice over large distances then with melting water enter the marine environment.

The current version of the hemispheric model includes the following processes describing the behaviour of a pollutant in the marine environment

- horizontal currents and vertical motion of water masses,
- distribution over the upper mixing layer, which changes dynamically,
- three-dimensional turbulent diffusion,
- POP partitioning between the dissolved phase and phases adsorbed on suspended particles,
- POP sedimentation with particles,
- influence of ice cover on POP transport,
- POP degradation.

In the current version of the model influence of ice cover, sedimentation and partitioning between different POP phases in seawater are described in quite a rough way. However, they can inflict an appreciable impact on some POPs budget ratios in the seawater. Below we present the investigation of model sensitivity to POP partitioning between different phases and processes connected with sea ice environment (simplified version). In this section we evaluate model sensitivity with respect to processes of POP partitioning in the marine environment and to consideration of ice cover.

### E.1. POP partitioning between different phases

**Model assumptions.** POP redistribution between the dissolved phase and the phase associated with particles essentially affects the dynamics of POP concentration fields in the marine environment. Under the condition of instantaneous phase equilibrium establishment the relation between particulate and dissolved phases is as follows:

$$c_p = k^p \cdot c_d. \quad (\text{E.1})$$

In its turn  $k^p$  may be estimated by the expression:

$$k^p = k_p^o K_p c_{prt} \quad (\text{E.2})$$

where  $k_p^o$  is fraction of organic matter in a particle;

$K_p$  is equilibrium constant for sorption/desorption processes (proportional to octanol-water coefficient  $K_{ow}$ );  
 $c_{prt}$  is particle concentration.

The concentration of sedimentating particles in the seawater to a considerable extent is defined by the availability of phytoplankton organisms evolving in the upper layers [Tusseau *et al.*, 1997]. Phytoplankton being a primary producer of carbon compounds in the seawater gives rise to the evolution of subsequent organisms in the food chain. As a result of biosystem evolution in the upper layer a flux of organic carbon in a particle form makes its way to the bottom. For the phytoplankton evolution a sufficient quantity of light energy and inorganic nutrient are required. The intensity of light energy in the upper layers (euphotic zone) depends on a season. The availability of inorganic nutrient depends on different characteristics of the marine environment: temperature, current pattern, vertical mixing, closeness of riverine and coastal runoff etc. The global pattern of phytoplankton intensity distribution is extremely complex and dynamic. In the majority of sea basins annual variation of phytoplankton evolution is characterized by the growth peak in spring ("spring blossom") and subsequent minimum intensity in summer [Dale *et al.*, 1999; Dutkiewicz *et al.*, 2001; Jackson and Burd, 2002]. As a very rough approximation we presume that the annual cycle of phytoplankton evolution intensity and correspondingly organic particle concentrations is like the curve depicted in Figure E.1.

Temperature conditions, the pattern of horizontal and vertical currents and internal properties of the evolution of marine ecocommunities is defined by the availability of productive (eutrophic) and underproductive (oligotrophic) zones [Monin, 1997; Garcon *et al.*, 2001]. The distribution of mean annual productivity over the World Ocean is demonstrated in Figure E.2.

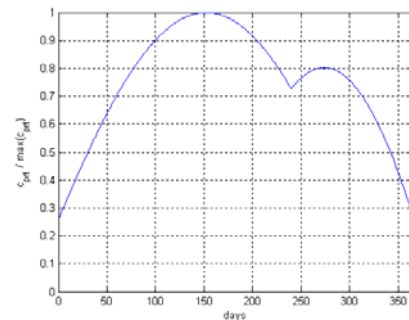


**Figure E.1.** Dependence of particle concentrations in an annual cycle for middle latitudes

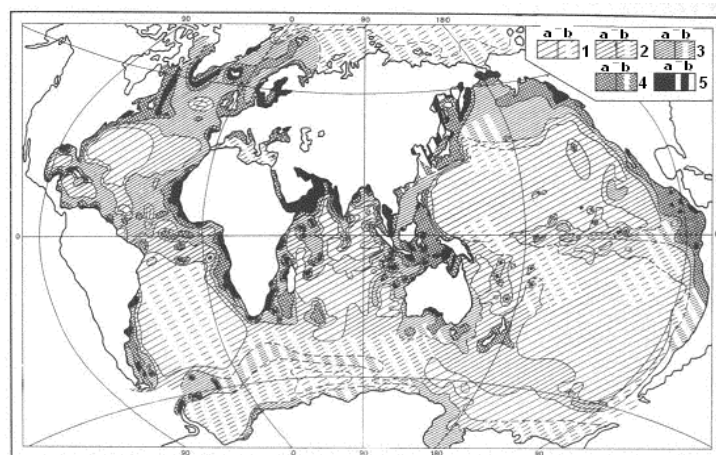


**Figure E.2.** Mean annual productivity distribution ( $\text{mg}/\text{m}^2$ ) over the World Ocean [Monin, 1997]

1 – <100, 2 – 100-150, 3 – 150-250, 4 – 250-500, 5 – >500

**a** – by radionuclide method, **b** – by indirect methods

In a first approximation at zonal averaging it may be supposed that waters in middle latitudes are most productive therefore the dependence of particle concentrations in the seawater on latitude shown in Figure E.3 is used.

The sedimentation process of organic particles is characterized by particle concentration decline with depth due to the formation of dissolved organic compounds and particle size increase as a result of coagulation. For this reason in the model the dependence of particle concentration on depth looks as displayed in Figure E.4 and particle sedimentation velocity – like in Figure E.5.

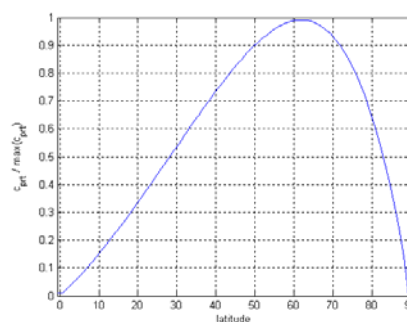


**Figure E.3.** Dependence of particle concentrations in the ocean on latitude

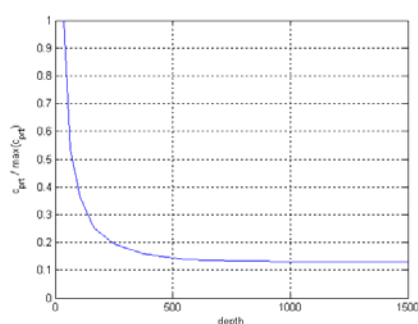


**Figure E.4.** Dependence of particle concentrations on the seawater depth

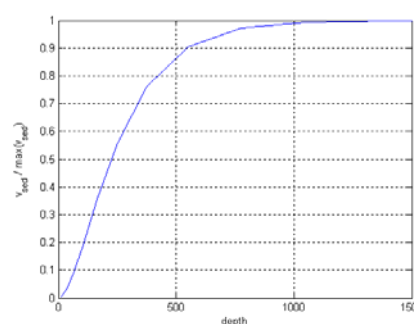


**Figure E.5.** Dependence of particle sedimentation velocity on the depth

**Numerical experiments.** To examine the developed model efficiency numerical experiments for the assessment of PCB transport over the Northern Hemisphere have been carried out. POP dynamics module for the seawater was integrated to the hemispheric multi-compartment model MSCE-POP. PCB emission scenario was prescribed on the base of available data for Russia [AMAP Report 2000:3, 2000] and for Europe [Pacyna et al., 1999].

POP transport dynamics in sea was calculated with the time step of 1 hour in knots of the calculation grid with horizontal spatial resolution  $1.25^{\circ} \times 1.25^{\circ}$  and vertical layer depths 12.5, 37.5, 65.0, 105.0, 250.0, 375, 550, 775, 1050, 1400, 1900, 2600, 3500, 4600 meters. Values of the velocity fields and the upper mixing layer thickness for sea were updated every day from previously prescribed data file [Zelenko and Resniansky, 1999] and it was interpolated for each time step. In the preliminary (“basic”) experiment the model spin-up was performed, that is calculations for a year period were repeated with input parameters of the same year. Characteristic of the marine environment affecting equilibrium constants between the dissolved and sorbed phase (particle concentration, organic matter content in particles, equilibrium coefficient  $K_{OW}$ ) and particle sedimentation velocities (particle density and size) were selected in such a way that the dissolved phase concentration was equal to that of the sorbed one [Schulz-Bull et al., 1998] and particle sedimentation velocity – about 100 m/day [Baldwin et al., 1998]. In the basic experiment sedimentation velocity did not depend on time and spatial co-ordinates. For the calculated period of about 30 years the model system has achieved quasi-steady state (like annual variation of dynamic fields). Figures E.6-E.8 show plots for PCB mass mean annual variation in the environmental compartments.

From the comparison of PCB mass dynamics in different environmental compartments (Fig. E.8) it is possible to conclude that most inertial is soil (Fig. E.6). PCB distribution over the seawater at the selected parameters is established during approximately 10 years (Fig. E.7). In subsequent experiments it was shown that at the decrease of sedimentation velocity by two orders of magnitude or similar reduction of the coefficient of phase partitioning (shift of distribution to the dissolved phase) the period of process establishment in the seawater was similar to that in soil (about 30 years). Figure D.17 demonstrates the dynamics of PCB mass loss velocities (outflow through the atmospheric boundaries, sea current transport through the equator, sedimentation to the seawater, pollutant degradation) for different environmental compartments. It is evident that about one third of PCB mass entering the environment is lost via seawater.

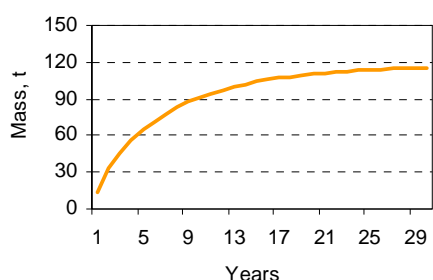


**Figure E.6.** PCB mass dynamics in soil

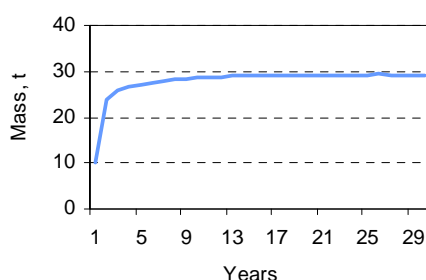


**Figure E.7.** PCB mass dynamics in the seawater

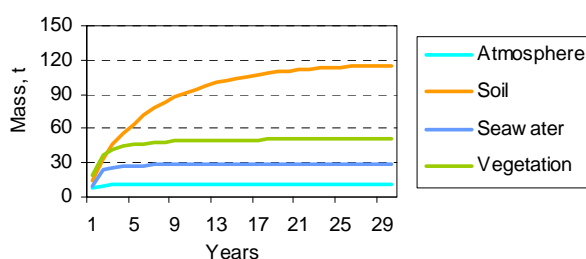


**Figure E.8.** PCB mass dynamics in different compartments

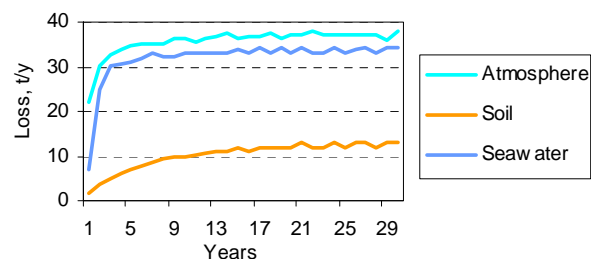


**Figure E.9.** Dynamics of PCB mass loss velocity in different compartments

In the experiment the highest concentrations were observed in internal seas and coastal zones. This distribution may be explained first by emission source distribution (Europe, Russia) and second by the absence of transport and sedimentation mechanisms in internal seas and coastal zones (cells with non-zero content of land elements) in the basic experiment.

In view of importance of sedimentation processes for the problem of POP distribution in the environment experiments with refined parameter influencing the sedimentation velocity. These parameters are the phase partitioning coefficient (in its turn depending upon particle concentrations) and the particle sedimentation velocity.

To evaluate the effect of heterogeneity and no steady state of phase partitioning coefficient we conducted experiments aimed at studying the dependence of particle concentrations on time, latitude and depth (Figs. E.1, E.3, E.4) of the integral dependence (the product of dependence on time, latitude and depth). Alongside the dependence of phase partitioning coefficient on depth, the dependence of particle sedimentation velocity shown in Figure E.5 was also introduced. All dependences of particle concentrations employed the normalization condition:

$$\frac{1}{T} \int_0^T \left( \frac{1}{V} \int_V k(\lambda, \varphi, z, t) dv \right) dt = \frac{1}{T} \int_0^T \left( \frac{1}{V} \int_V k^p dv \right) dt = 1, \quad (\text{E.3})$$

where  $T$  is annual period;

$V$  is volume of the calculated water reservoir.

As follows from Figures E.10 and E.11, introduction of particle concentration dependence on time, latitude and depth insignificantly changes integral characteristics of the system. At the combined dependence PCB mean annual mass in the seawater declines and PCB mass loss velocity for seawater increases.

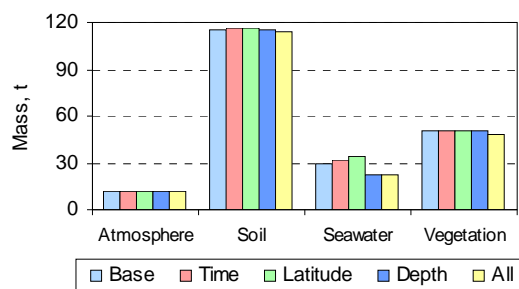


**Figure E.10.** PCB mean annual masses in different compartments in the basic experiment and in the experiment with phase partitioning coefficient dependence on time, latitude and depth and integral dependence

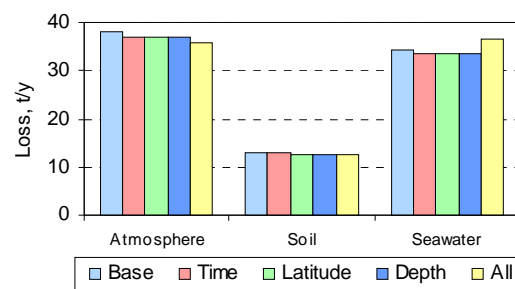


**Figure E.11.** PCB annual mass loss velocity in different compartments in the basic experiment and in the experiment with phase partitioning coefficient dependence on time, latitude and depth and integral dependence

Changes in the redistribution of concentration fields in the sea reservoir (Fig. E.12 compared to Fig. E.13) are more pronounced. In this experiment PCB concentration increases in regions of the open seawater manifesting the effect of sea currents on concentration field distributions.

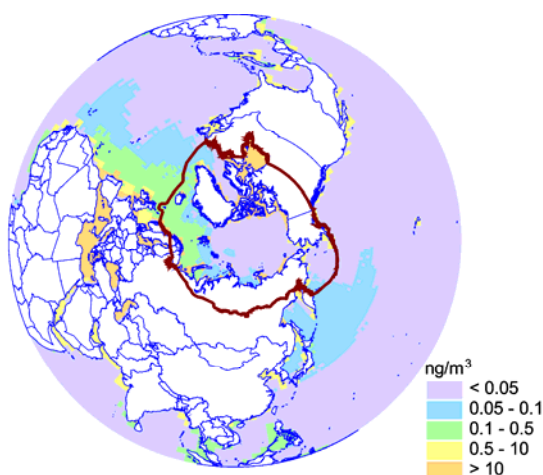


**Figure E.12.** PCB mean annual total concentration in the upper seawater layer in the basic experiment

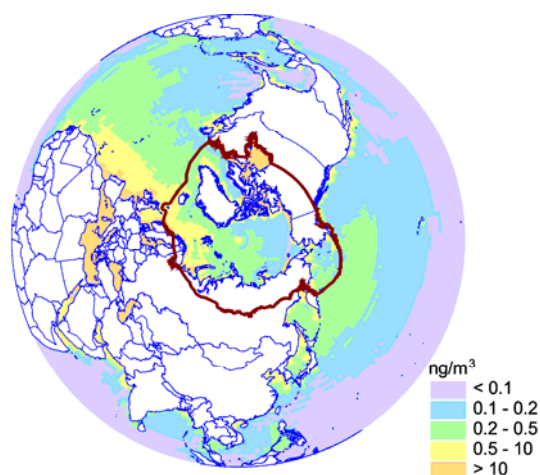


**Figure E.13.** PCB mean annual concentration in the upper seawater layer for combined dependence of phase partitioning dependence on time, latitude and depth

For further clarification of the effect of phase partitioning coefficient and particle sedimentation were performed experiments with maximum particle concentration  $\max(c_{prt})$  in dependences given in Figures E.1, E.3 and E.4 the integral coefficient of phase partitioning  $k^p$  from (E.1) decreases 10 times (experiment "Dissociation/10") and 100 times (experiment "Dissociation/100").

In a similar manner due to the uncertainty in mean diameter  $d^p$  and particle density  $\rho_o^p$  resulting in scattering of  $\max(v_{sed})$  (Fig. E.5) experiments with  $\max(v_{sed})$  reduced as much as 10 times ("Sedimentation/10") and 100 times ("Sedimentation/100") were performed. Diagrams of experimental results are demonstrated in Figures E.14–E.16.

As seen from Figures E.14 and E.15, PCB mass variation in the seawater is mostly affected by the phase partitioning coefficient and the rate of PCB removal outside the seawater calculation domain – by the particle sedimentation velocity. The variation of phase partitioning coefficient essentially affects PCB flux from the atmosphere to the seawater (Fig. E.16).

As follows from the comparison of Figures E.13 and E.17 decrease of sedimentation velocity by 2 orders increases PCB concentration in the upper layer by an order of magnitude and more.

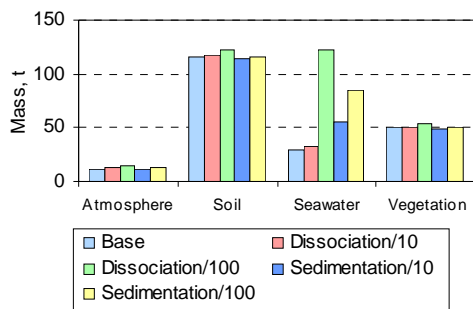


**Figure E.14.** PCB mean annual mass in different environmental compartments in the basic experiment and in experiments with reduced phase partitioning coefficient and particle sedimentation velocity

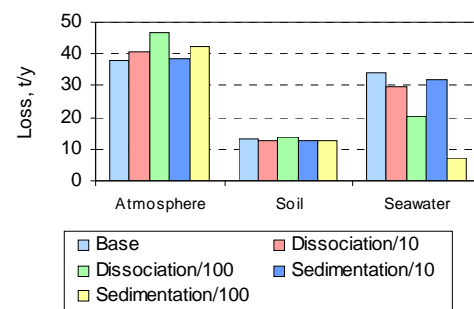


**Figure E.15.** PCB annual mass loss velocity in different environmental compartments in the basic experiment and in experiments with reduced phase partitioning coefficient and particle sedimentation velocity

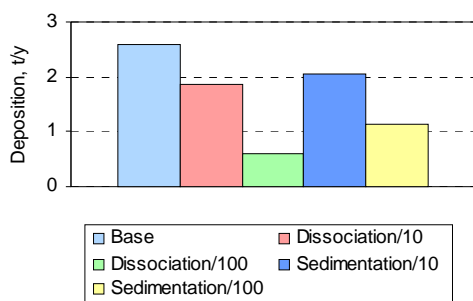


**Figure E.16.** PCB annual fluxes from the atmosphere to the seawater in the basic experiment and in experiments with reduced phase partitioning coefficient and particle sedimentation velocity

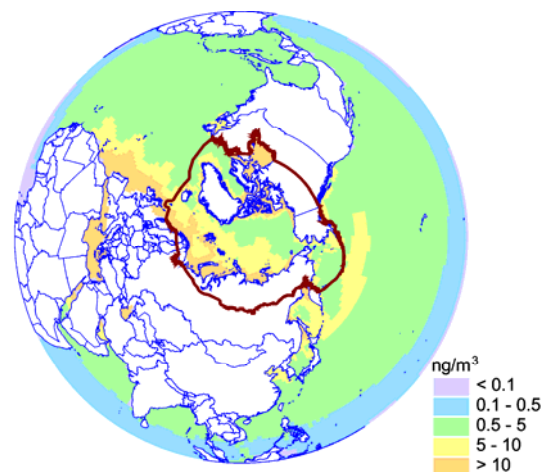


**Figure E.17.** PCB total mean annual concentration in the upper seawater layer for particle sedimentation velocity decreased 100 times in comparison with the velocity in the basic experiment

## E.2. POP transport with ice cover

In the hemispheric version of the model for proper description of the processes consideration of the ice cover is highly desirable. In the review [Macdonald *et al.*, 2000], it was pointed out, that sea ice has a potentially important role in the transport of contaminants. In particular, much of the ice in the Arctic is produced in shallow marginal seas during winter and exported to the interior seawater. Ice forming on shelves can incorporate contaminated sediments during suspension freezing, frazil ice formation or from bottom-anchored ice. This contaminated ice may then be transported thousands of kilometers undergoing little or no alteration. Besides, the ice cover acts as a barrier to exchange of gases including POP vapor-phase, limiting their direct entry from the atmosphere and evasion from sea to air.

**Model assumptions.** The ice module of POP transport describes the following processes:

- accumulation in the snow thickness and on the ice surface,
- gas phase exchange between the snow and the atmosphere,
- fluxes into the seawater as a result of snow and ice melting,
- fluxes from the seawater to the ice cover during ice bottom and lateral accretion,
- horizontal transport with drifting ice,
- degradation in the snow and ice environment.

Sea ice plays the role of a screen between the seawater and the atmosphere. At the same time POP may be accumulated in ice itself and in the snow above it. On the upper snow-ice surface the process of POP exchange with the atmosphere takes place. When snow and ice are melting on the surface and melting or frosting on the lower or lateral surfaces, POP pass to the water environment and return back. Besides POP trapped by the sea ice and snow thickness may be transported with ice drift.

Modules of POP dynamics in the marine ice cover were switched to the MSC-E multi-compartment model of POP transport. For the ice module the horizontal grid and time step were: horizontal step  $1.25^\circ \times 1.25^\circ$ , time step – 1 hour. Fields of snow and ice thickness, ice and snow melting rate, snow-ice surface temperature, ice drift velocity were read on the monthly basis from files previously calculated and were interpolated for each time step (see Section E.5 below).

**Numerical experiments.** The sensitivity of global POP transport model to the developed sea ice model was tested by numerical experiments of the global dispersion of selected POP (PCB-153) within the Northern Hemisphere.

Below we describe the results of the following numerical experiments.

- In the “Base” experiment PCB-153 concentrations were calculated for the period from 1970 to 1996. In this experiment we used the model of POP flux through the sea ice cover with additional introduced vertical “mixing” of POP concentrations in the snow and ice environment roughly parameterizing POP fluxes due to mechanical (hummocking) and thermal (melting) processes.
- The experiment “Noice 1994” was similar to the “Base” experiment, in which from 1994 to 1996 the sea ice cover was neglected. As initial concentration fields here appropriate fields for late 1993 from the “Base” experiment were selected.
- “Noice 1970” with parameters like in the “Base” but in this case sea ice cover was not considered from the beginning of the experiment (from 1970). POP initial concentrations equaled zero.

- “Nomix” was similar to the “Base” but in this experiment POP concentration “mixing” in the snow and ice environment was not calculated from 1994 to 1996. POP initial concentrations were the same as in the “Base” for late 1993.
- “Nodyn” with parameters as in the “Base” but without drift of the sea ice cover. The initial concentrations were zero.

The experiments “Noice 1994” and “Noice 1970” were aimed at studying the extent of sea ice cover impact on the dynamics of POP environmental concentrations. The “Nomix” results allow us to assess the effect on the introduced vertical mixing of POP concentrations between snow and ice. The experiment “Nodyn” was carried out for the evaluation of contribution of sea ice drift to the processes studied.

The comparison results of PCB-153 concentrations measured in seawater of different basins during the considered period with concentrations calculated in the experiment is shown in Table E.1.

The column “Calculated values” shows the lowest and the highest mean monthly values of PCB-153 concentrations for the reference year. The comparison of calculated against measured values demonstrates that the parameterization of POP transport processes in the marine environment including the transport through the ice cover is adequate enough.

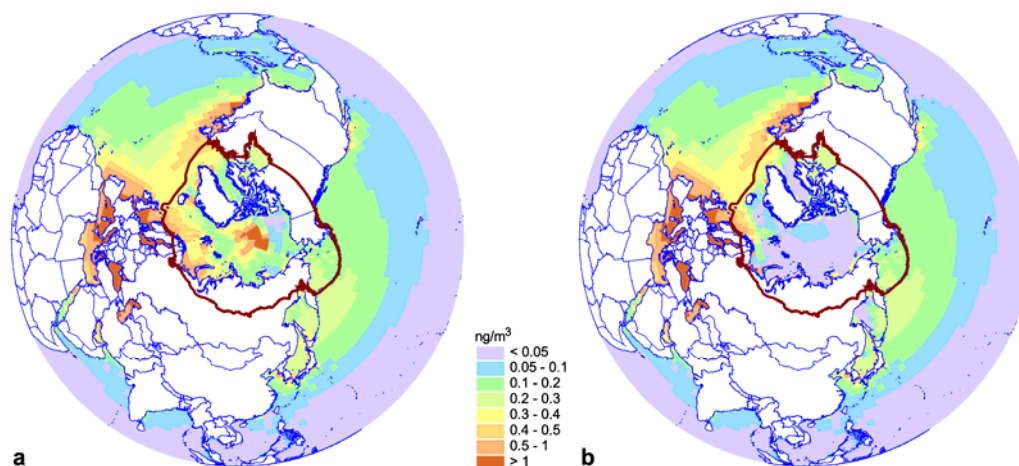
**Table E.1.** *The comparison results of PCB-153 concentrations measured in seawater with concentrations in the experiment “Base” (ng/m<sup>3</sup>)*

Year	Region	Geographical co-ordinates	Measured values	Calculated values	Reference for measured data
1986	North Atlantic	47-48N, 20-21W	0.34 – 2.70	1.07 – 1.63	<i>Broman and Axelman, 1997</i>
1986	Ice Island	81N, 97W	0.56	0.55 – 0.93	
1988	North Sea	54N, 1.6E	4.77	17.1 – 32.82	<i>Schulz-Bull et al., 1991</i>
1989	North Atlantic	40N, 40W	2.10	0.29 – 0.79	<i>Broman and Axelman, 1997</i>
1989	Caribbean Sea	15N, 70W	1.45	0.51 – 0.98	
1989	Gulf of Mexico	25N, 90W	1.29	0.28 – 0.4	
1989	Mediterranean Sea	35N, 20E	2.18	1.84 – 2.91	
1990	Chukchi Sea	70N, 180E	0.68	0.33 – 0.59	
1990	Bering Sea	62N, 170W	0.97	0.18 – 0.75	
1990	Gulf of Alaska	55N, 150W	0.97	0.2 – 0.46	
1990	Pacific Ocean	40-50N, 180E	1.13 – 1.14	0.14 – 0.68	
1990	New Bedford Bay	41N, 71W	1.45	0.58 – 1.3	<i>Bergen et al., 1993</i>
1992	North Atlantic	47-53N, 20-21W	0.10 – 0.40	0.52 – 1.12	<i>Broman and Axelman, 1997</i>
1993	North Atlantic	61-68N, 6-33W	0.13 – 1.21	0.14 – 0.93	<i>Schultz-Bull et al., 1998</i>
1994	Baltic Sea	54.1-57.2N, 10.6-17.5E	16.30 – 24.7	8.51 – 20.72	<i>Bigner et al., in Background document, No.64B</i>
1995	Japanese Sea	42.8-43.4N, 139.5-140.1E	0.035 – 0.6	0.32 – 0.65	<i>Kannan et al., 1998</i>

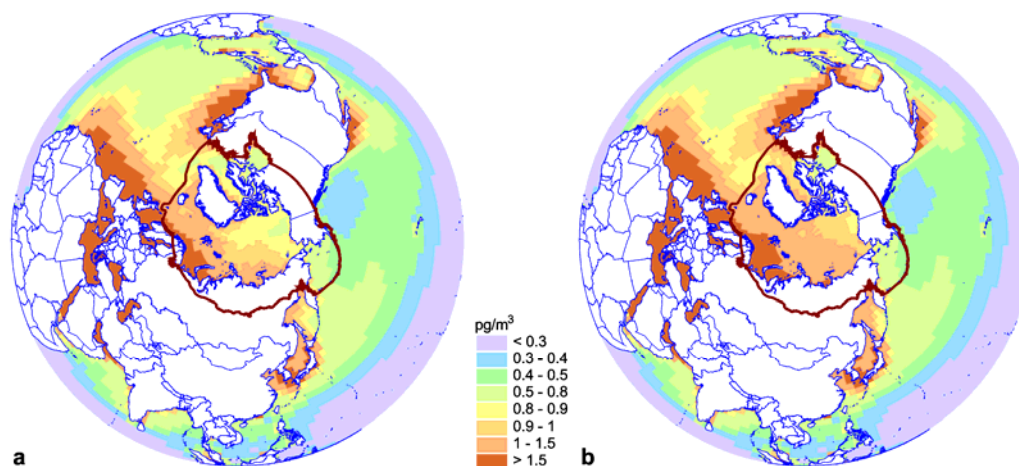
To estimate the effect of ice cover on concentration fields in various media incorporated to the model of POP global transport, numerical experiments with no ice on the ocean surface were made. In the experiment “Noice1994” PCB-153 concentration fields were calculated on the assumption that there is no ice in the Arctic from 1994 to 1996 included.

Figures E.18 and E.19 manifest the following result: the incorporation of the ice coverage increases PCB-153 concentration in the ocean and decreases it in the atmosphere. This “behaviour” of the

model may be explained by the fact that during the considered period (1994-96) the intensity of emission sources cut down (Fig. E.20) and the ocean became an additional POP emission source. In this case the ice coverage impedes POP to pass on to the atmosphere from the ocean thereby increasing concentrations in the ocean and decreasing them in the atmosphere.



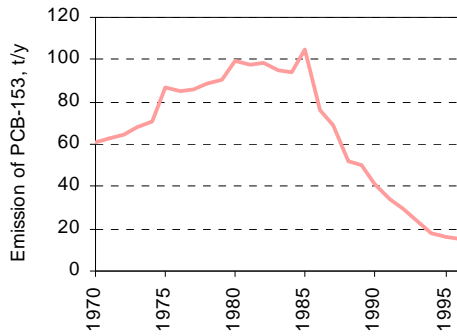
**Figure E.18.** Mean annual PCB-153 concentrations in the upper ocean layer for 1996 in the “Base” experiment with ice cover (a) and the experiment “Noice1994” without ice cover (b)



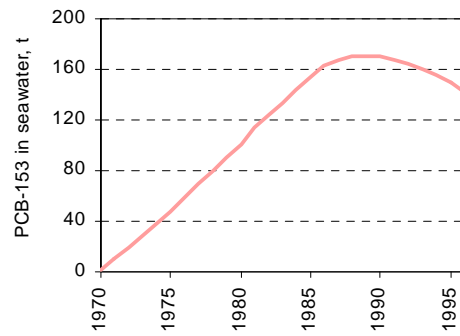
**Figure E.19.** PCB-153 mean annual concentrations in the lower atmosphere for 1996 in the “Base” experiment with ice cover (a) and the experiment “Noice1994” without ice cover (b)

Figure E.21 demonstrates the decrease of the pollutant content in the marine environment during 1994-96. This confirms the supposition about POP mass transfer from the ocean to the atmosphere during this period.

In the experiment “Noice1970” the initial concentration was assumed to be zero. During the increase of emission intensity, e.g. in 1972, (see Figs. E.20 and E.21) the ocean accumulates the pollutant mass coming from the atmosphere. Figures E.22 and E.23 present PCB-153 concentration fields in the ocean and in the atmosphere with the availability of the ice cover and without it.



**Figure E.20.** PCB-153 emissions during the calculated period



**Figure E.21.** Computed PCB-153 mass in seawater during the calculated period

The comparison of Figures E.22.a and E.22.b allows the following conclusion. Under the condition of POP intensive inflow from the atmosphere to the ocean the ice makes a screening effect.

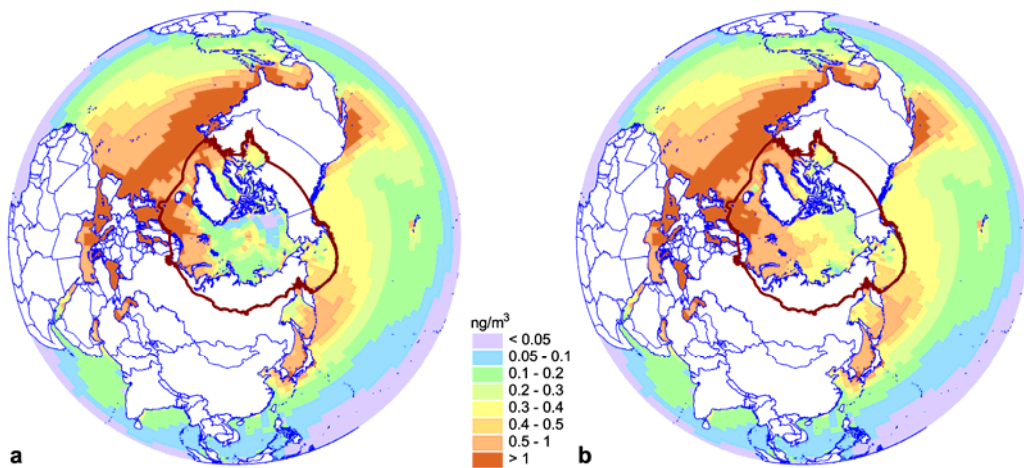


**Figure E.22.** PCB-153 mean annual concentrations in the top ocean layer in the experiments “Base” (a) and “Noice1970” (b) for 1972

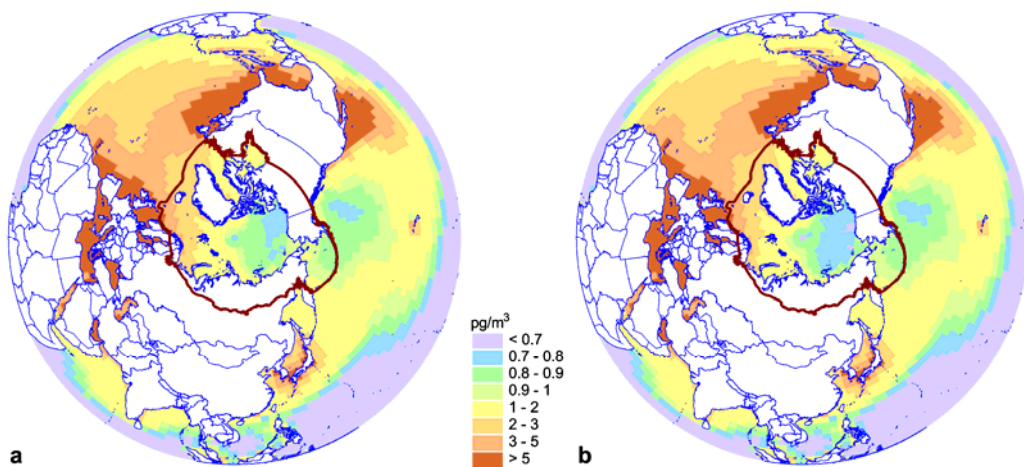


**Figure E.23.** PCB-153 mean annual concentrations in the lower atmospheric layer in the experiments “Base” (a) and “Noice1970” (b)

PCB-153 mean annual concentrations in the atmosphere in the experiment “Base” are slightly lower (D.23.a) than in the “Noice1970” without ice. This effect can be also explained by the screening effect of the ice cover.

POP mean annual concentration field in ice and snow in the experiment “Base” for 1996 is shown in Figure E.24.a. Figure E.24.b presents PCB-153 mean annual concentration field in the ice environment for the experiment “Nomix”, in which the “mixing” mechanism of POP concentrations in snow and ice is absent.

PCB-153 concentrations in ice in the experiment with concentration “mixing” in the snow and ice compartments (Fig. E.24.a) are appreciably higher than in the experiment without “mixing” (Fig. E.24.b). In the experiment “Nomix” in the absence of “mixing” in snow the concentrations reach considerable values (Fig. E.25). However, POP mass in snow is insignificant due to a small thickness of snow in the model (about 10 centimeters).

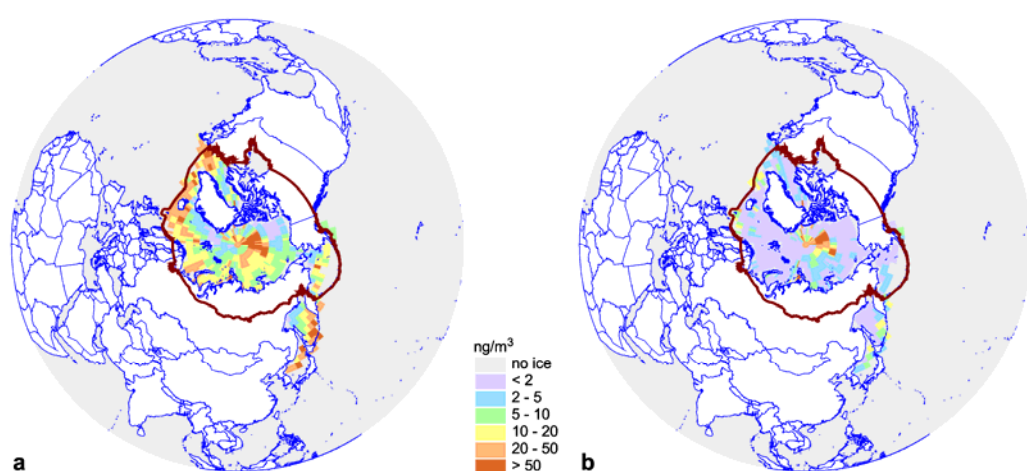


**Figure E.25.** PCB-153 mean annual concentrations in 1996 in snow and ice in the experiment “Base” (a) with “mixing” of POP concentrations in the snow and ice compartments in the experiment “Nomix” (b) (without “mixing”)

In the experiment “Base153” two extreme cases of parameterization of POP exchange between snow and ice compartments were assumed: absence of exchange and complete “mixing”. Obviously in reality some medium variant of exchange is realized: intrusion of POP molecules to the depth of snow and ice with melting water and mechanical mixing of media (hummocking). According to measurement data PCB concentrations in ice in the Arctic exceed PCB concentrations in water as much as several times [Pfirman, 1995]. It better correlates with the experiment “Nomix”. As follows from the numerical experiments, in the formulation of the problem “mixing” in snow and ice media does not exert a considerable effect on concentrations fields in the atmosphere and ocean.

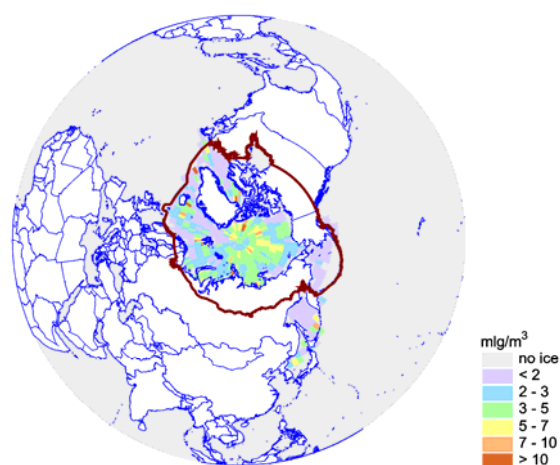


**Figure E.25.** PCB-153 mean annual concentrations in 1996 in snow without “mixing” of POP concentrations in the snow and ice compartments

A patch of elevated concentration in the experiment “Base” (Fig. E.26.a) in the region of Beaufort Sea coincides with the center of anticyclonic ice motion. The experiment “Nodyn” explains the reason for this patch. In this experiment sea ice drift was taken to be zero and no patch was observed in the Beaufort Sea (Fig. E.26.b). Results of this experiment testify that in the Beaufort Sea zones of PCB-153 accumulation are formed due to anticyclonic ice motion in this region.

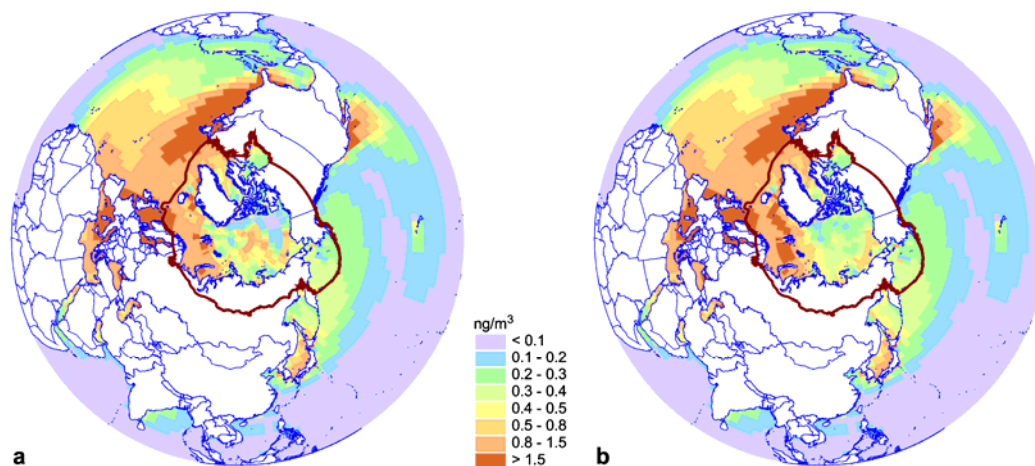


**Figure E.26.** PCB-153 concentrations in August 1972 in the marine environment in the experiment “Base” (a) and “Nodyn” (b), in which sea ice drift is absent

#### E.4. Model development

Further development of models of POP transport in the marine environment and sea ice cover is supposed to be performed in the following directions:

For POP marine transport model:

- Model should take into account different type of particles adsorbing POPs in seawater: bacteria cells, phytoplankton, microzooplankton, detrit, and particles with inorganic nucleus. Dissolved organic species able to sorbe POP molecules are also to be taken into account as POP carriers.
- Global 3D dynamic fields of concentrations of particles and dissolved organics in seawater are needed as model input. Such fields can be obtained on the basis of appropriate mathematical models.
- POP balance equations should take into account external POP sources such as rivers, coastal zones, etc.
- Parameterization of dynamic redistribution between sediments and seawater at ocean bottom is required.
- In parameterization of turbulent diffusion processes the dependence of diffusion coefficients on the characteristics of current velocities and other parameters of calculation domain is required.

For POP dynamics in ice/snow cover of the ocean:

- The exchange of POP containing in snow/ice environment with ocean and the atmosphere occurs mainly in surface layers. Under these conditions vertical distributions of POP concentrations in snow and ice may be essential. For more adequate description of exchange processes between

snow/ice cover, ocean and the atmosphere further parameterization of POP dynamics in the bulk of snow/ice taking into account vertical concentration profile, precipitation types (rain/snow), ice temperature, etc. is required.

- The presence of water in ice and snow leads to changes of physical parameters of ice/snow and to redistribution of all POP phases in snow/ice environment. To take this redistribution into account both description of POP redistribution dynamics and physical characteristics of snow/ice (presence of water phase, temperature, specific surface area of ice crystals, etc) is needed.

## **E.5. Seasonal evolution of sea ice**

In this section we consider issues related to obtaining sea ice evolution characteristics for modeling the contaminants transport in the Northern Hemisphere.

The evolution of the ice cover in the Arctic is governed by a great number of interconnected physical processes going on in the atmosphere, ocean and land. The present-day monitoring system allows us to receive on a regular basis only information about very limited number of the Arctic ice state parameters. First of all these are data on ice cover compactness and its extension obtained from several satellite systems. Direct observations of other parameters are of a fragmentary character and they make it impossible to obtain regular estimates of the sea ice evolution affecting processes of contaminants transport in the Arctic. In this situation modern numerical models become basic tools for the acquisition of required quantitative information about ice cover variability.

The description of sea ice dynamics is rather a complicated problem in terms of physics and computations. The sea ice cover is very fragmentary multi-component medium consisting of variety of ice proper, snow, firn, water and sea salt. This medium is non-uniform, possesses essential anisotropy both in horizontal and vertical directions. Besides the basic component of the medium, ice, is a crystal body with a complicated behaviour at mechanical loads (rheology).

### **E.5.1. *Basic approaches to sea ice modeling***

Originally sea ice models were one-dimensional and accounted for main thermodynamic processes involving vertical heat redistribution along the relevant phase transfers of water in the idealized horizontally uniform ice cover.

The next step of sea ice thermodynamic model development was so-called “dynamic” models. These models additionally accounted for processes of momentum redistribution in horizontally non-uniform medium, which in fact is sea ice. These models are more sophisticated since they describe mechanical interactions in the fragmentary ice cover with varying compactness within the framework of sea ice cover as a continuous media. Presumably the first indications to the necessity of a correct description of rheology in ice drift calculations are referred to the late 50s [Ruzin, 1959]. Subsequent to the simplest ice rheology models at present operating with viscous-plastic and cavitation rheology are most widely used. The difference between these approaches will be considered below after the discussion of basic elements of thermodynamic models.

Modern-day dynamic (comprehensive) models of sea ice use as a component a thermodynamic unit, the essentials of which was developed within the framework of global climate models. The three-layer thermodynamic model of sea ice [Semtner, 1976], main principles of which are in common use at present, is a certain generalization in term of construction of one-dimensional numerical models. In this work it is shown that the reduction of layers number to minimum in the suggested scheme does

not influence substantially the results and it is rather beneficial in view of the consumption of computational resources compared to a multi-layer model [Maykut and Untersteine, 1971].

The balance equation for heat fluxes on ice-snow upper and lower surfaces are used for ice melting/accretion calculations (the upper layer in the three-layer scheme represents the snow phase). Heat flux in the snow-ice interface is continuous while crossing the boundary.

The heat balance equation on the upper ice surface (or snow if exists) is written in the following way:

$$F_A = F_l + F_t + F_L + (1 - \alpha)F_r + \sigma T_s^4, \quad (\text{E.4})$$

where  $F_A$  is the net heat flux on the upper ice surface;  
 $F_l$  is the heat flux due to evaporation from the surface (latent heat flux);  
 $F_t$  is the sensible heat flux;  
 $F_L$  is the downward long-wave radiation flux;  
 $F_r$  is the downward short-wave (direct and scattered) solar radiation;  
 $\alpha$  is the surface albedo;  
 $\sigma$  is Stefan-Boltzmann constant;  
 $T_s$  is the surface temperature. All the fluxes are assumed positive if they are directed upward.

If snow is available on the ice surface,  $F_A$  is compared with the heat flux inside the snow  $F_s$  defined by its heat conduction:

$$F_s = k_s \frac{T_0 - T_s}{h_s / 2}, \quad (\text{E.5})$$

where  $k_s$  is the thermal diffusivity of snow;  
 $T_0$  is the temperature in the middle of the snow layer;  
 $h_s$  is the snow-layer thickness.

From the surface heat balance condition,  $F_A = F_s$ , after substitution into it expressions for  $F_A$  and  $F_s$  one derives the relationship for the underlying surface temperature  $T_s$ . If  $T_s$  determined in such a way reaches the freezing point, then the excess heat  $F_A - F_s$  is spent for snow melting. Snow depth changes  $\Delta h$  over a time step are given by the relationship:

$$\Delta h_s = \Delta t (F_A - F_s) / q_s, \quad (\text{E.6})$$

where  $q_s$  is the specific heat of snow melting.

In the absence of snow on the ice surface similar equations are solved with substitution of thermodynamic ice parameters for snow parameters.

In the work [Semter, 1976], in addition to the above mentioned parameters, processes of ice thickness variation due to bottom melting/accretion were considered; snow thickness increase at falling the precipitation solid fraction; the effect of heat accumulation and waste in salt pockets. Basic physical principles and the numerical scheme suggested in [Semtner, 1976] are used in the majority of thermodynamical sea ice models.

An example of more complete model involving, along with thermodynamics, the description of ice cover dynamics is the model of [Flato and Hibler, 1992] based on the approach suggested in the 60s by Nikiforov *et al.* [1967]. The dynamic model unit is developed within the approximation of cavitating

fluid, according to which ice resists to the compression (convergence), but it can be freely distributed over the basin if there are areas free of ice. Chronologically, this model appeared later than more sophisticated dynamic model of *Hibler* [1979], which was commonly used and in many respects defines the development of sea ice models up till now.

In the model [*Hibler*, 1979] the mechanical behaviour of the ice cover is described within the approximation of viscous-plastic solid medium, i.e. along with the action of tangential (viscous) stresses arising in the course of compact ice motion, plastic deformations at normal stresses leading to ice cover hummocking are taken into account. The equation of ice dynamics in the vector form is written as follows:

$$mD\bar{u}/Dt = -mf\bar{k} \times \bar{u} + \bar{\tau}_a + \bar{\tau}_w - mg\nabla H + \bar{F}, \quad (\text{E.7})$$

where  $D/Dt = \partial/\partial t + \bar{u} \cdot \nabla$  is the total time derivative;

- $\bar{k}$  is the normal to the surface vector;
- $\bar{u}$  is the vector of ice motion velocity;
- $f$  is the Coriolis parameter;
- $m$  is the ice mass per unit area;
- $\bar{\tau}_a, \bar{\tau}_w$  are the vectors of wind and water stress;
- $H$  is the dynamic height of the sea surface;
- $g$  is the gravity acceleration;
- $\bar{F}$  is the force of internal stress.

For the stresses induced by wind and water friction the following expressions are used:

$$\bar{\tau}_a = \rho_a C_a |\bar{U}_a| (\bar{U}_a \cos \phi + \bar{k} \times \bar{U}_a \sin \phi), \quad (\text{E.8})$$

$$\bar{\tau}_w = \rho_w C_w |\bar{U}_w - \bar{u}| ((\bar{U}_w - \bar{u}) \cos \theta + \bar{k} \times (\bar{U}_w - \bar{u}) \sin \theta) \quad (\text{E.9})$$

- where  $\bar{U}_a$  is the wind speed vector;
- $\bar{U}_w$  is the sea current velocity vector;
- $C, C_w$  are the friction coefficients for the atmosphere and water respectively;
- $\rho_a, \rho_w$  are the density of air and water respectively;
- $\phi, \theta$  are the angular rotation of wind and sea current stresses.

Components of internal friction forces  $F_i = \partial \sigma_{ij} / \partial x_i$  are expressed through derivatives of tensor components of the medium stress  $\sigma_{ij}$ . For viscous-plastic medium the stress tensor components are expressed through components of deformation rate tensor  $\varepsilon_{ij}$  and pressure  $P$  in the following way:

$$\sigma_{ij} = 2\eta(\varepsilon_{ij}, P) \varepsilon_{ij} + [\xi(\varepsilon_{ij}, P) - \eta(\varepsilon_{ij}, P)] \varepsilon_{kk} \delta_{ij} - P \delta_{ij} / 2, \quad (\text{E.10})$$

$$\varepsilon_{ij} = \frac{1}{2} \left( \frac{\partial u_i}{\partial x_j} + \frac{\partial u_j}{\partial x_i} \right) \quad (\text{E.11})$$

- where  $\delta_{ij}$  is the Kronecker symbol;
- $\eta, \xi$  are the bulk and shear of medium viscosity,  $x_i$  and  $x_j$  are the spatial co-ordinates.

In [*Hilber*, 1979] the following expressions were used for viscosity coefficients:

$$\xi = P/2\nabla, \quad \eta = \xi/e^2, \quad (E.12)$$

where  $\nabla = [(\varepsilon_{11}^2 + \varepsilon_{22}^2)(1 + 1/e^2) + 4\varepsilon_{12}^2/e^2 + 2\varepsilon_{11}^2\varepsilon_{22}^2(1 - 1/e^2)]^{1/2}$ ;

$e$  is the relation of axes of the main stress tensor.

The medium described by this rheological law experiences no internal stresses at pure divergence. The model developed within indicated approximations quite adequately simulates general features of sea ice drift and features of ice cover thickness associated with its dynamics. Among them - stationary region of maximum ice thickness near the northern coast of Greenland and Canadian Archipelago (Fig. E.27.c,d). Thermodynamic (one-dimensional) sea ice models cannot reproduce this structure even qualitatively.

At the same time, viscous-plastic models require large computer resources and the computational scheme can lead to computational instability [Gray and Killworth, 1995]. The appearance of cavitation models was, in part, an attempt to overcome these problems. The indicated difficulties are weakened partly by application of more effective numerical method [Zhang and Hibler, 1997].

In view of effective computational realization of sea ice model with the use of modern multi-processor computers it was suggested to employ more complicated rheological relationship [Hunke and Dukowicz, 1997].

Using similar notations the components of deformation rate tensor  $\varepsilon_{ij}$  and stress tensor  $\sigma_{ij}$  are connected by the expression:

$$\frac{1}{E} \frac{\partial \sigma_{ij}}{\partial t} + \frac{1}{2\eta} \sigma_{ij} + \frac{\eta - \xi}{4\eta\xi} \sigma_{kk} \delta_{ij} + \frac{P}{4\xi} \delta_{ij} = \varepsilon_{ij}^*, \quad (E.13)$$

where  $E$  is the Yuong module.

This rheological model is called elastic-viscous-plastic one. The model operates with two ice categories: thick and thin (up to 5 cm). In order to describe each category, different continuity equations are used: for ice compactness (specific area occupied by thick and thin ice), for mass (thickness) of thick and thin ice and for snow mass on the ice surface.

In other model [Polyakov et al., 1997; Polyakov, 1999] more detailed description of horizontal inhomogeneity of ice thickness field is achieved by introduction of six ice categories corresponding to gradations used in Russian monitoring network. In this model elastic-plastic rheology, which contrary to viscous-plastic approximation [Hibler, 1979] relates the stress in the ice cover not with the deformation rate tensor variation but with tensor itself.

In view of consideration of physical processes, more comprehensive model for the ice cover obviously is the model CSIM4 developed in US National Center of Atmospheric Research (NCAR). The model operates with five ice categories, elastic-viscous-plastic rheology, provides more detailed description of snow on the ice surface, improved model of surface albedo, salt pockets in ice, functional salinity profiles for each ice category etc. The detailed description of the model can be found in [Hunke and Dukowicz, 1997].

It might be well to point out that the comparison of results of this model with those obtained by a similar model with elastic-plastic rheology demonstrates [Hunke and Zhang, 1999] that in terms of reproducing long-term variability of the ice cover the results are actually identical but the first model is more effective from viewpoint of computations.

The considered models were employed both for problems of description of ice cover dynamics and as a constituent modules of climatic models.

### E.5.2. *Brief description of the model for sea ice cover dynamics*

As a basis for calculations of required ice field characteristics the CSIM2 model was used. It is a constituent of the coupled model of the climate system, which is under development in NCAR within the framework of CCSM project [Bruce *et al.*, 2001]. In this model ice is affected by heat fluxes, various force fields and fresh water fluxes from the atmosphere and the ocean. In its turn ice affects atmospheric and oceanic processes by similar fluxes. Interaction processes of media in the NCAR model are described by a special interface module.

The model adaptation for computations of sea ice characteristics was limited to separation of CSIM2 module from the coupled climate model, to organize input of information about external boundary conditions (atmospheric forcing), tuning of model parameters and fulfillment of numerical experiments. Below we discuss basic information about thermodynamic and dynamic modules and results of the model application to simulations of the ice cover evolution in the Arctic.

***The balance of vertical heat fluxes for snow-ice interface.*** Processes of vertical heat transfer are described by analogy with the model of Semtner [1976]. Two layers at total ice thickness exceeding 50 cm represent the total ice thickness. When ice thickness is between 25 cm and 50 cm, one ice layer is considered. If the ice thickness is less than 25 cm, zero-layer model is used. Snow on the ice surface is represented by one layer.

For the upper snow surface the balance equation for heat fluxes has the form:

$$S_1 + H_1 + L \uparrow_1 + k_s \frac{T_0 - T_s}{h_s / 2} = 0 \quad (\text{E.14})$$

where  $S_1$  is the net solar radiation flux;  
 $H_1$  is the sum of fluxes of long-wave radiation, heat consumption for evaporation and turbulent heat exchange;  
 $L \uparrow_1$  is the upward long-wave radiation flux;  
 $k_s$  is the heat conduction of snow;  
 $h_s$  is the snow layer thickness;  
 $T_s$  is the snow surface temperature;  
 $T_0$  is the temperature in the middle of snow layer.

The relationship for snow surface temperature (or ice in the absence of snow) is derived by substitution of  $T_s = T_p + \Delta T$  ( $T_p$  is the surface temperature at the previous time step;  $\Delta T$  is temperature increment per time step) in the heat balance Equation (E.14). At low  $\Delta T$  expansion of Equation (E.14) into series upon ignoring the terms of higher orders yields:

$$S_1 + H_1 + L \uparrow_1(T_p) + \Delta T 4\sigma(T_p)^3 + \Delta T \frac{\partial H_1}{\partial T_s} + k_s \frac{T_0 - T_p - \Delta T}{h_s / 2} = 0 \quad (\text{E.15})$$

From equation (E.15) the equation for  $\Delta T$  can be derived. Similar algorithm can be applied to the case of the ice surface without snow.

**Thermodynamic processes in polynyas.** The formation of new ice at the water surface in polynyas and marginal regions is expressed by the relationship:

$$Q_H = Q_i \frac{d(A_i h_i)}{dt} \quad (\text{E.16})$$

where  $Q_H$  is the net heat flux directed from the ocean to the atmosphere;  
 $Q_i$  is the latent heat of ice freezing (melting);  
 $A_i$  is the ice compactness;  
 $h_i$  is the thickness of the forming ice.

It is assumed that the thickness of newly formed ice  $h_i^*$  is constant and equals 20 cm. In this case, for ice compactness increment from (E.16) we have:

$$\Delta A_i = Q_H \Delta t / (Q_i h_i^*) \quad (\text{E.17})$$

After computation of new ice concentration the thickness of new and old ice in a cell is reduced to a single variable:

$$A_i' h_i' = A_i h_i + \Delta A_i \Delta h_i \quad (\text{E.18})$$

where  $A_i' = A_i + \Delta A$ ,  $\Delta h_i = h_i^*$ .

The model assumes limitation for the maximum ice concentrations.

$$A_i' = \begin{cases} A_{\max} & h_i' \leq 1 \text{ m} \\ 1 - (1 - A_{\max}) \exp[-(h_i' - 1) / \tau_1] & h_i' > 1 \text{ m} \end{cases} \quad (\text{E.19})$$

The value  $A_{\max}$  is assumed equal to 0.99 for the Northern Hemisphere and 0.96 for the Southern Hemisphere. The value  $\tau_1$  is selected equal to 3 m.

If the heat flux  $Q_H$  is directed from the atmosphere to the ocean, then a mechanism of lateral ice melting is acting, and the melting heat changes only the ice concentration. Processes of melting/accretion on the lower ice surface are not considered.

**Evolution of snow cover on sea ice.** The snow cover dynamics in the model involves processes of precipitation, evaporation, melting and conversion of snow into ice. Melting snow, snow from melting ice and snow entering the water in the absence of ice formation make a fresh water flow to the ocean. For the parameterization of the upper surface albedo the coefficient of snow distribution over the ice surface is introduced.

**Ice cover dynamics and drift velocities.** The dynamics of ice fields in cavitation approximation [Flato and Hibler, 1992] fits the medium behaviour, in which the final resistance is exerted to compression (convergence), but shear stress and resistance to divergence are absent. The equation of ice dynamics in spherical co-ordinates contains Coriolis forces, the stress induced by wind and sea currents, gravity forces arising due to sloping sea surface, and stress gradient due to ice compression:

$$\rho_i h_i f v_i + \tau_\lambda + C_w \cos \theta (u_w - u_i) - C_w \sin \theta (v_w - v_i) - \frac{\rho_i h_i g}{a \cos \phi} \frac{\partial \eta}{\partial \lambda} - \frac{1}{a \cos \phi} \frac{\partial p^*}{\partial \lambda} = 0,$$

$$-\rho_i h_i f u_i + \tau_\phi + C_w \cos \theta (v_w - v_i) + C_w \sin \theta (u_w - u_i) - \frac{\rho_i h_i g}{a} \frac{\partial \eta}{\partial \phi} - \frac{1}{a} \frac{\partial p^*}{\partial \phi} = 0 \quad (\text{E.20})$$

where  $u_i, v_i$  are zonal and meridian components of ice velocity respectively;  
 $\rho_i$  is the ice density;  
 $h_i$  is the ice thickness;  
 $f$  is the Coriolis parameter;  
 $\tau_\gamma, \tau$  are the components of wins stress;  
 $u_w, v_w$  are the components of current velocity;  
 $C_w$  is the drag coefficient at the lower ice surface;  
 $\theta$  is the angular rotation of the vector of sea current effect;  
 $\eta$  is the dynamic height of the ocean surface;  
 $g$  is the acceleration of gravity;  
 $a$  is the Earth's radius;  
 $p^*$  is the pressure in ice.

Instead of original set of Equations (E.20) it is possible to write the transformed set:

$$\begin{aligned} -Du_i + Ev_i + X &= \frac{1}{a \cos \phi} \frac{\partial p^*}{\partial \lambda}, \\ -Dv_i - Eu_i + Y &= \frac{1}{a} \frac{\partial p^*}{\partial \phi}, \\ D &= C_w \cos \theta, \\ E &= \rho_i h_i f + C_w \sin \theta, \\ X &= C_w \cos \theta u_w - C_w \sin \theta v_w - \frac{\rho_i h_i g}{a \cos \phi} \frac{\partial \eta}{\partial \lambda} + \tau_\lambda, \\ Y &= C_w \cos \theta v_w + C_w \sin \theta u_w - \frac{\rho_i h_i g}{a} \frac{\partial \eta}{\partial \phi} + \tau_\phi, \end{aligned} \quad (\text{E.21})$$

in which expressions for  $D, E, X$  and  $Y$  do not depend on ice velocity.

The system of Equations (E.21) is solved by iteration with initial  $p^* = 0$ . For cells with  $\nabla \cdot \bar{U}_i < 0$  correction term  $\bar{U}'_i$  is introduced. It ensures non-divergence of the corrected velocity field,

$$\nabla \cdot (\bar{U}_i + \bar{U}'_i) = 0 \quad (\text{E.22})$$

The conservation of the system of Equations (E.21) is possible in this case provided additional conditions for  $\bar{U}'_i$  are fulfilled:

$$-D\bar{U}'_i - E\bar{k} \times \bar{U}'_i = \nabla p' \quad (\text{E.23})$$

where  $p'$  is a certain correction pressure in a cell resisting convergent ice compression.

Velocity variations in a given cell may lead to the formation of convergent conditions in neighboring cells. In this case velocities and pressure in them are corrected to neutralize the convergence. This algorithm is applied in iterative way for the entire computation domain till conditions:

$$\max \left( \left| \bar{U}_i^n \right| - \left| \bar{U}_i^{n-1} \right| \right) < 0.002 \text{ m/s} \quad (\text{E.24})$$

are fulfilled.

The mechanism of correction pressure may be used until the pressure in a cell reaches its maximum,

$$P_{\max} = P^* h_i \exp[-20(1 - A_i)] \quad (\text{E.25})$$

In zones with constant convergence at correcting pressure exceeding the maximum excess convergence is distributed over cells without convergence.

**Advection.** The advection transport in the model affects all mass and thermodynamic parameters connected with sea ice. Upstream advection scheme is used:

$$\frac{\partial f}{\partial t} = -\nabla \cdot (f\bar{U}_i) \approx (u_l f_l \Delta y - u_r f_r \Delta y + v_b f_b \Delta x_b - v_t f_t \Delta x_t) / \Delta A \quad (\text{E.26})$$

where indices  $l, r, b, t$  imply that values belong to the left, right, lower (southern) and upper boundaries of a cell respectively. For the pole cell advection is specified as a sum of fluxes from cells neighboring all southern boundaries of the pole cell. In the model, instead of Equation (E.26), its analog in terms of ice velocity divergence is used:

$$\frac{\partial f}{\partial t} \approx -2\nabla \cdot \bar{U}_i \frac{f_l + f_r + f_b + f_t}{4} + \frac{\partial v_l}{\partial y} \frac{(f_l + f_r)}{2} + \frac{\partial u_l}{\partial x} \frac{(f_b + f_t)}{2} + \left\{ \frac{u_l + u_r}{2} (f_l - f_r) \Delta y + \frac{v_b \Delta x_b + v_t \Delta x_t}{2} (f_b - f_t) \right\} / \Delta A. \quad (\text{E.27})$$

The correction for excess convergence in cells with stable convergence is made in the following way:

$$f_n'' = f' \frac{(\bar{f}A - \bar{f}'_m A_m)}{\bar{f}'_n A_n} \quad (\text{E.28})$$

where  $f_n''$  are the new values of corrected values for points with positive divergence;

$f'_n$  are the previous values of the corrected variables for points with positive divergence;

$\bar{f}'_n$  is the mean value for the hemisphere;

$A$  are the cell areas, indices  $m$  and  $n$  are referred to cells with negative and positive divergence respectively.

**Consideration of oceanic processes.** Among essential parameters defining the ice cover evolution is the heat flux at the ice-water interface. Though mean flux value is only several  $\text{W/m}^2$  its long-term effects can result in essential redistribution of the ice cover. In combined models this heat flux is computed in the ocean model and it is delivered to the ice model as an external parameter.

In our case when the ice model is not directly connected with the ocean one the heat flux at the lower ice boundary should be determined with the use of additional conditions. One of reasonable approaches is the application of temperature of the upper mixed layer (as a rule coinciding with the ocean surface temperature) for computation of its enthalpy and heat flux using the difference in temperatures between water and ice. The latter is assumed to be equal to freezing point (typical value under Arctic conditions is  $-1.8^\circ\text{C}$ ).

Simpler but rather crude way of the parameterization of heat exchange processes at the water-ice interface is the prescription of constant heat flux. Obviously it is acceptable only in short-term calculations.

### E.5.3. Computation procedure

Prior to main calculations of ice characteristic evolution over a year time interval there was a stage of preparation of appropriate computation environment. It involves the configuration of the model domain, tuning of model parameters, preparation of atmosphere forcing fields specifying external (boundary) conditions for the model.

The ice cover dynamics model domain is represented by a grid superimposed on the sphere with grid points arranged according to B-grid of Arakawa's Classification. On the entire sphere the grid dimension is 150×110. Along the longitude the grid is uniform with spatial resolution 2.4°. Along the latitude the gridsize is 1.2° in latitude belts from the pole to 60°S and 60° N. In low latitudes the gridsize is larger. Time step is 20 min.

In a general case input data for the ice cover model integrations involve the following fields:

- wind stress at the upper ice surface and ocean current stress at its lower surface;
- solar radiation flux at the upper ice surface minus the reflected part;
- sum of fluxes of downward long-wave radiation, heat consumption for evaporation and turbulent heat exchange at the upper ice surface;
- derivative of the sum of fluxes including downward long-wave radiation, heat consumption for evaporation and turbulent heat exchange at the upper ice surface by the temperature of this surface  $\partial H_I / \partial T_s$ ;
- heat flux at the ice-water interface determined by potential enthalpy of the upper ocean surface;
- fresh water flux at the ice/snow interface;
- water surface slope.

To estimate these fields, a dataset of the reanalysis of meteorological fields [Kalnay *et al.*, 1996] was used. Mean monthly fields of relevant characteristics were used as initial ones. The reanalysis data are presented on a uniform geographical grid with dimension 144×72 with gridsize 2.5°×2.5°. With the use of bilinear interpolation these data were put on the knots of computation grid. When integrating the ice model atmospheric forcing was updated daily and the forcing fields were determined through the interpolation of mean monthly values. Derivative  $\partial H_I / \partial T_s$ , which is not incorporated to this dataset, was determined from expressions for turbulent heat exchange and heat consumption for evaporation in the following way:

$$\frac{\partial H_I}{\partial T_s} = -\bar{U}_a \left[ c_a k_t + L k_l k_q k_{sat} / P \exp(a T_a / (T_a + b)) a b / (T_a + b)^2 \right] \quad (E.29)$$

- where
- $c_a$  is the specific heat of air;
  - $L$  is the specific heat of evaporation;
  - $T_a$  is the air temperature at the reference height (usually 2 m);
  - $\bar{U}_a$  is the wind speed at the reference height (usually 10 m);
  - $P$  is the atmospheric pressure;
  - $k_{sat}$ ,  $a$ ,  $b$  are the coefficients in Magnus formula for saturated humidity;
  - $k_t$ ,  $k_l$  are the coefficients of heat- and moisture exchange in the near water air layer.

The required initial fields of ice characteristics were specified in two ways. In the first case constant thickness and compactness of ice were used as initial data, in the second case we employed fields

determined from numerical experiments with a coupled climate model used under CCSM project [Bruce *et al.*, 2001].

After preliminary model testing and tuning the required annual data set of sea ice characteristics has been calculated. Prior to these calculations integration for five years to spin-up the model and its adjustment to atmospheric forcing fields repeating in a cycling way from year to year were performed. Computations were made in local (thermodynamic) approach – neglecting dynamic processes, i.e. with zero ice drift velocity.

#### **E.5.4. Preliminary results**

In the course of integration of the sea ice model mean monthly fields of the following characteristics of sea ice were calculated and stored in the set of files for one year:

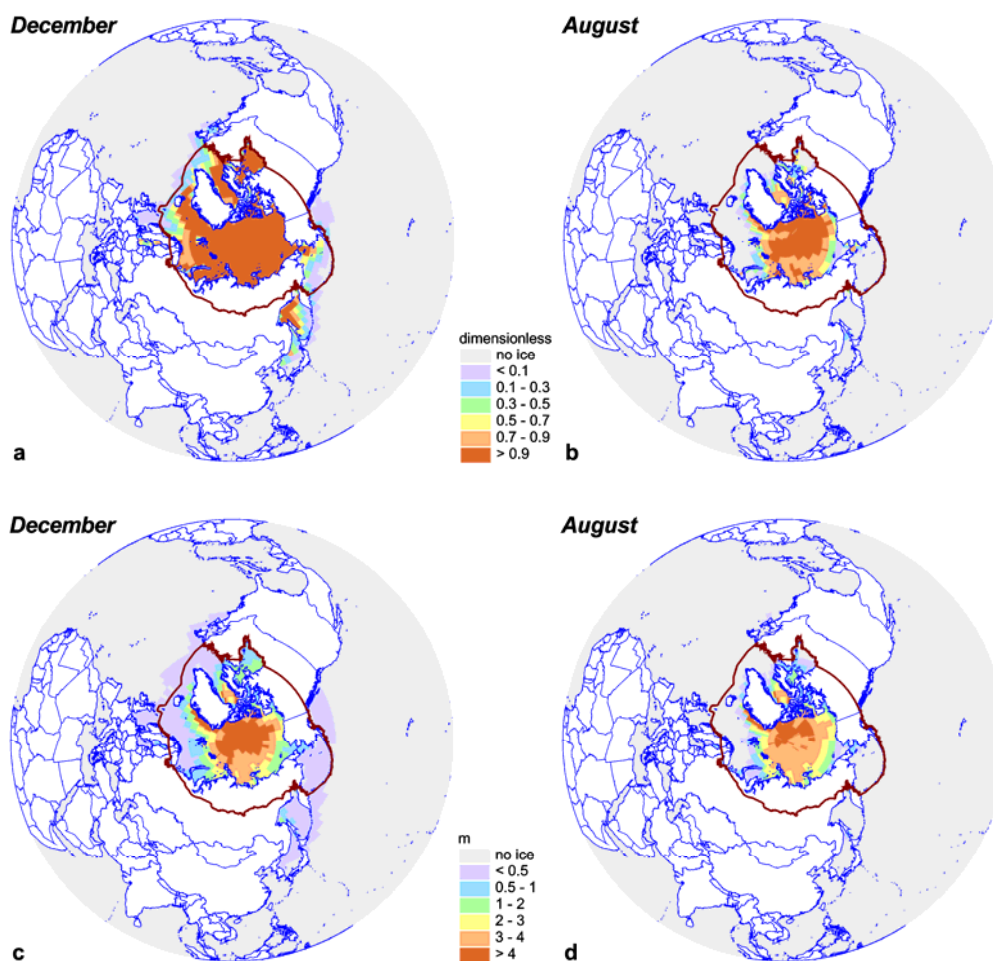
- ice thickness,
- ice compactness,
- ice/snow surface temperature,
- snow thickness on the ice,
- snow melting rate,
- ice melting rate at the upper boundary,
- ice melting rates at the lower and lateral boundaries.

Figure E.27 demonstrates the simulated distribution of sea ice thickness and compactness for December and August. A large-scale structure of simulated fields is mainly consistent with distributions obtained from observations. Seasonal variations of ice cover extension are accompanied by typical reduction of ice compactness. By summer the region of compact ice (9-10 balls) decreases by 3-4 times and it is located near the northern coast of Greenland and Canadian Archipelago (Figs. E.27.a,b). Similar area is occupied by ice with compactness 7-9 balls and much smaller regions are occupied by ice of less compactness. The formation of tongues protruded in the meridional direction to the Greenland Sea and the Labrador Sea and the Sea of Okhotsk characterize the distribution of winter ice. This is one of prominent features of the ice cover which have no analogy in the Antarctic.

The basic large-scale structure is well enough reproduced in fields of ice thickness in winter and summer – the region of the most powerful perennial ice (Figs. E.27 c,d).

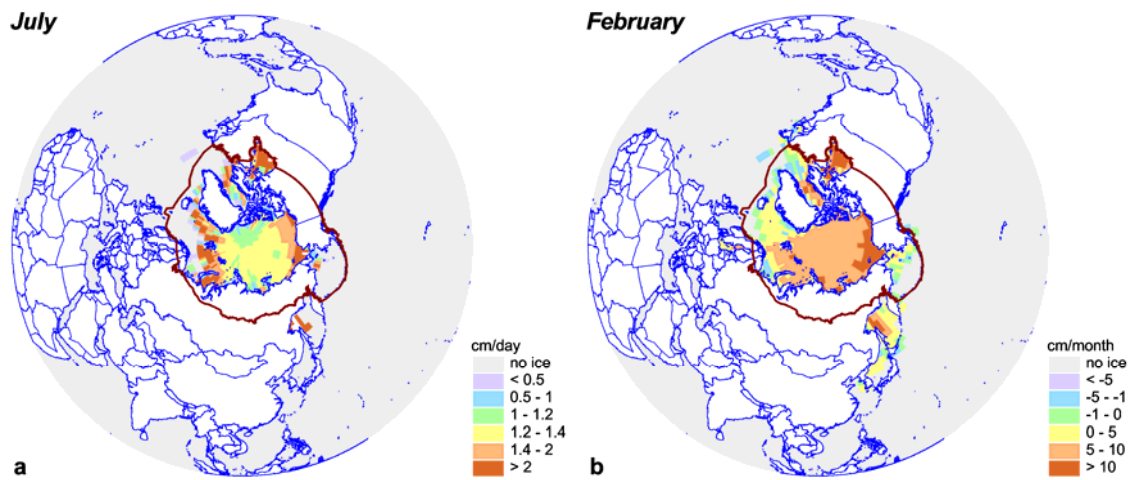
The notable discrepancy between model and climatic fields is observed in the Barentz Sea where the ice cover is overestimated especially during winter period (Fig. E.27.a). As it was mentioned above heat transport by ocean currents impedes the formation of ice. These effects are not described by a given model, and for their adequate consideration it is necessary to employ a coupled ocean-sea ice model.

Great seasonal variations of sea ice area essentially affect processes of contaminants distribution. In winter the ice cover over the major part of the Arctic screens out the direct exchange of contaminants being in different phases between the atmosphere and the ocean. During warm season the contact area increases approximately 2 times. From the onset of sea ice intensive-melting contaminants trapped by ice enter the ocean. For a correct account of these processes information about phase transfer of sea ice should be available. For this reason fields on intensive ice and snow melting are referred to essential calculation parameters.



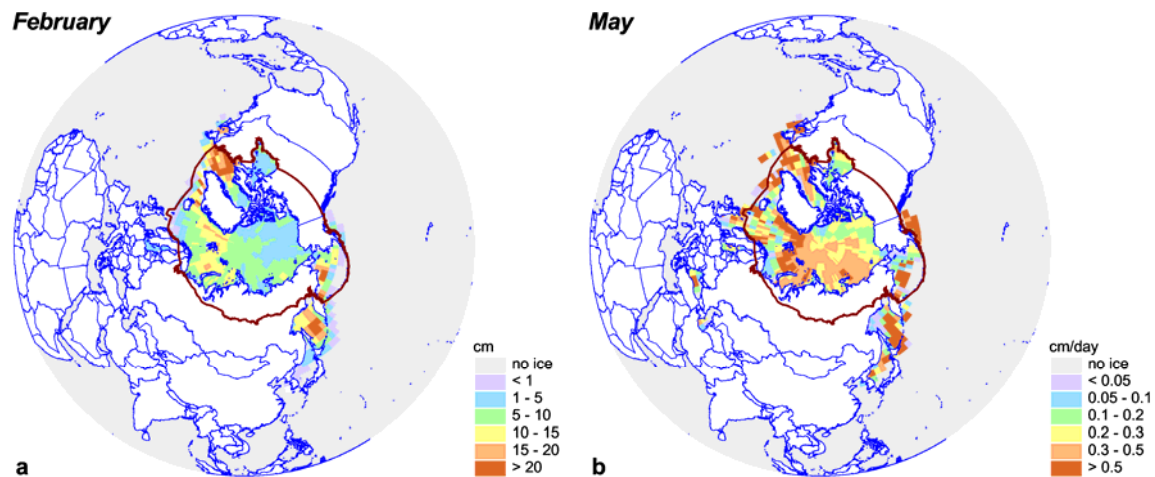
**Figure E.27.** Simulated distribution of ice compactness (a) and (b) and thickness (c) and (d) in December and August

Figure E.28 shows simulated fields of ice melting rate at the upper and lower boundaries for winter and summer seasons. Essential melting of the ice cover takes place on its surface mainly due to incoming short-wave radiation beginning from April. Melting stage is sufficiently shorter than the processes of ice accretion extended over a year. This asymmetry results in a kind of a “volley” discharge (June-July) of melted water to the ocean with all dissolved contaminants. Ice thickness variation at its lower boundary is characterized by much lower values (in Fig. E.28.b another color scale is used). However, the operation with these values should be very careful because the effect of oceanic processes on ice evolution is rather schematic in this model. More reliable data can be obtained with the use of a coupled ocean–sea ice model.



**Figure E.28.** Field of ice cover melting rates at upper boundary (a) in July and at the lower boundary (b) in February

Similar processes are related to the snow cover evolution on the ice surface (Fig. E.29.a). This cover also melts fast compared to the period of its accumulation. Although the rate of snow melting (Fig. E.29.b) is comparable with the ice melting rate (Fig. D.28.a) this source is less important for the transport of water and contaminants from the atmosphere to the ocean for the reason of rather thin snow cover (Fig. E.29.a). The latter is connected with the establishment of arctic anticyclone and week precipitation. More intensive precipitation falls along the periphery of the anticyclone over Arctic sea basins (Fig. E.29.a).



**Figure E.29.** Snow cover thickness in February (a) and snow melting rate in May (b)

Considering the obtained results as a whole it should be mentioned that model calculations make it possible to estimate characteristics of sea ice representing basic large-scale features of its evolution. In particular these data are applicable to the evaluation of impact on contaminants dispersion of such processes as ice screening impeding the exchange between the ocean and the atmosphere and comparatively long accumulation of contaminants in ice and their “rapid” discharge to the ocean during melting. To obtain more detailed and more accurate data on ice cover evolution comprehensive models of sea ice should be applied.

### E.5.5. Further activity

The obtained results are of a preliminary character and are intended for acquisition of qualitative estimates of the impact of the Arctic ice cover on contaminants distribution processes. To investigate in detail the sea ice behaviour it is supposed both further development of the model and application of more detailed characteristics of atmospheric forcing.

In order to improve the quality of calculated fields it is necessary to use a coupled model for ocean-sea ice since processes occurring in both media are closely connected. As follows from some investigations a number of important characteristics of ice cover evolution cannot be reproduced without adequate account of the influence of oceanic currents and heat redistribution processes associated with them.

For a correct description of the distribution of ice thickness and its variability, it is necessary to consider ice dynamics. Recent results show that the observed features are reproduced best of all by models with viscous-plastic rheology or its close variations. Therefore in further research connected with calculations of the Arctic ice evolution models of this type should be used.

A correct representation of the ice cover behaviour is closely connected with adequate specification of atmospheric forcing. In its importance, along with seasonal scale, synoptic variability in the atmosphere is distinguished which results in a number of significant effects, which become apparent both in the ocean [Resnyansky and Zelenko, 1999] and in the behaviour of the ice cover. The role of short-term variations can be exemplified by the comparison [Hanesiak and Barber, 1999] of experimental results with hourly and daily mean forcing of one-dimensional thermodynamic ice model. An hourly forcing, keeping mean diurnal values, leads to earlier commencement of snow melting, and the duration of ice-free period increases by 21 days! It is related to non-linearity associated with the absorption of solar radiation and sensible and latent heat fluxes.

Therefore, to improve simulation results of ice cover evolution, it is necessary to pass on to atmospheric forcing fields taking into account synoptic variability (daily mean fields instead of monthly mean fields).

## References

- AMAP Report 2000: 3. PCB in the Russian Federation: Inventory and proposals for priority remedial actions. Arctic Monitoring and Assessment Programme (AMAP), Oslo, 2000, published by: Centre For International Project (CIP), Moscow, 2000.
- Baldwin R.J., R.C. Glatts and K.L. Jr. Smith [1998] Particle matter fluxes into the benthic boundary layer at a long time-series station in the abyssal NE Pacific: composition and fluxes. *Deep-Sea Research II*, v. 45, 643-665.
- Bruce P.B., C. Hunke, C.M. Bitz, B. Lipscomb and V. Schramm [2001] DRAFT description of the CCSM2 Sea Ice Model: CSIM4, (<http://www.ccsm.ucar.edu/models/ice-csim4>)
- Dale T., F.Rey and B.R. Heimdal [1999] Seasonal development of phytoplankton at a high latitude oceanic site. *Sarsia*, v. 84, pp.419-435.
- Dutkiewicz S., M.Follows, J.Marshall and W.Gregg Watson [2001] Interannual variability of phytoplankton abundances in North Atlantic. *Deep-Sea Research II*, v.48, pp.2323-2344.
- Flato G.M. and W.D.Hibler [1992] Modeling pack ice as a cavitating fluid. *J.Phys.Oceanogr.*, v.22, pp.626-651.
- Garçon Veronique C., Andreas Oschlies, Scott C. Doney, Dennis McGillicuddy, Joanna Waniek [2001] The role of mesoscale variability on plankton dynamics in the North Atlantic.
- Gray J.M.N.T. and P.D. Killworth P.D. [1995] Stability of the viscous-plastic sea ice rheology. *J. Phys. Oceanogr.*, v. 25, No 5, pp. 971-978.
- Hanesiak J.M. and D.G. Barber [1999] Role of diurnal processes in the seasonal evolution of sea ice and its snow cover. *J. Geophys. Res.*, v. 104, No C6, pp. 13593-13603.
- Hibler III W. D. [1979] A dynamic thermodynamic sea ice model. *J. Phys. Oceanogr.*, v.9, No.4, pp. 815-846.
- Hunke E.C. and J.K.Dukowicz [1997] An elastic-viscous-plastic model for sea ice dynamics. *J. Phys. Oceanogr.*, v. 27, pp. 1849-1867.

- Hunke E.C. and Y. Zhang [1999] A comparison of sea ice dynamics models at high resolution. *Mon. Wea. Rev.*, v. 127, pp. 396-408.
- Jackson George A., and B. Burd Adrian [2002] A model for distribution of particle flux in the mid-water column controlled by subsurface biotic interactions. Deep Sea Research Part II: Topical Studies in Oceanography, v. 49, pp.193-217
- Kalnay et al., 1996 Kalnay E., Kanamitsu M., Kistler R., Collins W., Deaven D., Gandin L., Iredell M., Saha S., White G., Woollen J., Zhu Y., Leetmaa A., Reynolds R., Chelliah M., Ebisuzaki W., Higgins W., Janowiak J., Mo K.C., Ropelewski C., Wang J., Roy Jenne, and Dennis Joseph The NCEP/NCAR 40-Year Reanalysis Project // Bulletin of the American Meteorological Society, 1996, vol. 77, No. 3, p. 437-471.
- Macdonald R.W., Barrie L.A., Bidleman T.F., Diamond M.L., Gregor D.J., Semkin R.G., Strachan W.M., Li Y.F., Wania F., Alaee M., Alexeeva L.V., Backus S.M., Bailey R., Bewers J.M., Gobel C., Halsall C.J., Harner T., Hoff J.T., Jantunen L.M.M., Lockhart W.L., Mackay D., Muir D.C.G., Pudykiewicz J., Reimer K.J., Smith J.N., Stern G.A., Schroeder W.H., Wagemann R., Yunker M.B. [2000] Contaminants in the Canadian Arctic: 5 years of progress in understanding sources, occurrence and pathways. *The Science of the Total Environment*, V. 254, pp. 93-234.
- Maykut G.A. and N. Untersteine [1971] Some results from a time-dependent thermodynamic model of sea ice, *J. Geophys. Res.*, v.76, p.1550-1575.
- Monin A.S. (ed.) [1997] Oceanic biology. M., "Nauka".
- Nikiforov Ye.G., Z.M. Gudkovich, Yu.N. Yefimov and M.A. Romanov [1967] Principles of a method for calculating the ice redistribution under the influence of the wind during the navigation period in the Arctic seas. *Tr. Arkt., Antarkt. Int.*, v. 257, pp. 5-25.
- Pacyna J.M. et al. [1999] Final report for Project POPCYCLING-Baltic. EU DGXII, Environment and Climate Program ENV4-CT96-0214. Available on CD-rom including technical report, the emission and environmental databases as well as the POPCYCLING-Baltic model. NILU, P.O. Box 100, N-2027 Kjeller, Norway.
- Pfirman S.L., H.Eicken, D.Bauch and W.F. Weeks [1995] The potential transport of pollutants by Arctic sea ice. *Science of the Total Environment* (NLD), v.159, pp.129-146.
- Polyakov I.V. [1999] Modeling the Arctic ocean seasonal variability, *Okeanologiya*, v.39, No.4, pp.493-503, (*in Russian*).
- Polyakov I.V., Kulakov I.Yu., Kolesov S.A. et al. [1997]. Dynamic-thermodynamic model of the ocean covered with ice: description and experiments. *Izvestia of the Russian Academy of Sciences. Physics of the atmosphere and Ocean*, v.37, No.4, (*in Russian*).
- Resnyansky Yu.D. and A.A. Zelenko [1999] Effects of synoptic variations of atmospheric impacts in the model of ocean general circulation: direct and indirect manifestation. *Meteorology and Hydrology*, No.9, pp.66-71, (*in Russian*).
- Resnyansky Yu.D. and A.A.Zelenko [1999] Effects of synoptic variations of atmospheric forcing in an ocean general circulation model: direct and indirect manifestation. *Meteorology and Hydrology*, No.9 pp.66-77.
- Ruzin M.I. [1959] The wind drift of ice in a heterogeneous pressure field. *Tr. Arkt., Antarkt. Int.*, v. 226, pp. 123-135.
- Schulz-Bull D.E., G.Petrick, R. Bruhn and J.C. Duinker [1998] Chlorobiphenyls (PCB) and PAHs in water masses of the northern North Atlantic; *J. Marine Chemistry* (NLD); v.61; No.1-2; pp.101-114.
- Semtner A.J. [1976] A model for the thermodynamic growth of sea ice in numerical investigations of climate. *J. Phys. Oceanogr.*, v. 6, pp. 379-389.
- Tusseau M.-H., C.Lancelot, J.-M.Martin and B.Tassin [1997] 1-D coupled physical-biological model of the northwestern Mediterranean Sea. *Deep-Sea Research II*, v. 44, No 3-4, pp.851-880.
- Zhang J. and W.D. Hibler III [1997] On an efficient numerical method for modeling sea ice dynamics. *J. Geophys. Res.*, v. 102, No C4, pp. 8691-8702.

## Annex F

## ADDITIONAL COMPUTATION EXPERIMENTS

## F.1. Gas/aerosol partitioning

Here we present an evaluation of influence of variation of specific surface area of POP particles-carriers in the atmosphere on calculation results. This parameter is used for evaluation of POP fraction associated with particles in the atmosphere. As it was mentioned in Section 2.2, particle-bound POP fraction  $\phi$  is calculated in the MSCE-POP model using Junge-Pankow equation [Junge, 1977; Pankow, 1987]

$$\phi = \frac{c\theta}{p_L^0 + c\theta},$$

where  $c$  is the constant dependent on thermodynamic parameters of the adsorption process and on properties of aerosol particle surface ( $c = 0.17 \text{ Pa}\cdot\text{m}$  [Junge, 1977]);

$\theta$  is the specific surface of aerosol particles,  $\text{m}^2/\text{m}^3$  ( $\theta = 1.5\cdot 10^{-4}$  for background aerosol [Whitby, 1978]);

$p_L^0$  is the subcooled liquid-vapour pressure (Pa).

Value of  $p_L^0$  is supposed to be temperature-dependent:

$$\log p_L^0 = -\frac{A}{T} + B$$

where  $A$  and  $B$  are some constants depending on a POP in question;

$T$  is the ambient temperature (K).

At present, as a rough approximation, the value of specific surface of aerosol particles  $\theta$  in the model is chosen one and the same ( $1.5\cdot 10^{-4} \text{ m}^2/\text{m}^3$ ) for the whole Northern Hemisphere. Below we analyze the uncertainty due to application of this approximation since the observation data show that this value can vary essentially in different regions [Lohmann *et al.*, 2000]. The analysis is done on the example of PCB-153.

There are two types of changes caused by variation of the parameter  $\theta$ . First, lower values of  $\theta$  in clean regions (compared with those applied in the model) lead to the decrease of deposition velocities and, consequently, to the increase of air concentrations. Second, higher values of  $\theta$  lead to the increase of deposition velocities in contaminated regions, which results in decrease of air concentrations of the pollutant transported from these regions to clean regions (in particular, the Arctic).

Calculation experiments for transport of PCB-153 for one year under the assumption of zero initial concentrations in all the media are carried out. We compare two possible scenarios of calculations. The first scenario uses one and the same value  $\theta = 1.5\cdot 10^{-4} \text{ m}^2/\text{m}^3$  for all Northern Hemisphere. The second scenario assumes  $\theta = 0.42\cdot 10^{-4} \text{ m}^2/\text{m}^3$ ,  $\theta = 1.5\cdot 10^{-4} \text{ m}^2/\text{m}^3$  and  $\theta = 3.5\cdot 10^{-4} \text{ m}^2/\text{m}^3$  for clean, intermediate and contaminated regions, respectively. The corresponding spatial distribution of  $\theta$  is constructed on the base of emission fields for PCB-153. Namely, regions with PCB-153 emission flux less than  $0.005 \text{ g}/\text{km}^2/\text{y}$  are considered as clean with  $\theta = 0.42\cdot 10^{-4} \text{ m}^2/\text{m}^3$ , in regions where emission

flux ranges between 0.005 and 0.5 g/km<sup>2</sup>/y the value  $\theta = 1.5 \cdot 10^{-4}$  m<sup>2</sup>/m<sup>3</sup> is used (intermediate regions), and the regions with high emission density (more than 0.5 g/km<sup>2</sup>/y) are considered as contaminated with  $\theta = 3.5 \cdot 10^{-4}$  m<sup>2</sup>/m<sup>3</sup>.

The results of calculations using these two scenarios are displayed in Figure F.1.

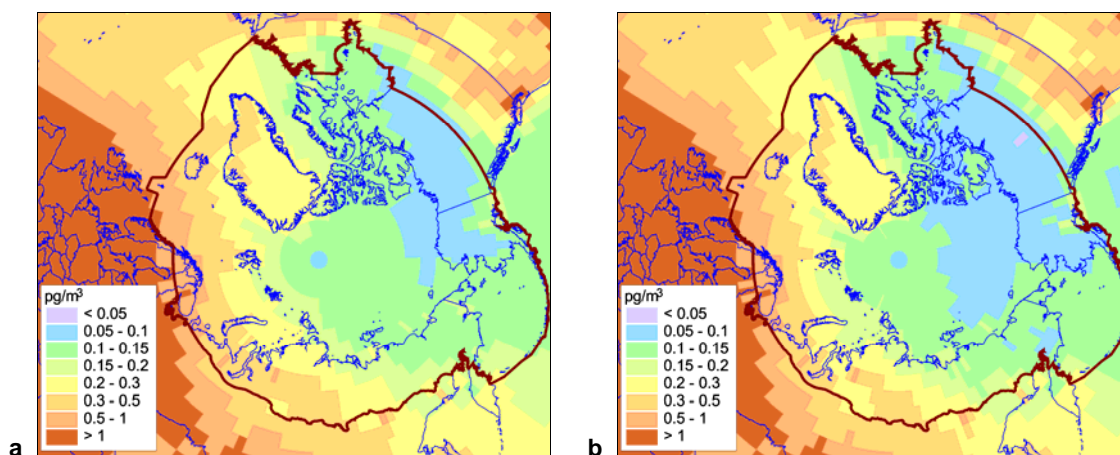


**Figure F1.** Air concentrations of PCB-153 (gas + particles) obtained under first (a) and second (b) scenario in the Arctic,  $pg/m^3$

As seen from these maps there are certain differences in air concentration fields obtained under the above scenarios. Namely, the difference of the results of these two simulations over the whole Northern Hemisphere ( $\Delta=(C_2-C_1)/C_1$ ) ranges from -20% to about 15% (depending on location, see Figure F.2).

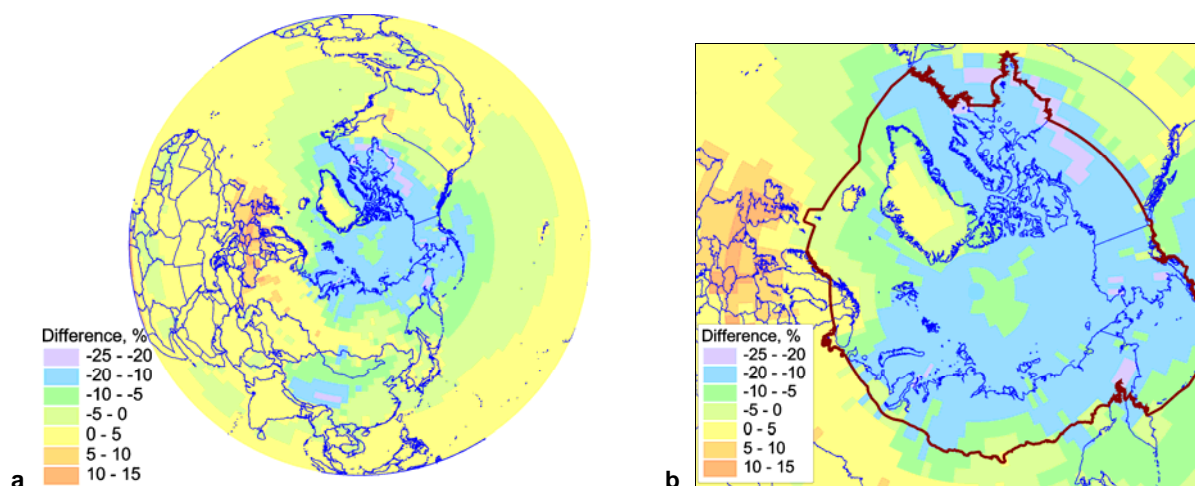


**Figure F.2.** Differences between values of air concentrations of PCB-153 obtained under first and second scenario, % for the whole hemisphere (a) and the Arctic (b)

Annual depositions obtained for two considered scenarios differ from -60% to 50% in different parts of the Northern Hemisphere (Figure F3).

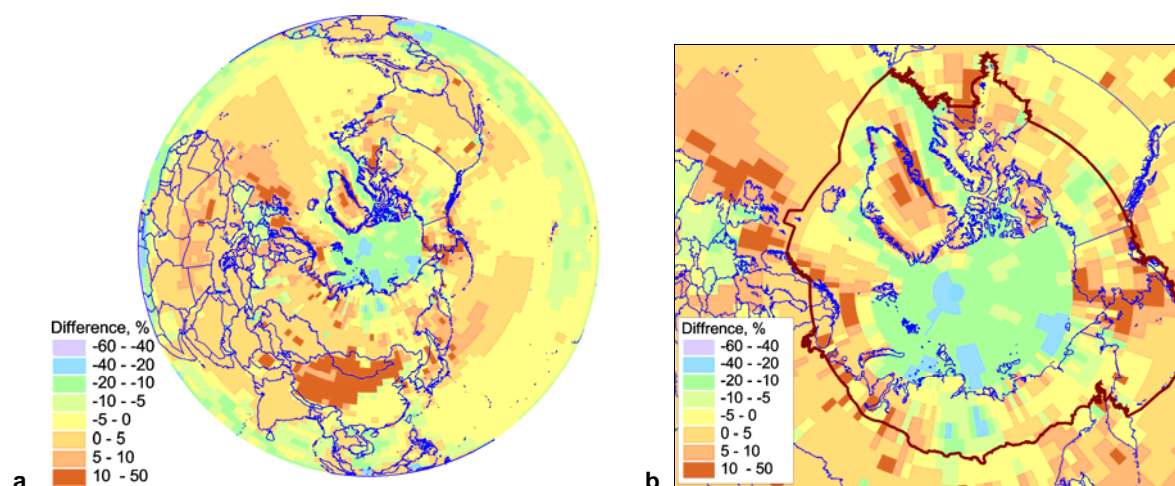


**Figure F.3.** Differences between values of depositions of PCB-153 obtained under first and second scenario, % for the whole hemisphere (a) and the Arctic (b)

It is reasonable to examine the sensitivity of seasonal variations of PCB-153 air concentrations and total depositions to five regions-receptors of the Russian North and to the Arctic as a whole with respect to variations of the parameter  $\theta$ . Table F1 displays the values of relative differences of these quantities obtained under the two described scenarios.

**Table F.1.** Relative differences (%) between calculations under first and second scenarios (monthly averaged air concentrations (gas + particles) and total monthly wet + dry particulate depositions) for five regions-receptors of the Russian North and annual averages

Region	Surface air concentrations		Total depositions	
	Max monthly	Annual	Max monthly	Annual
Murmansk Oblast	-3	-1	9	5
Nenets AO	-17	-10	17	7
Yamalo-Nenets AO and Taimyr AO	-23	-12	10	1
Republic of Saha	-26	-9	-9	-2
Chukotka AO	-24	-16	-23	-5
Arctic region	-13	-9	-13	-2

From these data it is seen that the values of PCB-153 monthly averaged air concentrations are changed up to -26% (decrease) for different months and regions. On the average the second scenario gives lower surface atmospheric concentrations. The deposition values vary from -23% to 10% depending on month and region. Application of more detailed description of  $\theta$  spatial distribution leads to increase of both monthly and annual deposition values in Murmansk oblast, Nenets AO and Yamalo-Nenets and Taimyr AO, and shows the decreased values in Republic of Sakha and Chukotka AO as well as for the Arctic as a whole.

The differences in seasonal variations of concentrations and depositions for Chukotka AO (where the differences for deposition are the largest, see Table F.1) are exemplified by plots of Figure F.4. Total increase of concentrations and depositions is explained by the fact that simulations were performed under the assumption that initial concentrations in all the media are zero and for one year only.

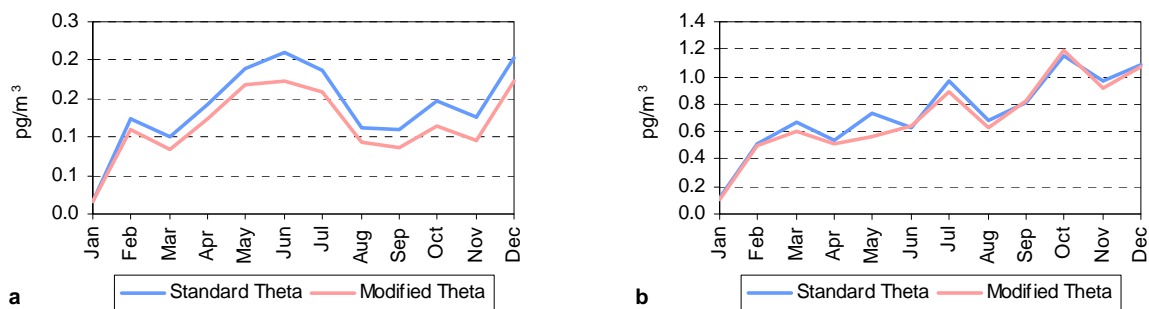


**Figure F.4.** Seasonal variations of monthly averages of air concentrations (a) and total monthly deposition (b) obtained under first and second scenario in Chukotka AO

It is seen that seasonal variations for both deposition and air concentrations for the two considered scenarios have similar characters.

In view of large enough uncertainties in emission data, the simplified approach (first scenario) seems to be reasonable at the first step of the assessment of contamination levels of the Arctic as a whole and of the Russian North. Moreover usage of second scenario needs detailed spatial distribution of aerosol particles, which in turn is rather uncertain. However, for modeling of POP long-range transport the application of detailed spatial distribution of specific aerosol surface is a priority task. These distributions are expected to be obtained as an output of aerosol dynamics and transport models.

## F.2. Diurnal variations of OH radical concentrations

According to observational data [Lee *et al.*, 1998, Mandalakis *et al.*, 2003], PCB atmospheric concentrations undergo substantial diurnal variations. Daily PCB concentrations for different congeners vary as much as 2-4 times. This phenomenon can be conditioned by atmospheric transport, deposition, gas exchange with the underlying surface and degradation, etc. One of the most important processes of PCB destruction in the atmosphere is reaction with OH radical. In the model this process is described by the following equation (see Section 2.2):

$$\frac{dC}{dt} = -k \cdot C \cdot [\text{OH}], \quad (\text{F.1})$$

where  $C$  is the pollutant concentration in the gas phase of the atmosphere,  $\text{ng/m}^3$ ;  
 $[\text{OH}]$  is the concentration of OH radical,  $\text{molecules/cm}^3$ ;  
 $k$  is the degradation rate constant for air,  $\text{cm}^3/\text{s/molecules}$ ,

where the temperature dependence of the parameter  $k$  is provided by the equation:

$$k = A \cdot \exp(-E_a / RT), \quad (\text{F.2})$$

where  $A$  is the exponential multiplier;  
 $E_a$  is the activation energy;  
 $R$  is the universal gas constant;  
 $T$  is the ambient air temperature.

Thus, as seen from the Eqs. (F.1, F.2) PCB degradation in the atmosphere is affected by temperature and OH radical concentration variations. In general, OH radical concentrations are subject to temporal and spatial variations. At present in the model as a first approximation OH radical concentrations have no diurnal variations and depend only on a season. Below the uncertainty caused by this assumption is roughly evaluated.

As a measure of uncertainty the relative deviation between pollutant concentrations obtained under two following scenarios is used: 1) with mean value of OH radical concentration round the clock within each season ( $\overline{OH}$ ) and 2) with diurnal variations of OH radical concentration. These scenarios are considered separately for three seasons: winter, spring/fall and summer. Spatial distribution of OH radical is uniform for each season. Mean values of OH radical concentrations over the Northern Hemisphere for each season used in scenario 1 are given in Table F.2.

**Table F.2.** Mean values of accepted OH radical concentrations ( $\overline{OH}$ ) used in scenario 1

Season	Mean daily OH radical concentration, molecules/cm <sup>3</sup> , [Yu Lu and Khall, 1991]
Winter	$0.09 \cdot 10^6$
Spring/Fall	$0.8 \cdot 10^6$
Summer	$2 \cdot 10^6$

For scenario 2, diurnal variation profile of OH radical concentrations is based on the data from paper [Mandalakis et al., 2003]. According to meteorological data used in the model, the day is divided into 4 periods 6 hours each. In the night concentrations of OH radical are taken to be zero, in the daytime concentrations are taken two times higher than averaged values (Table F.3). Experimental diurnal temperature variations with amplitude of 10 degrees are assumed the same for both scenarios (Table F.3).

**Table F.3.** Diurnal variations of OH radical concentrations accepted in the scenario 2 and ambient temperature variation used in both scenarios

Season	OH radical concentration, molecules/cm <sup>3</sup>		Temperature, C	
	Day	Night	Day	Night
Winter	$0.18 \cdot 10^6$	0	-5	-15
Spring/Fall	$1.6 \cdot 10^6$	0	10	0
Summer	$4 \cdot 10^6$	0	25	15

According to Eq. (F.1), under the assumption of equal initial air concentration, the relative deviation  $\Delta$  of air concentrations, between the first and the second scenario is evaluated as:

$$\Delta = \frac{C_2 - C_1}{C_1} = \exp \left[ \frac{Time}{4} \left( \sum_{i=1}^4 OH_i \cdot k_i - \overline{OH} \sum_{i=1}^4 k_i \right) \right] - 1, \quad (F.3)$$

where  $Time$  is the time period;

$OH_i$  and  $k_i = k(T_i)$  is OH radical concentrations and degradation rate constants for each day period respectively;

$\overline{OH}$  is the mean value of OH radical concentration.

The degradation process is more important for low chlorinated PCBs, which are present in the atmosphere mainly in the gas phase, than for high chlorinated PCBs, associated with the atmospheric particles in more extent. For this reason the uncertainty evaluation is carried out on the example of the PCB-28 degradation parameters ( $A = 1.7 \cdot 10^{-10} \text{ cm}^3/\text{s}/\text{molecules}$ ,  $E_a = 13700 \text{ J/mol}$  [Beyer and Matthies, 2001]). Temporal dependence of relative deviations between air concentrations calculated by two scenarios for each season is depicted in Figure F5.

The deviation gradually increases with time, the slope of the curves depends on the season. Maximum OH radical concentrations are estimated for summer, therefore the deviation curve has the steepest slope. From the figure it is seen that the deviation over a season (90 days) can reach values of 70-80%.

Degradation half-lives for the considered seasons, taking into account corresponding OH radical concentrations (Table F.2), equal to 4, 14 and 175 days for summer, spring/fall and winter respectively. These periods for summer and spring/fall are marked by vertical dotted lines in Figure F5. By the end of the respective half-lives the deviation  $\Delta$  is less than 10% for each season.

These calculations give lower estimates of the uncertainty. In reality the uncertainty is likely to be higher. This may be conditioned by a number of factors, for instance, by the diurnal variations of a pollutant concentrations caused by re-emissions or some other processes. This phenomenon seems to be rather important and should be properly studied in future.

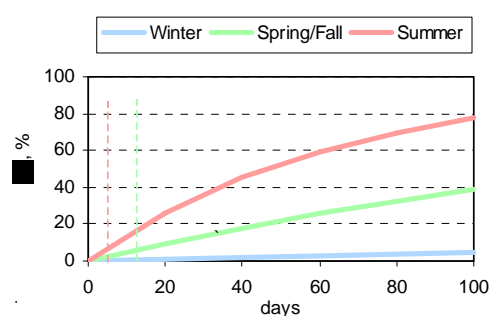


**Figure F.5.** Relative deviation (Eq. F.3) of calculation results obtained under two scenario for PCB-28,  $\Delta$ ,%. The dotted vertical lines denote degradation half-life in the atmosphere for corresponding season.

## References

- Beyer A and M.Matthies [2001] Criteria for Atmospheric Long-range Transport Potential and Persistence of Pesticides and Industrial Chemicals. Umweltforschungsplan des Bundesministerium für Umwelt, Naturschutz und Reaktorsicherheit. Stoffbewertung, Gentechnik, Förderkennzeichen (UFOPLAN) 299 65 402.
- Junge C.E. [1977] Basic considerations about trace constituent in the atmosphere is related to the fate of global pollutant. In: Fate of pollutants in the air and water environment. Part I, I.H. Suffet (ed.) (Advanced in *Environ. Sci. Technol.*, v.8), Wiley-Interscience, New York.
- Lee R.G.M., H.Hang, D.Makey and K.C. Jones [1998] Measurement and modelling of the diurnal cycling of atmospheric PCBs and PAHs, *Environ. Sci. Technol.*, v.32, pp.2172-2179.
- Lohmann R, T.Harner, O.Thomas and K.C. Jones [2000] A comparative study of the gas-particle partitioning of PCDD/Fs, PCBs and PAHs. *Environ. Sci. Technol.*, v.34, pp.4943-4951.
- Mandalakis M., Berresheim H. and Stephanou E.G. [2003] Direct Evidence for Destruction of Polychlorobiphenyls by OH Radicals in the Subtropical Troposphere ARTICLE IN PRESS: *Environmental Science and Technology*.
- Pankow J.F. [1987] Review and comparative analysis of the theories on partitioning between the gas and aerosol particulate phases in the atmosphere. *Atmos. Environ.*, v.21, pp.2275-2283.
- Whitby K.T. [1978] The Physical Characteristics of Sulphur Aerosols. *Atmos. Environ.*, v.12, pp.135 – 159
- Yu Lu and M.A.K. Khall [1991] Tropospheric OH: model calculation of spacial, temporal and secular variations. *Chemosphere*, v. 23, pp.397-444.